Micro and nanotools for sensing and therapy

Ana Mafalda Nunes Rodrigues

UNIVERSITAT DE BARCELONA

FACULTAT DE FARMÀCIA

DEPARTAMENT DE FARMACOLOGIA I QUÍMICA TERAPÈUTICA

Micro and nanotools for sensing and therapy

ANA MAFALDA NUNES RODRIGUES

Barcelona, 2014

UNIVERSITAT DE BARCELONA

FACULTAT DE FARMÀCIA

DEPARTAMENT DE FARMACOLOGIA I QUÍMICA TERAPÈUTICA

PROGRAMA DE DOCTORAT EN NANOCIÈNCIES

Micro and nanotools for sensing and therapy

Memòria presentada per Ana Mafalda Nunes Rodrigues per optar al títol de doctor per la Universitat de Barcelona

Directora de la tesi:
Drª Lluïsa Pérez-García

Doctorand:
Ana Mafalda Nunes Rodrigues

ANA MAFALDA NUNES RODRIGUES

Barcelona, 2014

El treball descrit en la present Memòria ha estat realitzat al Laboratori de Química Orgànica del Departament de Farmacologia i Química Terapèutica de la Universitat de Barcelona.

La tesi ha estat realitzada durant el període entre Setembre de 2010 fins a Setembre de 2014, dins del Programa de Doctorat: Nanociències.

Durant el període entre Setembre de 2010 i Juliol de 2011 s'ha obtingut el títol de Màster Oficial en Nanociència i Nanotecnologia per la Universitat de Barcelona.

El Maig de 2013 s'ha realitzat una estada de 1 mes a la Universidad de Zaragoza i el Novembre de 2013 s'ha realitzat una estada de 1 mes a la Universitat de Girona.

El treball d'investigació ha estat finançat per:

Ministerio de Ciencia e Innovación:

Projectes d'investigació: TEC2008-06883-C03-02 i TEC2011-29140-C03-02;

Generalitat de Catalunya

Projecte d'investigació: 2009 SGR 158.

“There is Plenty of Room at the Bottom.”

Richard Feynman

Agradecimientos

En primero lugar, quiero agradecer a mi Directora de tesis, Dr. Maria Lluïsa Pérez, por aceptarme como estudiante y darme la oportunidad de hacer el doctorado con ella. En su grupo he aprendido y evolucionado como científica.

A Dr. Oriol Penon, mi "compañero de poyata" durante estos 4 años en el laboratorio, por su buena disposición, su disponibilidad para ayudar, y por las sesiones de "brainstorming".

A nuestros colaboradores: Dr. Ana Calpena, mi cotutora de la tesis de máster, por su ayuda con todo el tema de la liberación de fármacos; Dr. David Amabilino, por las discusiones fructuosas; Dr. Lidia Feliu y Silvia, del grupo LIPPSO (Universitat de Girona), por la síntesis de los péptidos cíclicos; Dr. José Antonio Plaza, Marta, y Nuria, del Centro Nacional de Microelectrónica (CNM-CSIC), por la fabricación de las superficies; Dr. Manel Puig, Jordi y Laura, de la Facultad de Física, por el trabajo realizado con los "tuning fork"; Dr. Ángel Millán y Rafael, del Instituto de Ciencia de Materiales de Aragón (ICMA-CSIC) por el trabajo de los termómetros moleculares.

A Dr. Lyda Halbaut de la Facultat de Farmácia; Dr. Ana Linares, Dr. Irene Fernández, Dr. Manel Bosch, Dr. Lorenzo Calvo, Dr. Carmen Iglesias y Dr. Marta Taules de los Centres Cientifics i Técnics de la Universitat de Barcelona (CCiTUB), y a Judith Oró y Maite Simón de los servicios científicos del Institut de Ciéncia de Materials de Barcelona (ICMAB-CSIC).

A todos mis compañeros, en especial al "nanogrupo": Lucia, Dimitris, Paula, Aniuska, Kinga, Mari, David, Ezhil, Lorenzo, Israel y Alicia. Gracias por hacer que las horas en el laboratorio fueran más divertidas. A Faiza, y a los catalanes (Magda, Gisela y Carlos Luque), por las comidas compartidas entre risas. Espero seguir compartiendo esas risas con todos.

A Edgar y a Olfa, por me animaren a empezar esta aventura; a Pedro, Petra, Juan y Peggy, por vuestra alegría. A Rakelita, mi "compi de piso", por casi 4 años juntas siempre con mucha diversión (Ya tu sabe!) A Davinia & Cía., por las cenas en la terraza, las sesiones de petardeo, las noches "mágicas" y de "anti", y por ¡las sevillanas!

A Carlos, por su amistad (¡y donde eso nos llevó!). Gracias por tu cariño y por el apoyo que me das, y por estar a mi lado en esta nueva etapa de mi vida que tengo adelante, construyendo nuevos proyectos juntos.

Quero também agradecer ao Prof. João Pedro Conde, que me mostrou por primeira vez o campo da nanociência e com o seu entusiasmo motivou-me a seguir esta área. Aos meus amigos de Portugal: ao Rui e ao Fábio, ao Pedro e à Teresa, à Brigitte, Carina e Cláudia.

E por último, mas não menos importante, aos meus pais e aos meus padrinhos, por todo o apoio que me deram constantemente ao largo de todo o meu percurso académico, mesmo quando implicou estar longe deles. Obrigada por me darem asas para voar.

INDEX

Index

Chapter 1

Introduction

1.1. Prologue

This thesis has its main focus on using supramolecular chemistry as an approach to Nanomedicine, specifically the assembly of layers of molecules. From these, it is highlighted the formation of macroscopic or nanoscopic materials made of nanostructured assemblies of molecules, but also the assembly of molecules on surfaces, these being either macroscopic or nanoscopic (which are also obtained by supramolecular processes).

The work being presented here is an interdisciplinary effort that spawns through different areas within Nanomedicine, where applications of nanostructured materials (hydrogels and gold nanoparticles) as drug delivery vehicles, as well as sensing and studying molecular interactions by means of SAMs have been explored. This thesis is presented as a compilation of papers – already published or in preparation – that describes the work, and is structured into chapters that focus each of the aforementioned areas. Each chapter has its own corresponding state of the art review and objectives described at the beginning, for a better comprehension of the work.

This work begins with the assembly of structures derived from a gemini-type imidazolium derived amphiphile The nanostructured assembly of this amphiphile leads to the formation of hydrogels, and due to the nature of the polar head of the amphiphile that can recognize and bind anions, the gel presents the ability to incorporate and deliver anionic drugs. On the other hand, the gels have been used as a matrix to direct the templated-synthesis of gold nanoparticles (Chapter 2).

Gold nanoparticles can also be obtained in solution by two different methods that gave either organic-soluble or water-soluble nanoparticles, both showing ability to deliver drugs. Additionally, gold nanoparticles can be synthesized by other methods, such as the Turkevich synthesis using citrate as stabilizer or the synthesis in methanol using thiols as stabilizers, and the stabilizer can be exchanged, rendering the appropriate functional groups to covalently attach biomolecules, such as peptides (Chapter 3).

In Chapter 4 we describe the self-assembly process of molecules on macroscopic surfaces. These surfaces were used as thermometric sensors to measure temperature. Additionally, the functionalization of surfaces and quartz tuning fork with avidin and biotin was performed to study interactions between these two molecules, the interactions being measured in terms of

frequency of resonance. Additionally, the formation of layers of molecules on the surface of gold surfaces was used to study the binding kinetics between antibodies and antigens through the phenomenon called Surface Plasmon Resonance (SPR), present in the colloidal solutions of gold nanoparticles but also in surfaces with gold layers that have nanometric thickness.

1.2. Context of the work

Nanoscience is a scientific area that has found a big development over the last decades. One of the most commonly accepted definitions of nanotechnology, found in the US National Nanotechnology Initiative, describes it as the understanding and control of mater with dimensions in the order of 100 nm or less.[1] On the other hand, the EU Novel Food Regulation defines ''Engineered nanomaterial'' as "any intentionally produced material that has one or more dimensions of the order of 100 nm or less or is composed of discrete functional parts, either internally or at the surface, many of which have one or more dimensions of the order of 100 nm or less, including structures, agglomerates or aggregates, which may have a size above the order of 100 nm but retain properties that are characteristic to the nano-scale".[1]

The approaches to achieve such materials can be grouped in two: the top-down and the bottom-up approaches (**Figure 1.1**). In the top-down approach the bulk material is processed by different methods, that can be mechanical techniques (such as milling), lithographic techniques or laser-beam processing, to name a few.[2] On the other hand, the bottom-up strategy consists on the use of chemical synthesis and non-covalent interactions to obtain organized assemblies of molecules.[3,4]

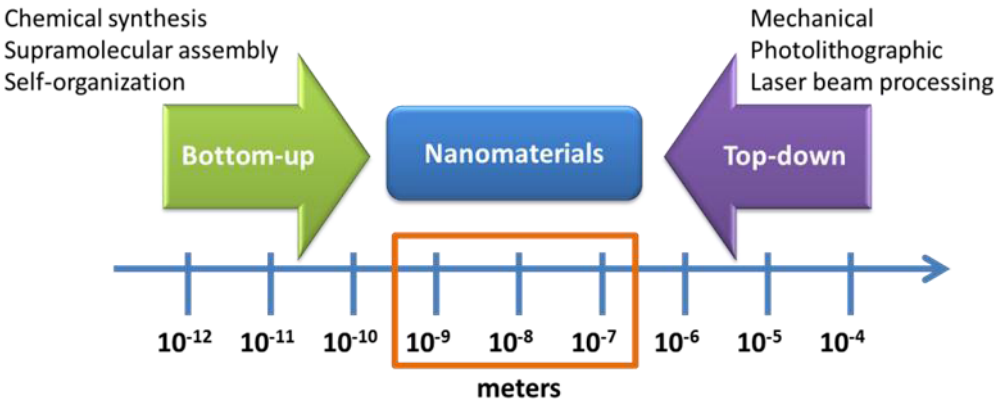

Figure 1.1: Top-down and bottom-up approaches for the preparation of nanomaterials.

The bottom-up approach resembles the processes that can be found in nature, namely the

formation of the DNA double-helix or the formation of the quaternary structure of proteins. The mechanisms are the same: the starting points are "construction blocks" that self-assemble through different processes -such as attractive and electrostatic forces, hydrophobic effects and hydrogen bonds- into more complex structures. These structures can acquire functions that were not present initially.

Many of these nanomaterials obtained by supramolecular chemistry may have many applications,[5] one of them being medicine (**Figure 1.2**). Nanomedicine can therefore be defined as the application of nanotechnology to solve medical problems.[6]

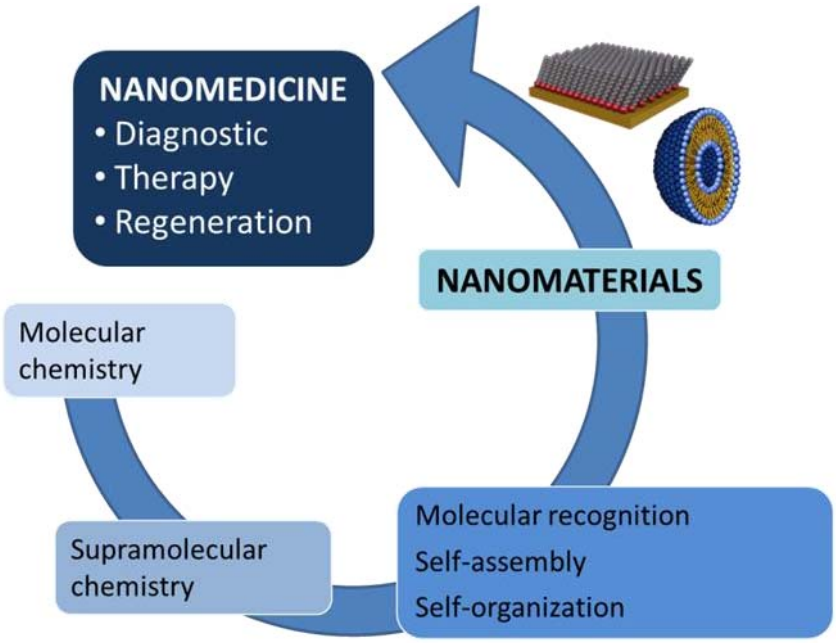

Figure 1.2: Bottom-up approach and applications in nanomedicine.

Their applications range from tissue regeneration to therapy and diagnostic.[7] Some of the main advantages of using nanomaterials are: the ability to obtain multimodal systems with different functions that can be used for targeting, therapy and/or imaging; the protecting effect on more easily degradable molecules that can be loaded into these materials; and the fact that the high surface/volume ratio enables a higher loading of molecules.[8–12]

Examples that can be found in literature, include synthetic polymers, hydrogels, liposomes and micelles, but also other materials such as nanoparticles (metallic, paramagnetic or polymeric),[13] quantum dots[14] and carbon nanotubes (**Figure 1.3**).[15]

For instance, we can find synthetic polymers used in tissue regeneration,[16] gene therapy[17] and in clinical use for drug delivery (albumin-bound paclitaxel Abraxane®)[18]. Hydrogels can also be used as scaffolds in tissue engineering[19,20] but also for drug delivery.[19,21] Micelles are systems that can find application as drug delivery systems[22] and liposomes are already being

commercialized as delivery vectors for drugs like doxorubicin or amphotericin B (as is the case of Doxil® and AmBisome® respectively) to cite a few.[23]

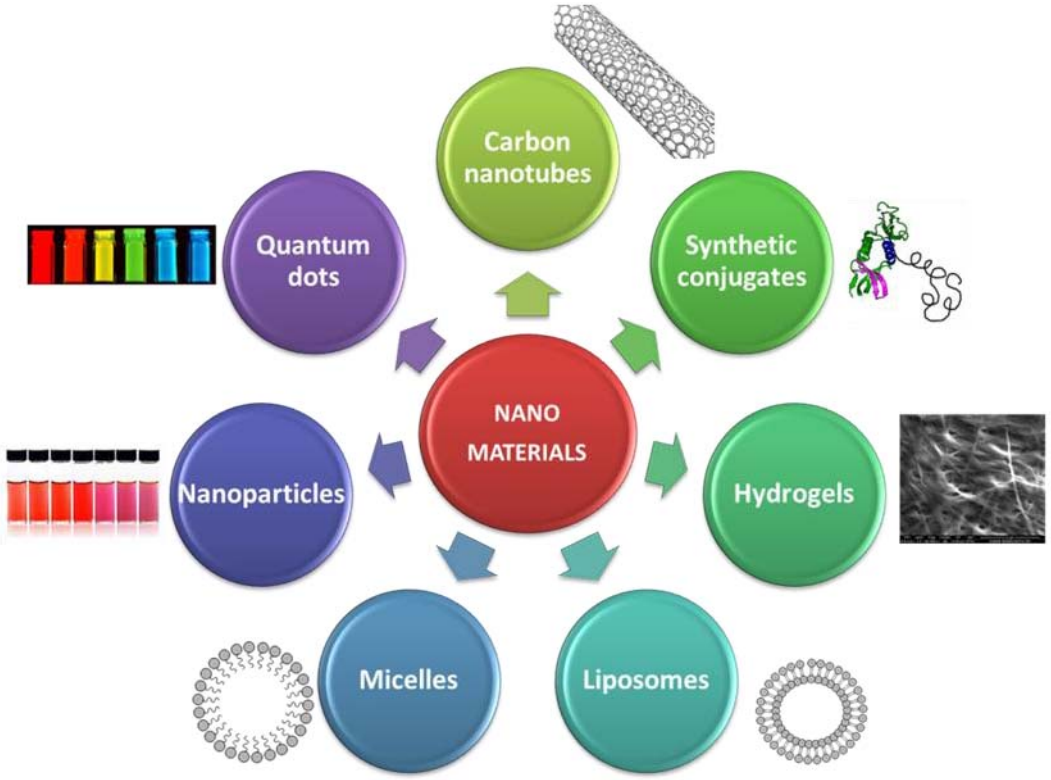

Figure 1.3: Different nanomaterials being developed and/or already in use in the field of nanomedicine.

Inorganic nanoparticles are also studied as therapeutic agents,[24] but also for imaging.[25] Due to their easy synthesis and surface characteristics, gold nanoparticles have been exploited as therapy agents for delivery of drugs, vaccines, gene therapy, imaging[26–29] but also in theranostics.[30] Superparamagnetic iron oxide nanoparticles (SPIONs) were of the first nanoparticle MRI contrast agents (Feridex®, Endorem® and Resovist®) and are still in use,[31] but their application as delivery vectors has also been gaining attention.[9,32,33] The nanometric size of these systems are especially important in the case of these inorganic non-biodegradable nanoparticles, since their dimensions have consequences in their fate in the organism that are yet to be fully understood.[34]

Quantum dots (also called semiconductor nanoparticles) are developed for imaging, because their characteristics allow multiplexed and robust labelling of proteins or organelles,[35] but also for imaging of cells and tissues.[36] Apart from application in other fields, carbon nanotubes are being studied as delivery agents.[37]

Being biocompatible and non-toxic are mandatory features that these materials must comply with.[23] This is a major drawback in the case of cadmium-containing quantum dots[38] and carbon

nanotubes.[39]

The above examples concern nanomaterials that are used for treatment or diagnostic *in vivo*. However, the nanomaterials can also be used for diagnostic and sensing *in vitro*. An example is the self-assembled monolayers (SAMs). SAMs are defined as ordered assemblies of molecules that are formed by the spontaneous adsorption of a head group from the molecule to the surface (substrate). The assembly of molecules on the surfaces of inorganic nanoparticles constitute a SAM. However, a SAM can be formed on macro or microscopic substrates, and according to the definition, it is still a nanostructured material because the monolayer constitutes a functional part on the surface, and has at least one dimension below 100 nm. The monolayers are obtained through spontaneous adsorption of molecules onto the surface in the liquid-solid interface, in solution[40] or by micro-contact printing.[41] One of the most popular applications of SAMs is its use to fabricate sensors, as for example DNA chips for diagnostic,[4,42–44] or through the immobilization of biomolecules[45] or cells,[46] or to tag cell, through the immobilization of biomolecules capable of recognizing specific types of cells (biosensors).[47,48] More particular applications of SAMs include the functionalization of tools to detect interactions using SPR-based sensors[49–51] and measurement of interactions between biomolecules using microscope probes.[51–53]

1.3. Objectives

The general objectives of the present thesis are:

- Assembly of nanostructures with adequate properties to be potentially used in therapy;
- Synthesis of gold nanoparticles with appropriate functionalization for drug delivery, using covalent and non-covalent interactions for incorporation of drugs;
- Self-assembly of monolayers and functionalization, of surfaces or probes, for sensing using biomolecules and chimiosensors.

Specific objectives are described, grouped by the chapters where they are discussed:

- Hydrogels assembly from bis-imidazolium ligands (Chapter 2):

a) Finding and optimizing the conditions for hydrogel formation;
b) Characterization of the obtained hydrogel;
c) Incorporation of anionic drugs and study of their release rate *in vitro*;
d) Permeation study *ex vivo;*
e) Determination of the drug activity *in vivo*;
f) Directed-synthesis of gold nanoparticles (GNP) using the hydrogels as templates.

- Synthesis of gold nanoparticles (Chapter 3):

a) Synthesis of GNP using biphasic system with bis-imidazolium ligands with linear structure;
b) Synthesis of GNP in aqueous medium using bis-imidazolium ligands with linear constitution;
c) Synthesis of GNP using biphasic system with bis-imidazolium ligands with macrocyclic structure;
d) Characterization of the obtained GNP;
e) Assessment of cytotoxicity, genotoxicity, and cell internalization of the synthesized GNP;
f) Incorporation of anionic drugs and study of their release rate *in vitro*;
g) Synthesis of GNP using thiols and functionalization with synthetic cyclic peptides with antimicrobial and antitumor properties.

- Monolayer assembly on surfaces for sensing (Chapter 4):

a) Functionalization of silicon surfaces surfaces with chimiosensors for temperature sensing;
b) Functionalization of Scanning Force Microscopy probes with biotin for sensing its molecular interaction with avidin;
c) Characterization of the functionalized structures using fluorescent conjugates;
d) Immobilization of anti-EGFR monoclonal antibodies and study of the interactions with the corresponding antigen EGFR using functionalized gold sensor chips.

Chapter 2

Nanostructured gels based on bis-imidazolium amphiphiles

2.1. Introduction

As it was described in Chapter 1, an engineered nanomaterial it is considered one that has one or more dimensions of the order of 100 nm. According to this definition, gels can be classified as nanomaterials.

A gel, as defined by Flory,[54] is a two-component colloidal system which is semi-solid, composed of small amounts of a solid – called gelator - that is dispersed in a large amount of an appropriate solvent (continuous phase), but having more solid-like characteristics.[55,56] The gelator self-assembles through chemical interactions that can be covalent or non-covalent (supramolecular). The self-assembly is responsible for the formation of a mesh network that - through surface tension forces- prevents the solvent to flow (**Figure 2.1**).[57]

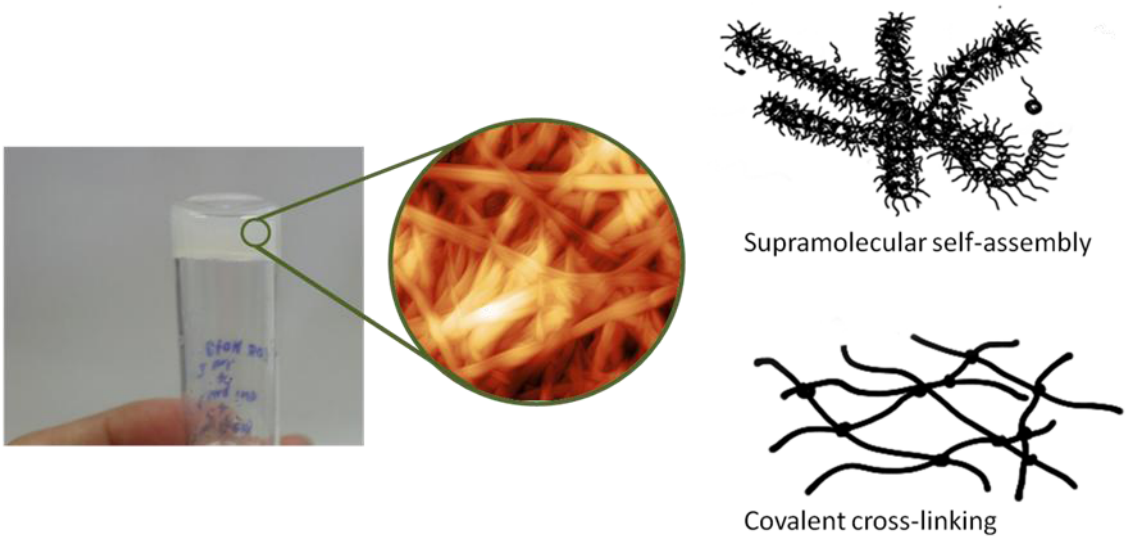

Figure 2.1: Macroscopic and nanoscopic images of a gel; the gelator molecule forms the gel by entrapping the continuous phase in a network that can be formed by supramolecular self-assembly or covalent cross-linking.

Initially, Flory classified the gels in terms of structure, where he described a) lamellar structures, composed of lamella with parallel arrangement; b) covalent polymeric networks, which form a three-dimensional network that is ramified and presents cross-linking between the structural units; c) polymer networks derived from physical aggregation that are mainly disordered but presents some regions of local order, and d) particulate structures, which are disordered and includes flocculent precipitates.[54]

In driving self-assembly for the gel formation, the covalent bonds account for the stronger and irreversible chemical interactions, while non-covalent interactions are weaker, such as hydrogen bonds, ionic interactions, electrostatic and hydrophobic interactions, van der Waals interactions, π-π stacking and London dispersion forces.[58,59] It has been observed that even though hydrogen bonds are one of the stronger intermolecular interaction that can stabilize the gelator network, in the cases where other interactions dominate, like the π-π stacking and London dispersion forces, they can be absent.[59]

Covalent interactions provide more robust gels, whereas non-covalent bonds give gels that are frailer, but often present thermoreversibility. This means that when the temperature increases, the gel becomes more fluid, due to the increasing disorder on the system. The temperature that corresponds to the sol-gel transition is called sol-gel transition temperature, t*gel*. This process is usually reversible, and upon cooling, the gel reassembles (**Figure 2.2**).

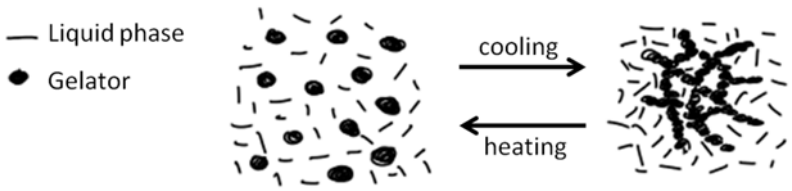

Figure 2.2: Schematic representation of the transitions between an isotropic liquid, an isotropic gel and an ordered liquid crystal anisotropic gel

Nowadays is still a tad difficult to have a generally accepted classification of the existing types of gels, which normally is based in the type of gelator used, the kind of intermolecular interactions that operate in the self-assembly process, and in the nature of the continuous phase.

Regarding the continuous phase, some consider a hydrogel one with water as continuous phase on which the gelator is cross-linked, otherwise defined as an aqueous gel.[55] On the other hand, others define hydrogel as a gel which has an aqueous continuous phase, further dividing them in a) physical, if the networks are assembled and maintained through molecular entanglements and intermolecular interactions, and b) chemical, if the networks are covalently linked.[60] When the continuous phase is mainly composed of an organic solvent they are called organogels,[57] or aerogels/xerogels when the gel is dried and there is no liquid continuous phase.[61] If the gel is composed of an ionic liquid mixed with another component, then it is defined as an ionogel.[62]

According to the type of gelator, the gels can be a) polymeric, when the gelator is a polymer, or b) Low Molecular Weight Gelator (LMWG) gels, when the small gelator molecules self-assemble forming fibber-like structures.. Polymers can be of natural or synthetic origin.

Although polymeric gels are normally associated to a cross-linked structure, the intermolecular interactions can also be non-covalent. The chemically stabilized gels, with the cross-linked structure, may be more robust but lacks thermal reversibility.[57,58] In the case of the gels formed by LMWGs, the type of interactions are mainly non-covalent chemical interactions. However, the type or organization of organogels from LMWGs can present two forms: in the first one the temperature is lowered below the gelator's solubility limit, with a consequent precipitation of the gelator molecules, and aggregates are formed through intermolecular interactions, resulting in solid fibbers; in the second case, a polar solvent is introduced in the organic solution of a surfactant-type gelator which reorganizes into cylindrical aggregates, thus immobilizing the solvent.[57]

Two important concepts regarding the LMWGs are the Critical Aggregation Concentration (CAC) and the Critical Gelator Concentration (CGC). CAC corresponds to the concentration at which the molecules aggregate in solution, and CGC to the lowest concentration at which the gelator is able to gelate a liquid at room temperature.[59]

According to their use, there are many examples of different applications for the gels: they can be used for removal of pollutants: gels made of the polysaccharide Konjac glucomannan were used to remove boron[63] and hydrogels prepared with poly(acrylic acid) to remove brilliant green dye from water.[64] Their robustness makes them useful as supports in the preparation of solar or fuel cells. For example dextran hydrogel electrolyte loaded with quantum dots to prepare quantum dot-sensitized solar cells[65] and chitosan to prepare hydrogel membrane electrolytes used in fuel cells.[66] Also in the preparation of sensors, for cation and anions[67] or nitric oxide[68] sensing, for example. Gels can also be used as templates or scaffolds: literature describes the use as templates to prepare metallic nanoparticles: poly(2-acrylamido-2-methyl-1-propansulfonic acid) hydrogels for the preparation *in situ* of cobalt nanoparticles[69]; in other example tripeptides with tyrosine residue were used to prepare gold and silver nanoparticles.[70] It is noteworthy that the tyrosine residues present in the peptide have the ability to reduce Au^{3+} to Au^{0}, with the consequent oxidation of the amino acid residue, so the gel as double function of template and reducing agent.

Their application as scaffolds can be associated to tissue engineering. Many examples are found in literature: a double network hydrogel made of two different polymers for cartilage tissue engineering,[71] a hydrogel of blended gelatine and glycosaminoglycans for the culture of hepatocytes,[72] or a scaffold of polycaprolactone included in a hydrogel of gelatine and chitosan for the culture of cardiac tissue,[73] just to name a few. It should be remarked the predominance of the natural polymers in these scaffolds, due to their biocompatibility and biodegradability, which makes them a first choice when performing cell and tissue culture. Besides tissue

engineering, hydrogels are also used in nanomedicine as drug delivery systems, and can be made responsive to some external stimuli, such as temperature[19,74] or the acidic pH found in tumour tissues.[75] Examples can be found of nanogels of lecithin for skin delivery of drugs,[76] hydrogels of α-cyclodextrin for delivery of doxorubicin,[77] polyethylene glycol-based hydrogels incorporating imidazole for the delivery of an antisense RNA oligonucleotide for cancer therapy along with iron oxide nanoparticles for imaging,[75] a hybrid composed of an interpenetrated chitosan-poloxamer 407 hydrogel loaded with micelles was studied for local delivery of the anticancer drug paclitaxel,[78] or hydrogel beads of alginate grafted with *N*-vinyl captrolactam for the delivery of 5-fluorouracil (a drug used in chemotherapy).[79] Most examples found are of natural polymers[80] that are combined with other molecules or modified.

Polymeric hydrogels have been widely studied, due to the robustness and good biocompatibility, but in the last decade LMWGs have been gaining attention, due to their thermoreversibility, and their structure that favours an easier degradation.[56] The drawback is finding such molecules, for there is no rationale design method that assures the gelating ability of the molecules. One of the options is the systematic synthesis of molecules with analogue structures to already known LMWGs.[59]

Imidazole- and imidazolium-derived polymers have been described as being able to form hydrogels.[81] For example, radical polymerization of an imidazolium-based ionic liquid with a vinyl group in water resulted in the formation of a polyionic hydrogel with improved thermostability when compared with a polyacrylamide hydrogel with covalent cross-linking and an alginate-based hydrogel with ionic cross-linking;[82] also photopolymerization of an acrylate imidazolium derivative afforded a hydrogel that was found to be more ordered structurally as before the polymerization step, when the monomers were only non-covalently assembled.[83]

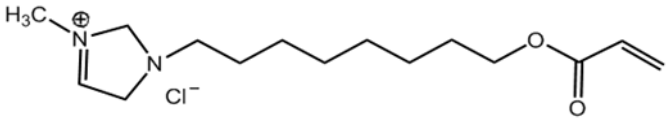

Figure 2.3: Example of imidazolium derivative with acrylate group.[83]

There are also examples where imidazolium-based ionic liquids could be gelated by LMWG derived from cholesterol, thus obtaining physical gels with good thermoreversible properties[84] Another important example shows imidazolium-based ionic liquids forming ionogels incorporating ibuprofenate as counterion.[85] Other examples include imidazolium-derived ionic liquids that upon addition of water self-assemble into an ionogel.[86] In this case, the water is responsible for breaking the bond between the imidazolium and its counterion, resulting in the self-assembly of the gelator.

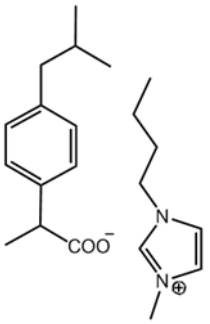

Figure 2.4: Example of imidazolium ionic liquid that forms gel with ibuprofenate as counterion.[85]

Besides the described examples of gels of imidazolium-based polymers and of imidazolium-based ionic liquids, examples are also found of imidazolium-based LMWG that can form gels in organic solvents and in water solutions of α-cyclodextran, both gemini imidazolium salts,[87] and simple chain imidazolium salt,[88] or imidazolium-bearing bolaamphiphiles that when brought together with other components, gain the ability to gel water.[89] LMWG of L-lysine bearing imidazolium groups could be used to gelate water.[90] it was found that bigger alkanoyl chains decreased the gelation ability.

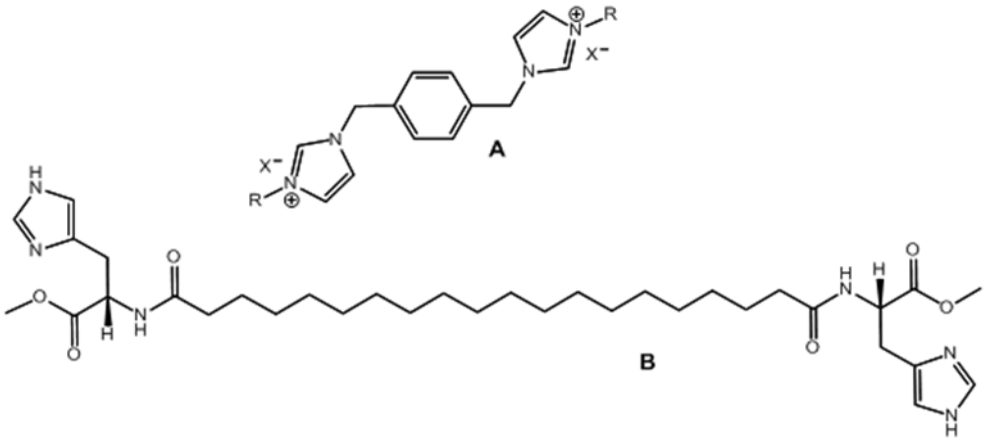

Figure 2.5: Example of (A) gemini imidazolium salt that forms gel with α-cyclodextran,[87] and of (B) imidazolium-bearing bolaamphiphile.[89]

To the light of the example found in literature, imidazolium-based derivatives seem promising molecules to assess their use as LMWG to obtain gels, which could be further used as drug delivery systems or as templates to grow metallic nanoparticles.

2.2. Objectives

Within the development of nanostructured materials, the study of hydrogels comprised of nanometric fibbers is described. The main goals of this study are:

a) Assembly of nanostructured LMWGs hydrogels, where the gelator's nature is based on bis-imidazolium amphiphiles, namely a bis-imidazolium based gemini amphiphile composed of two imidazolium moieties bearing an octadecyl chain, linked by a 1,3-dimethylenebenzene (**Figure 2.6**);
b) Incorporation of anionic drugs into the hydrogel's network,
c) Study the ability of the hydrogels to be used as delivery agents of anti-inflammatory anionic drugs for topical applications;
d) Investigate the use of the hydrogels as templates for the synthesis of gold nanoparticles (GNP) coated with bis-imidazolium amphiphiles.

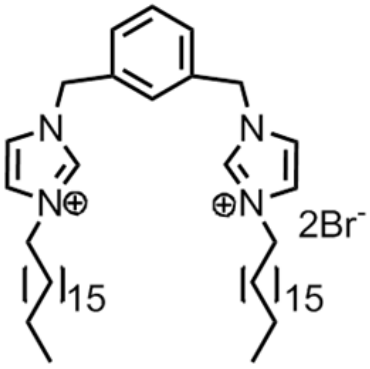

Figure 2.6: Structure of the bis-imidazolium based gemini amphiphile gelator.

This chapter is therefore divided in two sections, which objectives are explained in detail:

2.2.1. Bis-imidazolium hydrogels as potential carriers of anionic drugs

I. Study of the gelification by self-assembly to form hydrogel based on a bis-imidazolium based gemini-type amphiphile;
II. Optimization by changing solvent ratio and gelator amount:
III. Study of the incorporation in the hydrogel of anionic drugs (sodium ibuprofenate, indomethacin, diclofenac, sodium methotrexate) and optimization of the gelator:drug ratio;
IV. Characterization of the obtained gels through a variety of techniques, including: Rheology, Proton nuclear magnetic resonance spectroscopy (^{1}H NMR), Optical

Microscopy, Atomic Force Microscopy (AFM), Scanning Electron Microscopy (SEM), Transmission Electronic Microscopy (TEM) and X-ray powder diffraction (XRPD);

V. Study of the release rate *in vitro* of the incorporated anionic drugs using a Microette transdermal diffusion system with vertically assembled Franz-type diffusion cells;

VI. Assessment of the permeation through human skin of a model drug *ex vivo* and determination of the drug activity *in vivo*.

2.2.2. Bis-imidazolium hydrogels as templates for in situ synthesis of GNP

I. Formation of bis-imidazolium amphiphle gel incorporating $HAuCl_4$ and reduction of the Au^{3+} ions to Au(0), and extraction of the obtained GNP through a mechanical method;

II. Characterization of the obtained GNP by means of UV-visible absorption spectroscopy, High Resolution Transmission Electronic Microscopy (HRTEM), X-ray Photoelectron Spectroscopy (XPS) AFM and Rheology;

III. Comparison between the GNP obtained by templated synthesis with the GNP obtained by synthesis in liquid phase.

2.3. Supramolecular gels based on a gemini imidazolium amphiphile as molecular material for drug delivery

Publication in Journal of Materials Chemistry B, 2014, 2, 5419-5429.

Mafalda Rodrigues,[1,2] Ana C. Calpena,[2,3] David B. Amabilino,[4] Maria Luísa Garduño-Ramírez[5] and Lluïsa Pérez-García[1,2]

1 Departament de Farmacologia i Química Terapèutica, Universitat de Barcelona, Av. Joan XXIII s/n, 08028 Barcelona, Spain.

2 Institut de Nanociència i Nanotecnologia IN2UB, Universitat de Barcelona, 08028 Barcelona, Spain.

3 Departament de Farmàcia i Tecnologia Farmacèutica, Universitat de Barcelona, Av. Joan XXIII, 29-31 08028 Barcelona, Spain.

4 Institut de Ciència de Materials de Barcelona (ICMAB-CSIC), Campus Universitari, 08193 Bellaterra, Spain.

5 Centro de Investigaciones Químicas, Universidad Autónoma del Estado de Morelos, Av. Universidad 1001, Cuernavaca, Morelos, México.

Summary

In this work, a nanostructured gel, formed by fibbers of approximately 80 nm of width, is described. This gel incorporates drugs in its structure, and can be used as delivery vehicle for topical application.

The first step of the work consisted of obtaining the gel by dissolving a gemini imidazolium-based amphiphilic molecule in ethanol/water. The ratios of gelator, ethanol/water and drug load were varied in order to assess the optimal proportions. Some proportions favoured the correct assembly of the gel while others only resulted in a precipitate. After obtaining the best conditions, different drugs were incorporated: sodium ibuprofenate, indomethacin, and sodium methotrexate. Diclofenac was also used, but the system could not form a gel.

The successfully obtained gels were characterized by different techniques: optical microscopy confirmed that the gelator maintained its birefringent behaviour after forming the gel. AFM, SEM and TEM allowed the determination of the fibbers' size and tridimensional arrangement. XRPD, IR and ^{1}H NMR spectroscopies highlighted the presence of the drugs, and their localization within the nanostructure of the gel. The rheological behaviour showed no differences in the gel's resistance when compared with the gel loaded with ibuprofenate or indomethacin, but did show that the incorporation of methotrexate improves the resistance to sheer stress.

The study of the release from the incorporated drugs was performed, and shows that release rate varies with the structure of the drug. Ibuprofenate and indomethacin showed similar kinetics, although the released percentage of indomethacin is almost 3-fold of the ibuprofenate. Methotrexate showed a much slower release profile.

Furthermore, the *in vivo* anti-inflammatory efficacy of the gels containing ibuprofenate and indomethacin was studied and could be correlated with the release rate obtained *in vitro*.

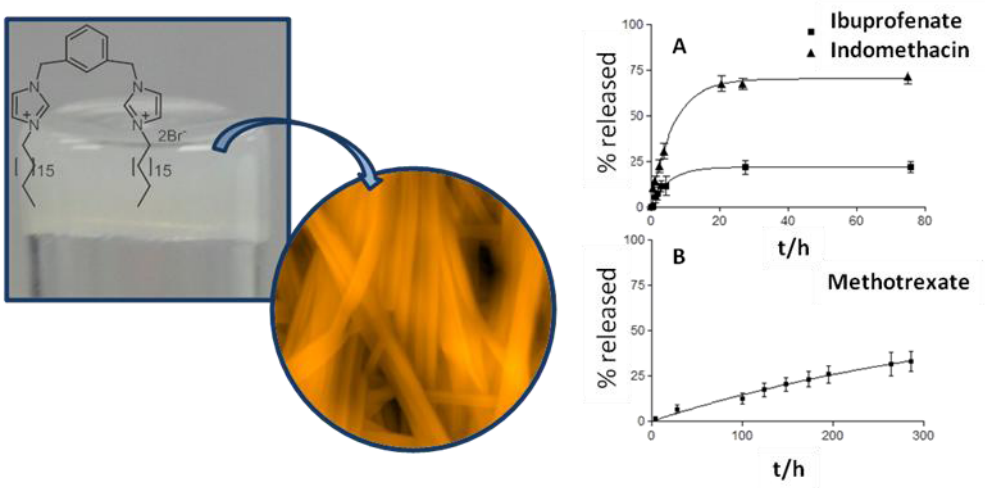

Figure 2.7: Photograph of the gel and corresponding AFM image (left) and release profiles obtained for the gels with the different drugs (right).

Journal of Materials Chemistry B

PAPER

View Article Online
View Journal | View Issue

Cite this: J. Mater. Chem. B, 2014, 2, 5419

Supramolecular gels based on a gemini imidazolium amphiphile as molecular material for drug delivery†

Mafalda Rodrigues,[ab] Ana C. Calpena,[bc] David B. Amabilino,[d] María Luisa Garduño-Ramírez[e] and Lluïsa Pérez-García*[ab]

Received 21st March 2014
Accepted 19th June 2014

DOI: 10.1039/c4tb00450g

www.rsc.org/MaterialsB

A novel physical gel was obtained using a gemini imidazolium-based amphiphilic molecule dissolved in ethanol–water mixtures. The structure of the gel is comprised of intertwining nanofibres with widths of approximately 80 nm. The ethanol/water ratio has an important influence on the gelation process: the gelator is sparingly soluble in water and soluble in ethanol. The gelator is capable of incorporating anionic drugs in its fibrillar network easily; sodium ibuprofenate, indomethacin and the sodium salt of methotrexate were used as model drugs that were incorporated into the quickly forming gels. The characterization of these composite xerogels was made by different microscopy techniques as well as X-ray powder diffraction. The ability of the amphiphile to form a gel is largely maintained in the presence of the different model drugs and the overall morphology of the gels (that present a fibre like structure in all cases with intertwined ribbons) is very similar. Furthermore the *in vitro* release of the drugs from the gel and the *in vivo* anti-inflammatory efficacy was studied. The overall results show better release profiles and anti-inflammatory efficacy for indomethacin, and prove the promise of this molecular gel in controlled drug release, in the present case dermatological application.

Introduction

Small molecule-based physical gels are attractive as drug delivery systems.[1,2] The term "gel" includes a wide variety of different chemical systems with distinct compositions and structures but that share some common features in their macroscopic properties and behaviour.[3] It is generally agreed that a gel is composed of a (macro)molecule that is able to immobilise a continuous liquid phase through the formation of a three-dimensional network, the active component maintaining a solid-like structure. Gelators can be classified based in the nature of the compound used (polymeric or low molecular weight) and also the liquid phase (aqueous, organic or ionic liquid). Often, the synthetic gels made out of polymers are chemical, meaning that they contain covalent links between the polymer molecules, making them very robust but also thermally irreversible. The robustness can be an advantage, but for certain biological applications the degradation of the gel could be advantageous and hence our focus on molecular gels.

Many examples can be found reporting the usage of molecule-based gels in a variety of fields[4] such as pollutant removal from water,[5,6] solar[7,8] and fuel cells,[9,10] sensors,[11,12] tissue engineering[13–15] and, the topic with which we are concerned here, drug delivery.[16–21] The prediction of the gelation process is not yet possible for a given molecular structure because of the lack of a full understanding of the intermolecular interactions between the gelators themselves and the solvent surrounding them. Thus, the design of gelator molecules is somewhat intuitive; many of the known gelators have been discovered by serendipity.

For biological applications, hydrogels – in which the fluid phase is water – are obviously the most appropriate. Gupta *et al.*[22] make a distinction between a hydrogel, which incorporates water and swells, and an aqueous gel, where further addition of water causes the polymeric fibres to dissolve, and may be attractive for drug delivery. Importantly, there are many commercial formulations where the gel is based on the use of co-solvents, particularly ethanol,[23] that widens the scope for preparing these nanomaterials and that we will take advantage of in this work.

[a]Departament de Farmacologia i Química Terapèutica, Universitat de Barcelona, Av. Joan XXIII, s/n, 08028 Barcelona, Spain. E-mail: mlperez@ub.edu; Fax: +34 934024539; Tel: +34 934035849

[b]Institut de Nanociència i Nanotecnologia IN2UB, Universitat de Barcelona, 08028 Barcelona, Spain

[c]Departament de Farmàcia i Tecnologia Farmacèutica, Universitat de Barcelona, Av. Joan XXIII, s/n, 08028 Barcelona, Spain

[d]Institut de Ciència de Materials de Barcelona (ICMAB-CSIC), Campus Universitari, 08193 Bellaterra, Spain

[e]Centro de Investigaciones Químicas, Universidad Autónoma del Estado de Morelos, Av. Universidad 1001, Cuernavaca, Morelos, México

† Electronic supplementary information (ESI) available: Additional optical microscopy photographs and AFM images of gels, kinetic models for drug release and rheology measurements. See DOI: 10.1039/c4tb00450g

On the other hand, the low molecular weight gelators (LMWGs) are gaining more attention recently. There are many different types of molecules in this category, often with amphiphilic character because it is during the study of their amphiphilic behaviour that gels of water are uncovered.[24] The gels obtained from these LMWGs are physical gels (or supramolecular gels): the gel is formed by the self-assembly of the molecules into fibres that arrange in an isotropic three-dimensional matrix through non-covalent interactions, and are normally obtained under mild conditions. These molecules are very often based on peptide derivatives,[25] although others are also effective.[1,2] One can refer to these assemblies as self-assembled fibrillar networks (SAFINs).[26] Because the intermolecular interactions are generally weaker than in polymeric systems, where multivalency can have an important role, the gels of LMWGs are thermoreversible, which means that upon heating above a certain temperature the gel becomes a homogeneous fluid (sol), and after cooling down, it turns back into the gel form. This property can be advantageous, because these gels can therefore be made thermoresponsive. Other advantages when comparing with polymeric gelators are the facile degradation because the molecules are shorter and LMWGs assemble through physical bonds based in intermolecular interactions, and because the interactions are not covalent, the structure of the gel is more flexible and dynamic.[27]

We have shown that gemini imidazolium-based salts – that have the ability to recognize and bind anions, in particular carboxylates – can present liquid crystal behaviour,[28] can form micelles in water[29] and also have potential use as delivery agent for the release of anionic drugs when used as ligands to decorate gold nanoparticles.[30,31] In these systems the carboxylate is incorporated into the bis(imidazolium) moieties in the colloid because of the ion pairing between the anion and the cationic head, as well as van der Waals interaction in the covering of the nanoparticle. Other groups have shown that imidazolium-based compounds can act as hydrogelators.[32–34] On the other hand, the influence of anions on gelator action is an area of great current interest.[35–37] Therefore, we considered that the gemini imidazolium based compounds could be attractive molecular gelators that could also display anion binding and release.

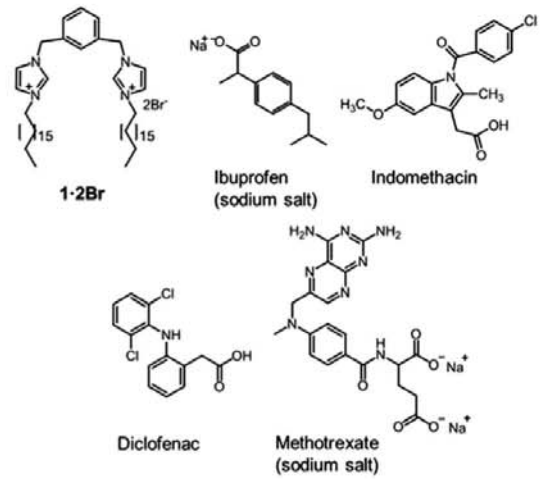

Fig. 1 Structure of **1**, the sodium salt of ibuprofen, indomethacin, diclofenac and sodium methotrexate.

Here, we present gels obtained using a gemini imidazolium-based amphiphile (**1**, Fig. 1) and also the results obtained from their application as both *in vitro* and *in vivo* delivery vehicles using different model drugs that bear carboxylate functional groups: sodium ibuprofenate, diclofenac and indomethacin, which are non-steroidal anti-inflammatory drugs (NSAID), and sodium methotrexate, which is a drug used in cancer therapy but also in the treatment of autoimmune diseases such as psoriasis and rheumatoid arthritis.[38] The recognition and complexation ability of **1** towards ibuprofenate had already been demonstrated, both in solution and as a ligand in gold nanoparticles,[30,31] whereas indomethacin and methotrexate were chosen because they have limited solubility in aqueous media, thus benefiting from the complexation ability of **1** to carry them.

Experimental

Materials

All reagents were of analytical grade. Compound 1,3-bis[(3-octadecyl-1-imidazolio)methyl]benzene dibromide (**1**) was prepared as reported previously.[30]

Gel preparation

Gels with **1** were obtained as follows: 10 mg of **1** was added to 0.8 mL of ethanol. After complete dissolution, 1.2 mL of distilled water was added and the solution was stirred gently. The solution was maintained at room temperature without any disturbance. After 1 hour, the formation of the gel was confirmed by its stability to inversion of the glass vial. The final concentration of **1** was 5 mg mL^{-1} in solution. The final composition of the solvent was 40 : 60 of ethanol–water. These values were maintained constant across all the experiments performed, except where stated otherwise. For the gel with **1** and sodium ibuprofenate, 10 mg of **1** were added to 0.8 mL of ethanol. After complete dissolution, 1.2 mL of an aqueous solution containing 1 mg of sodium ibuprofenate was added and the solution was gently stirred and then left to stand.

For the gel with **1** and indomethacin, 10 mg of **1** and 1 mg of indomethacin were added to 0.8 mL of ethanol. After complete dissolution, 1.2 mL of distilled water as added and the solution was gently stirred and allowed to stand.

For the gel with **1** and methotrexate, 10 mg of **1** were added to 0.9 mL of ethanol. After complete dissolution, 1.1 mL of an aqueous alkaline solution containing 0.5 mg of methotrexate and Na_2CO_3 (final concentration 0.5%) were added and the solution was gently stirred then left to stand.

Gel characterization

Optical images were collected with an Olympus BX51TRF polarising optical microscope.

SEM images were acquired by the Electron Microscopy Service in the ICMAB-CSIC on a QUANTA FEI 200 FEG-ESEM system on samples deposited on gold on mica from the gel. Contacts were made between the gold surface and the sample holder with graphite paste, in order to avoid charging of the unstained xerogels.

AFM images were recorded by the Scanning Probe Microscopy Service in the ICMAB-CSIC on a PicoSPM system (Molecular Imaging). The intermittent contact mode was used close to resonance frequencies of the silicon cantilevers (Nanosensors, FM type force constant 1.2–3.5 N m^{-1} and tip diameter 5 nm) of around 60–70 kHz. All the images were recorded under atmospheric conditions.

The freeze-fracture electron microscopy study was done according to the procedure described elsewhere.[39] The gel was sandwiched between two copper platelets using a 400-mesh gold grid as spacer. Then the samples were frozen by liquid propane immersion, at −189 °C and fractured at −150 °C and approximately 10 mbar in a BAF 060 freeze-etching system (Leica Microsystems, Vienna). The replicas were obtained by unidirectional shadowing at 45° with 2 nm of Pt/C and at 90° with 20 nm of C, and they were floated on distilled water for 5 minutes and observed in a Tecnai Spirit at 120 kv (FEI Company, Eindhoven, Netherlands) with Megaview III Soft Imaging System.

XRD measurements were performed with a Siemens D-5000 X-ray diffractometer. The source was a DRX ceramic tube (λ CuKα = 1.540560 Å and λ CuKα 2 = 1.544390 Å) with a voltage and current of 45 kV and 35 mA, respectively. The gel was mounted on a glass slide and dried under vacuum, and was scanned from 2Θ = 2–80°.

The rheological characterization was performed at 32 °C using a HAAKE Rheostress1 rheometer (Thermo Fisher Scientific, Karlsruhe, Germany) connected to a Thermo Haake Phoenix II + Haake C25P temperature controller. The rheological studies carried out on freshly prepared sample included:

(a) Flow behaviour. The rheometer was equipped with a cone-plate geometry set-up with a fixed lower plate and a mobile upper cone (Haake C60, 2° 60 mm diameter, 0.106 mm) and also a plate–plate geometry (PP60 Ti, 60 mm diameter, 0.5 mm gap between plates). The rheometer was connected to a computer provided with the software HAAKE RheoWin®Job Manager V.3.3 to carry out the test and RheoWin®Data Manager V.3.3 (Thermo Electron Corporation, Karlsruhe, Germany) to carry out the analysis of the obtained data.

Viscosity curves and flow curves were recorded under rotational runs at 32 °C for 3 min during the ramp-up period from 0 to 100 s^{-1}, 1 min at 100 s^{-1} (constant share rate period) and finally 3 min during the ramp-down period from 100 to 0 s^{-1}.

(b) Oscillatory test. The rheometer was equipped with a plate–plate set-up (Haake PP60 Ti, 60 mm diameter, 1 mm gap between plates). Oscillatory stress sweeps between 0.1 and 100 Pa were performed at 1 Hz and frequency sweep tests from 0.01 to 10 Hz at a constant shear stress within the linear viscoelastic region, in order to determine the related variation of storage modulus (G') and loss modulus (G'') at 32 °C. Both viscoelastic moduli are defined as follows: $G' = \tau_0/\gamma_0 \cos\delta$ and $G'' = \tau_0/\gamma_0 \sin\delta$ (where τ_0 and γ_0 are the amplitudes of stress and strain and δ is the phase shift between them).

^{1}H NMR spectra for the studied drugs (sodium ibuprofenate, indomethacin and methotrexate) and of the gels with increasing amounts of drug were recorded in a Varian VNMRS 400 MHz, in methanol-d4–D_2O 50 : 50.

In vitro release studies

The release of the drugs from the **1**-gel was performed in a Microette transdermal diffusion system (Microette plus-Hanson Research) with vertically assembled Franz-type diffusion cells (Crown Glass). Dialysis membranes (Cellu Sep T3 dialysis membrane, MWCO 12 000–14 000 Da, MFPI, USA), previously hydrated in water : methanol 1 : 1, were placed in the Franz-type diffusion cells. Known weights of gel were placed into the donor compartment onto the dialysis membranes. The dialysis membrane and the donor container were put onto the glass receptor chamber and the assembly was fixed with a joint. The receptor chamber contained Sorensen Buffer 67 mM pH 5.5, which complies with the SINK conditions. The Franz-type cells were connected to a controlled temperature system, with a heating bath set to 32 °C. Samples were taken at given time intervals, and the sample taken was replaced by equal volume of the receptor solution.

The permeation assay was done with human skin from the abdominal region obtained during plastic surgery of a healthy, 40-year-old woman who gave written, informed consent to the use of this material for research purposes. The skin was dermatomed at 0.4 mm thickness. The method was similar as described above, replacing the dialysis membranes with skin. The gel was applied on the donor compartment in contact with the epidermal side of the skin. The pH used for the donor solution was 5.5 (which is the skin pH) and the temperature was set to 32 °C. The samples were taken along 48 hours.

Drug determination in samples was done by HPLC in a Waters LC Module I, in a Waters Spherisorb 5 μmODS-2 (4.6 mm × 150 mm) column. The mobile phase consisted of acetonitrile–water (acidified to pH 3 with phosphoric acid) 65 : 35, with a flow rate of 1.5 mL min^{-1} and the detection wavelength was 220 nm for sodium ibuprofenate and 254 nm for indomethacin. The flow rate was 0.8 mL min^{-1} and the detection wavelength was 313 nm for methotrexate. The data was collected using Millennium32 version 4.0.0 software from Waters Corporation. All data was calculated as the average ± standard deviation of three replicates. A nonlinear least-squares regression was performed using the WinNonLin® software (WinNonlin® Professional edition version 3.3, Pharsight Corporation, USA), and the model parameters calculated. Modelistic parameters were statistically compared by using StatGraphics software version 5.1.

In vivo studies of anti-inflammatory efficacy

Anti-inflammatory efficacy of the gels was evaluated following the protocol described elsewhere.[40] TPA (12-*O*-tetradecanoylphorbol 13-acetate) was used to induce mouse ear inflammation. Adult male Wistar CD-1 mice with a body weight ranging

from 20 to 25 g were used. Oedema was induced by topical application of 2.5 μg per ear of TPA dissolved in EtOH. Gel formulations (100 mg) containing either ibuprofenate or indomethacin, or without any drug were applied to both sides of the right ear only, along with TPA. Four hours after the application of the gels, the animals were sacrificed and circular sections with 7 mm of diameter were cut from left and right ears and weighted to determine the anti-inflammatory activity. All experiments were performed in compliance with the Norma Oficial Mexicana NOM-062-ZOO-1999 and with the approval of the Academic Committee of Ethics of the Vivarium of the Universidad Autσnoma del Estado de Morelos.

Results and discussion

Characterization of the gel

In this work we characterized a nanostructured gel obtained with the amphiphilic molecule 1,3-bis[(3-octadecyl-1-imidazolio)methyl]benzene dibromide (**1**, Fig. 1), which has a bis-imidazolium gemini-type structure. This molecule has been described previously as having low cytotoxicity and genotoxicity, making it a promising ligand for biological applications.[30] During the study of the properties of **1**, we came upon the formation of a homogenous gel when it was dispersed in acetonitrile and heated to the boiling point of the solvent, but also when dissolved in a solution consisting of ethanol and water. This type of behaviour was already reported for other type of amphiphiles based on aromatic hydrazines.[41] Apart from that, the closest example in literature[34] of gelators relatively similar to **1** have shorter alkyl chains and need the addition of a cyclodextrin to form gels in water. For the application we are targeting, that of drug delivery where benign solvents are preferred, the water–ethanol mixtures were clearly the medium of choice for the formation of the gels.

In the present case, the gel can be formed upon introduction of water into an ethanolic solution of the gelator and allowing the mixture to stand at room temperature for a time (the gel does not form immediately upon mixing).[42] The amphiphile organizes itself into aggregates and subsequently fibres that trap the solvent, producing a gel that was stable at room temperature. In this type of physical gels, London dispersion forces between the gelator's alkyl chains are likely to play an important role in the stabilization of the gels.[34,43,44] Furthermore it has already been found that in the case of imidazolium-based gelators the charged ring (and accompanying anion) is important for the interactions that promote the gel formation; changing the imidazolium group by another moiety, or adding substituent groups, causes the initial molecule to lose its gelling ability.[32,45]

In order to verify the optimum conditions for gel formation different proportions of ethanol and water were tested as the solvent medium. The formation of the gels of **1** using the different ethanol/water ratios were attempted, and their general appearance as well as their thixotropic behaviour were qualitatively observed. The thixotropy was assessed by vigorously shaking the gel, and observing that the gel assembled again after resting for three to five hours, highlighting the time-dependence of the process. Table 1 summarises the findings. In the case of the sodium salts of ibuprofenate and methotrexate, different concentrations were tested. The same could not be done with indomethacin because of its poor solubility in the solvents used.

Table 1 Gels of **1** (10 mg) and its combination with different drugs prepared using different solvent mixtures (total volume 2 mL) and their thixotropic behaviour[a]

Ethanol : water proportion	Drug[b]	**1** : drug (mg mg^{-1})	**1** : drug ratio[c]		T.B.[d]
35 : 65	—	—	—	OG	No
40 : 60	—	—	—	**OG**	**Yes**
45 : 55	—	—	—	OG	Yes
50 : 50	—	—	—	OG	No
55 : 45	—	—	—	PG	—
40 : 60	**Ibu**	**1 : 0.100**	**1 : 0.40**	**OG**	**Yes**
40 : 60	**Ibu**	1 : 0.250	1 : 1.00	OG	No
45 : 55	**Ibu**	1 : 0.100	1 : 0.40	OG	Yes
40 : 60	**Diel**	1 : 0.100	1 : 0.30	PG	—
45 : 55	**Diel**	1 : 0.100	1 : 0.30	PG	—
40 : 60	**Ind**	**1 : 0.100**	**1 : 0.25**	**OG**	**Yes**
45 : 55	**Ind**	1 : 0.100	1 : 0.25	OG	Yes
40 : 60	**Mtx**	1 : 0.050	1 : 0.10	P	—
45 : 55	**Mtx**	**1 : 0.050**	**1 : 0.10**	**OG**	**Yes**
45 : 55	**Mtx**	1 : 0.075	1 : 0.15	PG	—
45 : 55	**Mtx**	1 : 0.100	1 : 0.20	PG	—
50 : 50	**Mtx**	1 : 0.050	1 : 0.10	PG	—

[a] OG – opaque gel; PG – partial gel; P – precipitate. [b] **Ibu** – ibuprofenate; **Diel** – diclofenac; **Ind** – indomethacin; **Mtx** – methotrexate. [c] mol/mol. [d] T.B. thixotropic behaviour.

The gel of **1** in 35 : 65 ethanol–water formed very quickly after mixing the water with the ethanol solution of the gelator, although some of the liquid phase did not incorporate into the gel and remained separate. The gel was not very stable to mechanical stress and could be easily disrupted upon very mild shaking. The gels formed with 40 : 60 and 45 : 55 ethanol–water incorporated the liquid phase completely upon formation. However, the gel with 50 : 50 ethanol–water did not present a thixotropic behaviour, meaning that after shaking the gel, it did not recover the gel form, and the gel with 55 : 45 ethanol–water also formed a gel partially, and it was not stable. The amount of ethanol present in solution is important because it is the component responsible for the solubilisation of **1** while the water acts as an antisolvent. As reported previously in literature, a change of the solvent that solubilises the gelator molecule can have drastic effects where no gelation occurs,[45] and in this case we can rationalise the lack of gel formation at high ethanol content because of the higher solubility of **1** under these conditions. Conversely, at high water content the compound is not sufficiently soluble to reach the concentration necessary to form large aggregates that lead to gel formation.

The rheological behaviour of the gel-**1** in a 60 : 40 water–ethanol was studied, as this behaviour can be important for biomedical applications.[46] Regarding the flow properties and viscosity, under the programmed increasing/decreasing shear rate sweep carried out in duplicate, the gel was found to exhibit

erratic behaviour due to the rigid structure of the gel fibres that broke in no reproducible way and therefore the viscosity could not be determined, and also no quantitative study of its thixotropic behaviour The viscoelastic properties were assessed through an oscillatory study, with a stress sweep test, and the critical stress was approximately 1 Pa for all the samples under study (see ESI Fig. S1†). These results indicated that the gel is quite fragile, confirming qualitative observations.

A constant shear stress of 0.5 Pa (50% of the critical value) was selected to perform the frequency sweep tests. Oscillatory measurements applied to the samples showed prevalence of the elastic over the viscous behaviour ($G' > G''$) (see ESI Fig. S2†). This means that the gel, due to this fragility, can be applied on the skin to treat inflammation and pain in a very easy way with just a mild massage.

The introduction of the drugs affects the gelling process: with diclofenac in the gelling with **1**, a degree of gelification was observed. However, the sample remained partially fluid, and did not turn into a solid gel completely, whereas the samples with the same solvent composition and content of **1** did. Thus diclofenac inhibits gel formation. In the case of methotrexate, the influence of the ethanol content was more important: with 40% ethanol no gelation took place, and with 50% ethanol, the gel could only form partially (with some supernatant liquid). We could obtain an opaque gel with 45% ethanol; however gelation occurred with a slight shrinkage of the colloidal material leaving clear liquid. The reasons for this partial phase separation – rather than homogeneous gel formation – are unclear at present. In the case of ibuprofenate and indomethacin opaque gels were formed with 40% and 45% of ethanol in water, but we chose the gel formed with 40% ethanol for further studies because it was the one that presented faster formation of the gel. These gels without any drug, with ibuprofenate, indomethacin, and methotrexate will be referred to as gel-**1**, gel-**Ibu**, gel-**Ind** and gel-**Mtx**, respectively. The amounts of drug incorporated in the studied gels correspond to the maximum loading of drug that allows a correct formation of the gel.

The appearance of the different gels can be appreciated in Fig. 2. During the preparation of the solutions, it was observed that gel-**1** had a relatively slow gelling speed (around 1 hour), while gel-**Ibu** and gel-**Ind** were formed more rapidly, with the latter being the one that showed a faster speed in the gelation process (within 15–30 minutes). Gel-**Mtx**, however, formed very slowly, as we could see the formation of the different gelling nuclei on the solution. Nevertheless, as we can observe, the overall appearance of the different gels was similar. Since the model drugs used were chosen because of their ability to interact with the amphiphile molecule, an enhancement in the formation of the gel structure due to intermolecular interactions between the positively charged polar head of the amphiphile and the negative charges of the anionic molecules and the apolar regions of the uncharged drugs may take place, presumably accompanied by the liberation of sodium bromide into the trapped fluid part of the system. In the case of methotrexate the gelation is slower, possibly because of the high solubility of the dianionic form of the drug in the solvent.

The rheological behaviour of the drug containing gels (gel-**Ibu**, gel-**Ind** and gel-**Mtx**, containing 1 mg of ibuprofenate, 1 mg of indomethacin, and 0.5 mg of methotrexate respectively) was also studied in the same conditions as gel-**1** (without any drug). It was found that gel-**Ibu** and gel-**Ind** had very similar profiles. When comparing with gel-**1**, it is clear that the latter has higher values of G' (elastic or storage modulus), G'' (viscous or loss modulus), and $|f^*|$ (viscosity), which means that gel-**1** is more consistent. However, the crossover values (storage modulus G' = loss modulus G'') are very similar between gel-**1**, gel-**Ibu** and gel-**Ind**, and therefore the three present the same fragility. On the other hand, gel-**Mtx** also has lower G', G'' and $|f^*|$ when compared with gel-**1**, but presents higher crossover value, indicating that this gel, even though apparently less viscous than the gel without drug, is more consistent and has more resistance to the applied tensions (see ESI Fig. S3–S7†). Table 2 presents the crossover values obtained for each of the gels.

In the case of ibuprofenate and indomethacin, the presence of these drugs did not appear to influence significantly the behaviour of the gel. The **1** : drug ratio (mol/mol) of the these gels were different (1 : 0.40 and 1 : 0.25 in the case of ibuprofenate and indomethacin, respectively), although the same weight of each were used in the preparation of the gel, indicating that for these gels the amount of drug can be varied slightly without affecting gel performance. However, in the case of methotrexate, despite a lower **1** : drug ratio the presence of the drug did exert a significant effect on the overall viscous properties of the gel.

Infrared spectroscopy was used to confirm the presence of the two components in the gel, and was particularly useful in the case of gel-**Mtx**. The bands from **1** in this mixed gel appear at the same position as they do in the bromide salt, for example the bands at 1154, 1469 and 1551 cm^{-1} stand out. The methotrexate is clearly present as the anion form, as the peak at 1643 cm^{-1} in the pure compound in its acid form is replaced as a shoulder on a medium-broad peak at 1600 cm^{-1}

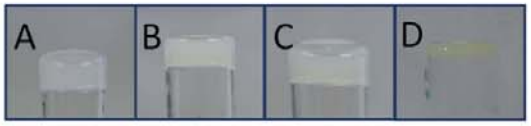

Fig. 2 Gels obtained with the bromide salt of bisimidazolium compound **1** without any drug (A), with sodium ibuprofenate (B), with indomethacin (C) and with the sodium salt of methotrexate (D); ethanol–water proportions are 40 : 60 (A–C) and 45 : 55 (D); **1** : drug ratio (mol/mol) are 2.5 : 1, 4 : 1 and 10 : 1, respectively.

Table 2 Crossover values and respective shear stress (τ) for gels in 60 : 40 water : ethanol, except for gel-**Mtx** (55 : 45 mixture)

Sample	Crossover/Pa	τ (shear stress)/Pa
Gel-**1**	165.0	25.78
Gel-**Ibu**	173.3	25.29
Gel-**Ind**	165.3	24.87
Gel-**Mtx**	421.5	39.96

View Article Online
Journal of Materials Chemistry B Paper

corresponding to the carboxylate form. The other bands corresponding to the drug component are also observed.

Proton nuclear magnetic resonance spectroscopy (^{1}H NMR) was used to probe the interaction between the gelator and the drug. ^{1}H NMR spectra were recorded for the drug alone, and for the respective gels with increasing amounts of drug. The spectra obtained for the gel with ibuprofenate (see ESI Fig. S8†) shows no sharp peak of ibuprofenate when incorporated in the gel, which indicates that the drug molecule is interacting strongly with the gelator, and not merely dissolved in the interstitial liquid phase of the solvent trapped between the fibres. A similar situation is true for the case of methotrexate (ESI Fig. S10†). However, in the case of indomethacin, for lower amounts of drug no signal is detected, but for higher proportions relatively well resolved peaks are visible; this suggests that part may be involved in interactions with the gelator fibres, but part is dissolved in the interstitial liquid phase (ESI Fig. S9†). It seems likely that this difference in behaviour is a result of the weaker interaction of carboxylic acid form of indomethacin with the gelator, compared with the other drugs that are carboxylate salts.

The temperature of transition gel-to-sol, T_{gel}, is defined as the temperature at which the gel melts and starts to flow from the glass vial in an inverted position. The T_{gel} of the different gels was determined by immersing the vial containing the gel in a thermostated bath and raising the temperature slowly at a rate of 1 °C min^{-1}. The results are presented in Table 3. They are an average of three measurements.

As we can see, the presence of the drugs did not have an effect in the T_{gel} of **1**. This study also allowed us to verify the thermoreversibility of the gel, since the gel was heated until complete solubilisation of the colloid and upon cooling down the gel formed again.

Fig. 3 shows transmission micrographs taken of the gels with an optical microscope with parallel and crossed polarisers. We can see that the gel fibres composed of the bis-imidazolium compound are birefringent, meaning that the molecules are organised in such a way that they have orientational order within the colloid. This behaviour was seen in all the different gel samples that were analysed (see ESI Fig. S11–S13†).

A higher resolution analysis of the fibre structure of the xerogels was performed by scanning electron microscopy (SEM) and atomic force microscopy (AFM). These microscopy techniques allow us to study how the fibres of the gel are arranged and their dimensions and morphology, and how the gel fibres are grouped together. Fig. 4 shows the micrographs obtained by

Table 3 Melting temperatures for gels in 60 : 40 water : ethanol except for gel-**Mtx** (55 : 45 mixture)[a]

Sample	T_{gel}/°C
Gel-**1**	38.5
Gel-**Ibu**	38.0
Gel-**Ind**	36.5
Gel-**Mtx**	35.0

[a] Temperatures are accurate to ±0.5 °C.

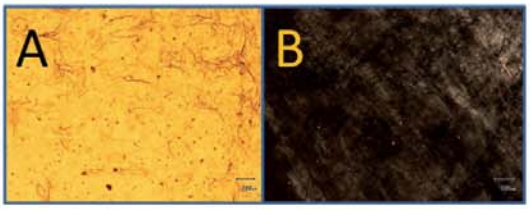

Fig. 3 Optical transmission micrographs taken with parallel polarisers (A) and with crossed polarisers (B) of the gel **1** (ethanol : water 40 : 60) without drug incorporated.

SEM for the gels without any drug, with sodium ibuprofenate, with indomethacin, and with sodium methotrexate. The micrographs of the three gels with a magnification of 20 000× show little difference between them, except in the case of incorporation of methotrexate. The gels are formed by long, narrow fibres, which are intertwined, not showing any particular three dimensional ordered arrangements in accord with the isotropic nature of the bulk sample. The fibres can clearly bend, and have lengths far longer than five micrometres. The gel incorporating methotrexate clearly has shorter fibres (that are more poorly defined) in the sample, which would explain the poorer stability of this gel when compared with the others in the series. In this sample, there are no fibres imaged with lengths of greater than five micrometres. When increasing the magnification to 40 000×, one can observe some additional slight differences between the samples: the xerogel of **1** appears to be compact, gel-**Ibu** seems to have a less dense structure, and in the case of gel-**Ind** the structure seems more compact, although these slight differences are partially dependent on the area being imaged. The structure of gel-**Mtx** appears quite different to the others again, with rougher fibres where the edges are poorly defined and the width is more variable than the other samples.

Atomic force microscopy (AFM) was also used in order to obtain more detailed information on the lateral dimensions of the fibres. In Fig. 5 some AFM images of the xerogels of gel-**1**, gel-**Ibu**, gel-**Ind** and gel-**Mtx** are shown, as well as profiles perpendicular to the fibre direction in the image, representing the topography, which can be analysed in order to obtain information about the width of the gel fibres.

From the AFM images we can observe that the width of the fibres is around 40–80 nm for gel-**1**, 100–120 nm for gel-**Ibu**, 60–100 nm for the gel-**Ind** and 100–120 nm for the gel-**Mtx**. In all cases the fibres are remarkably well defined and tend to bundle into yarns with parallel fibres over short distances (up to a few microns). Furthermore, AFM images of the gels with different ratios of ethanol/water were also obtained (see ESI Fig. S14–S16†). Apparently there is no significant influence of the medium on the organization of the fibres or on width, that is around 60–100 nm. A comparison between the gel with 1 mg and 2.5 mg of sodium ibuprofenate was also performed (see ESI Fig. S17†). The most important feature is that the width of the fibres is much higher in the case of the gel with 2.5 mg of sodium ibuprofenate, which confirms that the presence of the

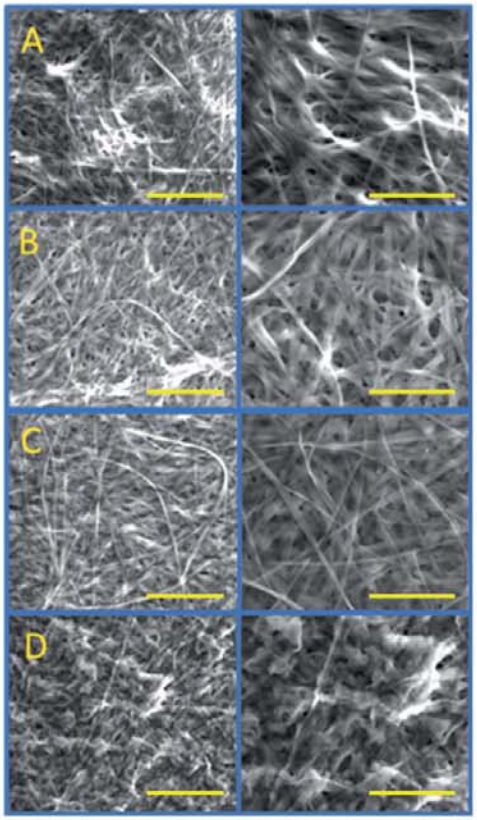

Fig. 4 SEM micrographs of the xerogel of **1** (A), gel-**Ibu** (B), gel-**Ind** (C), and gel-**Mtx** (D). Images taken with 20 000× magnification (left, scale bar = 5 μm) and 40 000× magnification (right, scale bar = 3 μm).

drug affects greatly the assembly of the fibres, thus also giving a possible explanation for the fact that this gel did not present thixotropic behaviour.

Furthermore, the structure of the gels was studied using transmission electron microscopy (TEM). For the preparation of the samples, the freeze-fracture technique was used. This allows obtaining images of the gel in its native state, in contrast with the previous techniques which can present modifications of the fibre structure due to the required drying of the sample.

In Fig. 6 the ribbon-like shape of the fibres is clearly visible: they are rather flat and have a regular height and width. Internal structure can also be seen, where several tapes form a single object – the dark lines within the tapes presumably correspond to places where individual fibres are connected. This observation shows the tendency of the fibres to agglomerate laterally, and explains the observation in the AFM measurements that fibres often run practically parallel to one another.

Additionally, the gels were characterized by X-ray powder diffraction (XRPD) in order to probe the degree of crystallinity of the samples. This would show either macroscopic fibre crystallinity or the presence of any crystalline drug in the bulk

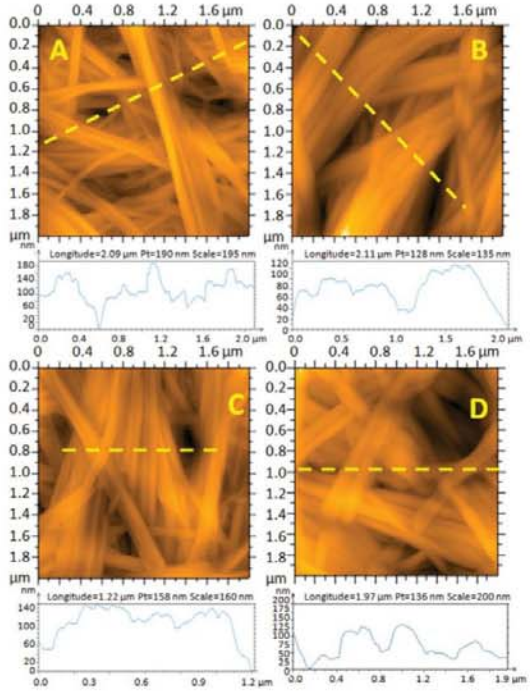

Fig. 5 AFM image of xerogels of **1** (A), gel-**Ibu** (B), gel-**Ind** (C), and gel-**Mtx** (D), with respective profiles in cross section (marked with yellow dash line).

sample. In Fig. 7 the diffractograms corresponding to gel-**1**, gel-**Ibu**, gel-**Ind**, and gel-**Mtx** are presented.

The main features in the diffractogram of the xerogel of **1** are the intense Bragg peaks at values of 2θ of 7 and 9° that correspond to spacings between lamellae of the amphiphile.[28] This aspect of the diffractogram and the presence of the other sharp peaks indicate a significant proportion of crystalline material in the sample of large enough dimensions to diffract the X-rays. On the other hand, the gels incorporating the drugs are essentially amorphous at the bulk level, they show only low intensity sharp peaks. Instead, the diffractograms are dominated by broad peaks between 2θ values of 30 and 40°, corresponding to distances of 2.2 to 3.2 Å, that probably arise from the short van

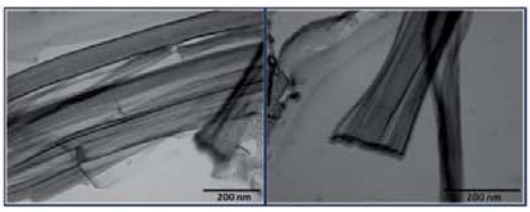

Fig. 6 Transmission electronic microscope photograph of gel-**1** in ethanol–water 40 : 60. Samples were prepared by the freeze-fracture method.

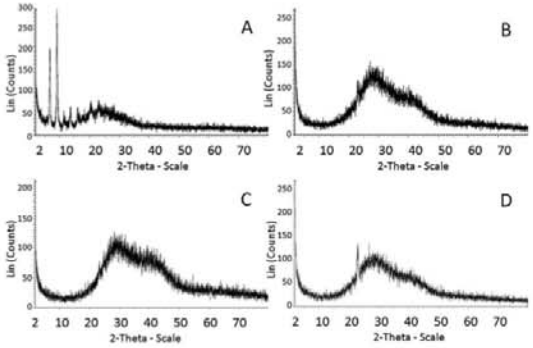

Fig. 7 X-ray powder diffractograms of gel-**1** (A), gel-**Ibu** (B), gel-**Ind** (C), and gel-**Mtx** (D).

der Waals contacts between alkyl chains. The drug molecules precipitated under the same solvent conditions but without gelator show sharp diffraction peaks (see ESI Fig. S18†). However, the gelator–drug hybrids show clearly broad peaks coming from a non-periodic structure (over a large length scale at least) and indicating incorporation of the drug into the gel fibres: should it merely be precipitated in between the fibres or adhered to the surface of the fibres the diffraction peaks of drug and gelator would be expected to be observed. The drug is not present in its free state in any case, but is incorporated into the gelator fibres, and so is not present in its free form. The results confirm that the drug limits the ordered growth of the fibres of the gelator, since the few diffraction peaks seen in the pure gelator are not present.

Drug release studies

Having characterised the gels structurally, their ability to deliver the drug load was explored. Aiming at an external application, the conditions that were chosen for the experiments correspond to the skin: acidic pH (5.5) and a slightly lower temperature than the internal one (32 °C). The delivery was tested with gel-**Ibu**, gel-**Ind**, and gel-**Mtx**,. Gel-**1** was used as a control, showing that the gelator was not taken into the receptor solution. The amount of released drug was calculated taking into account the total weight of the gel used, and it was measured as described in the experimental section. Different kinetic models (first order, Peppas–Korsmeyer and Higuchi), normally used to describe release from hydrogels, were used to fit the experimental data obtained in the drug release experiments.[47] The Akaike Information Criterion (AIC) was determined for each model, as it is an indicator of the model's suitability for a given dataset.[48] The kinetic model that best describes the experimental data, selected based on the lowest AIC value (see ESI Table S1†), is the first order kinetic for all of the analyzed gels. In Fig. 8 we can see the release profiles from: sodium ibuprofenate and indomethacin (A) and sodium methotrexate (B), and in Table 4 the equation parameters (Q_{max}, K, $t_{1/2}$ and R^2).

The most important difference in the materials used is the amount of drug released when comparing ibuprofenate and

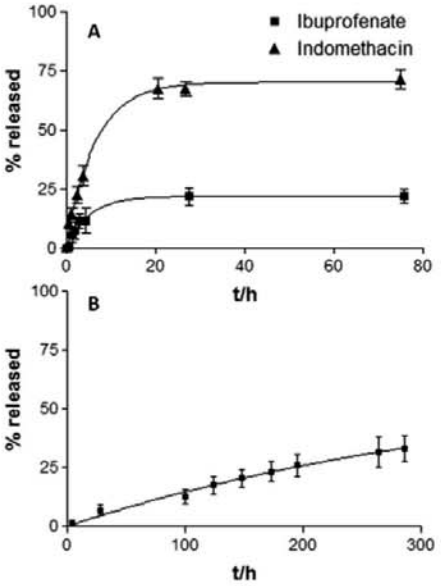

Fig. 8 Release profile of sodium ibuprofenate and indomethacin (A) and sodium methotrexate (B) from respective gels at pH 5.5 and 32 °C.

Table 4 Equation parameters for the release kinetic of sodium ibuprofenate, indomethacin and sodium methotrexate

Parameter[a]	Q_{max}	K	$t_{1/2}$	R^2
Ibuprofenate	21.8	0.19	3.6	0.996
Indomethacin	70.2	0.15	4.5	0.999
Methotrexate	64.0	0.0026	268.7	0.997

[a] Q_{max}: maximum amount released (%); K: release rate constant (h^{-1}); $t_{1/2}$: time to achieve the release of 50% of the Q_{max}; R^2: coefficient of determination for the equation.

indomethacin. In the first case, Q_{max} is almost 25% of the total ibuprofenate incorporated in the gel, whereas the gel with indomethacin can release up to 70% of its content. This probably results from the different interaction strength between **1** and each of the molecules. In the case of sodium ibuprofenate, the interaction is stronger, and thus the molecule is held relatively firmly in the gel fibres, making release to the medium more difficult.

Nevertheless, the rate is very similar, with both having similar $t_{1/2}$ and release rates. On the other hand, in the case of methotrexate, the release is much slower. The release rate is 0.0026 h^{-1}, two orders of magnitude inferior to the previous two. During the time that the experiment was carried out, approximately 30% release was achieved, which is approximately half of the Q_{max}.

Since the best results were obtained with the gel with indomethacin, this was used in the next experiment, which consisted of testing its permeation across human skin. The overall

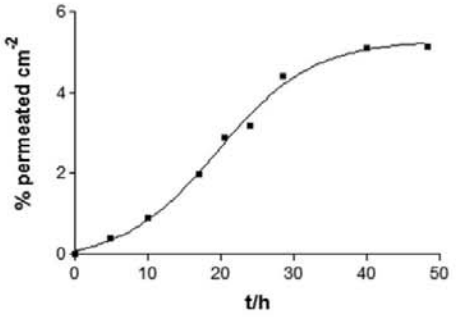

Fig. 9 Cumulative permeation profile of indomethacin as percentage of the drug by area of skin, at 32 °C.

procedure was the equivalent as for the release *in vitro* with the dialysis membranes except that these were replaced with human skin. The permeation profile is shown in Fig. 9.

The cumulative permeation curve (Fig. 9) presents a sigmoidal profile, which is in agreement with the fact that the experiments were done with a finite dose of drug and thus the donor compartment reaches a stage of drug depletion. We can observe that the percentage of total drug that crosses the skin and is recovered in the receptor, divided by the total area of the skin in contact with the gel, corresponds to 5.3% cm^{-2} and the flux J of indomethacin is 0.18% $cm^{-2}\ h^{-1}$.

Because the depletion stage was reached, J was calculated in the range where linearity is observed, between 10 and 30 hours. With these values, a linear regression was done and J corresponds to the slope of the curve. The curve obtained also allows us to obtain the value of the drug's partition (KH) and diffusion (D/H^2) parameters, and calculate the corresponding permeability coefficient (K_p).

$$\frac{D}{H^2} = \frac{1}{6t_0}$$

$$KH = \frac{J}{2.54C_0\frac{D}{H^2}}$$

$$K_p = KH\frac{D}{H^2}$$

In the above equations t_0 corresponds to the intercept of the x axis from the curve, C_0 is the initial concentration, that corresponds to 100% because all the values were defined as percentage of the total amount of drug added, and H is the thickness of skin sample used. Thus, the calculated value for the diffusion parameter is 0.03 h^{-1}, for the partition parameter is 0.06 cm^{-2}, and for the permeability coefficient K_p is 0.002 cm^{-2} h. These values appear lower than the ones obtained for the *in vitro* release because in the case of the permeation, apart from the drug that crosses the skin, an important part is retained. Besides, the flux is much lower in the case of the skin, which is a thicker and more complex barrier when compared with the dialysis membrane used in the *in vitro* experiment.

Besides the permeation assay, an *in vivo* test was performed to assess the action of the gel containing the anti-inflammatory drugs ibuprofenate and indomethacin. The percentage of anti-inflammatory activity was calculated as follows:

$$\%\ \text{anti-inflammatory activity} = \frac{\text{weight difference, control} - \text{weight difference, treated}}{\text{weight difference, control}} \times 100$$

The weight difference refers to the difference between the left ear, where only the inflammation inducer TPA was applied, and the right ear, where the gels were applied along with TPA. This measurement is based on the fact that the inflammatory process generates drainage of fluids that cause swelling, increasing the volume and weight of the tissues. When the inflammatory process decreases, the swelling also diminishes, and consequently the volume and weight. The obtained results are shown in Table 5.

The results show that the gel without any drug does not present any anti-inflammatory activity, since no change was observed comparing with the untreated ear. Furthermore, the activity showed by the gel with indomethacin is higher when compared with the one with ibuprofenate. These results can be rationalised by the fact that in the case of gel-**Ind** the drug is released at a faster rate than in the case of gel-**Ibu**, meaning that the real amount of drug that is available to exert the anti-inflammatory activity is also higher. Furthermore, when taking into account the permeation profile from Fig. 9, it is clear that within the time length of the *in vivo* study (4 hours) we are still in a phase where the drug is entering the skin, but little has yet passed, meaning that the amount of drug available is low. This may explain why the anti-inflammatory activity appears low. Regarding the drug's anti-inflammatory action without being in a gel, the drug was applied in acetone at the same concentration as used in the gel (0.5 mg mL^{-1}). The inhibition percentages found were 37.0 ± 0.7 and 77.5 ± 0.3 for ibuprofenate and indomethacin respectively. However, it must be noted that acetone is a powerful promoter of skin permeation, and may favour the availability of the drug. Also, being applied in a gel formulation, the hydrophilic character of the formulation and the molecular interactions between the nanofibre structure of the gelator and the drug may limit the availability of the drug in the area where it was applied, decreasing the percentage of inflammation inhibition.

Table 5 Anti-inflammatory activity of gel-**1** (control), gel-**Ibu** and gel-**Ind**

Drug	% anti-inflammatory activity
Gel-**1**	0
Gel-**Ibu**	29.7 ± 0.8
Gel-**Ind**	48.6 ± 0.4

Conclusions

The molecular gelator described here successfully incorporates three quite different pharmaceutically relevant drugs in its colloidal structure during the relatively fast gel formation that results after mixing aqueous and ethanolic solutions. Although the gels are relatively fragile, this mechanical feature does not prevent the nanomaterial from being effective in drug delivery. The synergy between gelator and drug molecule results in the formation of amorphous gels that are capable of releasing their drug load, showing anti-inflammatory efficacy both *in vitro* and *in vivo*. The release profile depends largely on the charge on the drug molecule. These results show that the use of charged molecular gelators may be a viable way of controlling the delivery of certain therapeutically relevant compounds. The results obtained from the rheological study of the gel show good characteristics for a dermal application. The fluidity of the gel, its big liquid content and its fragility are all factors that favour a good penetration of the drugs without having to press to much the body area with the inflammatory and painful process present. It would be more adequate, however, the formulation of the gel in single dose packaging, so that the gel could be maintained in its ideal conditions and to control the exact amount of drug to be applied. The development of formulations for local application of NSAIDs is important. Although a higher number of applications are required, when compared with oral formulations, there are benefits for the patient with chronic inflammation (especially in the case of rheumatoid arthritis) who may suffer gastric problems due to oral administration of this type of drugs.

Acknowledgements

This study was supported by a grant from the *Ministerio de Ciencia e Innovación* (MICINN) (project TEC2011-29140-C03-02) and from the Generalitat de Catalunya (2009SGR158). The authors thank Judith Oró and Maite Simón (Scientific Experimental Platforms, ICMAB-CSIC) for their help with the SEM and AFM measurements, respectively, Dr Lyda Halbaut Bellowa for rheology studies, and Berenice Andrade for her help with the *in vivo* studies.

References

1 K. J. Skilling, F. Citossi, T. D. Bradshaw, M. Ashford, B. Kellam and M. Marlow, *Soft Matter*, 2014, **10**, 237.
2 S. S. Sagiri, B. Behera, R. R. Rafanan, C. Bhattacharya, K. Pal, I. Banerjee and D. Rousseau, *Soft Matter*, 2014, **12**, 47.
3 P. J. Flory, *Faraday Discuss. Chem. Soc.*, 1974, **57**, 7.
4 *RSC Soft Matter No. 1, Functional Molecular Gels*, ed. B. Escuder and J. F. Miravet, The Royal Society of Chemistry, 2013.
5 K. Oishi and Y. Maehata, *Chemosphere*, 2013, **91**, 302.
6 S. R. Shirsath, A. P. Patil, R. Patil, J. B. Naik, P. R. Gogate and S. H. Sonawane, *Ultrason. Sonochem.*, 2013, **20**, 914.
7 H.-Y. Chen, L. Lin, X.-Y. Yu, K.-Q. Qiu, X.-Y. Lü, D.-B. Kuang and C.-Y. Su, *Electrochim. Acta*, 2013, **92**, 117.
8 Y. Rong, X. Li, G. Liu, H. Wang, Z. Ku, M. Xu, L. Liu, M. Hu, Y. Yang, M. Zhang, T. Liu and H. Han, *J. Power Sources*, 2013, **235**, 243.
9 N. A. Choudhury, J. Ma and Y. Sahai, *J. Power Sources*, 2012, **210**, 358.
10 L. An, T. S. Zhao and L. Zeng, *Appl. Energy*, 2013, **109**, 67.
11 I. Yoshimura, Y. Miyahara, N. Kasagi, H. Yamane, A. Ojida and I. Hamachi, *J. Am. Chem. Soc.*, 2004, **126**, 12204.
12 P. D. Wadhavane, M. A. Izquierdo, F. Galindo, M. I. Burguete and S. V. Luis, *Soft Matter*, 2012, **8**, 4373.
13 C. Fan, L. Liao, C. Zhang and L. Liu, *J. Mater. Chem. B*, 2013, **1**, 4251.
14 M. De Colli, M. Massimi, A. Barbetta, B. L. Di Rosario, S. Nardecchia, L. Conti Devirgiliis and M. Dentini, *Biomed. Mater.*, 2012, **7**, 055005.
15 S. Pok, J. D. Myers, S. V. Madihally and J. G. Jacot, *Acta Biomater.*, 2013, **9**, 5630.
16 H. Kuang, H. He, Z. Zhang, Y. Qi, Z. Xie, X. Jing and Y. Huang, *J. Mater. Chem. B*, 2014, **2**, 659.
17 C.-W. Lin, S. J. Tseng, I. M. Kempson, S.-C. Yang, T.-M. Hong and P.-C. Yang, *Biomaterials*, 2013, **34**, 4387.
18 C. Ju, J. Sun, P. Zi, X. Jin and C. Zhang, *J. Pharm. Sci.*, 2013, **102**, 2707.
19 C. Gong, Q. Wu, Y. Wang, D. Zhang, F. Luo, X. Zhao, Y. Wei and Z. Qian, *Biomaterials*, 2013, **34**, 6377.
20 B. Y. Swamy, J. H. Chang, H. Ahn, W.-K. Lee and I. Chung, *Cellulose*, 2013, **20**, 1261.
21 S. V. Vinogradov, T. K. Bronich and A. V. Kabanov, *Adv. Drug Delivery Rev.*, 2002, **54**, 135.
22 P. Gupta, K. Vermani and S. Garg, *Drug Discovery Today*, 2002, **7**, 569.
23 J. Réeff, A. Gaignaux, J. Goole, C. De Vriese and K. Amighi, *Drug Dev. Ind. Pharm.*, 2013, **39**, 1731.
24 M. de Loos, B. L. Feringa and J. H. van Esch, *Eur. J. Org. Chem.*, 2005, **2005**, 3615.
25 A. Altunbas and D. Pochan, in *Peptide-Based Materials*, ed. T. Deming, Springer, Berlin Heidelberg, 2012, vol. 310, ch. 206, p. 135.
26 N. M. Sangeetha and U. Maitra, *Chem. Soc. Rev.*, 2005, **34**, 821.
27 W. T. Truong, Y. Su, J. T. Meijer, P. Thordarson and F. Braet, *Chem.–Asian J.*, 2011, **6**, 30.
28 L. Casal-Dujat, O. Penon, C. Rodríguez-Abreu, C. Solans and L. Pérez-García, *New J. Chem.*, 2012, **36**, 558.
29 L. Casal-Dujat, P. C. Griffiths, C. Rodriguez-Abreu, C. Solans, S. Rogers and L. Perez-Garcia, *J. Mater. Chem. B*, 2013, **1**, 4963.
30 L. Casal-Dujat, M. Rodrigues, A. Yagüe, A. C. Calpena, D. B. Amabilino, J. González-Linares, M. Borràs and L. Pérez-García, *Langmuir*, 2012, **28**, 2368.
31 M. Rodrigues, A. C. Calpena, D. B. Amabilino, D. Ramos-López, J. de Lapuente and L. Pérez-García, *RSC Adv.*, 2014, **4**, 9279.
32 J. Zhang and X. Shen, *J. Phys. Chem. B*, 2013, **117**, 1451.
33 M. A. Firestone, J. A. Dzielawa, P. Zapol, L. A. Curtiss, S. Seifert and M. L. Dietz, *Langmuir*, 2002, **18**, 7258.

34 F. D'Anna, P. Vitale, S. Marullo and R. Noto, *Langmuir*, 2012, **28**, 10849.
35 G. O. Lloyd, M.-O. M. Piepenbrock, J. A. Foster, N. Clarke and J. W. Steed, *Soft Matter*, 2012, **8**, 204.
36 J. A. Foster, R. M. Edkins, G. J. Cameron, N. Colgin, K. Fucke, S. Ridgeway, A. G. Crawford, T. B. Marder, A. Beeby, S. L. Cobb and J. W. Steed, *Chem.–Eur. J.*, 2014, **20**, 279.
37 H. Maeda, *Chem.–Eur. J.*, 2008, **14**, 11274.
38 E. Gan, W.-S. Chong and H. Tey, *BioDrugs*, 2013, **27**, 359.
39 O. López, A. d. l. Maza, L. Coderch, C. López-Iglesias, E. Wehrli and J. L. Parra, *FEBS Lett.*, 1998, **426**, 314.
40 V. Domínguez-Villegas, B. Clares-Naveros, M. L. García-López, A. C. Calpena-Campmany, P. Bustos-Zagal and M. L. Garduño-Ramírez, *Colloids Surf., B*, 2014, **116**, 183.
41 L.-Y. You, G.-T. Wang, X.-K. Jiang and Z.-T. Li, *Tetrahedron*, 2009, **65**, 9494.
42 A. Vintiloiu and J.-C. Leroux, *J. Controlled Release*, 2008, **125**, 179.
43 D. J. Abdallah and R. G. Weiss, *Adv. Mater.*, 2000, **12**, 1237.
44 S. Brahmachari, S. Debnath, S. Dutta and P. K. Das, *Beilstein J. Org. Chem.*, 2010, **6**, 859.
45 A. Ballabh, D. R. Trivedi and P. Dastidar, *Chem. Mater.*, 2003, **15**, 2136.
46 C. Yan and D. J. Pochan, *Chem. Soc. Rev.*, 2010, **39**, 3528.
47 P. Costa and J. M. S. Lobo, *Eur. J. Pharm. Sci.*, 2001, **13**, 123.
48 K. Yamaoka, T. Nakagawa and T. Uno, *J. Pharmacokinet. Biopharm.*, 1978, **6**, 165.

Electronic Supplementary Information:

Supramolecular gels based on a gemini imidazolium amphiphile as molecular material for drug delivery

Mafalda Rodrigues,[a,b] Ana Calpena,[b,c] David B. Amabilino,[d] M Luisa Garduño-Ramírez,[e] Lluïsa Pérez-García[a,b,*]

[a]*Department of Pharmacology and Therapeutic Chemistry, Universitat de Barcelona, Av. Joan XXIII, 29-31 08028 Barcelona, Spain. Fax: +34 934024539, Tel: +34 934035849, E-mail: mlperez@ub.edu*

[b]*Institute of Nanoscience and Nanotechnology IN2UB, Universitat de Barcelona, 08028 Barcelona, Spain.*

[c]*Department of Pharmacy and Pharmaceutical Technology, Universitat de Barcelona, Av. Joan XXIII, 29-31 08028 Barcelona, Spain.*

[d]*Institut de Ciència de Materials de Barcelona (ICMAB-CSIC), Campus Universitari, 08193 Bellaterra, Spain.*

[e]*Centro de Investigaciones Químicas, Universidad Autónoma del Estado de Morelos, Av. Universidad 1001, Cuernavaca, Morelos, México.*

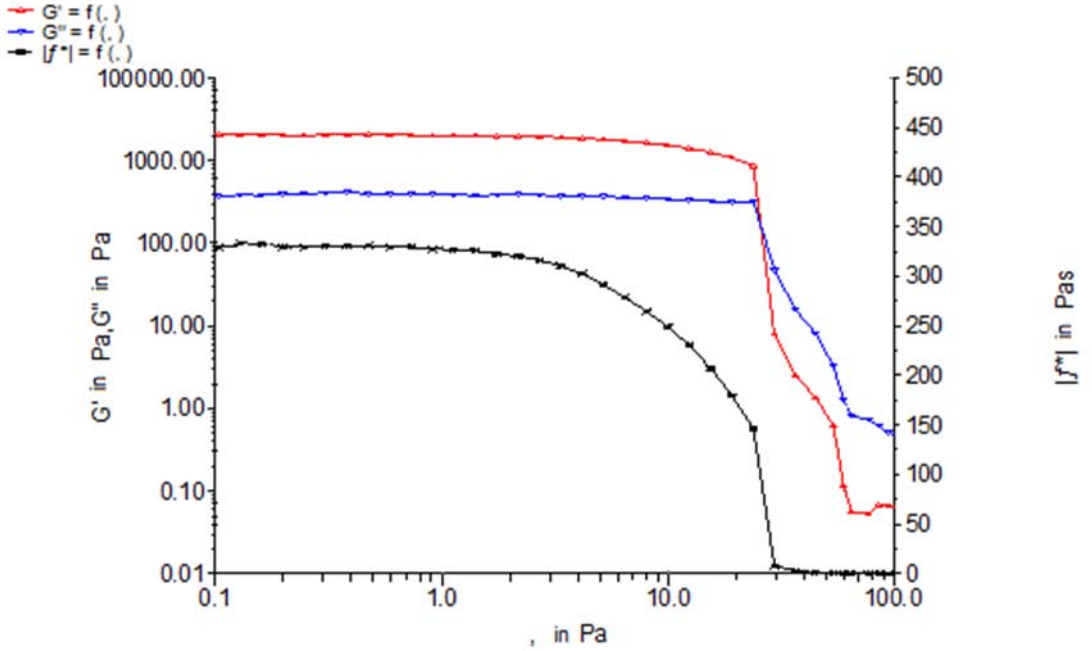

Fig. S1: Stress sweep of gel of gel-**1** in water-ethanol. G' (elastic or storage modulus), G" (viscous or loss modulus), and |*f**| (viscosity) are defined as function of τ (shear stress).

Sensor: PP60 Ti
A Factor: 23580 Pa/Nm
M Factor: 29.991 (1/s)/(rad/s)
Inertia: 1.234e-05 kg m²
Damping: 30.00
Thermal expansion coefficient: 1.100 µm/°C
Compliance: 0.003157 rad/Nm
Groove: 1.0 mm
Driver version: 45

Element definition:
ID 2: 108; CS; 0.000 Pa; t < 300 s; ; T 32.00 °C <± 1.00 °C;
ID 8: 3; CS; 0.000 Pa – 500.0 Pa log; f 1.000 Hz; t ---; #50; T 32.00 °C;

Evaluation:
CROSSOVER: G' (storage modulus) = G" (loss modulus) = 165.0 Pa when Tau = 25.78 Pa

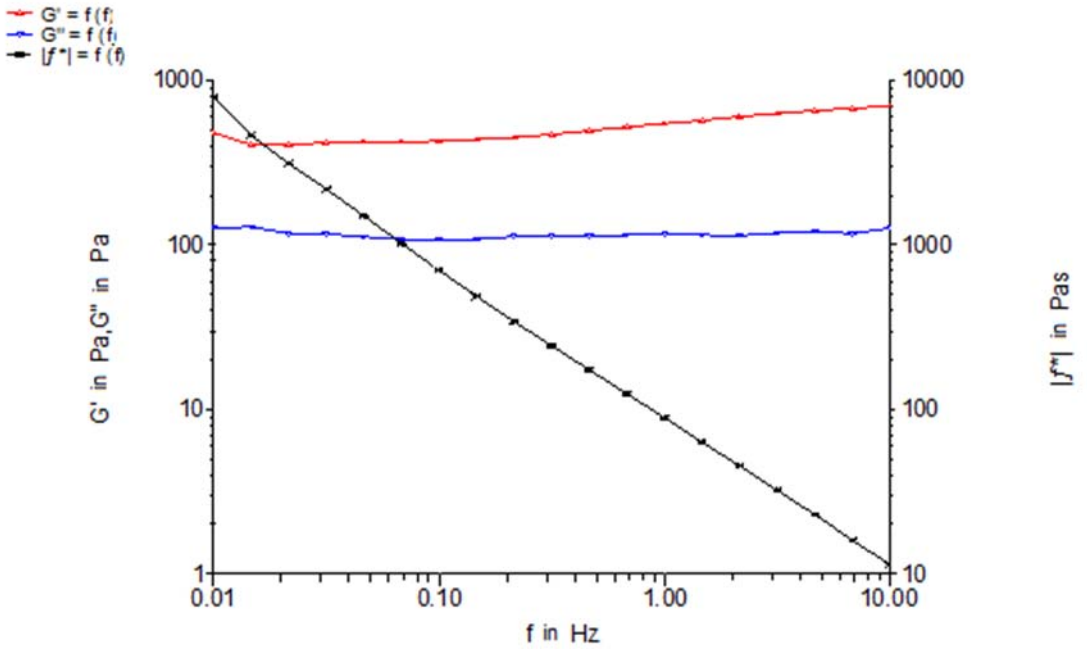

Fig. S2: Frequency sweep of gel-**1**: G' (elastic or storage modulus), G'' (viscous or loss modulus), and |*f**| (viscosity) defined as function of f (oscillatory frequency).

Sensor: PP60 Ti
A Factor: 23580.000 Pa/Nm
M Factor: 29.987 (1/s)/(rad/s)
Inertia: 1.234e-05 kg m²
Damping: 30.00
Thermal expansion coefficient: 1.100 µm/°C
Compliance: 0.003157 rad/Nm
Groove: 1.000 mm
Driver version: 45

Element definition:
ID 3: 2; CS; 0.5000 Pa; 10.00 Hz – 0.01000 Hz log; t ---; #6; T 32.00 °C;

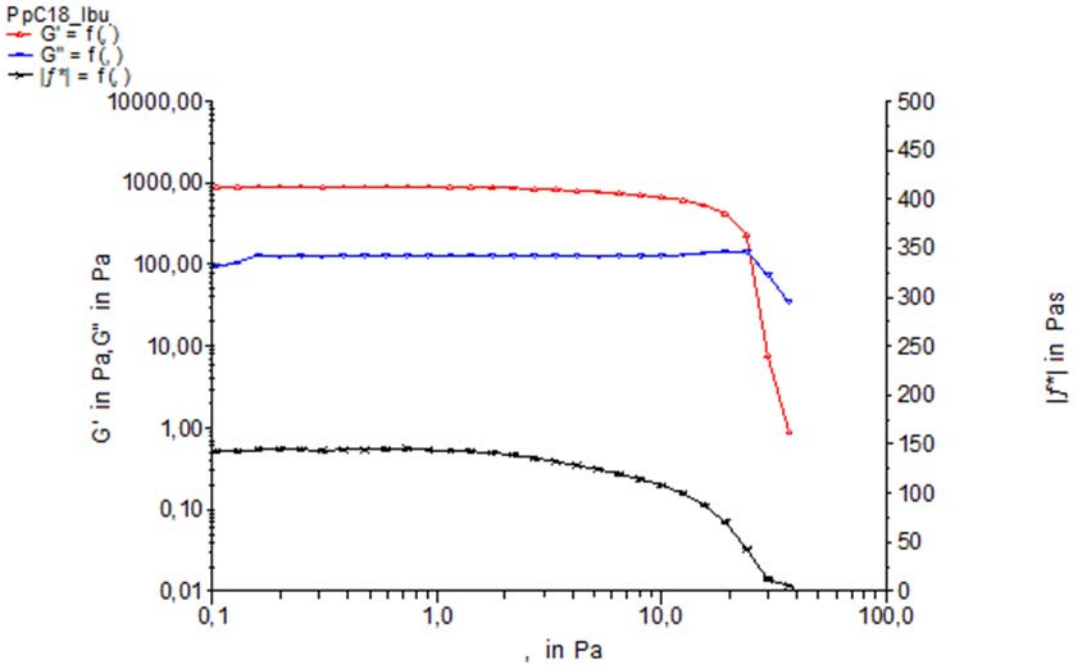

Fig. S3: Stress sweep of gel-**Ibu** in water-ethanol. G' (elastic or storage modulus), G" (viscous or loss modulus), and $|f^*|$ (viscosity) are defined as function of τ (shear stress).

Sensor: PP60 Ti
A Factor: 23580 Pa/Nm
M Factor: 29.979 (1/s)/(rad/s)
Inertia: 1.234e-05 kg m²
Damping: 30.00
Thermal expansion coefficient: 1.100 µm/°C
Compliance: 0.003157 rad/Nm
Groove: 1.001 mm
Driver version: 45

Element definition:
ID 2: 108; CS; 0.000 Pa; t < 300 s; ; T 32.00 °C <± 1.00 °C;
ID 8: 3; CS; 0.000 Pa – 500.0 Pa log; f 1.000 Hz; t ---; #50; T 32.00 °C;

Evaluation:
CROSSOVER: G' (storage modulus) = G" (loss modulus) = 173.3 Pa when Tau = 25.29 Pa

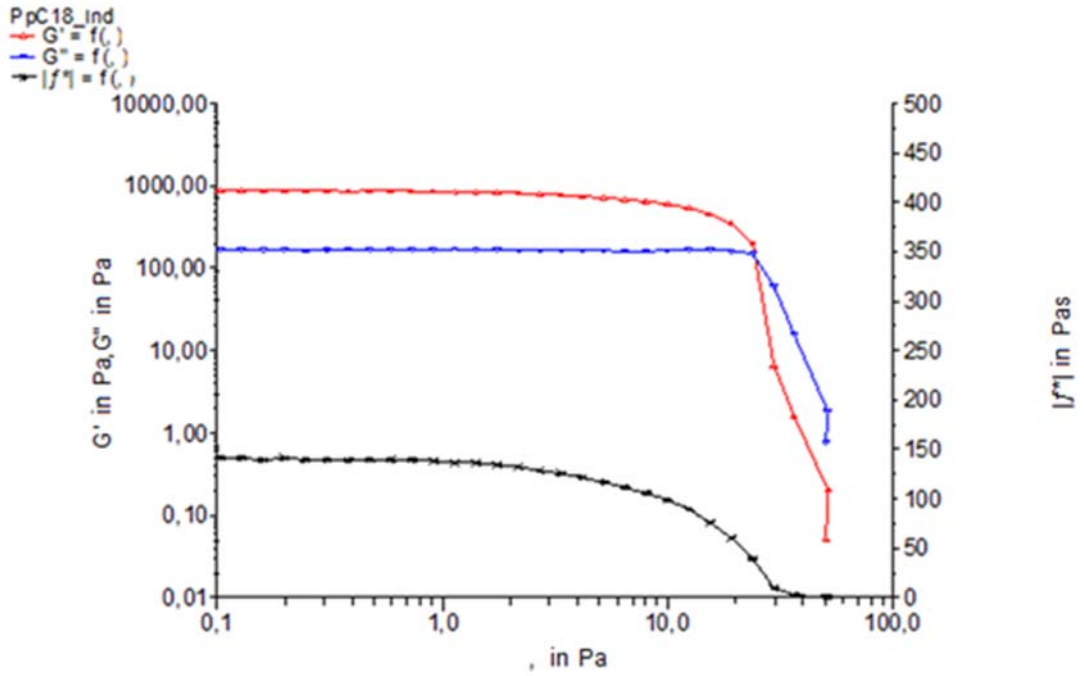

Fig. S4: Stress sweep of gel-**Ind** in water-ethanol. G' (elastic or storage modulus), G" (viscous or loss modulus), and |*f**| (viscosity) are defined as function of τ (shear stress).

Sensor: PP60 Ti
A Factor: 23580 Pa/Nm
M Factor: 29.979 (1/s)/(rad/s)
Inertia: 1.234e-05 kg m²
Damping: 30.00
Thermal expansion coefficient: 1.100 µm/°C
Compliance: 0.003157 rad/Nm
Groove: 1.001 mm
Driver version: 45

Element definition:
ID 2: 108; CS; 0.000 Pa; t < 300 s; ; T 32.00 °C <± 1.00 °C;
ID 8: 3; CS; 0.000 Pa – 500.0 Pa log; f 1.000 Hz; t ---; #50; T 32.00 °C;

Evaluation:
CROSSOVER: G' (storage modulus) = G" (loss modulus) = 165.3 Pa when Tau = 24.87 Pa

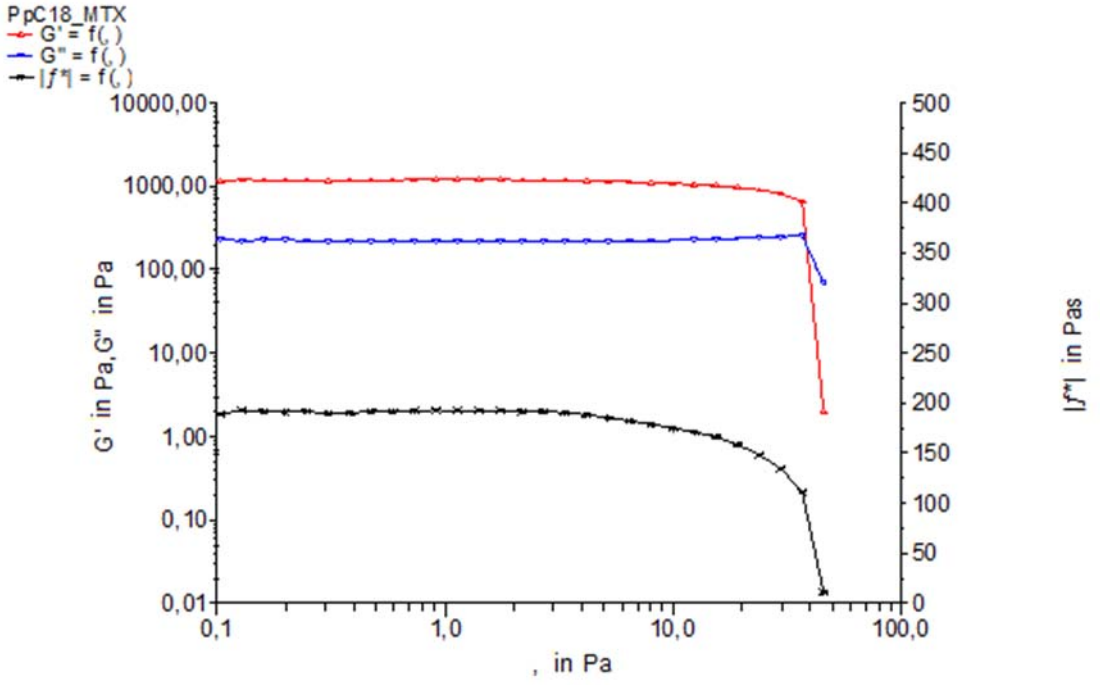

Fig. S5: Stress sweep of gel-**Mtx** in water-ethanol. G' (elastic or storage modulus), G" (viscous or loss modulus), and |*f**| (viscosity) are defined as function of τ (shear stress).

Sensor: PP60 Ti
A Factor: 23580 Pa/Nm
M Factor: 29.979 (1/s)/(rad/s)
Inertia: 1.234e-05 kg m²
Damping: 30.00
Thermal expansion coefficient: 1.100 µm/°C
Compliance: 0.003157 rad/Nm
Groove: 1.001 mm
Driver version: 45

Element definition:
ID 2: 108; CS; 0.000 Pa; t < 300 s; ; T 32.00 °C <± 1.00 °C;
ID 8: 3; CS; 0.000 Pa – 500.0 Pa log; f 1.000 Hz; t ---; #50; T 32.00 °C;

Evaluation:
CROSSOVER: G' (storage modulus) = G" (loss modulus) = 421.5 Pa when Tau = 39.96 Pa

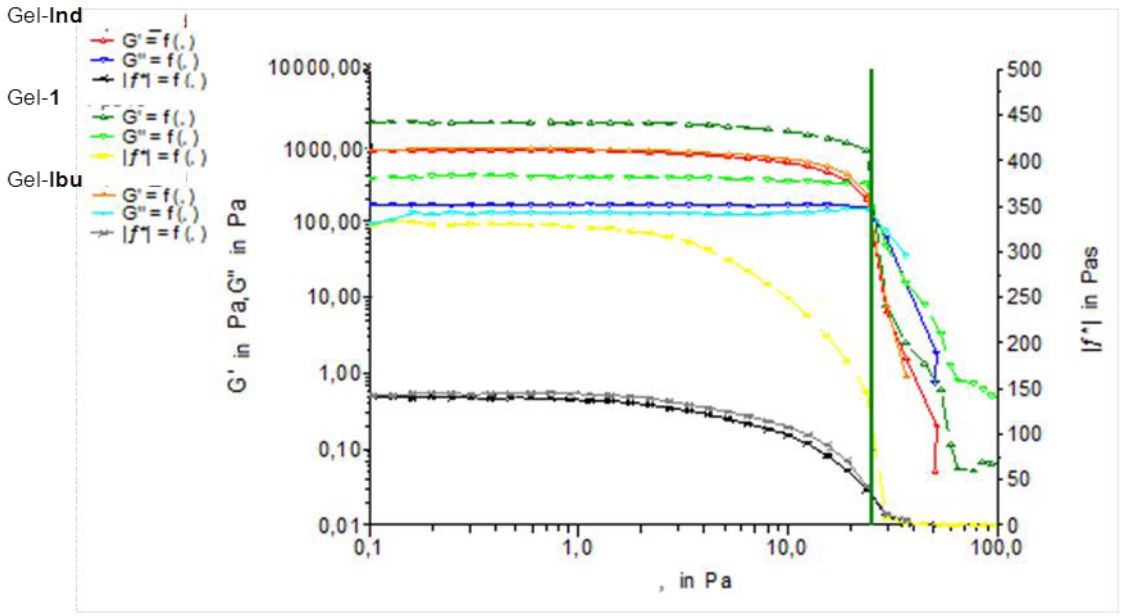

Fig. S6: Comparison of stress sweep of gel-1, gel-Ibu and gel-Ind in water-ethanol. G' (elastic or storage modulus), G" (viscous or loss modulus), and |f*| (viscosity) are defined as function of τ (shear stress). Green vertical line marks the crossover for gel-1.

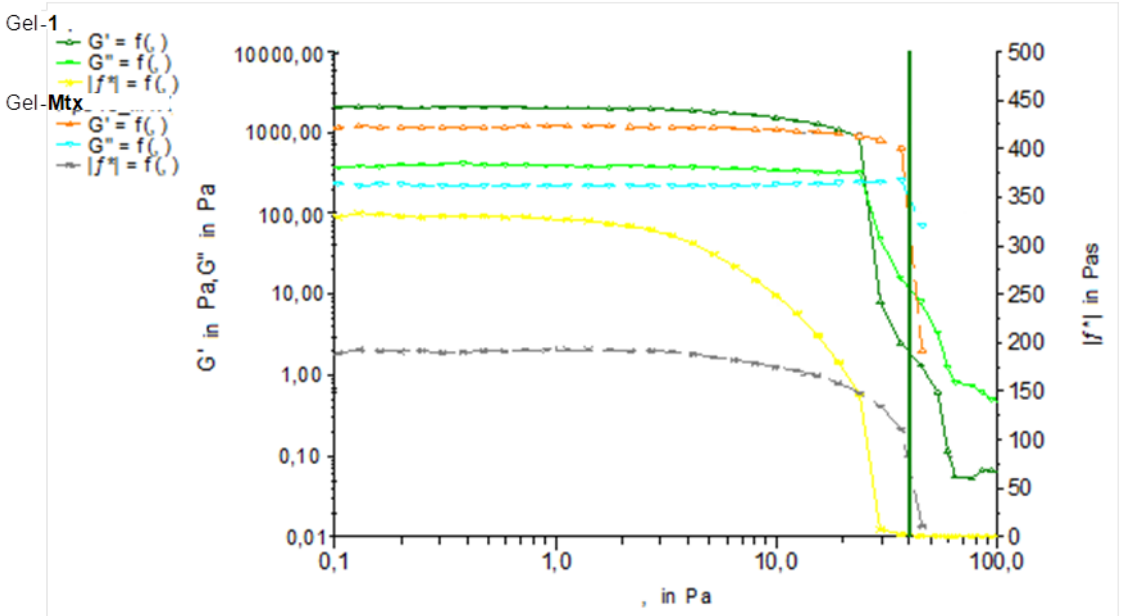

Fig. S7: Comparison of stress sweep of gel-**1** and gel-**Mtx** in water-ethanol. G' (elastic or storage modulus), G" (viscous or loss modulus), and |*f**| (viscosity) are defined as function of τ (shear stress). Green vertical line marks the crossover for gel-**Mtx**.

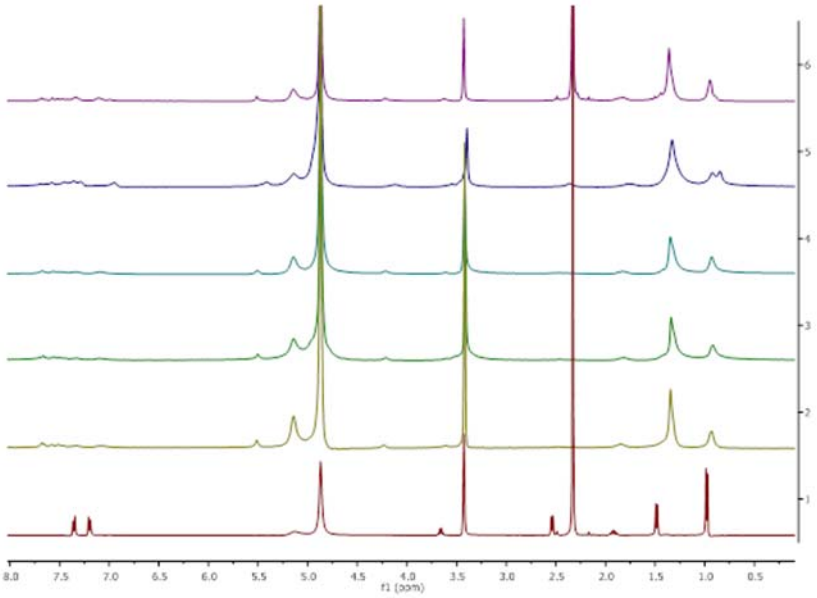

Fig. S8: ^{1}H NMR spectra of (1) sodium ibuprofenate in methanol/water (50:50) and of gel-**Ibu** containing increasing amounts of drug (2-6): **1**:ibuprofenate ratio (m/m) of 1:0.06; 1:0.08; 1:0.1; 1:0.15; 1:0.2.

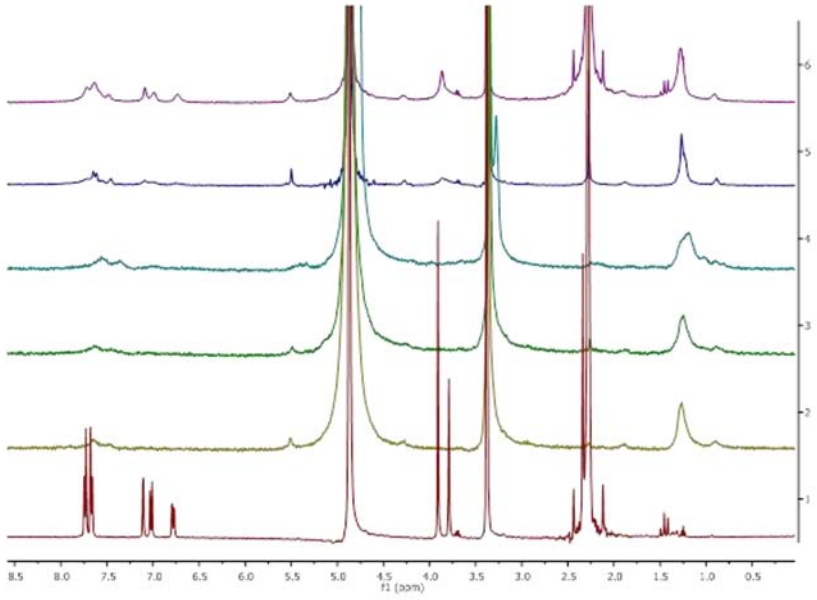

Fig. S9: ^{1}H NMR spectra of (1) indomethacin in methanol/water (50:50) and of gel-**Ind** containing increasing amounts of drug (2-6): **1**:indomethacin ratio (m/m) of 1:0.015; 1:0.030; 1:0.050; 1:0.10; 1:0.15.

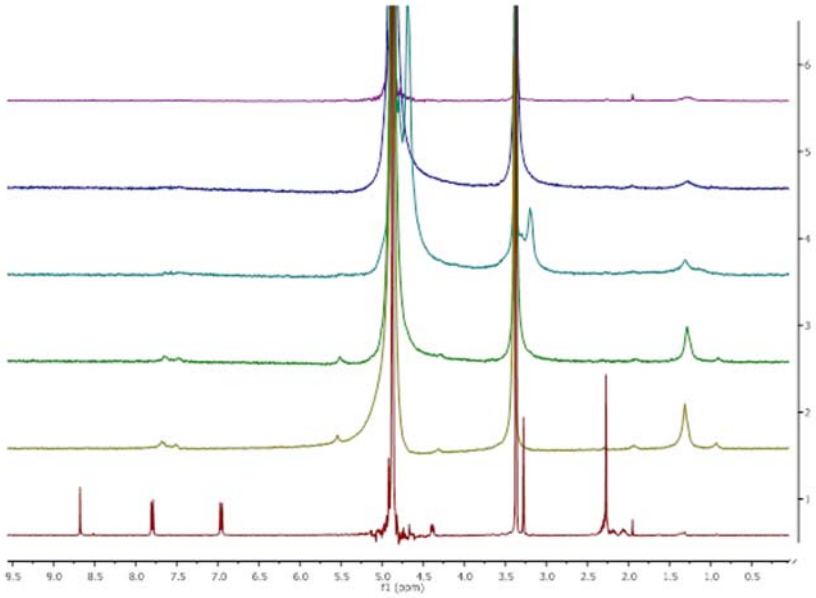

Fig. S10: ^{1}H NMR spectra of (1) methotrexate in methanol/water (50:50) and of gel-**Mtx** containing increasing amounts of drug (2-6): **1**:methotrexate ratio (m/m) of 1:0.011; 1:0.020; 1:0.040; 1:0.08; 1:0.10.

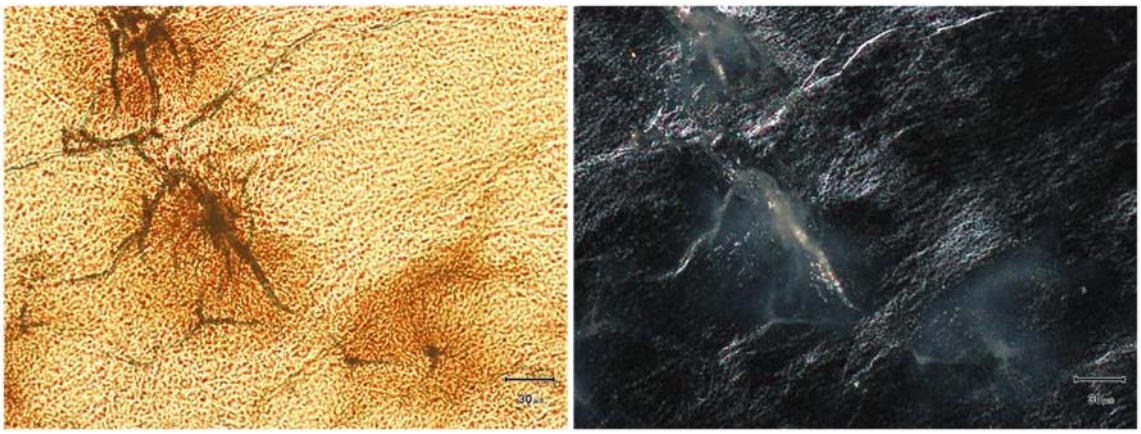

Fig. S.11: Optical microscopy photographs of gel-**1** in ethanol/water 35:65, taken with parallel polarisers and with crossed polarisers.

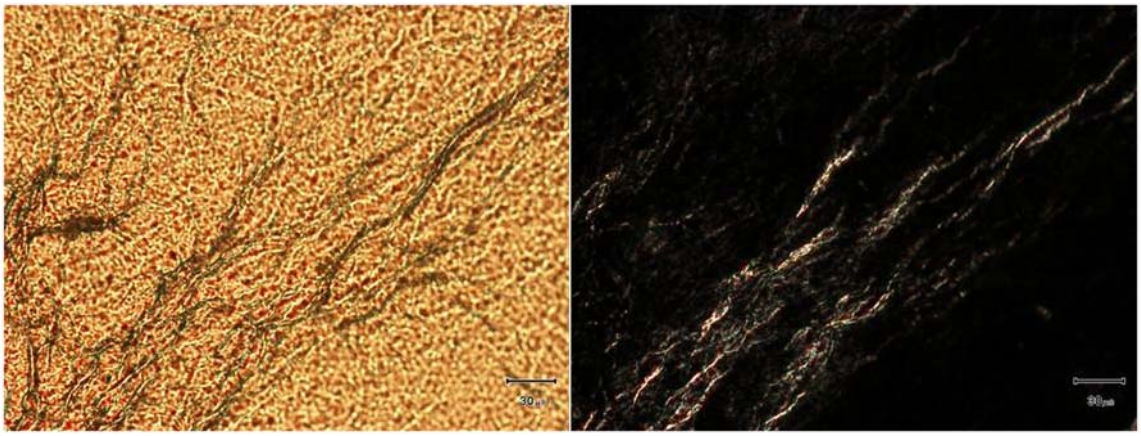

Fig. S.12: Optical microscopy photographs of gel-**1** in ethanol/water 45:55, taken with parallel polarisers and with crossed polarisers.

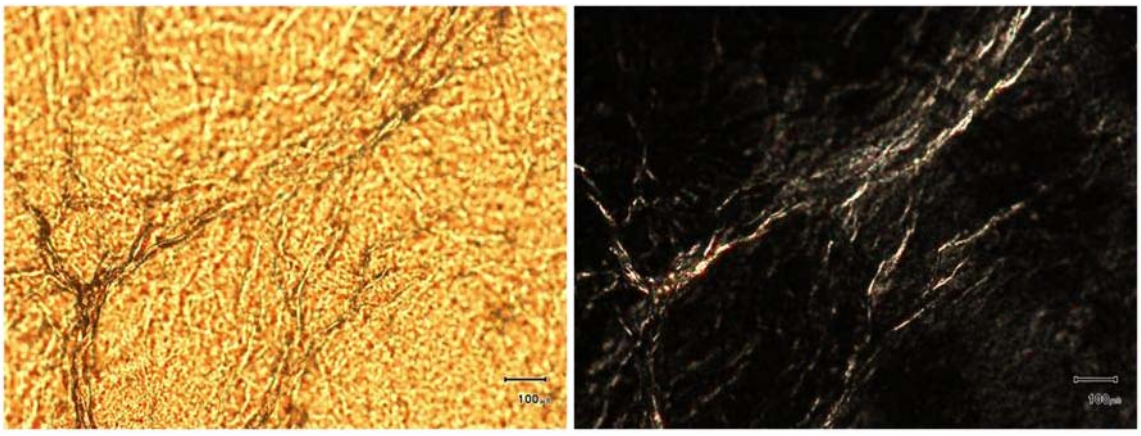

Fig. S.13: Optical microscopy photographs of gel-**1** in ethanol/water 50:50, taken with parallel polarisers and with crossed polarisers

.

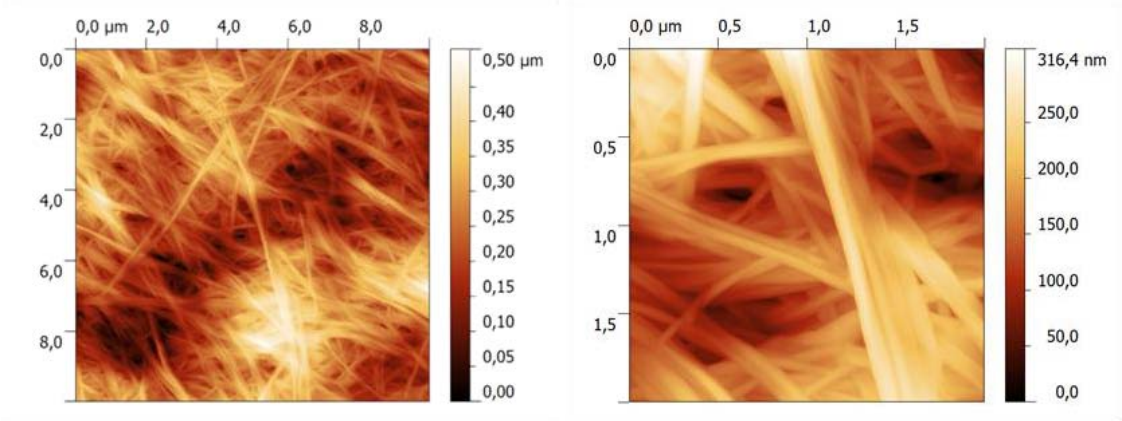

Fig. S.14: AFM image of gel-**1** in ethanol/water 40:60.

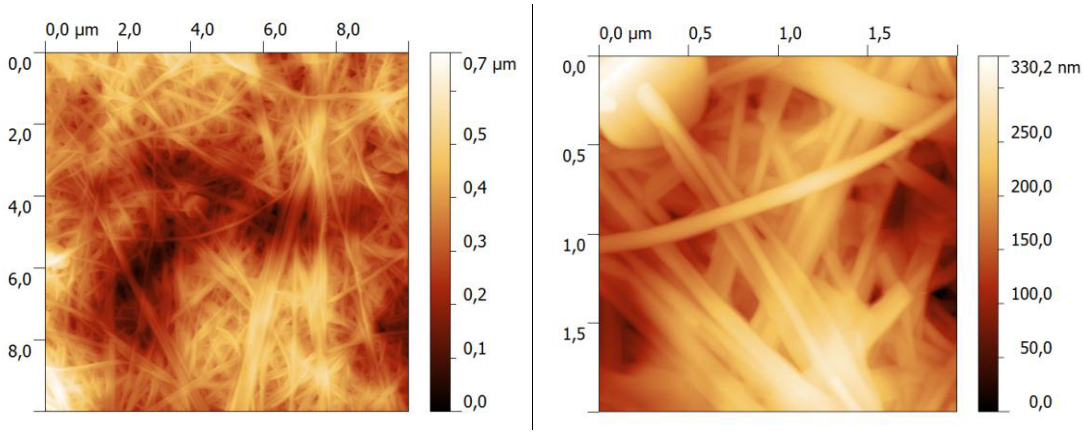

Fig. S.15: AFM image of gel-**1** in ethanol/water 45:55.

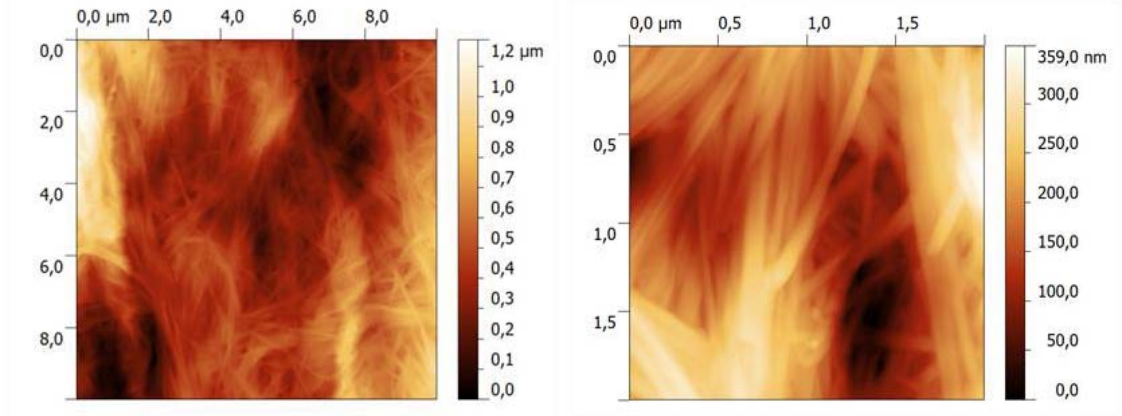

Fig. S.16: AFM image of gel-**1** in ethanol/water 50:50.

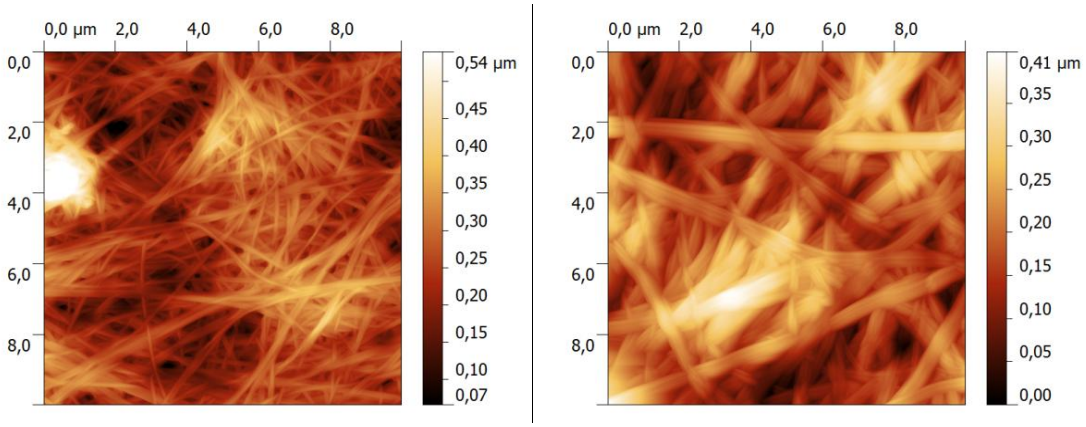

Fig. S.17: AFM image of gel-**Ibu** (10:1 w/w) (left) and gel-**Ibu** (10:2.5 w/w) (right) in ethanol/water 40:60.

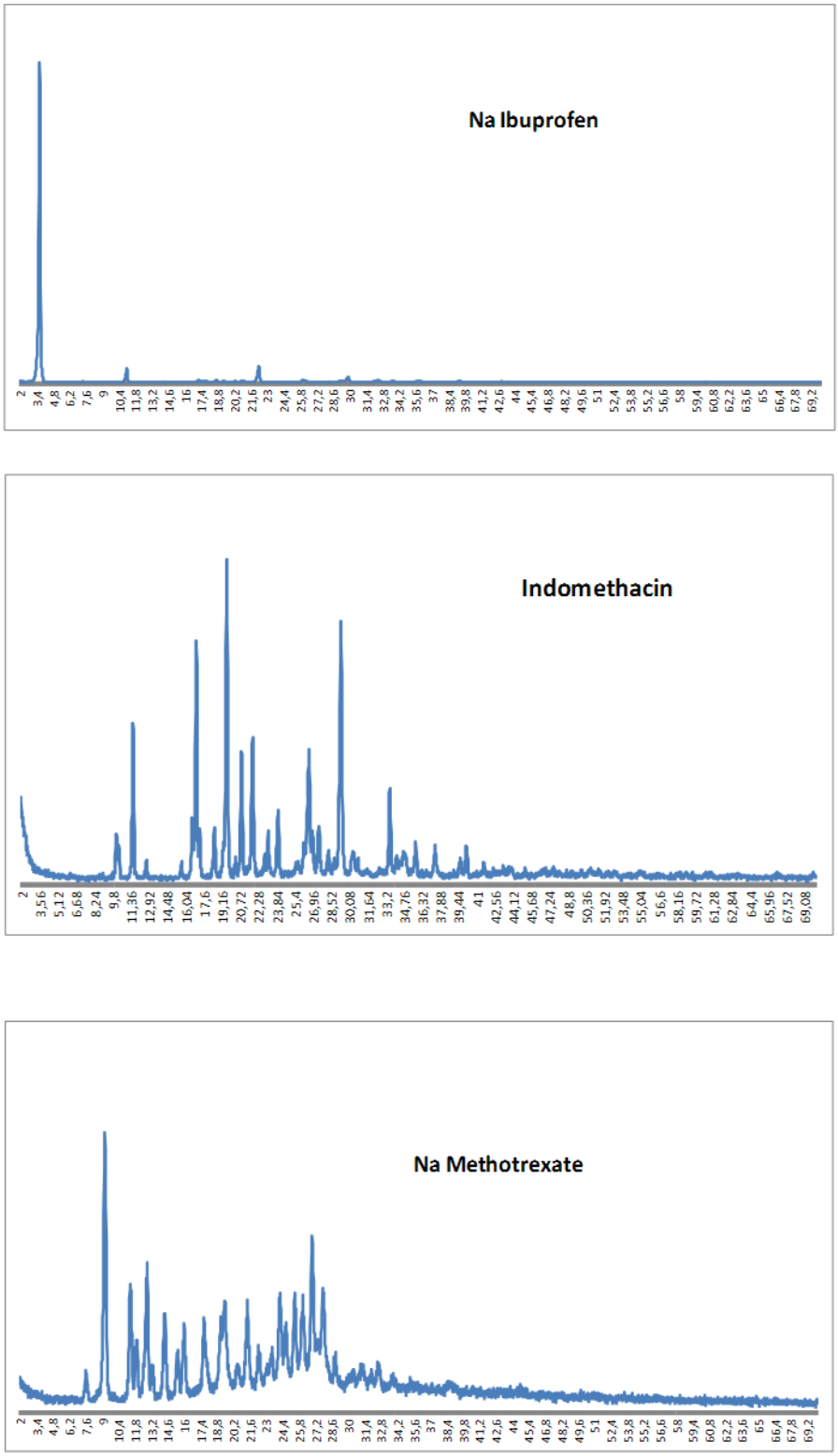

Fig. S18: X-ray powder diffractograms of sodium ibuprofenate (A), indomethacin (B), and sodium methotrexate (C).

Table S1: Kinetic models used to fit the data for the release of the different model drugs from the corresponding gel, and the respective AIC parameter:

Kinetic model	Equation	AIC		
		Gel-Ibu	Gel-Ind	Gel-Mtx
First Order	$Qt/Q\infty = 1-e^{-Kt}$	**11.30**	**15.67**	**8.29**
Higuchi	$Qt/Q\infty = K * t^{1/2}$	33.29	52.30	26.68
Korsmeyer-Peppas	$Qt/Q\infty = K*t^{n}$	35.29	47.75	9.61

Qt is the amount of drug released at time t
Q∞ is the total amount of drug released
Qt/Q∞ is the fraction of drug released at time t
K is the release rate constant
P is the Plateau (Q at t∞) and S is the Span (the difference between Q_0 and P)
n is the diffusion release exponent that could be used to characterize the different release mechanism ($n \leq 0.43$ (Fickian diffusion), $0.43 < n < 0.85$ (anomalous transport), and ≥ 0.85 (case II transport; i.e. zero order release)
t_d is the time in which the 63.2% of the drug is released and β is the shape parameter

2.4. *In situ* templated synthesis of gold nanoparticle using a bis-imidazolium amphiphile-based hydrogel

Manuscript in preparation

Mafalda Rodrigues,[ab] Aziz Genç,[c] Jordi Arbiol,[c,d] David B. Amabilino[c‡] and Lluïsa Pérez-García[ab]

a Department of Pharmacology and Therapeutic Chemistry, Universitat de Barcelona, Av. Joan XXIII, s/n, 08028 Barcelona, Spain. Fax: +34 934024539, Tel: +34 934035849

b Institut de Nanociencia i Nanotechnologia IN2UB, Universitat de Barcelona, 08028 Barcelona, Spain.

c Institut de Ciència de Materials de Barcelona (ICMAB-CSIC), Campus Universitari, 08193 Bellaterra, Spain.

d Institució Catalana de Recerca i Estudis Avançats (ICREA), Passeig Lluís Companys, Barcelona, Spain

‡ Present address: School of Chemistry, The University of Nottingham, University Park, Nottingham NG7 2RD, UK

Summary

The synthesis of GNP using the bis-imidazolium hydrogel was attempted. Examples in literature are found of the synthesis using a gel as template, and in some cases, the gelator itself causes the reduction of the gold from Au(III) to Au(0).[91] In this work, the imidazolium-based amphiphile gelator lacks reducing ability; therefore a sodium borohydride solution was added to reduce the gold. It was observed that, over a time span of 8 hours, the gel changed its colour from the initial yellow to a dark red tone, which indicated the formation of GNP.

To obtain the GNP in solution, the gel-GNP composite was disrupted through mechanical forces, and UV-visible absorption spectroscopy of the obtained solution showed the presence of the typical SPR peak in the spectrum, confirming that indeed GNP were obtained. The gel-templated GNP were further characterized by High Resolution Transmission Electron

Microscopy (HRTEM), that showed their icosahedral shape. Furthermore, the GNP obtained by templated synthesis showed lower size and monodispersion when comparing with the GNP obtained by synthesis in liquid phase with the same amphiphile.

It was found that the GNP were formed inside the gel fibbers, because AFM images show no evidence of the presence of GNP outside the fibbers. Cryo-TEM was used to observe the GNP in the gel fibbers, and the rheology of the gel was also assessed. An interesting finding is that the presence of the GNP inside the gel fibbers caused an improvement in the rheologic properties, with the gel containing the GNP being more viscous and more resistant to sheer stress comparing with the original gel without any nanoparticles or drugs.

In situ template synthesis of gold nanoparticle using a bis-imidazolium amphiphile-based hydrogel†

Mafalda Rodrigues,[ab]* Aziz Genç,[c] Jordi Arbiol,[c,d] David B. Amabilino[c‡] and Lluïsa Pérez-García[ab]

a Department of Pharmacology and Therapeutic Chemistry, Universitat de Barcelona, Av. Joan XXIII, s/n, 08028 Barcelona, Spain. Fax: +34 934024539, Tel: +34 934035849, E-mail: mafaldanunes@ub.edu
b Institut de Nanociencia i Nanotechnologia IN2UB, Universitat de Barcelona, 08028 Barcelona, Spain.
c Institut de Ciència de Materials de Barcelona (ICMAB-CSIC), Campus Universitari, 08193 Bellaterra, Spain.
d Institució Catalana de Recerca i Estudis Avançats (ICREA), Passeig Lluís Companys, Barcelona, Spain
‡ Present address: School of Chemistry, The University of Nottingham, University Park, Nottingham NG7 2RD, UK

Gold nanoparticles (GNP) with monodisperse sizes and well defined icosahedral geometry were synthesized in situ using a bis-imidazolium amphiphile-based hydrogel as template. Furthermore the gelator is also the stabilizing ligand of the GNP, which means that nanoparticles can be recovered by disassembling the gel without aggregation of the inorganic colloid.

In this paper we sought to develop an alternative medium for the formation of gold nanoparticles (GNPs) that could provide synthetic and structural versatility, and have found that this simple method can produce very well defined colloids, with improved size distribution, Furthermore, the bis-imidazolium gelator used is an ionophore,[1,2] meaning that, comparing with other examples in literature, the synthesized GNP can incorporate anions without further modification. NPs are the focus of increasing attention as drug delivery systems (DDS) with intense research being carried out in the last decade.[3,4] The most commonly used methods to obtain gold nanoparticles are the Brust-Schiffrin method,[5] in a biphasic system, where a thiol stabilizes the GNP, and the Turkevich method,[6] in aqueous solution, and the GNP are stabilized by the citrate anion through electrostatic interaction. However, alternative ligands used to stabilize GNPs are also viable, such as amines,[7] phosphines,[8] triazole ring-containing polymers,[9] and other polymers that may be synthetic[10] or extracts from natural sources,[11,12] amphiphiles that

both reduce and cap the GNP,[13,14] and imidazolium-based amphiphiles.[1]

Apart from the syntheses in solution, there have also been methods developed to obtain NPs of gold, and other metals, using gels as templates and a reducing agent, normally $NaBH_4$. For example, cobalt[15] and silver NPs, in hydrogels of pluronic,[16] chitosan,[17] or poly(acrylamide)/poly(ethylene glycol),[18] to name a few. Poly(ethylene oxide propylphosphonamidate) hydrogels were reported as being able to reduce anions of some metals, obtaining the respective NPs. The metals used were gold, silver, palladium, platinum and ruthenium.[19] Amphiphilic amino acid-based gelators[20,21] and oligopeptide gelators,[22] both also having the ability to reduce the gold ions and allowing the formation of GNPs. Some gels from amphiphilic derivatives based in urea[23] and in ascorbic acid[24] also proved to be able to reduce the gold ions *in situ* and stabilize the GNP. Furthermore, examples of gel formed by imidazolium-derived ionic liquids for the synthesis of GNP by irradiation with UV light were also found.[25] The gels act as template matrix, to control the size of the NP, but also prevent their aggregation. The NP included in the gel can form a composite with a defined function, as for example catalyst[19] or sensor[26] or antibacterial activity.[16]

In this work we describe the formation of GNPs using a newly reported hydrogel[27] of 1,3-bis[(3-octadecyl-1-imidazolio) methyl]benzene dibromide (**1·2Br**) (Fig. 1) as matrix, because this gelator is capable of binding drugs and therefore we envisage that the GNP modification could modulate this behaviour. The gel used as the template medium was formed by adding an ethanolic solution of the gelator **1·2Br** to an aqueous solution of $HAuCl_4$.

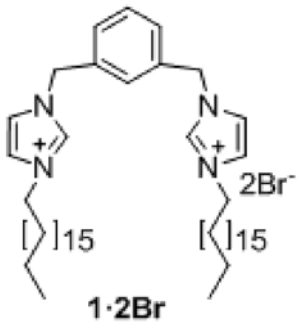

Figure 1: Structure of the gelator molecule 1·2Br

After the successful formation and aging of the gel, which took more than 24 hours, it had an appearance very similar to the gel with no gold salt even though the gelation process was much slower, and the remaining liquid not incorporated in the gel was removed. Then, an aqueous solution of $NaBH_4$ was added to the gel, to reduce the gold, and the mixture was allowed to stand. A clear change in the colour of the gel is visible 15 minute after addition of the reducing agent (Figure S1, ESI), whereby the initial yellow

colour was converted into a wine-red tone. After 8 hours, the $NaBH_4$ solution was removed and the resulting gel – that to the naked eye maintained its mechanical characteristics – was washed with water.

A rheological study was performed where the viscoelastic properties were determined through an oscillatory study, with a stress sweep test, in order to know if the GNP have any effect on the general viscous properties of the gel. Comparing with previously published results of the gel alone and containing different drugs,[27] we found that the gel with the GNP embedded and similar ethanol-water ratio (40:60) presents higher values of G' (elastic or storage modulus), G'' (viscous or loss modulus), and |η*| (viscosity) (see ESI Fig. S2), which means that they are more consistent. The crossover value, which corresponds to G' = G'', was found to be 1540 Pa, and this value is one order of magnitude higher when compared with the gel without GNP. The crossover occurs at a value of shear stress of 118,9 Pa, which is approximately four times higher, meaning that besides being more viscous, it also has more resistance to sheer stress. This means that the presence of GNP in the gel improves its rheological properties, which can open new applications besides the usage as matrix for the synthesis of the GNP.

Samples of the gels with the GNP were also observed by Atomic Force Microscopy (AFM). Two different areas of the gel were studied: one from the middle of the sample, and one from the edge of the gel, to see if there is any difference, because change of colour that indicates the formation of colloidal gold begins in the edges of the gel. Fig. 2 shows AFM images obtained from a sample taken from the central area of the gel.

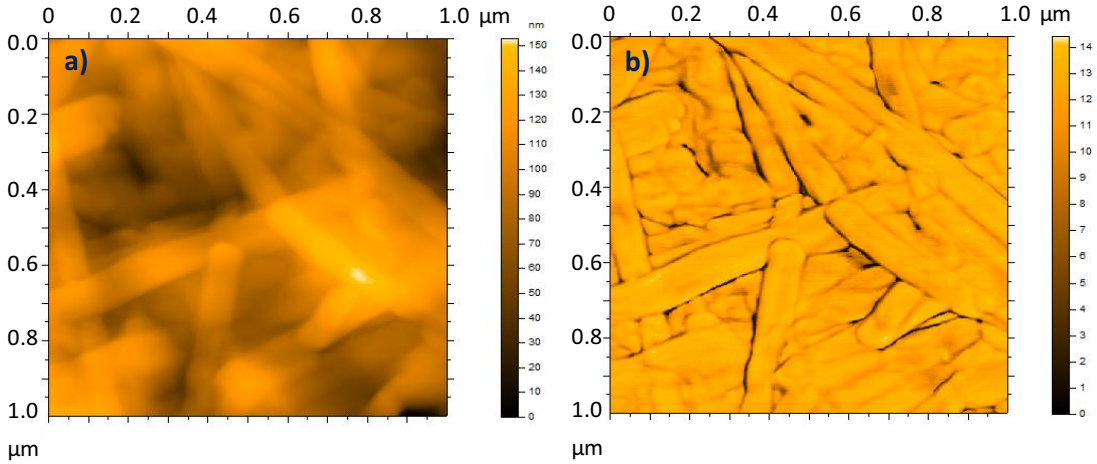

Figure 2: AFM topography image (a) and phase image (b) of a sample taken from the centre of the gel.

It is visible that no spherical formation, consistent with the presence of GNP, can be found in the surface of the gel fibbers. This can indicate that the GNP are found inside the nanostructure,

which would be consistent with the fact that drug incorporated in similar gels were found to be located inside the fibbers and not in the interstitial continuous phase (see also ESI Fig. S3-S5).

Transmission Electron Microscopy (TEM) of the whole assembly was performed using Freeze Fracture Direct Imaging,[28,29] to check if the GNP could be seen and also if it could indicate their location within the gel. Fig. 3 shows TEM images obtained of the gel. It can be clearly observed the presence of the GNP in the gel, confirming that the GNP cannot be observed by AFM on the surface of the gel, but that they are present, most likely contained inside the gel fibres. Furthermore, it appears that the GNP are widely distributed across the sample, in a fairly homogenous manner (see ESI Fig. S6).
The gel samples were destroyed through mechanical disruption to characterize the GNPs that were formed in this system. Water or dichloromethane were added, so that two different colloidal solutions could be obtained. This process is necessary (particularly for the transmission electron microscopic studies) to obtain a homogeneous sample that is not overly concentrated.
The dichloromethane solution was analysed by UV-visible absorption spectroscopy where the presence of the surface plasmon resonance (SPR) peak characteristic of the GNPs was observed at approximately 520 nm (see ESI, Fig. S7). Because of the low solubility of the gelator in water, the aqueous phase showed turbidity and a lower amount of nanoparticles when compared with the dichloromethane phase.

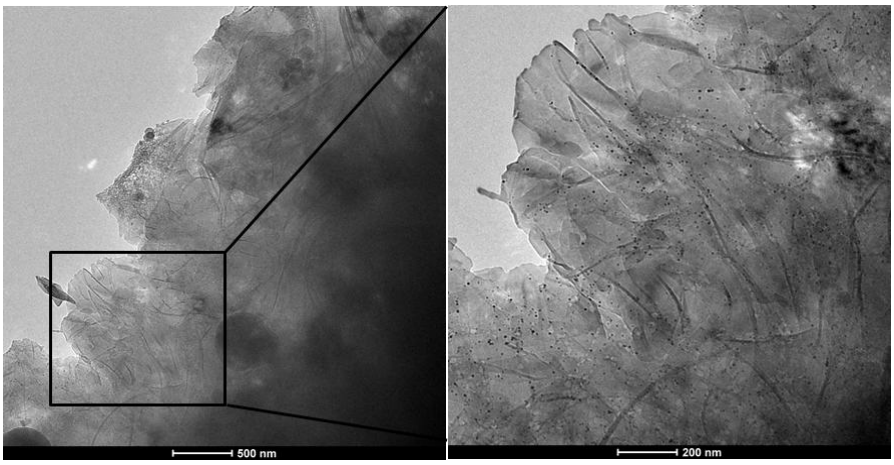

Figure 3: TEM micrograph of gel sample with GNP (top) and magnification of the marked area (bottom).

Furthermore X-ray photoelectron spectroscopy (XPS) was used to confirm the presence of gold in the reduced state. The spectrum (Fig. 4) shows the characteristic binding energies of Au0 at 88.2 and 84.5 eV corresponding to the double peaks of Au 4f5/2 and Au 4f7/2.

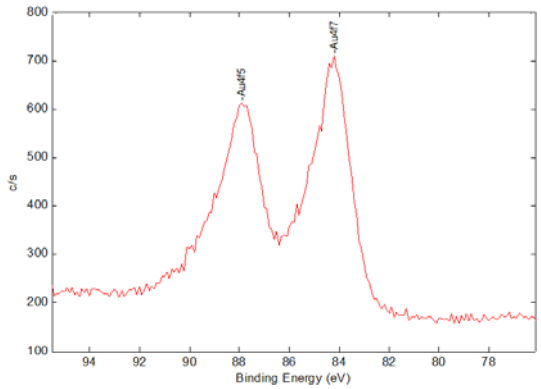

Figure 4: XPS spectrum showing the electron peaks with binding energy corresponding to Au^0.

Additionally, the samples of GNP re-suspended in dichloromethane were observed by High Resolution Transmission Electron Microscopy (HRTEM) which could afford a more accurate analysis of the geometry of the GNP.

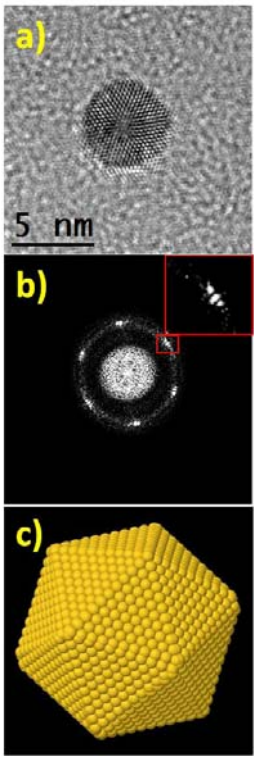

Figure 5: a) HRTEM micrograph, b) power spectrum and c) structural model of the icosahedral shape with relevant orientation.

For the fractions that were re-suspended in dichloromethane and deposited on TEM grids, the sample comprised nanoparticles with an average size of 5.4 ± 0.7 nm. HRTEM showed that the majority of the nanoparticles had faceted structure, and six different facets could be clearly observed (Fig. 5). Faceted nanoparticles have an icosahedral shape that is formed by twenty {111} facets.[30] The corresponding power spectra (FFTs) can also be seen in Fig. 5. It is also

noteworthy that single crystalline nanoparticles were occasionally observed as well, not spherical but containing the 6 facets. As seen in the power spectra, the spots form a ring shape (which corresponds to the {111} planes of face centered cubic Au structure) showing six more intense regions presenting three slightly mis-oriented spots. One of these triple-spot areas is highlighted as an inset figure in the upper power spectrum. This type of power spectrum is typical for icosahedron shape (see ESI Fig. 8).

In light of these findings, to assess if the template offers improvement regarding the size distribution and geometry of the synthesized GNP, we obtained the HRTEM images of previously prepared GNPs, synthesized with the same bis-imidazolium ligand. These samples were synthesized in solution with homogeneous reaction conditions, without a fibrillar pre-formed template, following two different methods that conferred to the GNP different solubility: in biphasic system,[1] which allowed obtaining GNP soluble in organic media, and water-soluble GNP obtained in aqueous solution.[31] HRTEM images showed that in general, the GNP prepared in solution presented bigger average sizes and standard deviation, indicating more dispersion of sizes, and also different geometric shapes were found (spheroid, tetrahedral and icosahedral) (Fig. 6).

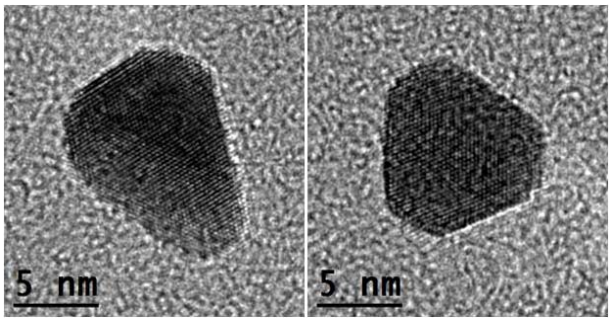

Figure 6: HRTEM micrograph showing different geometries found in water-soluble GNP synthesized in aqueous solution: 4-twinned spheroidal nanoparticle (left) and tetrahedra (right).

The gold core sizes found were 12 ± 0.8 and 7.2 ± 0.7 for the GNP synthesized in organic medium (Fig.S9, ESI), and much more disperse (5-25 nm) in the case of GNP synthesized in water (Fig.S10, ESI). These findings indicate clearly that the disposition of the imidazolium ligand in fibres favours one type of geometry, also acting as template to obtain a more homogeneous size distribution.

The corresponding 3D structural models of the icosahedron shape with the same orientation as the HRTEM micrographs can also be appreciated in Fig S11 (see ESI). The model was obtained using the Rhodius on-line software package,[32] and was created with ~5.7 nm icosahedron shape that contains 5195 atoms. The created 3D models perfectly match the experimental nanoparticles.

It can therefore be concluded that the bis-imidazolium amphiphilic-based hydrogel appears a good candidate for the *in situ* templated synthesis of GNPs with homogeneous size and geometry, representing an improvement to the previous methods in solution.[1,31] Additionally, the bis-imidazolium gelator which acts as stabilizer of the GNP has the ability to recognize and incorporate anions, giving an additional feature to these GNP. It was also observed that the GNPs are synthesized within the fibbers of the gel, which is responsible for improving the resistance of the gel, meaning that the GNP-embedded gel may be a material with interesting properties and applications besides just acting as template. An interesting study to follow up these promising results would be to determine if the GNP-containing gel maintains the capacity to load drugs and what effect the metal colloid has on the release properties.

Acknowledgements

This study was supported by a grant from the *Ministerio de Ciencia e Innovación* (MICINN) (project TEC2011-29140-C03-02). The authors thank Judith Oró and Maite Simón (Scientific Experimental Platforms, ICMAB-CSIC) for their help with the SEM and AFM measurements, respectively, and Carmen Iglésias (CCiTUB) for the TEM images.

Notes and References

1. L. Casal-Dujat, M. Rodrigues, A. Yagüe, A. C. Calpena, D. B. Amabilino, J. González-Linares, M. Borràs and L. Pérez-García, *Langmuir*, 2012, **28**, 2368–2381.
2. E. Amirthalingam, M. Rodrigues, L. Casal-Dujat, A. C. Calpena, D. B. Amabilino, D. Ramos-López and L. Pérez-García, *J. Colloid Interface Sci.*, 2014, DOI: 10.1016/j.jcis.2014.09.026S.
3. Rana, A. Bajaj, R. Mout and V. M. Rotello, *Adv. Drug Deliv. Rev*., 2012, **64**, 200–216.
4. A. Llevot and D. Astruc, *Chem. Soc. Rev*., 2012, **41**, 242–257.
5. M. Brust, M. Walker, D. Bethell, D. J. Schiffrin and R. Whyman, *J. Chem. Soc. Chem. Commun*., 1994, 801–802.
6. J. Turkevich, P. C. Stevenson and J. Hillier, *Discuss. Faraday Soc*., 1951, **11**, 55–75.
7. M. Aslam, L. Fu, M. Su, K. Vijayamohanan and V. P. Dravid, *J. Mater. Chem*., 2004, **14**, 1795–1797.
8. W. Weare and S. Reed, *J. Am. Chem. Soc*., 2000, **122**, 12890–12891.
9. N. Li, P. Zhao, N. Liu, M. Echeverria, S. Moya, L. Salmon, J. Ruiz and D. Astruc, *Chem. Eur. J.*, 2014, **20**, 1–8.
10. R. Bleach, B. Karagoz, S. M. Prakash, T. P. Davis and C. Boyer, *ACS Macro Lett*., 2014, **3**, 591–596.

11. R. Shukla, S. K. Nune, N. Chanda, K. Katti, S. Mekapothula, R. R. Kulkarni, W. V Welshons, R. Kannan and K. V Katti, *Small*, 2008, **4**, 1425–1436.
12. S. K. Nune, N. Chanda, R. Shukla, K. Katti, R. R. Kulkarni, S. Thilakavathi, S. Mekapothula, R. Kannan and K. V Katti, *J. Mater. Chem*., 2009, **19**, 2912–2920.
13. S. Si, E. Dinda and T. K. Mandal, *Chem. Eur. J*., 2007, **13**, 9850–9861.
14. C. Tu, G. Li, Y. Shi, X. Yu, Y. Jiang, Q. Zhu, J. Liang, Y. Gao, D. Yan, J. Sun and X. Zhu, *Chem. Commun*., 2009, 3211–3213.
15. N. Sahiner, H. Ozay, O. Ozay and N. Aktas, *Appl. Catal. B Environ*., 2010, **101**, 137–143.
16. S. Park, P. S. K. Murthy, S. Park, Y. M. Mohan and W.-G. Koh, *J. Ind. Eng. Chem*., 2011, **17**, 293–297.
17. G. Li, Q. Wen, T. Zhang and Y. Ju, *J. Appl. Polym. Sci*., 2013, **127**, 2690–2697.
18. Y. Murali Mohan, K. Vimala, V. Thomas, K. Varaprasad, B. Sreedhar, S. K. Bajpai and K. Mohana Raju, *J. Colloid Interface Sci*., 2010, **342**, 73–82.
19. L. Zhang, S. Zheng, D. E. Kang, J. Y. Shin, H. Suh and I. Kim, *RSC Adv*., 2013, **3**, 4692–4703.
20. R. N. Mitra and P. K. Das, *J. Phys. Chem. C*, 2008, **112**, 8159–8166.
21. T. Kar, S. Dutta and P. K. Das, *Soft Matter*, 2010, **6**, 4777–4787.
22. S. Ray, A. K. Das and A. Banerjee, *Chem. Commun*., 2006, 2816–2818.
23. P. K. Vemula and G. John, *Chem. Commun*., 2006, 2218–2220.
24. P. K. Vemula, U. Aslam, V. A. Mallia and G. John, *Chem. Mater*., 2007, **19**, 138–140.
25. M. A. Firestone, M. L. Dietz, S. Seifert, S. Trasobares, D. J. Miller and N. J. Zaluzec, *Small*, 2005, **1**, 754–760.
26. A. Baeissa, N. Dave, B. D. Smith and J. Liu, *ACS Appl. Mater. Interfaces*, 2010, **2**, 3594–600.
27. M. Rodrigues, A. C. Calpena, D. B. Amabilino, M. L. Garduño-Ramírez and L. Pérez-García, *J. Mater. Chem. B*, 2014, **2**, 5419–5429.
28. L. Belkoura, C. Stubenrauch and R. Strey, *Langmuir*, 2004, **20**, 4391–4399.
29. V. Agarwal, M. Singh, G. McPherson, V. John and A. Bose, *Langmuir*, 2004, **20**, 11–15.
30. J. Wu, L. Qi, H. You, A. Gross, J. Li and H. Yang, *J. Am. Chem. Soc*., 2012, **134**, 11880–11883.
31. M. Rodrigues, A. C. Calpena, D. B. Amabilino, D. Ramos-López, J. de Lapuente and L. Pérez-García, *RSC Adv*., 2014, **4**, 9279–9287.
32. S. Bernal, F. J. Botana, J. J. Calvino, C. López-Cartes, J. A. Pérez-Omil and J. M. Rodríguez-Izquierdo, *Ultramicroscopy*, 1998, **72**, 135–164.

Electronic Supplementary Information

In situ templated synthesis of gold nanoparticle using a bis-imidazolium amphiphile-based hydrogel

Mafalda Rodrigues,[a,b] Aziz Genç,[c] Jordi Arbiol,[c,d] David B. Amabilino[c‡] and Lluïsa Pérez-García[a,b,*]

a Department of Pharmacology and Therapeutic Chemistry, Universitat de Barcelona, Av. Joan XXIII, s/n 08028 Barcelona, Spain. Fax: +34 934024539, Tel: +34 934035849, E-mail: mafaldanunes@ub.edu

b Institute of Nanoscience and Nanotechnology IN2UB, Universitat de Barcelona, 08028 Barcelona, Spain.

c Institut de Ciència de Materials de Barcelona (ICMAB-CSIC), Campus Universitari, 08193 Bellaterra, Spain.

d Institució Catalana de Recerca i Estudis Avançats (ICREA), Passeig Lluís Companys, Barcelona, Spain

‡ Present address: School of Chemistry, The University of Nottingham, University Park, Nottingham NG7 2RD, UK

Experimental Procedure

All reagents were of analytical grade. Compound 1,3-bis[(3-octadecyl-1-imidazolio)methyl]benzene dibromide (**1**) was prepared as reported previously.[92]

The gels were prepared as follows:

Gels A1 and B1 (with a molar ratio **1·2Br**:Au of 10:1) were prepared with 10 mg of **1·2Br** dissolved in 0.8 mL of ethanol and 0.7 mL of ethanol (respectively). Then, 216 μL of a 2 mg mL^{-1} aqueous solution of $HAuCl_4.3H_2O$ was added and the volume was completed with MilliQ water until a final volume of 2 mL.

Gels A2 and B2 (with a molar ratio **1·2Br**:Au of 8:1) were prepared with 10 mg of **1·2Br** dissolved in 0.8 mL of ethanol and 0.7 mL of ethanol (respectively). Then, 270 μL of a 2 mg mL^{-1} aqueous solution of $HAuCl_4.3H_2O$ was added and the volume was completed with MilliQ water until a final volume of 2 mL.

The gels were left overnight for proper aging, because the gelling process occurred slowly. To prepare the GNP, 12 equivalents (with respect to Au^{3+}) of an aqueous solution of $NaBH_4$ were added to the gels, in a final volume of 2.5 mL. The solution was left in contact with the gels for 8 hours, then it was removed and the gels were washed with water.

UV absorption spectra were obtained on UV-1800 Shimadzu UV Spectrophotometer.

XPS experiments were performed at the *Centres Científics i Tecnològics de la Universitat de Barcelona* (CCiTUB), in a PHI 5500 Multitechnique System (from Physical Electronics) with a monochromatic X-ray source (Aluminium Kalfa line of 1486.6 eV energy and 350 W), placed perpendicular to the analyzer axis and calibrated using the 3 $d_{5/2}$ line of Ag with a full width at half maximum (FWHM) of 0.8 eV. The analyzed area was a circle of 0.8 mm diameter, and the selected resolution for the spectra was 187.5 eV of Pass Energy and 0.8 eV/step for the general spectra and 23.5 eV of Pass Energy and 0.1 eV/step for the spectra of the different elements. All Measurements were made in an ultra high vacuum (UHV) chamber pressure between $5 \cdot 10^{-9}$ and $2 \cdot 10^{-8}$ torr.

High Resolution Transmission Electron Microscopy images were performed at the Group of Advanced Electron Nanoscopy (GAeN) of the Institut de Ciència de Materials de Barcelona (ICMAB-CSIC).

AFM images were recorded by the Scanning Probe Microscopy Service in the ICMAB-CSIC on a PicoSPM system (Molecular Imaging). The intermittent contact mode was used close to resonance frequencies of the silicon cantilevers (Nanosensors, FM type force constant 1.2-3.5 N/m and tip diameter 5 nm) of around 60-70 kHz. All the images were recorded under atmospheric conditions.

Transmission Electron Microscopy using Freeze Fracture Direct Imaging was performed as follows: the sample was sandwiched between two copper platelets using a glow-discharged holey carbon grid as spacer. Then, the samples were frozen by liquid ethane immersion, and fractured later into liquid nitrogen. The grid with the fractured sample was transferred to a microscope Tecnai F20 (FEI Company, Eindhoven, Netherlands) using a Gatan cryo-holder (Gatan, Pleasanton, CA). The images were taken at 200 Kv with a 4096x4096 pixel CCD Eagle camera (FEI Company, Eindhoven, Netherlands) at a temperature between -170ºC and -175ºC and using low-dose imaging conditions.

The rheological study of the flow behaviour was performed with a HAAKE Rheostress1 rheometer (Thermo Fisher Scientific, Karlsruhe, Germany) connected to a Thermo Haake Phoenix II + Haake C25P temperature controller. The rheological studies carried out on freshly prepared sample included. The rheometer was equipped with a cone-plate geometry set-up with a fixed lower plate and a mobile upper cone (Haake C60, 2º 60 mm diameter, 0.106 mm) and also a plate-plate geometry (PP60 Ti, 60 mm diameter, 0.5 mm gap between plates). The rheometer was connected to a computer provided with the software HAAKE RheoWin®Job Manager V.3.3 to carry out the test and RheoWin®Data Manager V.3.3 (Thermo Electron Corporation, Karlsruhe, Germany) to carry out the analysis of the obtained data. Viscosity curves and flow curves were recorded under rotational runs at 32 ºC for 3 min during the ramp-up period from 0 to 100 s^{-1}, 1 min at 100 s^{-1} (constant share rate period) and finally 3 min during the ramp-down period from 100 to 0 s^{-1}.

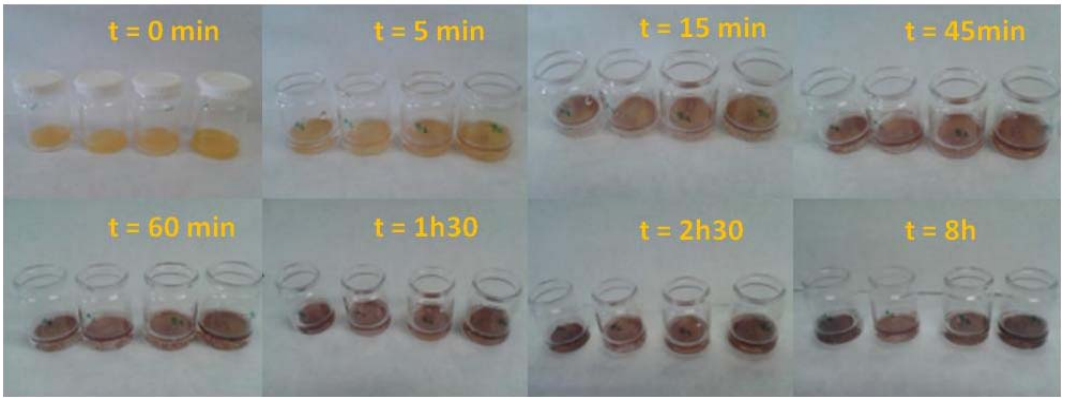

Figure S1: Gels with HAuCl4 before (t=0 minutes) and after the adition of NaBH4 at different times.

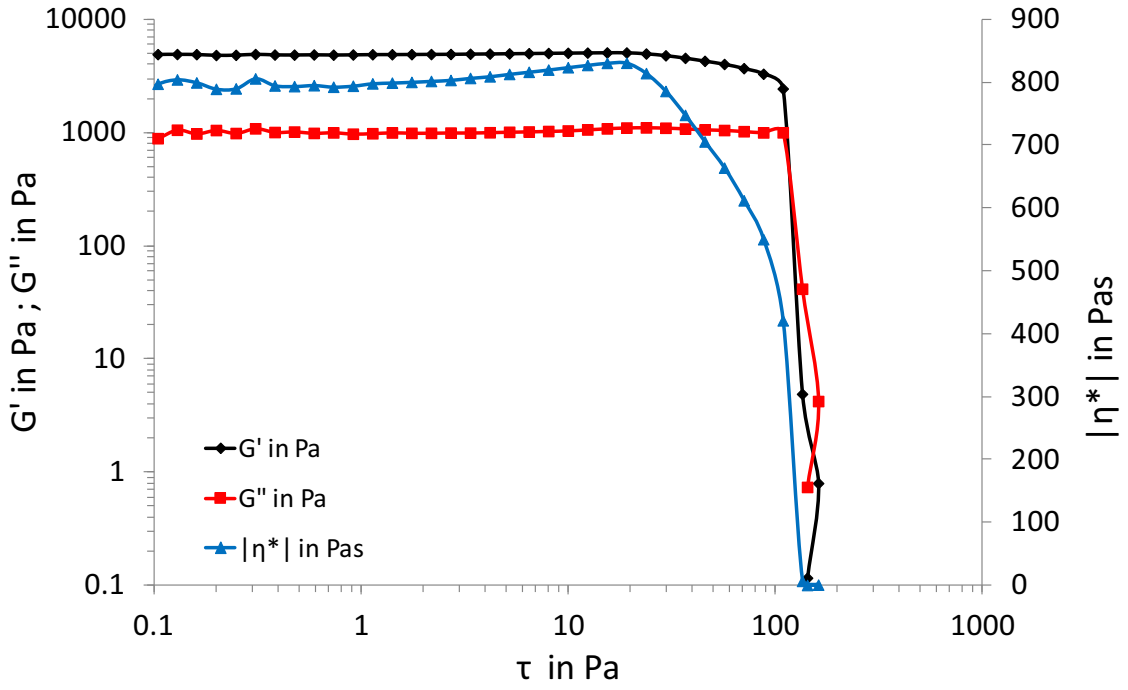

Figure S2: Stress sweep of gel-1 in water-ethanol. G' (elastic or storage modulus), G" (viscous or loss modulus), and |η*| (viscosity) are defined as function of τ (shear stress).

Sensor: PP60 Ti
A Factor: 23580 Pa/Nm
M Factor: 29.979 (1/s)/(rad/s)
Inertia: 1.234e-05 kg m²
Damping: 30.00
Thermal expansion coefficient: 1.100 µm/°C
Compliance: 0.003157 rad/Nm
Groove: 1.001 mm
Driver version: 45

Element definition:

ID 2: 108; CS; 0.000 Pa; t < 300 s; ; T 32.00 °C <± 1.00 °C;
ID 8: 3; CS; 0.000 Pa – 500.0 Pa log; f 1.000 Hz; t ---; #50; T 32.00 °C;

Evaluation:

CROSSOVER: G' (storage modulus) = G" (loss modulus) = 1540 Pa when Tau = 118,9 Pa

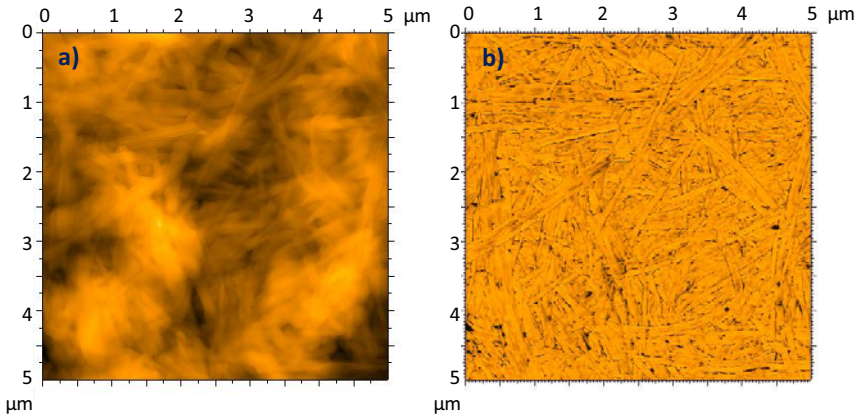

Figure S3: AFM topography image (a) and phase image (b) of a sample taken from the centre of the gel.

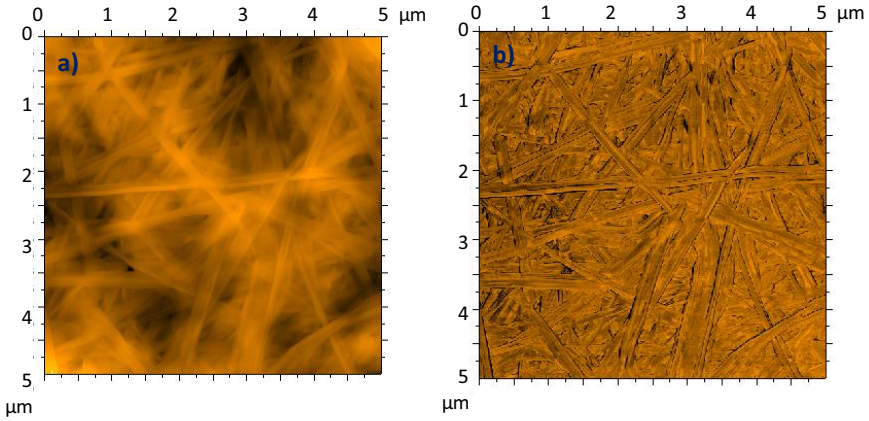

Figure S4: AFM topography image (a) and phase image (b) of a sample taken from the edge of the gel.

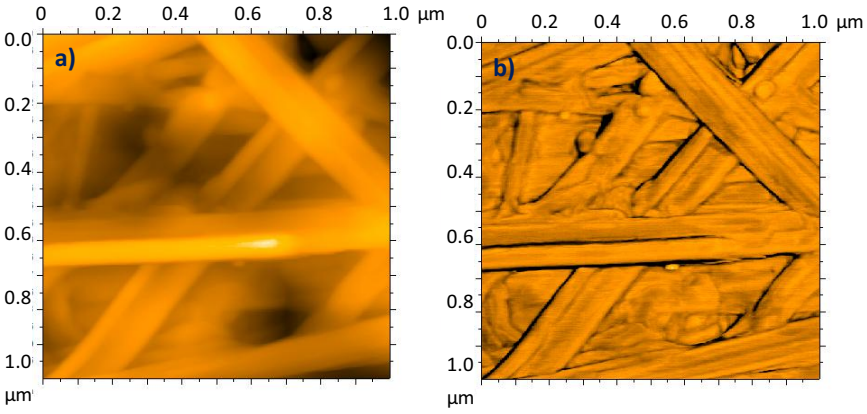

Figure S5: AFM topography image (a) and phase image (b) of a sample taken from the edge of the gel.

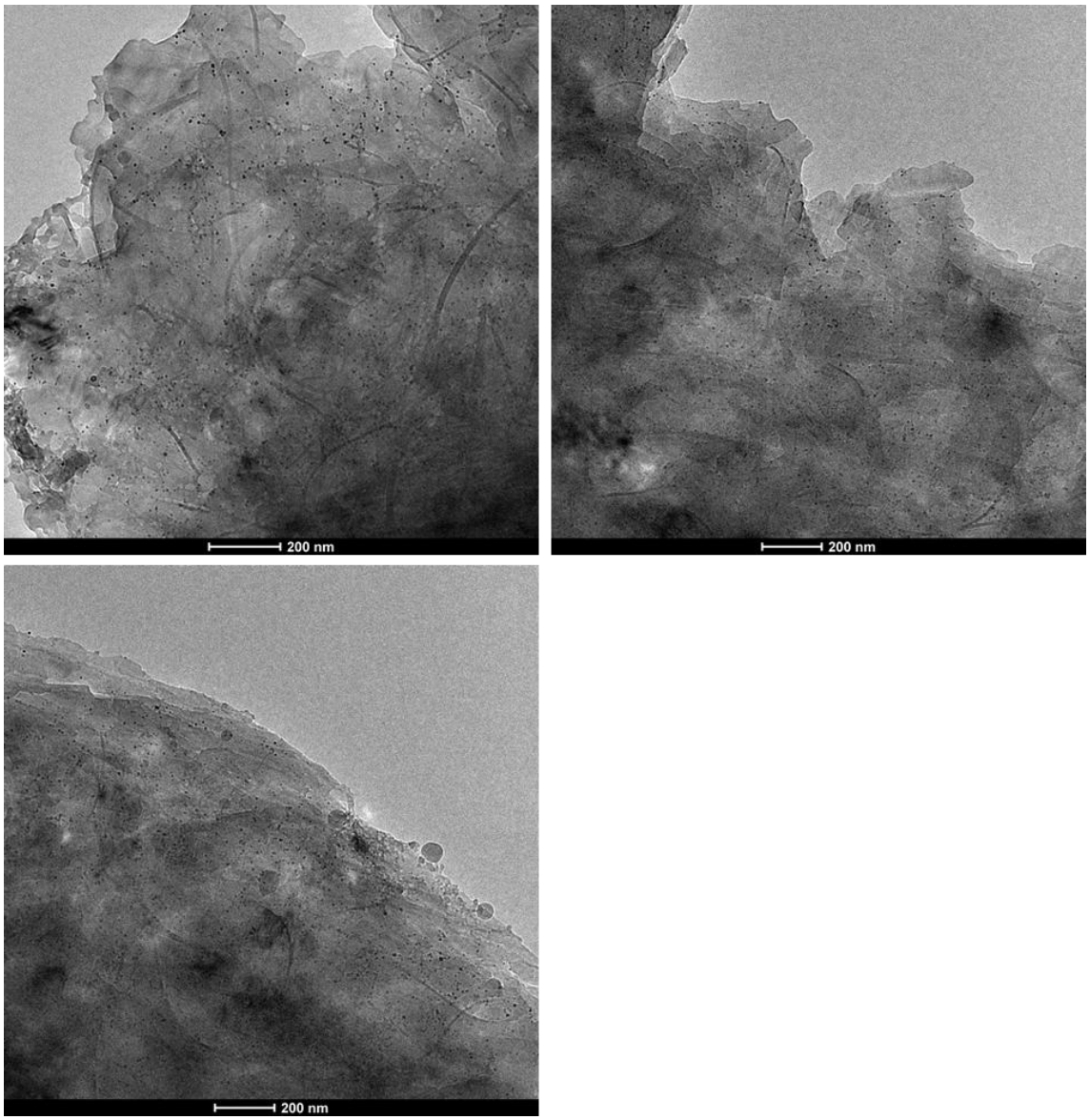

Figure S6: TEM micrographs of the GNP distributed within the gel.

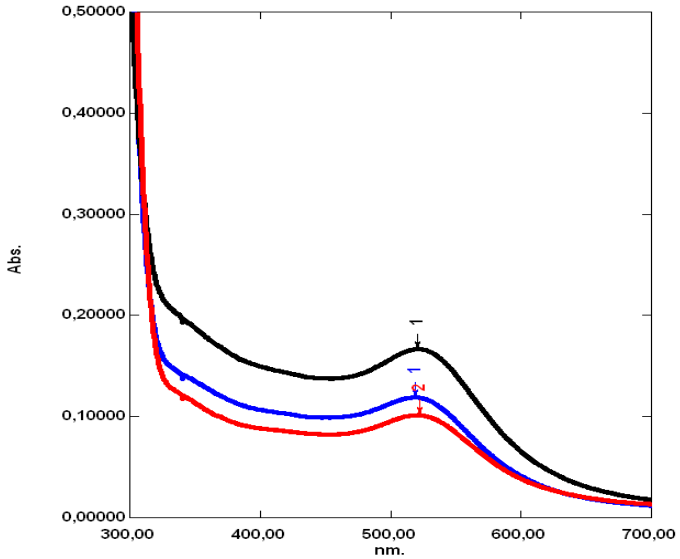

Figure S7: UV-visible absorption spectrum showing the typical SPR peak of the GNP solutions: A1 (black), B1 (red) and A2 (blue).

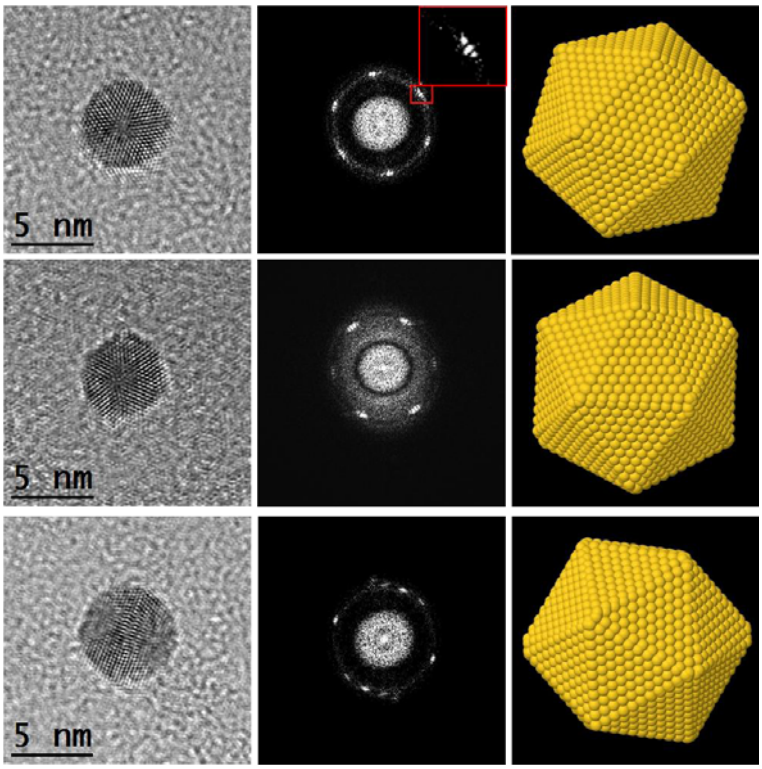

Figure S8: HRTEM micrographs and their corresponding power spectra (FFTs). On the right, structural 3D atomic models of the icosahedral morphology. Notice that the orientation of the models corresponds to the one of the experimental GNPs on the left.

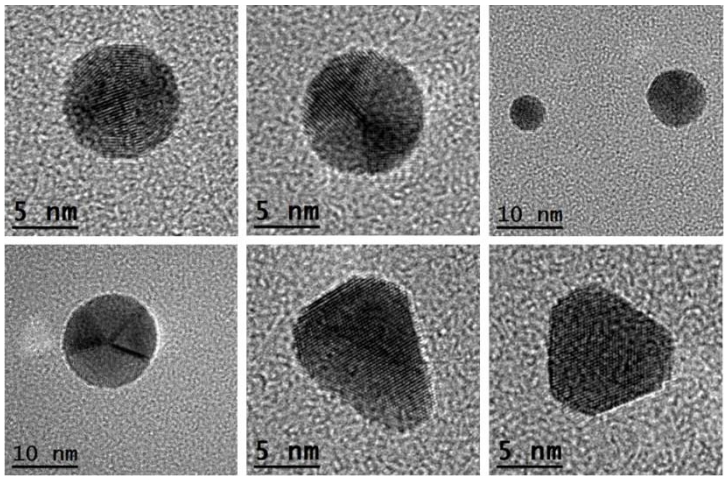

Figure S9: HRTEM micrographs showing different structural morphologies present in a sample of GNP synthesized with ligand molecule **1·2Br** in biphasic system.

Fig. S9 shows icosahedron faceted nanoparticles with different sizes, 4-twinned spheroidal nanoparticle and tetrahedral obtained by synthesis in solution using a biphasic system (Casal-Dujat *et al*, 2012). Power spectra taken from these structures are revealed that all of them are gold-based. The sample was composed by multifaceted spheroidal nanoparticles with different sizes and tetrahedral, that was divided in two groups which cover about 80% of the sample. The first group is composed by multitwinned faceted spheroidal nanoparticles with an average size of 12 nm. Another group has multitwinned faceted nanoparticles with an average size of 7.2 nm.

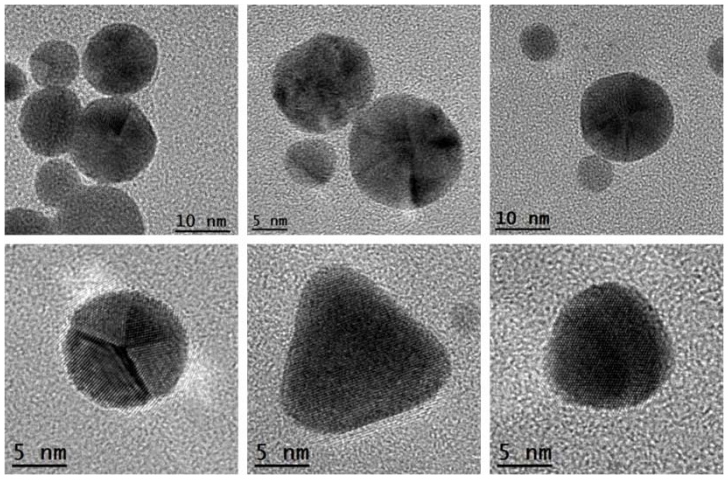

Figure S10: HRTEM micrographs showing different structural morphologies present in the sample of GNP synthesized with ligand molecule **1·2Br** in aqueous phase.

The sample of GNP shown in **Fig. S10** was synthesized in aqueous phase (Rodrigues *et al*, 2014) and contains a variety of structures. Most of them are multitwinned faceted spheroidal nanoparticles with different sizes, which vary between ~ 5 nm and ~ 25 nm. In addition to the spheroidal nanoparticles, tetrahedra are occasionally observed in the sample.

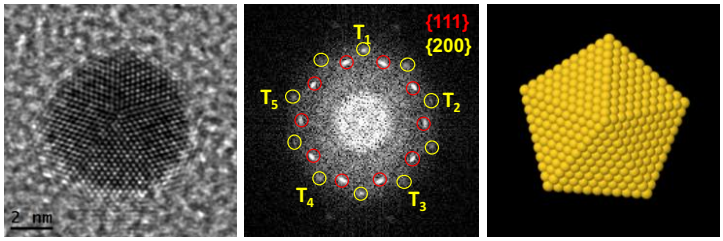

Figure S11: HRTEM micrograph of a 6.4 nm decahedron GNP synthesized with ligand molecule **1·2Br** in aqueous phase and its corresponding power spectrum and 3D structural model.

As seen in the power spectrum in **Fig. S11**, diffraction spots corresponding to {111} and {200} family of planes form a perfect symmetry, which is typical for decahedra. Regular decahedron shape consists of mergence of 5 {111} faceted tetrahedron. Yet, the theoretical angle between two (111) planes is 70.53° and combination of 5 tetrahedra to form a decahedron results in a 7.35° gap, which must be filled by some form of internal strain such as twin dislocations and other structural defects.

L. Casal-Dujat, M. Rodrigues, A. Yagüe, A. C. Calpena, D. B. Amabilino, J. González-Linares, M. Borràs and L. Pérez-García, Langmuir, 2012, 28, 2368–2381.

M. Rodrigues, A. C. Calpena, D. B. Amabilino, D. Ramos-López, J. de Lapuente and L. Pérez-García, RSC Adv., 2014, 4, 9279–9287.

Chapter 3

Gold Nanoparticles for delivery of drugs and peptides

3.1. Introduction

Gold has been used in medicine for centuries, because of its inertness (it resists to chemical corrosion unlike other metals) thus appearing as an "immortal metal" associated with longevity. Its use in China can be traced back to 2500 BC, where pure gold applied topically was believed to cure skin conditions like furuncles or ulcers, as well as smallpox. Later, a way to produce gold in a liquid preparation that could be drunk was pursued by many alchemists, as found in documents from 81 BC. Some of these recipes indeed allowed obtaining gold salts in solution.[93] Around 1300 it was described the preparation of *aqua regia*, the first known solution to dissolve gold.[94]

Colloidal gold was also used in art, to decorate objects, as is the case of the famous Lycurgus Cup, exhibited in the British Museum in London, which is made of dichroic glass that contains colloidal gold and silver. The presence of the colloids within the glass is the responsible for its property of being translucent when a light is shone through it.[95] Although colloidal gold had been used since many centuries it was Faraday, in his lecture from 1857, who first described different ways of obtaining gold preparations, including colloidal gold. Furthermore, he also described the sizes of the particles and the relation between the size and response to light, in a very complete study.[96] Colloidal gold is composed of small gold particles with nanometric size, known as gold nanoparticles (GNP), that when dispersed in an adequate solvent have the appearance of a solution.

Gold is an inert and resistant metal, and this property is also found in GNP. Furthermore, the small size of GNP renders a very important property, named the Surface Plasmon Resonance (SPR). This phenomenon is caused by the collective oscillation of electrons at the surface of the gold due to the electromagnetic radiation of the incident light. According to Mie's theory, the SPR band of the particles with spherical shape, visible in the absorption spectra, results from the dipole oscillations of the free electrons in conduction band that are occupying the energy states immediately above the Fermi energy level. A decrease in the size of the GNP translates into a broadening of the SPR band and a decrease in the intensity of the peak. GNP with sizes below 2 nm do not present SPR band, as well as bulk gold.[95,97,98] The SPR maximum peak can range from 518 nm to 565 nm, corresponding to sizes ranging from 9 nm to 100 nm.[99] This band is also present in gold thin films. It is important to highlight that the band depends not only of the

size of the GNP, but also of the type of ligand that is on the nanoparticles' surface, and the solvent where they are resupended. The dependence of the SPR relative to the GNP size allows the determination of the later by UV-visible absorption spectroscopy.[100,101] The SPR band also experiences shifts on its absorption wavelength upon aggregation of the GNP, which can be macroscoscopically easily seen because of the changes in the colour of the colloidal solution. Recently it has been found that SPR depends more on the plasmon length (distance along which occurs the oscillation, that depends on the size) rather than the shape.[102] As far as characterization of GNP is concerned, the development of the electron microscope allowed the study of these colloids, since the particles' size is small and cannot be properly studied with a regular optical microscope.

One of the milestones for GNP preparation revolves around Turkevich's work. In 1951 Turkevich published his work, where different methods of preparing gold colloids were compared, and his own method, adapted from existing literature, and showed that spherical particles could be obtained with a narrow distribution and good reproducibility. This method, known as the Turkevich method, uses citrate as the reducing agent of Au(III) salts, and is one of the most widely used methods to obtain gold nanoparticles dispersed in water.[103] The method was further studied, and it was proved that tuning the citrate:Au ratio affords GNP with distinct sizes.[104] The citrate is the responsible for the reduction of the gold, but recently, it was found that it is not citrate itself but the dicarboxyl acetone resulting from its oxidation the responsible for the stabilization of the nanoparticles.[105]

Another method developed for the synthesis of GNP that could also render good reproducibility is the method developed by Brust and Schiffrin, in which a two phase system is used.[106] A gold(III) salt is solubilized in water and transferred by tetraoctylammonium bromide (TOAB) to an organic phase containing a thiol that will stabilize the GNP, once is formed. The reduction of the gold is performed by adding an aqueous solution of $NaBH_4$ with vigorous stirring. The GNP is stabilized by the formation of a monolayer of thiols on its surface, and for that reason the so-obtained GNP are referred to as monolayer-protected clusters (MPC). The normally accepted theory for the synthetic route was that the thiol would reduce Au(III) to Au(I) and form a complex with Au(I), that would then be reduced to Au(0) by the addition of $NaBH_4$.[107] Nowadays is known that the Au-S bond is formed only after adding the reducing agent.[108] The strength of $NaBH_4$ as reducing agent is bigger than citrate's, which could account for their smaller size when compared with the ones obtained by Turkevich's method. In the biphasic system, the presence of the transfer agent TOAB represents an additional contaminant to the GNP solution that requires removal. Therefore, an improvement was introduced later, where the synthesis was performer in methanol, thus avoiding the use of TOAB.[109]

Before the publication of the Brust-Schiffrin method, reports had already been made where the GNP synthesized by the Turkevich method were afterwards stabilized by a thiol by simple exchange,[110] because thiol has binds with gold through the sulphur atom by a quasi-covalent bond. This exchange process can be very useful when the functional group of the thiol can also be reduced by the reducing agent used in the GNP synthesis or a given GNP size is required. The exchange is not, however limited to GNP obtained by the Turkevich method: GNP already stabilized by one thiol may undergo ligand exchange for a different thiol (**Scheme 3.1**).[111,112]

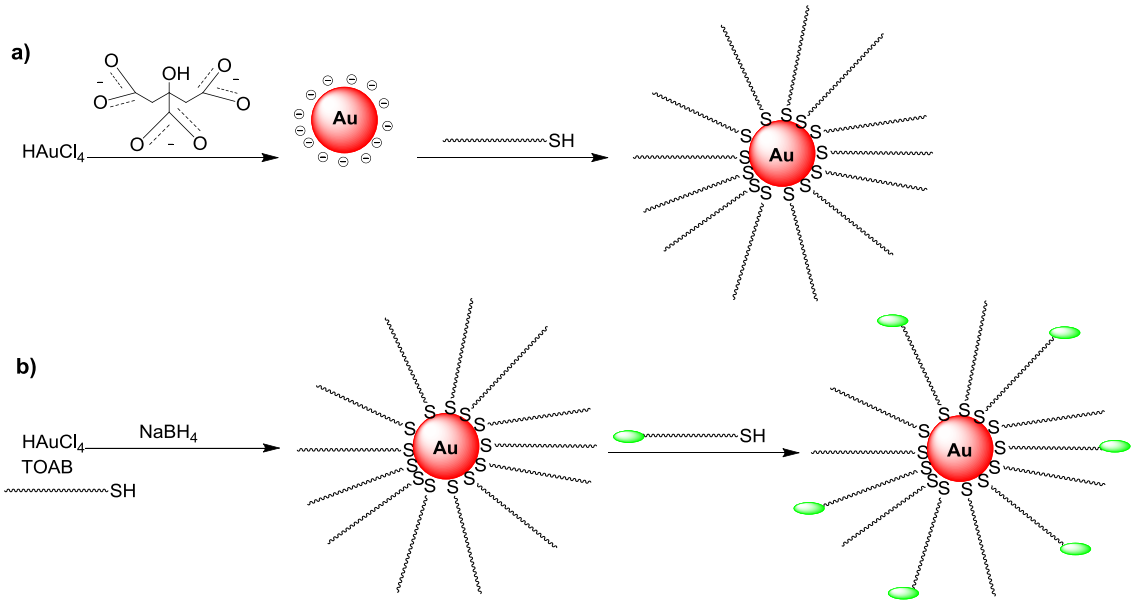

Scheme 3.1: Synthesis of gold nanoparticles: a) by the Turkevich method and subsequent exchange between the citrate and a thiol, and b) by the Brust-Schiffrin method and subsequent exchange of the thiolate from the synthesis by a second thiol.

GNP can also be stabilized by cysteíne[113]. This amino acid is present in glutathione (abundantly found in the cytoplasm of cells and in blood plasma), and therefore GNP can also be stabilized by this molecule through the thiol group from the cysteine residue.[114] Aditionally, thiolates stabilizing GNP can be released through exchange with glutathione.[115] Cysteine also mediates protein adsorption and stabilization of GNP.[116] Other examples of ligands that are found in literature include natural ligands, such as chitosan,[117,118] ligands with phosphine as functional group,[119] bipyridyls,[120] polymers,[121] as for example Pluronic or Poloxamer,[122] amphiphilic molecules such as TOAB, which apart from being a transfer agent in the Brust-Schiffrin method can also be used as stabilizer in the absence of thiols,[123] didodecyldimethyl ammonium bromide,[124] or cetyltrimethylammonium bromide (CTAB), although the last is more popular for the synthesis of nanorods.[125,126] and surfactants with a gemini structure.[127,128] Additionally GNP can also be stabilized by ionic liquids containing imidazolium groups.[129,130] It has been observed that the imidazolium moiety is involved in the stabilization.[131] Recently examples of

imidazolium-bearing gemini surfactants have been reported as ligands to stabilize GNP.[132] Some examples are shown in **Figure 3.1**.

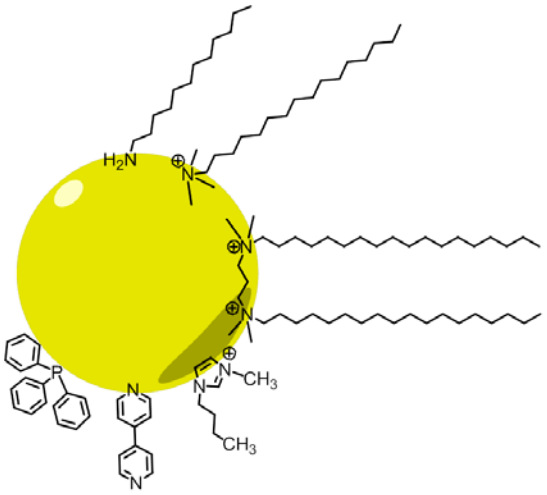

Figure 3.1: Schematic representation of a GNP with different ligands that can be used for stabilization. Clockwise, from top to bottom:amine, amphiphile with single chain (CTAB) and gemini-type, imidazolium-based, bipyridyl, and phosphine.

Groups like amino, carboxy, carbonyl and phenol are also known to stabilize GNP. Some efforts are made to achieve a "greener" synthesis of GNP by using ligands that possess such groups found in natural extracts, as for example leaf extracts of *Magnolia kobus* and *Diospyrus kaki*,[133] *Rosa rugosa*[134] or *Morus alba*,[135] and fruit extract from *Punica granatum*.[136] A more unusual method to obtain the GNP is using extracellular filtrates from microbes as reducing agents and stabilizers. Examples found in literature include extracts from *Trichoderma viride* and *Hypocrea lixii*.[137] Other examples describe the reduction of Au(III) and formation of GNP by contact with the biomass of *Fusarium oxysporum*,[138] *Verticillium sp.,*[139] or *Rhodopseudomonas capsulata.*[140]

In addition to the various types of stabilizers that can be used in their synthesis, the fact that GNP can be functionalized with appropriate thiols, that furthermore can be used to immobilize (bio)molecules in the surface, makes them a very versatile tool. Therefore, GNP have been widely studied to be used in different types of applications. Some examples are listed.

Catalysis: Although gold in its bulk form is not reactive,[141] when in the form of GNP, it can catalyse the oxidation of styrene[142] and volatile organic compounds like CO, CH_3OH and HCHO,[143] selective hydrogenation,[144] 1,2 addition to alkynes,[145] C-C coupling reactions,[146] and also as catalyst in the synthesis of carbon nanotubes,[147] to name some examples.

Diagnosis: The inertness and easy functionalization of GNP makes them useful in the development of lateral flow assays for diagnosis, for example for the detection of pathogens.[148,149] Generally, this type of assays is based on a sandwich design and the needed device can be formed by the following parts: a sample pad (where the analyte is placed), a conjugate pad (where GNP-conjugated antibodies are placed), a nitrocellulose membrane (where the analyte solution flows) as well as test and control lines, and finally an absorbent pad (**Figure 3.2**).

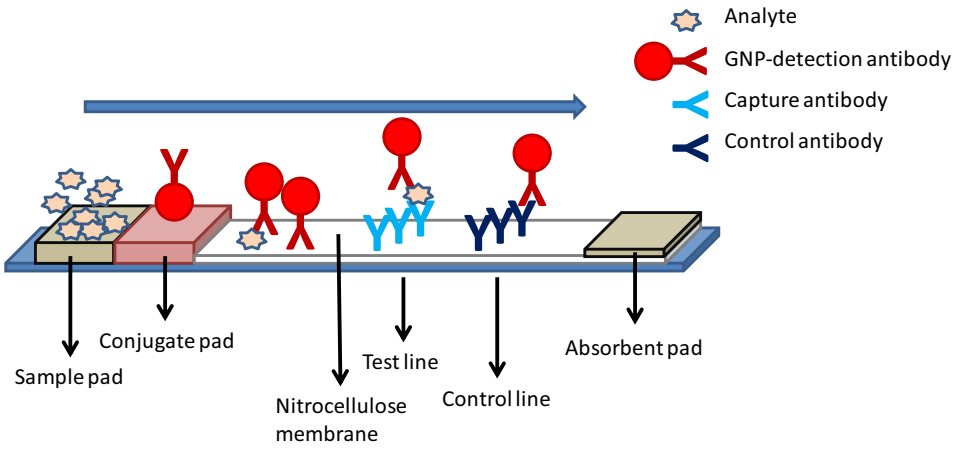

Figure 3.2: Schematic representation of a lateral flow assay with colloidal gold for the detection of analytes.

Basically, the analyte is introduced in the assay system and, due to capillarity, it migrates along the conjugate pad and nitrocellulose membrane. Antibodies specific for the analyte are placed in the conjugate pad linked to GNPs, so that when the analyte solution passes, they bind to the analyte (when present). In the test line, another antibody specific for the analyte is also placed, and the control line has antibodies that are specific for the detection of the former antibody. The detection of the presence of the analytes is easy because of the colour of the colloidal gold. When the analyte is present, a line is visible in the test line, and the control line assures that the solution with the analyte migrated through the membrane.

Sensing: When GNP experiment aggregation, the gold core of the GNP become closer, the SPR band shifts, since absorption occurs at longer wavelength, and the solution changes its colour. The most common is the change from a red-wine to a dark blue colour. This feature can be used for label-free sensing. For instances, Gooding's group described GNP functionalized with a thiol bearing azide groups. This solution is placed together with 1,4-diethynylbenzene that has two alkyne groups, and therefore act as cross-linker. In the presence of copper (I), which is a catalyst in the Huisgen reaction of cycloaddition, GNP are cross-linked and the solution turns from red to blue (**Figure 3.3**). The intensity of the colour is proportional to the amount of

copper present.[150]

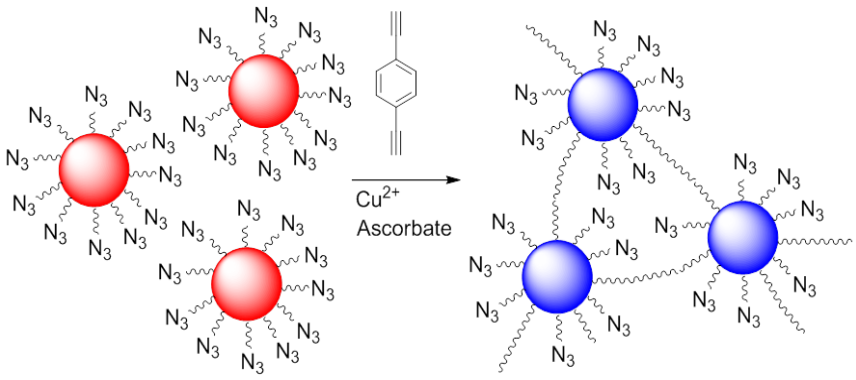

Figure 3.3: Schematic representation of the aggregation of GNP functionalized with an azide upon addition of copper in the presence of 1,4-diethynylbenzene.

A similar strategy is applied to detect the activity of blood coagulation Factor XIII. Different GNP are synthesized, a batch incorporating peptides containing terminal lysine residues, and another incorporating peptides containing terminal glutamine residues. When activated, the Factor XIII is responsible for the formation of bonds between the terminal residues of each type of particle, which results in their aggregation.[151] Other examples of the colorimetric detection use DNA-modified GNP and the change in the melting temperature (T*m*) between DNA complementary strands, and could be used, for example, in the detection of Hg^{2+} and Cu^{2+} cations.[152,153] An example of for the detection of Hg^{2+} is shown in **Figure 3.4**.

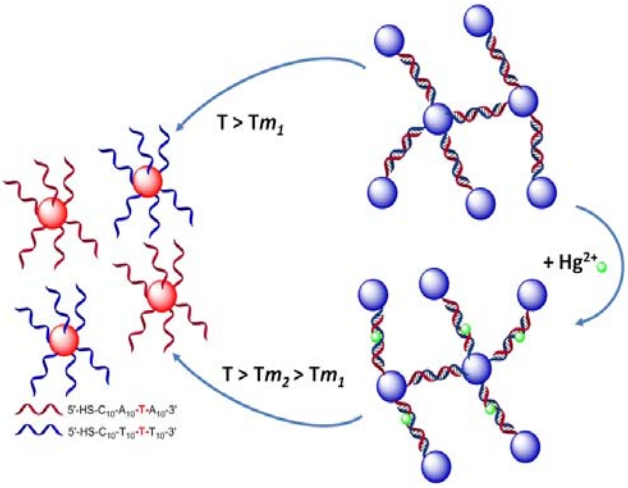

Figure 3.4: Example of GNP with complementary DNA strands and a T-T mismatch: The GNP aggregate but when the temperature increases above T*m*, the DNA strands separate and the solution turns red. When adding Hg^{2+}, this cation complexates with the T-T mismatch between the complementary strands, and the temperature at which the two strands separate increases when comparing with the initial solution with no Hg^{2+}.

The aggregation of GNP can furthermore be used along with fluorescent probes, because GNP have a quenching effect on their fluorescence. For instance, a method to detect DNA hybridation based on fluorescence was developed. A solution is prepared containing Rhodamin B, GNP and single strand DNA, this being responsible for the stabilization of the GNP upon the addition of NaCl. The stabilized GNP quench the fluorescence of Rhodamin B. However, when the complementary DNA is added, the double strand DNA is formed and can no longer stabilize the GNP, which aggregate in the presence of NaCl and no longer quench Rhodamin B's fluorescence. Thus, this aggregation translates into an increase in the Rhodamine B fluorescence in solution (**Figure 3.5**).[154]

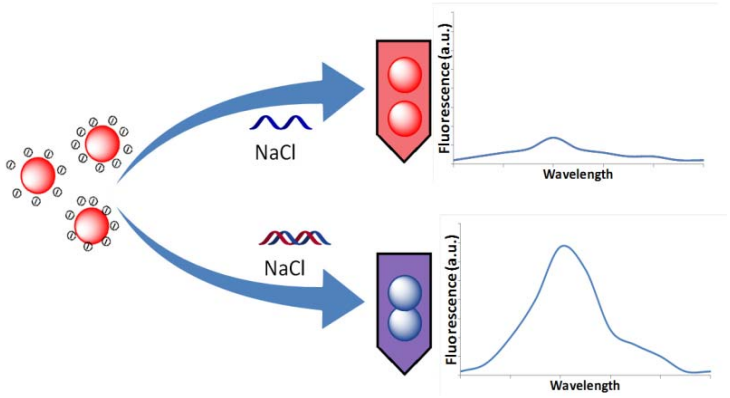

Figure 3.5: Example of a solute of GNP containing rhodamine. Upon the addition of NaCl, the presence of ssDNA can stabilize the GNP and the quenching of rhodamine occurs. When the hybridization occurs, the GNP aggregate and the fluorescence of rhodamine is detected in solution.

The quenching effect can also be used to detect DNA hybridization by combining ssDNA with a reporter that emits fluorescence. For instance, ssDNA labelled with a fluorophore, with hairpin structure, thus making the fluorophore closer to the GNP. A quenching effect occurs (the emitted radiation is transferred to the gold core), and no fluorescence is observed. Upon hybridization, the hairpin opens, the reporter is separated from the gold core, no energy transfer occurs, and the fluorescence becomes visible (**Figure 3.6**).[155]

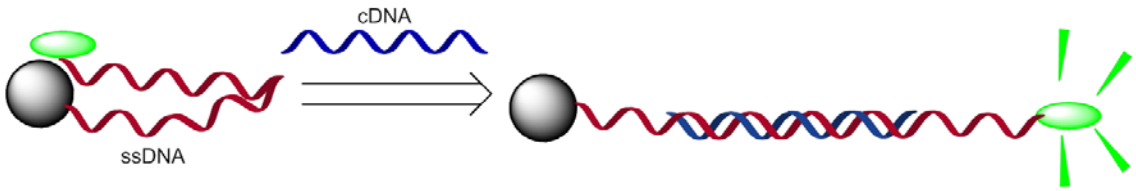

Figure 3.6: Fluorescence-based sensor with GNP. The ssDNA attached to the GNP forms a hairpin structure. Upon addition of the complementary DNA, the hairpin unwinds and no quenching occurs.

The SPR effect found on GNP can also be used for the development of sensors based in GNP immobilized on matrices. For example, GNP embedded in a gel could be successfully used to

sense dopamine. The presence of the analyte causes a swelling in the gel, and this causes a bigger separation between the GNP, which results in shifts in the SPR (**Figure 3.7**).[156]

Figure 3.7: Example of gel with embedded GNP. Upon swelling of the gel, the distance between the GNP increases.

The technique has become very popular with the development of sensor chips with thin gold layers that also present SPR, and can be used to sense deposition of materials but also determine interaction constants between biomolecules (see Chapter 4 for more details).

Imaging: There are different features of the GNP that can be taken advantage of for its use as imaging agents. For instance, GNP can be observed by optical microscopy in phase contrast or differential interface contrast (DIC) mode when their size is bigger than 20 nm.[157] On the other hand, the fact that gold atoms have high atomic mass allows the gold core to be seen by TEM without the need of additional staining. This was what allowed the study of the influence of citrate:gold ratio on the size of the GNP,[104] and therefore, TEM is used in their characterization, but also means that GNP can be visualized inside cells, allowing the study of their biodistribution.[158] On the other hand, it has been demonstrated that GNP are also able to scatter X-ray, which means they can be used as contrast agent in X-ray imaging.[159]

GNP can also be used for imaging using Surface-Enhanced Raman Scattering (SERS). Raman scattering consists on the inelastic scattering of photons by a given molecule. This scattering has associated a different energy to the incident light. The energy shifts are specific for certain molecular structures. More complex molecules have therefore their own specific spectrum, which allows them to be identified. The energy shift does not depend of the wavelength, and the signals have low intensity, but can be highly amplified by a factor of 10^{14} if the molecules are sufficiently closer to a curved surface of gold, like for instance the surface of gold nanoparticles. This phenomenon of electromagnetic enhancement is caused by the SPR of the GNP: when a laser is shone through the GNP, the incoming and outgoing radiations' electric field are enhanced. This enhanced electric field interacts with the molecule that is near the GNP's surface, and thus the name Surface-Enhanced Raman Scattering.[160,161] This allows GNP loaded with these reporter molecules to be used as sensors[162,163] and as imaging agents.[164] For example, SERS was used to image the cellular transport pathways. In this example[165] the GNP are introduced inside a cell and are tracked through the SERS signal, allowing the mapping of the

transport in organelles and accumulation in lisosomes. In the field of cancer diagnosis, SERS has been tested for real-time release of anticancer drugs inside living cells,[115] but can also be used for histological detection *in vitro* and for *in vivo* imaging (**Figure 3.8**).[166] SERS agents were prepared using lipoic acid as linker between the reporter molecules and the gold core, for *in vivo* detection of cancer through antibodies targeting HER2 and EGFR, which are overexpressed in many cancer cells.[167,168]

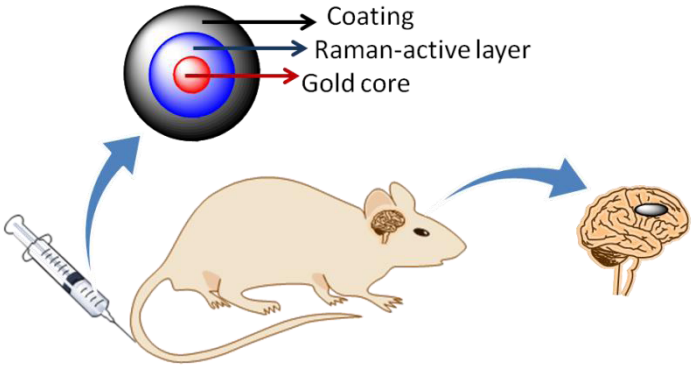

Figure 3.8: Example of GNP covered with a Raman-active layer. The GNP solution is injected and the GNP target a specific organ, where they accumulate in the tumour, allowing this to be observed through SERS.

Additionally, it was found that thiol-coated GNP present permanent magnetism, for which they can also be used as an enhancer in Magnetic Resonance Imaging (MRI) when associated with gadolinium.[169–171] GNP can also be capped with other ligands, like manganese[172] to be used as MRI contrast agent or combined with iron oxide nanoparticles to be used as both MRI and SERS contrast agents.[173]

Therapy: One of the most promising applications of GNP is in therapy. Due to their easy synthesis to obtain GNP with appropriate ligands, their high surface/volume ratio (which allows high molecule loading) and good biocompatibility, GNP have seen an increase in their study to deliver drugs.[174]

Some examples of applications in the promising field of gene delivery can be found. GNP that were functionalized with lysine and lysine dendron structures proved to be good ligands to bind DNA and posterior delivery of the cargo through response to the glutathione levels inside the cell.[175] Another strategy involves GNP coated with charge-reversal copolymer, which could shift the charge from positive to negative according to the pH. The delivery of siRNA by such GNP, and consequent gene silencing, could be successfully achieved.[176] GNP stabilized with this type of polymers with siRNA can enter the cell inside endosomes. The influx of protons to acidify the medium inside the endosome leads to a change in the charge of the polymer, wich

disassembles and releases the cargo. At the same time, because the copolymer has the capacity to disrupt the endosome, the released siRNA can exit the endosome (**Figure 3.9**).

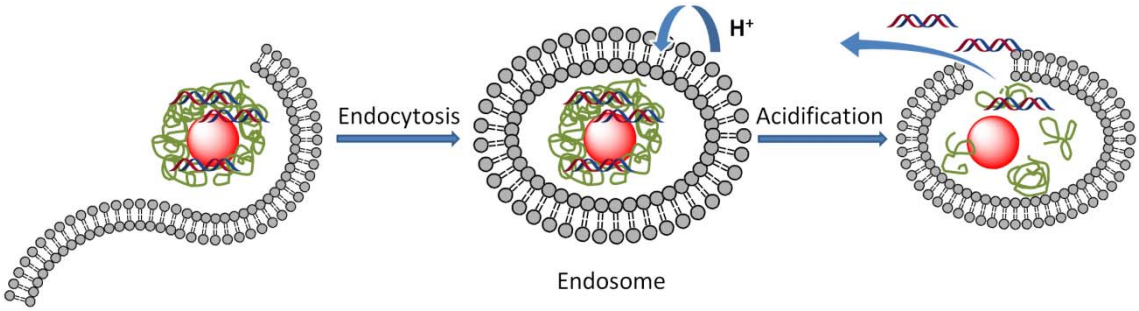

Figure 3.9: GNP covered with pH-responsive copolymer enters the cell through endocytosis; the newly formed endosome suffers an influx of protons to acidify the medium, and the change in the pH causes the copolymer to disassemble, thus releasing the siRNA.

GNP have also been studied for the delivery of drugs. For example, water soluble GNP, with propansulfonate groups on the surface, could interact with dexamethasone through the formation of a bond between the fluorine atom of the drug and Au(I) atoms on the surface of the GNP. This interaction resulted in the incorporation into the GNP of 70-80% of the added drug. These GNP can be used to load and release drugs that are not water-soluble.[177] Another example shows GNP encapsulated inside dendrimers and having the drug attached to the GNP by a thiol group. Captopril and 6-mercaptopurine, which are thiol-containing drugs, and doxorubicin and cisplatin, drugs modified in order to introduce thiol group, were tested. The levels of the thiol-reducing agent glutathione trigger the release of the drug from the GNP.[178] Another example that relies on the glutathione-triggered release is the synthesis of GNP with tiopronin, a drug that also has a thiol group and is used to treat acute liver injuries.[179]

Pluronic-based micelles, with GNP are forming an outer shell, have also been developed, where after the uptake of the structure by the cell, the glutathione levels cause the disruption of the shell and the release of the inside cargo, in this case paclitaxel.[180] Other possible strategy for the delivery of cargo from GNP consists on the assembly of vesicles directed by the ligand composition. These vehicles incorporate the drug in the interior, and upon a trigger, the vesicle disassembles, releasing the cargo. Because of the proximity of the GNP in the vesicle, the SPR is different from the SPR of individual GNP, and thus allows the screening of the release. The release may be triggered by light, inducing chemical changes in the photoresponsive ligands (**Figure 3.10**).[181] Other approach involves the construction of structures which are pH-responsive; for example, a supramolecular conjugate of GNP inside β-cyclodextrin molecules could be successfully obtained and could incorporate and release various anticancer drugs depending on the pH.[182]

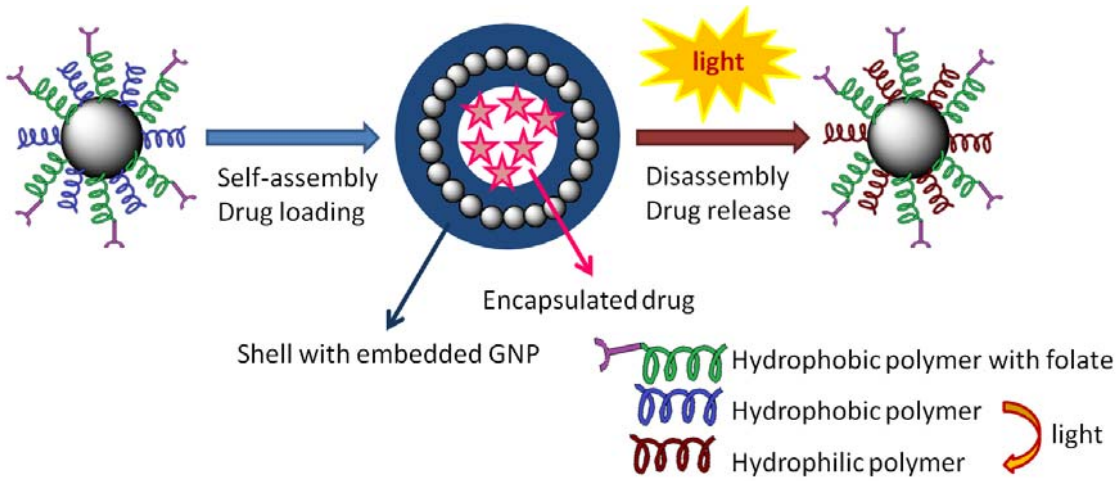

Figure 3.10: GNP coated with two polymers, one hydrophobic and other hydrophilic, which causes a polymeric vesicle to form with the GNP embedded and the drug encapsulated inside. Upon irradiation with light, the hydrophobic polymer is converted into hydrophilic and consequently the vesicle opens up and releases the cargo.

Besides allowing controlled release of drugs, in some cases the association of a drug to GNP enhances the drug's activity. For example, BSA-capped GNP were used to incorporate methotrexate, and it was found that the they had anticancer activity on MCF-7 cancer cells, and this was higher than the obtained for the free drug alone.[183] In the case of XAV939, a small molecule that inhibits the Wnt/β-catenin pathway, it was found that this molecule could inhibit 100 times more the Wnt proteins signalling pathway when it was conjugated to GNP than it did in the free form. This conjugation was performed through sulphide linkage. The efficacy depends on the amount of GNP that were internalized by the cell, through endocytosis.[184] Yet another example, where the synthesis of the GNP is done using natural extracts, shows that the GNP could target MCF-7 cells by conjugation with folic acid, and were used to deliver 5-fluorouracil to these cells with better results than the free drug.[185] Selectivity can also be enhanced by targeting specific cells through the conjugation of the GNP with antibodies that specifically recognize and bind to molecules present in the surface of those cells. The use of antibodies to target specific cells is found in many examples of GNP for both therapy and diagnostic.[186–188] In **Figure 3.11** we can see an example of GNP that are conjugated with antibodies anti-HER2, an epidermal growth factor receptor that is overexrpessed in breast cancer cells. The overexpression is responsible for a higher accumulation of the GNP in the tumour, because the antibodies bind to the receptors on the membrane of the cells. The GNP may be designed to deliver a cargo (drug delivery) or have conjugated another molecule for specific therapy, or may be used for diagnosis purposes: the accumulation in the tumour allows it to be detected through imaging techniques.

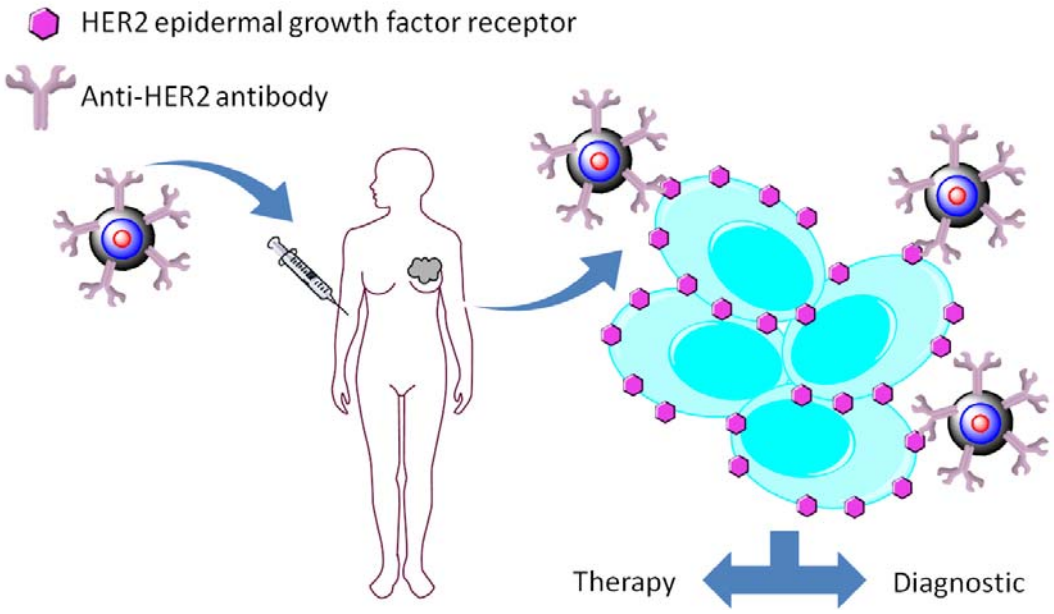

Figure 3.11: Example of GNP conjugated with antibodies anti-HER2 epidermal growth factor receptor that is overexpressed in breast cancer cells. The presence of the antibody targets the cells with this receptor, and because it is overexpressed in the cancer cells, its accumulation is higher in these tissues.

Special advantage can be taken from the fact that GNP themselves have a high tendency to accumulate in tumours. Because the tumour cells multiply so quickly, there are anatomical and physiological differences in respect with cells in normal tissue; thus, because tumour tissues need high vascularisation, large gaps form between the endothelial cells of the blood vessels, allowing macromolecules and nanoparticles to cross the endothelium. This is known as the Enhanced Permeability and Retention (EPR) effect.[189] Recently it was found that GNP may exert an anti-angiogenic effect, inhibiting the formation of new blood vessels around the tumour which are necessary for its growth.[190] This effect appears to be related with the inhibition of the vascular endothelial growth factor (VEGF) signalling cascade, involved in the angiogenesis. Furthermore, it was found that the size and charge of the GNP influence their activity,[190] and coating of GNP with different functional peptides, specific for determined cell receptors, could inhibit or activate angiogenesis.[191] For this reason, GNP are also used in non-pharmacological cancer therapy.

One promising treatment is cancer immunotherapy, which consists of stimulating the host immune system in order to detect and kill the cancer cells. It is known that cancer cells evade recognition by the immune system due to some mechanisms, like the downregulation in the expression of antigens in the cell surface, which reduces recognition and stimulation of T-cells.[192] One way of stimulating the immune system is to conjugate the GNP with tumour associated antigen peptides. This strategy could improve immune *in vivo* cell stimulation.[193] The same was also done with a thiol-modified CpG 1668 oligodeoxynucleotide that is known to

stimulate immune responses.[194] Briñas *et al* synthesized GNP that were coated with a tumour associated carbohydrate antigen along with a peptide derived from the B-cell activating C3d protein, acting as adjuvant.[195] This vaccination strategy can also be applied to other cases. A multifunctional GNP has been synthesized with a tetrasaccharide epitope from *Streptococcus pneumoniae* type 14, the T-helper $OVA_{323–339}$ peptide and D-glucose, and could successfully trigger the production of IgG antibodies (**Figure 3.12**).[196]

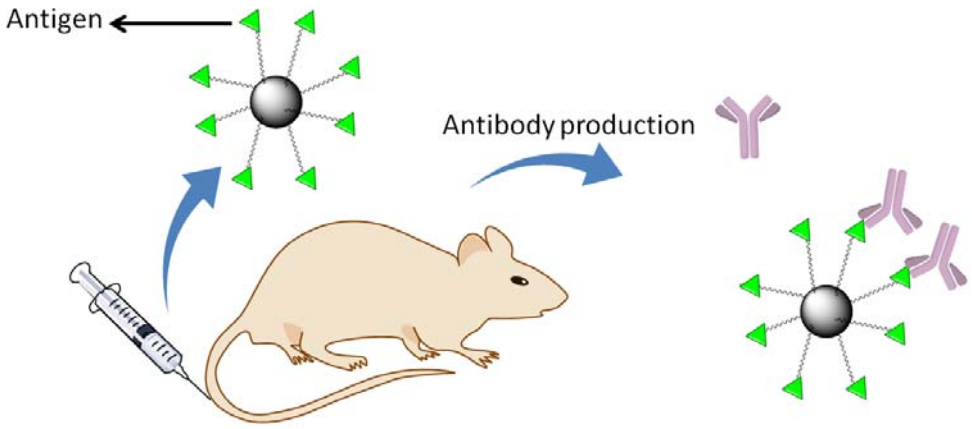

Figure 3.12: GNP conjugated with molecules known to trigger immune response. They are introduced in the body, and stimulate the production of antibodies. These antibodies bind to the antigens present in the GNP and initiate the process of opsonisation of the complex.

Other application of GNP is in radiotherapy: due to the fact that gold can absorb X-rays, the introduction of GNP inside the tumours enhances greatly the dosage of radiation applied to the tumour cells in comparison with the radiation absorbed by healthy tissue.[197] It has been demonstrated that in the case of superficial treatment, lower doses of radiation are needed in the presence of GNP to destroy the same fraction of cells obtained with higher radiation doses in the absence of GNP.[198] It has also been found that this enhancement helped in the therapy of radiation-resistant squamous cell carcinoma model cells.[199]

Due to the fact that GNP can convert electromagnetic radiation into heat, they have been also tested for laser based hyperthermia to treat cancer, because cells start to show signs of apoptosis when heated to temperatures between 41ºC and 47ºC.[200] The main advantage is that, besides the therapeutic paper, the conjugation of the GNP with appropriate antibodies can target specifically the tumour cells. For example, oral squamous carcinoma cell lines HSC 313 and HOC 3 Clone 8, and one benign epithelial cell line (HaCaT) were targeted with anti-EGFR antibody-conjugated GNP and it was proven that the irradiation not only caused cells death, but also that the malignant cells require less laser energy.[201] Also, using lower laser power resulted not in the complete disruption of the cell due to hyperthermia, but localized small disruptions were obtained, which did not kill the cells but could be used to enhance the uptake of anticancer

drugs by the cell, resulting in a combined therapy.[187] Furthermore, it was recently found that hyperthermia and radiotherapy have synergistic effect, and that the radiation needed in the radiotherapy process could be decreased.[202] When the hyperthermia technique is combined with chemotherapeutics, activity enhancement can be obtained. For instance, gold half-shell with anti-DR4 antibody conjugated with polymer with doxorubicin were used. The GNP moiety allows the targeting and the application of near IR radiation to increase the temperature. This heating of the cells allows the drug to accumulate inside and overcome the tumour cell's mechanisms of drug resistance.[188] An example was also found where the GNP aggregate in acidic pH, like the one found in the cancer cells' vicinity (**Figure 3.13**). From the aggregation arises a collective plasmon mode that causes the GNP aggregate to heat upon certain irradiating light, and at the same time release the cargo (in this case the drug tested was doxorubicin).[203]

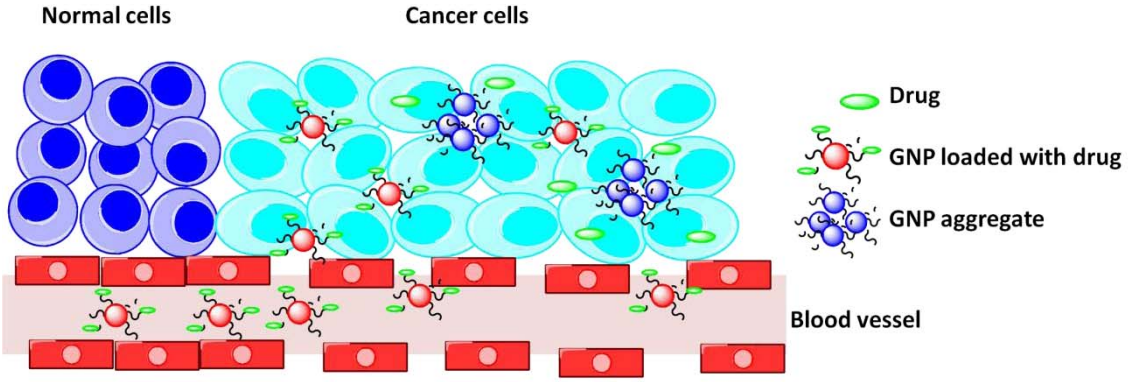

Figure 3.13: Example of drug-loaded GNP that are sensitive to acidic pH. The GNP cross the blood vessel (due to the EPR effect) and accumulate in the tumour. Because of the low pH found in this tissue, the GNP aggregate, releasing the drug. The aggregates can act as photothermal agent.

GNP can also be used as delivery and targeting agents for photodynamic therapy (PDT). PDT consists basically in using radiation to produce Reactive Oxygen Species (ROS). The photosensitizer is the molecule that is excited upon irradiating it with a specific wavelength. The relaxation of the molecule back to its ground state can occur with the emission of a fluorescent photon, or to an excited triplet state, from which can relax to ground state with the emission of a phosphorescent photon or by transference of energy to another molecule. In the presence of oxygen, the energy transfer occurs easily between the photosensitizer and molecular oxygen, and because the energy to form singlet oxygen is low, oxygen singlet is produced in this transfer.[204] The oxygen singlet is responsible for the cytotoxic effect of the photosensitizer on cells. Therefore, PDT appears promising in the treatment of cancer. One of the challenges is to target the photosensitizer cells to tumours, which can be achieved by conjugating with carriers such as GNP.[205,206] For example, Russell's group used phthalocyanine-conjugated GNP to generate singlet oxygen.[207] These conjugated GNP proved to have *in vivo* activity against

melanoma cells.[208] To improve their distribution, GNP can be additionally conjugated with antibodies. The targeting of breast cancer cells with anti-HER2 antibodies, which recognize the HER2 factor (overexpressed in many breast cancer cells) led to the accumulation of the GNP in the tumour, and cell death was induced upon the radiation.[186]

If the particles are to be used in biomedical application, whether it is imaging or therapy, it is very important to assess the toxicity of the GNP. There has been work done in this area, with findings that sum up to an overall understanding of the GNP safety in living organisms. For instance, when using Cos-1 cells the toxicity of the GNP present is closely related to their surface charges, which interact electrostatically with the cell membrane.[209] The charges interact with the lipid bilayer of the cell membrane, damaging its integrity. On the other hand, positively-charged GNP appear to induce structural changes in the cell membrane, and furthermore induce cytotoxicity due to changes in the membrane potential and increase in the concentration of Ca^{2+}. The cellular uptake of GNP positively charged is improved, but the cell proliferation decreases and cell death is induced.[210] Three types of GNP, with positive, negative, and neutral charge were studied and it was found that even the neutral-charge GNP proved toxic for HaCaT human keratinocyte cells, showing that not only the the synthesis and the surface charges of the GNP influence their toxicity behaviour, but also the reactions that can take place between the groups on the surface of the GNP and the cells. For example, the charged GNP elicited an apoptotic response whereas the neutrally charged ones showed minimum levels of caspase-3, and therefore the cell death was probably through necrotic process.[211] In K562 cells leukemia cells, the GNP are uptaken and up to a concentration of 250 μM (concentration expressed in gold atoms) they did not show toxicity. On the other hand, GNP with CTAB on the surface had significant toxicity: 50% of viable cells were found with a concentration of 0.01 μM (concentration expressed in gold atoms). It was found however that this high toxicity was associated with unbound CTAB on the surface of the GNP.[212] Gold nanorods, which are typically stabilized by CTAB, are highly toxic to human skin cells, due to the presence of this amphiphilic ligand. If, however, the CTAB-containing nanorods are coated with poly(styrenesulfonate), which proved to be biocompatible no toxic effect is observed.[213]

Regarding the influence of the size of the GNP in their toxicity, studies were performed using phosphine-stabilized GNP in four different cell lines: HeLa cells, SK-Mel-28 cells, L929 mouse fibroblasts and mouse monocytic/macrophage cells J774A1. It appears that for these particles the cytotoxicity, as well as the cell death, depends on the size and not on the ligand. An increase in the size of the GNP from 1-2 nm to 15 nm causes the increase in the percentage of apoptotic cells from the total cells that died, indicating a faster cytotoxic action.[214] A study was performed with HeLa cells that showed the influence of the size of the GNP on the toxicity. Smaller GNP (~2 nm) are less prone to form aggregates; they can enter the cells through endocytosis and

show lower toxicity. Bigger GNP (~25 nm) form aggregates inside the cells and show higher toxicity. But if the GNP aggregate outside the cell to a size that can no longer enter the cells through endocytosis, then the GNP aggregates adhere to the cell surface, resulting in an increase in the growth rate of the cells and no toxicity is observed.[215]

In an assay to determine the bioaccumulation of GNP in mice, the nanoparticles were administered through intraperitoneal route. After 8 days of daily GNP administration, no toxicity was observed. The weight of the animal did not suffer changes, nor the organ morphology or the tissue histology. Evidences pointed out that GNP can cross the blood-brain barrier because low concentration of GNP was found in the organ.[216] PEGylated GNP were found to accumulate in the liver and spleen of mice. Gold nanorods however accumulated more than gold nanospheres on the remaining studied organs, and also showed better accumulation in tumours.[217] Recently it was found that glutathione-cooated GNP may be a good alternative to PEG, because studies *in vivo* showed clearance of the GNP from the body through the kidneys and for higher concentration of GNP the clearance is done through the reticuloendothelial system.[114]

The ability of the GNP to penetrate through the skin has also been object of study. For instances, smaller GNP (~6 nm) appear to penetrate the skin, and bigger GNP (~15 nm) can penetrate depending on the ligand around the core. Bigger sizes may require enhancement to penetrate, such as dermabrasion or ballistic delivery.[218]

Due to the gold inertness and good biocompatibility, the versatility of ligands that can be used and also because the toxicity can be tuned with the appropriate molecules so that they can be made less toxic, GNP appear as promising vehicles for biomedical applications. Some were explored in this chapter dedicated to the delivery of active molecules by gold nanoparticles.

3.2. Objectives

In the field of GNP for drug delivery, the main objectives of this work are:

a) Synthesis of GNP using bis-imidazolium-based amphiphiles (**Figure 3.14**);
b) Non-covalent incorporation and release of anionic drugs from the synthesized GNP;
c) Preparation of GNP using thiols with functional groups for immobilization;
d) Covalent immobilization of synthetic cyclopeptides with therapeutic activities.

e)

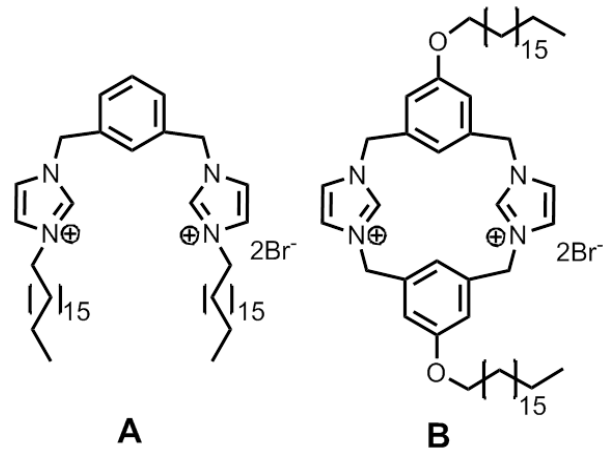

Figure 3.14: Structure of the bis-imidazolium amphiphiles with linear (A) and cyclic (B) structure.

The chapter is divided in four sections, which objectives are described in more detail:

3.2.1. Preparation of GNP from bis-imidazolium amphiphilic protophanes in a biphasic system

I. Synthesis of GNP through a biphasic method, using bis-imidazolium-derived amphiphiles as transfer agents and stabilizers of the GNP;
II. Characterization of the newly synthesized GNP by means of UV-visible absorption spectroscopy, TEM, Dynamic Light Scattering (DLS), Matrix Assisted Laser Desorption Ionization Time-of-Flight Mass Spectroscopy (MALDI-TOF-MS) and XPS;
III. Study of the cytotoxicity and genotoxicity of the imidazolium ligands and the so-formed GNP, as well as assessment of their internalization in Caco-2 Cells;
IV. Study of the incorporation, and *in vitro* release of ibuprofenate as anionic model drug, and *ex vivo* permeation study in human skin.

3.2.2. Preparation of GNP from bis-imidazolium amphiphilic protophanes in aqueous medium

I. Synthesis of GNP in aqueous solution, using bis-imidazolium-derived amphiphiles as stabilizers of the GNP;
II. Characterization of the newly synthesized GNP by means of UV-visible absorption spectroscopy, TEM and Thermogravimetric Analysis (TGA);
III. Study of the cytotoxicity and genotoxicity of the GNP; and internalization in Caco-2 Cells;
IV. Study of the incorporation and *in vitro* release of piroxicam, and piroxicam activity evaluation through the study of cyclooxygenase inhibition.

3.2.3. Preparation of GNP from bis-imidazolium amphiphilic macrocycles in a byphasic system

I. Synthesis of GNP through a biphasic method, using bis imidazolium-derived macrocycles as transfer agents and stabilizers of the GNP;
II. Characterization of the newly synthesized GNP by means of UV-visible absorption spectroscopy, TEM, SEM, DLS, XPS, MALDI-TOF-MS and TGA;
III. Study of the cytotoxicity and genotoxicity of the macrocycle ligands;
IV. Study of the incorporation, and *in vitro* release of ibuprofenate as anionic model drug.

3.2.4. Preparation of thiol-stabilized GNPs coated with bioactive synthetic peptides

I. Synthesis of thiol stabilized GNP, the thiols containing different functional groups for the immobilization of cyclopeptides with antimicrobial and anticancer activity;
II. Synthesis of GNP with peptides with antimicrobial and anticancer activity containing a thiol group;
III. GNP characterization by means of UV-visible absorption spectroscopy, TEM, DLS and XPS;
IV. Comparison between *in vivo* activity of the cyclopeptides in solution and immobilized in the GNP.

3.3. Gemini Imidazolium Amphiphiles for the Synthesis, Stabilization, and Drug Delivery from Gold Nanoparticles

Publication in Langmuir, 2012, 28, 2368-2381.

Lucía Casal-Dujat,[1] Mafalda Rodrigues,[1] Alex Yagüe,[1] Anna C. Calpena,[2] David B. Amabilino,[3] Javier González-Linares,[4] Miquel Borràs,[4] and Lluïsa Pérez-García[1]

1 Department of Pharmacology and Therapeutical Chemistry and Institute of Nanoscience and Nanotechnology UB (IN2UB), Universitat de Barcelona, Avda. Joan XXIII s/n, 08028 Barcelona, Spain

2 Department of Pharmacy and Pharmaceutical Technology and Institute of Nanoscience and Nanotechnology UB (IN2UB), Universitat de Barcelona, Avda. Joan XXIII s/n, 08028 Barcelona, Spain

3 Institut de Ciència de Materials de Barcelona (ICMAB-CSIC), Campus Universitari, 08193 Bellaterra, Spain

4 UTOX-PCB – Unitat de Toxicologia Experimental i Ecotoxicologia, Baldiri i Reixac 10-12, 08028 Barcelona, Spain

Summary

The synthesis of GNP using bis-imidazolium amphiphiles was achieved, following a method based on the Brust-Schiffrin biphasic system.

Since the amphiphilic molecules used as ligands were newly described compounds, they were first synthesized and characterized individually. Then, the GNP were prepared, by first transferring the gold precursor from the aqueous to the organic phase using a bis-imidazolium amphiphile, that acted as transfer agent, followed by phase separation. Afterwards, a freshly prepared aqueous solution containing the reducing agent was added.

Previous analysis of the organic phase by UV-visible absorption spectroscopy confirmed the presence of GNP that were further characterized: XPS confirmed the presence of gold in its reduced form. Two methods were used to determine the GNP size: through TEM it was

measured the size of the gold core and DLS allowed determining the hydrodynamic size of the GNP. The hydrodynamic size was found to be approximately 19.5 nm and the gold core 8.8 nm. These values correlated well with the proposed model of the GNP.

Besides the characterization, toxicity studies of both the GNP and the free ligands were performed, as well as internalization studies of the GNP in Caco-2 cells. The GNP proved to have low toxicity (the EC_{50} could not be determined) and could be internalized.

The bis-imidazolium amphiphile containing alkyl chains with 18 carbons that was used as ligand has the ability to recognize anions in solution, so the incorporation of an anionic drug in the GNP was performed, and its release was studied. Clearly, pH had a major influence on the release rate but also in the release kinetics: at pH 7.4 the release followed a first-order kinetic, and at pH 5.5 the release followed a zero-order.

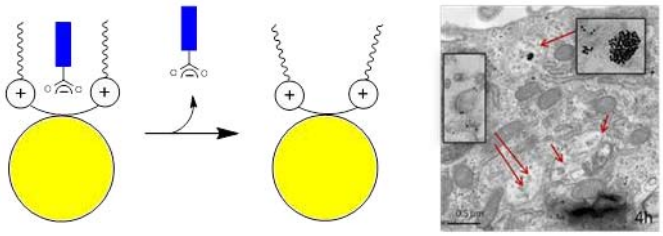

Figure 3.15: Scheme depicting the proposed disposition of the anionic drug inside the GNP ligand layer, and the release (left) and TEM image of the GNP internalized by Caco-2 cells (right).

Langmuir

ARTICLE

pubs.acs.org/Langmuir

Gemini Imidazolium Amphiphiles for the Synthesis, Stabilization, and Drug Delivery from Gold Nanoparticles

Lucía Casal-Dujat,[†] Mafalda Rodrigues,[†] Alex Yagüe,[†] Anna C. Calpena,[‡] David B. Amabilino,[§] Javier González-Linares,[∥] Miquel Borràs,[∥] and Lluïsa Pérez-García*[,†]

[†]Department of Pharmacology and Therapeutical Chemistry and Institute of Nanoscience and Nanotechnology UB (IN2UB), Universitat de Barcelona, Avda. Joan XXIII s/n, 08028 Barcelona, Spain

[‡]Department of Pharmacy and Pharmaceutical Technology and Institute of Nanoscience and Nanotechnology UB (IN2UB), Universitat de Barcelona, Avda. Joan XXIII s/n, 08028 Barcelona, Spain

[§]Institut de Ciència de Materials de Barcelona (ICMAB-CSIC), Campus Universitari, 08193 Bellaterra, Spain

[∥]UTOX-PCB—Unitat de Toxicologia Experimental i Ecotoxicologia, Baldiri i Reixac 10-12, 08028 Barcelona, Spain

Supporting Information

ABSTRACT: Gold nanoparticles (AuNPs) are considered useful vehicles for medical therapy and diagnosis. Despite the progress made in this field, there is need to find direct, reliable, and versatile synthetic procedures for their preparation as well as new multifunctional coating agents. In this sense, we have explored the use of imidazolium amphiphiles to prepare new AuNPs designed for anion recognition and transport. Thus, in this work we describe (a) the synthesis, by a phase transfer method, of new gold nanoparticles using gemini-type surfactants as ligands based on imidazolium salts, those ligands acting as transfer agents into organic media and also as nanoparticle stabilizers, (b) the examination of their stability in solution, (c) the chemical and physical characterization of the nanoparticles, using a variety of techniques, including UV—visible spectroscopy (UV—vis), transmission electron microscopy (TEM), and X-ray photoelectron spectroscopy (XPS), (d) toxicity data concerning both the imidazolium ligands and the imidazolium coated nanoparticles, (e) the assessment of their molecular recognition ability toward molecules of biological interest, such as anions and carboxylate containing model drugs, such as ibuprofen, (f) the study of their toxicity and those of their coating ligands, as well as their ability for cell internalization, and (g) the study of their ability for delivering anionic pharmaceuticals. The structurally governed triple role of those new gemini-type surfactants is responsible for the preparation, remarkable stability, and delivery properties of these functional AuNPs.

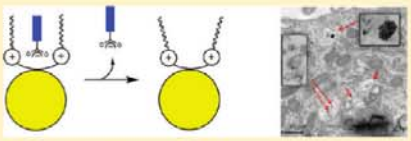

INTRODUCTION

There is ever increasing interest in the study of gold nanoparticles (AuNPs) because of their applications in catalysis[1] and nanomedicine,[2] potential use for diagnosis[3] and drug delivery,[4] as well as their use as probes for sensing and imaging.[5] Some of the advantages of using AuNPs as carriers for drugs are the inertness and nontoxic nature of the gold core, the ease of their synthesis, and their properties for drug release.[2]

The use of AuNPs in nanomedicine relies on the existence of a simultaneously reliable synthetic methodology capable of leading to NPs in an efficient manner and introducing active functional units in the coating ligands. A variety of synthetic strategies for the preparation of AuNPs have been described,[2] mainly based on bottom-up strategies using chemical or electrochemical reduction of a gold(III) precursor in the presence of a capping agent or stabilizer, this meaning a compound able to bind to the nanoparticle exterior blocking its growth beyond the nanometer scale and also stabilizing the nanoparticles surface. AuNPs can be prepared and stabilized with a large variety of capping agents, and the most common approach is the use of thiolates, due to their strong affinity to gold, where the most reliable synthetic method is the Schiffrin—Brust biphasic synthesis,[6] which uses $HAuCl_4$, a thiol (as stabilizer), tetraoctylammonium bromide (as a surfactant that acts as a transfer agent into the organic solvent that is eventually replaced with a thiol), and $NaBH_4$ (as reducing agent) in water—toluene media. Additionally, many of the thiol ligands used as capping agents incorporate additional chemical groups in their structure to be used as binding or recognition elements, capable of different functionalities, such as sensors or delivering agents.[5] Also, glutathione-mediated release of thiolate ligands could be exploited in delivery applications.[4]

Therefore, it appears clear there is still need for improvement, and the synthetic methodology could be simplified and made more economic in terms of material, for instance, by using new capping agents that could function at the same time as transfer agents and functional stabilizers. In this context, various examples in the literature attempt the use of dual agents, acting as both reducing and capping agents.[7−9] On the other hand, room temperature ionic liquids (ILs) are regarded as environmentally respectful solvents because of their nonvolatility, high stability, and low toxicity.[10] The use of ionic liquids based on imidazolium salts for the generation and stabilization of metal nanoparticles

Received: September 16, 2011
Revised: October 27, 2011
Published: October 28, 2011

has been reported.[11] In particular, some ILs based on the imidazolium cation have been exploited to study the synthesis and stabilization of AuNPs, some incorporating the imidazolium moiety within a sulfur ligand (the latter is coordinated to the gold)[12] and a few recent examples using the imidazolium cation as the main motif in the ligand,[13] although the nature of the interaction between the imidazolium moiety and the surface of the gold cluster is not fully understood. An inconvenience of this approach is that the excess of IL has to be removed if the nanoparticles are to be isolated in pure form, and this process is far from trivial. On the other hand, gemini surfactants display excellent properties in the preparation and stabilization of monodisperse gold nanoparticles,[14] but the combination of a gemini nature and imidazolium functionality has not been reported.

On the other hand, anion sensing is a relevant topic for the design of biosensors of use in diagnosis and environmental analysis, and supramolecular chemistry has provided many approaches to the make of synthetic receptor for this purpose.[15] We reported previously the anion binding properties in solution of some imidazolium containing macrocycles.[16] As a step forward in this research we have focused our attention on the use of imidazolium based gemini amphiphiles, regarded as potential anion sensors and anion deliverers, to explore the ionophoric behavior of these imidazolium scaffolds both on surfaces and in the solid state. For instance, our preliminary studies[17] indicated that some bis-imidazolium salts with sulfur atoms in their alkyl chains self-organize, forming monolayers on gold surfaces, where we have also explored the anion recognition phenomenon.[18] On the other hand, ionogels containing imidazolium ibuprofenate have been shown to be an efficient drug releasing system with kinetics controlled by the nature of the silica wall.[19]

In this context, we aimed to prepare gold nanoparticles coated with bis-imidazolium amphiphiles, to explore their ability toward anion recognition, and their potential use in nanomedicine. Thus, we report here (a) a solution based preparation of new gold nanoparticles with bis-imidazolium ligands, where the ligands act both as transfer agents into organic media and also as nanoparticle stabilizers (b) their chemical and physical characterization, including their stability in solution toward aggregation and ligand exchange, (c) toxicity data concerning both the imidazolium ligands and the imidazolium coated nanoparticles, including cell internalization studies, (d) their molecular recognition ability toward valproate and ibuprofenate, as models of carboxylate containing drugs, and (f) in vitro studies of the ability of the new gold nanoparticles for delivering anionic pharmaceuticals.

The system investigated is based on dicationic amphiphiles formed by two imidazolium rings linked by a 1,3-dimethylene-phenylene spacer, where the imidazolium rings incorporate long alkyl chains of different lengths and functionality. Two different types of amphiphiles were considered (Figure 1): compounds **1·2Br**−**3·2Br**, bearing an alkyl chain of 10, 12, or 18 carbon atoms, respectively, and compound **4·2Br**, incorporating a dodecylthioundecyl moiety.

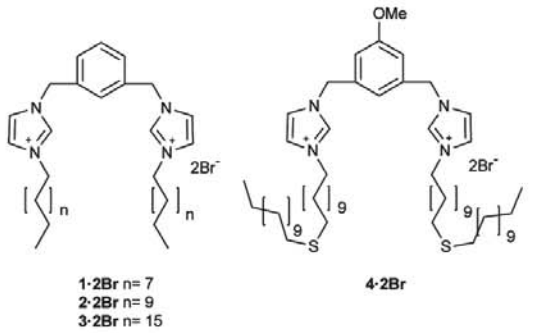

Figure 1. Bis-imidazolium amphiphiles **1·2Br**−**4·2Br**.

EXPERIMENTAL SECTION

General Methods. Melting point: CTP-MP 300 hot-plate apparatus with ASTM 2C thermometer. ^{1}H NMR: Varian Gemini 300 and Varian Mercury 400 spectrometers (300 and 400 MHz). ^{13}C NMR: Varian Gemini 300 and Varian Mercury 400 spectrometers (75.4 and 100 MHz). HMQC and HMBC: Varian VXR 500 spectrometer (500 MHz). COSY-2D and ROESY-2D: Bruker 500 spectrometer (500 MHz). NMR spectra were determined in $CDCl_3$ or $(CD_3)_2SO$, and chemical shifts are expressed in parts per million (δ) relative to the central peak of the solvent. Thin layer chromatography (TLC) was performed on Merck coated 60 F_{254} silica gel plates; the spots were located with UV light and developed with an iodine/silica or (1% w/v) potassium permanganate solution. Chromatography: SDS silica oxide 60 ACC (30−75 μm). UV absorption spectra were obtained on UV-1800 Shimadzu UV spectrophotometer. Absorption spectra were determined in CH_2Cl_2, THF, and toluene. In general, the compounds were dried overnight at 25 °C in a vacuum oven. Solvents: tetrahydrofuran, dichloromethane, toluene, acetonitrile, and absolute ethanol. The solvents were dried over basic aluminum oxide. Milli-Q water obtained from a Millipore system. Microanalysis were performed on a Carlo Erba Fisons EA 1108 analyzer in the Serveis Científico-Tècnics de la Universitat de Barcelona.

Mass Spectra (MS) from the Serveis Científico-Tècnics de la Universitat de Barcelona. Electron impact (EI) technique in Agilent 6890 with the 5975 mass spectrometer was used for neutral molecules. For cationic molecules, the ion ESI-MS was performed on a LC/MSD-TOF mass spectrometer from Agilent Technologies. Electrospray interface had the following conditions: the nebulizing nitrogen gas flow at 15 psi and drying nitrogen 7 L min^{-1}; the source temperature was maintained at 300 °C with a capillary voltage of 4 kV and a fragmentor voltage of 80 or 215 V. The eluent flowing through the probe was H_2O:MeCN (1:1) at a flow rate of 200 μL min^{-1}. High resolution mass spectra (HR-MS): electrospray (ESI) with high resolution in Agilent (2006) LC/MSD-TOF mass spectrometer.

MALDI-TOF-MS were performed on a 4800 Plus MALDI TOF/TOF mass spectrometer from AB Sciex. The laser operated at 355 nm, at a frequency of 200 Hz and at a pulse of 3−7 ns. When a matrix was used, it was DHB (2,5-dihydroxybenzoic acid) or α-ciano-γ-hydroxy-cinnamic acid.

Transmission electron microscopy (TEM) was from the Serveis Científico-Tècnics de la Universitat de Barcelona. The samples were observed with an electronic microscope Tecnai SPIRIT (FEI Co.) at 120 kV. The images were captured by a Megaview III camera and digitalized with the iTEM program. The size of the nanoparticles gold core was measured with the Analysis software (Olympus). The size of the nanoparticles was determined by dynamic light sctatering (DLS) using a Zetasizer Nano ZS series (Malvern Instruments).

The TOF-SIMS analyses were performed using a TOF-SIMS IV (IONTOF, Munster, Germany) operated at a pressure of 5×10^{-9} mbar. Samples were bombarded with a pulsed bismuth liquid metal ion source (Bi^{3+}), at an energy of 25 keV. The gun was operated with a 20 ns pulse width, 0.3 pA pulsed ion current for a dosage lower than 5×10^{11} ions/cm^2, well below the threshold level of 1×10^{13} ions/cm^2 generally accepted for static SIMS conditions. Secondary ions were detected with

a reflectron time-of-flight analyzer, a multichannel plate (MCPs), and a time-to-digital converter (TDC). Measurements were performed with a typical acquisition time of 20 s, at a TDC time resolution of 200 ps. Charge neutralization was achieved with a low energy (20 eV) electron flood gun. Secondary ion spectra and images in both positive and negative mode were acquired from a randomly rastered surface areas of 500 μm × 500 μm along the sample's surface. Secondary ions are extracted with 2 kV voltage and are postaccelerated to 10 keV kinetic energy just before hitting the detector. The maximum mass resolution, $R = m/Dm$, was around 9.000, where m is the target ion mass and Dm is the resolved mass difference at the peak half-width.

XPS experiments were performed at the Serveis Cientifico-Tècnics de la Universitat de Barcelona, in a PHI 5500 Multitechnique System (from Physical Electronics) with a monochromatic X-ray source (Al Kα line of 1486.6 eV energy and 350 W), placed perpendicular to the analyzer axis and calibrated using the 3 $d_{5/2}$ line of Ag with a full width at half-maximum (fwhm) of 0.8 eV. The analyzed area was a circle of 0.8 mm diameter, and the selected resolution for the spectra was 187.5 eV of pass energy and 0.8 eV/step for the general spectra and 23.5 eV of pass energy and 0.1 eV/step for the spectra of the different elements. All measurements were made in an ultra high vacuum (UHV) chamber pressure between 5×10^{-9} and 2×10^{-8} Torr.

For the release studies: Biodialysers system, double side type with inner diameter of 16 mm, and Dialysis membrane CelluSep T3, MWCO 12000−14000 Da, MFPI. Franz diffusion cell equipment: Crown Glass and Microetteplus-Hanson Research. Dialysis area: 2.54 cm^2. Volume of receptor compartment: 13 mL. Ibuprofenate determination in samples was done by HPLC in a Waters LC Module I, in a Waters Spherisorb 5 μm ODS-2 (4.6 mm × 150 mm) column; the detection wavelength was 220 nm.

Materials. Commercial compounds: 1-bromodecane, 1-bromododecane, 1-bromooctadecane, 1,3-bis(bromomethyl)benzene, *N*-bromosuccinimide (NBS), 1,3-dimethyl-5-methoxybenzene, hexadecanethiol, hydrogen tetrachloroaurate(III), 1,3-bis(hydroxymethyl)-5-methoxybenzene, ibuprofen (sodium salt), 1,8-octanethiol 97%, phosphorus tribromide (PBr_3) (1.0 M solution in CH_2Cl_2), sodium borohydride, tetrabutylammonium chloride, tetrabutylammonium acetate 97%, tetraoctylammonium bromide, valproate (sodium salt), were purchased from Aldrich. α,α'-Azoisobutyronitrile (AIBN), 1*H*-imidazole, and tetrabutylammonium chloride were purchased from Fluka. Potassium hydroxide (KOH pellets) 85% was purchased form Scharlau. $CDCl_3$, CD_3OD, or $(CD_3)_2SO$ were purchased from Euriso Top. Compounds prepared according to literature procedures: 1,3-bis(imidazolylmethyl)benzene,[16] 11-bromoundecylthiododecane.[20]

1,3-Bis[(3-alkyl-1-imidazolio)methyl]benzene Dibromide (1·2Br, 2·2Br). 1,3-Bis(imidazolylmethyl)benzene (0.30 g, 1.26 mmol) was dissolved in dry MeCN (25 mL) at room temperature under an argon atmosphere, and 1-bromoalkane (2 equiv) was added via a syringe. The colorless solution was heated to 80 °C, and the stirring was continued for 5 days. The yellow solution was cooled to room temperature, and the solvent was evaporated. The yellow residue was washed twice with *n*-hexane (2 × 8 mL). Dicationic protophanes (**1·2Br**, **2·2Br**) were obtained as dark yellow very dense oils that solidified at room temperature (99% and 92%, respectively).

1·2Br: ^{1}H NMR (300 MHz, $CDCl_3$, 25 °C, TMS): δ 0.88 (t, J = 7.5 Hz, 6H, CH_3), 1.25−1.32 (m, 28H, $(CH_2)_7$), 1.89 (m, N−CH_2−C**H**$_2$), 4.27 (t, J = 7.5 Hz, 4H, N−CH_2), 5.64 (s, 4H, CH_2), 7.17 (dd, J = 9 Hz, J = 6 Hz, 1H, Ar-H(5)), 7.29 (s, 2H, Im-H(4)), 7.61 (d, J = 6 Hz, 2H, Ar-H(4,6)), 8.12 (s, 1H, Ar-H(2)), 8.20 (s, 2H, Im-H(5)), 10.43 (s, 2H, Im-H(2)). ^{1}H NMR (300 MHz, $(CD_3)_2SO$): δ 0.85 (t, J = 6 Hz, 6H, CH_3), 1.23 (m, 28H, $(CH_2)_7$), 1.79 (m, 4H, N−CH_2−CH_2), 4.19 (t, J = 9 Hz, 4H, N−CH_2), 5.47 (s, 4H, CH_2), 7.40−7.50 (m, 3H, Ar-H(4, 5, 6)), 7.61 (s, 2H, Ar-H(2)), 7.86 (m, 4H, Im-H(4, 5)), 9.48 (s, 2H, Im-H(2)). ^{1}H NMR (300 MHz, CD_3OD): δ 0.92 (t, J = 6 Hz, 6H, CH_3), 1.32−1.38 (m, 28H, $(CH_2)_7$), 1.93 (m, 4H, N−CH_2−CH_2), 4.26 (t, J = 7.5 Hz, 4H, N−CH_2), 5.50 (s, 4H, CH_2), 7.47−7.71 (m, 8H, Ar-H(2,4,5,6), Im-H(4,5)). ^{13}C NMR (100 MHz, $CDCl_3$): δ 14.2 (CH_3), 22.8−31.9 ($(CH_2)_8$), 50.4 (N−CH_2), 52.5 (CH_2), 121.8 (Im-C(4)), 123.6 (Im-C(5)), 130.0 (Ar-C(4,5,6)), 130.5 (Ar-C(2)), 134.8 (Ar-C(1,3))/(ImC(2)), 136.7 (Ar-C(1,3))/(ImC(2)). MS (ESI) m/z: (260.7, $[(M - 2Br)/2]^{2+}$, 100%), (379.3, $[M - (CH_2)_9CH_3)$, $-2Br]^+$, 91%), (601.4, $[M - Br]^+$, 79%). HMRS (ESI) m/z: $(C_{34}H_{56}N_4Br_2 - 2Br)^{2+}$ calculated 260.2247, found 260.2257; $(C_{34}H_{56}N_4Br_2 - Br)^+$ calculated 599.3682, found 599.3684. R_f: 0.80 (MeOH:NH_4Cl 2 M H_2O:$MeNO_2$, 7:2:1).

2·2Br: ^{1}H NMR (300 MHz, $CDCl_3$, 25 °C, TMS): δ 0.88 (t, J = 6 Hz, 6H, CH_3), 1.25−1.32 (m, 28H, $(CH_2)_9$), 1.89 (m, 4H, N−CH_2−C**H**$_2$), 4.27 (t, J = 7.5 Hz, 4H, N−CH_2), 5.64 (s, 4H, CH_2), 7.16 (dd, J = 9 Hz, J = 6 Hz, 1H, Ar-H(5)), 7.29 (s, 2H, Im(4)), 7.61 (d, 2H, Ar-H(4,6)), 8.11 (s, 1H, Ar-H(2)), 8.21 (s, 2H, Im-H(5)), 10.44 (s, 2H, Im-H(2)). ^{13}C NMR (100 MHz, $CDCl_3$): δ 14.3 (CH_3), 22.9−32.1 ($(CH_2)_{10}$), 50.6 (N−CH_2), 52.9 (CH_2), 122.3 (Im-C(4)), 123.5 (Im-C(5)), 130.2 (Ar-C(4,5,6)), 130.9 (Ar-C(2)), 134.9 (Ar-C(1,3))/(ImC(2)), 136.6 (Ar-C(1,3))/(ImC(2)). MS (ESI) m/z: (288.6, $[(M - 2Br)/2]^{2+}$, 100%), (407.3, $[M - ((CH_2)_{11}CH_3)$, $-2Br]^+$, 6%), (657.4, $[M - Br]^+$, 16%). HMRS (ESI) m/z: $(C_{38}H_{64}Br_2N_4 - 2Br)^{2+}$ calculated 288.2560, found 288.2574; $(C_{38}H_{64}Br_2N_4 - Br)^+$ calculated 655.4308, found 655.4301.

1,3-Bis[(3-octadecyl-1-imidazolio)methyl]benzene dibromide (3·2Br). A solution of 1,3-bis(bromomethyl)benzene (0.50 g, 1.89 mmol) in dry MeCN (5 mL) was added to a solution of 1-octadecyl-1*H*-imidazole (1.2 g, 3.79 mmol) at 80 °C under argon atmosphere, and the stirring was continued for 22 h. The yellow solution was cooled to room temperature and a white solid precipitated. The solvent was evaporated, and the yellow residue was dissolved in CH_2Cl_2 (8 mL). Acetone (9 mL) was added until a white solid precipitated, which was filtered off and dried under vacuum to obtain **3·2Br** as a white powder (1.45 g, 85%).

3·2Br: ^{1}H NMR (400 MHz, $CDCl_3$, 25 °C, TMS): δ 0.88 (t, J = 7.5 Hz, 6H, CH_3), 1.26−1.32 (m, 60H, $(CH_2)_{15}$), 1.90 (m, 4H, N−CH_2−C**H**$_2$), 4.27 (t, J = 6 Hz, 4H, N−CH_2), 5.63 (s, 4H, CH_2), 7.16 (dd, J = 3 Hz, J = 6 Hz, 1H, Ar-H(5)), 7.26 (s, 2H, Im-H(4)), 7.59 (d, J = 6 Hz, 2H, Ar-H(4,6)), 8.09 (s, 1H, Ar-H(2)), 8.16 (s, 2H, Im-H(5)), 10.41 (s, 2H, Im-H(2)). ^{1}H NMR (300 MHz, $(CD_3)_2SO$, 25 °C): δ 0.85 (t, J = 6 Hz, 6H, CH_3), 1.23 (m, 60H, $(CH_2)_{15}$), 1.79 (m, 4H, N−CH_2−CH_2), 4.17 (t, J = 7.5 Hz, 4H, N−CH_2), 5.43 (s, 4H, CH_2), 7.38−7.50 (b.a., 4H, Ar-H(2,4,5,6)), 7.82 (dd, J = 9 Hz, J = 9 Hz, 2H, Im-H(4,5)), 9.32 (s, 2H, Im-H(2)). ^{13}C NMR (100 MHz, $CDCl_3$, 25 °C, TMS): δ 14.3 (CH_3), 22.9−32.1 ($(CH_2)_{16}$), 50.4 (N−CH_2), 52.6 (CH_2), 121.8 (Im-C(4)), 123.7 (Im-C(5)), 130.1 (Ar-C(4,5,6), 130.6 (Ar-C(2)), 134.8 (Ar-C(1,3)), 136.8 (Im-C(2)). MS (ESI) m/z: (372.4, $[(M - 2Br)/2]^{2+}$, 100%), (573.6, $[M - (Br, ((CH_2)_{17}CH_3)]^+$, 7%), (825.6, $[M - Br]^+$, 17%). HRMS (ESI) (m/z): $(C_{50}H_{88}N_4Br_2 - 2Br)^{2+}$ calculated 372.3499, found 372.3494; $(C_{50}H_{88}N_4Br_2 - Br)^+$ calculated 823.6186, found 823.6189. R_f: 0.55 (CH_2Cl_2:MeOH, 4:1). Elemental analysis calculated (%) for $C_{50}H_{88}N_4Br_2.3H_2O$: C 62.61, H 9.88, N 5.84; found: C 62.73, H 9.69, N 5.86

1,3-Bis(imidazolylmethyl)-5-methoxybenzene (6). Potassium hydroxide (0.46 g, 8.16 mmol) and 1*H*-imidazole (0.46 g, 6.80 mmol) were stirred vigorously in dry MeCN (120 mL) at room temperature under an argon atmosphere for 1 h until a solution was obtained. A solution of 1,3-bis(bromomethyl)-5-methoxybenzene (**5**) (1.00 g, 3.40 mmol) in dry MeCN (30 mL) was added, the reaction mixture turned turbid, and the stirring was continued for 15 h at room temperature. After this time, the suspension was filtered, and the solid was washed with CH_2Cl_2 (6 mL). The solution was concentrated in the rotary evaporator, and then the residue was dissolved in CH_2Cl_2 (250 mL). The organic solution was washed with water (3 × 150 mL),

dried over $MgSO_4$, filtered, and evaporated in vacuum to give **6** as a yellow oil (0.91 g, 99%).

6: ^{1}H NMR (400 MHz, $CDCl_3$, 25 °C, TMS): δ 3.73 (s, 3H, OCH_3), 5.06 (s, 4H, CH_2), 6.52 (s, 1H, Ar−H(2)), 6.59 (s, 2H, Ar-H(4,6)), 6.89 (s, 2H, Im-H(5)/Im-H(4)), 7.09 (s, 2H, Im-H(4)/Im-H(5)), 7.53 (s, 2H, Im-H(2)). ^{13}C NMR (100 MHz, $CDCl_3$, 25 °C, TMS): δ 50.6 (CH_2), 55.6 (OCH_3), 112.7 (Ar−C(4,6)), 118.2 (Ar-C(2)), 119.5 (Im-C(4)/(5)), 130.2 (Im-C(4)/(5)), 137.6 (Im-C(2)), 138.9 (Ar-C-(1,3)), 160.9 (Ar-C(5)). MS (EI) *m/z*: (160.1, [M − (CH_2−Im), − (OCH_3)]$^+$, 79%), (186.1, [M − (CH_2−Im)]$^+$, 56%), (201.1, [M − Im]$^+$, 59%), (268.1, [M]$^+$, 100%). HRMS (ESI) *m/z*: ($C_{15}H_{16}N_4O$ + H)$^+$ calculated 269.1396, found 269.1408. R_f: 0.44 (MeOH:CH_2Cl_2, 1:9). Mp: 71−75 °C.

1,3-Bis[(3-dodecylthioundecyl-1-imidazolio)methyl]-5-methoxybenzene Dibromide (4·2Br). 1,3-Bis(imidazolylmethyl)-5-methoxybenzene (**6**) (0.38 g, 1.42 mmol) and 11-bromoundecylthiododecane[20] (1.23 g, 2.83 mmol) were dissolved in anhydrous THF (30 mL) under reflux and argon atmosphere for 2 days. The solvent was evaporated, and the residue was dissolved in CH_2Cl_2 (50 mL). The white solid that precipitated with acetone (20 mL) was filtered off to give **4·2Br** as a white powder (0.75 g, 46%).

4·2Br: ^{1}H NMR (400 MHz, $CDCl_3$, 25 °C, TMS): δ 0.88 (t, 6H, J = 8 Hz, CH_3), 1.26−1.36 (m, 32H, $(CH_2)_{16}$), 1.57 (m, 8H, S−CH_2-−CH_2), 1.89 (m, 4H, N−CH_2−CH_2), 2.50 (t, J = 8 Hz, 8H, S−CH_2), 3.71 (s, 3H, OCH_3), 4.27 (t, J = 8 Hz, 4H, N−CH_2), 5.58 (s, 4H, CH_2), 7.16 (s, 4H, Ar−H(4,6)), 7.19 (s, 2H, Im-H(4)/Im-H(5)), 7.65 (s, 1H, Ar-H(2)), 8.22 (s, 2H, Im-H(4)/Im-H(5)), 10.53 (s, 2H, Im-H(2)). ^{13}C NMR (100 MHz, $CDCl_3$, 25 °C, TMS): δ 14.3 (CH_3), 22.9−32.1 ($(CH_2)_{19}$), 32.4 (S−CH_2), 50.5 (N−CH_2), 52.7 (CH_2), 56.3 (OCH_3), 115.7 (Ar-C(4,6)), 121.6 (Im-C(4)/Im-H(5)), 122.3 (Ar-C(2)), 123.9 (Im-H(4)/Im-C(5)), 136.1 (Ar-C(1,3)), 137.1 (Im-C(2)), 160.6 (Ar-C(5)). MS (ESI) *m/z*: (489.4, [(M − 2Br)/2]$^{2+}$, 100%), (1059.7, [M − Br]$^+$, 18%). HRMS (ESI) *m/z*: ($C_{61}H_{110}N_4Br_2OS_2$ − Br)$^+$ calculated 1057.7298, found 1057.7294. R_f: 0.57 (CH_2Cl_2:CH_3OH, 4:1). Mp: 126−127 °C.

Synthesis of AuNP with Hexadecanethiol (HDT). An aqueous solution of hydrogen tetrachloroaurate (5 mL, 0.16 mmol) was mixed with a solution of tetraoctylammonium bromide in toluene (10 mL, 0.37 mmol). The two-phase mixture was stirred and hexadecanethiol (0.014 mmol) was added to the organic phase while stirring. An excess of an aqueous solution of sodium borohydride (20 equiv) was slowly added with vigorous stirring. After 4 h the organic phase was separated and evaporated in a rotary evaporator. Finally, the mixture was subjected to three subsequent cycles of suspension in ethanol (3 mL) and acetone (3 mL) and centrifugation to remove completely the non-nanoparticulate materials to obtain a dark brown solid, which was dissolved in dichloromethane.

Synthesis of AuNP with Imidazolium Salts. The gold nanoparticles (**1·AuNPs**−**4·AuNPs**) encapsulated with an imidazolium shell were synthesized by the standard two-phase method. $AuCl_4^-$ was transferred from aqueous $HAuCl_4$ solution (10 mL, 0.32 mmol) to a dichloromethane phase (10 mL) by the phase transfer reagent **1·2Br**−**4·2Br** (0.24 mmol). The organic phase was separated, and an excess (20 equiv) of aqueous reducing agent ($NaBH_4$) was slowly added. The reaction was allowed to occur under stirring at room temperature for 4 h. The organic phase of the resulting dark red solution was separated using an extraction funnel and was subjected to solvent removal in a rotary evaporator, followed by multiple washings using ethanol (3 × 5 mL) and acetone (3 × 5 mL). Finally, a red solid was obtained, which was dissolved in dichloromethane.

Anion Binding. The titration experiments were performed by ^{1}H NMR measurements of **1·2Br** solutions in $(CD_3)_2SO$ (0.5 mM) containing increasing concentrations of valproate and ibuprofenate sodium salts in the following bis-imidazolium:drug ratios: 1:0, 1:2, 1:3, 1:5, 1:7, 1:10, 1:13, 1:15, and 1:20. The samples were obtained by mixture and dilution of stock solutions of **1·2Br**, where the 0.6 mL volume sample contained 0.5 mM bis-imidazolium receptor. The titration data were analyzed using Origin 7.0 SR0 (1991−2002) from OriginLab Corporation, Northampton, MA, USA.

Transmission Electron Microscopy (TEM). For the preparation of the samples suitable for TEM study, 5 μL of solution of **HDT·AuNPs**, **3·AuNPs**, and **4·AuNPs** in CH_2Cl_2 were deposited onto a carbon-coated copper grid, which were previously kept under UV light for 5 min to provide static charge and therefore to enhance the nanoparticle adsorption on it. Then, the CH_2Cl_2 was allowed to evaporate and the sample was ready to be observed by TEM. All the samples were kept in the dark and visualized just after preparation or the following day.

Toxicity Study. For cytotoxicity assay Caco-2 cells were cultured in Dulbecco's modified Eagle's medium (DMEM, Sigma-Aldrich) containing 10% fetal calf serum (Hyclone), 2 mM glutamine (Sigma-Aldrich), and antibiotics (Sigma-Aldrich, 50 U/mL penicillin and 50 μg/mL streptomycin). Cells were exposed for 48 h under 5% CO_2 at 37 °C and the viability was assessed by the MTT assay based in mitochondrial dehydrogenase enzyme capability to hydrolyze chromogen bromide (3-(4,5-dimethylthiazol-2-yl)-2,5-diphenyltetrazolium bromide). Data were statistically analyzed by SPSS v15 using U of MannWihtney statistic.

The genotoxicity study performed was the Comet Assay, which was done according to the guidelines.[43] In the assay, the percentage of DNA in the tail was determined with respect to the intensity of the total DNA, in 50 cells. The determination was done using the software *Comet Assay IV*. The cell line used was also the Caco-2 cell line.

Cell uptake was studied in Caco-2 cells by transmission electron microscopy (TEM). A subcytotoxic dose of 70 μg/mL of AuNP (1% dichloromethane) was administered to Caco-2 cells grown until confluence. After 15 and 30 min and 1, 4, and 24 h, cells were fixed with 2.5% glutaraldehyde and then harvested in microtubes and maintained at 4 °C. The recollection in microtubes allowed cell pellet obtaining by centrifugation and next steps. Cell pellets were rinsed with phosphate buffer 0.1 M and fixed with 1% osmium tetroxide for 2 h. Samples were washed again in phosphate buffer and dehydrated in acetone: 50% for 10 min, 70% twice for 10 min, 90%, 96%, and 100% three times for 15 min. Subsequently, cell pellets were infiltrated in increasing proportion of EPON 12 resin (47% Eponate 812, 25% DDSA (dodecenyl succinic anhydride), 28% NMA (NADIC methyl anhydride)) 3:1, 1:1, 1:3 in acetone for 1 h, before a final infiltration step in 100% resin. At this point samples were included in resin with DMP-30 catalyst and polymerized overnight in a stove at 60 °C for 48 h. Then 50 nm thin sections were cut in a LEICA EM FCS ultramicrotome and post-stained with uranyl acetate for 30 min and plumb citrate for 5 min. Samples were observed with a JEOL 1010 transmission electron microscope (TEM) at 80 kV.

Transfer of Sodium Ibuprofenate with 3·AuNPs to an Organic Phase. An aqueous solution of 1.9 mM sodium ibuprofenate was prepared (solution a). Three milliliters of this solution were added to 3 mL of dichloromethane, and they were mixed in a separatory funnel; the aqueous phase was recovered (solution b). Also 3 mL of solution a was added to 3 mL of **3·AuNPs** and they were mixed in a separatory funnel; the aqueous phase was recovered (solution c). The aqueous phases of the three solutions were studied by UV−vis. The concentration of ibuprofen in the aqueous phases was determined by the Beer−Lambert law. The quantity of ibuprofenate in solutions b and c was 96.1% and 33.3%, respectively, of the initial solution.

Release Study. To obtain the ibuprofenate-loaded gold nanoparticles, a 10 mM sodium ibuprofenate aqueous solution was prepared. Five milliliters of this solution was added to 9 mL of **3·AuNPs** solution in dicloromethane, and they were mixed in a separation funnel. The organic phase was collected and extracted twice with water to remove

Scheme 1. Synthesis of Amphiphilic Protophanes 1·2Br−3·2Br.

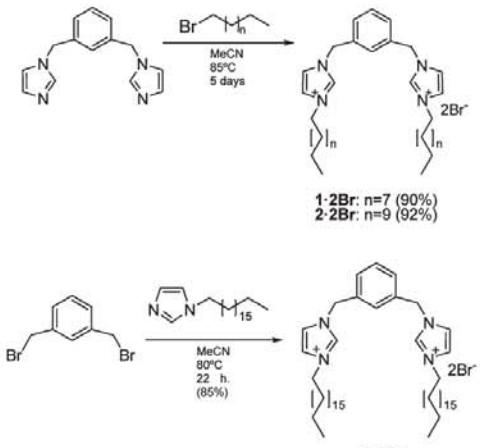

Scheme 2. Synthesis of the Amphiphilic Protophane 4·2Br

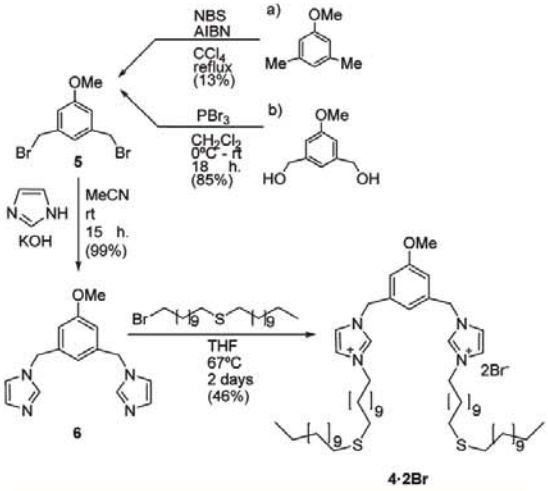

ibuprofenate excess. To obtain the ibuprofenate−**3·2Br** complex, 5 mL of the same sodium ibuprofenate solution was added to 9 mL of **3·2Br** solution 2 mM in dicloromethane and they were mixed in a separation funnel. The extraction was performed as described above. The presence of ibuprofenate was determined in organic and aqueous phases through UV−vis spectroscopy.

Dynamic Dialysis Experiments. Dialysis membranes were hydrated in Milli-Q water and placed in one end-cap of the biodialyzer. Solutions of ibuprofenate−**3·AuNPs** (0.6 mL), **3·AuNPs** (0.3 mL) (as control), and ibuprofenate−**3·2Br** (0.7 mL) (as control) in CH_2Cl_2 were placed into the biodialyzers. The CH_2Cl_2 was allowed to evaporate, and Milli-Q water (0.8 mL) was added to every biodialyzer. Hydrated dialysis membranes were placed on the other side of the end-caps, and the biodialyzers were closed. Five replicas of biodialyzers containing ibuprofenate−**3·AuNPs** were prepared. All the containers were placed into a reactor with water jacket to keep the systems at a fixed temperature of 32 °C by using a circulating bath with temperature control. The whole setup experienced a continuous left−right movement (for details see Figure S8 in the Supporting Information). The fixed diffusing area of the dialysis membranes per biodialyzer was 2 × 2.01 cm^2, and the diffusion experiments lasted 8 days. At known time intervals, samples (3 mL) were extracted from the receptor phase, and the volume was replaced by fresh Milli-Q water (3 mL). The amount of permeated ibuprofenate was determined by UV−vis spectrophotometry by using a calibration curve of ibuprofenate for the peak at 273 nm in the same absorbance range.

Static Dialysis Experiments. Hydrated dialysis membranes were placed in the donor chamber of the Franz-type diffusion cells. Solutions of ibuprofenate−**3·AuNPs** (0.197 mL), **3·AuNPs** (0.099 mL) (as control), and ibuprofenate−**3·2Br** (0.230 mL) (as control) in CH_2Cl_2 were poured into the donor compartment onto the dialysis membranes; the volumes were determined to ensure that the amount of ibuprofenate per mm^2 in these cells was equivalent to the dynamic dialysis experiments. The organic solvent was allowed to evaporate, and the appropriate solution (Sorensen Buffer 0.067 M pH 7.4 or Milli-Q water acidified to pH 5.5) (0.263 mL) was added to the donor chamber. The dialysis membrane and the donor container were put onto the glass receptor chamber, which contained 67 mM NaOH pH 11 and was fixed with a joint. The Franz-type cells were connected to a controlled temperature system, with a heating bath set to 32 °C (in the case of pH 5.5 donor solution) or 37 °C (in the case of pH 7.4 donor solution) (for details see Figure S9 in the Supporting Information). The fixed diffusing area of the dialysis membranes was 2.54 cm^2. Samples of 0.3 mL were taken at regular intervals, and the volume was replaced with Milli-Q water. The concentration of ibuprofenate in samples was determined by in a Waters LC Module I. The column used was a Waters Spherisorb 5 μm ODS-2 (4.6 mm × 150 mm); the mobile phase was acetonitrile−water pH 3, adjusted with orthophosphoric acid (65:35 v/v). The flow rate was 1.5 mL/min, and the detection wavelength was 220 nm. The data was collected using Millennium32 version 4.0.0 software from Waters Corporation.

RESULTS AND DISCUSSION

Synthesis and Characterization of Amphiphilic Bis-imidazolium Salts. Dicationic protophanes **1·2Br** and **2·2Br** were obtained in >90% yield by treatment of 1,3-bis(imidazolylmethyl)benzene,[16] with different 1-bromoalkanes (Scheme 1), whereas, following an alternative approach, quaternization of *N*-octadecyl-1*H*-imidazole with 1,3-bis(bromomethyl)benzene proceeded in 85% yield to give dicationic protophane **3·2Br** (Scheme 1).

Protophane 1,3-bis(imidazolylmethyl)-5-methoxybenzene (**6**) (Scheme 2) was obtained in good yield and purity by means of reaction of potassium imidazolate with the bis(bromomethyl) derivative **5** in MeCN at room temperature. Compound **5** was previously prepared by either (a) radical bromination of 1,3-dimethyl-5-methoxybenzene with *N*-bromosuccinimide (NBS) in CCl_4 under reflux in presence of α,α'-azoisobutyronitrile (AIBN) or (b) bromination of the 1,3-bis(hydroxymethyl)-5-methoxybenzene using PBr_3 in CH_2Cl_2 at room temperature. Clearly, bromination using PBr_3 is the method of choice for the preparation of the bromoderivative **5** according to the higher yield obtained (85%), compared to the radical bromination yield (13%) (Scheme 2). Finally, reaction of protophane **6** and 11-bromoundecylthiododecane[20] in darkness, afforded the dicationic open chain protophane **4·2Br** in moderate yield (46%), probably due to the difficulty of its purification (Scheme 2).

These newly synthesized bis-imidazolium amphiphiles had a high degree of purity, and their structural properties were

examined in solution by ^{1}H and ^{13}C NMR spectroscopy and electrospray ionization (ESI) and matrix assisted laser desorption ionization time-of-flight (MALDI-TOF) mass spectrometry prior to the assessment of their complexation behavior (see later). Selected ^{1}H NMR spectroscopic data for all the new dicationic protophanes **1·2Br**−**4·2Br** is included in Table 1, and ^{1}H and ^{13}C NMR spectroscopic data for all the new compounds is collected in Tables S1 and S2 (Supporting Information). The ^{13}C NMR chemical shifts for dications **1·2Br**−**4·2Br** were consistent with data from correlative systems and individual assignments were made by HMQC. The results from the mass spectrometry analysis are incorporated in Table 2.

The ^{1}H NMR spectra of dications **1·2Br**−**4·2Br** in $CDCl_3$ showed sharp singlets for the interannular methylene protons, which indicated conformational mobility; this flexibility was also observed in the previously prepared [1$_4$]*meta*heterophane frameworks and dicationic protophanes.[16,21] A selection of the most representative hydrogen atoms are listed in Table 1, which

Table 1. ^{1}H NMR Spectroscopic Data from Compounds 1·2Br−4·2Br

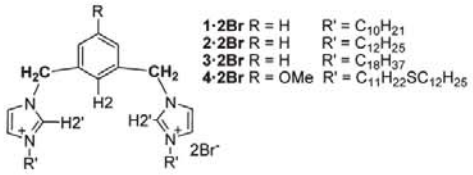

compound	solvent	CH_2	H-2	H-2′
1·2Br	$CDCl_3$	5.64	8.12	10.43
	$(CD_3)_2SO$	5.47	7.61	9.48
	CD_3OD	5.50	7.47−7.71	*b*
$\Delta\delta^a$		−0.17	−0.51	−0.95
2·2Br	$CDCl_3$	5.64	8.11	10.44
3·2Br	$CDCl_3$	5.63	8.09	10.41
	$(CD_3)_2SO$	5.43	*c*	9.32
$\Delta\delta^a$		−0.20		−1.09
4·2Br	$CDCl_3$	5.58	7.65	10.53

[a] $\Delta\delta$ chemical shift difference between the ^{1}H NMR spectrum recorded in $CDCl_3$ and $(CD_3)_2SO$. [b] The signal cannot be observed due to the H/D exchange of the hydrogen atom of this position. [c] Broad signal.

indicate a good correlation for the chemical shifts of all the structures and are in agreement with the data previously reported for parent compounds.[21] The only significant difference relates to the chemical shift of the spacer phenyl in **4·2Br**, with hydrogen atoms shielded 0.5 ppm as a consequence of the influence of the alkoxy substituent (Table 1). The proton chemical shifts of the C(2′)−H are indicative of the acidity of these hydrogen atoms, and therefore, of their ability to coordinate anions. The amphiphilic protophanes are soluble in organic solvents such as chloroform or dichloromethane, and we have observed a clear solvent effect by ^{1}H NMR spectroscopy when comparing the chemical shifts of their aromatic protons in solvents of different polarity. As can be seen in Table 1, the solvent influence is observed with a general shielding effect when the solvent polarity is increased by comparing the chemical shifts (δ) of acidic protons of in $CDCl_3$ with those in polar solvents such as $(CD_3)_2SO$ or CD_3OD (Table 1), although H/D exchange precludes a clear observation of the signals when CD_3OD is used. The measurements were performed by keeping the product concentration always below the aggregation values, to avoid the influence of self-association in chemical shift values. Thus, for **1·2Br**, the protons of Ar-H(2) and Im-H(2′) are shifted upfield 0.51 ppm and 0.95 ppm, respectively, when $(CD_3)_2SO$ is used as the solvent. Likewise, in the same solvent, **3·2Br** experiences a variation in chemical shift in 1.09 ppm upfield for Im-H(2′) protons. These observations are the result of the increasingly higher polarity of the solvent and the diminished hydrogen bonding interaction between the imidazolium receptor and its corresponding anion in the polar solvent.

The length of the hydrophobic chain does not seem to influence significantly the ^{1}H NMR chemical shifts of dicationic protophanes. For instance, in the spectrum recorded in $CDCl_3$, of imidazolium protophanes **1·2Br**−**3·2Br** no appreciable variation in δ can be accounted (max $\Delta\delta$ = 0.04 ppm) for any of the aromatic hydrogen atoms, as indicated in Table 1.

Electrospray ionization mass spectrometry (ESI-MS) has been used to examine the charged protophanes **1·2Br**−**4·2Br**. For recording their positive ion ESI-MS the samples were dissolved in a 1:1 mixture of H_2O/MeCN at 200 μL min^{-1} at a cone potential of 215 V. Table 2 collects the observed peaks originating from the positive ESI response of the open-chain imidazolium dications, which resulted in the formation of two main characteristic ions for all the compounds, although there are variations in their abundances. Thus, the most representative peaks correspond to (a) the dication arising from the loss of the two bromide counterions $[(M - 2Br)/2]^{2+}$, which is the highest

Table 2. Positive-Ion Mode MS for Compounds 1·2Br−4·2Br

		ions[b] (*m*/*z*)					
compound	MW[a] (g mol^{-1})	$[(M - 2Br/2)]^{2+}$	$[M - 2Br - [(CH_2)_nCH_3]]^+$	$[M - Br - [(CH_2)_nCH_3]]^+$	$[M - 2Br - 2H]^+$	$[M - Br - 2H]^+$	$[M - Br]^+$
1·2Br[c]	680.6	260.7 (100%)	379.3 (91%)				601.4 (79%)
2·2Br[c]	736.8	288.6 (100%)	407.3 (6%)				657.4 (16%)
3·2Br[c]	905.1	372.4 (100%)		573.6 (7%)			825.6 (17%)
3·2Br[d]		372.4 (100%)		573.6 (3%)	743.6 (1%)	823.6 (2%)	825.6 (3%)
3·2Br[e]				(6%)	(78%)		(100%)
3·2Br[f]					(3%)		(2%)
4·2Br[c]	1139.5	489.4 (100%)					1059.7 (18%)

[a] Molecular weight. [b] Ions, *m*/*z* ratio relative abundance (%). [c] ESI-MS at V_c = 215 V in CH_3CN:H_2O (1:1, v/v). [d] ESI-MS at V_c = 80 V in CH_3CN:H_2O (1:1, v/v). [e] MALDI-TOF-MS with matrix DHB. [f] MALDI-TOF-MS without matrix.

dx.doi.org/10.1021/la203601n |*Langmuir* 2012, 28, 2368–2381

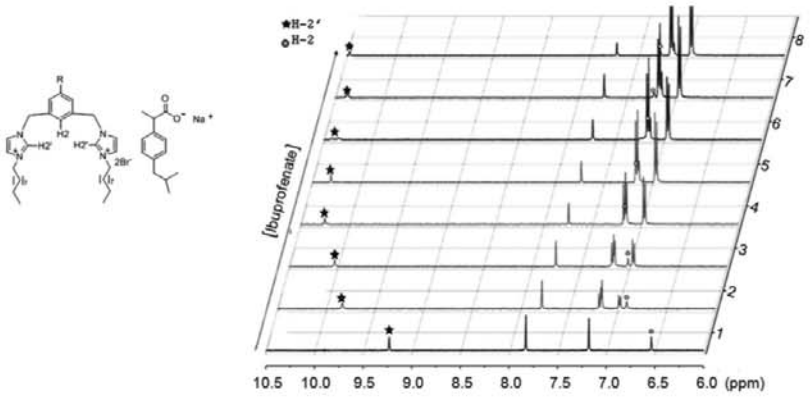

Figure 2. Chemical shifts of the aromatic interval which show the upfield effect of the proton signals H-2 and H-2′ of **1·2Br** in 0.5 mM $(CD_3)_2SO$ solutions, with an increasing **1·2Br**:ibuprofenate ratio: 1:0, 1:2, 1:3, 1:7, 1:10, 1:10, 1:13, 1:15, and 1:20.

intensity peak in all the cases, and (b) the monocation formed by the loss of one bromide counterion $[M - Br]^+$ (Table 2).[21,22]

The peaks corresponding to the loss of the hydrocarbon chain in compounds **1·2Br**−**4·2Br** are not very common, partly due to the experimental conditions of the ESI employed, and their intensity is lower when the hydrophobic chain length increases (Table 2). Thus, other representative peaks correspond to (a) for compounds **1·2Br** and **2·2Br**, the singly charged ion formed by the loss of two bromide ions and loss of one alkyl chain $[(M - 2Br - (CH_2)_nCH_3]^+$, and (b) for compound **3·2Br**, the singly charged ion formed by the loss of one bromide ion and loss of one alkyl chain $[(M - Br - (CH_2)_nCH_3]^+$.

Peaks indicative of the formation of *N*-heterocyclic carbenes, originated by deprotonation of imidazolium species, were not observed for compounds **1·2Br**−**4·2Br**, as was previously reported for related compounds,[21,22] partly because carbene fragments are normally detected at lower voltages. Thus, when the ESI-MS spectrum of **3·2Br** was registered using V_c = 80 V, peaks corresponding to singly charged imidazolylidene ions were also observed assigned to the carbene species $[M - Br - 2H]^+$ and $[M - 2Br - 2H]^+$, resulting from the loss of two protons and one or two bromide ions, respectively. However, the abundance of these carbene peaks was very low (<2%).

Interestingly, when MALDI-TOF-MS was used, the results were significantly different. Thus, when DHB was used as the matrix, the spectra of **3·2Br** indicated (Table 2) that the main peak corresponded to the ion $[M - Br]^+$, but the carbene $[M - 2Br - 2H]^+$ showed a 78% abundance, indicating that this is a much more sensitive technique to generate and detect carbene species. Instead, the MALDI-TOF spectrum recorded without matrix shows very low peaks corresponding to these ions, as well as some fragmentation (Table 2).

Supramolecular Behavior and Anion Binding Properties of the Amphiphilic Bis-imidazolium Salts. In this work we will show that, despite their relatively low preorganization, open-chain imidazolium analogues exhibit anion binding properties that could be used for the complexation of anions. We have previously reported the anion binding properties of preorganized imidazolium-based macrocycles in polar solvents such as CD_3CN and $(CD_3)_2SO$ by ^1H NMR spectroscopy, and the study revealed the importance of the hydrogen bonds in controlling anion binding, showing that the maximum association constant obtained was formed between and imidazolium heterophane and acetate anions (TBA·AcO).[16] The bis-imidazolium amphiphile **1·2Br** was selected to examine its complexation ability toward organic carboxylate ions. Sodium ibuprofenate and sodium valproate were chosen as models of anionic drugs, and their sodium salts were used as guests. Additionally, ibuprofen is a nonsteroidal anti-inflammatory drug, whose control of adsorption and release is of interest in medicinal applications.[19,23] Likewise, valproate is an antiepileptic drug, whose increasing concentration in blood can induce adverse effects; therefore, it is important to exert controlled delivery and release, besides its monitorization.[24] Titration experiments were performed using increasing concentrations of a specific carboxylate sodium salt of the drug that were added to a fixed concentration (0.5 mM) of bis-imidazolium **1·2Br** solution in $(CD_3)_2SO$. The ^1H NMR spectrum of each solution was recorded to observe the variations in the chemical shift ($\Delta\delta$) corresponding to the hydrogen atoms more involved in the hydrogen bonds established with the anion, H-2 and H-2′ (Figure 2).

Binding isotherms were obtained after plotting the variation in the chemical shift of these protons as a function of valproate or ibuprofenate concentration, and a selection is shown in Figure S1 (Supporting Information). The binding isotherms allowed deduction of the degree of anion binding by fitting the data in a nonlinear curve fitting program applying a one-site binding model using Origin 7.0 software. Thus, K_a was obtained from the fitting process, and ΔG° was deduced from the Eyring equation ($\Delta G = -RT \ln K_a$). The values obtained for complexation between **1·2Br** and sodium ibuprofenate (K_a = 279 M^{-1}, corresponding to a complexation free energy of $-\Delta G^\circ$ = 13.95 kJ/mol) were similar to those obtained for valproate (K_a = 358 M^{-1}, corresponding to a complexation free energy of $-\Delta G^\circ$ = 14.6 kJ/mol) in this polar solvent.

Therefore, the binding studies indicate a considerable anion interaction between the protophane **1·2Br** and the carboxylate anions contained in both ibuprofenate and valproate sodium salts. Remarkably, the energy associated with this interaction has a very similar value to that estimated for analogous macrocycles and tetrabutylammonium acetate, indicating that the anion recognition ability of the macrocycles is also present in their open-chain analogues, a clear advantage considering the greater simplicity of the synthesis and structure of the protophanes.

It is worth mentioning that water was always observed to some extent in the ^{1}HNMR spectra recorded for the titration experiments. This solvent is as a competing agent for hydrogen bonds in the anionic drugs titration experiments because it is very difficult to obtain completely anhydrous solutions. However, water solvation does not prevent binding between the imidazolium salts and the carboxylate anions of the drugs. At this stage it is not possible to weigh the relative importance of interference with hydrogen bonding and the hydrophobic effect which might plausibly enhance binding of the relatively hydrophobic drugs. Be that as it may, the binding constants of the drugs with the protophanes are comparable with those of the macrocycles.

Synthesis of Gold Nanoparticles Using Amphiphilic Bis-imidazolium Salts as Transfer Agents and Stabilizers. The synthesis of gold nanoparticles in organic media was used for the preparation of the colloids in this work because it has some characteristic advantages over other methods, such as the relative ease of isolation and the control of the size of the particles.[25] It is achieved following the Brust−Schiffrin method[6] consisting of a phase transfer protocol that habitually relies in the use of thiol ligands and is performed in a biphasic system because the thiol group binds strongly to the gold; the gold(III) salt is transferred to an organic phase, generally toluene, by a tetraoctylammonium salt acting as the transfer method and then reduced by sodium borohydride in the presence of the alkanethiol. The AuNPs generally have a diameter between 1.5 and 5.2 nm, although size and shape could be tuned by experimental conditions.[26] The AuNPs prepared by this methodology can be stored, and redissolved in organic solvents, without changes in their properties.

The synthesis of gold nanoparticles **1·AuNPs**−**4·AuNPs** using the imidazolium amphiphiles **1·2Br**−**4·2Br**, both as phase transfer agents and as colloid stabilizers, was achieved by using a modified Brust−Schiffrin methodology[6] particularly regarding the solvent. Our imidazolium salts are not soluble in toluene, so dichloromethane was employed as it has been shown to perform well in AuNP synthesis.[27] Notably, although no additional stabilizing ligands are incorporated, the bis-imidazolium capped AuNPs are perfectly stable, unlike those intermediate AuNPs capped with tetraoctylammonium salts. The colloidal suspensions resulting from the reaction are stable for months.

One concern during the synthesis is the fate of the imidazolium ligands in the reaction conditions, especially in the presence of $NaBH_4$, because their reduction could lead to the formation of carbenes.[28] Despite their likely stability,[29] carbenes have been inferred in the stabilization[30] and formation[31] of AuNPs. However, ^{1}H NMR experiments indicated the stability of the imidazolium moieties. Additionally, in our hands, the lack of $NaBH_4$ in the experimental conditions used did not lead to the formation of nanoparticles, whatever the proportion of imidazolium salts to gold(III) salts, judging by the absorption spectra and the TEM analysis of the solutions.

Also the experimental conditions are known to influence the morphology of the AuNPs. For instance, larger thiol/gold mole ratios give smaller average core sizes, and fast reductant addition and cooled solutions produced smaller, more monodisperse particles.[2a] Another aspect we are interested to explore is the effect of the alkyl chain variation on the formation constitution, and stability of the new nanoparticles, as this effect had been explored for some previously described coating surfactants.[32]

The size and morphology of the AuNPs obtained with our imidazolium ligands was compared with the size and morphology

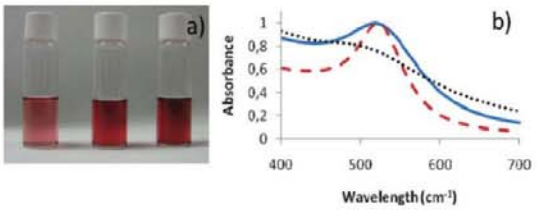

Figure 3. (a) Images of gold nanoparticles **3·AuNPs**, **2·AuNPs**, and **4·AuNPs** in dichloromethane, prepared with **3·2Br**, **2·2Br**, and **4·2Br**, from left to rigth. (b) UV−vis absorption spectra of the gold nanoparticles: coated with hexadecatethiol **HDT·AuNPs** (dotted line), **3·AuNPs** (solid line), and **4·AuNPs** (dashed line).

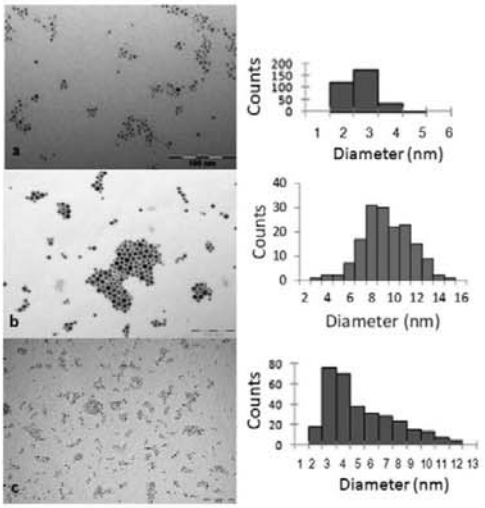

Figure 4. TEM pictures of the gold nanoparticles **HDT·AuNPs** (a), **3·AuNPs** (b), and **4·AuNPs** (c) and their corresponding size distribution histograms.

of those nanoparticles synthesized using hexadecanethiol and tetraoctylammonium bromide, reproduced in our laboratories to ensure direct comparison. The best synthetic conditions were found to be using a ratio 1:0.75:20 for gold(III)/imidazolium salt/sodium borohydride, using dichloromethane as the organic phase, whereas using higher imidazolium amphiphile ratio only produced slightly smaller nanoparticles. The main observations deduced from the different experiments that were carried out are included in Table S3 (Supporting Information).

■ CHARACTERIZATION OF THE GOLD NANOPARTICLES

Absorption Spectroscopy (UV−Vis). The gold nanoparticles prepared in this work give solutions with colors ranging from light to dark red as shown (Figure 3a). The absorption spectroscopy (UV−vis), showing absorption peaks at approximately 519 nm for **3·AuNPs**, and 521 nm for **4·AuNPs**, originated from the surface plasmon absorption of the particles (Figure 3b).

Transmission Electron Microscopy (TEM) and Dynamic Light Scattering (DLS). A morphological study of the different

Table 3. Size of 3·AuNPs in Dichloromethane Measured by DLS Sequentially at Different Temperatures ($n = 3$)

temp/°C	size/nm
25	15.2 ± 0.1
37	19.5 ± 0.3
4	19.9 ± 0.1
25	18.3 ± 0.1
37	22.7 ± 0.2

AuNPs was carried out using transmission electron microscopy (TEM), allowing assessment of the morphology and size of the nanoparticles. Figure 4 shows the size distribution as well as the TEM micrographs of the differently coated nanoparticles. The samples were prepared by drop casting the different AuNPs solutions in CH_2Cl_2 over a carbon-coated copper grid and were imaged in the electron microscope after drying in air. The images corresponding to **HDT·AuNPs** (Figure 4a) show that their diameter lies in the range 1−5 nm, with a maximum in the particle size distribution at 2−3 nm. On the other hand, nanoparticles with an imidazolium coat **3·AuNPs** and **4·AuNPs** (Figure 4b,c, respectively), display an average core size of 8.8 ± 2.2 and 5.3 ± 2.4 nm, respectively. These results are in agreement with the size difference inferred by the UV−vis spectra. It has also been observed (Figure 4) that gold nanoparticles encapsulated with the imidazolium salts **3·AuNPs** and **4·AuNPs** show different types of polydispersity, which are greater than the thiol capped particles.

The size of the **3·AuNPs** nanoparticles was also measured through dynamic light scattering (DLS). The average size measured was 15.2 ± 0.1 nm. This result implies a slightly higher diameter than that observed by TEM, in agreement with the fact that this technique measures the hydrodynamic size of the particles, in contrast with TEM that only gives us the gold core size, because no contrast agent was used and the imidazolium ligand is relatively transparent to the electron beam compared with the gold. Thus, the size measured by DLS gives the diameter that includes not only the core but also the alkyl chains of the **3·2Br** coating protophane, and the values obtained are in agreement with the formation of a monolayer. As indicated in Table 3, a sample of **3·2Br** was heated from 25 to 37 °C, cooled to 4 °C and warmed again to 25 and 37 °C. Variations in the temperature of DLS measurements did not affect significantly the size of the nanoparticles, as indicated by the small differences in the nanoparticles size values included in Table 3, suggesting that they are stable and do not aggregate easily (see later). The polydispersity value obtained using this technique was low, having a PDI value of 0.18.

Mass Spectrometry. Matrix assisted laser desorption ionization time-of-flight mass spectroscopy (MALDI-TOF-MS) was used to study the gold nanoparticles **3·AuNPs** and **4·AuNPs**, and the results are gathered in Table 4. Despite precedence from the literature reports,[33] the experimental conditions to observe AuNPs were difficult to find. The spectra were recorded in the absence of a matrix or using different matrices for the purpose (α-cyano-γ-hydroxycinnamic acid and DHB). In all cases, for both **3·AuNPs** and **4·AuNPs**, the most abundant peak was the singly charged peak corresponding to the gold complex with the two imidazolylidene moieties of one molecule of the corresponding protophane. Depending on the matrix used, different peaks corresponding to the loss of one bromide ion from the original protophane, or peaks corresponding to loss of alkyl chains, were detected with low intensity (Table 4). The use of no matrix also allowed the observation of gold clusters (Figure S2, Supporting Information).

Time-of-flight secondary ion mass spectrometry (TOF-SIMS) was used to confirm the presence of gold nanoclusters in the sample, prior to attempting a quantitative analysis. The samples were prepared by a drop casting of the AuNPs solution (CH_2Cl_2) onto a silicon substrate.

Initial difficulty to find the right experimental conditions to run the samples seemed to be caused by low loading concentrations of the metallic particles. For this reason two different samples of **3·AuNPs** at different concentrations were analyzed by TOF-SIMS. Different mass peaks corresponding to Au were found, as seen in Figure S3 in the Supporting Information, which shows four different peaks corresponding to one, two, three, and four gold atoms, respectively. These results indicate the presence of various gold atoms on the surface of the core of the nanoparticle. On the other hand, it was not possible to obtain information about the disposition of the imidazolium coating units with respect to the gold nanoparticles because of the limitations of the apparatus regarding the size of the discrete aggregate molecules in the samples. To observe clearly the gold signals in the core, it was necessary to clean the sample (sputtering). This fact emphasizes that TOF-SIMS is a surface analysis technique that is sensitive to the length of coating molecules that can hinder effective ionization. It can also be taken as another indication of the dense packing of the imidazolium coating ligands.[34]

X-ray Photoelectron Spectroscopy (XPS). X-ray photoelectron spectroscopy (XPS) was used to determine the valence state of gold in the synthesized nanoparticles. The samples were prepared by drop casting of the different AuNP solutions (CH_2Cl_2) onto a silicon substrate. As stated for the TOF-SIMS experiments, sputtering of the sample was necessary to identify clearly the peaks corresponding to Au, N, and Br in the gold nanoparticles **3·AuNPs** and **4·AuNPs**, but the signals were identified after this process, indicating the proximity of the imidazolium ring to the gold core of the nanoparticles. This fact was also supported by the very broad signals of the aromatic signals of the imidazolium moiety in a ^{1}H NMR spectrum of **3·AuNPs** recorded in $CDCl_3$. The values and relative intensities of the peaks in the XPS gave additional information to confirm the structure of the imidazolium coated AuNPs. The characteristic binding energies of Au^0 at 88.2 and 84.5 eV corresponding to the double peaks of Au $4f_{5/2}$ and Au $4f_{7/2}$ can be observed for **3·AuNPs** and **4·AuNPs** (Figure S4, Supporting Information), these being typical values for Au^0. The absence of signals corresponding to Au^I eliminates the possibility that the ligand interaction with the gold atoms is stabilized through a carbene structure.[30] This observation is also supported by the presence of bromine (and chlorine, possible due to an anion exchange in the synthesis process), which indicates the integrity of the ligand in the AuNPs. Quantitative analysis of the XPS signals, especially for Au 4f and N 1s, indicated a proportion of coating ligand:Au 1:3 in **3·AuNPs**, which is in agreement with the dimensions of the imidazolium coating agent and their type of mutual interaction assuming a close packed structure.

In **4·AuNPs** a peak that corresponds to the binding energy of S 2p can also be observed (Figure S5, Supporting Information). Additionally, angle resolved XPS (ARXPS) analysis were carried out to know how the **4·AuNPs** molecules were attached to the

Table 4. Positive-Ion Mode MALDI-TOF-MS for the Gold Nanoparticles 3·AuNPs and 4·AuNPs

compound	$[(M - 2Br - 2H]^+$	$[M - Br]^+$	$[M - 2Br - 2H + Au/2]^{2+}$	$[M - 2Br - 2H + Au]^+$	$[M - Br - 2C_{18}H_{37}]^+$	$[M - Br - C_{18}H_{37}]^+$
3·AuNPs[a]				939.6 (100%)		
3·AuNPs[b]	743.8 (100%)	625.7 (25%)		939.9 (100%)		
3·AuNPs[c]				939.8 (100%)	321.3 (12%)	573.6 (15%)
4·AuNPs[a]				1173.9 (100%)		
4·AuNPs[c]			586.5 (95%)	1173.9 (100%)		

[a] No matrix. [b] Matrix = α-ciano-γ-hydroxycinnamic acid. [c] Matrix = DHB.

Table 5. EC_{50} Values of 3·2Br, 3·AuNPs, and Reference Compounds[a]

	EC_{50} /μg mL^{-1}
7·2Br	>1000[b]
1·2Br	7
3·2Br	13.18
3·AuNPs	>70[b]

[a] Cells were exposed for 48 h and the viability was assessed by the MTT assay. [b] Maximum concentration tested.

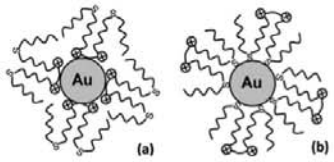

Figure 5. Some possible schematic representations of gold nanoparticles coated with **4·AuNPs** bound by imidazolium moieties (a) and S atom (b).

gold nanoclusters, i.e., which is the preferential disposition of the ligands **4·2Br** on the gold surface, linked through either the thioether or the imidazolium moieties (Figure 5). Measuring the spectra with different takeoff angles, it was possible to determine which element is found in a higher ratio near the gold and, therefore, to explain what the binding disposition of the imidazolium amphiphiles is to gold. At the lower takeoff angle (15°) it was found that the ratio N:S was 2.2:1, whereas at the highest angle (75°) the ratio was 1.7:1. In addition, at middle takeoff angles (60°, 45°, and 30°) the lowest N:S ratio (1.25:1) was obtained. All these results combined with that obtained when the data were recorded at the usual takeoff angle (the N:S ratio was 1.9; the theoretical rate is 2) proved that the molecules are bound to the gold nanoclusters mainly by their imidazolium groups, and this preference can be a clear advantage in delivery applications (see later).

Stability Studies. The stability in solution of **3·AuNPs** and **4·AuNPs** was examined both at room temperature and under reflux in three different solvents (dichloromethane, tetrahydrofuran, and toluene), and the absorption spectra of these solutions were recorded daily for one 1 month. No obvious change in the shape or maximum in the plasmon resonance was observed, which indicates that the as-prepared gold nanoparticles are stable for at least 1 month in air at room temperature. In addition, the stability of the nanoparticles in the same three solvents at increasing temperatures was also studied by UV−visible absorption spectroscopy. The solutions were heated starting at room temperature at a rate of 10 °C/day until the reflux temperature was reached. Samples were checked after 2, 6, and 24 h for each temperature. We found out that gold nanoparticles **3·AuNPs** and **4·AuNPs** remained stable after being heated at reflux temperature for 48 h. As no additional antiaggregation agent was added to the system, the stability of the nanoparticles should be attributed to the bis-imidazolium salts, opening the possibility of considering the nanoparticles suitable for storage.

To attempt the exchange of the imidazolium cations on the AuNP surface by different ligands, for instance, thiols, would be of interest from the point of view of expanding the versatility of this material, and considering them as a potentially replaceable by a specific ligand (exchanging of cargoes). Several examples have been reported in the literature using the exchange of thiol coatings by a different type of thiols, the induced aggregation by bisthiols, to assemble, for instance, nanoparticles thin films,[35] and also aggregation of the nanoparticles via hydrogen bonds[36] or π−π stacking[37] interactions of their coating ligands. The exchange of the bis-imidazolium cations on the AuNP surface by different ligands, for instance, thiols, was also examined by means of two different experiments in dichloromethane at room temperature: (a) treatment of **3·AuNPs** with hexadecanethiol and (b) addition of an excess of 1,8-octanedithiol to a solution of **3·AuNPs**. No thiolate exchange at all was observed under these conditions, indicating the strong interaction between the imidazolium ligands and the gold, a fact that could also contribute to the controlled release in delivery applications.

It will be plausible to consider that some extra stabilization is due to the formation of a bilayer of imidazolium dicationic protophanes (gemini surfactant) on the surface of the gold core, according to some literature examples.[14b,38] However, this possibility could be almost ruled out for two additional reasons: First, the insolubility of **3·AuNPs** in aqueous solution (which would be expected if a second layer were present with the cations facing the solvent); second, the ^1H NMR of **3·AuNPs** recorded in $CDCl_3$ shows very broad bands, whereas the resonances of the protons at the end of the alkyl chains are relatively sharp, indicating the proximity of the imidazolium cation to the metallic core.

Toxicity of the AuNPs and Protophanes. Because the synthesized gold nanoparticles used in delivery studies were stabilized with the dication **3·2Br**, it is valuable to study the toxicity of the protophane, besides the overall toxicity of the nanoparticles, because they are aimed at biomedical usage. The cytotoxicity, expressed here as EC_{50}, was determined on human colon carcinoma cell line Caco-2 using the MTT assay. This assay is based on the conversion of yellow tetrazolium salts to purple formazan crystals in the mitochondria of active, viable cells. The Caco-2 cell line can be used in cytotoxicity assays because dedifferentiated cancer cell lines provide a good rough estimation

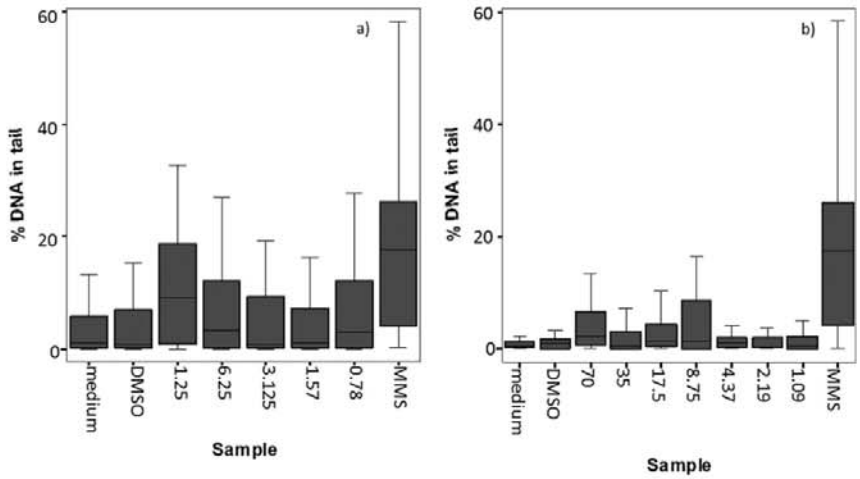

Figure 6. Genotoxicity assay performed with (a) **3·2Br** and (b) **3·AuNPs**. Determination was performed by the Comet assay.

for the toxic potential of the studied substance, as suggested in literature.[10b] Table 5 shows the EC_{50} values obtained for different bis-imidazolium compounds: **1·2Br**, **3·2Br**, the reference compound 1,3-bis[(3-methyl-1-imidazolio)methyl]-benzene dibromide (**7·2Br**) and the nanoparticles **3·AuNPs** after 48 h of exposure.

There are many examples of single imidazolium-derived ionic liquids in the literature,[39] but our coating ligands are gemini-type surfactants, i.e., double imidazolium-alkyl chain, linked through a 1,3-dimethylenebenzene spacer. In the case of **3·2Br** with two octadecyl chains, the EC_{50} is 13.18 μg mL^{-1} (Figure 6a), which corresponds to 14.6 μM. The cytotoxicity was also determined for similar molecules, but with shorter alkyl chains (methyl for **7·2Br** and decyl for **1·2Br**), and for **7·2Br** the EC_{50} value is higher than the one obtained for **3·2Br** (Figure 6a), whereas **1·2Br** has a EC_{50} similar to that of the latter. These results are in good agreement with literature reports, regarding the relation between the length of the alkyl chain and the cytotoxicity: Previous studies of imidazolium-derived ionic liquids show that toxicity increases with the increase of the alkyl chain length.[10b,39] Because the alkyl chain is responsible for the lipophilicity, this behavior is expected, and indeed there is a correlation between the lipophilicity and the cytotoxicity of the imidazolium-derived ionic liquids:[40a,d] A longer alkyl chain will increase the lipophilicity of the molecule, making the molecule more likely to pass the cell membranes and insert into them. Interestingly, the EC_{50} value obtained for **3·2Br** is not lower (it is not more toxic) than the one reported in literature for imidazolium-derived ionic liquids with shorter alkyl chains, also tested in Caco-2 cell line,[10b] meaning that **3·2Br** has a similar toxicity, although it has two alkyl chains. Also, according to the literature, the anion has little or no influence in the overall cytotoxicity of the ionic liquid.[39a]

As can be observed in Table 5, the EC_{50} value for **3·AuNPs** is higher than the range of concentrations studied. Solubility limitations mean that the maximum concentration of nanoparticles that can be studied is 70 μg mL^{-1}, which is below any observed toxic effect. More importantly, the toxicity of **3·AuNPs** is considerably lower than that of the imidazolium coating **3·2Br**. This result suggests that the interaction of the polar headgroup with the gold nucleus of the nanoparticle prevents, in some way, a higher toxicity, because the positive charge of the imidazolium is not available to interact with the cells.

Also, the Comet Assay was performed to evaluate the genotoxicity of **3·2Br** and **3·AuNPs**. Many concentrations were tested, and after statistical analysis, it was concluded that no significant genotoxicity was observed for both the amphiphile molecule **3·2Br** (Figure 6a) and the nanoparticles **3·AuNPs** (Figure 6b). Again, dimethyl sulfoxide ($(CD_3)_2SO$) and dichloromethane were the solvents used to study **3·2Br** and **3·AuNPs**, respectively. In both cases, the statistical analysis of the assay showed no significant differences between the solvent and the **3·2Br** or **3·AuNPs**, except between the solvent and the highest concentration of **3·AuNPs** tested (70 μg/mL). However, because the damage produced in the DNA was low, we conclude that no real genotoxicity was observed. The DNA-damaging alkylating-agent methylmethanesulfonate (MMS) was used as positive control.

Models for the Delivery of Anionic Drugs: Ibuprofenate Transport Studies. Several examples of anion sensing by AuNPs have been reported in the literature, and in all the cases the anion recognition motif (amides, thiourea, or organometallic clusters) was attached to the end of a large thiol agent coating the nanoparticle.[40] The ultimate goal of our research consists of evaluating if the anion recognition exhibited by the imidazolium containing dications, and previously evaluated binding in solution,[16,17] was still operating in the AuNPs prepared in this work.

We have shown in this paper (see before, complexation studies) that the protophanes bind to the carboxylate-containing drugs valproate or ibuprofenate. It would be expected that bis-imidazolium surfactants, such as the ones described in this work, would exhibit a higher anion complexation once attached to the AuNPs.

Initially, the anion recognition properties of **3·AuNPs** were studied by UV−visible spectroscopy. For this purpose, different solutions of TBA·Cl and TBA·Ac with a range of concentrations from 5×10^{-6} to 0.05 M were prepared. The solutions that were analyzed consisted of a 1:1 mixture of solutions of **3·AuNPs** and the corresponding tetrabutylammonium salt in CH_2Cl_2. No significant changes in either the absorbance or the wavelength were observed for the plasmon resonance band on **3·AuNPs**,

and a quantitative analysis was discounted. The lack of anion complexation under these conditions could be the consequence of the hydrophobic coating of the Au core preventing the penetration of a solvated anion, and therefore the interaction with the imidazolium moiety near the surface.

Ibuprofen (sodium salt) was chosen as an anionic drug often used as a model for controlled delivery, and a protocol based on a biphasic transfer system was used to estimate the capability of **3·AuNPs** for transferring the carboxylate (ibuprofenate) from water into an organic solvent (dichloromethane), following changes in the absorbance spectrum of the anion. Binding of the ibuprofenate by the nanoparticles showed that, as in control experiments, using extraction with dichloromethane and with dichloromethane saturated with **3·2Br**, the anion is not transferred appreciably into the organic phase. Instead, it is possible to observe a decrease in the absorption band intensity of the ibuprofen when the ibuprofenate aqueous solution is extracted with **3·AuNPs**, indicating that the AuNPs promote the transfer of ca. 70% of ibuprofenate to the organic phase (Figure S7, Supporting Information), and demonstrating that **3·AuNPs** interact with anionic drugs and have the ability to transport them.

Delivery and permeation of ibuprofenate complexed to gold nanoparticles **3·AuNPs** was examined by dialysis experiments in aqueous media to study the potential application of gold nanoparticles coated with bis-imidazolium salts as systems for controlled delivery of drugs. Experiments of dynamic and static dialysis were performed to evaluate the ibuprofenate diffusion through a dialysis membrane in aqueous media. To establish conditions similar to those of the skin medium, the experiments were carried out using Milli-Q water (pH 5), and at 32 °C. The dynamic analysis experiments were performed as detailed in the Experimental Section; however, the amount of ibuprofenate detected in the samples taken from the receptor aqueous phase for up to 500 h was always at the limit of detection. For this reason, no clear liberation profile could be established, which made the results nonconclusive. A plausible explanation could be that the high volume of each extraction (3 mL) and its replacement with water could cause a progressive dilution in the receptor phase, making negligible the detection of increasing ibuprofenate concentration in the receptor containers.

Additionally, the liberation rate of ibuprofenate from the obtained ibuprofenate−**3·AuNPs** complex was assessed using Franz-type diffusion cells and dialysis membranes.[41] The samples were resuspended in Sorensen Buffer pH 7.4, to simulate physiological conditions, and the receptor solution used was NaOH pH 11, to ensure ibuprofenate solubility, complying with the SINK conditions. The liberation rate from the ibuprofenate−**3·2Br** complex was also studied, and as a control, samples with free ibuprofenate were taken in the same conditions, to ensure that the release rate was independent of the diffusion rate of ibuprofenate between the solutions. Figure 7 shows the plot of cumulative delivered (Q) amount of ibuprofenate versus time (t). The total amount of ibuprofenate added was calculated to be the same in all the samples.

The diffusion rate of free ibuprofenate across the dialysis membrane is higher than the rates obtained with ibuprofenate−**3·AuNPs** and ibuprofenate−**3·2Br**, thus showing that diffusion is not limiting the liberation rates obtained. The values of the dissociation constants K_D, obtained by nonlinear fitting, were 39.98 and 65.47 h^{-1} for ibuprofenate−**3·AuNPs** and ibuprofenate−**3·2Br**, respectively, following first-order kinetics (Figure 7a). Therefore, although the imidazolium ligand

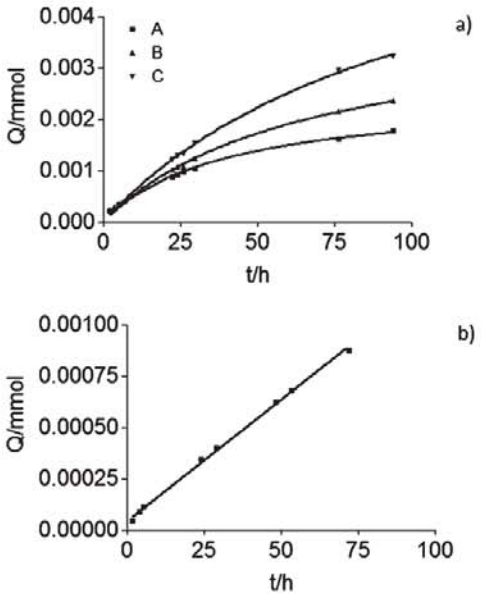

Figure 7. (a) Liberation profile at pH 7.4 of (A) ibuprofenate−**3·AuNPs**, (B) ibuprofenate−**3·2Br**, and (C) sodium ibuprofenate. (b) Liberation profile at pH 5.5 from ibuprofenate−**3·AuNPs**.

3·2Br is involved in the recognition and binding of ibuprofenate, the behavior is different when it is stabilizing gold nanoparticles, and the release of ibuprofenate takes place at a slower, more sustained rate.

Additionally, release of ibuprofenate from ibuprofenate−**3·AuNPs** was also studied at pH 5.5, closer to the value in inflamed tissues. Figure 7b shows the ibuprofenate release profile from **3·AuNPs**, according to a zero-order kinetics (K_D is 0.00001265 h^{-1}). This result expresses the slower release of ibuprofenate in more acidic media, as a consequence of its lower aqueous solubility at this pH, despite its lower ionization and subsequently reduced interaction with the bis-imidazolium carrier.

It is remarkable that analysis of the receptor phase by UV−vis spectroscopy revealed only the presence of ibuprofenate, indicating that neither **3·AuNPs** nor **3·2Br** diffused into the solution.

Internalization Studies. Cell uptake was studied in Caco-2 cells by transmission electron microscopy (TEM). Figure 8 shows the TEM images obtained from Caco-2 cells after 15, 30, and 60 min, and after 4 and 24 h of exposure to a 70 $\mu g\ mL^{-1}$ of a solution of **3·AuNPs**; this concentration was chosen to be used in these assays because it was the maximum concentration of nanoparticles used in the toxicity assay, and a value lower than the EC_{50}. **3·AuNPs** were quickly internalized in Caco-2 cells, because nanoparticles uptake was already visible at 15 min. As can be seen (Figure 8a), after only 15 min a few AuNPs were found inside a vesicle structure, probably an early endosome. After 30 min, isolated AuNPs or groups of AuNPs (Figure 8b,c, respectively) were entering the cell inside a vesicle structure. Absorbed AuNPs were situated inside lysosomes (Figure 8d,e) and in the cell membrane (Figure 8f) 1 h after exposure. **3·AuNPs** were observed in the cell membrane and in vesicular structures (early endosomes and lysosomes) inside cells; there were no nanoparticles free at the cytoplasm or in any other

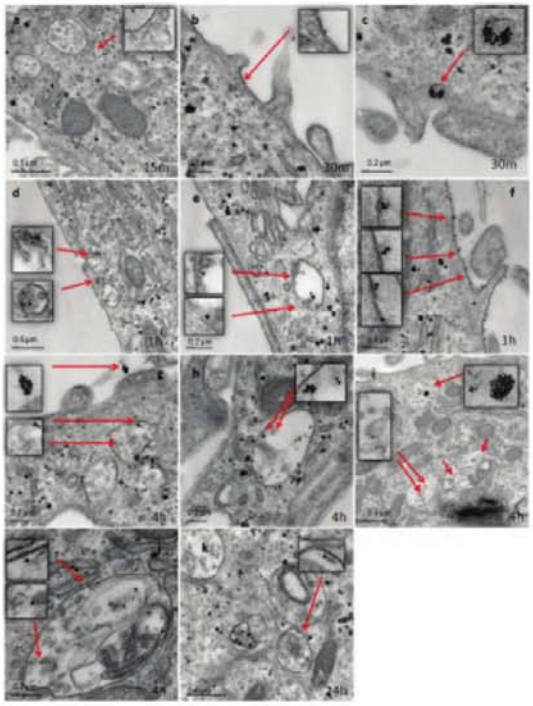

Figure 8. TEM images from Caco-2 cells treated with **3·AuNPs** at 15 (a), 30 (b, c) and 60 (d−f) min, and after 4 (g−j) and 24 (k) h.

organelle. High amounts of AuNPs were found in lysosomes (Figure 8g−j) after 4 h of exposure, and after 24 h few AuNPs were found in the lysosomes (Figure 8k), suggesting that the nanoparticles are eliminated from the cell. These results indicate that the nanoparticles **3·AuNPs** are successfully absorbed by the cell as expected[42] and have a short residence time inside the cell.

CONCLUSION

In conclusion, we have synthesized new AuNPs with imidazolium ligands of the gemini-type surfactant that are stable in solution and where the capping agent plays a unique triple role: phase transfer of the gold salt during the synthesis, stabilization of the gold colloid, and binding agent for a guest. The new AuNPs are stable, and the bis-imidazolium capping molecules do not exchange with thiolate ligands. Indeed, given the choice, the gold surface prefers bis-imidazolium to thioether ligands. Finally, the capability of these nanoparticles to complex ibuprofenate was shown, a model for carboxylate-containing anionic drugs, and to release it at a sustained rate. The low toxicity and internalization capability of the reported **3·AuNPs**, as well as the fact that the dication **3·2Br** used to stabilize the nanoparticles presents a reduced cytotoxicity, make this kind of nanoparticulate carrier appear as promising vehicles for nanomedical applications.

ASSOCIATED CONTENT

Supporting Information. (1) Synthesis of 1-octadecyl-1*H*-imidazole. (2) Synthesis of 1,3-bis(bromomethyl)-5-methoxybenzene (**5**). (3) ^{1}H NMR spectroscopic data from compounds **1·2Br**−**4·2Br** (Table S1). (4) ^{13}C NMR spectroscopic data from compounds **1·2Br**−**4·2Br** (Table S2). (5) Compounds and ratios used for the AuNPs synthesis (Table S3). (6) Experimental fitting data of chemical shifts variation ($\Delta\delta$) plotted versus drug concentration, from titrations with **1·2Br** with ibuprofenate and valproate (Figure S1). (7) ALDI-TOF MS spectrum of **3·AuNPs** (Figure S2). (8) TOF-SIMS spectra of **3·AuNPs** (Figure S3). (9) XPS spectrum of the **3·AuNPs** (Figure S4). (10) XPS spectrum of **4·AuNPs** (Figure S5). (11) EC_{50} values of **3·2Br**, **3·AuNPs**, and reference compounds, and the effect of **3·AuNPs** and **3·2Br** on the viability of Caco-2 cells (Figure S6). (12) UV−vis spectra of the binding process of ibuprofenate to **3·AuNPs** (Figure S7). (13) Stages of the experimental setup of the dynamic dialysis for the ibuprofenate diffusion evaluation from the **3·AuNPs**−ibuprofenate complex (Figure S8). (14) Franz cells setup for evaluation of the ibuprofenate diffusion from the **3·AuNPs**−ibuprofenate complex in static dialysis experiments (Figure S9). This material is available free of charge via the Internet at http://pubs.acs.org.

AUTHOR INFORMATION

Corresponding Author

*E-mail: mlperez@ub.edu. Telephone: (+34) 934035849. Fax: (+34) 934024539.

ACKNOWLEDGMENT

Financial support from the Ministerio de Ciencia e Innovación (MICINN) (TEC2008-06883-C03-02) and the Generalitat de Catalunya (2009SGR158) is acknowledged. L.C. thanks the UB and the MEC for predoctoral grants.

REFERENCES

(1) Hvoalbæk, B.; Janssens, T. V. W.; Clausen, B. S.; Falsig, H.; Christensen, C. H.; Nørskov, J. K. *Nano Today* **2007**, *2*, 14–18.

(2) (a) Daniel, M.-C.; Astruc, D. *Chem. Rev.* **2004**, *104*, 293–346. (b) Boisselier, E.; Astruc, D. *Chem. Soc. Rev.* **2009**, *38*, 1759–1782.

(3) Baptista, P.; Pereira, E.; Eaton, P.; Doria, G.; Miranda, A.; Gomes, I.; Quaresma, P.; Franco, R. *Anal. Bioanal. Chem.* **2008**, *391*, 943–950.

(4) Ghosh, P.; Han, G.; De, M.; Kim, C. K.; Rotello, V. M. *Adv. Drug Delivery Rev.* **2008**, *60*, 1307–1315.

(5) Wang, Z.; Ma, L. *Coord. Chem. Rev.* **2009**, *253*, 1607–1618.

(6) Brust, M.; Walker, M.; Bethell, D.; Schiffrin, D. J.; Whyman, R. *J. Chem. Soc., Chem. Commun.* **1994**, 801–802.

(7) (a) Dhar, S.; Reddy, E. M.; Shirar, A.; Pokharkar, V.; Prasad, B. L. V. *Chem. Eur. J.* **2008**, *14*, 10244–10250. (b) Shukla, R.; Nune, S. K.; Chanda, N.; Katti, K.; Mekapothula, S.; Kulkami, R. R.; Welshons, W. V.; Kannan, R.; Katti, K. V. *Small* **2008**, *4*, 1425–1436. (c) Nune, S. K.; Chanda, N.; Shukla, R.; Katti, K.; Kulkarni, R. R.; Thiakavathy, S.; Mekapothula, S.; Kannan, R.; Katti, K. V. *J. Mater. Chem.* **2009**, *19*, 2912–2920.

(8) Si, S.; Dinda, E.; Mandal, T. *Chem. Eur. J.* **2007**, *13*, 9850–9861.

(9) Tu, C.; Li, G.; Shi, Y.; Yu, X.; Jiang, Y.; Zhu, Q.; Liang, J.; Gao, Y.; Yan, D.; Sun, J.; Zhu, X. *Chem. Commun.* **2009**, 3211–3213.

(10) (a) *Ionic Liquids in Synthesis*; Wasserscheid, P., Welton, T., Eds; Wiley-VCH: Weinheim, 2003. (b) Fei, Z.; Geldbach, T. J.; Zhao, D.; Dyson, P. J. *Chem. Eur. J.* **2006**, *12*, 2122–2130. (c) García-Lorenzo, A.; Tojo, E.; Teijeira, M.; Rodríguez-Berrocal, F. J.; González, M. P.; Martínez-Zorzano, V. S. *Green Chem.* **2008**, *10*, 508–516. (d) Frade, R. F. M.; Rosatella, A. A.; Marques, C. S.; Branco, L. C.; Kulkarni, P. S.;

Mateus, N. M. M.; Afonso, C. A. M.; Duarte, C. M. M. *Green Chem.* **2009**, *11*, 1660–1665. (e) Ranke, J.; Mölter, K.; Stock, F.; Bottin-Weber, U.; Poczobutt, J.; Hoffmann, J.; Ondruschka, B.; Filser, J.; Jastorff, B. *Ecotoxicol. Environ. Saf.* **2004**, *58*, 396–404.

(11) Dupont, J.; Scholten, J. D. *Chem. Soc. Rev.* **2010**, *39*, 1780–1804.

(12) (a) Itoh, H.; Naka, K.; Chujo, Y. *J. Am. Chem. Soc.* **2004**, *126*, 3026–3027. (b) Kim, K.; Demberelnyamba, D.; Lee, H. *Langmuir* **2004**, *20*, 556–560. (c) Tatumi, R.; Fujihara, H. *Chem. Commun.* **2005**, 83–85. (d) Luo, L.; Yu, N.; Tan, R.; Jin, Y.; Yin, D. *Catal. Lett.* **2009**, *130*, 489–495.

(13) (a) Zhao, D.; Fei, Z.; Ang, W. H.; Dyson, P. J. *Small* **2006**, *2*, 879–883. (b) Schrekker, H. S.; Gelesky, M. A.; Stracke, M. P.; Schrekker, C. M. L.; Machado, G.; Teixeira, S. R.; Rubim, J. C.; Dupont, J. *J. Colloid Interface Sci.* **2007**, *316*, 189–195. (c) Khatri, O. P.; Adachi, K.; Murase, K.; Okazaki, K.; Torimoto, T.; Tanaka, N.; Kuwabata, S.; Sugimura, H. *Langmuir* **2008**, *24*, 7785–7792. (d) Dash, P.; Scott, R. W. J. *Chem. Commun.* **2009**, 812–814.

(14) (a) Xu, J.; Han, X.; Liu, H.; Hu, Y. *J. Disper. Sci. Technol.* **2005**, *26*, 473–476. (b) Liu, Q.; Guo, M.; Nie, Z.; Yuan, J.; Tan, J.; Yao, S. *Langmuir* **2008**, *24*, 1595–1599.

(15) Gale, P. A., Gunnlaugsson, T., Guest editors. Themed issue: Supramolecular chemistry of anionic species. *Chem. Soc. Rev.* **2010**, *39*, 3581−4008.

(16) Alcalde, E.; Mesquida, N.; Pérez-García, L. *Eur. J. Org. Chem.* **2006**, 3988–3996and references therein.

(17) Casal-Dujat, L. *Ph.D. Thesis*, University of Barcelona, 2010.

(18) Sporer, C.; Casal, L.; Caballero, D.; Samitier, J.; Errachid, A.; Pérez-García, L. *Sensor Lett.* **2009**, *7*, 757–764.

(19) Viau, L.; Tourné-Péteilh, C.; Devoisselle, J.-M.; Vioux, A. *Chem. Commun.* **2010**, 228–230.

(20) Casilli, S.; Malitesta, C.; Conoci, S.; Petralia, S.; Sortino, S.; Valli, L. *Biosens. Bioelectron.* **2004**, *20*, 1190–1195.

(21) Alcalde, E.; Mesquida, N.; Alemany, M.; Alvarez-Rúa, C.; García-Granda, S.; Pacheco, P.; Pérez-García, L. *Eur. J. Org. Chem.* **2002**, 1221–1231.

(22) (a) Alcalde, E; Mesquida, N.; Fernández, I.; Giralt, E. *Rapid Commun. Mass. Spec.* **2000**, *14*, 1014–1016. (b) Alcalde, E.; Mesquida, N. *Int. J. Mass. Spectrom.* **2007**, *262*, 80–87.

(23) Carafa, M.; Marianecci, C.; Rinaldi, F.; Santucci, E.; Tampucci, S.; Monti, D. *J. Lipos. Res* **2009**, *19*, 332–340.

(24) Döse, G.; Arhan, E.; Unal, B.; Ozaydin, E.; Guven, A.; Sayli, T. R. *J. Child Neurol.* **2009**, *24*, 1493–1498.

(25) Sastry, M. *Curr. Sci.* **2003**, *85*, 1735–1745.

(26) Zhou, J.; Ralston, J.; Sedev, R.; Beattie, D. A. *J. Colloid Interface Sci.* **2009**, *331*, 251–262.

(27) (a) Chen, Q.; Zhao, L.; Li, C.; Shi, G. *J. Phys. Chem. C* **2007**, *111*, 18392–18396. (b) Ju-Nam, Y.; Allen, D. W.; Gardiner, P. H. E.; Light, M. E.; Hursthouse, M. B.; Bricklebank, N. *J. Organomet. Chem.* **2007**, *692*, 5065–5070. (c) Huo, Q.; Worden, J. G. *J. Nanopart. Res.* **2007**, *9*, 1013–1025.

(28) (a) Alcarazo, M. *An. Quim.* **2009**, *105*, 173–179. (b) Migowski, P.; Dupont, J. *Chem. Eur. J.* **2007**, *13*, 32–39.

(29) (a) Benjelloun, A. T.; Morel, G.; Marchand, E. *Heteroatom Chem.* **2000**, *11*, 16–26. (b) Flahaut, A.; Baltaze, J. P.; Roland, S.; Mangeney, P. *J. Organomet. Chem.* **2006**, *691*, 3498–3508.

(30) Hurst, E. C.; Wilson, K.; Fairlamb, I. J. S.; Chechik, V. *New J. Chem.* **2009**, *33*, 1837–1840.

(31) Zhao, L.; Zhang, C.; Zhuo, L.; Zhang, Y.; Ying, J. Y. *J. Am. Chem. Soc.* **2008**, *130*, 12586–12587.

(32) Zhu, H.; Tao, C.; Zheng, S.; Wu, S.; Li, J. *Colloids Surf. A* **2005**, *256*, 17–20.

(33) (a) Reilly, S. M.; Krick, T.; Dass, A. *J. Phys. Chem. C.* **2010**, *114*, 741–745. (b) Dass, A.; Stevenson, A.; Dubay, G. R.; Tracy, J. B.; Murray, R. W. *J. Am. Chem. Soc.* **2008**, *130*, 5940–5946. (c) Dass, A.; Guo, R.; Tracy, J. B.; Balasubramanian, R.; Douglas, A. D.; Murray, R. W. *Langmuir* **2008**, *24*, 310–315.

(34) Ionita, P.; Wolowska, J.; Checkik, V.; Caragheorgheopol, A. *J. Phys. Chem. C* **2007**, *111*, 16717–16723.

(35) Leibowitz, F. L.; Zheng, W.; Maye, M. M.; Zhong, C. J. *Anal. Chem.* **1999**, *71*, 5076–5083.

(36) Mayer, C. R.; Neveu, S.; Secheresse, F.; Cabuil, V. *J. Colloid Interface Sci.* **2003**, *273*, 350–355.

(37) (a) Laromaine, A.; Koh, L.; Murugesan, M.; Ulijn, R. V.; Stevens, M. M. *J. Am. Chem. Soc.* **2007**, *129*, 4156–4157. (b) Yang, Z.; Gu, H.; Zhang, Y.; Wang, L.; Xu, B. *Chem. Commun.* **2004**, 208–209.

(38) Zhang, L.; Sun, X.; Song, Y.; Jiang, X.; Dong, S.; Wang, E. *Langmuir* **2006**, *22*, 2838–2843.

(39) (a) Stolte, S.; Arning, J.; Bottin-Weber, U.; Matzke, M.; Stock, F.; Thiele, K.; Uerdingen, M.; Welz-Biermann, U.; Jastorff, B.; Ranke, J. *Green Chem.* **2006**, *8*, 621–629. (b) Stolte, S.; Matzke, M.; Arning, J.; Böschen, A.; Pitner, W. R.; Welz-Biermann, U.; Jastorff, B.; Ranke, J. *Green Chem.* **2007**, *9*, 1170–1179. (c) Jaitely, V.; Karatas, A.; Florence, A. T. *Int. J. Pharm.* **2008**, *354*, 168–173.

(40) (a) Watanabe, S.; Sonobe, M.; Arai, M.; Tazume, Y.; Matsuo, T.; Nakamura, T.; Yoshida, K. *Chem. Commun.* **2002**, 2866–2867. (b) Kubo, Y.; Uchida, S.; Kemmochi, Y.; Okubo, T. *Tetrahedron Lett.* **2005**, *46*, 4369–4372. (c) Ruiz Arazaes, J.; Belin, C.; Astruc, D. *Chem. Commun* **2007**, 3456–3458. (d) Chaterjee, A.; Oh, D. J.; Kim, K. M.; Youk, K.-S.; Ahn, K. H. *Chem. Asian J.* **2008**, *3*, 1962–1967. (e) Kado, S.; Furui, A.; Akiyama, Y.; Nakahara, Y.; Kimura, K. *Anal. Sci.* **2009**, *25*, 261–265.

(41) Morales, M. E.; Gallardo Lara, V.; Calpena, A. C.; Domenech, J.; Ruiz, M. A. *J. Controlled Release* **2004**, *95*, 75–81.

(42) (a) Shukla, R.; Bansal, V.; Chaudhary, M.; Basu, A.; Bhonde, R. R.; Sastry, M. *Langmuir* **2005**, *21*, 10644–10654. (b) Nativo, P.; Prior, I. A.; Brust, M. *ACS Nano* **2008**, *2*, 1639–1644. (c) Krpetić, Z.; Nativo, P.; Sée, V.; Prior, I. A.; Brust, M.; Volk, M. *Nano Lett.* **2010**, *10*, 4549–4554.

(43) ASTM-E2186. "Standard Guide for Determining DNA Single-Strand Damage in Eukaryotic Cells using the Comet Assay", June 2003.

Electronic Supplementary Information

Gemini imidazolium amphiphiles for the synthesis, stabilization and drug delivery from gold nanoparticles

Lucía Casal-Dujat,[1] Mafalda Rodrigues,[1] Alex Yagüe,[1] Anna C. Calpena,[2] David B. Amabilino,[3] Javier González-Linares,[4] Miquel Borràs,[4] and Lluïsa Pérez-García[1]

1 Department of Pharmacology and Therapeutical Chemistry and Institute of Nanoscience and Nanotechnology UB (IN2UB), Universitat de Barcelona, Avda. Joan XXIII s/n, 08028 Barcelona, Spain

2 Department of Pharmacy and Pharmaceutical Technology and Institute of Nanoscience and Nanotechnology UB (IN2UB), Universitat de Barcelona, Avda. Joan XXIII s/n, 08028 Barcelona, Spain

3 Institut de Ciència de Materials de Barcelona (ICMAB-CSIC), Campus Universitari, 08193 Bellaterra, Spain

4 UTOX-PCB – Unitat de Toxicologia Experimental i Ecotoxicologia, Baldiri i Reixac 10-12, 08028 Barcelona, Spain

Corresponding Author

*E-mail: mlperez@ub.edu. Telephone: (+34) 934035849. Fax: (+34) 934024539

1-Octadecyl-1H-imidazole: 1*H*-Imidazole (1.0 g, 14.69 mmol) and potassium hydroxide (0.99 g, 17.63 mmol) were stirred in dry MeCN (60 mL) under argon atmosphere and at room temperature until dissolved (2 hours). A solution of 1-bromooctadecane (4.90 g, 14.69 mmol) in dry MeCN at 40ºC (50 mL) was added. After cooling down at room temperature, the solution was stirred for 24 hours, and a white solid precipitated. The solvent was evaporated, and the residue was partitioned between CH_2Cl_2 (40 mL) and water (35 mL). The aqueous phase was extracted with CH_2Cl_2 (2 x 40 mL), then the organic phase was washed with water (70 mL), dried over $MgSO_4$, filtered, and the solvent was evaporated to obtain 1-octadecyl-1*H*-imidazole as a yellow oil that solidified at room temperature under vacuum (4.07 g, 87 %).

^{1}H NMR (300 MHz, $CDCl_3$, 25°C, TMS): δ= 0.88 (t, *J*=6 Hz, 3H, OCH_3); 1.25 (m, 30H, $(CH_2)_{15}$); 1.79 (m, 2H, N-CH_2-C**H**$_2$); 3.92 (t, *J*=7.5 Hz, 2H, N-CH_2); 6.94 (s, 1H, Im-H(5)); 7.12 (s, 1H, Im-H(4)); 7.72 (s, 1H, Im-H(2)). R_f: 0.34 (CH_2Cl_2). mp: 49ºC (110ºC/0.01 Torr).[1]

1. Tosoni, M.; Laschat, S.; Baro, A. *Helv. Chim. Acta*, **2004**, *87*, 2742-2748.

1,3-Bis(bromomethyl)-5-methoxybenzene (5)

Method 1: A suspension of 1,3-dimethyl-5-methoxybenzene (13.10 g, 0.10 mol), *N*-bromosuccinimide (36.6 g, 0.20 mol) and α, α'-azoisobutyronitrile (0.20 g, 1.22 mmol) in dry CCl_4 (500 mL) was stirred at 77ºC under argon atmosphere for 21 hours under radiation (standard light bulb). The mixture was cooled down to room temperature, filtered and, the solution was evaporated in vacuum. The yellow syrup obtained was stored at 4ºC until white solid precipitated. The white precipitate was isolated and purified by crystallisation from *n*-hexane (20 mL) to obtain 5 as white needles (3.7 g, 13%). Method 2: 1,3-Bis(hydroxymethyl)-5-methoxybenzene (1.00 g, 5.95 mmol) was stirred in dry CH_2Cl_2 (40 mL) at room temperature under an argon atmosphere for 40 minutes. The suspension was cooled to 0 ºC with an ice-bath, and phosphorous tribromide (5.40 mL, 5.35 mmol) was added via a syringe under argon. After stirring for 18 hours, the solution was evaporated in the rotary evaporator. The brown residue was partitioned between CH_2Cl_2 (15 mL) and water (15 mL), and the aqueous phase was extracted with CH_2Cl_2 (2 x 15 mL). The whole organic phase was washed with water (75 mL), dried over $MgSO_4$, filtered, evaporated and dried in vacuum to obtain 5 as a brown oil that crystallised spontaneously at room temperature as white crystals (1.50 g, 85%).

5: ^{1}H NMR (300 MHz, $CDCl_3$, 25°C, TMS): δ= 3.82 (s, 3H, OCH_3); 4.44 (s, 4H, CH_2); 6.87 (s, 2H, Ar-H(4,6)); 7.01 (s, 1H, Ar-H(2)). ^{1}H NMR (300 MHz, $(CD_3)_2SO$, 25°C): 3.76 (s, 3H, OCH_3); 4.66 (s, 4H, CH_2); 6.97 (s, 2H, Ar-H(4,6)); 7.10 (s, 1H, Ar-H(2)). ^{13}C NMR (75.4 MHz, $(CD_3)_2SO$, 25°C): δ= 33.9 (CH_2); 55.3 (OCH_3); 114.7 (Ar-C(4,6)); 122.3 (Ar-C(2)); 139.8 (Ar-C(1,3)); 159.3 (Ar-C(5)). MS (EI) *m/z*: (134.1, $[M-2Br]^+$, 66%); (213.1, $[M-Br]^+$, 100%); (294.0, $[M]^+$, 24%). R_f: 0.20 (CH_2Cl_2: *n*-hexane, 1:10). mp: 74-76ºC.[2]

2. Gilat, S. L.; Andronov, A.; Fréchet, J. M. J. *J. Org. Chem.*, 1999, *64*, 7474-7484.

Table S1: ^{1}H NMR spectroscopic data from compounds **1·2Br**, **2·2Br**, **3·2Br** and **4·2Br**

	CH_3	$(CH_2)_n$	SCH_2-C**H$_2$**	N-CH_2-C**H$_2$**	S-C**H$_2$**	O-C**H$_3$**	N-C**H$_2$**	CH_2	Ar-H(5)	Im-H(4)	Ar-H(4,6)	Ar-H(2)	Im-H(5)	Im-H(2)
1·2Br	0.88	1.25-1.32	--	1.89	--	--	4.27	5.64	7.17	7.29	7.61	8.12	8.20	10.43
2·2Br	0.88	1.25-1.32	--	1.89	--	--	4.27	5.64	7.16	7.29	7.61	8.11	8.21	10.44
3·2Br	0.88	1.29-1.32	--	1.90	--	--	4.27	5.63	7.16	7.26	7.59	8.09	8.16	10.41
4·2Br	0.88	1.26-1.36	1.57	1.89	2.50	3.71	4.27	5.58	--	7.19	7.16	7.65	8.22	10.53

1·2Br and **2·2Br** – 300 MHz, $CDCl_3$, **3·2Br** and **4·2Br** – 400 MHz, $CDCl_3$; n=7 (**1·2Br**), 9(**2·2Br**), 15 (**3·2Br**), 16(**4·2Br**)

Table S2: ^{13}C NMR spectroscopic data from compounds **1·2Br**, **2·2Br**, **3·2Br** and **4·2Br**

	CH_3	$(CH_2)_n$	S-CH_2	N-CH_2	CH_2	O-C**H**$_3$	Im-C(4)	Im-C(5)	Ar-C(4,6)	Ar-C(5)	Ar-C(2)	Ar-C(1,3)	Im-C(2)
1·2Br	14.2	22.8-31.9	--	50.4	52.5	--	121.8	123.6	130.0	130.0	130.5	134.8	136.7
2·2Br	14.3	22.9-32.1	--	50.6	52.9	--	122.3	123.5	130.2	130.2	130.9	134.9	136.6
3·2Br	14.3	22.9-32.1	--	50.4	52.6	--	121.8	123.7	130.1	130.1	130.6	134.8	136.8
4·2Br	14.3	22.9-32.1	32.4	50.5	52.7	56.3	121.6	123.9	115.7	160.6	122.3	136.1	137.1

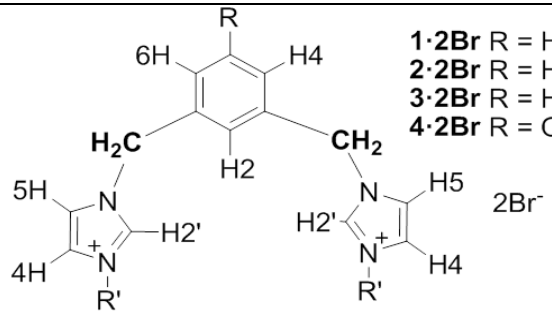

1·2Br R = H R' = $C_{10}H_{21}$
2·2Br R = H R' = $C_{12}H_{25}$
3·2Br R = H R' = $C_{18}H_{37}$
4·2Br R = OMe R' = $C_{11}H_{22}SC_{12}H_{25}$

100 MHz, $CDCl_3$; n=8 (**1·2Br**), 10(**2·2Br**), 16 (**3·2Br**), 19(**4·2Br**)

Table S3. Compounds and ratios used for the AuNPs synthesis and the absorption plasmon resonance bands.

Number of experiment	Transfer agent (TA)	Additional Stabilizer agent (SA)	TA:$HAuCl_4$:SA:$NaBH_4$	λ (nm)
1	TOAB	-	2.5:1:0:24	-
2	TOAB	HDT	2.5:1:0.25:24	519.0
3	TOAB	HDT	2.5:1:0.16:24	[a]
4	TOAB	HDT	2.5:1:0.09:24	[a]
5	**3·2Br**	-	2.5:1:0:24	518.5
6	**3·2Br**	-	0.75:1:0:20	519.0
7	**4·2Br**	-	2.58:1:0:24	517.0
8	**4·2Br**	-	0.75:1:0:20	521.5
9	**1·2Br**	-	0.75:1:0:21	521.0
10	**2·2Br**	-	0.75:1:0:22	524.5

[a] Broad signal in the plasmon resonance with an undefined maximum in the absorption band.

The main observations deduced from the different experiments that were carried out, included in Table S1, are:

i) In experiment 1 no hexadecanethiol (HDT) was added in order to prove if AuNPs could be synthesized using purely a tetraalkyl ammonium salt as stabiliser. The formation of black solids in suspension demonstrated that the AuNPs cannot be stabilized by the tetraoctylammonium bromide (TOAB) salt for long periods of time. The particles coalesce and precipitate.

ii) With the purpose of inducing an increase on the nanoparticle's size, the Au/HDT ratio was reduced. The UV-Vis spectra of experiments 2 and 4 did not show any significant differences with those from experiment 1, suggesting their sizes are similar (see later). Also, the AuNPs from experiments 3 and 4 have a very broad absorption band probably due to their high polydispersity.

iii) Experiments 5 and 7 were performed in the same conditions as experiment 1 but changing the transfer agent (**3·2Br** or **4·2Br** instead of TOAB). The formation of the AuNPs without adding an additional stabilizer proved that dicationic protophanes, apart from transfer agents, also acted as passivators.

iv) The reduction of the amount of protophanes used in experiments 6 and 8 compared to 5 and 7 respectively, without affecting the formation of the AuNPs can be interesting in green chemistry.

v) AuNPs stabilized with **1·2Br and 2·**2Br were also successfully synthesised. However, the kinetics of the phase transfer with these molecules were appreciably slower than with **3·2Br** and **4·2Br**.

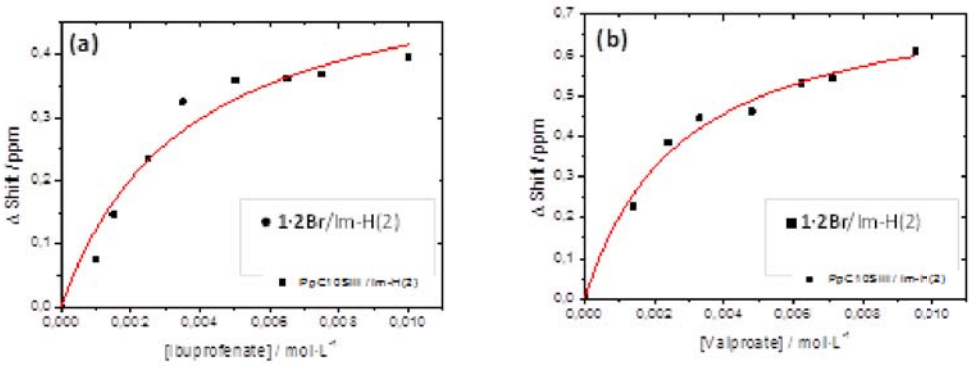

Figure S1. Experimental (points) and fitting (line) data of chemical shifts variation (Δδ) plotting versus drug concentration, from titrations with **1·2Br** with ibuprofenate and valproate: (a) Δδ of Im-H(2) in presence of ibuprofenate, and (b) Δδ of Im-H(2) in presence of valproate.

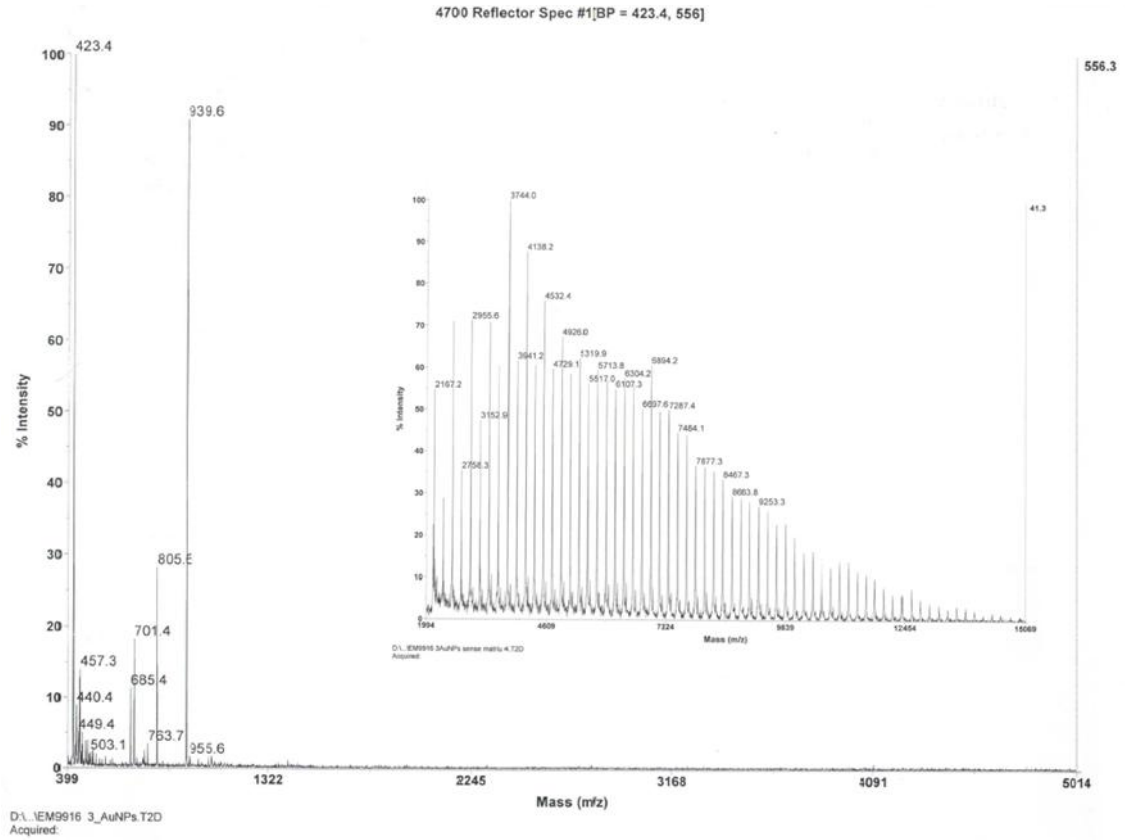

Figure S2. LDI-TOF spectrum of **3·AuNPs** (without matrix)

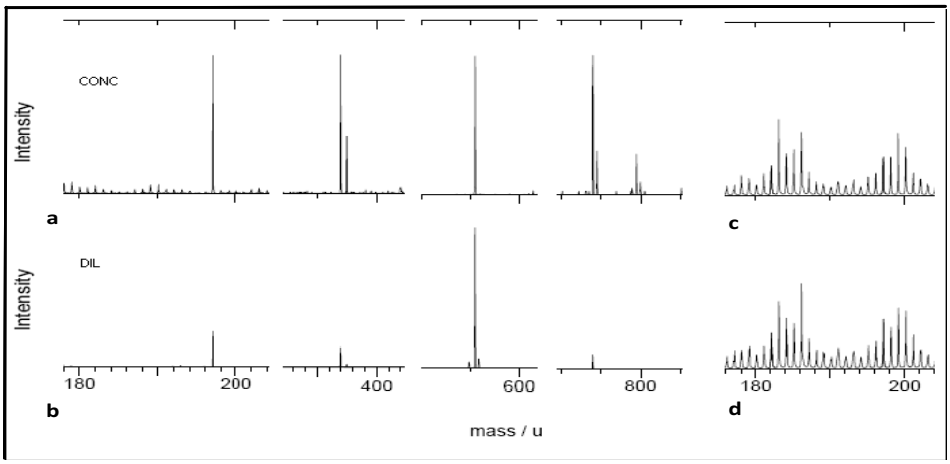

Figure S3. TOF-SIMS spectra of concentrated (a) and diluted (b) samples of **3·AuNPs** after sputtering. Peaks corresponding to one, two, three and four atoms of gold can be observed. (c) and (d) spectra show the pick corresponding to one gold atom before sputtering..

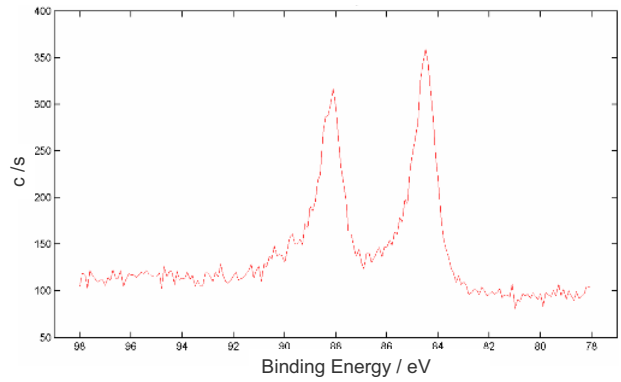

Figure S4. XPS spectrum of the **3·AuNPs** (identical to **4·AuNPs**) showing the Au 4f7/2 and 4f5/2 doublet with binding energies of 84.5 and 88.2 eV, respectively.

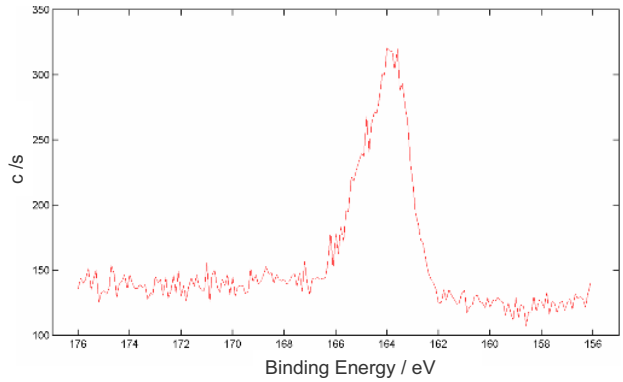

Figure S5. XPS spectrum of S 2p of **4·AuNPs** with a binding energy of 163.8 eV.

a)

	EC_{50} /µg ml^{-1}
7·2Br	> 1000[a]
1·2Br	7
3·2Br	13.18
3·AuNPs	> 70[a]

[a] Maximum concentration tested

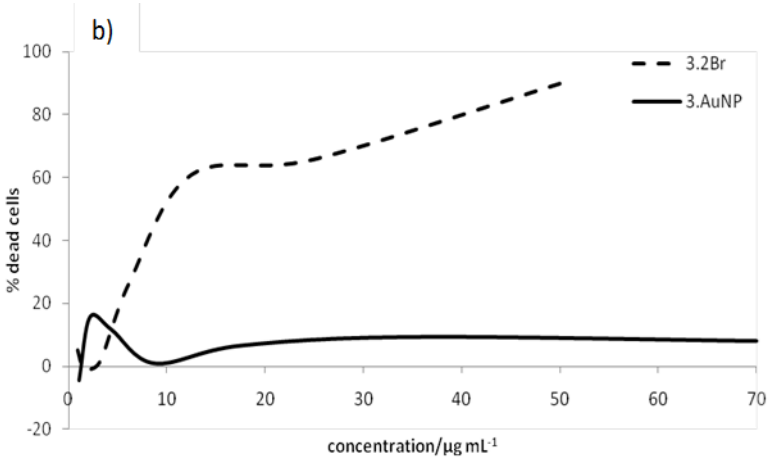

Figure S6. a) EC_{50} values of **3·2Br**, and **3·AuNPs** and reference compounds, and b) effect of **3·AuNPs** and **3·2Br** on the viability of Caco-2 cells. Cells were exposed for 48 hours and the viability was assessed by the MTT assay.

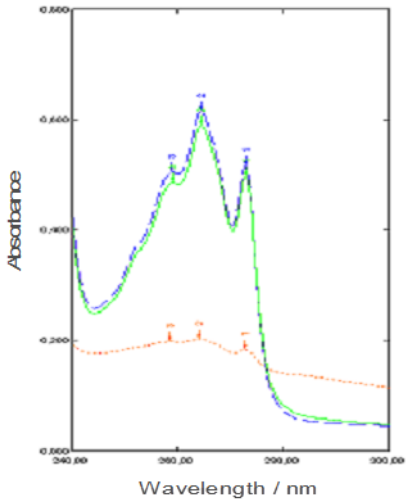

Figure S7. UV-Vis spectra of ibuprofenate aqueous solution (dashed line), aqueous solution of ibuprofenate after extraction with CH_2Cl_2 (solid line), and aqueous solution of ibuprofenate after extraction with CH_2Cl_2 containing **3·AuNPs** (dotted line). In the later case, a decrease in the intensity of the characteristic absorption band of ibuprofenate can be clearly observed, corresponding to an extraction of ca. 70% of ibuprofenate by **3·AuNPs**.

Figure S8. Stages of the experimental set-up of the dynamic dialysis for the ibuprofenate diffusion evaluation: Dichloromethane solutions of **3·AuNPs**-ibuprofenate complex, 3·2Br–ibuprofenate complex (as control) and **3·AuNPs** (as control), were placed in biodialysers (a) with one end cap covered with dialysis membrane and closed. Five replicas were prepared for **3·AuNPs**-ibuprofenate complex to obtain a reproducible measure. The solvent was allowed to evaporate and Milli-Q water (0.8 mL) was added in every biodialyser, which were closed on the other end with a dialysis membrane. Every biodialyser was placed on a closed container with 25 mL of MilliQ-water as receptor phase (b), those with **AuNPs** were covered with aluminium foil. All the containers were placed inside a reactor with a water jacket (c) which kept the dialysis systems at 32ºC by using a circulating water bath with temperature control (d). The whole set-up was on a platform with a constant horizontal shake (e).

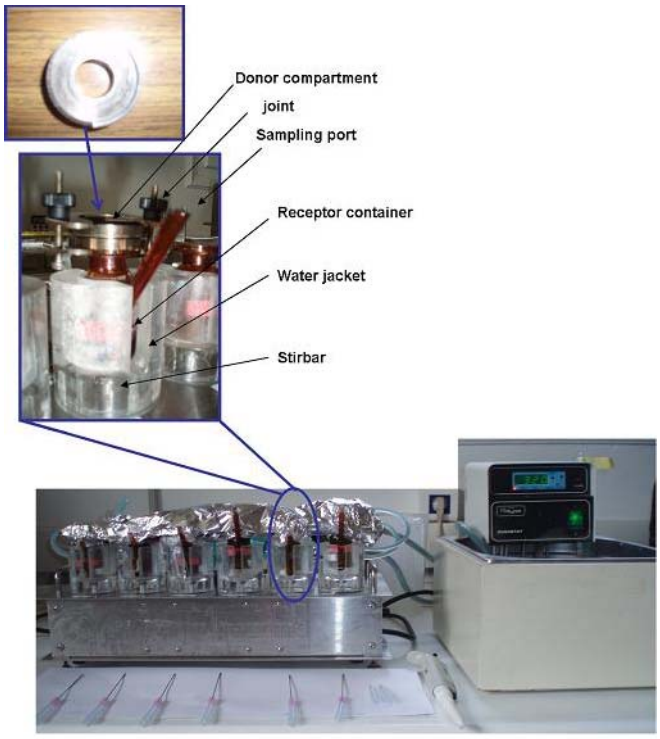

Figure S9. Franz cells set-up for evaluation of the ibuprofenate diffusion in static dialysis experiments: Dichloromethane solutions of 3·AuNPs-ibuprofenate complex (0.197 mL), 3·2Br –ibuprofenate complex (as control) (0.099 mL) and 3·AuNPs (as control) (0.230 mL), were placed on the donor chamber of the Franz cell (a). Four replicas were prepared for 3·AuNPs-ibuprofenate complex to obtain a reproducible measure. The solvent was allowed to evaporate and Milli-Q water (0.263 mL) was added in every donor container. The donor compartments were kept in darkness, placed onto the receptor glass chambers, and fixed with a joint (b). The water jacket of the Franz cells kept the system at 32ºC by using the circulating water bath (c), and the stirbar maintained the receptor phase as a homogeneous solution. Samples of 0.3 mL were taken at regular intervals, and the volume was replaced with MilliQ water from the sampling port.

3.4. Water-soluble gold nanoparticles based on imidazolium gemini amphiphiles for delivery of piroxicam

Publication in RSC Advances, 2014, 4, 9279-9287.

Mafalda Rodrigues,[a,b] Anna C. Calpena,[b,c] David B. Amabilino,[d] David Ramos-Lopez,[e] Joaquin de Lapuente[e] and Lluïsa Pérez-García[a,b]

a Department of Pharmacology and Therapeutic Chemistry, Universitat de Barcelona, 08028 Barcelona, Spain.

b Institute of Nanoscience and Nanotechnology IN2UB, Universitat de Barcelona, 08028 Barcelona, Spain.

c Department of Pharmacy and Pharmaceutical Technology, Universitat de Barcelona, 08028 Barcelona, Spain.

d Institut de Ciència de Materials de Barcelona (ICMAB-CSIC), Campus Universitari, 08193 Bellaterra, Spain.

e Unitat de Toxicologia Experimental i Ecotoxicologia (UTOX-PCB), Baldiri i Reixac 10-12, 08028 Barcelona, Spain.

Summary

In the previous work, a bis-imidazolium ligand containing alkyl chains with 18 carbonswas used to synthesize GNP in a biphasic system. In the present work, that same ligand was used in aqueous solution, rendering GNP that were water-soluble.

Different ligand:Au ratios were tested, and the success in the synthesis of GNP was assessed by UV-visible absorption spectroscopy. The successfully obtained GNP were further characterized by TEM and TGA. TEM showed a gold core of around 12 nm, and TGA provided data to determine the amount of ligand per GNP. Comparing the amount found by the GNP previously obtained, which were formed by a monolayer of ligand around the gold core, and the one obtained for the water-soluble ones, we could conclude that they present a bilayer of ligand.

Having such a structural difference, it was also important to study the toxicity and

internalization. We found they were slightly more cytotoxic than the previously described GNP that were synthesized in a biphasic system and were comprised of a monolayer.This increase in cytotoxicity is in agreement with the fact that the surface has a high density of positive charges, but also that they could enter the cell probably by a different route, suggested by the fact that the GNP were found free in cytoplasm and not confined to endosomes.

The incorporation of a poorly water-soluble drug was successfully achieved, as the bilayer structure of the ligand around the gold core would represent a favourable environment. The release rate of the incorporated drug was assessed, and the pH appeared to have little influence on the process, inside the values tested. At both pH 7.4 and 5.5, the release followed the same zero-order kinetic and very similar release rates. Furthermore, the anti-inflammatory activity of the released drug was performed *in vitro* through the determination of the inhibition of COX activity. However, the GNP exerted alone an inflammatory response, and therefore the effect of the drug appeared to be small.

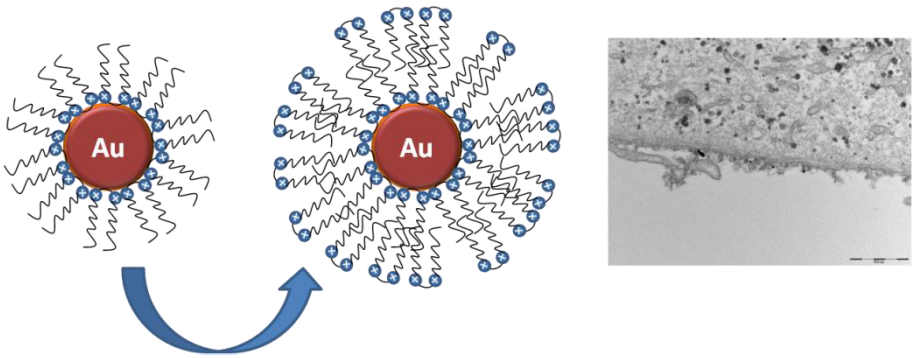

Figure 3.16: Schematic representation of the GNP previously synthesized in biphasic system in contrast with the GNP synthesized in aqueous medium, bearing a double layer of ligand (left) and TEM micrograph of Caco-2 cells with the novel GNP found dispersed inside the cytoplasm (right).

RSC Advances

PAPER

Water-soluble gold nanoparticles based on imidazolium gemini amphiphiles incorporating piroxicam†

Cite this: *RSC Adv.*, 2014, 4, 9279

Mafalda Rodrigues,[ab] Ana C. Calpena,[bc] David B. Amabilino,[d] David Ramos-López,[e] Joaquin de Lapuente[e] and Lluïsa Pérez-García*[ab]

Water soluble gold nanoparticles were synthesized in a single step using a double layer of a gemini imidazolium-based amphiphile as both reagent and stabilizer. The synthetic strategy exploits the amphiphilic nature of the ligand, and different ratios of ligand to Au(III) precursor were tested in order to favour the formation of amphiphile bilayer-coated nanoparticles, as indicated by their solubility and the thermogravimetric analysis, which proved the gold/organic ratio. The approximately 10 nm nanoparticles display cytotoxicity on Caco-2 cells similar to gold nanomaterials coated with other cationic surfactants, mainly because of their bilayer coating. Instead, genotoxicity was proven to be low, and the gold nanoparticles showed cell internalization being able to leave endosomes and without entering the nuclei. The incorporation of piroxicam, a poorly water soluble drug that has anti-inflammatory and antitumoral activity, was achieved thanks to anion binding by the amphiphile. Subsequently *in vitro* release of piroxicam from these nanoparticles was demonstrated, indicating their potential in combined chemotherapy.

Received 22nd August 2013
Accepted 22nd January 2014

DOI: 10.1039/c3ra44578j

www.rsc.org/advances

Introduction

Gold nanoparticles (GNPs) are presently seen as powerful components in the development of nanoscale-based platforms, such as drug delivery vehicles, to be used in therapy[1,2] or for diagnosis.[3] The most commonly used methods for their synthesis are the citrate method, developed by Turkevich to prepare water-soluble GNPs,[4] and the Brust–Schiffrin method,[5] which consists of a two-phase system to synthesize GNPs that have low polydispersity and are soluble in organic media. The former are more suited for applications in nanomedicine, because of their solubility in physiological media, while the latter can be used in other fields, where the presence of organic solvents in the synthesis does not compromise the contact of the nanomaterial with the biological media.[6] Although the organic synthetic methodology generally allows a better control over quality and polydispersity of the nanoparticles,[7] the fact that the synthesis of lipophilic GNPs requires a transfer agent that later has to be removed could result in a more complex preparation, which could in turn affect their toxicity profile, leaving room for improvement in the methodology. It is also possible to generate water-soluble GNPs following the Brust methodology,[8] although there is an increase in the complexity of the systems generated. The need to obtain water-soluble GNPs is driven by the fact that, when intended for biological applications, they have to be re-suspended in the physiological fluids. Besides, it is important that the synthetic method avoids as much as possible using organic solvents, which are restricted for final biomedical applications, as well as to maintain the delivery platforms at their simplest composition, *e.g.* reducing the number of their functional components.

However, the most common approach to obtain GNPs to be used as delivery agents is to use a thiol-terminated or amine-terminated ligands to which the molecule of interest to be delivered is loaded in a covalent manner,[2,9,10] or alternatively in a non-covalent manner.[2,11,12] The chemical nature of the coating agent determines the properties of the nanoparticles. Despite many articles in the literature describing the use of amphiphiles to stabilize gold nanoparticles, examples focussing on their use as drug delivery systems are scarce. Different types of ligands have also been studied as alternative stabilizers in the synthesis of water soluble GNPs, like water-soluble polymers,[13–17] some based on imidazolium salts,[18,19] but also amino acid based

[a]Department of Pharmacology and Therapeutic Chemistry, Universitat de Barcelona, 08028 Barcelona, Spain. E-mail: mlperez@ub.edu; Fax: +34 934024539; Tel: +34 934035849

[b]Institute of Nanoscience and Nanotechnology IN2UB, Universitat de Barcelona, 08028 Barcelona, Spain

[c]Department of Pharmacy and Pharmaceutical Technology, Universitat de Barcelona, 08028 Barcelona, Spain

[d]Institut de Ciència de Materials de Barcelona (ICMAB-CSIC), Campus Universitari, 08193 Bellaterra, Spain

[e]Unitat de Toxicologia Experimental i Ecotoxicologia (UTOX-PCB), Baldiri i Reixac 10-12, 08028 Barcelona, Spain

† Electronic supplementary information (ESI) available. See DOI: 10.1039/c3ra44578j

amphiphiles[20] or peptides.[21] Some examples of amphiphilic molecules are also used as templates, in the form of hydrogels, in the synthesis and stabilization of GNPs.[22–25] Ionic liquids based on imidazolium salts have received attention as stabilizers of metallic nanoparticles,[26] but only some examples use gemini amphiphiles as capping agents – such as bis ammonium quaternary salts.[27–29] We found only two examples of gemini-type imidazolium surfactants with a flexible spacer giving water soluble GNPs[30] and flower-shaped gold nanostructures,[31] but none directly related to the preparation of delivery systems.

In our group we developed[32] a family of gemini-type amphiphile molecules bearing a polar head incorporating two imidazolium groups linked through a rigid 1,3-bis(methylene)-benzene spacer, such as **1·2Br** (Fig. 1). These easily synthesized molecules showed a good ability to complex anions, particularly carboxylates, and this feature could be exploited for the recognition of anionic drugs, both in sensing applications and as delivery vectors. Thus, bearing in mind their complexation ability, and the fact that imidazolium salts were reported as ligands for the stabilization of GNPs, our next step was the use of this amphiphilic molecules in the synthesis of gold nanoparticles through a modified Brust–Schiffrin[32] without the need for a transfer agent, which resulted in the formation of very stable colloids. Besides this advantage, the fact that the ligand can complex anionic molecules permits loading of the GNPs with an anionic model drug in a non-covalent manner, which means that no prodrug or chemical modification of the drug was needed to incorporate it in the GNPs, making the whole delivery platform much simpler and controllable.

However, the obtained nanomaterials[32] were only soluble in organic media, which limits their applications in therapy. For this reason, finding an alternative methodology to obtain water-soluble gold nanoparticles using the same gemini imidazolium amphiphilic ligand represented a challenge and the main objective of this work, which could be faced by attempting the formation of a double layer of surfactant around the metallic gold core. In fact, examples in the literature[33,34] showed the successful use of surfactant molecules, namely cetyltrimethylammonium bromide and didodecyldimethylammonium bromide, to obtain GNP that are soluble in water, stabilized through a double layer of the molecules on the surface. In these cases, the surfactants used were quaternary ammonium salts, which are known to be cytotoxic.[35]

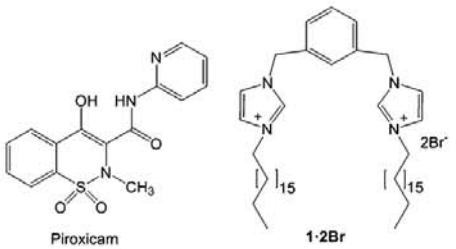

Fig. 1 Molecular structures of piroxicam and the gemini-type surfactant **1·2Br**.

In order to prepare water soluble GNPs with lower cytotoxicity, we have explored the stabilization of gold nanoparticles forming a bilayer of a gemini-amphiphile imidazolium salt **1·2Br**. The GNPs obtained can be used as a vehicle for drugs that have low solubility in water, such as piroxicam (Fig. 1) a non-steroidal anti-inflammatory drug (NSAID) widely used in inflammatory arthritis and osteoarthritits. Besides this application, piroxicam already proved to be useful as a chemopreventive drug in the case of colorectal cancer.[36,37] In studies performed with dogs with transitional cell carcinoma, which can be considered a good model for human invasive urinary bladder cancer, it showed ability to induce apopotosis.[38] This apoptotic effect is thought to be the responsible for its antitumor activity, and the inhibition of Cyclooxygenase (COX) activity can be one of the mechanisms,[39] as well as regulation of proto-oncogenes.[40]

Consequently, in this work we have explored the preparation of a delivery platform for non-water soluble drugs, based on simple and stable, and easily prepared water soluble GNPs consisting only of a gold core coated with a single type of ligand. This ligand is a gemini amphiphile playing a triple role for the preparation of the water soluble gold nanoparticles, their stabilization through an imidazolium amphiphile bilayer coating and the incorporation and release of non-water soluble drugs, by means of non-covalent interactions. We have targeted a potent anti-inflammatory drug as a proof of principle for the delivery of compounds, given that the percentage of active component in the delivery vehicle–drug complex in this work – and in all the other work on nanoparticle carriers – is relatively low so that high activity is required. The ultimate aim of the nanoparticle vehicles is to provide greater selectivity in the delivery process.

In this paper we report a method to synthesize GNP that were soluble in water but not in organic solvents, by using the gemini imidazolium amphiphile **1·2Br** (Fig. 1) for their synthesis and stabilization. The synthetic methodology directs the obtained GNP to have a bilayer coat, in which the first layer stabilizes the gold core, and the second is responsible for their solubility in water. This type of GNP can therefore be used as vehicle for anionic drugs that have low solubility in water, using the ability of the imidazolium coating ligands to bind anions. As a proof of principle, we studied the GNP incorporation of the drug piroxicam. It was observed that the amphiphile ligand maintained the ability to complex this drug in a non-covalent way and to release it at a sustained rate. Furthermore, the toxicity of the GNPs synthesized and their internalization by cells was assessed.

Results and discussion

Synthesis and characterization of 1·GNP

We chose the gemini imidazolium-based amphiphilic ligand **1·2Br** (Fig. 1) as the stabilizer for the formation of gold nanoparticles that disperse in water. Basically, the GNP preparation consisted of the addition of a small amount (below 50 mg) of the imidazolium based amphiphile stabilizer in water (because of its low solubility in this medium) and then adding the aqueous

Table 1 GNP prepared using different **1·2Br**:gold ratio, and their corresponding peaks of the SPR band, size of the gold core and PDI

Experiment	**1·2Br** : Au ratio	UV-vis peak (nm)	Size (nm)[a]	PDI[b]	Stability in water
1	0.5 : 1.0	547	[c]	[c]	Poor
2	1.0 : 1.0	549	12 ± 4	0.09	Poor
3	1.5 : 1.0	539	12 ± 4	0.10	Poor
4	2.3 : 1.0	534	10 ± 4	0.16	Good

[a] Size of the gold core in the nanoparticle as determined by TEM. [b] PDI was calculated as the square of the quotient of the standard deviation divided by mean size. [c] Not analysed.

$HAuCl_4$ solution (the precursor of the metallic gold core) and the reducing agent ($NaBH_4$).

The formation of GNPs was monitored by UV-visible absorption spectroscopy, following the appearance of a characteristic peak around 530–550 nm (ESI, Fig. S1†), originated from the surface plasmon resonance (SPR) absorption of the nanosized gold particles, which is responsible for their characteristically coloured solutions (ESI, Fig. S2†). Table 1 summarizes the results obtained regarding the SPR peak and the size of the different GNP obtained using different ligand to gold proportions and their respective polydispersity index (PDI).

As shown in Table 1, **1·2Br** could be successfully used for the synthesis of water soluble GNPs in aqueous medium employing $NaBH_4$ as the reducing agent. The UV-visible absorption analysis showed a characteristic peak that shifts with the proportion of **1·2Br** used. The average size (diameter) of the gold core, measured by TEM, also shows variations. These differences can be related to the fact that the different proportions of ligand influence the size of the gold nucleus, and small variations in the nucleus account for differences in the SPR peak that we observe. Thus, as the **1·2Br**/Au ratio increases, the size of the gold core is reduced as indicated by the shift of the SPR peaks. If we compare them with the previously obtained GNPs,[32] soluble in organic medium, those presented an SPR peak at 519 nm. This correlates well with the fact that the core size was slightly smaller (8.8 nm) than the ones obtained in this synthesis in aqueous medium.

The solubility and stability of the GNPs prepared using different proportions of surfactant to metal were also clearly dependent on the amount of surfactant (Table 1). To eliminate any non-specifically bound **1·2Br** from the colloidal suspension of nanoparticles, an extraction was performed using dichloromethane. Interestingly, in the case of the GNP from experiment 1 (see Table 1) addition of dichloromethane induced a transfer of gold nanoparticles from the aqueous to the organic phase. This could be understood considering that in this experiment we used the lower surfactant:gold ratio, and thus the amount of **1·2Br** used for the synthesis was insufficient to form a complete bilayer coating, and the removal of unbound stabilizer render gold nanoparticles insoluble in water. Instead, the GNP from experiments 2 and 3 were not stable, as they flocculated after some time, showing a solid deposit after some days. The synthesized GNP from experiment 4, referred to as **1·GNP**, were the most stable nanoparticles in water solution, and for this reason were further studied.

Morphological characterization of the synthesized **1·GNP** was performed by TEM. Fig. 2 shows a micrograph of the water-soluble **1·GNP** where their spherical shape and uniformity can be appreciated. The average size of their gold core is *ca.* 10 nm (Table 1). Details of the size distribution are shown in ESI, Fig. S3.†

1·GNP were further characterized by thermogravimetric analysis. This allowed determination of the mass of ligand **1·2Br** and gold in the analyzed GNP samples. With their respective molecular weight, we could determine the number of moles of each, and establish a ratio of surfactant:gold. Taking into account the size of the gold nanoparticles, the number of gold moles per nanoparticles was determined, and with the ratio surfactant:gold we calculated the number of ligands per nanoparticle. Furthermore, calculating the nanoparticles' surface area we found the presence of approximately 72 molecules of ligand per nm^2. For comparison purposes we analysed the gold nanoparticles synthesised in organic medium,[32] and thermogravimetry indicated that those GNPs had *ca.* 30 ligand molecules per nm^2 (ESI, Fig. S4 and Table S1†). This data confirms that the ligand forms a double layer around the gold core, so that the formed nanoparticles have positively charged heads from the first layer stabilizing the gold core, and the charges from the second layer facing outwards and making the particles soluble in water (Fig. 3).

Incorporation and release of piroxicam in 1·GNP

A model drug was used to be incorporated and released from water soluble **1·GNP** in order to set up the proof of principle

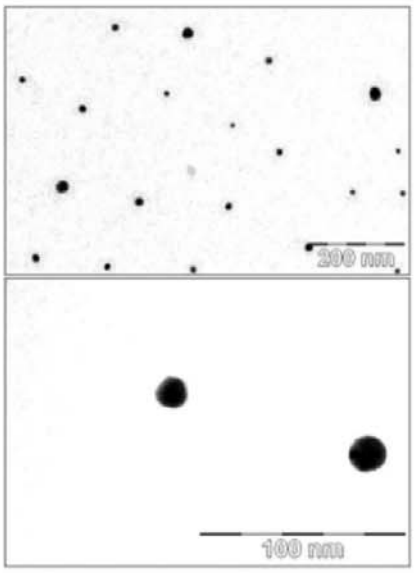

Fig. 2 TEM micrograph of the water-soluble gold nanoparticles 1·GNP.

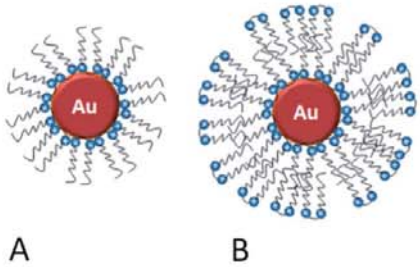

Fig. 3 Schematic representation of GNP with (A) one layer of ligand around the nucleus core, and (B) a double layer around the gold nucleus core (water soluble).

and assess the potential application of these new GNPs as delivery vehicles. The model drug used was piroxicam (Fig. 1), which is a poorly water soluble drug, used extensively in cases of arthritis and osteoarthritits for its anti-inflammatory activity, as well as in cases of colorectal cancer due to its preventive properties. Piroxicam is an acidic molecule, but acidity is attributed to the enolic group and not to a carboxylate group (as was the case in our previous work[32]), and its binding to gold nanoparticles coated with imidazolium amphiphiles had yet to be proven. Thus, extraction of piroxicam from an organic (dichloromethane) solution to the aqueous phase, containing the water soluble **1·GNP**, was performed.

The mean value for the diameter of **1·GNP** obtained by TEM allows us to determine the concentration of synthesized nanoparticles.[41] eqn (1) is used to determine the number of atoms of gold per nanoparticle, N:

$$N = \frac{\pi \rho D^3}{6M} N_A \quad (1)$$

where ρ is the fcc density of gold (19.3 g cm^{-3}), D is the average diameter of the AuNPs, M is the atomic mass of gold (196.97 g mol^{-1}) and N_A is the number of Avogadro (6×10^{23} mol^{-1}). Once N is known, eqn (2) is used to calculate the molar concentration of the nanoparticles in solution (C):

$$C = \frac{N_T}{NVN_A} \quad (2)$$

where N_T is the number of gold atoms added as $HAuCl_4$ (assuming 100% reduction of Au) and V is the volume of solution. The GNP solution was centrifuged to concentrate it, and using the equations, it was possible to calculate the final concentration of **1·GNP** as 71.3 nM, which corresponds to 2.3 mg mL^{-1}. After the extraction, the aqueous phase was washed three times with dichloromethane, to remove any unbound piroxicam. The aqueous phase with the **1·GNP** and piroxicam incorporated exhibits, besides the **1·GNP** peak at 540 nm, the peak at 360 nm corresponding to piroxicam (ESI, Fig. S5†). This peak was not visible in the organic phases used to extract piroxicam from the nanoparticles. This means that the drug was well incorporated in the nanoparticles, and that the imidazolium ligands are able to bind enolate incorporating compounds. Also a slight change in the SPR peak of the GNP was registered, that initially was at 533 nm and shifted to 540 nm. It is known that the SPR peak depends not only of the size of the GNPs but also of the ligand that is covering the metal, so we could explain this shift because of the incorporation of the piroxicam drug in the structure.

According to our calculations, we could incorporate 15 μg of piroxicam per mg of **1·GNP**. The release of piroxicam from the GNPs was determined as previously described,[42] using Franz cells system. The samples were resuspended in Sorensen Buffer at pH 5.5 and 7.4, to simulate physiological conditions, and the receptor solution used was NaOH pH 11, in which piroxicam is soluble, as tested prior to the experiments, and thus complying with the SINK conditions. Given the size of the gold nanoparticles, dialysis membranes were selected with a cut-off which allows the pass of piroxicam (molecular weight 331.35 Da) but prevents the passage of the nanoparticles (membrane dialysis pore diameter is equivalent to 2.4 nm).

The amount of released drug was measured as described in the experimental section. Six different kinetic models (zero order, first order, one phase exponential, Peppas-Korsmeyer, Higuchi and Weibull function) were used to fit the experimental data obtained in the drug release experiments.[43] The Akaike Information Criterion (AIC) was determined for each model, as it is an indicator of the model's suitability for a given dataset.[44] The kinetic model that best describes the experimental data was selected based on the lowest AIC value (see ESI, Table S2†). From the AIC data, we can say that the kinetic model that best describes the release of piroxicam from the gold nanoparticles, for both pH values tested, is the one phase exponential. This means that the release rate depends only on the amount of drug present. Furthermore, the presence of a delay in the beginning of the release means that the drug is well encapsulated by the ligand **1·2Br**, and suffers other diffusion processes from the interior of the nanoparticle, specifically a partition between the inner environment and the donor solution. This partition favours the slow release of the drug, because the donor solution must comply with the physiological conditions, opposite to the receptor solution.

Regarding the amodelistic parameters medium dissolution time (MDT), area under curve (AUC), and efficiency (Table 2), we can see important differences between the releases at the two pH values that were tested. At pH 7.4 the efficiency of the release is higher than at pH 5.5 (95.4% *vs.* 43.5%, respectively), meaning that it is more suited for delivery under physiological conditions and not for an external application in the skin since a higher amount of drug can be released from the GNP. On the other hand, the value of MDT registered at pH 7.4 is also higher.

Table 2 Amodelistic parameters for release of piroxicam at pH 5.5 and 7.4

pH	MDT[a] (h)	AUC[b]	% Effic.[c]
5.5	183.50	0.037	43.5
7.4	67.67	0.190	95.4

[a] Medium dissolution time. [b] Area under curve. [c] Efficiency (in percentage).

It can indicate that the release of this drug from the GNP complex is favoured at this pH.

Fig. 4 shows the release profiles of piroxicam at pH 5.5 and 7.4 with the fitting of the kinetic model that better adjusts to the release, along with the corresponding equation parameters.

Toxicity studies of 1·GNP

Along with the studies of the piroxicam liberation, the cytotoxicity and genotoxicity of the synthesized **1·GNP** were also determined.

Comparison of values found in the literature for cytotoxicity of gold nanoparticles is hampered by the different experimental protocols reported as well as the differences in the composition of the nanomaterials, for which a precise composition is not always defined.[45] Several reports indicate that interaction with the biological media depends of many factors, such as size, shape and charge of gold nanoparticles.[46] Additionally, the moderate toxicity of cationic particles has been evaluated,[47,48] with the toxicity mainly attributed to the cationic surfactant used as coating agent.[35] Interestingly, when cell damage is evaluated in gold nanorods,[49] cytotoxicity is closely related to the bilayer structure of the ammonium salt surfactant.

The cytotoxicity, expressed here as EC_{50}, was determined on human colon carcinoma cell line Caco-2 using the MTT assay. The cell line can be used in cytotoxicity assays because dedifferentiated cancer cell lines provide a good rough estimation for the toxic potential of the studied substance.[50] From the results obtained (ESI, Fig. S6†), the value for the EC_{50} of **1·GNP** is 30 μg mL^{-1}, which is a much smaller than the EC_{50} value obtained for the amphiphile **1·2Br** alone, which is 13.2 μg mL^{-1}.[32] Comparison with the organic media soluble GNP coated with a monolayer of the same amphipile,[13] which had an EC_{50} higher than >70 μg mL^{-1}, clearly indicates the higher toxicity of the water soluble nanoparticles **1·GNP**.

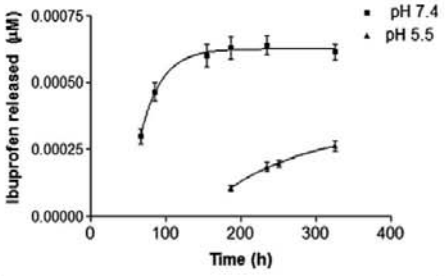

Parameter	pH 7.4	pH 5.5
S	-0.0037	-0.0010
K	0.0367	0.0081
P	0.0006	0.0003
Half Life	18.88	85.09
R^2	0.9979	0.9993

Fig. 4 Profiles and equation parameters for the release of piroxicam incorporated in **1·GNP** at pH 5.5 and pH 7.4.

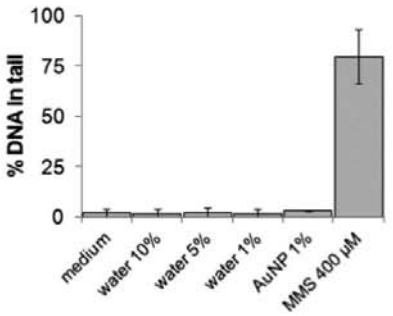

Fig. 5 Genotoxic effect of the **1·GNP** on Caco-2 cells, by the Comet assay.

According to our model, and in good agreement with the literature,[49] the disposition of a double layer around the gold core favours a dense interface containing positively charged polar heads to contact the cells, which explains the higher toxicity of **1·GNP**, compared to the GNP with a single layer in which the positive charge of the amphiphile is in contact with the metal in the colloid or the isolated amphiphile which has a low density of positive charges. However, this structural property of the **1·GNP** had interesting effects regarding the internalization in cells (see later). Furthermore, the EC_{50} for the surfactant indicates that toxicity should be mostly attributed to the cationic nature of surfactant coat.

To evaluate the genotoxicity of **1·GNP**, the Comet Assay was also performed. It consists of extracting and running an electrophoresis of the cells' DNA, and analysing the amount of DNA that forms a tail for each band. This tail indicates damage in the genetic material. Only the concentration of **1·GNP** that was below the EC_{50} was tested. For statistical analysis, different proportions of distilled water in culture medium were used, along with the **1·GNP**, and the results are shown in Fig. 4. It was concluded that no significant genotoxicity was observed for **1·GNP** (Fig. 5). The statistical analysis of the assay showed no significant differences between water and **1·GNP**. The DNA-damaging alkylating-agent methylmethane sulfonate (MMS 400 mM) was used as positive control.

Cell penetration study

Cell uptake was studied in Caco-2 cells exposed to 0.4 nM of **1·GNP** for 15 and 30 minutes, 1, 4 and 24 hours. Fig. 6 shows TEM images of the internalization of **1·GNP** in Caco-2 cells at the aforementioned time-points.

Aggregates were not observed in any case. Instead **1·GNP** were always observed as single nanoparticles. After 15 minutes only single **1·GNP** were found attached outside the cell membrane (Fig. 6A). At 30 minutes the GNP could also be found on the cell membrane (Fig. 6B) and inside the cell, in early endosomes (Fig. 6C). The same was observed at 1 hour (Fig. 6D–E). However, after 4 hours of exposure **1·GNP** were widely

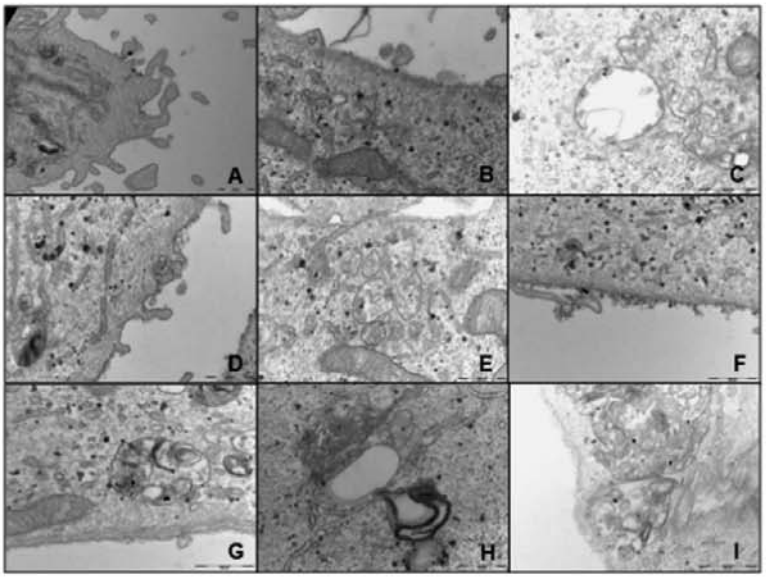

Fig. 6 TEM images from Caco-2 cells treated with **1·GNP** after 15 minutes (A), 30 minutes (B, C), 1 hour (D, E), 4 hours (F–H) and 24 hours (I) of exposure.

dispersed within the cell, located in cell membrane (Fig. 6F), within vesicles (Fig. 6G), lysosomes and also free in the cytoplasm (Fig. 6H). In any case, though, **1·GNP** have not been observed in the nuclei at any exposition time. At the last time of observation (24 hours) GNP remained as single particles within vesicles, lysosomes and cytoplasm (Fig. 6I). The fact that the GNP can be found in the cytoplasm after a few hours of exposure is important. In the first hour they could only be found confined inside vesicles, which meant that the internalization process is most likely to be through endocytosis. However, the ligand around the gold nucleus favours in some way the exit of the particles from the vesicles.

Piroxicam activity evaluation

Finally, we studied if the **1·GNP** loaded with piroxicam could express the drug bioactivity. We performed an assay which is based in the colorimetric detection of the peroxidase activity of the cyclooxygenase (COX) through the formation of the oxidized form of *N*,*N*,*N*,*N*-tetramethyl-*p*-phenylenediamine (TMPD), measured at 590 nm, using A549 p6 cell line. The final results of COX-2 activity are shown in Table 3 (further data included in ESI, Table S3†).

The cells were exposed to **1·GNP**, to **1·GNP** with piroxicam, and to **1·GNP** with piroxicam in the presence of LPS, which is commonly used to induce inflammation, in order to increase the COX activity. Regarding **1·GNP**, it was observed that they exert a certain level of inflammatory response in the cell line that was used, because the COX-II activity increased from day 1 (10.04 U mL^{-1}) to day 10 (22.63 U mL^{-1}). Also, **1·GNP** with piroxicam had an effect in the inflammatory response, reducing

Table 3 COX activity in cells exposed to **1·GNP**, **1·GNP** with piroxicam (**1·GNP-pxc**) and **1·GNP** with piroxicam and LPS (**1·GNP-pxc + LPS**). LPS is used to induce inflammation

	$t_{exposure}$/days	COX total activity/U[a] ml^{-1}	COX-2 activity/U[a] ml^{-1}
1·GNP	1	9.92	10.04
	10	24.79	22.63
1·GNP-pxc	1	8.96	9.22
	10	19.83	18.18
1·GNP-pxc + LPS	1	9.85	10.11
	3	12.27	11.44
	5	17.23	17.23
	8	22.31	19.70
	10	22.95	21.93

[a] Units of enzymatic activity.

it around 20%. In the assay with LPS, that induces inflammation, the reduction in the activity of COX-II was around 3%. However this is a good result, because it must be taken into account that piroxicam had to reduce the inflammatory effect of both LPS and **1·GNP**. The overall results can hence be attributed to the fact that the amount of **1·GNP** dose that was used was too high and that the amount of drug loaded was not enough to reduce substantially the inflammation in the 10 days of the assay.

Future work might include increasing the amount of pyroxicam incorporated into the gold nanoparticles, and further proofs with different cell lines should be done in order to determine if this response is transversal or is observed in specific tissues.

Conclusions

The use of novel delivery scaffolds for non-water soluble drugs based on amphiphilic coated gold nanoparticles is proven. Thus, it has been shown that the gemini imidazolium based amphiphile **1·2Br** can be used to form and stabilize GNP in aqueous medium. The water soluble **1·GNP** are spherical and uniform, with an average core size of *ca.* 10 nm. They have a well-defined structure, with the gold core coated with a bilayer of gemini-imidazolium surfactant, as proved by thermogravimetric analysis. This bilayer coating has an influence in the cytotoxicity of the nanomaterials based on **1·2Br** and gold, since their EC_{50} ($\mu g\ mL^{-1}$) is slightly lower than in the nanoparticles stabilized by a monolayer of the same cationic surfactant. Nevertheless, cytotoxicity seems comparable to that of other cationic nanoparticles. Cell uptake studies indicated that **1·GNP** do not enter the cell nuclei, as well as the capability of these nanoparticles to escape endosomic vesicles, stressing the potential of the surfactant **1·2Br** as an anti-lysosomal agent. More importantly, **1·GNP** showed the ability to incorporate piroxicam and to release it in a sustained manner at pH 7.4, indicating their suitability for delivery in physiological conditions. However, the inflammatory response that **1·GNP** produces has to be taken into account, since the drug loaded seems to be enough to reduce inflammation and inhibit cyclooxygenase, but has to reduce both the initial inflammation and the one that is being produced by the vehicle itself.

All these findings point out the potential of **1·GNP** for biomedical applications, mainly in combined therapies that take advantage of the combination of their cytotoxicity and their ability to incorporate drugs. Their usage in combined cancer therapy is an area of particular interest.

Experimental section

Reagents

All reagents were of analytical grade. Piroxicam was purchased from Sigma-Aldrich. Compound **1·2Br** was synthesized as described in literature.[32]

Instrumentation

UV-visible absorption spectra were obtained on UV-1800 Shimadzu UV Spectrophotometer. Thermogravimetric analysis was performed on Mettler Toledo TGA/SDTA 851e from 30 °C to 600 °C with a heating rate of 10 °C min^{-1}. TEM images were obtained with a transmission electron microscope JEOL 1010 at 80 kv. The images were captured by a Megaview III Soft Imaging System camera. The size of the nanoparticles was measured with the Analysis software (Olympus).

Synthesis of 1·GNP

The water-soluble gold nanoparticles **1·GNP** were prepared as follows: 30 mg (0.033 mmol) of **1·2Br** were dissolved in 60 mL of water and sonicated for 2 hours. The solution was mixed with 300 μL of an aqueous $HAuCl_4$ solution (different ratios of $HAuCl_4$ were tested, see Table 1) under vigorous stirring. Freshly prepared $NaBH_4$ solution in water (200 μL, 4 equivalents) was added dropwise to the previous solution. The colour of the solution changed from yellow to dark within a few minutes. The mixture was stirred for 3 hours, and the final solution was purple. The aqueous solution was extracted with dichloromethane (10 mL), to remove unbound **1·2Br**, and centrifuged at 13 400 rpm during 20 min and resuspended in water, to remove the excess of $NaBH_4$.

Encapsulation of piroxicam by 1·GNP

For the incorporation of drugs and release assays the **1·GNP** were centrifuged at 13 400 rpm during 20 min to concentrate them. 2 mL of concentrated GNP solution were added to 2 mL of a 0.05% (w/v) solution of piroxicam in dichloromethane. After energic shaking, the phases were allowed to separate and the organic phase was removed. The aqueous phase was washed with dichloromethane (3 × 1.5 mL). The presence of piroxicam was determined in the organic and aqueous phases through UV-vis absorption spectroscopy.

In vitro release of piroxicam

The study of the release of piroxicam from GNPs was performed in a Microette transdermal diffusion system with vertically assembled Franz-type diffusion cells with dialysis membranes (Cellu Sep T3 dialysis membrane, MWCO 12 000–14 000 Da, MFPI, USA). Sorensen buffer 67 mM pH 5.5 and 7.4 was used as donor solutions. 250 μL of samples were placed on top of the dialysis membrane, and 800 μL of the respective buffer were added. The receptor compartment was filled with NaOH 67 mM pH 11. The system was held at 32 ± 0.5 °C (for pH 5.5) to mimic skin conditions, and at 37 ± 0.5 °C (for pH 7.4) to mimic *in vivo* physiological conditions. The cells were sealed and 300 μL samples were withdrawn at appropriate time intervals for 240 h and were replaced with the same volume of fresh receptor medium. The *in vitro* accumulated amounts of piroxicam were assayed by HPLC in a Waters LC Module I. The column used was a Waters Spherisorb® 5 μm ODS-2 (4.6 mm × 150 mm). The mobile phase was acetonitrile – acetic acid 4% pH 2.4 (65 : 35 v/v). The flow rate was 1.0 mL min^{-1}, and the detection wavelength was 361 nm. The data was collected using Millennium32 version 4.0.0 software from Waters Corporation. All data was calculated as the average ± standard deviation of three replicates. A nonlinear least-squares regression was performed using the WinNonLin® software (WinNonlin® Professional edition version 3.3, Pharsight Corporation, USA), and the model parameters calculated. In addition, amodelistic parameter values for area under the curve (AUC), efficiency and medium dissolution time (MDT) were estimated. Both modelistic and amodelistic parameters were statistically compared by using StatGraphics software version 5.1.

Cytotoxicity and genotoxicity evaluation

Caco-2 cell line was were cultured in Dulbecco's modified Eagle's medium (DMEM, Sigma-Aldrich) containing 10% foetal calf serum (Hyclone), 2 mM glutamine (Sigma-Aldrich), antibiotics (Sigma-Aldrich, 50 U mL^{-1} penicillin and 50 μg mL^{-1}

streptomycin), Cells were exposed for 48 hours under 5% CO_2 at 37 °C and the viability was assessed by the MTT assay. Data was statistically analysed by SPSS v15 using U of MannWihtney statistic.

The genotoxicity was assessed by the Comet Assay according to the ASTM-E2186 guidelines. In the assay, the percentage of DNA in the tail was determined in respect to the intensity of the total DNA, in 50 cells. The determination was done using the software Comet Assay IV.

Cell penetration study

Cell uptake was studied as in Caco-2 cells by transmission electron microscopy (TEM) described before.[32] A sub-cytotoxic dose of **1·GNP** 0.4 nM was administered to Caco-2 cells grown until confluence. Exposure times were 15, 30 minutes, 1, 4 and 24 hours. Samples were observed with a transmission electron microscope JEOL 1010 at 80 kv.

Piroxicam activity evaluation

The anti-inflammatory activity of piroxicam released from the **1·GNP** was assayed by determination of the inhibition of COX activity with the kit CAY-760151 (Biomol, GmbH), following the manufacturer's instructions. The cell line used was A549 p6. Briefly, a solution of either (a) **1·GNP**, (b) **1·GNP** with piroxicam, or (c) **1·GNP** with piroxicam and lipopolysaccharide (LPS) was added to a confluent cell culture (1×10^6 cell per mL). The final concentrations used were 30 μg mL^{-1} of nanoparticles (blank or with piroxicam) and 1 μg mL^{-1} of LPS.

Acknowledgements

This study was supported by a grant from the *Ministerio de Ciencia e Innovación* (MICINN) (project TEC2011-29140-C03-02) and from the Generalitat de Catalunya (2009SGR158), and a predoctoral grant to M. Rodrigues from *Institut de Bioenginyeria de Catalunya* (IBEC).

References

1 E. Boisselier and D. Astruc, *Chem. Soc. Rev.*, 2009, **38**, 1759–1782.
2 C.-K. Kim, P. Ghosh and V. M. Rotello, *Nanoscale*, 2009, **1**, 61–67.
3 P. Baptista, E. Pereira, P. Eaton, G. Doria, A. Miranda, I. Gomes, P. Quaresma and R. Franco, *Anal. Bioanal. Chem.*, 2007, **391**, 943–950.
4 J. Turkevich, P. C. Stevenson and J. Hillier, *Discuss. Faraday Soc.*, 1951, **11**, 55–75.
5 M. Brust, M. Walker, D. Bethell, D. J. Schiffrin and R. Whyman, *J. Chem. Soc., Chem. Commun.*, 1994, 801–802.
6 K. M. L. Taylor-Pashow, J. Della Rocca, R. C. Huxford and W. Lin, *Chem. Commun.*, 2010, **46**, 5832–5849.
7 I. Ojea-Jiménez, L. García-Fernández, J. Lorenzo and V. F. Puntes, *ACS Nano*, 2012, **6**, 7692–7702.
8 T. R. Tshikhudo, Z. Wang and M. Brust, *Mater. Sci. Technol.*, 2004, **20**, 980–984.
9 L. Vigderman and E. R. Zubarev, *Adv. Drug Delivery Rev.*, 2013, **65**, 663–676.
10 B. Duncan, C. Kim and V. M. Rotello, *J. Controlled Release*, 2010, **148**, 122–127.
11 C. K. Kim, P. Ghosh, C. Pagliuca, Z.-J. Zhu, S. Menichetti and V. M. Rotello, *J. Am. Chem. Soc.*, 2009, **131**, 1360–1361.
12 T. Doane and C. Burda, *Adv. Drug Delivery Rev.*, 2013, **65**, 607–621.
13 I. Hussain, S. Graham, Z. Wang, B. Tan, D. C. Sherrington, S. P. Rannard, A. I. Cooper and M. Brust, *J. Am. Chem. Soc.*, 2005, **127**, 16398–16399.
14 A. Nagai, R. Yoshii, T. Otsuka, K. Kokado and Y. Chujo, *Langmuir*, 2010, **26**, 15644–15649.
15 S. Manju and K. Sreenivasan, *J. Colloid Interface Sci.*, 2012, **368**, 144–151.
16 R. Sardar, N. S. Bjorge and J. S. Shumaker-Parry, *Macromolecules*, 2008, **41**, 4347–4352.
17 K. Rahme, P. Vicendo, C. Ayela, C. Gaillard, B. Payré, C. Mingotaud and F. Gauffre, *Chem. – Eur. J.*, 2009, **15**, 11151–11159.
18 I. Biondi, G. b. Laurenczy and P. J. Dyson, *Inorg. Chem.*, 2011, **50**, 8038–8045.
19 N. R. Jana, P. K. Patra, A. Saha, S. Basiruddin and N. Pradhan, *J. Phys. Chem. C*, 2009, **113**, 21484–21492.
20 S. Si, E. Dinda and T. K. Mandal, *Chem. – Eur. J.*, 2007, **13**, 9850–9861.
21 R. Lévy, N. T. K. Thanh, R. C. Doty, I. Hussain, R. J. Nichols, D. J. Schiffrin, M. Brust and D. G. Fernig, *J. Am. Chem. Soc.*, 2004, **126**, 10076–10084.
22 P. K. Vemula and G. John, *Chem. Commun.*, 2006, 2218–2220.
23 P. K. Vemula, U. Aslam, V. A. Mallia and G. John, *Chem. Mater.*, 2007, **19**, 138–140.
24 R. N. Mitra and P. K. Das, *J. Phys. Chem. C*, 2008, **112**, 8159–8166.
25 D. Das, S. Maiti, S. Brahmachari and P. K. Das, *Soft Matter*, 2011, **7**, 7291–7303.
26 J. Dupont and J. D. Scholten, *Chem. Soc. Rev.*, 2010, **39**, 1780–1804.
27 M. S. Bakshi, P. Sharma and T. S. Banipal, *Mater. Lett.*, 2007, **61**, 5004–5009.
28 F. Xu, Q. Zhang and Z. Gao, *Colloids Surf., A*, 2013, **417**, 201–210.
29 Q. Liu, M. Guo, Z. Nie, J. Yuan, J. Tan and S. Yao, *Langmuir*, 2008, **24**, 1595–1599.
30 M. Murawska, A. Skrzypczak and M. Kozak, *Acta Phys. Pol., A*, 2012, **121**, 888–892.
31 L. Zhong, X. Zhai, X. Zhu, P. Yao and M. Liu, *Langmuir*, 2010, **26**, 5876–5881.
32 L. Casal-Dujat, M. Rodrigues, A. Yagüe, A. C. Calpena, D. B. Amabilino, J. González-Linares, M. Borràs and L. Pérez-García, *Langmuir*, 2012, **28**, 2368–2381.
33 A. Swami, A. Kumar and M. Sastry, *Langmuir*, 2003, **19**, 1168–1172.
34 L. Zhang, X. Sun, Y. Song, X. Jiang, S. Dong and E. Wang, *Langmuir*, 2006, **22**, 2838–2843.
35 E. E. Connor, J. Mwamuka, A. Gole, C. J. Murphy and M. D. Wyatt, *Small*, 2005, **1**, 325–327.

36 F. M. Giardiello, G. J. A. Offerhaus and R. N. Dubois, *Eur. J. Cancer, Part A*, 1995, **31**, 1071–1076.
37 R. F. Jacoby, D. J. Marshall, M. A. Newton, K. Novakovic, K. Tutsch, C. E. Cole, R. A. Lubet, G. J. Kelloff, A. Verma, A. R. Moser and W. F. Dove, *Cancer Res.*, 1996, **56**, 710–714.
38 S. I. Mohammed, P. F. Bennett, B. A. Craig, N. W. Glickman, A. J. Mutsaers, P. W. Snyder, W. R. Widmer, A. E. Degortari, P. L. Bonney and D. W. Knapp, *Cancer Res.*, 2002, **62**, 356–358.
39 T. A. Chan, *Lancet Oncol.*, 2002, **3**, 166–174.
40 S. S. Husain, I. L. Szabo and A. S. Tarnawski, *Am. J. Gastroenterol.*, 2002, **97**, 542–553.
41 X. Liu, M. Atwater, J. Wang and Q. Huo, *Colloids Surf., B*, 2007, **58**, 3–7.
42 M. E. Morales, V. Gallardo Lara, A. C. Calpena, J. Doménech and M. A. Ruiz, *J. Controlled Release*, 2004, **95**, 75–81.
43 P. Costa and J. M. S. Lobo, *Eur. J. Pharm. Sci.*, 2001, **13**, 123–133.
44 K. Yamaoka, T. Nakagawa and T. Uno, *J. Pharmacokinet. Biopharm.*, 1978, **6**, 165–175.
45 N. Khlebtsov and L. Dykman, *Chem. Soc. Rev.*, 2011, **40**, 1647–1671.
46 N. M. Schaeublin, L. K. Braydich-Stolle, A. M. Schrand, J. M. Miller, J. Hutchison, J. J. Schlager and S. M. Hussain, *Nanoscale*, 2011, **3**, 410–420.
47 C. M. Goodman, C. D. Mccusker, T. Yilmaz and V. M. Rotello, *Bioconjugate Chem.*, 2004, **15**, 897–900.
48 S. T. Kim, K. S. Kim and V. M. Rotello, *Acc. Chem. Res.*, 2013, **46**, 681–691.
49 L. Wang, X. Jiang, Y. Ji, R. Bai, Y. Zhao, X. Wu and C. Chen, *Nanoscale*, 2013, **5**, 8384–8391.
50 A. García-Lorenzo, E. Tojo, J. Tojo, M. Teijeira, F. J. Rodríguez-Berrocal, M. P. González and V. S. Martínez-Zorzano, *Green Chem.*, 2008, **10**, 508–516.

Electronic Suplementary Information

Water-soluble gold nanoparticles based on imidazolium gemini amphiphiles for delivery of piroxicam

Mafalda Rodrigues,[ab] Anna C. Calpena,[bc] David B. Amabilino,[d] David Ramos-Lopez,[e] Joaquin de Lapuente[e] and Lluïsa Pérez-García*[ab]

a Department of Pharmacology and Therapeutic Chemistry, Universitat de Barcelona, 08028 Barcelona, Spain.

b Institute of Nanoscience and Nanotechnology IN2UB, Universitat de Barcelona, 08028 Barcelona, Spain.

c Department of Pharmacy and Pharmaceutical Technology, Universitat de Barcelona, 08028 Barcelona, Spain.

d Institut de Ciència de Materials de Barcelona (ICMAB-CSIC), Campus Universitari, 08193 Bellaterra, Spain.

e Unitat de Toxicologia Experimental i Ecotoxicologia (UTOX-PCB), Baldiri i Reixac 10-12, 08028 Barcelona, Spain.

Corresponding Author

*E-mail: mlperez@ub.edu. Telephone: (+34) 934035849. Fax: (+34) 934024539

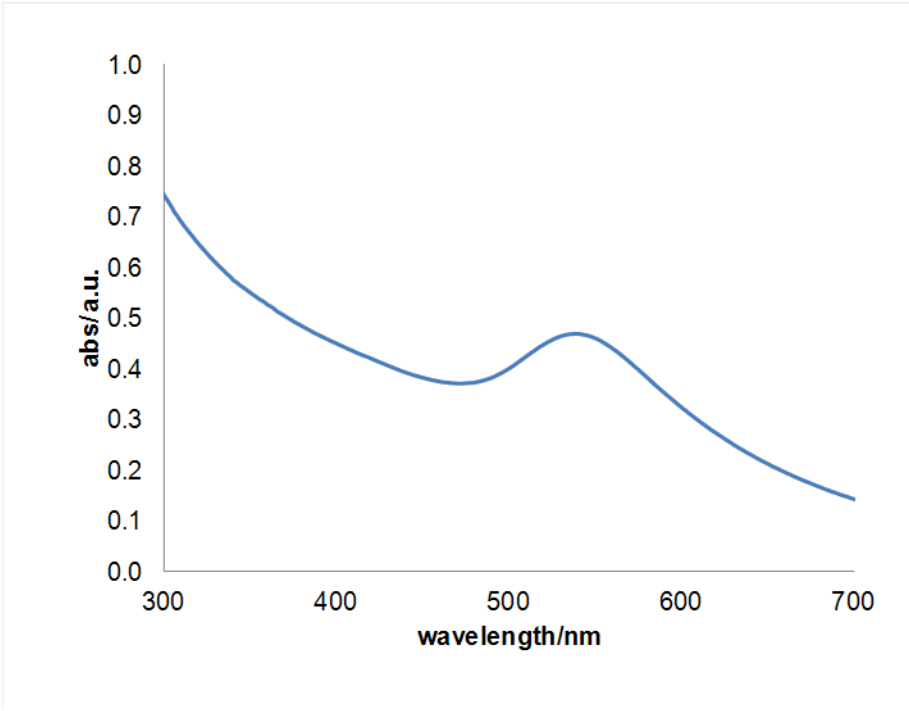

Figure S1: UV-vis spectra of **1·GNP**, showing the typical SPR peak around 533 nm**.**

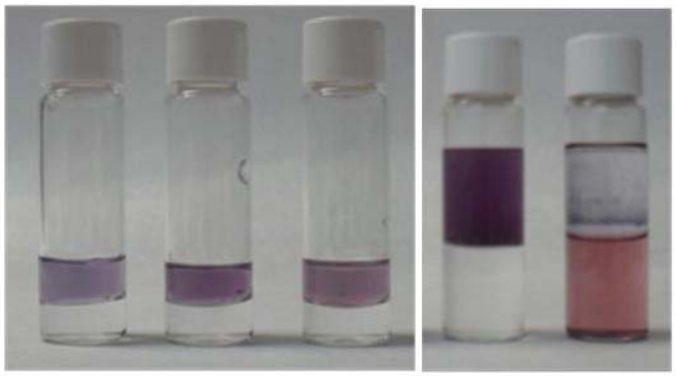

Figure S2: From left to right: GNP from experiments 2 to 4 (in Table 1) in aqueous phase (organic dichloromethane phase below without any GNP), GNP from experiment 4 (after centrifugation to concentrate them) and from experiment 1 (transferred to organic dichloromethane phase).

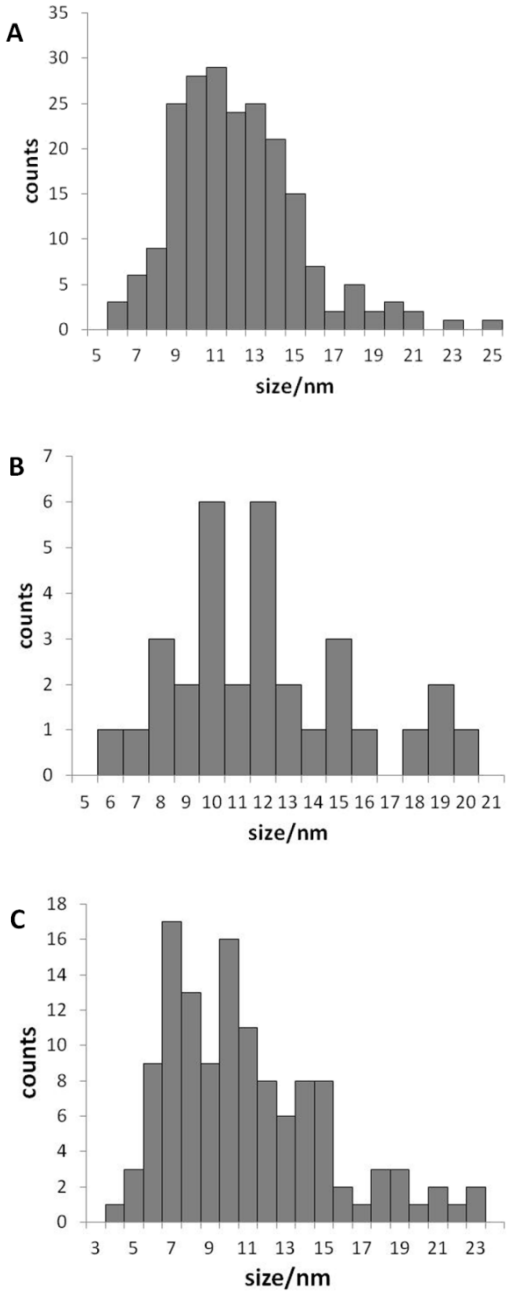

Figure S3: Histograms corresponding to the size distributions (measured in the TEM micrographs) for the GNP from experiment 2 (A), experiment 3 (B) and experiment 4 (C).

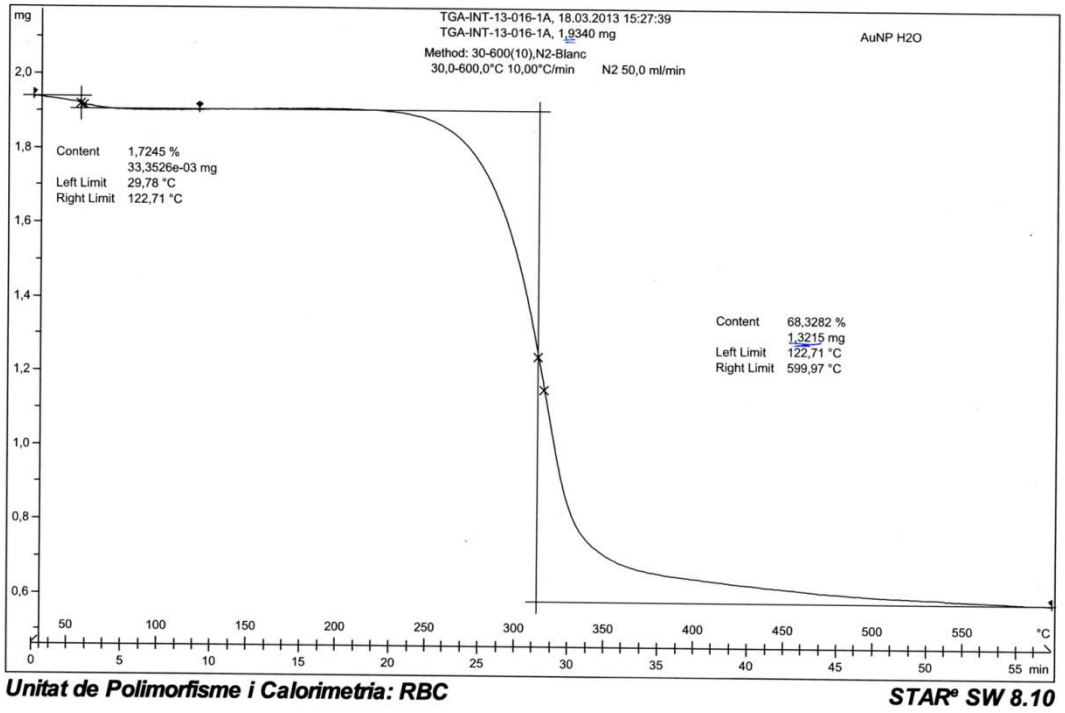

Figure S4: Termogravimetry curve obtained for the **1·GNP**

Table S1:

Thermogravimetry results and calculations of amount of ligand per NP and per area of NP surface based on the ratio of ligand to gold present in the GNP and their gold core size obtained by TEM.

Sample	Total mass (mg)	Ligand mass (mg)	Ligand:Au (mmol)	Average diameter (nm)	Moles Au/NP	Ligand/NP	**Ligand/nm^2**
1·GNP	1.8605	1.2861	0.62969	11.6	8.0×10^{-20}	30255	**71.57**
GNP[1]	5.8230	3.1521	0.32610	8.8	3.5×10^{-20}	6840	**28.12**

[1] L. Casal-Dujat, M. Rodrigues, A. Yagüe, A. C. Calpena, D. B. Amabilino, J. González-Linares, M. Borràs and L. Pérez-García, *Langmuir*, 2012, **28**, 2368-2381

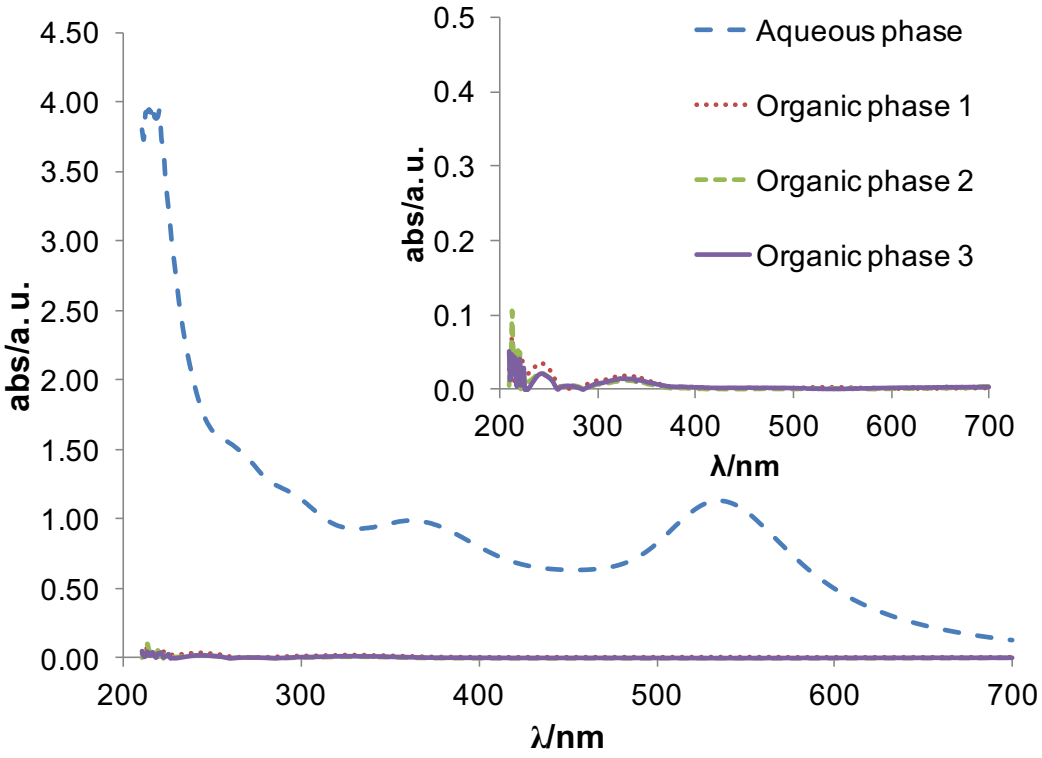

Figure S5: UV/Vis spectrum of the **1·GNP** after extraction of piroxicam, presenting the peak corresponding to piroxicam at 360 nm and the SPR of the GNP, and the organic phases (amplified scale included)**.**

Table S2:

Kinetic models used to fit the data for the release of Piroxicam from 1·GNP, and the respective AIC parameter

Kinetic model	Equation	AIC	
		pH 5.5	pH 7.4
Zero order	$Qt/Q\infty = K0*t$	-77.2	-95.1
First order	$Qt/Q\infty = 1-e^{-K1*t}$	-77.1	-107.7
One phase exponential	$Qt/Q\infty = 1+(S/P)*e^{-Kt}$	-96.1	-128.2
Higuchi	$Qt/Q\infty = KH * t^{1/2}$	-72.1	-101.4
Weibull	$Qt/Q\infty = 1-e^{-(t/td)\beta}$	-89.0	-118.0
Korsmeyer-Peppas	$Qt/Q\infty = K*t^{n}$	-80.7	-102.0

Qt is the amount of drug released at time t
Q∞ is the total amount of drug released
Qt/Q∞ is the fraction of drug released at time t
K is the release rate constant
P is the Plateau (Q at t∞) and S is the Span (the difference between Q_0 and P)
n is the diffusion release exponent that could be used to characterize the different release mechanism ($n \leq 0.43$ (Fickian diffusion), $0.43 < n < 0.85$ (anomalous transport), and ≥ 0.85 (case II transport; i.e. zero order release)
td is the time in which the 63.2% of the drug is released and β is the shape parameter

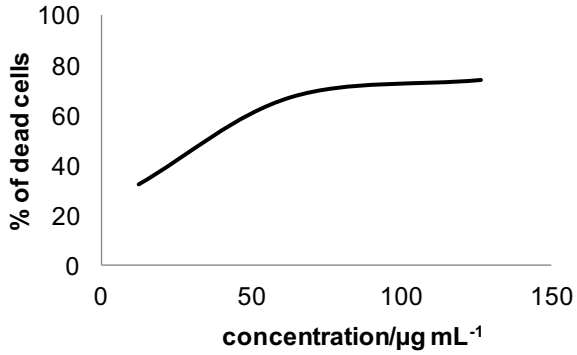

Figure S6: Effect of the **1·GNP** on the viability of Caco-2 cells, by the MTT method.

Table S3:

COX activity in cells exposed to 1·GNP, 1·GNP with piroxicam (1·GNP-pxc) and 1·GNP with piroxicam and LPS (1·GNP-pxc + LPS). LPS is used to induce inflammation.

	$t_{exposure}$/days	Optical density		Activity/U[a] mL^{-1}		% activity	
		COX-total	COX-II	COX-total	COX-II	COX-I	COX-II
1·GNP	1	0.156	0.158	9.915	10.042	-1.3	101.3
	10	0.39	0.356	24.788	22.627		91.3
1·GNP-pxc	1	0.141	0.145	8.962	9.216	-2.8	102.8
	10	0.312	0.286	19.831	18.178	8.3	91.7
1·GNP-pxc + LPS	1	0.155	0.159	9.852	10.106	-2.6	102.6
	3	0.193	0.18	12.267	11.441	6.7	93.3
	5	0.271	0.271	17.225	17.225	0.0	100.0
	8	0.351	0.31	22.309	19.703	11.7	88.3
	10	0.361	0.345	22.945	21.928	4.4	95.6

[a]Units

3.5. Macrocyclic imidazolium-based amphiphiles for the synthesis of gold nanoparticles and delivery of anionic drugs

Accepted in Journal of Colloid and Interface Science (DOI: 10.1016/j.jcis.2014.09.026).

Ezhil Amirthalingam,[1,2] Mafalda Rodrigues,[1,2] Lucía Casal-Dujat,[1,2] Ana C. Calpena,[2,3] David B. Amabilino,[4] David Ramos-López,[5] and Lluïsa Pérez-García[1,2,*]

1 Departament de Farmacologia i Química Terapèutica, Universitat de Barcelona, Avda. Joan XXIII s/n, 08028 Barcelona, Spain

2 Institut de Nanociència i Nanotecnología UB (IN2UB), Universitat de Barcelona, 08028 Barcelona, Spain

3 Departament de Farmàcia i Tecnologia Farmacèutica, Universitat de Barcelona, Avda. Joan XXIII s/n, 08028 Barcelona, Spain

4 Institut de Ciència de Materials de Barcelona (ICMAB-CSIC), Campus Universitari, 08193 Bellaterra, Spain.

5 Unitat de Toxicologia Experimental i Ecotoxicologia (UTOX-PCB), Parc Científic de Barcelona, Baldiri i Reixac 10-12, 08028 Barcelona, Spain.

Summary

Within the family of the synthesized bis-imidazolium amphiphiles, it was found that the analogues with a cyclic structure have higher affinity for anions. This suggested that GNP synthesized with these ligands could have improved ability to incorporate anionic drugs, translating into a higher loading capacity. Therefore, the synthesis using the biphasic system based in the Brust-Schiffrin method was attempted. We proved that the macrocyclic amphiphile could be successfully used to obtain GNP. Ligands with different alkyl chain lengths were tested, and it was observed that the length has influence in their ability to form the

nanoparticles: short alkyl chain (methyl) does not render the necessary characteristics to obtain GNP, whereas longer (decyl and octadecyl) ones did.

The correct synthesis of the GNP was confirmed by the presence of the SPR peak around 520 nm by UV-visible absorption spectroscopy. They were further characterized by TEM and DLS to assess their size, by SEM to study the morphology of the core and the amphiphilic layer, and TGA, to determine the amount of ligand present per nanoparticles. By TEM it was determined that he gold core had approximately 8 nm for the GNP with ligand with decyl chains, and 5 nm in the case of GNP with octadecyl one, and DLS showed a hydrodynamic size of 34.8 nm and 73.5 nm respectively. SEM images confirmed that the gold core was spherical, as well as the outer ligand layer, that was composed of around 240 ligands per particle.

Besides their physical characterization, their toxicity was also assessed. As before, the incorporation and release of an anionic drug was also assessed, but it was found that the release was much slower, which can be explained by the bigger affinity of the ligand, that can therefore difficult the release of the drug.

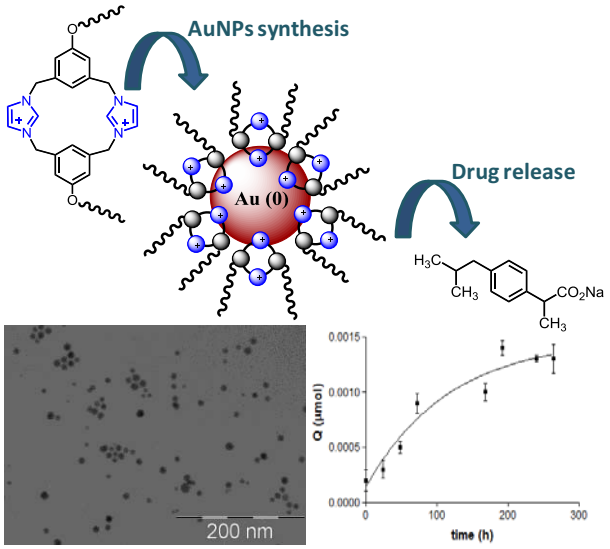

Figure 3.17: Schematic representation of the work: beginning with the synthesis of the compound, then the synthesis of the GNP and finally the incorporation of sodium ibuprofenate (top), TEM micrograph of the GNP (bottom left) and release profile of ibuprofenate from the GNP (bottom right).

Macrocyclic imidazolium-based amphiphiles for the synthesis of gold nanoparticles and delivery of anionic drugs

Ezhil Amirthalingam,[1,2] Mafalda Rodrigues,[1,2] Lucía Casal-Dujat,[1,2] Ana C. Calpena,[2,3] David B. Amabilino,[4] David Ramos-López,[5] and Lluïsa Pérez-García[1,2,*]

[1]Departament de Farmacologia i Química Terapèutica, Universitat de Barcelona, Avda. Joan XXIII s/n, 08028 Barcelona, Spain

[2]Institut de Nanociència i Nanotecnología UB (IN2UB), Universitat de Barcelona, 08028 Barcelona, Spain

[3]Departament de Farmàcia i Tecnologia Farmacèutica, Universitat de Barcelona, Avda. Joan XXIII s/n, 08028 Barcelona, Spain

[4]Institut de Ciència de Materials de Barcelona (ICMAB-CSIC), Campus Universitari, 08193 Bellaterra, Spain.

[5]Unitat de Toxicologia Experimental i Ecotoxicologia (UTOX-PCB), Parc Científic de Barcelona, Baldiri i Reixac 10-12, 08028 Barcelona, Spain.

*Corresponding author

Lluïsa Pérez-García - mlperez@ub.edu

Telephone: (+34) 934035849. Fax: (+34) 934024539

Abstract

In the present work, we have explored the use of amphiphilic bis-imidazolium based macrocycles and an open chain analogue for the successful synthesis of gold nanoparticles (AuNPs). The macrocyclic ligands incorporate hydrophobic chains of different lengths, and the newly synthesized ligands were further used for the synthesis of AuNPs in a biphasic system. The successfully synthesized AuNPs were thoroughly characterized. The sizes of the AuNPs were ca. 8 nm, using macrocyclic ligands bearing two 10 carbon atoms alkyl chains, ca. 5 nm in the case of macrocyclic ligands with two 18 carbon atoms alkyl chains, and ca. 7 nm for the open chain ligand with two 18 carbon atoms alkyl chains. Their possible application as vehicles to load and release anionic drugs (such as sodium ibuprofenate) was also assessed and compared with previously described open chain analogues. In this case, it was observed that the AuNPs had high efficiency in extracting sodium ibuprofenate from an aqueous solution. The application as a drug delivery vehicle was confirmed by *in vitro* release experiments at different pH values.

Keywords: Amphiphiles; imidazolium macrocycles; gold nanoparticles; drug delivery anionic drugs.

Introduction

Drug delivery systems (DDS) provide positive attributes to a 'free' drug by improving its pharmacokinetic properties, controlling its sustained release and, very importantly, lowering its systemic toxicity. The ideal nanoscale DDS ensures that the conjugated or bound drug–carrier complex arrives and acts specifically at the selected target [1, 2]. The field of particle-based drug delivery is currently focused on two chemically distinct colloidal particles: liposomes and drug conjugated nanoparticles. Although liposomes have been studied for longer, AuNPs have been widely explored in recent years, especially in the context of emerging biomedical nanotechnology [3]. AuNPs, due to their unique physical and chemical properties, could be used in almost all medical applications [4, 5] such as biosensors [6], target-specific drug delivery [7, 8], immunoanalysis [9], clinical chemistry [10, 11], photothermolysis of micro-organisms and cancer cells [12, 13] and optical bioimaging [14]. AuNPs are also highly stable metal nanoparticles [15]. Together with their unique subcellular size, that allows them to enter human cells by endocytosis, and good biocompatibility, their low toxicity [16] and reduction of the level of reactive oxygen species [17], makes them promising drug delivery vehicles [18-21].

Numerous methods can be found in the literature for the synthesis of AuNPs [22], among which the Brust-Schiffrin biphasic methodology [23] is commonly used. The gold precursor is transferred from an aqueous phase to an organic phase – using a surfactant such as tetraoctylammonium bromide – where the gold is reduced and the newly formed AuNPs are frequently stabilized by a thiolate. Examples are also found in literature of imidazolium-based ionic liquids being able to stabilize AuNPs through coordination with the imidazolium cation [24].

Among all the potential surfactants one could consider for AuNPs synthesis, the gemini-type amphiphiles possess at least two hydrophobic chains and two ionic or polar groups, linked through spacers of varied flexibility [25]. The gemini structure presents some advantages when comparing to a simpler amphiphile structure, such as lower Critical Micelle Concentration (CMC) [26, 27], higher capacity for reducing oil/water surface tension, and better wetting, solubilizing and foaming properties, which makes them attractive for drug entrapment and release applications.

Our group has developed a family of gemini-type imidazolium-based amphiphiles formed by two imidazolium rings linked by a 1,3-dimethylenebenzene spacer, and having an open chain structure [28] or cyclic structure [29]. This family of imidazolium-derived ligands are known to have the ability to recognize anions and also to behave as ionic liquid crystals [29]. The propensity of the imidazolium moiety to anion coordination has been studied by the ability of forming weak hydrogen bonds with their corresponding counterions [29-31]. This is important since anions are ubiquitous throughout biological systems, for example nucleic acids and also, the majority of enzyme substrates and co-factors are anionic [32]. Furthermore, from the synthesized compounds, the open chain structure **1·2Br** was found to interact with valproate [30] and **2·2Br** with valproate and ibuprofenate [28], two model drugs used to assess their possible use in DDS.

We have previously developed AuNPs synthesis based on a modified Brust-Schiffrin method using the open chain bis-imidazolium amphiphile **2·2Br** (Figure 1) where the imidazolium rings bear alkyl chains of 18 carbon atoms. In the reported synthesis of the AuNPs, the bis-imidazolium **2·2Br** amphiphile played two roles: transfer agent and stabilizer of the AuNPs, which resulted in the advantageous simplification of the synthetic process and subsequent purification [28]. Furthermore, our group successfully developed water soluble gold nanoparticles using the same ligand, that formed a double layer around the gold core [33]. Finally, in order to study their potential application as DDS, different anionic drugs such as sodium ibuprofenate [28] and piroxicam [33] were incorporated in the bis-imidazolium amphiphile particles. Successful incorporation and release of the anionic drugs from different

nanostructured particles with this imidazolium ligand confirms their possible use as DDS for anionic compounds.

Now we are going to explore how structural variations could affect their behavior as ionophores and in the synthesis of AuNPs. For this purpose, macrocyclic analogues **3·2Br** - **5·2Br** (Figure 1), with benzene rings bearing alkyl chains of either 1, 10 or 18 carbon atoms respectively, were used to study the influence of the polar head and the length of the alkyl substituent. **4·2Br** and **5·2Br** are known to behave as macrocyclic ionic liquid crystals [29]. The open chain analogue **6·2Br**, isomer of **2·2Br** but with a 1,4-dimethylenebenzene spacer, was also studied to assess how this change in the molecular constitution would influence the behavior of the ligand. Macrocycles have more rigid conformations than open chain compounds and in principle could be useful for DDS because it is more likely to show slow and sustained drug release due to its stronger affinity with the drug. The aim of this work was to prepare AuNPs coated with bis-imidazolium amphiphilic macrocycles, in order to explore the ability of the colloids towards anion recognition, and their potential use in nanomedicine. Thus, we describe the synthesis and characterization of **3·2Br** and **6·2Br**, anion binding studies of the bis-imidazolium compounds **1·2Br** - **5·2Br**, and the synthesis and characterization of AuNPs using imidazolium macrocyclic compounds **3·2Br** - **5·2Br** and open chain compound **6·2Br**.The successfully synthesized AuNPs were characterized using UV-Visible Absorption Spectroscopy, X-ray Photoelectron Spectroscopy (XPS), Matrix Assisted Laser Desorption Ionization – Time-of-Flight Mass Spectrometry (MALDI-TOF-MS), Thermogravimetric Analysis (TGA), Dynamic Light Scattering (DLS), Transmission Electron Microscopy (TEM) and Scanning Electron Microscopy (SEM). We also report on the molecular recognition ability towards sodium ibuprofenate, a model anionic drug, which could be successfully incorporated in the synthesized AuNPs, and the *in vitro* release studies of the incorporated drug.

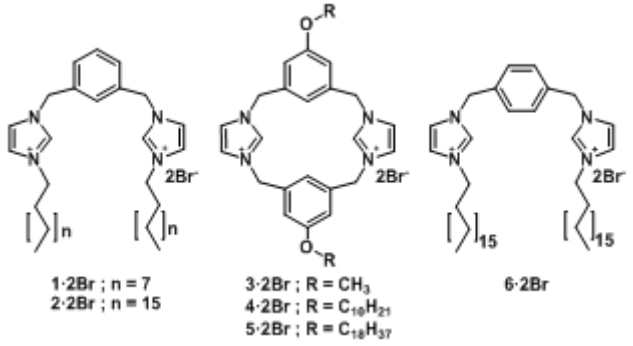

Figure 1: Structure of bis-imidazolium derivatives 1·2Br – 6·2Br.

Experimental Section

Commercial compounds: 1,4-bis(bromomethyl)benzene, hydrogen tetrachloroaurate(III), sodium borohydride, ibuprofen sodium salt, tetrabutylammonium chloride, tetrabutylammonium acetate and tetrabutylammonium dihydrogen phosphate were purchased from Sigma-Aldrich. Compounds 1,3-bis(bromomethyl)-5-methoxybenzene [28], 1-octadecyl-1*H*-imidazole [28], 1,3-bis(imidazolylmethyl)-5-methoxybenzene [28], **4·2Br** and **5·2Br** [29] were synthesized according to literature methods. General methods, synthesis of **3·2Br** and **6·2Br**, and anion exchange protocol are included in the Supporting Information.

Anion binding properties

Titration experiments were carried out as follows. First, the ^{1}H NMR spectra were acquired for the bis-imidazolium salts **1·2Br**, **3·2PF$_6$**, **4·2Br** (0.5 mM in 0.7 mL of $(CD_3)_2SO$) and **2·2PF$_6$**, **5·2PF$_6$** (0.5 mM in 0.7 mL of $CDCl_3$). Consecutive additions of 10 µL of tetrabutylammonium salts (TBA·X, X= Cl^-, $H_2PO_4^-$, AcO^-) corresponding to 1 equivalent were done to the initial solutions, with bis-imidazolium:TBA·X ratios of 1:0, 1:1, 1:2, 1:3, 1:7, 1:10, 1:13, 1:15, 1:20. The spectra were interpreted and the increment in chemical shifts was plotted as a function of salt concentration. The degree of anion binding was determined by nonlinear curve-regression fitting using Origin 7.0 software. The fitting procedure allowed the calculation of the stability constant (K_a) from the best approximation curve for experimental points, which corresponded to a one-site binding model. Additionally, the complexation free energy ($\Delta G°$) was deduced using the equation: $\Delta G° = - RT\ln K_a$.

Toxicity Study

The cytotoxicity assay was evaluated using the protocol Invittox 17 "MTT (Methylthiazolyldiphenyl-tetrazolium bromide) assay" following PNT TOX-EXP-045 and the study of DNA damage follows the standard ASTM-E2186 and PNT TOX-EXP-007. The products were treated by dissolving in DMSO at various concentrations, but were insoluble and therefore dissolved directly in the culture medium. For that, the highest concentration was prepared and the solution was sonicated to 80 Hz with 10 pulses for 0.5 seconds. The concentrations were prepared by serial dilution. A detailed protocol for cytotoxicity and genotoxicity assays is included in the Supporting Information.

Synthesis of AuNPs

For the preparation of the AuNPs, a solution of $HAuCl_4.H_2O$ (0.12 g, 0.32 mmol) in water 10 mL was added to an extraction funnel containing 10 mL of a chloroform solution with 0.24 mmol of the imidazolium derivatives **3·2Br - 6·2Br**. The shaken organic phase was separated and collected in a round bottom flask to which a freshly prepared solution of $NaBH_4$ (1.28 g, 6.40 mmol) in water (5 mL) was added drop wise under constant stirring. The stirring continued for 4 hours in the dark at room temperature. Later, the organic phase was separated using an extraction funnel and the solvent were evaporated in a rotary evaporator. The residue was washed with ethanol (2 x 1 mL), and with acetone (2 x 1 mL) and centrifuged at 13400 rpm for 10 minutes after each washing.

Drug incorporation with 5·AuNP and in vitro release study

The drug incorporation and release was done as described previously [28]. Briefly, to 5 mL of **5·AuNP** solution in chloroform, 5 mL of an aqueous solution of 10 mM sodium ibuprofenate were added and mixed in an extraction funnel. The organic phase was collected and was extracted with water (2 x 5 mL) to remove the excess ibuprofenate. The presence of ibuprofenate was determined in aqueous and organic phases through UV/Visible absorption spectroscopy. The release of the drug incorporated in the AuNPs was performed in a Microette transdermal diffusion system with vertically assembled Franz-type diffusion cells. The dialysis membrane (Cellu·Sep T3 dialysis membrane, MWCO12000-14000Da, MFPI, USA) was treated overnight in a solution of water:methanol 2:1 to hydrate the membrane and remove grease prior to the start of the experiment. The membranes were then placed in the Franz-type diffusion cells and 260 µL of the nanoparticle solution loaded with the drug was placed on top of the membranes. The solutions were air dried and resuspended with 250 µL of Sorensen buffer 1/15 M pH 5.5 that was used as the donor solution. NaOH 71 mM solution was taken as a receptor solution. The Franz-type cells were connected to a controlled heating water bath set to 32°C. The cells were sealed and samples were taken along 2 weeks at 24 hours intervals. The same protocol was followed to study the release at the physiological pH 7.4 at 37°C.

Drug determination in samples

Drug determination in samples was done by HPLC in a Waters LC Module I. The column used was ODS-2 5 µm (4.6 mm x 150 mm) from Waters Spherisorb®. The mobile phase was acetonitrile-water pH 3, adjusted with orthophosphoric acid (65:35 v/v). The flow rate was 1.5

mL min^{-1} and the detection wavelength was 220 nm. The data was collected using the software Millennium 32 version 4.0.0 from Waters Corporation.

Results and Discussion

Synthesis and characterization of bis-imidazolium salts

The macrocyclic bis-imidazolium compound **3·2Br** consists of two imidazolium rings linked by two 1,3-dimethylenebenzene spacers, whose phenyl rings bear a methoxy group. **3·2Br** was obtained with good yield by means of a convergent synthesis by coupling 1,3-bis(imidazolylmethyl)-5-methoxybenzene [28] with 1,3-bis(bromomethyl)-5-methoxybenzene [28] in acetonitrile under reflux (**Scheme 1**) under anion-templated conditions, meaning the synthesis is controlled by the bromide generated in the reaction, which involves interaction established between the bromide and the acidic hydrogen atoms in the aromatic rings by non-covalent bonds, both hydrogen and ionic bonds, which explains the high yield obtained (90 %) for the macrocyclization step.

Scheme 1. Synthesis of 3·2Br

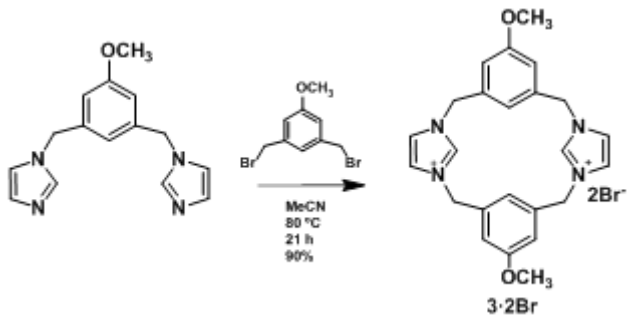

The open chain bis-imidazolium amphiphile **6·2Br** consists of two imidazolium rings linked by one 1,4-dimethylenebenzene spacer, and N-alkyl chains of 18 carbon atoms bearing on the imidazolium rings. Compound **6·2Br** was obtained by halogen substitution of 1,4-bis(bromomethyl)benzene in acetonitrile under reflux with 1-octadecyl-1*H*-imidazole [28] (**Scheme S1**, Supporting Information). **6·2Br** was obtained with 60 % yield and needed no further purification.

The newly synthesized bis-imidazolium compounds had a high degree of purity as seen by TLC, and were characterized by ^{1}H and ^{13}C NMR spectroscopy in $(CD_3)_2SO$ or $CDCl_3$ to study their structural properties in solution (Figure S1-S4, Supporting Information), and ESI-MS to examine the charged compounds. Several peaks are observed by ESI-MS (Table S1, Supporting Information); in the case of **3·2Br** the most important peak corresponds to a dication resulting

from the loss of two counter-ions $[(M-2Br)/2]^{2+}$, and other characteristic peaks found, with lower intensity, are singly charged ions that correspond to the loss of one or two counter-ions ($[M-H-Br]^+$ and $[M-H-2Br]^+$ respectively) and of one proton, which indicates the formation of *N*-heterocyclic carbenes under these experimental conditions. Instead, **6·2Br** showed only one peak that corresponded to $[(M-2Br)/2]^{2+}$, and no additional peaks could be seen, showing therefore no evidence of the formation of carbenes, as similarly reported for the **2·2Br** analogue [28].

Anion binding properties of bis-imidazolium salts

We have previously reported the anion binding properties of bis-imidazolium based open chain compounds, revealing the importance of weak hydrogen bonds (C-H···X^-) controlling the anion binding specially for organic carboxylates [28]. Here, we study the binding affinity in solution of the bis-imidazolium salts for three different anions (chloride, dihydrogen phosphate and acetate) to have general data on the affinity for different anions found in biological systems. To do so, titration experiments were performed and the solutions were analyzed using ^{1}H NMR spectroscopy. It is possible to determine the anion complexation with the bis-imidazolium salts through this technique by observing changes in the chemical shifts ($\Delta\delta$) of the acidic protons that are more involved in the anion binding. Different bis-imidazolium salts were chosen for the study, in order to determine how the structural differences in the alkyl chain length and head spacer can affect the compound's affinity. The open chain amphiphiles **1·2Br** and **2·2Br**, and the macrocycles **3·2Br**, **4·2Br** and **5·2Br** were chosen. To study the anionic interaction, in some cases (**2·2Br**, **3·2Br** and **5·2Br**), the first step was to replace the bromide counter ions in the molecules with hexafluorophosphate, as this anion associates weakly with the imidazolium units and therefore does not have a competitive binding scenario. TBA salts TBA·X (X= Cl^-, $H_2PO_4^-$, AcO^-) were used as the source of the target anion. ^{1}H NMR analysis of the bis-imidazolium salt solutions (0.5 mM) were performed in $CDCl_3$ or $(CD_3)_2SO$, containing increasing concentrations of TBA salts and observing the chemical shifts of the acidic protons (C(2)-H and C(2)'-H) in the ^{1}H NMR spectrum of the solution (selected examples are included in Figure S5-S11, Supporting Information). The chemical shifts were then plotted as a function of the anion concentration (Figure S12-S16, Supporting Information) and the stability constant (K_a) were calculated. The values are shown in Table 1. The complexation free energy ($-\Delta G^o$) was calculated and the values can be seen in Table S2 in Supporting Information. The first remark is that for the anions Cl^- and AcO^-, upon addition of the inorganic salts a moderate to strong NMR shift of the protons corresponding to the imidazolium moieties C(2)-H and xylyl units C(2)'-H was observed. As shown in Table 1, for the two ligands with 18 carbon alkyl chain it was found that **2·2PF$_6$** has more affinity than **5·2PF$_6$** for acetate, but **5·2PF$_6$** has more affinity for chloride

than **2·2PF$_6$**. Regarding the two ligands with 10 carbon alkyl chain, for both acetate and chloride the macrocycle **4·2Br** shows more affinity than **1·2Br**, and both show more affinity for acetate than for chloride. When comparing the macrocycle compounds, we can see that there is a trend for the affinity to increase with increase in the alkyl chain. Although the constant for **4·2Br** is lower than the one for **3·2PF$_6$**, one must take into account that the counterion is different. Also importantly, the solvent used for **5·2PF$_6$** was $CDCl_3$ and because **4·2Br** and **3·2PF$_6$** were not soluble, $(CD_3)_2SO$ was used. Comparing the two open chain compounds, we can see the same trend in the affinity with increasing alkyl chain: the affinity of **2·2PF$_6$** for both chloride and acetate is higher than the found for **1·2Br**. Again the compound **1·2Br** has different counterion, and the solvent was $(CD_3)_2SO$, however the difference in the affinity constants is one order of magnitude higher. Finally, except **5·2PF$_6$**, which showed more affinity for chloride than for acetate, the remaining ligands showed more affinity for acetate than for chloride.

On the other hand, in the case for dihydrogen phosphate, the ^{1}H NMR spectra had no signal from the bis-imidazolium compound upon increasing additions of TBA·H_2PO_4 salt. The solution had a cloudy appearance as the concentration of the salt increased. One of the solutions, **5·2PF$_6$,** was further studied using DLS and particles with 2000 nm were detected in the sample, which might indicate the formation of solid particles thus explaining the absence of signal in the spectra.

Synthesis and characterization of AuNPs using imidazolium derivatives

AuNPs can be readily obtained in a biphasic system using the appropriate transfer agent and stabilizer [23]. In our case, the bis-imidazolium amphiphiles play these two roles.

We tested the macrocyclic gemini surfactants with different chain length: **3·2Br** (1 carbon atom), **4·2Br** (10 carbon atoms) and **5·2Br** (18 carbon atoms) (Figure 1). In addition, to test the influence of the spacing between the imidazolium rings we also tried synthesizing AuNPs using **6·2Br**, where the bis-imidazolium rings are linked by a 1,4-dimethylenebenzene spacer instead of a 1,3-dimethylenebenzene spacer.

The solution obtained using **3·2Br** did not present the typical red-colored solution of colloidal AuNPs; instead, a precipitate was formed. Presumably the lack of alkyl chains means that the colloids agglomerate to form higher aggregates. A possible explanation is that **3·2Br** has high CMC value [30], because of the shorter alkyl chain, and therefore lacks the needed amphiphilic character that allows it to stabilize the gold nanoparticles. On the other hand, synthesis of AuNPs using longer chain macrocycles **4·2Br** and **5·2Br** resulted in red-colored solutions, and

those nanoparticles were named as **4·AuNP** and **5·AuNP** respectively. Additionally, preparation of AuNPs using **6·2Br** was also successful and they were named as **6·AuNP**.

UV-Visible absorption spectra were recorded for all the above solutions. The solution obtained for the synthesis using **3·2Br** did not show any characteristic band of AuNPs, originated from Surface Plasmon Resonance (SPR) on the UV-Visible spectrum, confirming that no AuNPs were obtained. Consequently, the use of **3·2Br** for the synthesis of AuNPs was not further studied. Instead, **4·AuNP** solution in dichloromethane showed the characteristic SPR peak for AuNPs at 527 nm, the **5·AuNP** solution in chloroform showed the peak at 524 nm and the **6·AuNP** solution in chloroform at 525 nm (Figure 2).

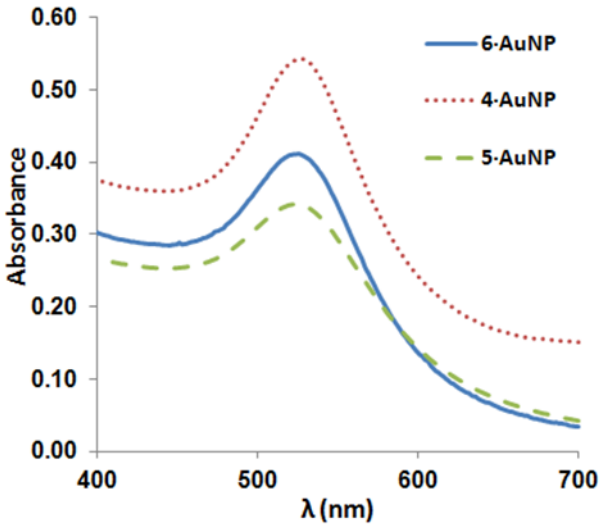

Figure 2: UV-Vis absorption spectra of 4·AuNP in dichloromethane, and 5·AuNP and 6·AuNP in chloroform solution.

MALDI-TOF-MS was used to study **5·AuNP**. The data was obtained using 2,5-dihydroxybenzoic acid (DHB) as matrix. The sharpest peaks were at m/z = 1073.7, corresponding to loss of two bromide $[M+Au-2Br]^+$. A peak with very low intensity was found corresponding to loss of one bromide ($[M+Au-Br]^+$) at m/z = 1153.6, whereas in the case of **2·AuNP** [28] the peaks for loss of each bromide were not present. Additionally, peaks corresponding to the macrocycle with gain of one hydrogen and loss of two bromides ($[M+H-2Br]^+$) at m/z = 877.7 was also observed with very low intensity (Table S3, Supporting Information). The same peak did not appear in the **2·AuNP** mass spectrum [28]. We found therefore that the particles **5·AuNP** show peaks corresponding to carbene species.

The oxidation state of gold in the synthesized nanoparticles was determined by XPS. Sputtering of the sample was necessary to identify clearly the peaks corresponding to gold (Au^0) in the **5·AuNP**. The obtained XPS spectrum (Figure S17, Supporting Information) shows the binding

energy of the typical peaks of $4f_{5/2}$ and $4f_{7/2}$ at 88.2 eV and 84.5 eV respectively for gold in the reduced state thereby confirming there are no residues of Au (III) precursor.

The AuNPs solutions were further characterized using TEM, DLS, and SEM. Figure 3 shows TEM micrographs obtained for **4·AuNP**, **5·AuNP** and **6·AuNP** colloidal solutions. All the AuNPs are spherical, and present low dispersity. **4·AuNP** shows an average size of 8.2 ± 3.7 nm, **5·AuNP** present an average size of 5.3 ± 3.0 nm and **6·AuNP** an average size of 6.5 ± 2.3 nm.

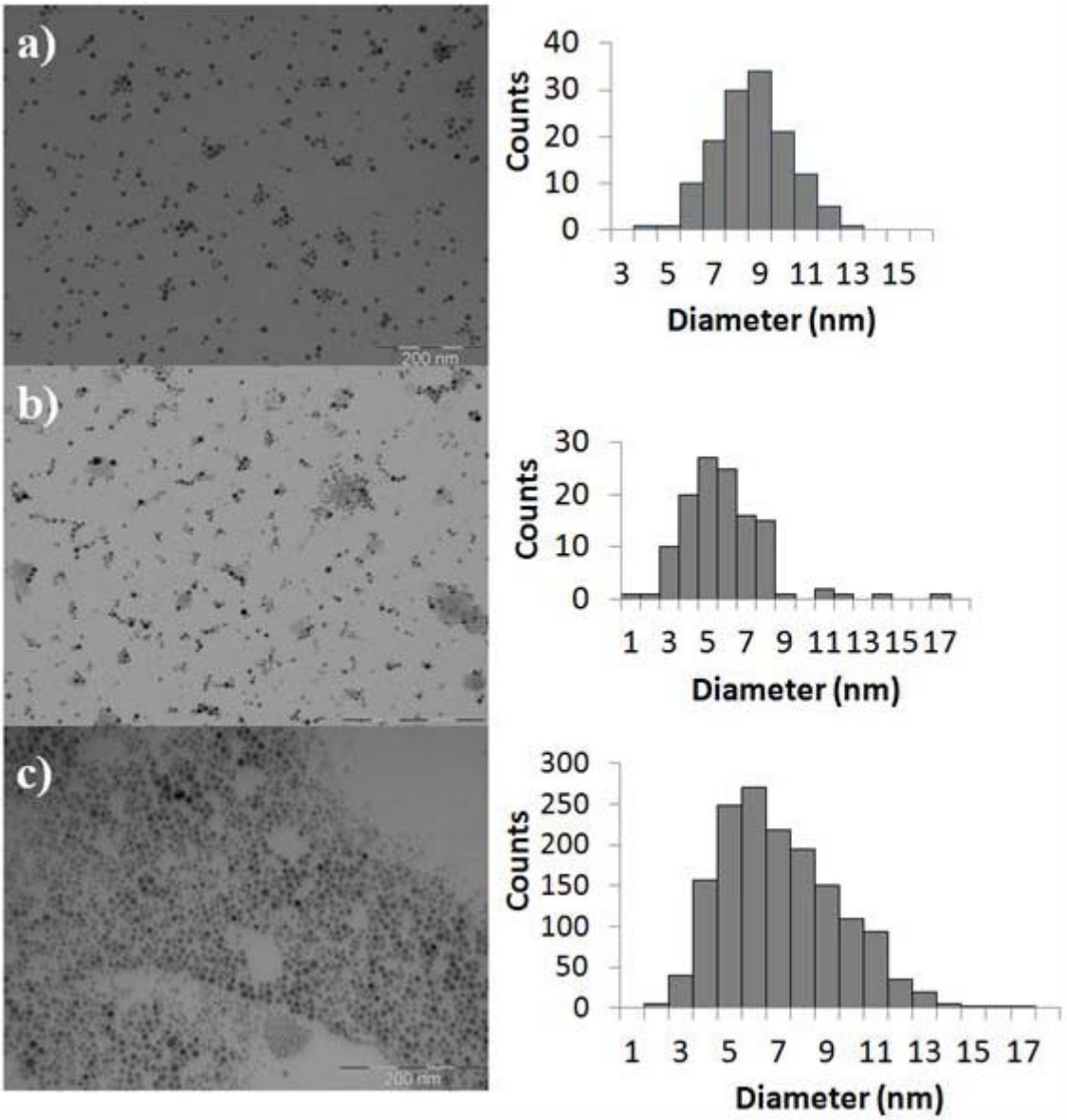

Figure 3: TEM micrographs for (a) **4·AuNP** and (b) **5·AuNP** and (c) **6·AuNP** and their corresponding size distribution histograms.

The size of **4·AuNP**, **5·AuNP** and **6·AuNP** was also assessed by DLS at 25°C. The hydrodynamic diameter and Polydispersity Index (PDI) of the AuNPs, and also the SPR absorption band determined by UV spectroscopy and gold core sizes determined by TEM are

summarized (Table S4, Supporting Information). Regarding the sizes obtained by DLS, the average size in the case of **4·AuNP** was 35 nm, for **5·AuNP** was 74 nm and for **6·AuNP** was 37 nm. The sizes measured by DLS are higher than those observed by TEM because this technique gives the hydrodynamic size of the particles that includes not only the core but also the alkyl chains of the coating ligands; instead TEM only indicates the gold core size, because no contrast agent was used. Knowing that the ligand **5·2Br** has a longer chain, it is normal that the hydrodynamic diameter is higher in the case of **5·AuNP**. On the other hand, in the case of **2·AuNP** the hydrodynamic diameter was around 20 nm, which is lower than that of the macrocycles. A possible explanation could be the structural orientation of the macrocycles that are more bulky than the open chain.

SEM was used to study the topography and morphology of the AuNPs, through secondary electron image, as well as their composition, using the backscattered image, which allows detecting the presence of metals (in our case, the reduced gold from the core). Figure 4 shows the SEM micrographs of **4·AuNP** and **5·AuNP**. The samples were drop casted on carbon tabs, and selective areas with good contrast were sampled to record both the secondary and the backscattered images. In Figure 4a) spherical particles are visible, whereas in the backscattered image shown in Figure 4b) the gold core is visible, confirming that gold is present in its reduced form, as seen by XPS, and that the gold core has a spherical shape, which is in agreement with the observed by TEM. Since in the secondary electron image the gold is not visible, the spherical particles seen correspond to the macrocycle layer around the gold core, thus confirming the presence of the coating. In the case **4·AuNP**, it is visible that the nanoparticles show a spherical morphology but formed aggregates in these experimental conditions. However, it was also possible to see the presence of the macrocycle layer around the core in Figure 4c), and the core of gold in reduced form with spherical shape in the backscattered image in Figure 4d).

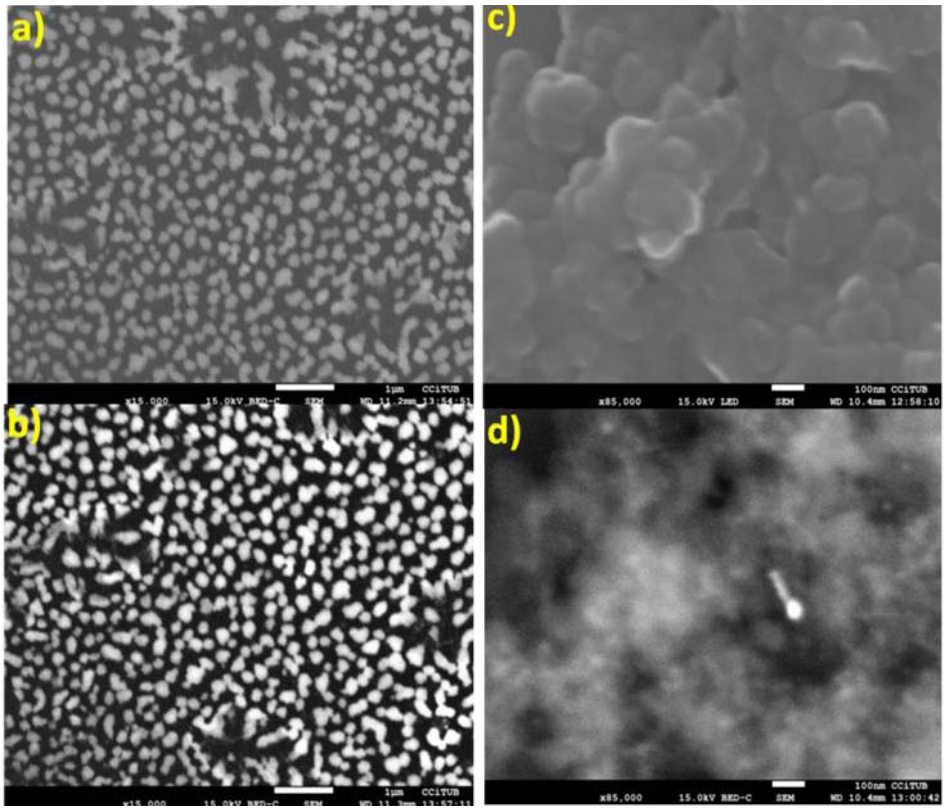

Figure 4: SEM micrographs obtained for 4·AuNP of a) secondary electron image and b) backscattered electron image; and for 5·AuNP of c) secondary electron image and d) backscattered electron image.

5·AuNP and **6·AuNP** were further analyzed using thermogravimetric analysis (Figure S18, Supporting Information), in order to assess the amount of organic material present in the AuNPs sample. Together with the size of the gold core measured by TEM, is possible to calculate the amount of ligands per nanoparticles (Table S5, Supporting Information). In the case of **5·AuNP** the amount of ligands resulted in ca 3 ligand molecules per nm^2 whereas **6·AuNP** resulted a high value of ca 30 ligand molecules per nm^2. In the case of open chain **2·AuNP** synthesized by the same biphasic method, ca 28 ligand molecules per nm^2 were observed [33]. Therefore there is no significant difference in the number of ligand molecules between **6·AuNP** and **2·AuNP**. The higher number of ligands can be due to the non-bulky and open chain structure of these two ligands, since the open chain structure confers molecular flexibility and both must adopt similar conformations on the surface of the AuNPs. Instead, the number of ligand molecules in **5·AuNP** is dramatically reduced to ca 3 ligand molecules per nm^2 as a consequence of the conformational rigidity of the macrocyclic structures, as well as of the larger dimensions of the polar head on the amphiphilic macrocycle.

Cytotoxicity and genotoxicity studies

The toxicity of **5·2Br** and **6·2Br** were studied *in vitro* on mouse fibroblast cell line 3T3/NIH. The cells were exposed to a range of concentrations of ligands **5·2Br** and **6·2Br** for 24 hours. After exposure, the viability of the cell culture was calculated using the MTT Assay, which is based on the conversion of yellow tetrazolium salts to purple formazan crystals in the mitochondria of active, viable cells, and the percentage of viable cells was determined and plotted against the ligand concentrations. The IC_{50} concentration values calculated for both ligands are shown in Table S6 in Supporting Information. As can be seen, the IC_{50} values that were found were 66 μM for **5·2Br** and 45 μM for **6·2Br**, whereas in the case of **2·2Br** the previously determined IC_{50} is 14.6 μM [28], meaning that the tested macrocycle **5·2Br** and its 1,4–open chain analogue **6·2Br** are less toxic when compared to the open chain **2·2Br**.

Additionally, to study the genotoxicity of **5·2Br** and **6·2Br**, the Single Cell Gel Electrophoresis, also known as Comet Assay, was used. This assay consists on determining DNA damage and repair by the analysis of its fragmentation, which translates in the formation of a tail of DNA when performing electrophoresis of the DNA samples. Figure 5 shows the percentage of tail intensity referring to the DNA fragmentation in both bis-imidazolium ligands **5·2Br** and **6·2Br** at the same range of concentrations used for testing their cytotoxicity. It was observed that neither **5·2Br** nor **6·2Br** show any significant formation of a tail of cellular DNA fragments within the studied concentrations, which mean that below the IC_{50} no genotoxicity is observed (Table S7-S8, Supporting Information).

We already know that during the formation of the AuNPs the polar head of the ligand binds to the AuNPs and the alkyl chains are facing outwards, and that even though **2·2Br** had determined toxicity, its corresponding AuNPs showed no toxicity within the range of concentrations that were studied [28], meaning that the **2·AuNP** were safe. From this we can expect that in the case of **5·2Br** and **6·2Br**, which present slightly lower IC_{50} values than **2·2Br**, their AuNPs will exhibit similar safety.

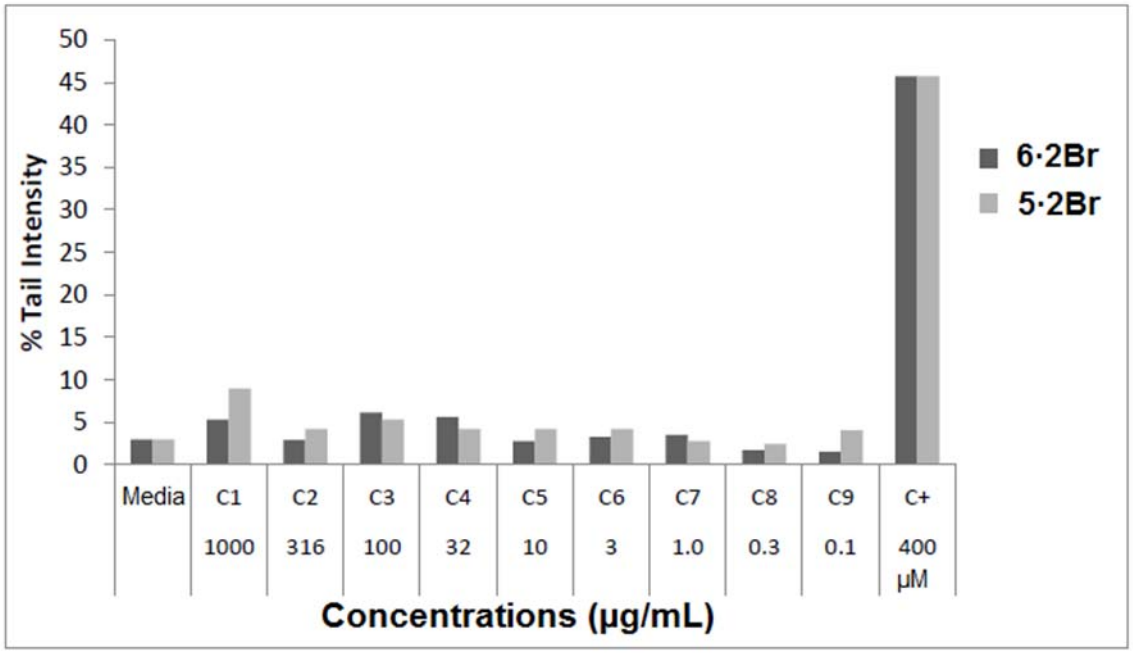

Figure 5: Comparison chart of the effect on DNA of **5·2Br** and **6·2Br**.

Interaction of carboxylate incorporating drugs and AuNPs: loading and release of sodium ibuprofenate

In vitro experiments were performed in order to study the interaction of an anionic drug with the AuNPs and to obtain the release profile of the drug incorporated in the AuNPs. The macrocycles used in the preparation of the AuNPs had already proven to have good recognition ability towards anions (see before, binding studies section). Thus, to evaluate the anionic incorporation ability of the macrocycles, **5·2Br** was chosen in order to compare with **2·2Br,** that has the same alkyl chain present in the gold nanoparticles [28]. Sodium ibuprofenate was used as a model drug because it has a carboxylate group, and also because previous reports showed that this drug could be successfully incorporated in AuNPs with imidazolium ligands [28]. Sodium ibuprofenate dissolved in water could be successfully extracted from the aqueous phase into the organic phase containing the **5·AuNP**. This was confirmed by the UV-Visible absorption spectrum of the organic phase (Figure S20, Supporting Information). The organic phase was then further washed twice with milliQ water in order to remove the free ibuprofenate molecules that were not incorporated in the **5·AuNP**. Following each washing step, both the organic and aqueous phases were analyzed by UV-Visible absorption spectroscopy. In the organic phase there was a slight decrease in the absorption peak of ibuprofenate, whereas in the collected aqueous phases the peaks corresponding to ibuprofenate were visible, meaning recovery of unbound ibuprofenate from the organic phase. The total amount of ibuprofenate that was extracted into the aqueous phases during the washing steps allowed us to determine the

amount of ibuprofenate that remained specifically bound in the **ibuprofenate-5·AuNP** complex. Since we know the initial mass of ibuprofenate, we can therefore say that we loaded 9.8 mg of ibuprofenate in the AuNPs, which was calculated to be ca 85% of the total sodium ibuprofenate.

After it was confirmed that ibuprofenate could be incorporated in **5·AuNP**, the release rate of ibuprofenate from the **ibuprofenate-5·AuNP** complex was assessed using Franz-type diffusion cells with dialysis membranes, as described previously [34]. The samples were tested at pH 7.4 and 5.5, the first one corresponding to physiological pH and the second one to simulate the human skin pH. The samples were resuspended in Sorensen buffer with the appropriate pH and the release took place at 32°C for pH 5.5 and at 37°C for pH 7.4. The receptor solution used was NaOH 71 mM to ensure the ibuprofenate solubility, thus complying with the SINK conditions, so that the rate of release and diffusion across the dialysis membrane was only due to the release from the AuNPs and not because of low solubility of the drug in the receptor solution. Figure 6 shows the plot of cumulative amount of ibuprofenate versus time, and Table 2 the respective dissociation constant K_D and half life time $t_{1/2}$.

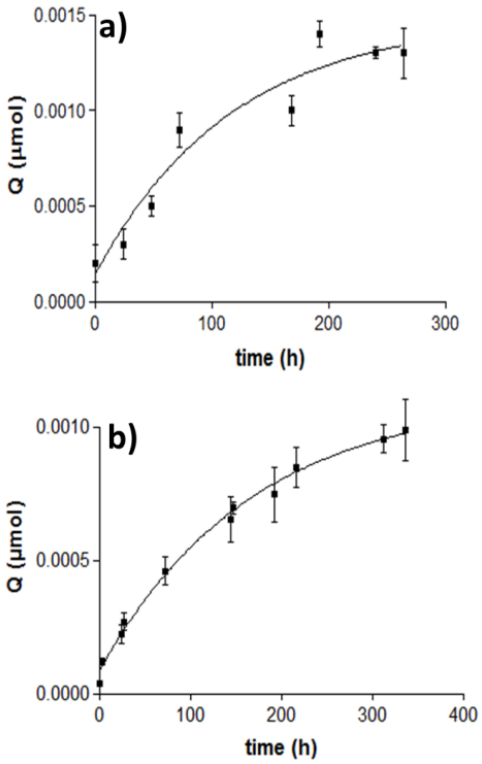

Figure 6: Release profile of ibuprofenate from sodium **ibuprofenate-5·AuNP** at (a) pH 5.5 and at (b) pH 7.4.

The analysis of the data showed that the release at pH 5.5 followed a first order kinetics, with a value of the dissociation constant K_D of 0.0085 h^{-1}. At physiological conditions, the same kinetics was observed, and the dissociation constant found was 0.0060 h^{-1}. Additionally, the amodelistic parameters were calculated and are also shown on Table 2. The calculated half life time and mean release time (MRT) were lower in the case of the release at pH 5.5 (82.8 h and 72.9 h respectively at pH 5.5 versus 116.3 h and 108.5 h at pH 7.4). The release efficiency shows similar results in both cases. Therefore, Student´s t-test analysis was performed and no significant differences were found between the release at pH 5.5 and 7.4 (Table S9, Supporting Information).

The kinetic profiles obtained in both cases are typical of Fickian diffusion. Hence, they can be potentially used in local drug delivery system. When comparing with the previous work with **2·AuNP** [28], in the same conditions, ibuprofenate release kinetics changed in function of the pH, which means that the interaction of the drug with the macrocyclic ligand is different. Thus, it is clear that the limiting factor in this case is the strong interaction of the macrocycle with the drug whereas in the case of the open chain analogue was the pH of the surrounding media. The fact that the pH does not significantly influences the release can be seen as an advantage, because although the skin pH is 5.5, it can present some variations that in the case of the macrocycle will not affect the release rate of the drug from the formulation. This same study was performed with **6·AuNP**. However, the amount of ibuprofenate released was very low, and no signal could be obtained from the collected samples analyzed by HPLC.

Conclusions

With this work we proved that the synthesis of AuNPs can be performed using new imidazolium based amphiphilic macrocycles **4·2Br** and **5·2Br,** and **6·2Br**, an open chain analogue, following a described biphasic system [23, 28]. The macrocycles used play a double role in the synthesis and stabilization of the AuNPs, making the synthesis easier than the habitual two-step process. It is interesting to note that the structural difference on the polar head of the amphiphiles did not have an influence on the synthetic process, when comparing with previous work [28], and this feature opens up the possibility to introduce new recognition sites near the surface of the colloid. However, care in the molecular design is required: an influence of the chain length on the stabilization process was observed, because **3·2Br**, which has shorter chain length than **4·2Br** and **5·2Br**, could not stabilize the AuNPs. This situation might be explained by its low CMC [30], implying that the amphiphilic character of the molecule is an important factor in the synthesis and stabilization of the AuNPs. The release of ibuprofenate from **ibuprofenate-5·AuNP** complex follows Fickian diffusion and is slower when compared

with the open chain analogues [28]. When correlating these findings with the studied stability constants of the amphiphiles, it is clear that the lower release rate observed for the **ibuprofenate-5·AuNP** complex is governed by the high affinity of the macrocyclic moiety for anions, whereas with the open chain imidazolium compound the affinity is relatively lower. This finding suggests a balance between the binding affinity of the specific local moiety near the colloid surface and other forces (probably electrostatic). In any case, we have shown how the topology of the head group can influence in the release of any bound drug. This study may aid in the understanding of the release of other anionic molecules of interest from the AuNPs complexes.

This newly synthesized AuNPs can be used as vehicle for delivery of drugs that requires long-term release. The next step in this research would be the incorporation of other anionic drugs of higher therapeutic interest and testing the *in vivo* efficacy through alternative routes to oral administration. Clearly, ibuprofenate serves here as an example and future work would involve *in vivo* testing where we include the use of more biologically active drugs where – because of the proportion of drug per carrier (the AuNP) is low – the dose required for therapeutically significant effect is low. We envisage physical application of the system or selective uptake for certain maladies. The incorporation of a second anionic molecule capable of sensing would also be assessed in order to convert the AuNPs from a delivery vehicle into a theranostics tool.

Acknowledgements

This study was supported by the Ministerio de Ciencia e Innovación (MICINN) (project TEC2011-29140-C03-02). E. A. thanks Kinga Szarpak for a sample of **6·2Br** and Dr. M. Sridharan from SASTRA University for the opportunity to carry out Master thesis in the Semester Abroad Program.

References

[1] K. Park, J. Control. Release 178 (2014) 126.

[2] R.K. Upadhyay, BioMed Research International 2014 (2014) 1.

[3] E. Boisselier, D. Astruc, Chem. Soc. Rev. 38 (2009) 1759.

[4] E.C. Dreaden, A.M. Alkilany, X. Huang, C.J. Murphy, M.A. El-Sayed, Chem. Soc. Rev. 41 (2012) 2740.

[5] L.A. Dykman, N.G. Khlebtsov, Acta Naturae 3 (2011) 34.

[6] M. Kajiura, T. Nakanishi, H. Iida, H. Takada, T. Osaka, J. Colloid Interface Sci. 335 (2009) 140.

[7] G.F. Paciotti, L. Myer, D. Weinreich, D. Goia, N. Pavel, R.E. McLaughlin, L. Tamarkin, Drug Deliv. 11 (2004) 169.

[8] S. Manju, K. Sreenivasan, J. Colloid Interface Sci. 368 (2012) 144.

[9] R. Cui, H. Huang, Z. Yin, D. Gao, J.-J. Zhu, Biosens. Bioelectron. 23 (2008) 1666.

[10] D. Tang, R. Yuan, Y. Chai, Anal. Chem. 80 (2008) 1582.

[11] A.T.N. Lam, J. Yoon, E.-O. Ganbold, D.K. Singh, D. Kim, K.-H. Cho, S.J. Son, J. Choo, S.Y. Lee, S. Kim, S.-W. Joo, J. Colloid Interface Sci. 425 (2014) 96.

[12] Y. Malam, M. Loizidou, A.M. Seifalian, Trends Pharmacol. Sci. 30 (2009) 592.

[13] D.O. Lapotko, E. Lukianova, A.A. Oraevsky, Lasers Surg. Med. 38 (2006) 631.

[14] H.S. Mader, P. Kele, S.M. Saleh, O.S. Wolfbeis, Curr. Opin. Chem. Biol. 14 (2010) 582.

[15] S.K. Balasubramanian, L. Yang, L.-Y.L. Yung, C.-N. Ong, W.-Y. Ong, L.E. Yu, Biomaterials 31 (2010) 9023.

[16] E.E. Connor, J. Mwamuka, A. Gole, C.J. Murphy, M.D. Wyatt, Small 1 (2005) 325.

[17] A.M. Alkilany, C.J. Murphy, J. Nanopart. Res. 12 (2010) 2313.

[18] V. Voliani, G. Signore, R. Nifosí, F. Ricci, S. Luin, F. Beltram, Recent Patents Nanomed. 2 (2012) 34.

[19] S. Rana, A. Bajaj, R. Mout, V.M. Rotello, Adv. Drug Del. Rev. 64 (2012) 200.

[20] P. Ghosh, G. Han, M. De, C. Kim, V. Rotello, Adv. Drug Del. Rev. 60 (2008) 1307.

[21] R. Raghavendra, K. Arunachalam, S.K. Annamalai, A.M. Arunachalam, Int J Pharm Pharm Sci 6 (2014) 74.

[22] C.N.R. Rao, H.S.S. Ramakrishna Matte, R. Voggu, A. Govindaraj, Dalton Transactions 41 (2012) 5089.

[23] M. Brust, M. Walker, D. Bethell, D.J. Schiffrin, R. Whyman, J. Chem. Soc., Chem. Commun. (1994) 801.

[24] H.S. Schrekker, M.A. Gelesky, M.P. Stracke, C.M.L. Schrekker, G. Machado, S.R. Teixeira, J.C. Rubim, J. Dupont, J. Colloid Interface Sci. 316 (2007) 189.

[25] S.K. Hait, S.P. Moulik, Curr. Sci. 82 (2002) 1101.

[26] T.A. Camesano, R. Nagarajan, Colloids Surf. Physicochem. Eng. Aspects 167 (2000) 165.

[27] M. Ao, G. Xu, Y. Zhu, Y. Bai, J. Colloid Interface Sci. 326 (2008) 490.

[28] L. Casal-Dujat, M. Rodrigues, A. Yagüe, A.C. Calpena, D.B. Amabilino, J. González-Linares, M. Borràs, L. Pérez-García, Langmuir 28 (2012) 2368.

[29] L. Casal-Dujat, O. Penon, C. Rodríguez-Abreu, C. Solans, L. Pérez-García, New J. Chem. 36 (2012) 558.

[30] L. Casal-Dujat, P.C. Griffiths, C. Rodríguez-Abreu, C. Solans, S. Rogers, L. Pérez-García, J. Mater. Chem. B 1 (2013) 4963.

[31] J. Yoon, S.K. Kim, N.J. Singh, K.S. Kim, Chem. Soc. Rev. 35 (2006) 355.

[32] C. Tarmann, A. Jungbauer, J. Sep. Sci. 31 (2008) 2605.

[33] M. Rodrigues, A.C. Calpena, D.B. Amabilino, D. Ramos-López, J. de Lapuente, L. Pérez-García, RSC Adv. 4 (2014) 9279.

[34] M.E. Morales, V.G. Lara, A.C. Calpena, J. Domenech, M.A. Ruiz, J. Control. Release 95 (2004) 75.

Tables

TABLE 1: Values of K_a from anion binding studies with chloride and acetate for bis-imidazolium salts **1·2Br**, **2·2PF$_6$**, **3·2PF$_6$**, **4·2Br** and **5·2PF$_6$**

		TBA Salts	
		Cl^-	**AcO^-**
		K_a / M^{-1}	K_a / M^{-1}
1·2Br[b]	C(2)-H	53.59	120.63
	C(2)'-H	[a]	[a]
2·2PF$_6$[c]	C(2)-H	473.5	1636.6
	C(2)'-H	307.8	1310.7
3·2PF$_6$[b]	C(2)-H	80.65	401.61
	C(2)'-H	92.42	389.11
4·2Br[b]	C(2)-H	96.15	364.96
	C(2)'-H	[a]	[a]
5·2PF$_6$[c]	C(2)-H	11,308	752.4
	C(2)'-H	10,133	[a]

[a] no significant shift is observed; [b] solution in $(CD_3)_2SO$; [c] solution in $CDCl_3$

TABLE 2: Modelistic and amodelistic parameters for the release of ibuprofenate from the **ibuprofenate-5·AuNP**.

	Modelistic		**Amodelistic**	
pH	K_D[a]	$t_{1/2}$[b]	MRT[c]	Efficiency
	(h^{-1})	(h)	(h)	(%)
5.5	0.0085	82.8	72.9	72.4
7.4	0.0060	116.3	108.5	67.7

[a] Dissociation constant; [b] Half life time; [c] Mean Release Time

Electronic Suplementary Information

Macrocyclic imidazolium-based amphiphiles for the synthesis of gold nanoparticles and delivery of anionic drugs

Ezhil Amirthalingam,[1,2] Mafalda Rodrigues,[1,2] Lucía Casal-Dujat,[1,2] Ana C. Calpena,[2,3] David B. Amabilino,[4] David Ramos-López,[5] and Lluïsa Pérez-García[1,2,*]

1Departament de Farmacologia i Química Terapèutica, Universitat de Barcelona, Avda. Joan XXIII s/n, 08028 Barcelona, Spain

2Institut de Nanociència i Nanotecnología UB (IN2UB), Universitat de Barcelona, 08028 Barcelona, Spain

3Departament de Farmàcia i Tecnologia Farmacèutica, Universitat de Barcelona, Avda. Joan XXIII s/n, 08028 Barcelona, Spain

4Institut de Ciència de Materials de Barcelona (ICMAB-CSIC), Campus Universitari, 08193 Bellaterra, Spain.

5Unitat de Toxicologia Experimental i Ecotoxicologia (UTOX-PCB), Parc Científic de Barcelona, Baldiri i Reixac 10-12, 08028 Barcelona, Spain.

*Corresponding autor:
Maria Lluïsa Pérez-García - mlperez@ub.edu
Telephone: (+34) 934035849. Fax: (+34) 934024539

General methods

^{1}H NMR were performed on Varian Mercury 400 spectrometers (400 MHz) and ^{13}C NMR on Varian Mercury 400 spectrometers (100 MHz) from the *Centres Cientifics i Tecnològics of the Universitat de Barcelona* (CCiTUB). NMR spectra were determined in $CDCl_3$ or $(CD_3)_2SO$, and chemical shifts are expressed in parts per million (δ) relative to the central peak of the solvent.

Thin layer chromatography (TLC) was performed on Merck coated 60 F_{254} silica gel plates; the spots were located with UV light and developed with an iodine/silica or potassium permanganate solution (1% w v^{-1}). Chromatography was performed on SDS silica oxide 60 ACC (30-75 μm).

The melting points were determined using CTP-MP 300 hot-plate apparatus with ASTM 2C thermometer.

Electrospray Ionization Mass Spectra (ESI-MS) and Electrospray Ionization High Resolution Mass Spectra (ESI-HRMS) were performed on an LC/MSD-TOF mass spectrometer from Agilent Technologies (CCiTUB). The electrospray interface had the following conditions: nebulizing nitrogen gas flow at 15 psi, drying nitrogen 7 L min^{-1}, source temperature was maintained at 300°C with a capillary voltage of 4 kV and fragmentor voltage of 80 or 215 V. The eluent flowing through the probe was H_2O: Acetonitrile (1:1) at a flow rate of 200 μL min^{-1}.

UV-Vis absorption spectra were obtained on a UV-1800 Shimadzu UV Spectrophotometer.

MALDI-TOF-MS analysis was performed using a Voyager-DE-RP mass spectrometer (Applied Biosystems, Framingham, USA) from CCiTUB. A 3 ns pulse nitrogen laser (337 nm) was used for desorption and ionization with an accelerating voltage of 20 kV. Positive ions were detected in a time-of-flight mass detector in the reflector mode. The matrix used was 2, 5-dihydroxybenzoic acid (DHB).

XPS spectra were obtained in a PHI 5500 Multitechnique System (from Physical Electronics) at the CCiTUB, with a monochromatic X-ray source (Al Kα line of 1486.6 eV energy and 350 W), placed perpendicular to the analyzer axis and calibrated using the 3 $d_{5/2}$ line of Ag with a full width at half maximum (fwhm) of 0.8 eV. The analyzed area was a circle of 0.8 mm diameter, and the selected resolution for the spectra was 187.5 eV of pass energy and 0.8 eV/step for the general spectra and 23.5 eV of pass energy and 0.1 eV/step for the spectra of the different elements. All measurements were made in an ultra high vacuum (UHV) chamber pressure between 5 x 10^{-9} and 2 x 10^{-8} Torr.

TEM images were obtained with a JEOL JEM-1010 transmission electron microscope at 80 kV, from CCiTUB. The images were captured by a Megaview III Soft Imaging System camera and the size of the nanoparticles was measured with Analysis software (Olympus).

The hydrodynamic size of the AuNPs was determined by Dynamic Light Scattering using a Malvern Zetasizer Nano ZS series from Malvern Instruments.

SEM images were obtained using a JEOL JSM-7100F field emission scanning electron microscope at 5 kV, at CCiTUB. Samples were mounted on microscope holders using carbon tabs and then they were coated with a thin film of amorphous carbon. The images were captured using the software PC-SEM version 5.1.

TGA was performed on a Mettler Toledo TGA/SDTA 851e, at CCiTUB, with a temperature ramp from 30°C to 600°C and a heating rate of 10°C min^{-1}.

*Synthesis of **3·2Br***

A solution of 1,3-bis(bromomethyl)-5-methoxybenzene (0.68 g, 2.31 mmol) in dry acetonitrile (50 mL) was added to a solution of 1,3-bis(imidazolylmethyl)-5-methoxybenzene (0.62 g, 2.31 mmol) in dry acetonitrile (60 mL) at 80°C under argon atmosphere. The stirring was continued for 21 hours. The white precipitate was filtered off, washed with acetonitrile (10 mL) and dried to give **3·2Br** as a white solid (1.17 g, 90 %). The NMR chemical shifts in $(CD_3)_2SO$ are listed below. Imidazolium and phenyl rings are referenced as (Im) and (Ar) respectively.

3·2Br: ^{1}H NMR (400 MHz, $(CD_3)_2SO$): 3.82 (s, 6H, OCH_3); 5.38 (s, 8H, CH_2); 6.61 (s, 2H, Ar-H(2)); 7.21 (s, 4H, Ar-H(4,6)); 7.85 (s, 4H, Im-H(4,5)); 9.34 (s, 2H, Im-H(2)). ^{13}C NMR (100 MHz, $(CD_3)_2SO$): 51.7 (CH_2); 55.2 (OCH_3); 114.7 (Ar-C(4,6)); 117.7 (Ar-C(2)); 123.1 (Im-C(4,5)); 136.0 (Im-C(2)); 137.7 (Ar-C(1,3)); 159.5 (Ar-C(5)). ESI-MS *m/z*: (201.1, $[(M-2Br)/2]^{2+}$, 100 %); (401.2, $[M-2Br]^{+}$, 37 %); (481.1, $[M-Br]^{+}$, 26 %). ESI-HRMS (*m/z*): $(C_{24}H_{26}N_4Br_2O_2$ -Br, $-H)^{+}$ calculated 481.1, found 481.1. Rf: 0.44 ($MeOH:NH_4Cl$ 2M $H_2O:MeNO_2$, 7:2:1). mp: 200°C. (dec.)

*Synthesis of **6·2Br***

A solution of 1,4-bis(bromomethyl)benzene (0.50 g, 1.88 mmol) was dissolved in dry acetonitrile at room temperature (5 mL). To this, a solution of 1-octadecyl-1*H*-imidazole (1.20 g, 3.70 mmol) was added at 80°C through a syringe and the mixture was kept under argon atmosphere with continuous stirring for 26 hours (**Scheme S1**). A yellow colored solution with white precipitate was obtained and allowed to cool down to room temperature. The solution was then filtered and the solid was washed with methanol (40 mL) and dried to give **6·2Br** (1.0 g, 60

%). The NMR chemical shifts in $CDCl_3$ are listed below. Imidazolium and phenyl rings are referenced as (Im) and (Ar) respectively.

Scheme S1. Synthesis of 6·2Br

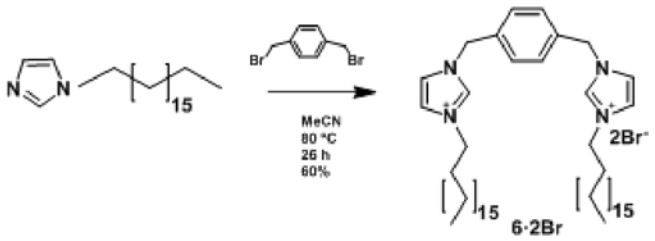

6·2Br: ^{1}H NMR (400 MHz, $CDCl_3$): 0.88 (t, 6H, CH_3), 1.26-1.32 (m, 60H, $(CH_2)_{15}$), 1.88 (m, 4H, N-CH_2-C**H**$_2$), 4.3 (t, 4H, N-CH_2), 5.67 (s, 4H, CH_2), 7.34 (s, 2H, Im-H(4)), 7.49 (s, 4H, Ar-H(2,3,5,6)), 7.92 (s, 2H, Im-H(5)), 10.33 (s, 2H, Im-H(2)). ^{13}C NMR (100 MHz, $CDCl_3$): 14.11 (CH_3); 22.67-31.91 ($(CH_2)_{16}$); 50.19 (N-CH_2); 52.45 (CH_2); 121.69 (Im-C(4)); 123.15 (Im-C(5)); 130.16 (Ar-C(2,4,5,6)); 134.23 (Ar-C(1,3)); 136.67 (Im-C(2)). ESI-MS m/z: (372.4, [(M-2Br)/2]$^{2+}$, 100%), (573.6, [M- (Br, $((CH_2)_{17}CH_3)]^+$, 7%), (825.6, [M-Br]+, 17%). ESI-HRMS (*m/z*): $(C_{50}H_{88}N_4Br_2\text{-}2Br)^{2+}$ calculated 372.3499, found 372.3494; $(C_{50}H_{88}N_4Br_2$ -Br)$^+$ calculated 823.6186, found 823.6189. Rf: 0.55 (CH_2Cl_2:MeOH, 4:1). mp: The phase behavior is similar to that described in [29] for related compounds where liquid crystal behavior was seen.

Anion exchange protocol

A solution of silver hexafluorophosphate (0.11 g, 0.42 mmol) in dry acetonitrile (2 mL) was added to a solution of **2·2Br** (0.13 g, 0.14 mmol) in dry acetonitrile (54 mL) at 40°C. The stirring was continued in darkness for 1 hour. A yellow solid precipitated, which was filtered off and the solvent was evaporated. The white residue was washed with water (10 mL) and filtered off to give **2·2PF$_6$** as a pale brown solid (0.13 g, 93 %). The same protocol was followed for compounds **3·2Br** and **5·2Br**.

Toxicity Study

The cells were cultivated in DMEM supplemented with 10 % Fetal Bovine Serum (FBS), 2 mM Glutamine and 0.5% penicillin/ streptomycin (a stock of 10000 IU/10 mg respectively). The cells were incubated (ThermoForma) at 37°C in a humid atmosphere of 5% CO_2 in culture T75 (Nunc) flascones. Cells were seeded in a density of approximately $1x10^5$ cells mL^{-1} on the plate

with 96 wells. The cells were exposed to 9 concentrations for both **5·2Br** and **6·2Br** separated by a factor of √ 10: 1000, 316, 100, 32, 10, 3, 1, 0.3 and 0.1 μg mL^{-1}. The culture medium was used as negative control for the test. SDS 0.02 % was used as a positive control in the case of MTT Assay and to assess genetic damage, as a positive control, MMS 400 μM was used. The plates were incubated for 24 hours before the start of the experiment followed by ligand exposure for 24 hours. The cells after exposure were washed with PBS. The treatment was followed by adding MTT (5 mg mL^{-1}) to the growth medium solution and incubated for 2 hours. Later, the media was removed and DMSO was added 100 μL per well. Finally the absorbance at 550 nm was read using spectrophotometer. The cell viability under the different conditions was assessed by comparison of optical density obtained with the control.

For the evaluation of DNA damage, some of the cells were collected in microtubes. The cells collected were mixed with a suspension of agarose with low melting at 0.9 % and were spread on the slides previously coated with a layer of 1 % agarose. After solidification of the agarose, the slides were dipped in liquid lysis for 1 hour to break the membranes and sequester proteins, followed by treating with electrophoresis buffer at 4°C for 40 minutes to allow DNA unwinding and finally electrophoresis was carried out at 25 V and 300 mA (at 4°C) for 30 minutes. The DNA was then washed thrice with Tris buffer to bind the DNA. Then, they were allowed to dry and were protected from light until analysis. For analysis, the slides were stained with the fluorochrome DAPI (4,6-Diamidin-2-phenylindole, at a concentration of 5 mg mL^{-1}) and the tail Intensity was analyzed, whose fluorescence was analyzed using Comet software Assay IV. Tail intensity was measured by treatment of 50 cells and was expressed as the percentage of fluorescence intensity with respect to the total fluorescence in the tail.

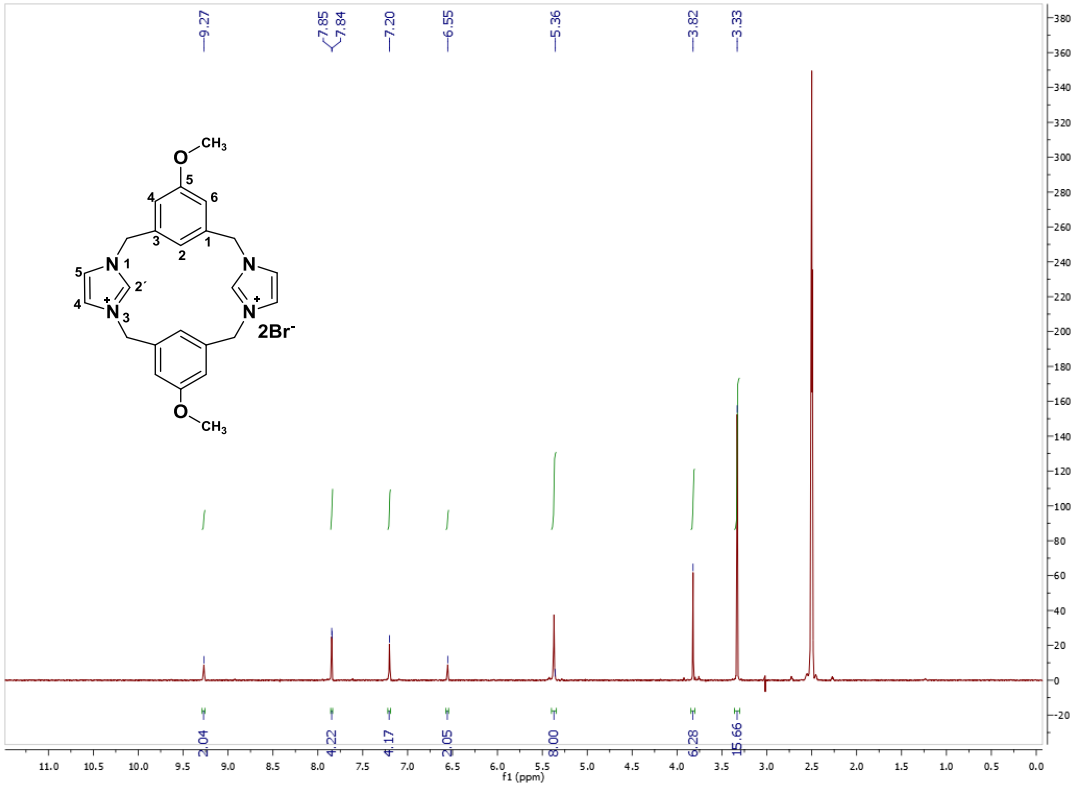

Figure S1: ^{1}H NMR spectrum of **3·2Br**

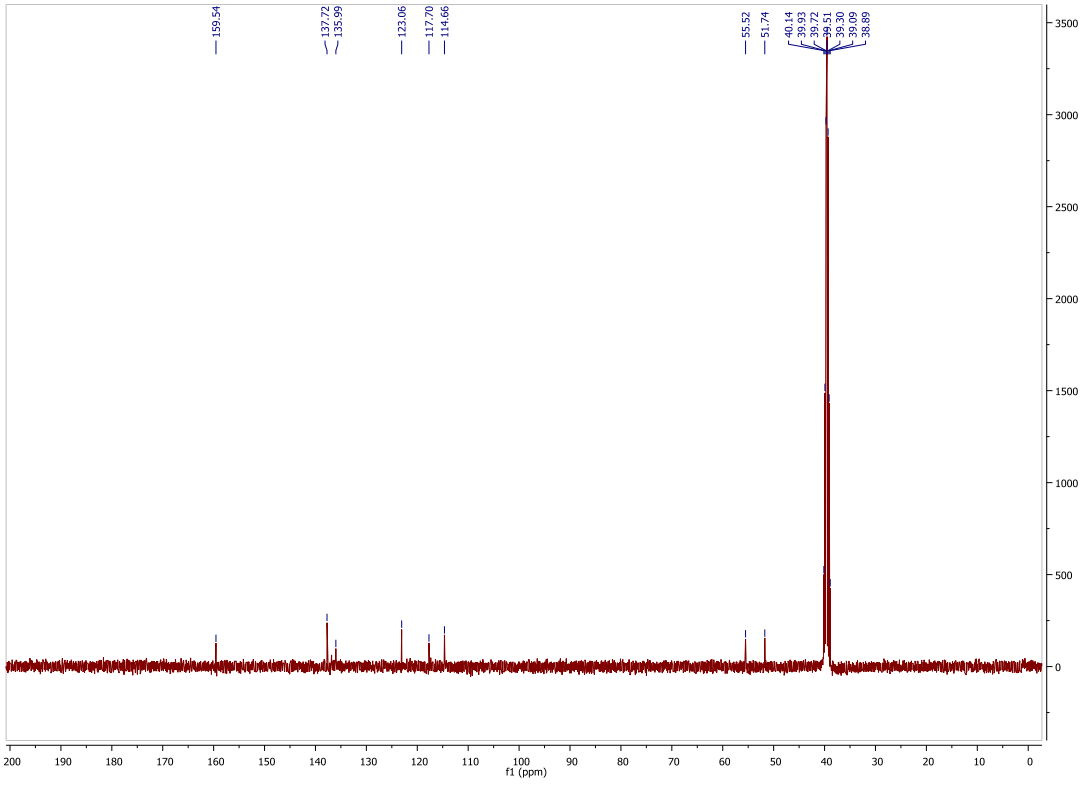

Figure S2: ^{13}C NMR spectrum of **3·2Br**

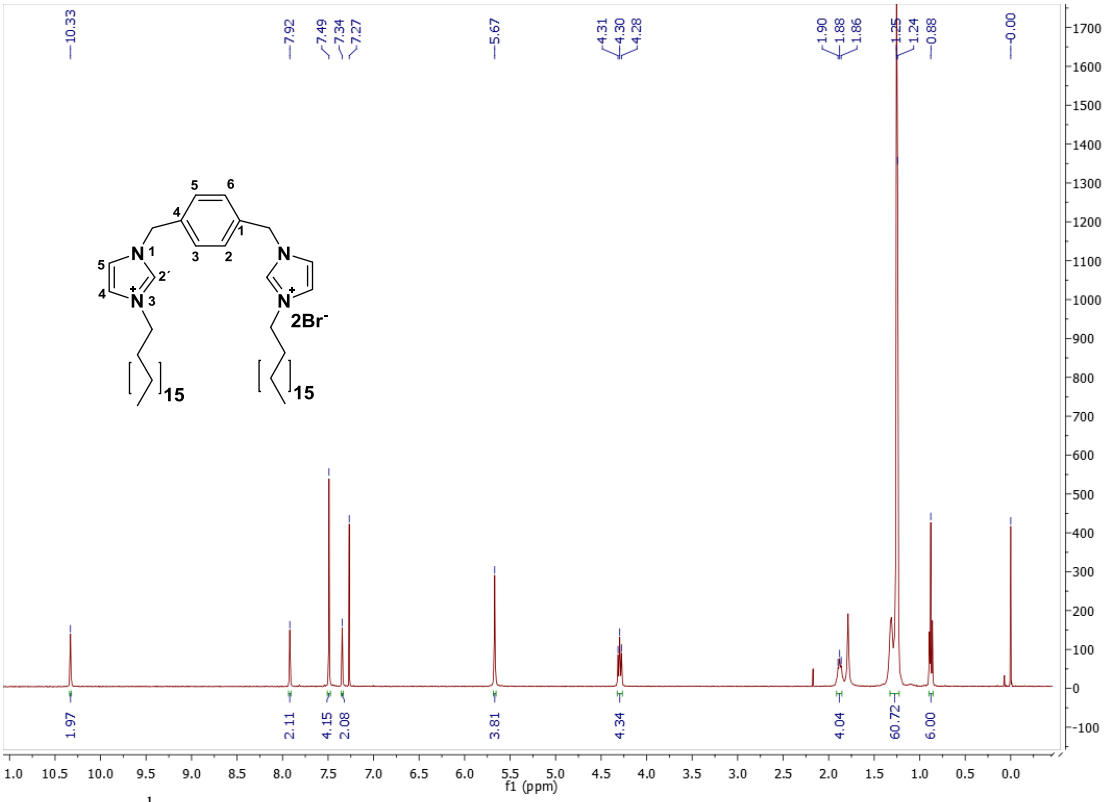

Figure S3: ^{1}H NMR spectrum of **6·2Br**

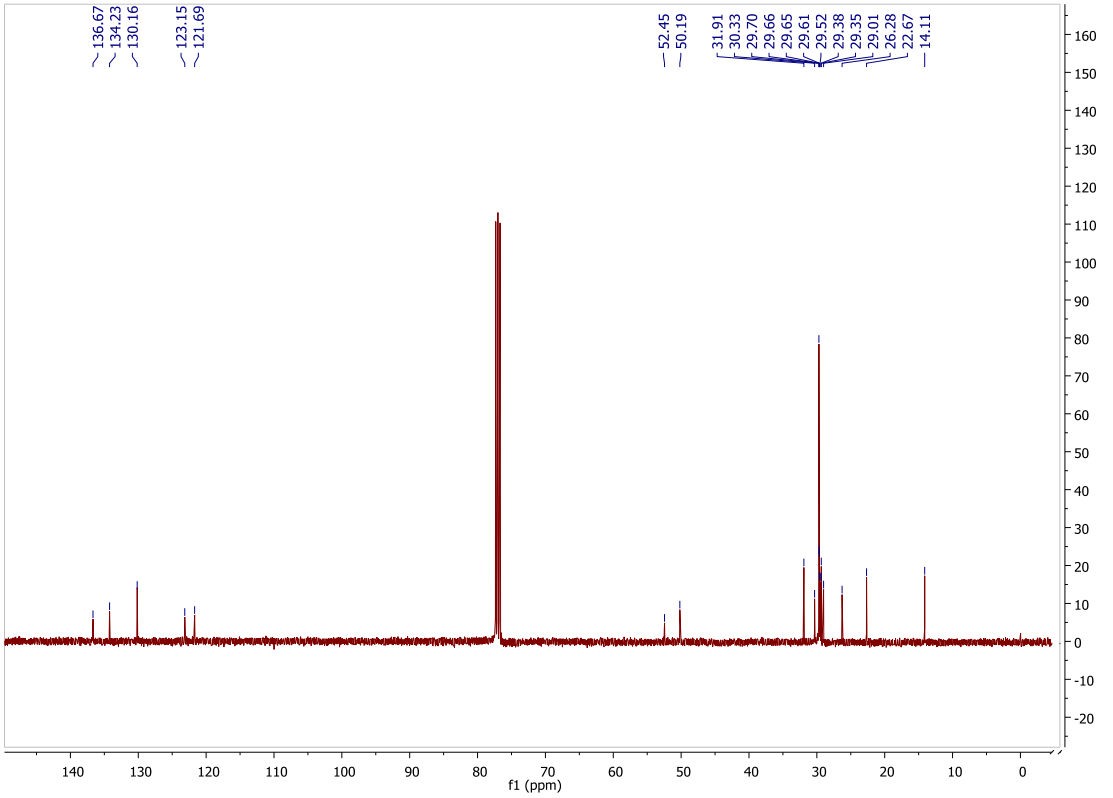

Figure S4: ^{13}C NMR spectrum of **6·2Br**

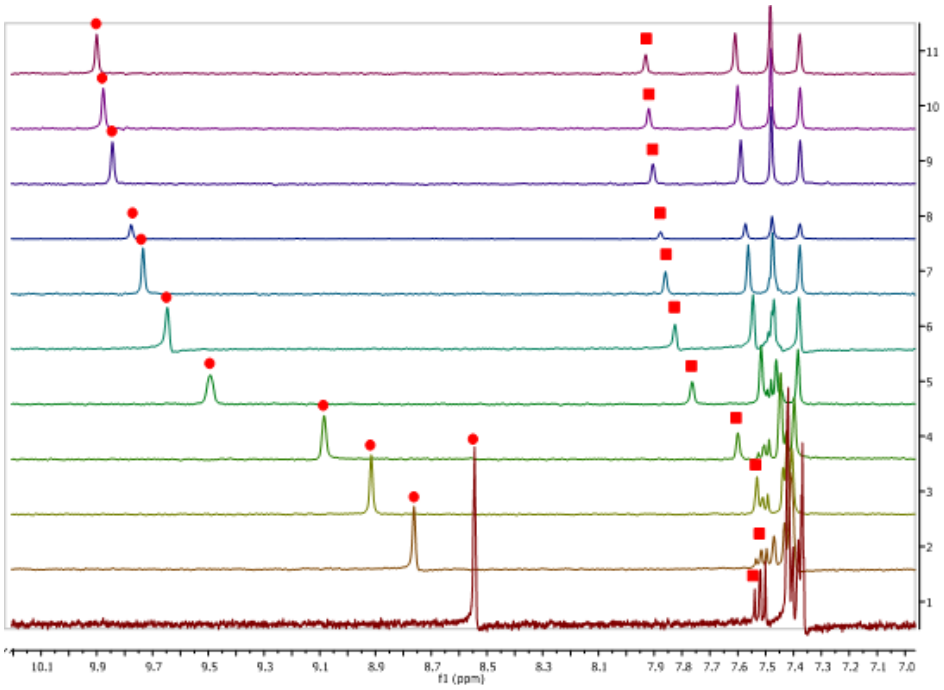

Figure S5: NMR spectra of **2·2PF$_6$** 0.5 mM solution in $CDCl_3$ show the chemical shifts, depicting the downfield effect of the proton signals C(2)-H (•) and C(2)'-H (▪), with increasing **2·2PF$_6$**: chloride ratio (from bottom to top: 1:0, 1:1, 1:2, 1:3, 1:7, 1:10, 1:13, 1:15, 1:20, 1:25 and 1:30).

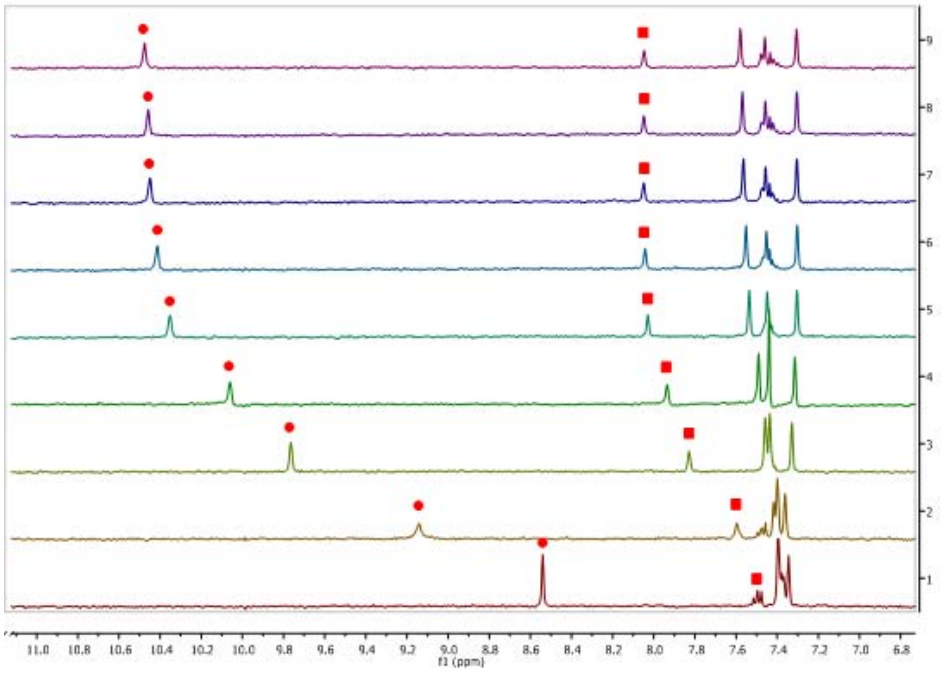

Figure S6: NMR spectra of **2·2PF$_6$** 0.5 mM solution in $CDCl_3$ show the chemical shifts, depicting the downfield effect of the proton signals C(2)-H (•) and C(2)'-H (▪), with increasing **2·2PF$_6$**: acetate ratio (from bottom to top: 1:0, 1:1, 1:2, 1:3, 1:7, 1:10, 1:13, 1:15 and 1:20).

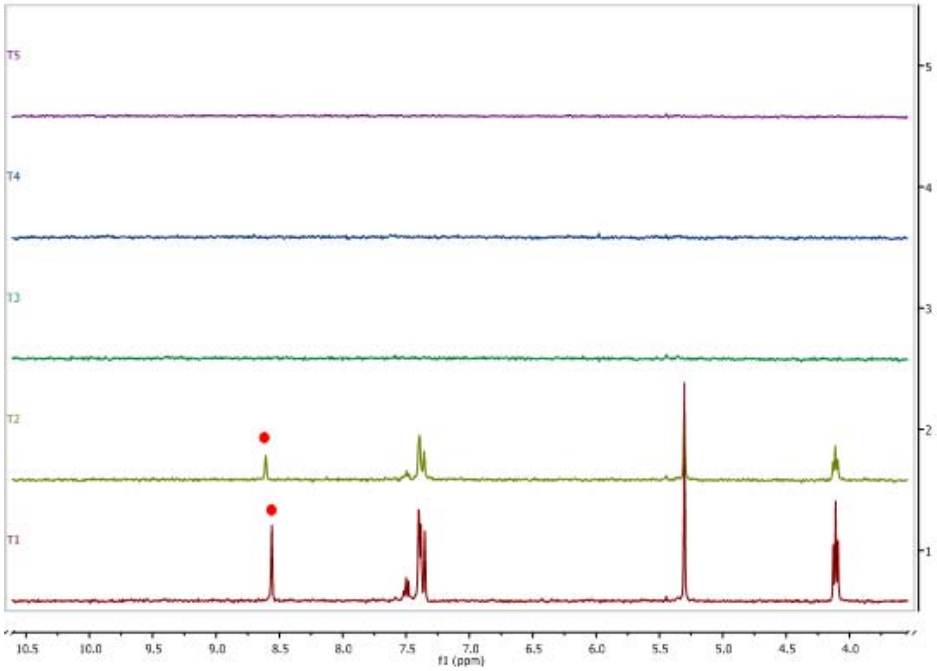

Figure S7: NMR spectra of **2·2PF$_6$** 0.5 mM solution in $CDCl_3$ show the disappearance of the peaks with increasing **2·2PF$_6$**: dihydrogen phosphate ratio (from bottom to top: 1:0, 1:1, 1:2, 1:3 and 1:7).

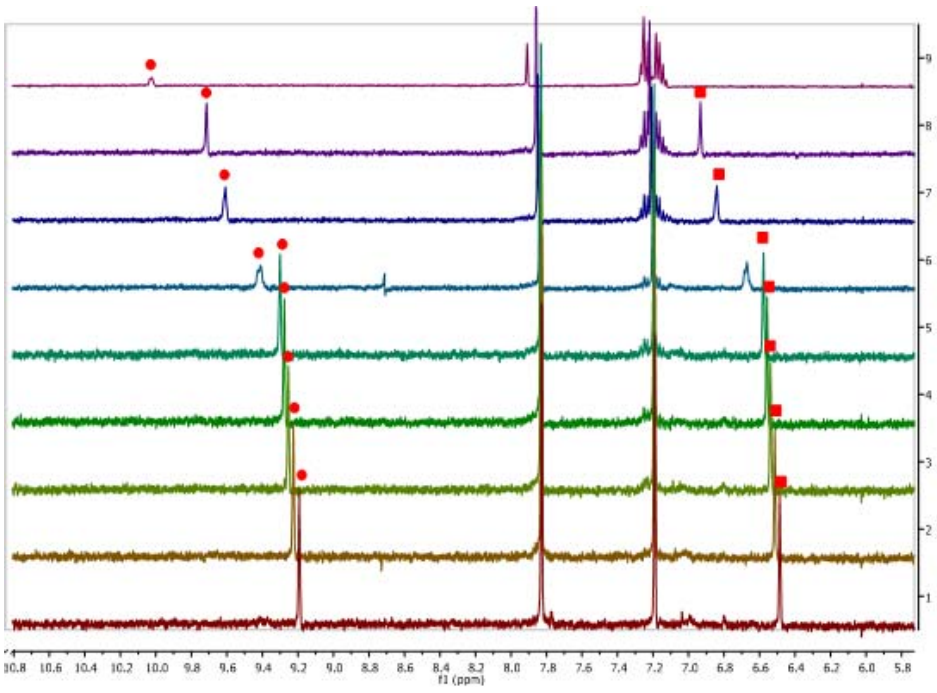

Figure S8: NMR spectra of **3·2PF$_6$** 0.5 mM solution in $(CD_3)_2SO$ show the chemical shifts, depicting the downfield effect of the proton signals C(2)-H (•) and C(2)'-H (▪), with increasing **3·2PF$_6$**: chloride ratio **(**from bottom to top: 1:0, 1:1, 1:2, 1:3, 1:7, 1:10, 1:13, 1:15 and 1:20)

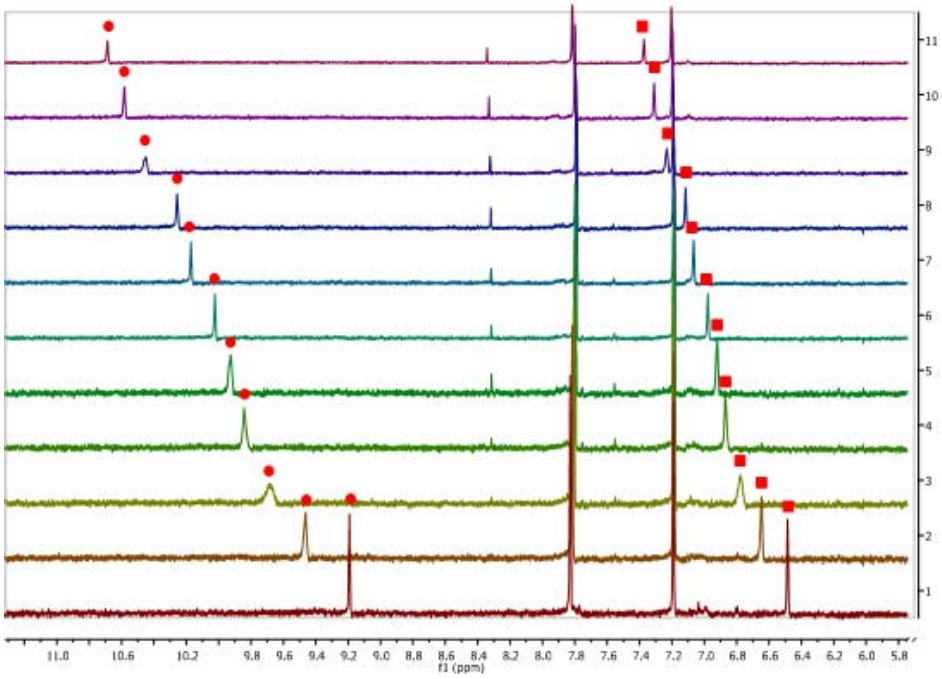

Figure S9: NMR spectra of **3·2PF$_6$** 0.5 mM solution in $(CD_3)_2SO$ show the chemical shifts, depicting the downfield effect of the proton signals C(2)-H (•) and C(2)'-H (▪), with increasing **3·2PF$_6$**: acetate ratio. **3·2PF$_6$** (from bottom to top: 1:0, 1:1, 1:2, 1:3, 1:7, 1:10, 1:13, 1:15, 1:20, 1:40 and 1:60).

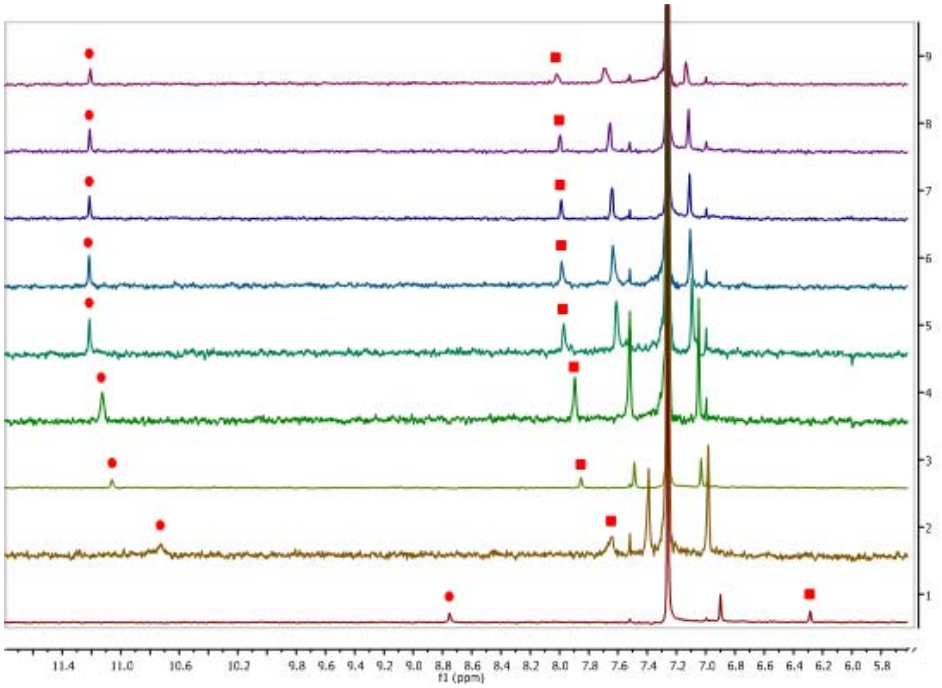

Figure S10: NMR spectra of **5·2PF$_6$** 0.5 mM solution in $CDCl_3$ show the chemical shifts, depicting the downfield effect of the proton signals C(2)-H (•) and C(2)'-H (▪), with increasing **5·2PF$_6$**: chloride ratio (from bottom to top: 1:0, 1:1, 1:2, 1:3, 1:7, 1:10, 1:13, 1:15 and 1:20).

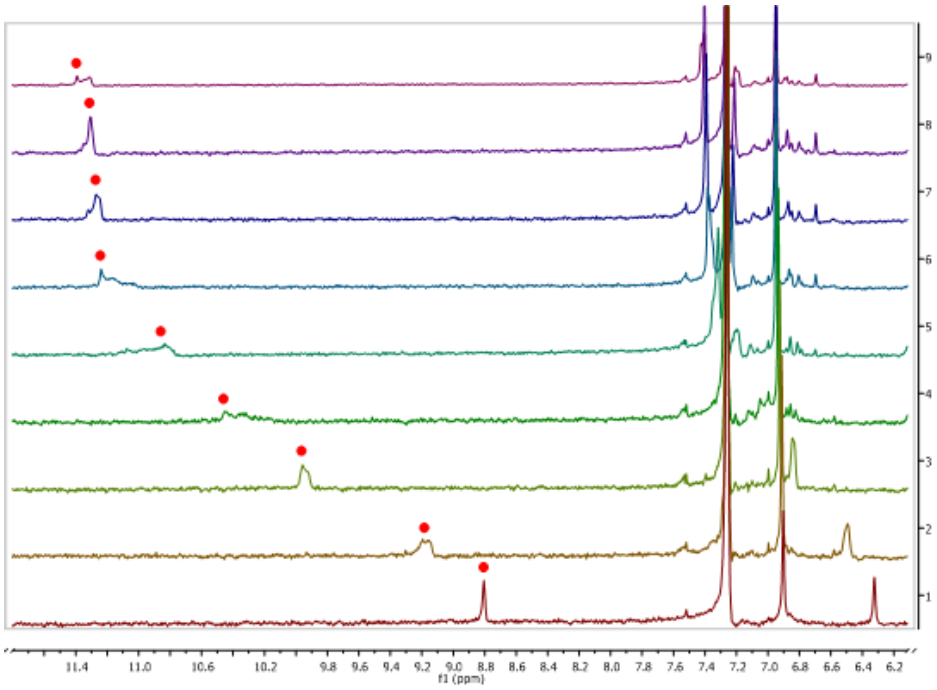

Figure S11: NMR spectra of **5·2PF$_6$** 0.5 mM solution in $CDCl_3$ show the chemical shifts, depicting the downfield effect of the proton signals C(2)-H (•) and C(2)'-H, with increasing **5·2PF$_6$**: acetate ratio (from bottom to top: 1:0, 1:1, 1:2, 1:3, 1:7, 1:10, 1:13, 1:15 and 1:20).

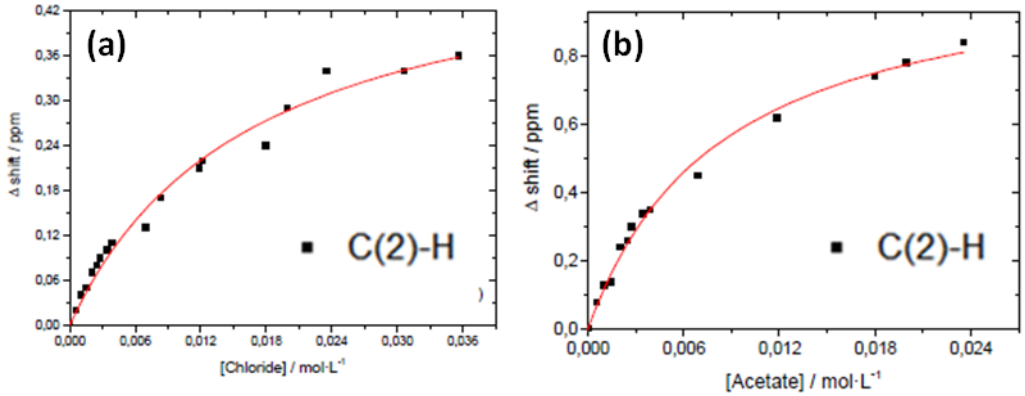

Figure S12: Experimental points and fitting (line) data from titrations with bis-imidazolium and TBA salts: a) **1·2Br**: chloride and b) **1·2Br**: acetate.

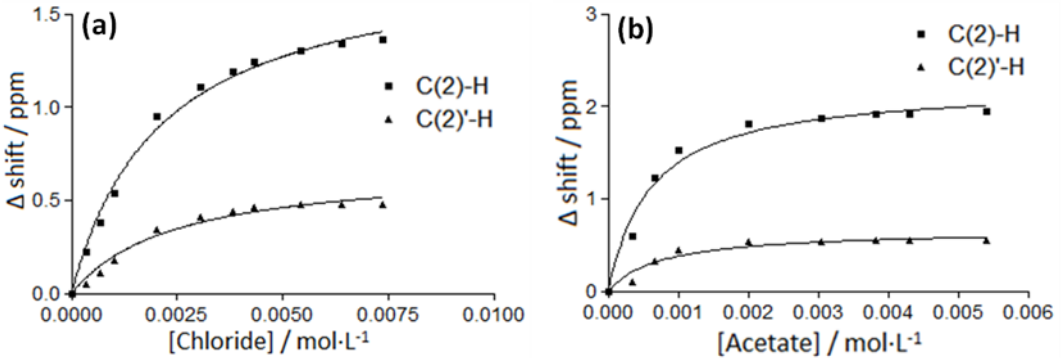

Figure S13: Experimental points and fitting (line) data from titrations with bis-imidazolium and TBA salts: a) **2·2PF$_6$**: chloride and b) **2·2PF$_6$**: acetate.

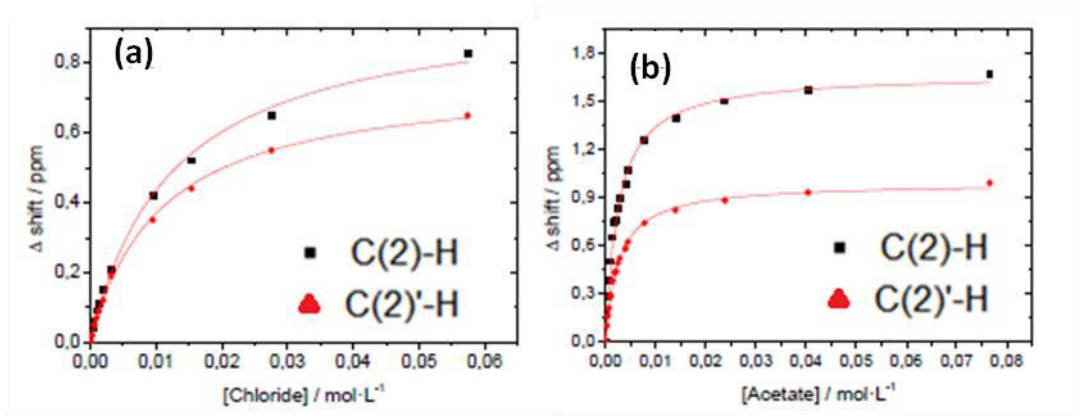

Figure S14: Experimental points and fitting (line) data from titrations with bis-imidazolium and TBA salts: a) **3·2PF$_6$**: chloride and b) **3·2PF$_6$**: acetate.

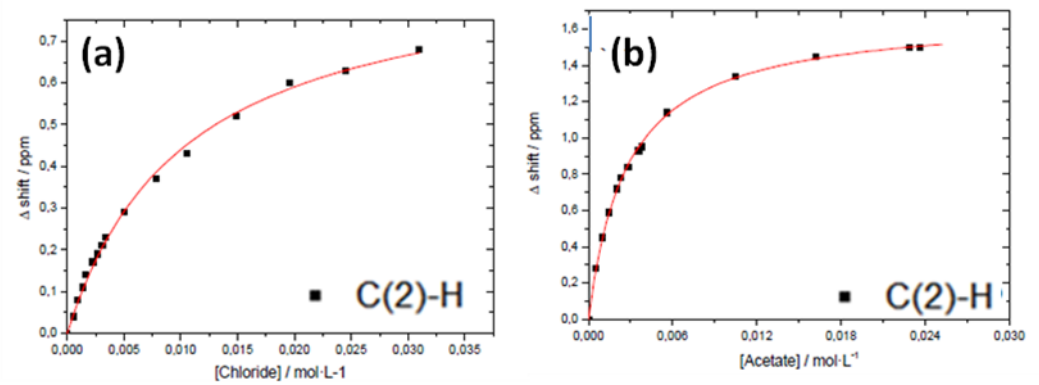

Figure S15: Experimental points and fitting (line) data from titrations with bis-imidazolium and TBA salts: a) **4·2Br**: chloride, b) **4·2Br**: acetate.

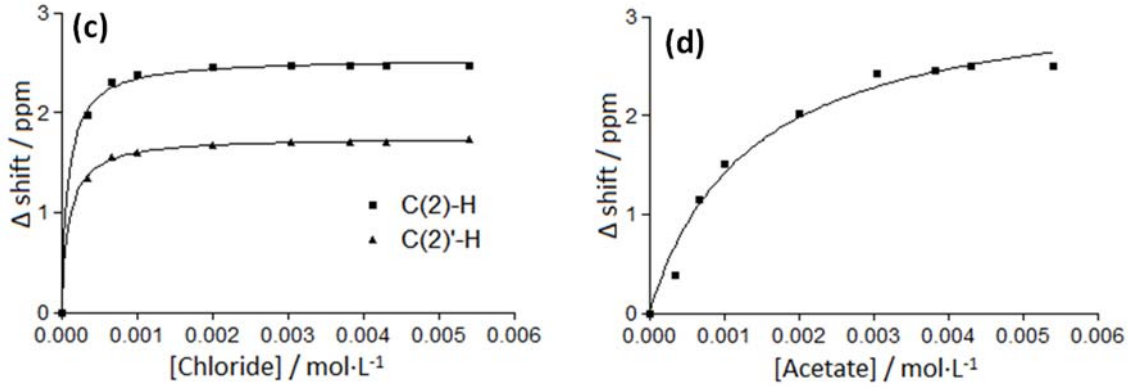

Figure S16: Experimental points and fitting (line) data from titrations with bis-imidazolium and TBA salts: a) **5·2PF$_6$**: chloride and b) **5·2PF$_6$**: acetate

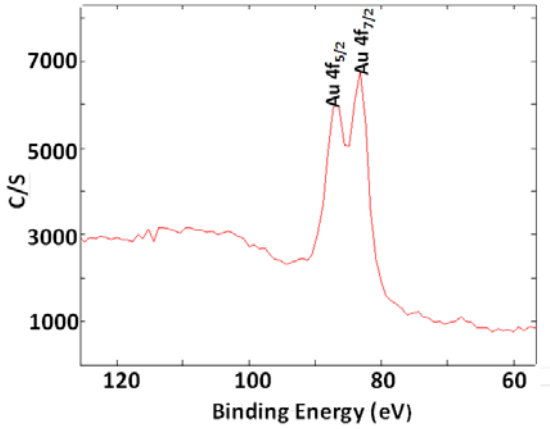

Figure S17: XPS spectrum of **5·AuNP** showing the Au $4f_{7/2}$ and $4f_{5/2}$ peaks with binding energies of 84.5 eV and 88.2 eV, respectively.

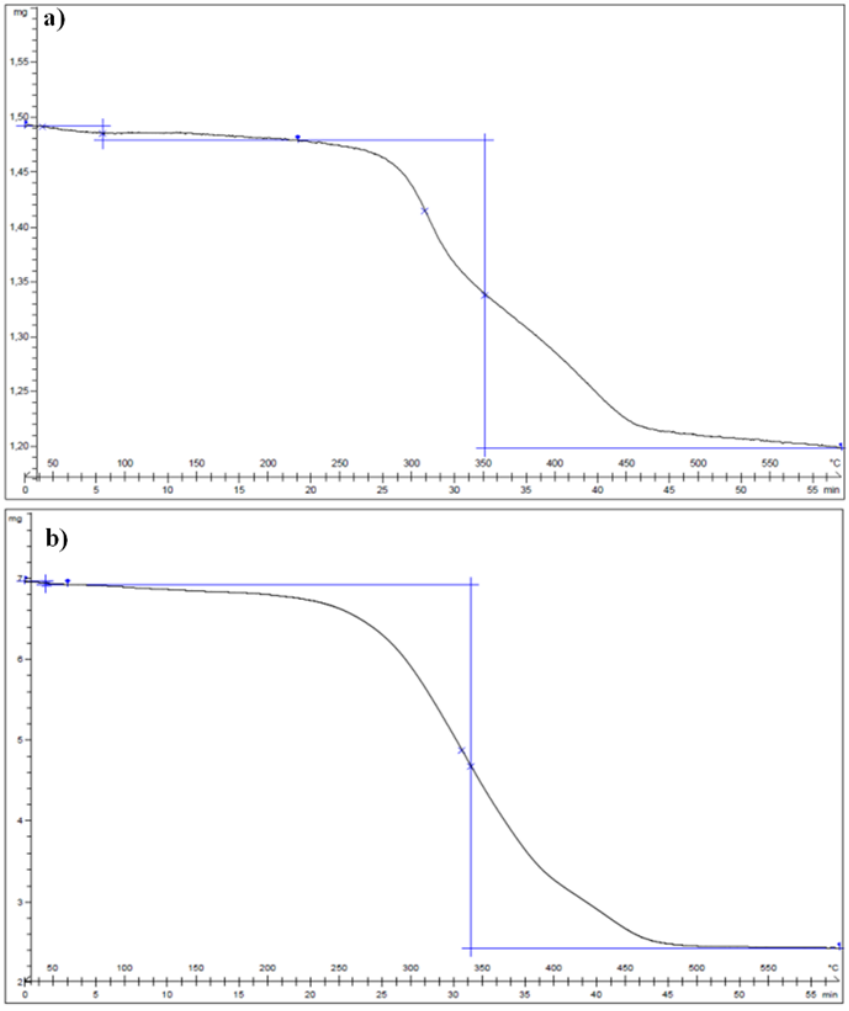

Figure S18: Thermogravimetry curve obtained for a) **5·AuNP** and b) **6·AuNP**.

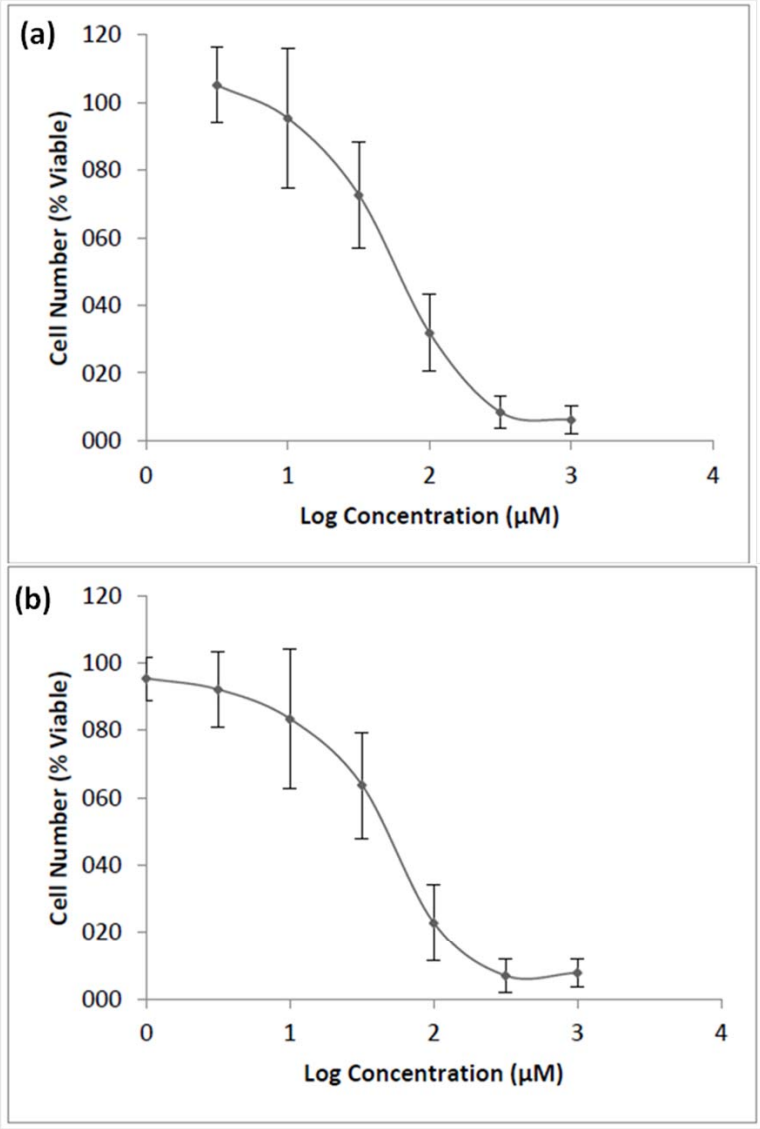

Figure S19: Dose-response curve for (a) **5·2Br** and (b) **6·2Br**.

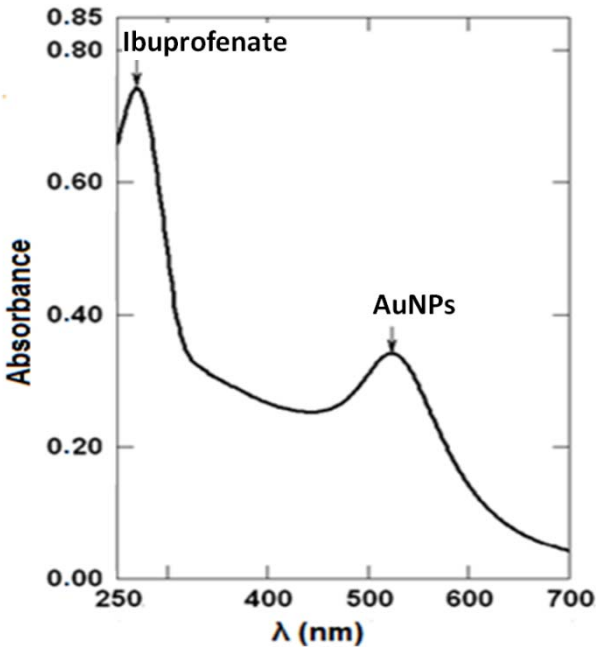

Figure S20: UV-Vis absorption spectrum of sodium **ibuprofenate-5·AuNP** from the organic phase

TABLE S1: Positive-Ion Mode ESI-MS data for **3·2Br** and **6·2Br**

	MW (g mol^{-1})	$[(M-2Br)/2]^{2+}$ (*m/z*)	$[M-H-2Br]^{+}$ (*m/z*)	$[M-H-Br]^{+}$ (*m/z*)
3·2Br	562.3	201.1	401.2	481.1
		100 %	37 %	26 %
6·2Br	372.3	372.4	-	-
		100 %	-	-

TABLE S2: Values of K_a and ΔG° from anion binding studies with chloride and acetate for bis-imidazolium salts **1·2Br**, **2·2PF$_6$**, **3·2PF$_6$**, **4·2Br** and **5·2PF$_6$**

		TBA Salts			
		Cl$^-$		**AcO$^-$**	
		K_a / M^{-1}	-ΔG° /kJmol^{-1}	K_a / M^{-1}	-ΔG° /kJmol^{-1}
1·2Br[b]	C(2)-H	53.59	9.86	120.63	11.87
	C(2)'-H	[a]	[a]	[a]	[a]
2·2PF$_6$[c]	C(2)-H	473.5	15.3	1636.6	18.3
	C(2)'-H	307.8	14.2	1310.7	17.8
3·2PF$_6$[b]	C(2)-H	80.65	10.88	401.61	14.85
	C(2)'-H	92.42	11.21	389.11	14.78
4·2Br[b]	C(2)-H	96.15	11.31	364.96	14.62
	C(2)'-H	[a]	[a]	[a]	[a]
5·2PF$_6$[c]	C(2)-H	11,308	23.1	752.4	16.4
	C(2)'-H	10,133	22.9	[a]	[a]

[a] no significant shift is observed; [b] solution in $(CD_3)_2SO$; [c] solution in $CDCl_3$

TABLE S3: Values of peaks from MALDI-TOF mass spectrometry for **5·AuNP**

$[M+Au-2Br]^+$ (*m/z*)	$[M+Au-Br]^+$ (*m/z*)	$[M-2Br+H]^+$ (*m/z*)
1073.7	1153.6	877.7
100%	2%	2%

Matrix – DHB

TABLE S4: Size of the gold core using TEM, and hydrodynamic size using DLS

Sample	**λ (nm)**	**Size/nm (TEM)**	**Size/nm (DLS)**	**PDI**[a]
4·AuNP	527	8.2 ± 3.6	34.8	0.1
5·AuNP	524	5.3 ± 3.0	73.5	0.2
6·AuNP	525	6.5 ± 2.3	36.9	0.1

[a] Polydispersity Index

Together with the size of the gold core measured by TEM, it is possible to calculate the number of moles of ligands per nanoparticle, N using the following formula:

$$N = \frac{\pi \rho D^3}{6\ M}$$

Where,

ρ = face centered cubic (fcc) density of gold (19.3 g cm^{-3}),

D = average diameter of the nanoparticles gold core and

M = atomic mass of atomic gold (196.97 g mol^{-1}).

TABLE S5: Thermogravimetry results and calculations of amount of ligand per nanoparticle and per area of nanoparticle surface based on the ratio of ligand to gold present in the AuNPs and their gold core size obtained by TEM.

Sample	Total mass (mg)	Ligand mass (mg)	Ligand:Au (mmol)	Average diameter[a] (nm)	Au/NP[b] ratio (mol mol^{-1})	Ligands per NP[b]	Ligands per nm^2
5·AuNP	1.5	0.3	0.05	5.3	7.6 x 10^{-21}	242	2.7
6·AuNP	7.3	4.6	0.46	6.5	1.4 x 10^{-20}	396	29.9

[a] measured by TEM; [b] Nanoparticle

TABLE S6: IC_{50} values of **5·2Br** and **6·2Br**

Ligand	**IC_{50}**	
	$\mu g\ mL^{-1}$	μM
5·2Br	68.7	66.1
6·2Br	40.7	45.0

TABLE S7: Results obtained for Cell viability and genotoxicity results for **5·2Br**

Concentration ($\mu g\ mL^{-1}$)	Viability	Cell death	Tail moment
C- (Media)	100	0.0	2.9
1000	6.1 ± 1.6	93.9 ± 1.6	8.9
316.2	8.5 ± 5.9	91.6 ± 5.9	4.2
100.0	31.8 ± 22.5	68.2 ± 22.5	5.3
31.6	72.7 ± 25.7	27.3 ± 25.7	4.2
10.0	95.3 ± 6.9	4.7 ± 7.0	4.2
3.2	105.1 ± 5.9	-5.1 ± 6	4.2
1.0	96.9 ± 8.4	3.1 ± 8.4	2.8
0.3	106.3 ± 0.1	-6.3 ± 0.1	2.5
0.1	83.5 ± 7.8	16.5 ± 7.8	4.1
C+ (SDS/ MMS)	1.8 ± 0.2	98.2 ± 0.2	45.7

TABLE S8: Results obtained for Cell viability and genotoxicity results for **6·2Br**

Concentration ($\mu g\ mL^{-1}$)	Viability	Cell death	Tail moment
C- (Media)	100	0.0	3.0
1000	7.7 ± 4.2	92.3 ± 4.2	5.3
316.2	6.9 ± 4.9	93.1 ± 4.9	2.9
100.0	22.8 ± 11.3	77.2 ± 11.3	6.2
31.6	63.8 ± 15.8	36.2 ± 15.8	5.6
10.0	83.4 ± 20.7	16.6 ± 20.7	2.8
3.2	92.1 ± 11.1	7.9 ± 11.1	3.3
1.0	95.4 ± 6.5	4.6 ± 6.5	3.5
0.3	97.6 ± 3.4	2.4 ± 3.4	1.7
0.1	100.3 ± 0.4	-0.3 ± 0.4	1.5
C+ (SDS/ MMS)	2.6 ± 1.6	97.5 ± 0.6	45.7

TABLE S9: Results obtained from Student´s t-test

	K_D[a]	MRT[b]	Efficiency
N[c]	3	3	3
P[d]	0.37	0.06	0.2
Mean ± SEM[e] (pH 7.4)	0.01 ± 0.002	72.9 ± 12.12	72.40 ± 3.00
Mean ± SEM[e] (pH 5.5)	0.01 ± 0.0004	108.5 ± 5.77	67.70 ± 1.04
Significant difference	No	No	No

[a] Dissociation constant; [b] Mean Release Time; [c] Number of replicates; [d] probability; [e] Standard error of the mean (SEM)

3.6. Gold nanoparticles decorated with cyclic peptides with antimicrobial and anticancer applications

Manuscript in preparation

Summary

GNP can also be used as delivery vehicles for bioactive molecules that are covalently attached, as in the case of peptides. In this work, we present the covalent immobilization of decapeptides with cyclic structure that are known to possess antimicrobial and antitumor activity. The cyclic peptide was chosen based on the high antitumor activity and low haemolytic action.

Three different strategies were used to perform the immobilization of the peptides on the GNP: through EDC/NHS activation, through azide-alkyne Huisgen cycloaddition and using a peptide containing an alkyl chain with a thiol.

It was concluded that the best strategy is using a thiol-containing peptide, because is the most straightforward method, however is necessary to mix the peptide with another thiol with hydrophilic groups. The methodology that presented more problems during the optimization of the process was through EDC/NHS activation.

The GNP obtained were analysed by TEM, DLS, and also the zeta potential was measured, to assess the correct immobilization of the peptides: In the case of the GNP functionalized though Huisgen cycloaddition, the hydrodynamic size increased from 35 nm to 57 nm, accompanied by an increase in the zeta potential from -24 mV to -5 mV. The GNP synthesized with a thiol-bearing peptide showed an hydrodynamic size of 46.12 nm, and the found zeta potential was -29.6 mV

Gold nanoparticles decorated with cyclic peptides for antimicrobial and anticancer applications

Mafalda Rodrigues,[a,b] Silvia Vilà,[c] Lidia Feliu,[c] and Lluïsa Pérez-García.[a,b,*]

a Departament de Farmacologia i Química Terapèutica, Universitat de Barcelona, Av. Joan XXIII, s/n 08028 Barcelona, Spain; Fax: +34 934024539, Tel: +34 934035849, E-mail: mlperez@ub.edu

b Institut de Nanociències i Nanotecnologia IN2UB, Universitat de Barcelona, 08028 Barcelona, Spain.

c Laboratori d'Innovació en Processos i Productes de Síntesi Orgànica (LIPPSO), Departament de Química, Universitat de Girona, Campus Montilivi, 17071 Girona, Spain

1. Introduction

In the research for strategies in cancer therapy, peptides rise as promising tools. Cell-penetrating peptides are being used to target tumours and improvement in the internalization of markers or chemotherapeutic drugs can be obtained by using cyclic peptides that can enhance the uptake and selectivity.[1] Additionally many antimicrobial peptides appear as promising anticancer agents. Antimicrobial peptide is a term that generally described the small peptide molecules that are able to kill or inhibit the growth of microorganisms. They normally are composed of 10-50 amino acid residues and possess positive charges which are the responsible for the interaction with the membranes from the microorganisms. They can show activity against bacteria, virus and fungi.[2] This is important as they appear as an alternative against bacteria which nowadays present multi-resistance against many known antibiotics.[3] These peptides can be found in nature (many have been isolated from plants, insects, amphibians, humans and bacteria),[3] where they compose one of the defence mechanisms. Peptides that possess anticancer activity found in nature can be easily synthesized in solid-phase,[4] but the screening of libraries of synthetic peptides is also performed in order to discover new molecules that have anticancer activity.[5]

Recent examples of peptides with anticancer activity found in literature include, among others, cyclic peptides that showed high cancer activity against a human Burkitt's lymphoma cell comparing with their linear counterparts,[6] peptides able to specifically bind to LDL receptor present in acute myeloid leukemia,[7] cationic antimicrobial peptides with activity against squamous skin cancer cells and also human keratinocytes,[8] peptides synthesized in the human heart that inhibit cancer cell proliferation *in vivo*,[9] peptide derivatives from a known antimicrobial peptide Ixosin-B-amide that inhibit the proliferation and cell migration of breast cancer cell line MCF-7.[10]

The advantage of using anticancer peptides in therapy is that peptides can recognize membrane

proteins in tumours and bind to them. They can also penetrate the cells and present better pharmacokinetic profiles when comparing with monoclonal antibodies which are used to target and treat cancer.[5] The mechanisms of action of the peptides include inhibition of angiogenesis, induction of apoptosis, induction of necrosis, immunomodulatory, inhibition of kinases/proteases activities and interference with functional proteins. It is thought that the anticancer activity presented by antimicrobial peptides can be linked to the glycosylation of the cell membrane of cancer cells.[11]

However, the *in vivo* delivery of the peptides to the cancer cells can be a drawback. One of the most studied solutions is the conjugation of the anticancer agents to vehicles that can target and improve the delivery to the correct site of action.[12,13] One of such vehicles that are widely studied is the gold nanoparticles (GNP). Due to their good biocompatibility and low toxicity, they are seen as good candidates for delivery systems for cancer treatment.[14,15] Besides the ability to incorporate drugs,[16,17] they can also be conjugated with antibodies to target specific cancer cells,[18,19] or rely on the enhanced permeability and retention effect to accumulate in the tumour tissues.[20]

In this work, we chose from a library of cyclic decapeptides, found to have antimicrobial activity and high cytotoxicity against HeLa cells,[21] the sequence that presented the best results in terms of anticancer activity while showing low haemolytic activity and also low cytotoxicity to normal fibroblasts. The aim was to immobilize them in gold nanoparticles (GNP) that would act as vehicle and also to improve the action on tumours through accumulation on the cancer tissue. To achieve so, different methodologies for the conjugation of the peptides to the GNP were used assessed, in order to determine the best strategy for the peptide immobilization.

2. Results and Discussion

In this work the main goal was the decoration of GNP with cyclic peptides, which are known to have antibacterial and antitumor activity.[21] We sought to improve their bioavailability through the immobilization on GNP, and after that, the next step would be targeting of specific cells or tissues by the GNP, through the conjugating with the adequate antibody or other biomolecules.

Since these are synthetic peptides, we can tailor them in order to introduce certain modifications. However, the first approach pursued took advantage of the fact that the peptides already have amine groups on their structure, that could be further used for their immobilization to an adequate functional group on the surface of the GNP. The used cyclopeptides are composed of 10 amino acid residues, with a cyclic conformation and the following amino acid sequence: K-K-L-K-K-F-K-K-L-Q.

Two different strategies to obtain water-soluble GNP were used for this study: in the first one, the GNP were synthesized by the citrate reduction method and then the citrate was exchanged

by the desired thiol. The citrate, which stabilizes the gold core through electrostatic interactions, is replaced by the thiols because they have high affinity for gold, which forms a monolayer through quasi-covalent bond. The second GNP were synthesized by a modification of the method developed by Kimura *et al*.[22,23] The synthesis is performed in methanol in the presence of the thiol that stabilizes the GNP. The difference between both of them is mainly in the synthetic strategy, and the fact that the second method avoids the additional step of replacing the citrate by the thiol. Both synthesized GNP were observed by TEM, to assess their shape and size. **Figure 1** shows the micrographs obtained for the GNP synthesized by the citrate reduction method and the ones obtained by direct synthesis with MUA in methanol.

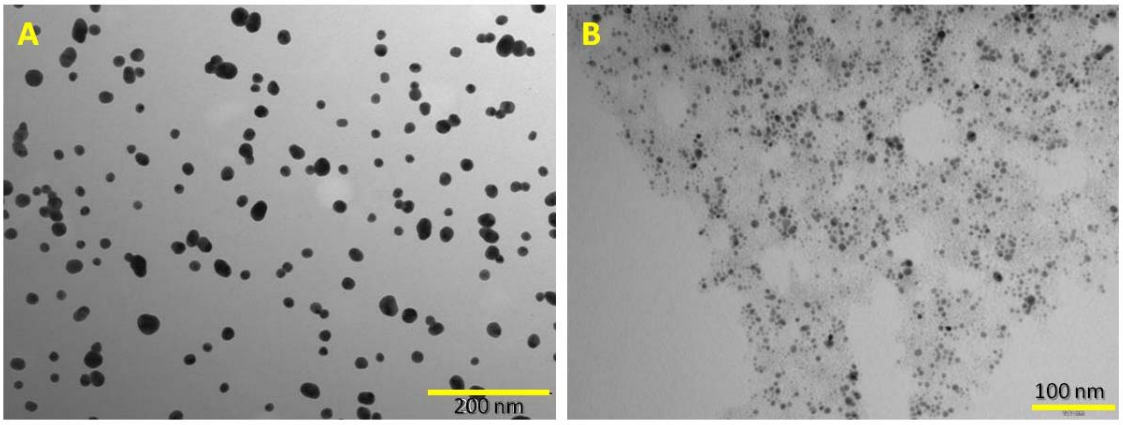

Figure 1: TEM micrograph of GNP synthesized by citrate reduction (A) and synthesized with MUA in methanol (B).

We can see from the images that both GNP have spherical shape, but the GNP synthesized in methanol present some GNP with bigger sizes than the average. The measured sizes of the gold cores of the GNP synthesized by citrate reduction and with MUA in methanol are 18 ± 3 nm and 7 ± 2 nm, respectively. The GNP obtained by citrate reduction were also used for citrate exchange with the other thiols.

Immobilization of peptides through EDC/NHS activation

The first approach that was tested was based on using a thiol with a carboxylic acid group (MUA). After the stabilization of the GNP with this thiol, the carboxylic acid group of the MUA is activated with NHS to later react with free amines from amino acid residues from the peptides (**Scheme 1**). The concentration of the coupling agents (EDC and NHS) is an important factor because if too many carboxylic groups react, the equilibrium is disrupted and the GNP end up precipitating or aggregating. Different amounts of EDC/NHS were tested until the conditions were found where the GNP solution maintained its stability.

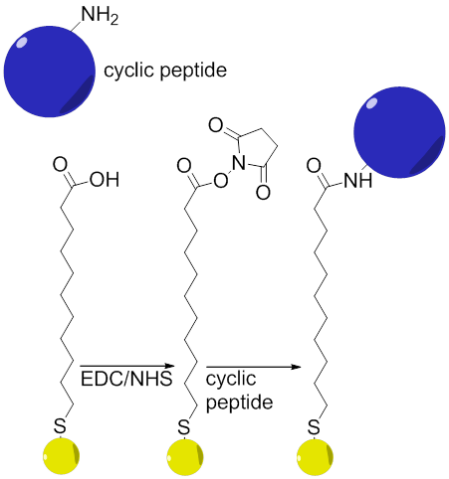

Scheme 1: GNP with MUA, activation of the carboxylic group with EDC and NHS, and immobilization of peptide through amine group.

Initially two peptides were tested. One of the peptides has a lysine group modified with fluorescein, and their structures are shows in **Figure 2**.

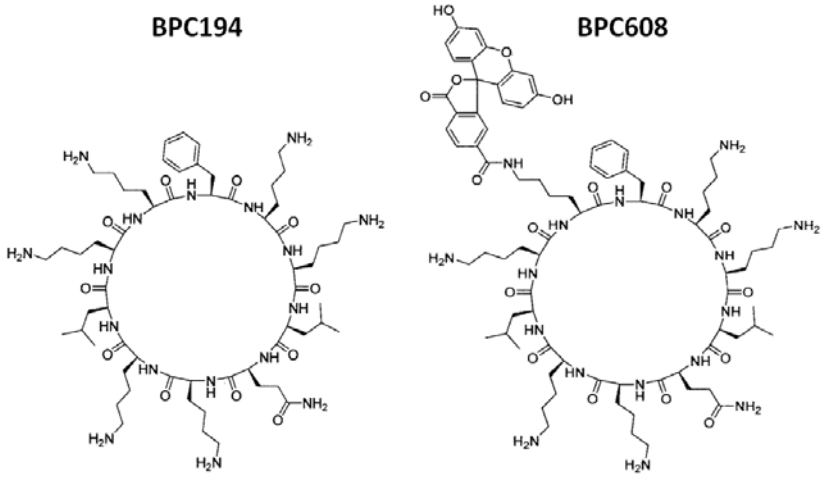

Figure 2: Cyclic peptides with free amines without fluorescein BPC194 and with fluorescein BPC608.

Upon addition of the peptides, the GNP would aggregate, and therefore we could not obtain stable GNP with these peptides after activation. The fact that they are small molecules with a great number of amines per molecule of peptide could caused the aggregation of the nanoparticles, as the same peptide molecule is thought to act as cross-linker between different GNP and thus causing the aggregation. **Figure 3** shows a schematic representation of the possible assembly of the GNP due to the cross-linking performed by the cyclopeptides.

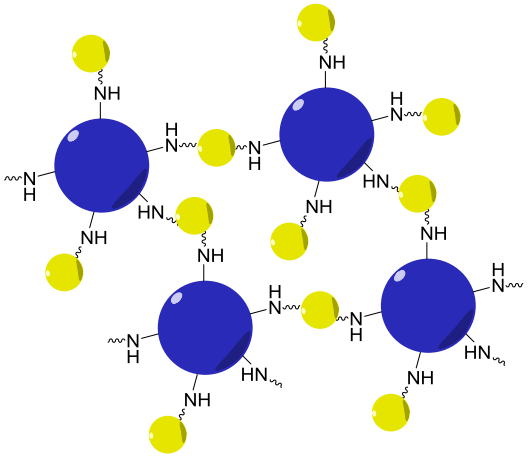

Figure 3: Schematic representation of GNP (in yellow) cross-linked by the peptides (in blue).

For this reason, after some preliminary experiments, this reaction, as it was designed, was put aside. A new strategy was devised using cyclopeptides with the same sequence as before, but with the amines from the lysine residues protected with ivDde group except the amine from the second lysine residue, left free to react with the hydroxysuccinimide group present in the GNP, thus trying to avoid the possible cross-linking between the nanoparticles. **Figure 4** shows the structures of the new peptides.

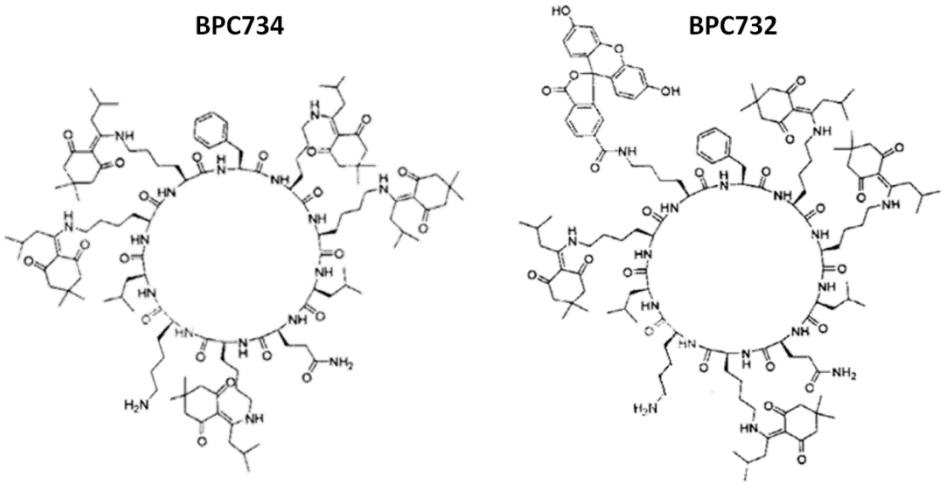

Figure 4: Cyclic peptides with ivDde-protected amines without fluorescein BPC734 and with fluorescein BPC732.

Apart from testing these new cyclopeptides, in order to assure that the conditions from the previous steps were not influencing the stability, different amounts of MUA were tested to exchange with the citrate. The solutions were analyzed by UV-visible absorption spectroscopy (UV-vis) and the size was measured by DLS, before and after the activation and addition of the peptide BPC734, and the stability of the solutions was assessed macroscopically by watching the overall appearance of the solutions along 1-2 weeks. The results are summarized in **Table 1**.

Table 1: Final concentrations of MUA for exchange with citrate, SPR absorbance peak measured by UV-visible absorption spectroscopy, hydrodynamic size measured by DLS, and peaks observed 1 hour after the addition of the peptide, and overnight (ON), size measured by DLS and stability.

MUA (% m/v)	**λ_{SPR}**	**Size (nm)**	**UV-vis 1h**	**UV-vis ON**	**Size (nm)**	**stability**
0.022	524.0	31,7 ± 1,2	528,0 259,0	536,0 343,0		flocculation
0.066	524.0	23,8 ± 1.4	527,5 259,0	535,5 259,0		flocculation
0.10	527.5	24,6 ± 0.1	528,0 259,0	527,5 260,5	45.2 ± 0.2	flocculation
0.20	527.5	26,6 ± 0.9	528,0 259,5	528,0 258,5	37.8 ± 1.0	**transparent**
0.40	525.5	33,4 ± 0.1	528,0 258,5	527.5 259,5	47.32 ± 1.7	**transparent**

As it could be observed, the amount of MUA used is important for the final stabilization of the GNP; when lower concentrations of thiol were used, the final solution appeared red and transparent, but after activation by the end of some days the solution would show aggregates. We concluded that a final concentration of MUA in solution for the exchange process had to be at least 0.2%. The solution with 0.1% appeared more stable, but through a longer time length also presented flocculation. The fact that the peak typically found in peptides around 250 nm is found and that the hydrodynamic size of the nanoparticles increased by approximately 12-14 nm suggests that the peptides was immobilized.

Because the lysine groups are protected, the peptide does not have enough ionisable groups that contribute to the electrostatic stabilization of the solution. We thus tried resuspending them in the solvents in which the peptides are more soluble such as DMF and DMSO. This however did not help increase the stability.

We also assessed the exchange of citrate with MUA dissolved in THF with success.

Regarding the GNP that were synthesized in methanol with MUA, the activation was performed and the two peptides BPC732 and BPC734 were added to the solution. Analysis of the UV-visible spectra of the peptides, free in solution and coupled to the GNP, shows that the typical peaks of the peptides are present in the GNP solution the UV-visible absorption spectra are shown in **Figure 5**.

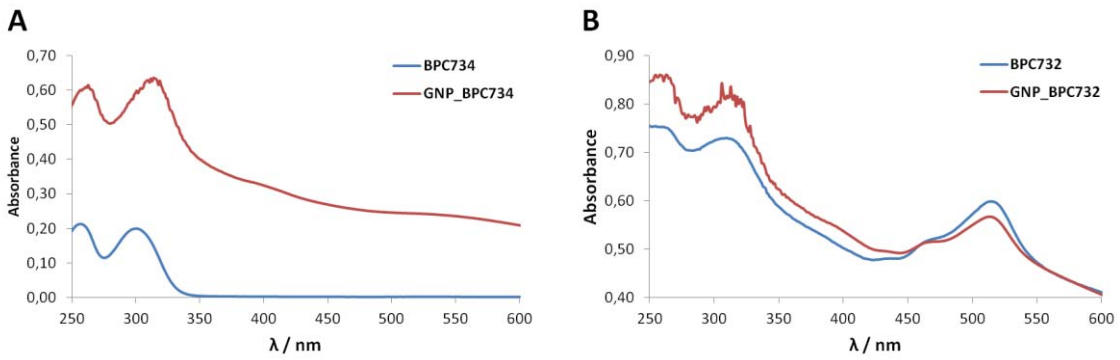

Figure 5: UV-visible spectra of peptide BPC734 (A) and fluorescein-conjugated peptide BPC732 (B), free in solution and coupled to GNP.

Observing the spectra of the free and coupled peptides, it is visible the peaks of the peptides present in the samples of GNP. These results make us think that the peptide was successfully immobilized on the GNP. In the case of the peptide with fluorescein, the peak of the fluorophore overlaps the SPR peak of the GNP (≈ 520 nm).

Immobilization of peptides through "click" chemistry

The second strategy for the immobilization of peptides was through an azide-alkyne Huisgen cycloaddition reaction between a peptide with an alkyne group with a thiol, previously immobilized, that has an azide function at the terminal end. The structure of the used cyclopeptide is shown in **Figure 6**. The structure is very similar to the previously ones, except that in this case an alkyne group was introduce.

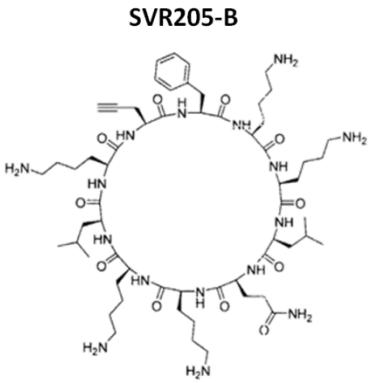

Figure 6: Cyclic peptide with alkyne group: SVR205-B.

GNP were synthesised by two different methods: the Brust-Schiffrin method and by the citrate reduction method. The first ones are synthesized with hexadecanethiol, and some molecules of thiolate are exchanged with a second thiol (in our case, the thiol with the azide function). Previous analysis by nuclear magnetic resonance (^{1}H NMR) showed an approximate rate of 1:6.5 of thiol-azide/hexadecanethiol on the GNP surface. However these GNP were not soluble

in aqueous medium, and therefore this strategy was no longer followed. In the second case, the GNP were synthesised by the citrate reduction method and afterwards were modified with two different thiols bearing the azide group, as described previously with MUA. The alternative synthesis in methanol could not be performed with the thiol with azide group because the reducing agent that is used for the formation of the GNP also reduces the azide group.

Scheme 2 shows the main strategy for the peptide immobilization on the GNP surface. Two different thiols were used: without PEG (AUT) and with PEG (MEG), to see if the PEG groups would influence in some way the solubility of the GNP in aqueous medium, but no differences were observed. After the functionalization of the GNP with the thiols, both proved to be water soluble. However, the GNP functionalized with MEG presented lower stability after addition of the peptide.

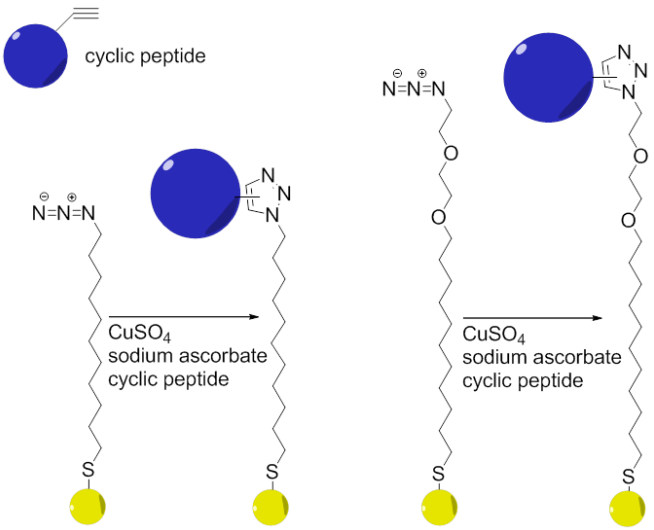

Scheme 2: Immobilization of the peptide bearing an alkyne group onto GNP (obtained by citrate reduction) using two different thiol molecules with azide group: one without PEG and other with PEG.

In the case of these peptides, there are no characteristic peaks that can be detected by UV-visible absorption spectroscopy. So we used other techniques to assess the immobilization of the peptides on the GNP. Dynamic Light Scattering (DLS) was used to detect the hydrodynamic size before and after functionalization, and in replicate samples, we observed an increase of the diameter from around 35 nm to 57 nm. The change in the size was accompanied by an increase in the zeta potential which changed from -24 mV to -5 mV.

Additionally, we also attempted to increase the amounts added of catalysers in order to obtain an improved immobilization of the peptide. Therefore, different conditions from the ones used initially were tested. The summary is shown in **Table 2**.

The results obtained with different amounts of catalyst showed us that, as in the case of the activation with EDC/NHS, it is also important that the amount added is not very high. The GNP from experiment 1 were analysed and showed an hydrodynamic size of 73 nm, that was bigger

than the obtained previously with lower amount of catalysts, but the increase in the zeta potential was lower (-12 mV).

Table 2: Experiments performed with different amounts of $CuSO4.5H_2O$, sodium ascorbate and SVR205-B for optimization of conditions. $CuSO4.5H_2O$ 20 mM, 90 µL of sodium ascorbate 10 mM and 75 µL of SVR205-B

Experiment	$CuSO4.5H_2O$ 20 mM	sodium ascorbate 10 mM	SVR205-B 300 µg/mL	Stability
1	75	270	60	Stable
2	150	540	120	Aggregated
3	225	810	180	Aggregated
4	300	1080	240	Aggregated

Besides the peptides, the addition of PEG with an alkyne group was also attempted. The aim was to prove that we could use one thiol with azide for the functionalization of the GNP and later introduce a mixture of peptide and PEG, both with alkyne groups, to obtain GNP with two different molecules on the surface. Surprisingly after some trials we could not obtain GNP that were stable in aqueous media after the reaction with the PEG containing molecule. We therefore tried an alternative: we exchanged the citrate in the GNP with a mixture of MUA and AUT. The obtained GNP appeared stable and showed and hydrodynamic size around 36 nm, which is in agreement with the sizes obtained so far for similar GNP with MUA or AUT alone. AUT would be used to immobilize PEG with an alkyne and MUA to immobilize a peptide. The outcome was the same as before: the addition of the PEG along with the catalyser resulted in the aggregation of the GNP. We tried adding first the peptide to the MUA, but the addition of EDC/NHS also caused the aggregation of the GNP.

Immobilization of peptides through thiol group

The final and more straightforward strategy was the synthesis of GNP with peptides with thiol group. This strategy was the most direct one, because it would allow obtaining the GNP with the peptides directly, without any additional immobilization steps. Two peptides were also synthesized, one with fluoresceín (BPC736) and other without fluoresceín (BPC738). Their structures are represented in **Figure 7**.

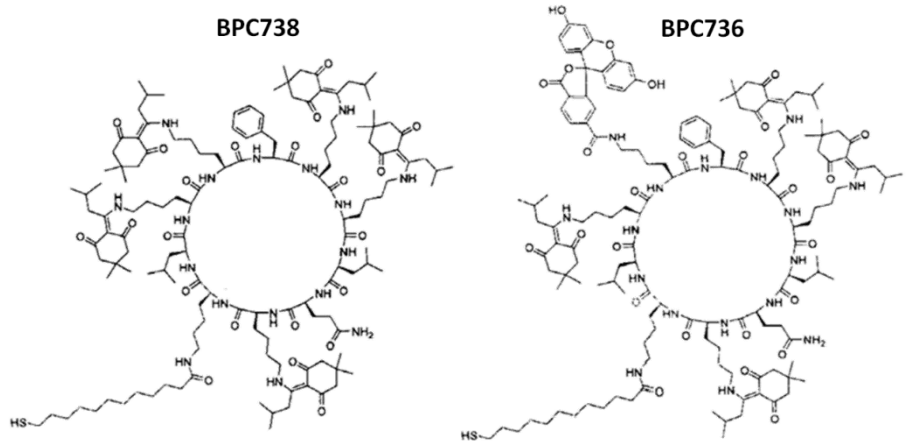

Figure 7: Cyclic peptides with a thiol group and with ivDde-protected amines without fluorescein BPC738 and with fluorescein BPC736.

Initially the same strategy was used consisting of the interchange between citrate and the thiol. However, because a big amount of thiol is necessary to obtain a satisfactory covering of the GNP meaning that a part of the thiol is discarded, which is not desired. Therefore, the synthesis was performed in methanol using the same method developed by Kimura *et al* as described before.[22,23] The thiol with the peptide was mixed with a thiol with PEG (MEG). The process was performed using the peptide and the PEG-containing thiol with ratio of 1:20 and 1:10. This way, we assure the presence of hydrophilic groups (PEG) that will render water-soluble GNP. We also performed the synthesis with other thiols without PEG, to assess alternatives in the synthesis, due to the fact that the purification was hard due to very good solubility in water. Therefore, the synthesis was performed changing MEG with MUA and with 11-mercaptoundecanol. The GNP obtained with MUA and BPC738 tended to aggregate with time, and the GNP obtained with BPC738 and 11-mercaptoundecanol showed poor solubility in water.

The GNP obtained with MEG and BPC738 were observed by TEM, to determine the size of the core. **Figure 8** shows a micrograph of the GNP. It is visible that the obtained GNP appear monodisperse, and present a spherical shape. The measured size of the gold core was 4 ± 1 nm, which explains why no evident peak of SPR was visible by UV-visible absorption spectrosocpy. The hydrodynamic size determined by DLS was 46.12 nm, giving evidence of the presence of the thiols on the surface of the GNP, and the found zeta potential was -29.6 mV.

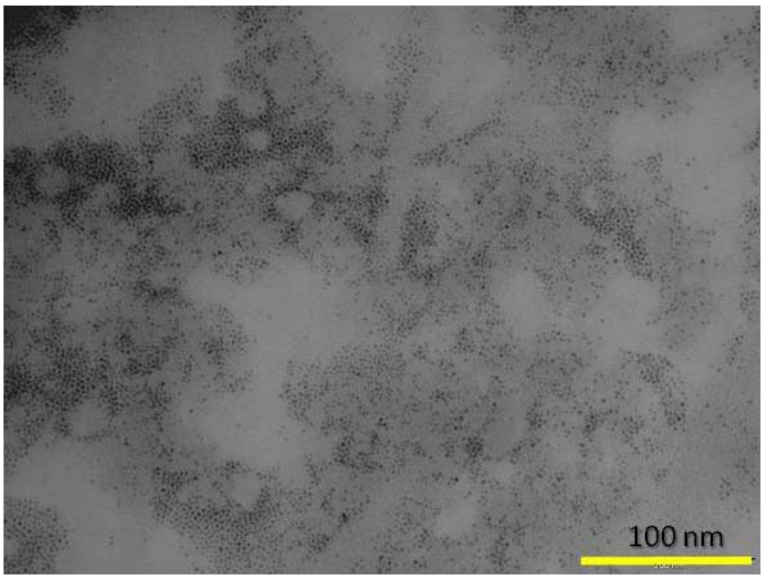

Figure 8: TEM micrograph showing GNP synthesized in methanol with BPC738

3. Conclusions

From all the alternative methods, it is clear that the direct immobilization of peptides with thiol group is the better strategy, because less amount of peptide can be used (and also avoiding waste of peptide) and is also faster. The purification is however less straightforward, due to their high solubility in water, which makes it difficult to purify by centrifugation and washing. The second method that also showed good results with fewer drawbacks is through "click" chemistry. The process was repeated many times and the results obtained by DLS are reproducible. The process which presents more drawbacks is the activation with EDC/NHS. The GNP functionalized with MUA and conjugated with the peptides with free amines showed no stability, which forced us to use peptides with protected amine groups except one to react with the thiol. The absence of charges leads to sedimentation of the GNP with time, and also means that the GNP need additional processing for the deprotection of the amine groups, which are protected with ivDde groups. This process is normally performed by adding hydrazine.
The next step would be testing the activity of the peptides immobilized on the GNP, by performing *in vivo* assays which are yet to be done.

4. Materials and methods

All reagents were of analytical grade. $CuSO_4.5H_2O$, $HAuCl_4.3H_2O$, $NaH_2PO_4.2H_2O$, $Na_2HPO_4.12H_2O$, phosphate buffered saline (PBS), sodium ascorbate, sodium azide, sodium borohydride, sodium citrate tribasic dihydrate, Tween 80, (*N*-(3-Dimethylaminopropyl)-*N*′-ethylcarbodiimide hydrochloride (EDC), *N*-hydroxysuccinimide (NHS), S-(11-bromoundecyl)thioacetate, 2-(2-aminoethoxy)ethanol and 11-mercaptoundecanoic acid (MUA)

were purchased from Sigma-Aldrich. (1-Mercaptoundec-11-yl)hexa(ethylene glycol) (MEG) and (1-Mercaptoundec-11-yl)hexa(ethylene glycol) azide (MGA) were purchased from Prochimia. Phosphate buffer (PB) 10 mM pH 6.8 was prepared by mixing stock solutions of $NaH_2PO_4.2H_2O$ and $Na_2HPO_4.12H_2O$ in distilled water. The cyclopeptides were prepared following the solid-phase method using standard Fmoc chemistry as described elsewhere.[21,24] 11-azidoundecilthiol (AUT) was prepared as described elsewhere.[25]

UV-visible absorption spectra were obtained on UV-1800 Shimadzu UV Spectrophotometer. Transmission electron microscopy (TEM) images were obtained with a transmission electron microscope JEOL 1010 at 80 kv. The images were captured by a Megaview III Soft Imaging System camera. The size of the nanoparticles was measured with the Analysis software (Olympus). The hydrodynamic size of the nanoparticles was detected by Dynamic Light Scattering (DLS) and the zeta potential was determined by Electrophoretic Light Scattering (ELS), using a Zetasizer Nano ZS series (Malvern Instruments, UK).

All the glassware was cleaned with aqua regia (3:1 HCl/HNO_3) prior to its use with the GNP. MilliQ water (Millipore system) was used throughout the work.

4.1. Preparation of Gold Nanoparticles by citrate reduction method (GNP)

GNP were prepared using the citrate reduction method. Briefly 20 mg of $HAuCl_4.3H_2O$ were added to 35 mL of water and the solution was heated until reflux. Then, 50 mg of sodium citrate in 2 mL of water was added with vigorous stirring and the reflux was continued for 15 minutes. The solution was then left to cool to room temperature before further use.

4.2. Functionalization of GNP with thiol

To functionalize the GNP with MUA, the as prepared GNP were dissolved to a concentration of 0.8 nM and final volume of 2 mL with water, and 2 mL of PB with 2% Tween 80 were added. After stirring for 15-20 minutes, 3 mL of MUA solution in 1:2 ethanol/water were added and left stirring overnight. The solution was then centrifuged 15 minutes at 13400 rpm, washed with PB with 2% Tween 80 and resuspended in equal volume of PB. The same process was used with BPC738 and BPC 736, using 2 mg of thiol in 3 mL of 1:2 ethanol/water.

4.3. Preparation of GNP with MUA in methanol

The synthesis was done as described elsewhere.[22,23] Briefly 44 mg of MUA were dissolved in 5 mL of methanol and 39.4 mg of $HAuCl_4.3H_2O$ in 10 mL of methanol were added. After stirring for 20 minutes, 5 mL of an aqueous solution of $NaBH_4$ (0.3 M) was added dropwise with continuous stirring. The stirring was continued for 1 hour, and the solution was centrifuged 15

minutes at 13400 rpm. The supernatant was discarded and the pellet was washed with methanol and then resuspended in water. To further purify the GNP solution, the solution was dialysed for 4 days.

4.4. Immobilization of peptides in GNP with MUA using EDC/NHS

The immobilization was performed as follows: the GNP solution was diluted with PB pH 6.8 with 2% Tween 80 until the SPR peak showed an absorbance of 0.5; then, for each mL of GNP solution, 0.43 mg of EDC and 1.5 mg of NHS were added and the solution was stirred for 30 minutes. The solution was centrifuged at 13400 rpm for 15 minutes and the pellet resuspended in PB. 5.6 µg of BPC734 was added, and after 3 hours with stirring 250 ng of 2-(2-aminoethoxy)ethanol were added. The solution was left stirring overnight, then Tween 80 was added for a final concentration of 2%, and the solution was centrifuged 15 minutes at 13400 rpm, washed with PB pH 6.8 with 2% Tween 80 and resuspended in PB.

4.5. Preparation of GNP with peptides in methanol

GNP with peptides BPC738, bearing thiol groups, were prepared as follows: 4.6 mg of BPC738 together with 18.7 mg of MEG were dissolved in 1 mL of methanol and 7.8 mg of $HAuCl_4.3H_2O$ in 2 mL of methanol were added under stirring. After 20 minutes, 1mL of an aqueous solution of $NaBH_4$ (0.3 M) was added dropwise with continuous stirring. After stirring for 1 hour, the solution was dialyzed. The same procedure was followed using 9.2 mg of BPC738.

4.6. Functionalization of GNP with AUT and immobilization of peptides by "click" chemistry

To functionalize the GNP with AUT, the prepared GNP by citrate reduction were dissolved to a concentration of 1.6 nM and final volume of 2 mL with water, and 2 mL of PB with 2% Tween 80 were added. After stirring for 15-20 minutes, 0.250 mL of AUT solution 20 mg/mL in 1:1 ethanol/water were added and left stirring overnight. The solution was then centrifuged 15 minutes at 13400 rpm, washed with PB with 2% Tween 80 and resuspended in equal volume of water. To 3 mL of the functionalized GNP solution in water, it was added 22.5 µL of $CuSO4.5H_2O$ 20 mM, 90 µL of sodium ascorbate 10 mM and 75 µL of SVR205-B 300 µg/mL. The solution was left stirring overnight, then 40 µL of Tween 80 were added prior to centrifugation at 13400 rpm for 15 minutes. The pellet was washed with PB with 2% Tween 80 and the pellet was resuspended in PB.

References

1. J. K. Ko and K. K. Auyeung, *Curr. Med. Chem*., 2014, **21**, 2346–2356.
2. L.-O. Brandenburg, J. Merres, L.-J. Albrecht, D. Varoga and T. Pufe, *Polymers (Basel*)., 2012, **4**, 539–560.
3. J. D. Steckbeck, B. Deslouches and R. C. Montelaro, *Expert Opin. Biol. Ther*., 2014, **14**, 11–14.
4. P. W. R. Harris, S.-H. Yang, A. Molina, G. López, M. Middleditch and M. A. Brimble, *Chemistry*, 2014, **20**, 5102–5110.
5. D. Wu, Y. Gao, Y. Qi, L. Chen, Y. Ma and Y. Li, *Cancer Lett*., 2014, **351**, 13–22.
6. A. Sivertsen, V. Tørfoss, J. Isaksson, D. Ausbacher, T. Anderssen, B.-O. Brandsdal, M. Havelkova, A. E. Skjørholm and M. B. Strøm, *J. Pept. Sci.,* 2014, **20**, 279–291.
7. M. Liu, W. Li, C. A. Larregieu, M. Cheng, B. Yan, T. Chu, H. Li and S. Mao, *Mol. Pharm.,* 2014, **11**, 2305–2312.
8. N. Do, G. Weindl, L. Grohmann, M. Salwiczek, B. Koksch, H. C. Korting and M. Schäfer-Korting, *Exp. Dermatol*., 2014, **23**, 326–331.
9. D. L. Vesely, *Anticancer Res*., 2014, **34**, 1459–1466.
10. Y.-C. Hsiao, K.-S. Wang, S.-H. Tsai, W.-T. Chao and F.-D. T. Lung, *Bioorg. Med. Chem. Lett*., 2013, **23**, 5744–5747.
11. Y.-Y. Han, H.-Y. Liu, D.-J. Han, X.-C. Zong, S.-Q. Zhang and Y.-Q. Chen, *Biochem. Pharmacol.,* 2013, **86**, 1254–1262.
12. O. Farokhzad and R. Langer, *ACS Nano*, 2009, **3**, 16–20.
13. T. Kim and T. Hyeon, *Nanotechnology*, 2014, **25**, 012001.
14. J. P. M. Almeida, E. R. Figueroa and R. A. Drezek, *Nanomedicine*, 2014, **10**, 503–514.
15. R. Cao-Milán and L. M. Liz-Marzán, *Expert Opin. Drug Deliv*., 2014, **11**, 741–752.
16. D. N. Heo, D. H. Yang, H.-J. Moon, J. B. Lee, M. S. Bae, S. C. Lee, W. J. Lee, I.-C. Sun and I. K. Kwon, *Biomaterials*, 2012, **33**, 856–66.
17. W.-H. Chen, X.-D. Xu, H.-Z. Jia, Q. Lei, G.-F. Luo, S.-X. Cheng, R.-X. Zhuo and X.-Z. Zhang, *Biomaterials,* 2013, **34**, 8798–807.
18. A. Kumar, H. Ma, X. Zhang, K. Huang, S. Jin, J. Liu, T. Wei, W. Cao, G. Zou and X.-J. Liang, *Biomaterials,* 2012, **33**, 1180–9.
19. T. Stuchinskaya, M. Moreno, M. J. Cook, D. R. Edwards and D. A Russell, *Photochem. Photobiol. Sci*., 2011, **10**, 822–831.
20. M. Ferrari, *Nat. Rev. Cancer*, 2005, **5**, 161–71.
21. L. Feliu, G. Oliveras, A. D. Cirac, E. Besalú, C. Rosés, R. Colomer, E. Bardají, M. Planas and T. Puig, *Peptides*, 2010, **31**, 2017–2026.
22. W. Shi, Y. Sahoo and M. T. Swihart, *Colloids Surfaces A Physicochem. Eng. Asp.,* 2004, **246**, 109–113.
23. S. Chen and K. Kimura, *Langmuir,* 1999, **1**, 1075–1082.
24. A. Afonso, L. Feliu and M. Planas, *Tetrahedron*, 2011, **67**, 2238–2245.
25. W. J. Sommer and M. Weck, *Langmuir*, 2007, **23**, 11991–11995.

3.7. Appendix: Functionalization of surfaces with cyclic peptides

Prior to the immobilization of the synthetic cyclopeptides in the GNP (Chapter 3.6), some experiments performed on surfaces were done to assure that it could be possible to perform the reactions between the thiols' and peptides' functional groups in the surface of the gold nanoparticles. All these preliminary studies were not included in the manuscript in preparation, for they would not fit entirely in the main goal of the work.

The first peptides that were tested had only amine groups, from the lysine amino acid residues. Has we had no means of detecting them easily on surface, the cyclopeptides were conjugated fluoresceín and the surfaces observed under an optical fluorescence microscope.

Silicon surfaces with patterned polysilicon squares were initially used. The procedure is the one described in Chapter 4 of this work, for the immobilization of proteins through their amine groups from amino acid residues, using TESUD. **Figure 3.18** shows images obtained by optical fluorescence microscopy of surfaces that were functionalized with the fluoresceín-conjugated cyclopeptide and its non-conjugated counterpart, which would serve as negative control.

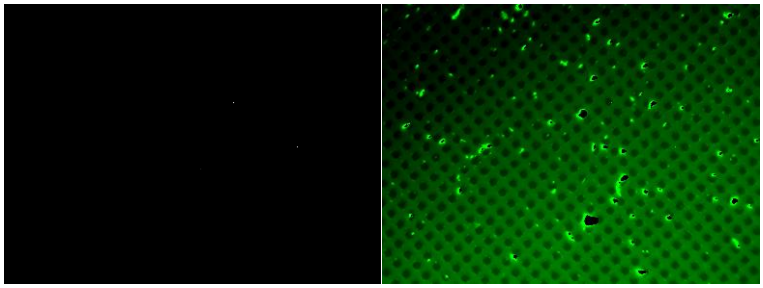

Figure 3.18: Optical microscopy images of silicon surface with cyclopeptide BPC194 (left) and fluoresceín-conjugated cyclopeptide BPC608, with 400x magnification and 30 seconds of exposure time.

It can be clearly seen the fluorescence in the case of the conjugated cyclopeptide but not on the non-conjugated, which confirms that is not due to auto-fluorescence of the material, and also indicating that the amine groups are available for covalent binding. The next step was the immobilization of the peptides on gold surfaces and analysis by MALDI-TOF-MS, but due to the small molecular weight of the molecule, the results obtained were never conclusive.

The second class of cyclopeptides that were provided had an alkyne group in one of the amino acid residues, to immobilize through a Huisgen cycloaddition reaction with azide group from the thiol. Because it was synthetically complicated to conjugate these cyclopeptides with a fluorophore, the first proofs were done with an alternative molecule from the coumarin family, that was modified in order to bear also an alkyne group (**Figure 3.19**).[220] This compound presented fluorescence in the ultraviolet range, which could not be observed through the

fluorescence microscope due to lack of appropriate filters. Therefore, the fluorescence was detected using a spectrofluorometer.

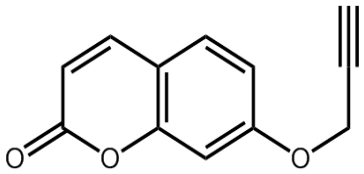

Figure 3.19: Structure of the Coumarin molecule bearing an alkyne group

The surfaces used were again the silicon surfaces with patterned polysilicon squares, which were functionalized with a silane beairng an azide group, and through a Huisgen cycloaddition the coumarin was immobilized. **Figure 3.20** show the fluorescence emission spectrum obtained.

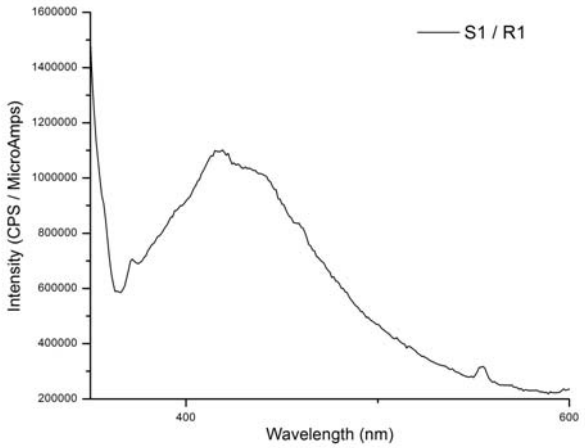

Figure 3.20: Fluorescence emission spectrum of coumarin immobilized on silicon surface through a Huisgen cycloaddition reaction.

Besides this experiment, after each step, the surface was analysed using a goniometer (THETALITE100 with the software One Attention, Finland)to measurethe static contact angles in order to determine the hydrophobicity of the modified surfaces. Values of the contact angle on at least three samples were measured to give statistical significance. The results are shown on **Table 3.1**

Table 3.1: Contact angle measurements for the different surfaces, after each of the steps required for the coumarin immobilization.

	Contact angle
Activation	18.2 ± 1.7
Silane (Functionalization)	71.3 ± 2.9
Coumarin (Immobilization)	62.9 ± 1.4

It is clear the presence of the silane, due to the drastic change in the contact angle, that rose from 18.2 (highly hydrophilic surface) to 71.3 (hydrophobic). However, after immobilizing coumarin, the contact angle showed a lower value. The next step was to perform the same functionalization and immobilize the cyclopeptide SVR205-A (**Figue 3.21**) also on silicon surface.

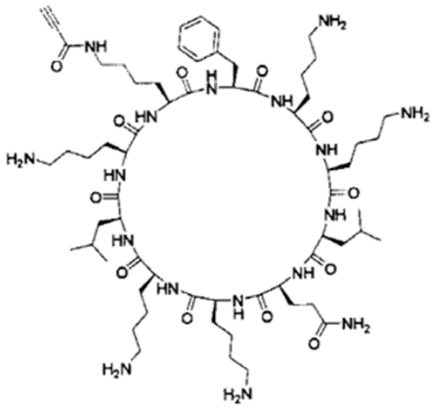

Figure 3.21: Structure of the cyclopeptide SVR205-A.

The successful immobilization was assessed again through contact angle measurements. The results are shown in **Table 3.2**.

Table 3.2: Contact angle measurements for the silicon surfaces, after each of the steps required for the cyclopeptide SVR205-A immobilization.

	Contact angle
Activation	8.23 ± 0.2
Silane (Functionalization)	72.3 ± 2.4
SVR205-A (Immobilization)	45.1 ± 2.6

It is visible from these results that the contact angle decreased after the cyclopeptide immobilization, and the decrease was higher than the one obtained for the coumarin, possibly

because the cyclopeptide, unlike the coumarin, has polar groups that are more hydrophilic. After having this positive result, the cyclopeptide SVR205-A was then immobilized on top of a gold surface. The contact angle measurements were also performed for these surfaces and the results are shown on **Table 3.3**. Two different thiols were used, one that contained an ethylene glycol before the terminal azide, and other that had an alkyl chain of 11 carbons and the azide functional group.

Table 3.3: Contact angle measurements for the gold surfaces, after each of the steps required for the cyclopeptide SVR205-A immobilization, with two different thiols.

	Contact angle
Blank	57.4 ± 2.3
Thiol[a] (Functionalization)	65.9 ± 3.0
SVR205-A (Immobilization)	45.4 ± 0.9
Thiol[b] (Functionalization)	73.8 ± 1.6
SVR205-A (Immobilization)	46.1 ± 3.4

[a] thiol with ethylene glycol; [b] thiol without ethylene glycol

As can be observed, there are slight differences between the surfaces functionalized with each of the thiols, the one with ethylene glycol having a slightly lower contact angle value. The presence of the ethylene glycol renders some hydrophilic character to the surface.

Due to the poor results obtained with MALDI-TOF-MS, the surfaces were analysed by XPS. Although no quantification is possible, it can be seen the differences in each element's percentage after each immobilization step. The results are shown in **Table 3.4**.

Table 3.4: Atomic percentage for selected elements calculated from XPS spectra results.

Atomic %	Au surface	Thiol	Peptide	Peptide (2)
Au4f	53.0	34.9	13.4	15.2
C1s	42.5	55.5	64.2	61.7
O1s	<0.1	1.9	15.2	11.8
S2p	--	1.8	1.3	1.6

It is noteworthy that sulphur (from the thiol) was only detected after the functionalization with the thiol, and that the detected percentage of gold decreased with each layer of molecules on top of the surface, indicating a correct immobilization of the peptide onto the surface.

Chapter 4

Functionalization of microtools for sensing temperature and biomolecular interactions

4.1. Introduction

One can define self-assembly, in a material point of view, as the arrangement of building blocks into complex hierarchical structures in a spontaneous fashion. A self-assembled monolayer (SAM) is, therefore, the spontaneous ordered assembly of molecules through their adsorption into a surface for which it has some degree of affinity (**Figure 4.1**).[221] In the case of the silanes, the SAM is formed through covalent bond, whereas thiols will form the monolayer through chemisorption.

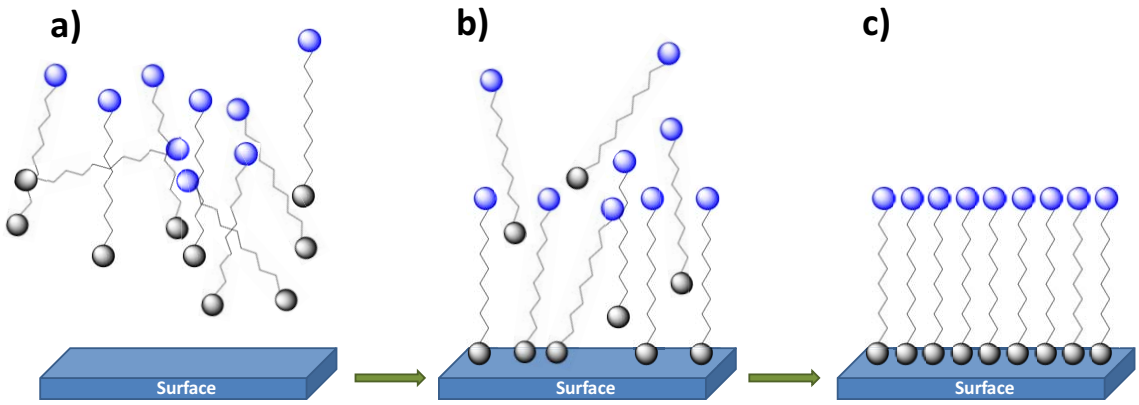

Figure 4.1: Formation of a SAM: the molecules are free in liquid or vapour phase (a), and due to their movement, they approach the surface and start adsorbing in a random way (b). Given more time, the layer of molecules packs itself on an ordered way (c).

SAM has important advantages: the preparation is rather easy, because it can be done in solution (wet chemistry) and thus no specialized equipments are necessary (for example Ultra High Vacuum or Langmuir-Blodgett Troughs) and they can be assembled on objects with different sizes and shapes, adding them specific functions (for example, Force Microscopy probes, nanowires or nanoparticles). Besides this, they make the connection between the external media and the surface's electronic or optical properties.[222]

The approach used in flat surfaces, is similar to the adsorption of ligands on the surface of metallic nanoparticles to stabilize them (like thiols on GNP).[222,223] **Figure 4.2** shows the

schematic representation of a SAM: the substrate is a surface of a specific material, on top of which the molecules assemble.

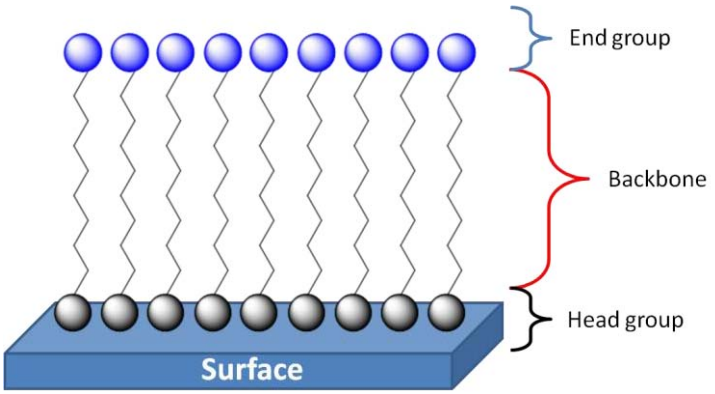

Figure 4.2: Schematic representation of a Self-assembled monolayer on a surface, with its different functional parts.

The assembly is spontaneously made by the interaction of the ***head group*** of the molecules with the substrate. The ***backbone*** is normally composed of an alkyl chain with the desired length to be used as spacer, and finally an ***end group***, which may also have a functional group that can be used to attach molecules to the SAM.[221]

This type of supramolecular assembly has been vastly exploited for sensing and diagnostic, due to the possibility of the deposited molecules to have specific functional groups that allow them to react and thus immobilize other molecules of interest.

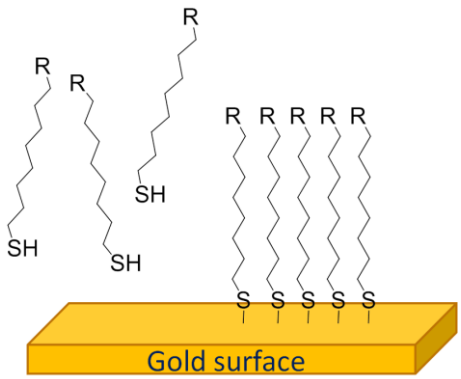

Scheme 4.1: Representation of free thiols in solution and immobilized on top of a gold surface forming the SAM through a quasi-covalent bond between sulphur and gold.

The functionalization can be made with different surfaces and molecules: one of the most commonly used are thiols, for their good affinity for gold surfaces where they form compact and well-ordered layers (**Scheme 4.1**); silicon surfaces can be activated to bear either hydroxyl

groups, to react with alkylchlorosilanes or alkylalkoxysilanes, or hydrogen, to react with 1-alkenes and 1-alkynes [224,225]

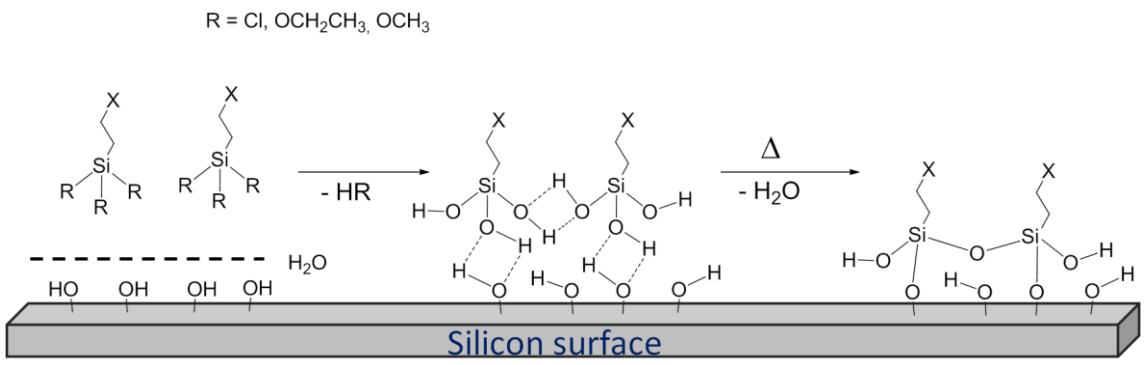

Scheme 4.2: Schematic representation of the silanization mechanism of a silicon surface, activated to bear hydroxyl groups, and a silane which can be alkylchlorosilane or alkylalkoxysilane. The silane establishes hydrogen bonds with adjacent hydroxyl groups from the surface or other silane, and water is eliminated on order to obtain a reticular network.

We can see in **Scheme 4.2** that a layer of water present on the silicon surface is responsible for the hydrolysis of the R group (which can be chloride or an alkoxy, normally methoxy or ethoxy) and the silane molecules establishes hydrogen bonds with the hydroxyl groups on the silicon surface but also with adjacent silane molecules. Upon heating, water molecules are eliminated, resulting in the formation of a reticular network.

After the SAM is formed, with an appropriate end group, the immobilization of the molecule of interest can be performed. It is noteworthy that the end group is chosen according to the functional groups present in the molecule of interest and the strategy to follow. A selection of the most common examples is described:[225,226]

- Activation with carbodiimide

In this case, the SAM has a carboxylate as end group. The carboxylate is activated with a carbodiimide, normally *N*-(3-Dimethylaminopropyl)-*N*′-ethylcarbodiimide hydrochloride (EDC) which is water-soluble. The formed O-acylurea intermediate is however prone to hydrolysis, and *N*-hydroxysuccinimide (NHS) is used to react with the intermediate forming a succinimide ester. The molecule of interest is then immobilized through reaction of amine groups with the formed succinimide ester (**Scheme 4.3**). An alternative is the formation of a SAM where the end group is already the succinimide ester.[53]

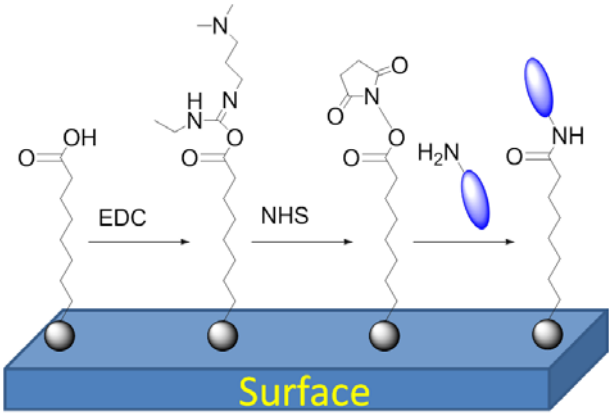

Scheme 4.3: SAM with carboxylate end group that is first activated with EDC, forming an intermediate that then reacts with NHS, and the formed ester reacts with amines forming an amide bond.

- Coupling with heterobifunctional linkers

One of the most used heterobifunctional linkers is *N*- [ε-maleimidocaproyloxy]sulfosuccinimide ester (sulfo-EMCS). This cross-linker has two groups: the sulfosuccinimide ester reacts with amines (normally present in the SAM) and the maleimide moiety reacts with thiols (**Scheme 4.4**).[227]

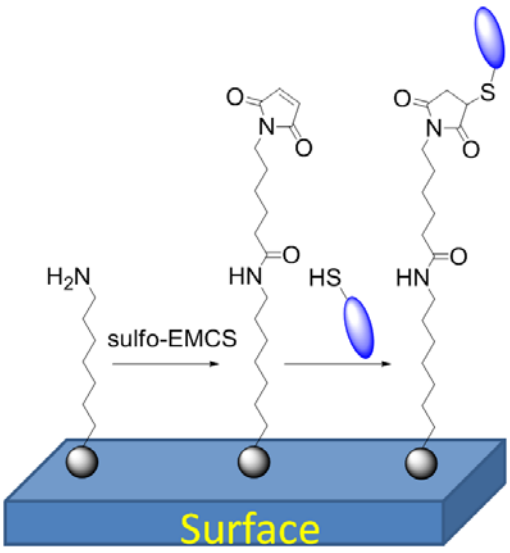

Scheme 4.4: SAM activated with the heterobifunctional linker sulfo-EMCS, which reacts with the amine through the NHS moiety forming an amide bond, and reaction of the maleimide moiety with a thiol.

- "Click" chemistry

This strategy relies on the Huisgen 1,3-dipolar cycloaddition between an alkyne and an azide group. The reaction results in the formation of a triazole, and although generally is necessary the

presence of copper Cu(I) as catalyst, strategies are being developed where instead of the alkyne being present in a linear alkyl chain it is in the cyclic form, and thus the presence of copper is not required for the reaction to occur.[228]

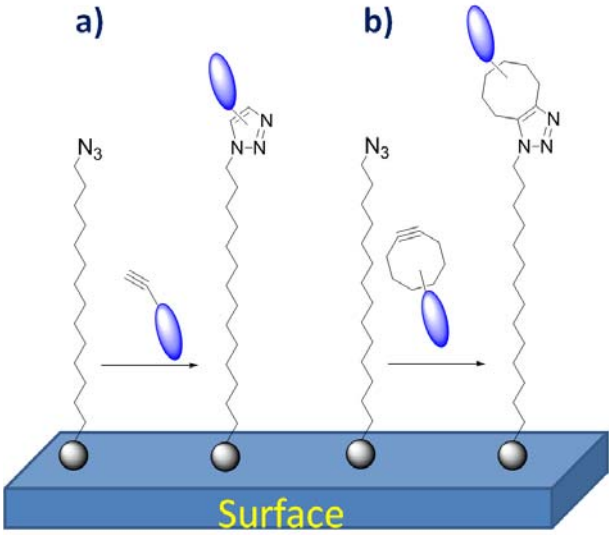

Scheme 4.5: SAM with terminal azide group, and reaction with an alkyne group on a linear alkyl chain and on a cyclic alkyl chain.

- Reaction between amine and aldehyde-derivatized surface

In this example, the surface presents a SAM with aldehyde terminal group that reacts with amines, forming an imine. The presence of a reducing agent (for example, sodium cyanoborohydride) reduces the imine to amine (**Scheme 4.6**).[48]

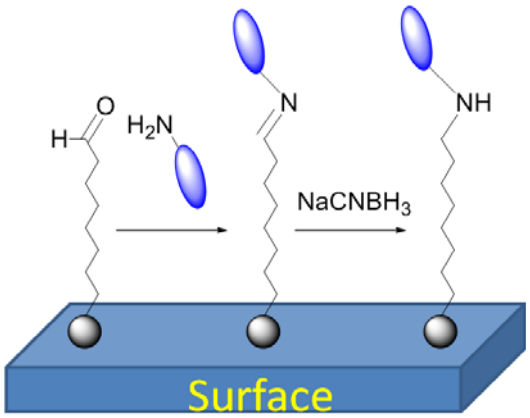

Scheme 4.6: SAM with an aldehyde group, reaction with an amine forming an imine and posterior reduction of the imine to amine by addition of the reducing agent sodium cyanoborohydride.

- Protein immobilization

Even though protein possesses amine and thiol groups on the amino acid residues, there are strategies developed specifically for their immobilization. For example, the strong interaction between biotin and avidin allows the later to be immobilized on a surface functionalized with biotin molecules; also specific is the interaction between Protein A or Protein G and antibodies from the IgG family. The recognition allows the immobilization to be oriented, because these proteins recognize specifically the region of the IgG molecules that are not involved in the antigen recognition.

It is important to characterize the SAM, whether it is after the formation of the monolayer or after the immobilization of other molecules, to assure that the process is occurring as desired. One of the simplest methods to assess changes in the surface is to determine the wettability of the surface through contact goniometry, which consists of measuring the contact angle formed by a drop of water on the surface. This method is based on the fact that the surface has different affinities for water, depending if the groups on the surface are hydrophobic or hydrophilic: more hydrophobic surface will present less "wettability" and therefore will present higher contact angles, whereas hydrophilic surfaces will have better "wettability" and thus lower contact angles.[229] **Figure 4.2** shows a clear example of a silicon oxide surface that was activated to bear hydroxyl groups, and therefore is very hydrophilic (a) and how this character changes upon the formation of a SAM of triethoxyundecanal, a silane that has an 11 carbon alkyl chain with an aldehyde function as end group, and renders the surface hydrophobic (b).

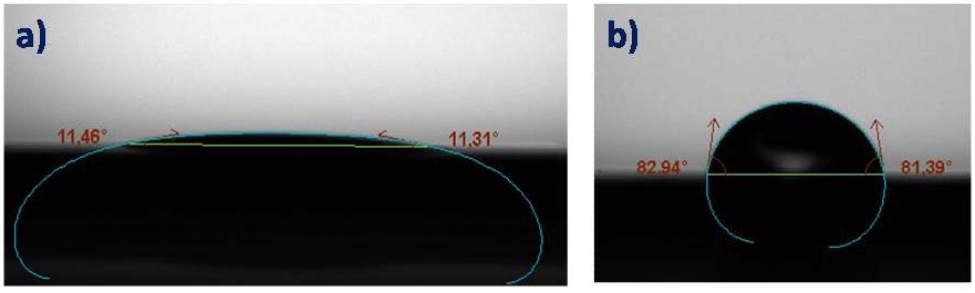

Figure 4.3: Contact angle measurement on hydrophilic (a) and hydrophobic (b) surfaces. The hydrophilic surface presents a better wetting that translates into a lower contact angle between the water drop and the surface. The opposite happens in a hydrophobic surface.

Mass spectrometry can also be used to analyze surfaces. Mrksich's group has proved this technique to be useful in the determination of the structure of the molecules that are immobilized on the surface.[230] Additionally, when the SAM was further functionalized with

other oligonucleotides, this technique can also be used to determine their presence and the hybridization with their complementary strands.[231] the advantage presented by the technique was the fact that it did not require the complementary oligonucleotides to be labelled in order to be detected. Through XPS it is possible to determine the elemental composition of the formed layers, and further analysis can highlight the nature of the bond that the elements are establishing.[227] This information is important to determine the reactions through which the molecules are immobilized. Ellipsometry measurements can be performed to determine the coverage of a surface. This technique allows the determination of the thickness of the layer being deposited, and can be used both in gold[232] and in silicon[233] surfaces. AFM is also a valuable tool in the characterization of SAM. In this technique, a probe located in a cantilever scans the surface, sensing the topography of the sample. The data obtained can be used to form an image of the surface and to determine its roughness.[227] Recently, techniques such as Quartz Crystal Microbalance (QCM) can also be used to determine not only the coverage but also the kinetic of the binding. The measurement is performed with a quartz crystal that has a determined resonation frequency. Upon addition or removal of mass on top of the resonator, the frequency changes, and the changes can be translated into mass, thus allowing the determination of the mass per unit that is adsorbed on the surface. Because the measurement can be made across time, it is possible to determine the kinetic of the adsorption process of the molecules on the surface.[234]

One of the main applications of the SAM is their use to build sensors. Different types of sensors can be found in literature, and the detection can be made by different approaches: the detected ligand can be conjugated with fluorophore, or can cause a change in the sensing group of the SAM (fluorescence, electrochemical signal, among others).

DNA chips are one of the best known examples. In this case, a substrate is functionalized with an appropriate molecule that serves as base for the synthesis of ssDNA with different sequences. Among the first ones to be commercialized we find the high-density DNA chips from the company Affymetrix.[235] The drawback is the need to conjugate the complementary ssDNA with a fluorophore (**Figure 4.5**), and the detection is done optically, requiring specific equipment. Recently the immobilization of DNA on surfaces was reviewed,[236] and examples are given of the use of the biotin-streptavidin system, where biotin is immobilized on the surface, then conjugated with streptavidin. Because each streptavidin molecule can bind at least four biotin molecules, the immobilized protein acts as the intermediary to bind biotin-conjugated oligonucleotides. Immobilized DNA can also be used to sense proteins, as in an example found

in literature of a silicon nanowire biosensor, where a SAM with vinyl group is used to immobilize specific dsDNA to bind and detect estrogen receptor present on breast cancer cells.[42]

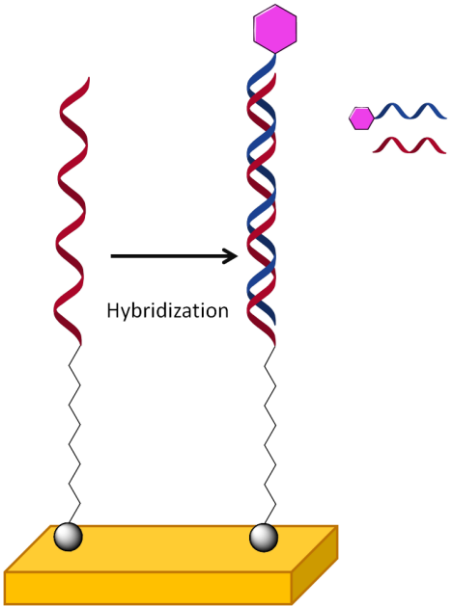

Figure 4.4: Schematic representation of a SAM with an immobilized oligonucleotide. The detection of the hybridization is done because of the presence of a fluorofore conjugated with the complementary oligonucleotides.

Many label-free approaches are currently found in literature. For instance, an electrochemical sensor was developed for the detection of antibodies against proteins found in peanut that are known to trigger allergic response. The sensor is produced through SAM formation and using click chemistry to achieve immobilization.[237] The same electrochemical approach can be found in recent examples, to detect the antibody for the human Influenza virus hemagglutinin,[238] or the PTEN gene from prostate tissue, which is a tumour suppressor gene.[239] Electrochemical sensors are also found for applications other than in diagnostics, for example, the detection of bisphenol A, a compound which can be released in the wastewater from plastic industries into the environment and is associated with higher cancer risk.[240] The Schiff's base of 2-{[(Z)-1-(2-methoxyphenyl) ethylidene] amino}-1-benzenethiol has been reported for electrochemical detection of uranyl cations.[241] The electrochemical detection of reactive oxygen species such as superoxide radicals can be performed through biosensors composed of immobilized redox proteins such as superoxide dismutase or cytochrome *c*.[242] SAM of rotaxanes or catenanes were obtained and studied for the detection of anions. When these discrete anion-receptor units are conjugated with transition metals, lanthanides, and organic fluorophores, the binding of the anion guest causes a change in the emission profile of the reporter conjugate. By integrating redox-active ferrocene group, the detection of the binding can be performed

electrochemically.[243] One recent publication reviews the formation of self-assemblies containing lanthanides that are being explored as biological probes or sensors for gas and temperature.[244]

The sensors can also be based in fluorescence. For instance, a pyrene-based fluorescent sensor was used the detection of nitroaromatic compounds such as picric acid, 2,4,6-trinitrotoluene, 2,4-dinitrotoluene and nitrobenzene,[245] and other example describes a pyrene-based sensor for Cu^{2+}.[246] Chemosensors based on fluorophores have also been described to detect, like rhodamine-based sensors for Hg^{2+},[247] or for Pb^{2+}.[248]

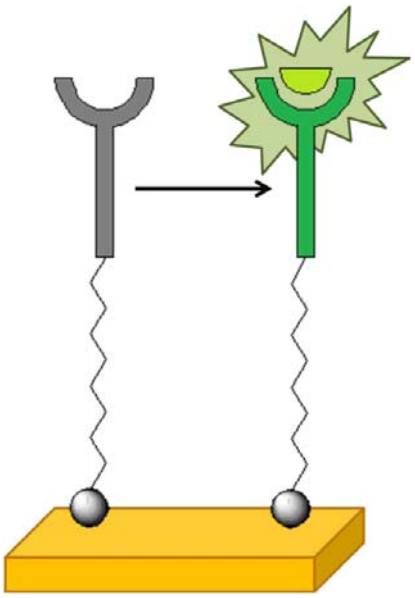

Figure 4.5: Example of a SAM with a chemosensor. The binding of the ligand to the host sensor causes a conformational change that translates into a signal that can emission of radiation (fluorescence) or electrical.

SAM are also found in mechanical sensors. For example, a cantilever for the detection of endotoxins produced by sepsis-associated Gram-negative bacteria. The cantilever has immobilized antibodies that are specific for specific toxins.[249] The QCM can also be used for the detection of molecules such as, for example, kaempferol.[250]

Aditionaly, the correct biofunctionalization of a surface can have applications other than sensing, as in this example where microscopic codes were functionalized with a lectin that recognized carbohydrates present in the *zona pellucid* of the embryos and were used to tag them, for identification of each individual embryo.[47]

Among the characterization techniques that can be used to study the SAM, AFM can be used together with functionalization of the probe for detection of molecules or interactions between molecules. The probe is functionalized through the same techniques used to obtain a SAM on a

surface,[224] and then a host or guest molecule is immobilized, and the surface to probe is functionalized with its corresponding pair that is to be studied. The use of modified AFM probes to determine the affinity between molecules is also known as Chemical Force Microscopy. The forces, established between the tip and the surface, are the result of the affinity between both molecules.[251] For example, the interaction between Concanavalin A and its guest has been widely studied,[53,252–254] or between another lectin, the wheat germ agglutinin and its guest *N*-acetyl-D-glucosamine.[51] This type of interaction study can also be performed with membrane proteins under physiological conditions.[255] Recently, QTF probes, an alternative to AFM cantilever probes, were also described for the detection of molecular interactions.[256,257] These probes are similar to the ones used in the tuning of musical instruments: they are composed of two prongs that are connected to one another in one of the extremities. Their resonance frequency depends on the properties of the material from which they are built and also from their geometry.

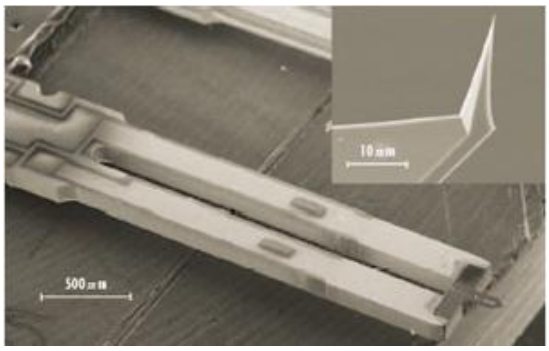

Figure 4.6: Micrograph of a quartz tuning fork with a cantilever mounted on its tip (*http://machinedesign.com/archive/using-microtechnology-get-nanotechnology).*

Another technique that recently has been used for sensing is based in the Surface Plasmon Resonance (SPR). The functionalized surface must be a metal that can be produce surface plasma waves of electrons at the surface of the metal through the excitation with an appropriate light wave. These surface plasmons propagate with a specific constant, which depends on the medium on top of the metal. Alteration in the medium causes changes to occur between the surface plasmons and the optical wave that interacts with them. The interaction between the surface plasmons and the optical wave can be measured in terms of wavelength, angle, intensity or phase modulation.[50] The medium refractive index is influenced by some factors, such as the solvent and the molecules on the surface. For this reason, SPR sensors can be used to study interactions between molecules, due to the fact that molecular interactions near the metal surface cause the local refractive index to change, and these changes can translate into shifts in the SPR peak, which can be determined.[49,258] **Figure 4.7** shows a typical graphic of the light intensity as function of the angle or wavelength detected by the SPR sensor.

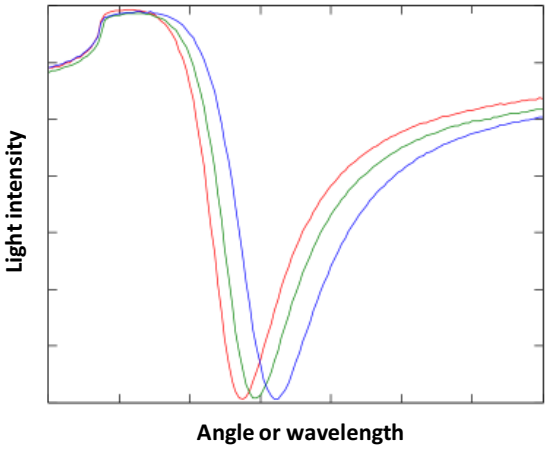

Figure 4.7: Graphic showing the intensity of light in function of the light angle or wavelength, for gold surfaces with different media in contact with the metal surface. Image adapted from http://upload.wikimedia.org/wikipedia/commons/d/d0/SPR-adsorption-data.png (licensed under Creative Commons license http://creativecommons.org/licenses/by-sa/3.0/)

The gold surfaces of the sensors are modified in order to immobilize the biomolecules.[50] Examples are found of the use of SPR sensors to detect proteins and DNA molecules,[259] for the detection of antigens by antibodies immobilized on the sensor,[260] and for the determination of antibody-antigen binding constants.[261] An example of a typical sensorgram of the response as function of the immobilization of a molecule on the surface is shown in **Figure 4.8**.

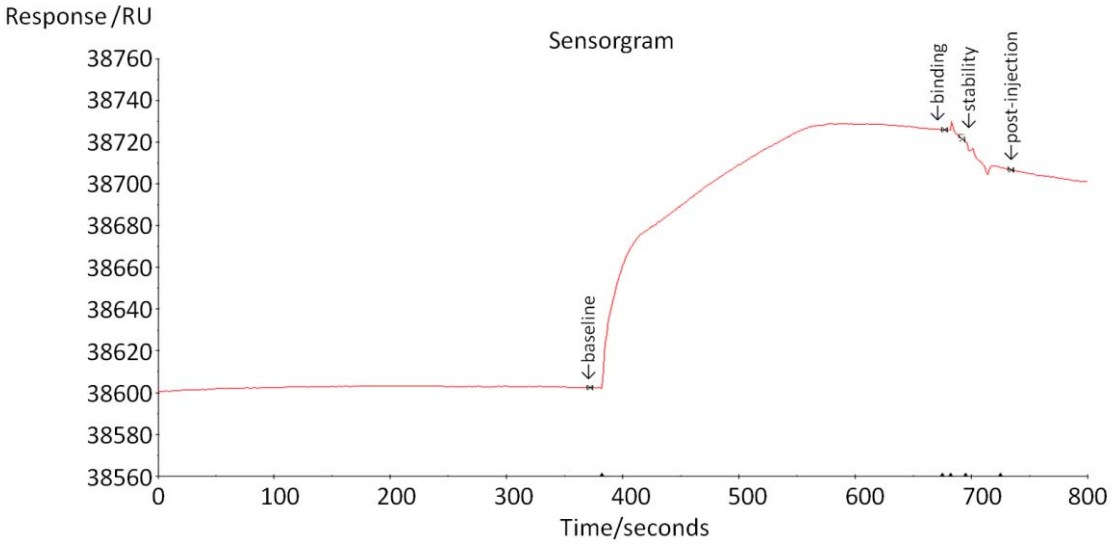

Figure 4.8: Example of a sensorgram showing the response units in function of time obtained for the immobilization of a molecule on the sensor chip surface.

The response increases with the presence of the molecule that comes into contact with the chip. A buffer washes the unbound molecule and the difference between the initial baseline response

(before immobilization) and the response after washing corresponds to the response units obtained due to the molecule that remained immobilized on the surface. In the case of an interaction between molecules, the ligand is immobilized, and the analyte is brought into contact with the ligand. In the typical case of an SPR-based system, the sensor chip is regenerated after measuring the response units obtained due to the interaction ligand-analyte. The sensorgram obtained along with the scheme of the corresponding events are shown in **Figure 4.9**.

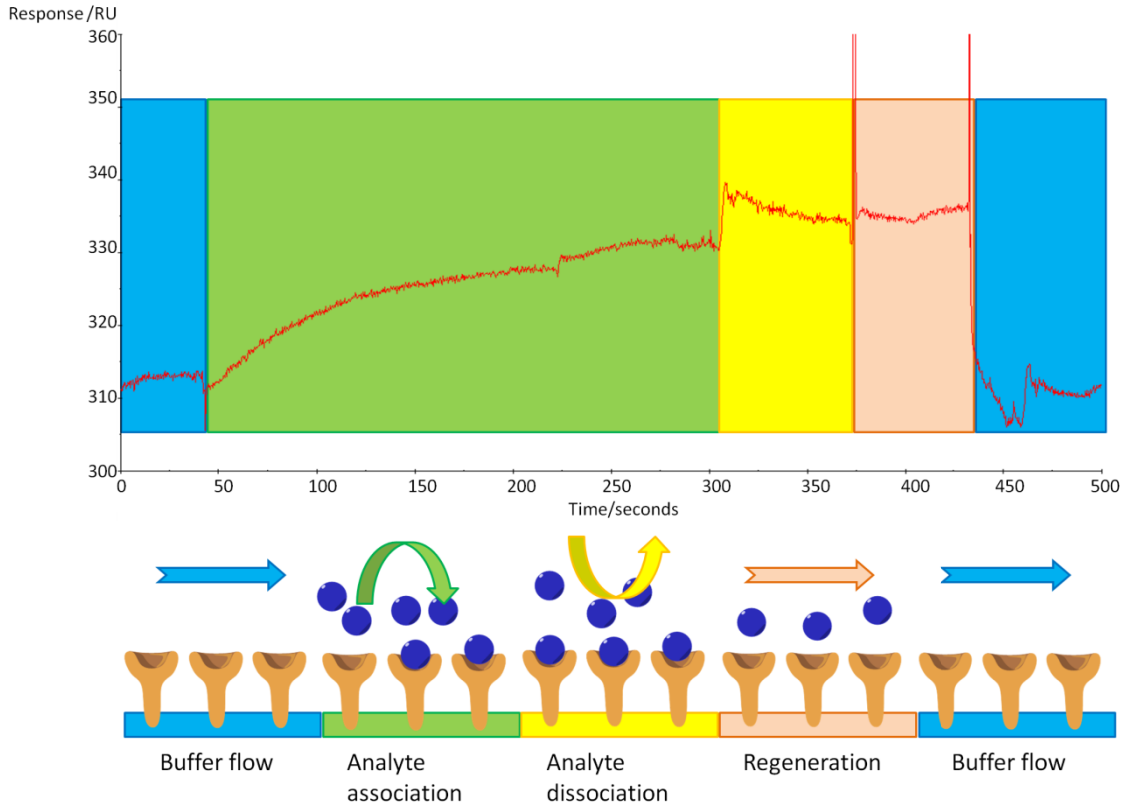

Figure 4.9: Example of sensorgram showing the response as function of time for the affinity binding between ligand and analyte with schematic representation of each step.

The analyte (in run buffer) is flown through the sensor, with the corresponding increase in the response due to the association between the analyte and the ligand; run buffer is then flown to dissociate the analyte from the ligand. This dissociation is limited by the higher or lower affinity of the analyte for the ligand and causes a decrease in the response level, and finally the analyte is completely removed by a regeneration solution, with an acidic pH, to force the dissociation of the analyte from the ligand. For the affinity study between ligand and host, like for example antibody-antigen, interaction, different concentrations of the analyte are flown into the sensors, and the response curves are recorded.[262] **Figure 4.10** shows a typical sensorgram of the interaction between ligand and different concentrations of an analyte.

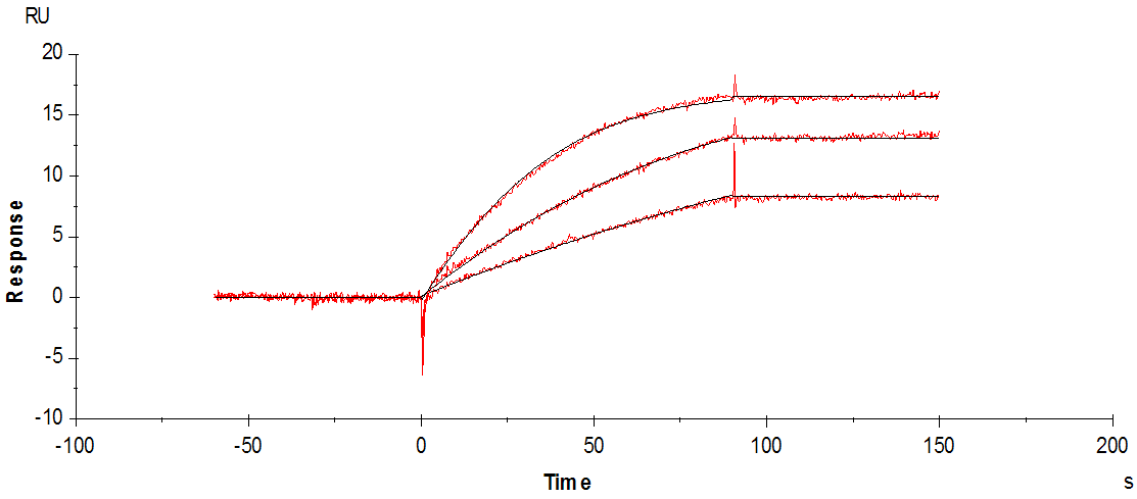

Figure 4.10: Example of sensorgram of response in function of time obtained for different concentrations of the guest molecule.

Because more analyte is brought into contact with the ligand, increasing responses are obtained, until saturation occurs, corresponding to the binding to all available sites of the ligand, meaning that a steady-state was achieved.

4.2. Objectives

This chapter focus on the supramolecular assembly of monolayers for sensing purposes, through different techniques. The main goals are:

a) Functionalization of surfaces for temperature sensing;
b) Functionalization of Quartz Tuning Fork probes for the study of molecular interactions;
c) Study of antibody/antigen affinity through Surface Plasmon Resonance.

Each of the different methods and its application is listed separately below:

4.2.1. Functionalization of silicon surfaces with chimiosensors for temperature measurements

I. Functionalization of three different silicon surfaces with alternative methods for surface activation and their silanization with aminopropyltriethoxysilane;
II. Immobilization of the polymeric ligand with PEG and coordination with the temperature sensor;
III. Characterization of the functionalized surfaces through: contact angle measurement, AFM and XPS;
IV. Study of the temperature sensing with the prepared surfaces.

4.2.2. Study of biotin/streptavidin interactions using biofunctionalized QTF probes

I. Functionalization of silicon patterned surfaces with different silanes and different solvents to choose best conditions;
II. Functionalization of substrate and QTF probes and immobilization of biotin on QTF probe and streptavidin on the substrate;
III. Characterization of the surfaces by fluorescence optical microscopy;
IV. Assessment of the interaction between avidin and biotin through Scanning Force Microscopy.

4.2.3. Study of interactions between anti-EGFR monoclonal antibodies and their antigen EGFR using SPR

I. Study of two different methods for anti-EGFR antibody immobilization on SPR sensor chips;

II. Determination of binding affinities of the immobilized antibodies for their antigen EGFR.

4.3. Implementing thermometry on silicon surfaces with a molecular thermometer working in the physiological range

Manuscript in preparation

Mafalda Rodrigues[1], Rafael Piñol[2], Guillermo Antorrena,[3] Carlos D. S. Brites[4], Nuno J. O. Silva[4], J.L. Murillo[2], R. Cases[2], Fernando Palacio[2], José Antonio Plaza,[5] Lluïsa. Pérez-García,[1] Luís D. Carlos[4], Angel Millán[2]

[1]*Department de Farmacologia i Química Terapèutica and Institut de Nanociència i Nanotecnologia UB (IN2UB), Universitat de Barcelona, Avda. Joan XXIII s/n, 08028 Barcelona, Spain*

[2]*Departamento de Física de la Materia Condensada, Facultad de Ciencias and Instituto de Ciencia de Materiales de Aragón, CSIC–Universidad de Zaragoza, 50009 Zaragoza (Spain).*

[3]*Laboratorio de Microscopías Avanzadas (LMA), Instituto de Nanociencia de Aragón (INA), Universidad de Zaragoza, Edificio I+D, C./Mariano Esquillor s/n., 50018 Zaragoza (Spain).*

[4]*Departamento de Física and CICECO, Universidade de Aveiro, 3810–193 Aveiro (Portugal)*

[5]*Institut de Microelectrònica de Barcelona, IMB-CNM (CSIC), Campus UAB, 08193 Bellaterra, Barcelona, Spain*

Summary

In this work, we studied the ability of lanthanide complexes to be used as temperature sensor after being immobilized on surfaces. The first step was to determine the best activation conditions. Afterwards, the silanization was performed in gas phase, which according to some examples in literature renders a more homogeneous layer. The successful silanization through this method was determined by contact angle measurement. The polymer that will form the complex with the lanthanides was then immobilized on the surface, and the lanthanides and remaining molecules that complete the coordination sphere were added. The surfaces were characterized by AFM and by XPS, to determine the homogeneity of the samples and also to assure the complex was formed. With the whole assembly formed, the surfaces were then used in the sensing of temperatures through changes in the emission of the complexes. This was done along with an AFM analysis, to determine if there are structural changes in the coating while heating. The emission spectra were recorded between 298 K and 338 K with 5K steps and an

excitation wavelength of 280 nm. The integrated areas of Eu^{3+} transition ($^5D_0 \rightarrow {}^7F_2$) and Tb^{3+} transition ($^5D_4 \rightarrow {}^7F_5$) in this range showed a sensitivity about $0.3\% \cdot K^{-1}$ for temperatures above 325 K, and hysteresis was observed between 298 and 330K.

Implementing thermometry on silicon surfaces with a molecular thermometer working in the physiological range

Mafalda Rodrigues[1], Rafael Piñol[2], Guillermo Antorrena,[3] Carlos D. S. Brites[4], Nuno J. O. Silva[4], J.L. Murillo[2], R. Cases[2], Fernando Palacio[2], José Antonio Plaza,[5] Lluïsa. Pérez-García,[1] Luís D. Carlos[4], Angel Millán[2]

[1]*Department de Farmacologia i Química Terapèutica and Institut de Nanociència i Nanotecnologia UB (IN2UB), Universitat de Barcelona, Avda. Joan XXIII s/n, 08028 Barcelona, Spain*

[2]*Departamento de Física de la Materia Condensada, Facultad de Ciencias and Instituto de Ciencia de Materiales de Aragón, CSIC–Universidad de Zaragoza, 50009 Zaragoza (Spain).*

[3]*Laboratorio de Microscopías Avanzadas (LMA), Instituto de Nanociencia de Aragón (INA), Universidad de Zaragoza, Edificio I+D, C./Mariano Esquillor s/n., 50018 Zaragoza (Spain).*

[4]*Departamento de Física and CICECO, Universidade de Aveiro, 3810–193 Aveiro (Portugal)*

[5]*Institut de Microelectrònica de Barcelona, IMB-CNM (CSIC), Campus UAB, 08193 Bellaterra, Barcelona, Spain*

Introduction

Surface functionalization is a recurrent way for endorsing a substrate with additional properties[1]. Among the wide scope of possible surface functionalities, thermometry is probably one of the most universal and useful. And among the possible substrates silicon is one of the most employed materials in device construction.[2, 3] It is thus worthy to develop thermometric coatings for silicon devices[4]. However, from our knowledge, there are no precedents of such coatings in the literature.

The strategy for implementing thermometry is based on the use of a molecular dual-lanthanide coordination compound system that has already been proved successfully in bulky and nanoparticle materials.[5-7] The sensing part is a molecule, and the reading is optic. The molecule can be covalently attached to the silicon surface so that the whole surface is accessible for temperature screening with a spatial resolution just limited by the optical detector. The thermometric process is based on electronic interactions between the lanthanide ions, the coordination ligands and the substrate. In this case, the lanthanide ions are Eu^{3+} and Tb^{3+} that are linked by diketonate chelate bonds to the end of polyethylene glycol (PEG) chains attached to the silicon surface. The coordination sphere of lanthanide ions is completed with aromatic ligands (DPA or fenantroline) that act as antennas for light harvesting[8]. The PEG host presents

an excited triplet state with energy slightly above that of the Tb^{3+} $^5D_4$ emitting state, thus permitting the occurrence of thermally-driven $^5D_4$→host energy transfer and, consequently, the determination of the temperature dependence of the $^5D_4$ emission. Whereas, the energy difference between that triplet state and the Eu^{3+} $^5D_0$ emitting level is too large for thermally-driven depopulation, and therefore the absolute temperature can be obtained from the Tb^{3+}/Eu^{3+} relative intensity[5].

As pointed out above, silicon surface must be coated with a PEG monolayer before the molecular thermometric molecules can be incorporated to the silicon surface. There are several strategies to functionalize silicon surfaces with organic monolayers, usually with the purpose to develop chip-based chemical or biological sensors.[3, 9] Some of them work directly on Si(111) or Si(100) surfaces. The functionalization is usually achieved by formation of Si-C bonds with alkenes or alkynes.[10] Others are based on the formation of Si-O-C bonds and require a previous surface oxidation to form a thin SiO_2 layer. The functionalization is then performed by sol-gel chemistry routes. This is the choice here for an initial activation of the surface with NH_2 groups. The silicon substrate is oxidized and then it is reacted with APTES precursors to leave NH2 groups on the surface. In a second step, PEG-acrylate chains are attached by Michael addition of the acrylate onto the amine surface groups. This strategy works at room temperature, does not leave by-products, and it has been used in our group for the production of aqueous suspensions of magnetic nanoparticles.[11, 12]

One of the most interesting applications of the materials presented in this report is biotechnology. The use of nanomaterials such as quantum dots metal or metal oxide nanoparticles as multifunctional probes for cell studies is an emergent area in nanobiotechnology. These materials are prepared by chemical methods. As an alternative, microfabrication opens up huge opportunities to obtain new materials with a controlled structure. This concept has been recently demonstrated[13] with the fabrication of biofunctionalized silicon barcodes for extracellular tagging. The polysilicon barcode surface was biofunctionalized using a self-assembled monolayer (SAM) as the connector with a lectin (wheat germ agglutinin, WGA) biomolecule capable of recognizing some specific carbohydrates present on the surface of most mammalian cells.

The thermometric system proposed in this report yields absolute temperatures by reading the optical emission of the material. It provides a high precision and a spatial resolution only limited by the optical detection system, and it works in the physiological temperature range. The thermometric system shows an interesting physical phenomenon consisting on a hysteresis of optical emission with temperature variation.

Experimental

All chemicals were purchased from Sigma-Aldrich and used as received. Three types of substrates were used for the coatings: 1) monocrystalline silicon; 2) monocrystalline silicon with a 1μm external layer of SiO2; and 3) polycrystalline silicon with a domain size of 500 nm.

Synthesis of precursors

: PEG acrylate ligands, lanthanide coordination compounds

Film deposition

All the substrates used to obtain the different surfaces were P-type monocrystalline silicon wafers of 100 mm of diameter and 525 ± 15 μm thick (Okmetic) which were considered as the first substrate type for the present study. Then, in two different wafers, a 1083.0 ± 11.3 nm layer of silicon oxide TEOS (tetraethylorthosilicate, $Si(OC_2H_5)_4$) was deposited by Plasma-Enhanced Chemical Vapor Deposition (PECVD) at 380ºC, and a pressure of 1000 mTorr, to form the second substrate type. Finally, the third substrate type was obtained by depositing a 518.8 ± 3.9 nm layer of polycrystalline silicon by Chemical Vapor Deposition (CVD) at 580°C and a pressure of 350 mTorr, on top of the previous silicon oxide layer.

Surface activation

The different surfaces were cut in 1x1 cm squares. Two different methods were used for activation. In the first one the surfaces were washed with ethanol and acetone and dried under nitrogen. The hydroxylation of the surface was performed by ozone for 10 minutes using a UVO-cleaner Model 342 (Jelight Company Inc., USA). Alternatively the activation was performed as described elsewhere:[14] the surfaces were immersed in piranha solution (H_2SO_4/H_2O_2 7:3) for 1 hour at room temperature, and then washed thoroughly with distilled water and immersed in a solution of (NH4/ H_2O_2/H_2O 1:1:5) for 30 minutes at room temperature. The surfaces were washed with distilled water and dried under nitrogen.

APTES deposition

The APTES covering was done by vapour deposition, as described elsewhere.[15] Briefly, a desiccator was connected to a vacuum pump and the temperature was raised to 80°C. Then, the surfaces were placed inside the desiccator, together with 1 mL of APTES, and the desiccator was pumped down and sealed off. The samples were left in contact with the APTES vapour for 3h. Afterwards, the samples were washed with acetone, dried under nitrogen, and cured on an oven at 50-60°C for 20 minutes.

Functionalization with PEGA

To introduce the PEG-acrylate group, the surfaces were brought into contact with a solution of PEG-acrylate 0.3% in water with pH adjusted to 8.5, and left for 24, 48 and 70 hours at 60°C, washed with distilled water and dried under nitrogen. The same procedure was performed with PEG-acrylate 0.3% in dioxane (24, 48 and 70 hours) and in ethanol (70 hours). The functionalized surfaces were used to form complexes with DPA, or alternatively with fenantroline.

Complex formation with DPA

To form the complex with the lanthanides, each surface was placed in individual vials with 2 mL of water, to which it was added 15.8 µL of NaOH 1M, 100 µL of a solution of $EuCl_3.6H_2O$ 1.44% and 100 µL of a solution of $TbCl_3.6H_2O$ 4.42%, and the pH was adjusted to 6.7. After3 hours, 84 µL of a solution of 2,6-pyridinedicarboxylic acid (DPA) 63mg/mL pH 6.76 were added. The complex was allowed to form overnight. The surfaces were then thoroughly washed with distilled water and dried under nitrogen.

Complex formation with fenantroline

The procedure was the same as above, but instead of DPA, 4 mg of ethylacetoacetate were added. After 1 hour, the whole solution was discarded, and 1 ml of ethanol containing 2.8 mg of fenantroline was added to each surface.

Instrumental and characterization of the samples

Contact angle experiments were performed using a contact angle goniometer (THETALITE100 with the software One Attention, Finland). Values of the contact angle on at least three samples were measured to give statistical significance. AFM observations were carried out with a Ntegra Aura (NT-MDT) equipment. SEM observations were carried out in a Quanta FEG 250 equipped with a Peltier sample heating/cooling system.

X-ray photoelectron spectroscopy analysis

All XPS analysis was carried out using a Kratos Axis Ultra spectrometer employing a monochromatic Al Kα (1486,6 eV)10 mA, 15 kV) X-ray source and a power of 150 W. All samples were introduced in the analysis chamber simultaneously and were analyzed in the same experimental conditions. Pressures near 1×10^{-8} Torr were observed in the analytical chamber during surface analysis. All XPS analysis employed an analysis area of 700µm×300µm. Survey spectra were recorded using an analyzer pass energy of 160 eV and a 1.0 eV energy step. High

resolution spectra of C 1s, O 1s, N 1s, Si 2p Eu 3d and Tb 3d regions were collected using a pass energy of 20 eV and 0.1 eV energy step. Differential surface charging was minimized using charge a neutralizer system (flood gun). A degradation control test was carried out in every sample by registering High Resolution C 1s spectra before and after the completion of data acquisition process. No significant differences were observed.

Spectra were analyzed using Casa software. The background for all spectra was substracted using a Shirley baseline. Due to the use of charge neutralizer spectra need to be calibrated. Binding energies (BEs) were referenced to the C 1s (C-C) peak at 284.9 eV.

Photoluminescence and Temperature Control

Photoluminescence. The photoluminescence spectra were recorded with a modular double grating excitation spectrofluorimeter with a TRIAX 320 emission monochromator (Fluorolog-3, Horiba Scientific) coupled to a R928 Hamamatsu photomultiplier, using a front face acquisition mode. The excitation source was a 450 W Xe arc lamp. The emission spectra were corrected for detection and optical spectral response of the spectrofluorimeter and the excitation spectra were corrected for the spectral distribution of the lamp intensity using a photodiode reference detector.

Temperature controller. The temperature was controlled using an IES-RD31 controller and a Kapton thermofoil heater from Minco mounted on a copper holder and monitored using a thermo-couple thermometer Barnant 100 (model 600-2820) with a temperature accuracy of 0.1K, accordingly to the manufacturer.

Results and Discussion

Surface functionalization and characterization

To obtain surfaces with the functional thermometers based on lanthanides, different materials were used: monocrystalline silicon, silicon oxide deposited by PECVD, and polycrystalline silicon deposited by CVD. Scheme1 shows the different steps of the functionalization of the surfaces. The first step to obtain a functional surface was to activate it so that hydroxyl groups are present on the surface. This activation was done by two different methods: one in solution, through a method already described[48] that affords good activation. The second consists of plasma activation by treatment with ozone. It was of our interest to see if the plasma activation with ozone could deliver similar results, since it is simpler method. The activated surface was then put into contact with APTES so that a layer of the silane could assemble. The functionalization with the polymer occurs through the reaction between the acrylate group of the

polymer and the amine from the monolayer, through an aza-Michael addition. In the case of the used polymer, it is known that it can successfully react through Michael addition in water with a slightly basic pH.

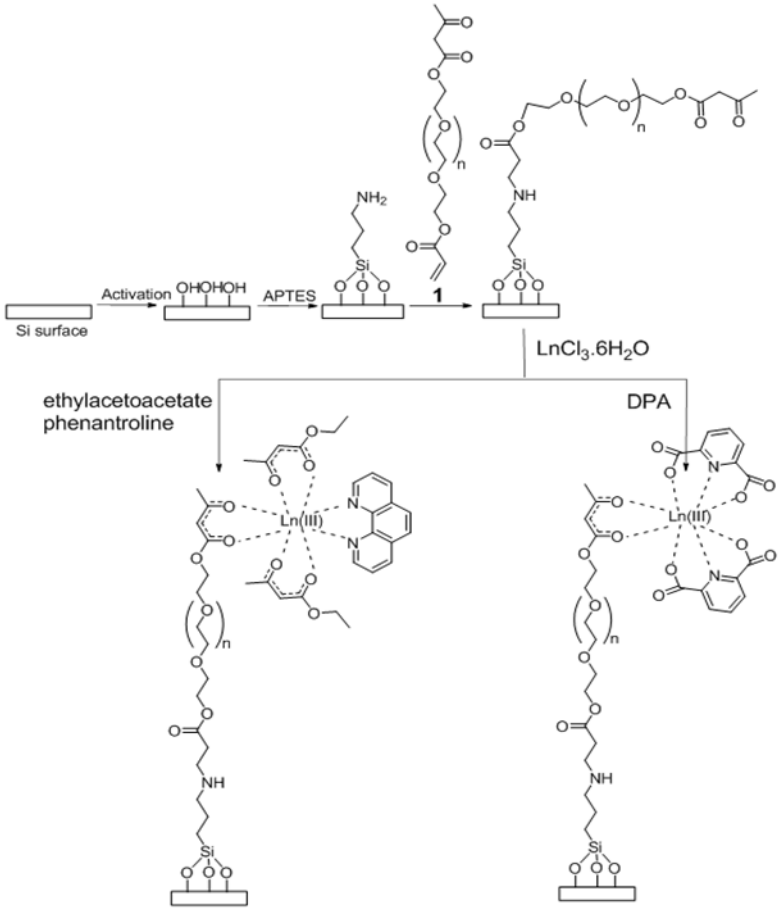

Scheme 1: Functionalization of the Surface with PEG polymer: 1) activation; 2) functionalization with APTES; 3) reaction with PEGA-polymer; 4) formation of the lanthanide (Ln = Eu or Tb) complex.

Apart from this solvent, ethanol (also protic solvent) and dioxane (apolar solvent) were also tested as alternatives to water. The different parameters that were tested, such as the initial surface activation process, the solvent in the Michael addition reaction and the time of reaction are described in Table 1.

The characterization of the surfaces after the functionalization process was performed initially by determining the wettability of the surface, through contact angle measurement, as a rough indication of the changes in the hydrophobicity (derived from the different reaction steps), then by atomic force microscopy (AFM), to determine the roughness of the surface after each step, and finally by XPS, that allowed us to determine the composition of the surface, and detect if the lanthanides from the complexes were present in the samples.

Table 1: Different conditions used for the immobilization of the PEG-polymer on silicon surfaces

Functionalization step		Time
Activation	Plasma	10 min
	Piranha // NH4/ H_2O_2/H_2O	1 hour // 30 min
Reaction with PEG-polymer	water	24 hours
		48 hours
		70 hours
	dioxane	24 hours
		48 hours
		70 hours
	ethanol	70 hours

All the surfaces, after activation, presented a more hydrophilic character, which translated into smaller contact angles. Depending on the material, we found some differences, ranging from 46° in the case of SiOx surfaces to 67° in the case of the polysilicon surfaces. For all surfaces, after the deposition of APTES, the found contact angle was between 91° and 95°. This was expected, because the presence of the silane gives a hydrophobic character to the surface, and therefore the contact angle increases after the deposition when compared to the one we had after activation, where the surface is rich in hydroxyl groups. However, the reaction with the polymer also reflects in a change in the hydrophobicity, and the contact angle decreases to around 46°.

The characterization of the surfaces by AFM gives us important information about the roughness and its changes derived by the different layers of molecules that are being added. We can therefore determine if the layers are homogeneous, which is of particular interest in the case of APTES deposition. This step is critical because depending on the deposition conditions, heterogeneous layer with islands can be formed, especially when depositing APTES in solution.[16] This was the main reason why a vapour deposition of APTES was chosen. Figure 1 shows the AFM images of the monocrystalline silicon surfaces treated with piranha, before and after APTES deposition, and monocrystalline silicon with a 500 nm layer of polycrystalline silicon surfaces treated with ozone, before and after APTES deposition.

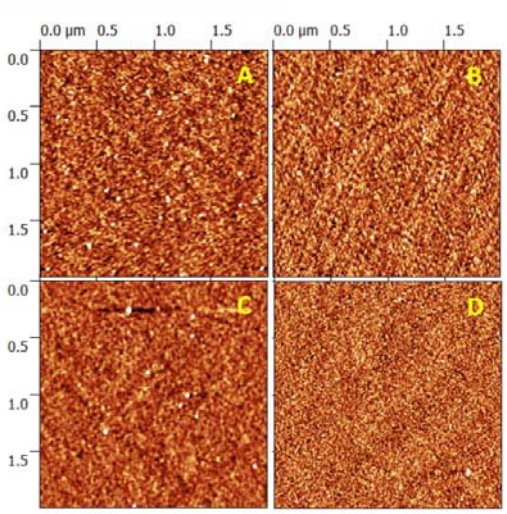

Figure 1: AFM images of monocrystalline silicon surfaces treated with piranya, before (A) and after (B) APTES deposition, and surfaces treated with ozone, before (C) and after (D) APTES deposition.

There are almost no visible differences in the surface morphology between the surfaces that were activated by the two different methods. Table 2 shows the roughness of the different materials, activated by the two different methods, and after the deposition of the silane.

Table 2: Roughness (RMS) of the different surfaces after the initial activation step, and after the deposition of the APTES film

Material	Surface	RMS (nm)
Monocrystalline Si	no activation	0.13
	-OH (piranha)	0.10
	APTES	0.10
	-OH (plasma)	0.12
	APTES	0.18
Silicon oxide 1000 nm	no activation	0.30
	-OH (piranha)	0.33
	APTES	0.34
	-OH (plasma)	0.73
	APTES	0.47
Polycrystalline Si 500 nm	no activation	0.78
	-OH (piranha)	0.23
	APTES	0.14
	-OH (plasma)	0.30
	APTES	-

There are no differences in the roughness after the activation with plasma or with piranha, except for the surfaces with a silicon oxide film, where apparently the activation with plasma has some effect in the material. The RMS measured was bigger in the case of the plasma activated surface. Other important feature is that after the deposition of APTES, the roughness suffers little changes in the case of surfaces activated with piranha. This means that a rather homogeneous layer of APTES was grown on the surface by vapour deposition.

Because the roughness of the surfaces depends on the initial smoothness of the surface, and the density and shape of the molecules instead of their functional groups, it is not possible to establish a relation between the contact angle values and the RMS measured.

X-ray photoelectron spectroscopy analysis

XPS analysis of samples along the whole the functionalization process has been performed. Table 3 presents the relative quantifications of C1s, O 1s N 1s and Si 2p peaks from the survey spectra.

Table 3. XPS analysis at every step of the functionalization process.

Sample	**C 1s %**	**N 1s %**	**O 1s %**	**Si 2p %**
Si-SiO2 (C2)	11,9	0,6	50,3	37,2
Si-SiO2-APTES (C1)	21,9	2,5	50,3	25,3
Si-SiO2-APTES- PEGA (C3c)	43,0	1,0	32,5	23,5
Si-SiO2-APTES- PEGA (C4c)	33,9	2,4	36,1	27,5
Si-SiO2-APTES- PEGA (C5c)	51,7	1,2	30,5	16,5
Si-SiO2-APTES- PEGA-Ln(DPA) (C3b)	38,2	1,2	35,9	24,7
Si-SiO2-APTES- PEGA-Ln(DPA) (C5a)	38,5	2,0	37,4	22,2

The presence of C in the silicon wafer after activation of the surface with plasma (Table 3, sample C2) may be explained by adsorption of hydrocarbon in the surface (adventitious carbon). A small amount of N contamination is also detected. Si 2p presents two distinct doublets characteristic of bulk silicon (98,8 eV) and Silicon bonded to oxygen (103,3 eV). Some contribution of Intermediate oxidation states of Si is also detected. After deconvolution of the spectra it is possible to estimate relative concentration of Si species: 48.2% Si^0 and 48% SiO_2 (Figure 2).

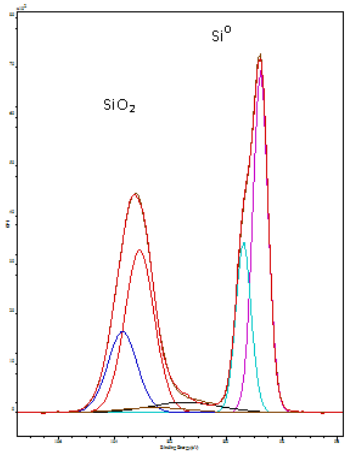

Figure 2: X-ray photoelectron spectrum of the Si 2p signal of initial oxidized silicon wafer (sample C2). The peak near 99eV represents bulk silicon and the peak near 103 eV represents SiO2.

.After APTES deposition (Table 3, sample C1), the presence of APTES on the surface is corroborated by the N 1s spectrum. The C:N ratio = 8.8, is higher than expected for a fully polymerized APTES molecule perfectly adsorbed to the surface (3 C:N ratio = 3). This ratio may indicate partial hydrolysis of APTES. An unknown amount of contaminating hydrocarbon overlay also contributes to increase the C:N ratio.[17, 18]

High resolution N 1s spectrum (Figure 3) presents two peaks at 399.7 eV and 401.6 eV. The lower energy peak is attributable to free amines (NH_2) and the higher energy peak to protonated (NH_3^+) and hydrogen bonded amines. These components are consistent with an APTES modified surface.[17] From the deconvolution of the spectra it is possible to estimate that the fraction of free amines in the surface is 53.5%.

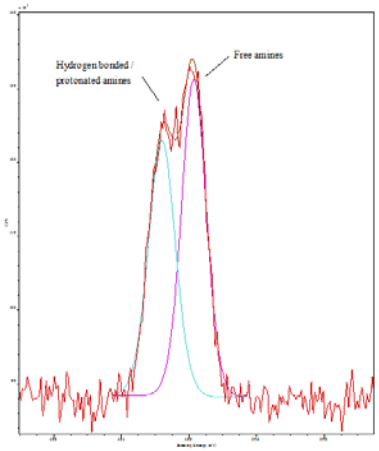

Figure 3: X-ray photoelectron spectrum of the N 1s signal after deposition of APTES (sample C1.) Lower BE peak corresponds to free amines and Higher BE peak corresponds to hydrogen bonded / protonated amines.

Photoemission spectra of surfaces after reaction with PEG-acrylate in three different media (water, dioxane and ethanol; samples C3c, C4c and C5c respectively) are qualitatively similar. The two main signals on Si 2p and N 1s previously explained are still present. In the case of Si 2p signal, several intermediate oxidation states are detected with concentration dependent upon the samples. Deconvolution of C 1s spectra requires four main differentiated peaks at 284.9 eV (C-C, calibration), +1.6(2) eV, +3.2(2) eV and +4.2(2) eV, which can be assigned to C-O, C=O / O-C-O and O-C=O respectively. Carbon – Nitrogen bonds are convoluted with previous signals but low concentration of Nitrogen in samples and proximity to oxygen bonded carbon signals makes it difficult to deconvolute.[18] As expected, the relative concentration of C increases in a ratio that increases when the reaction medium changes from dioxane to water and then to ethanol (see Table 4). Figure 4 shows a comparison of high resolution spectra of Si 2p, N1s and C 1s regions, deconvolution of C1s, N1s and Si 2p as an example.

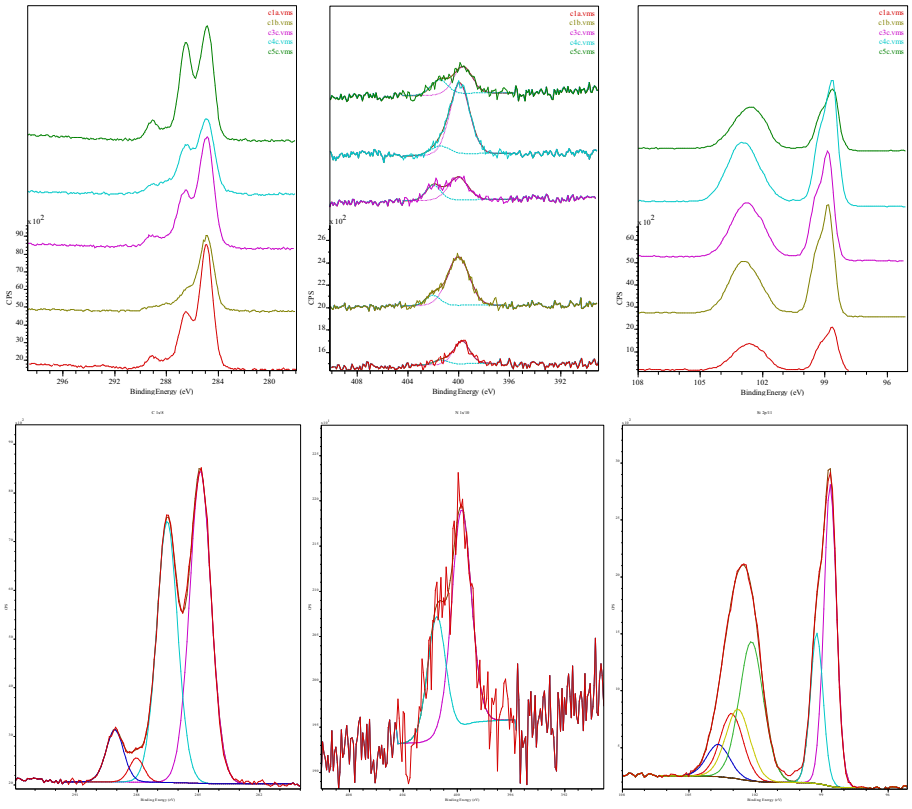

Figure 4: Comparative spectra of C1s, N1s and Si2p photoemission region of the studied samples (up from left to right). Deconvolution of XPS signal of sample C5c. Regions C1s, N1s and Si 2p. (Down)

XPS analysis of samples after the addition of the lanthanide compounds show the presence of Terbium and Europium in Samples C3b and C5a. Figure 5 shows comparative spectrum of Eu 3d and Tb 3d core levels in the samples. A sample prior Ln conjugation (C1a sample) is also

included as a reference. From Tb 3d and Eu 3d spectra is possible to estimate that the ratio of Tb:Eu in sample C5c is 2.7, which is close to the nominal ratio (3).

Table 4: C 1s and N 1s relative emissions in samples after PEGA addition.

Ref/BE	C 1s				N 1s	
	284,9 eV	+1,6 eV	+3,2 eV	+4,2 eV	399,8 (2) eV	401,8(2) eV
C1a	61,1±0,5%	30,6±0,5%	2,9±0,5%	5,6±0,5%	83,5±0,5%	16,5±0,5%
C1b	68,7±0,5%	24,3±0,5%	3,4±0,5%	3,6±0,5%	87,4±0,5%	12,6±0,5%
C3c	60,6±0,5%	31,9±0,5%	2,5±0,5%	5,1±0,5%	65,7±0,5%	34,3±0,5%
C4c	55,6±0,5%	34,2±0,5%	4,9±0,5%	5,3±0,5%	88,6±0,5%	11,4±0,5%
C5c	49,9±0,5%	40,6±0,5%	2,6±0,5%	6,8±0,5%	65,8±0,5%	34,2±0,5%

Typical Eu 3d core level XPS spectra of Eu^{3+} presents four main peaks assigned to Eu^{3+} $3d_{5/2}$ end Eu^{3+} $3d_{3/2}$ and their corresponding shake down satellites.[17] It is also reported that the relative intensity of the satellites versus the corresponding main peaks seems to be correlated with the chemical environment of europium ion.[17] Tb 3d spectrum of sample C5a is shown in Figure 5. The peaks at 1134.7 eV and 1124.8 eV may be assigned to main peak and satellite of Eu $3d_{5/2}$ (see table 5 comparing present work with published data) and the corresponding peaks at 1164.4 eV and 1154.4 eV main peak and satellite of Eu $3d_{3/2}$. We can conclude that XPS data in sample C5a is consistent with the reported data for Eu(III). It is worth to note that as shake down / shake up signals of Eu^{3+}/ Eu^{2+} overlaps respectively with the corresponding main peaks of the other oxidation state, is not possible just with XPS to discard the possibility of any Eu^{2+} contribution.

Table 5: Comparison on XPS energy data for Eu main peaks.

Eu(III) compound	Eu $3d_{5/2}$ Main peak	Eu $3d_{5/2}$ Shake down sat	Ref
Eu_2O_3	1133.7	1123.5	[17]
$Eu_2(C_2O_4)_3$	1133.9	1124.0	[17]
$Eu(acac)_3$	1135.0	1124.9	[17]
$Eu_2(CO_3)_3$	1135.3	1125.2	[17]
$Eu_2(SO_4)_3$	1135.9	1125.7	[17]
$Eu(NO_3)_3$	1136.4	1126.0	[17]
C5a	1134.7	1124.8	This work

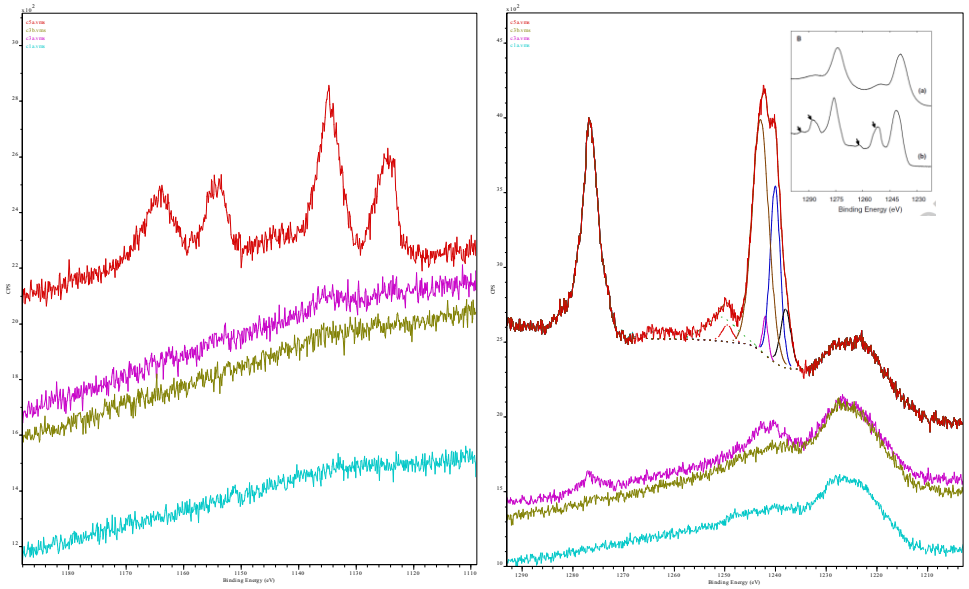

Figure 5. (Left) Eu 3d core level XPS spectra in C1a.C3a, C3b, C5a samples. (Right)Tb 3d core level XPS spectra in C1a.C3a, C3b, C5a samples. In the insert THE-XPS spectra of two pure terbium oxides (a) $TbO_{1.5}$ (100% Tb^{3+}), and (b) $TbO_{1.82}$ (36% Tb^{3+} / 64% Tb^{4+}).[19]

In the case of Terbium, the most intense core level in photoemission spectra is Tb 3d. Several combined facts make it difficult to accurately distinguish the chemical oxidation states of Tb: the high binding energy of the region (1230 – 1290 eV) (traduced in an intense energy loss spectra in the region and energetically unsuitable for Mg Kα X-rays), the proximity of Auger CKLL (when using Al Kα X-rays), the similar binding energy for the different oxidation states and the presence of shake up / multiplet structure in the signal.

Tb 3d core level XPS spectra presents two principal components related to Tb $3d_{3/2}$ and the Tb $3d_{5/2}$ binding energy peak positions. Previously published data reports in case of Tb^{3+} two doublets, one at 1239.1 and 1274.0 eV (for $3d_{5/2}$ and $3d_{3/2}$, respectively), and the corresponding satellites at 1250.4 and 1286.3 eV. Tb^{4+} signals appear at 1241.4 eV and 1276.0 eV. Terbium in the tetravalent state shows relatively intense satellites at 1251.5 and 1287.7 eV for the 3d5/2 and 3d3/2 components respectively, and weaker doublets at 1262.1 and1294.1 eV.[19] In figure 5, the spectra show two main peaks at 1241.6 eV and 1276.7 eV (between these main peaks, two main satellites are detected around 1250 eV and 1262 Ev.). These values are shifted to the high energy binding side respect to the reported values for Tb^{3+}. These results suggest that that both oxidation states (Tb^{3+} and Tb^{4+}) are present in the sample. Deconvolution of the $3d_{5/2}$ region shown in figure 5 makes it clearer. $3d_{3/2}$ signal shows the presence of two main peaks at 1240.1 eV and 1243.0 eV, which could be assigned to the coexistence of both oxidation states.[19, 20] The detected satellites at 1249.5, 1250.8, 1262.4 eV, also seem to corroborate it (see table). The complexity of the Tb 3d spectrum (presence of shake up and/or multiplet structure[21]) do not

allow us to be confident in any temptative estimation of the fraction of these oxides. However, according to published data pointing out that the higher the relative intensity of the satellites, the higher the tetravalent terbium content in the sample[19] it is most probable that Tb^{4+} is not dominant in the sample. The presence of Tb^{4+}might be explained by and oxidation process of Tb^{3+} induced by XPS analysis.

Table 6: Comparison on XPS energy data for Tb main peaks.

	Tb^{3+} $3d_{5/2}$ Main peak	Tb^{4+} $3d_{5/2}$ Main peak	Tb^{3+} $3d_{5/2}$ Sat 1	Tb^{4+} $3d_{5/2}$ Sat 1	Tb^{4+} $3d_{5/2}$ Sat 2
ref[19]	1239.1 eV	1241.4 eV	1250.4 eV	1251.5 eV	1262.5 eV
C5a	1240.1 eV	1243.0 eV	1249.5 eV	1250.8 eV	1262.4 eV

Temperature Dynamics

The setup used in the temperature cycling experiments is schemed in Figure 6. The setup consists on a heater, an excitation source and a detection system. Inside the sample chamber of the spectrofluorometer a Kapton thermofoil heater was put in contact **B6B – DPA** and the temperature controlled with accuracy up to 0.1 K. The excitation source was a 450 W Xe arc lamp coupled to a TRIAX 320 emission monochromator and the emission spectra measured as function of the temperature using the R928 Hamamatsu photomultiplier.

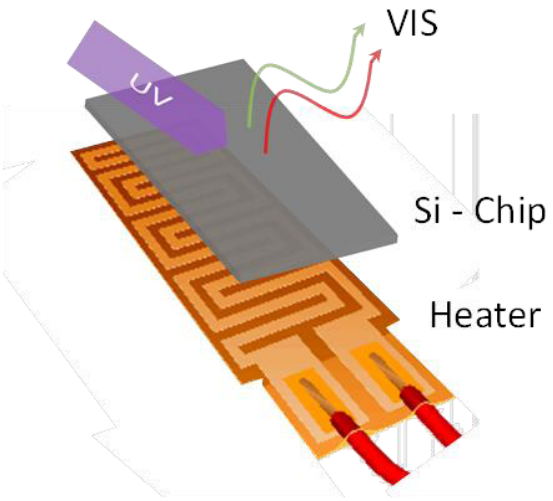

Figure 6: Scheme of the experimental setup used for the temperature control. Upon 280 nm UV excitation the functionalized Si-chip presents the typical transitions of Eu3+ and Tb3+ ions.

First, the **B6B – DPA** emission and excitation spectra were recorded at 300 K. The excitation spectrum (Figure 7A) in the range 280–350 nm presents a band of centered at 285 nm, for Eu^{3+}

and Tb^{3+}ions. The emission spectrum (Figure 7B) presents the straight lines characteristic of the lanthanide ions.

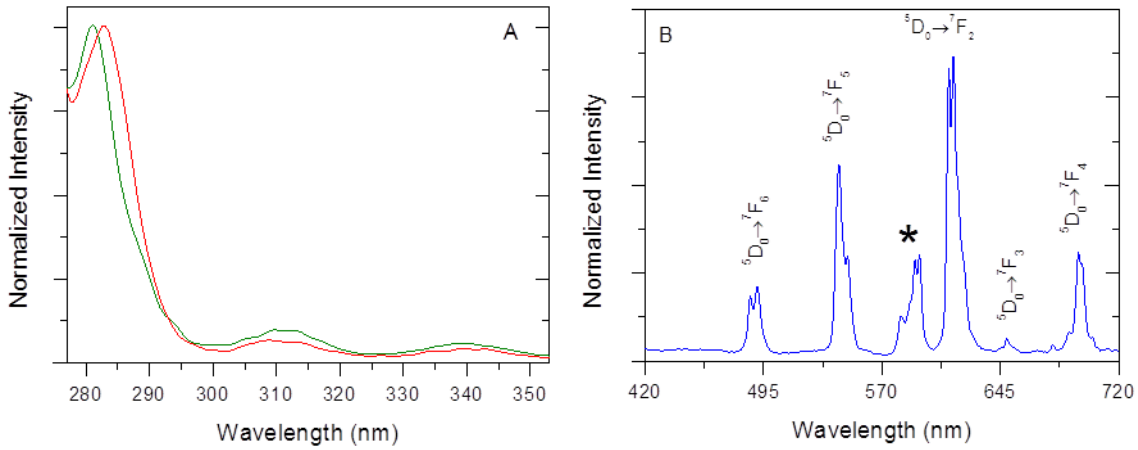

Figure 7: Excitation and emission spectra of B6B–DPA at 300 K. (A) Excitation spectrum of B6B–DPA. The red and green lines corresponds to the monitoring of the Tb^{3+} $^5D_4 \rightarrow {}^7F_5$ (542.5 nm) and Eu^{3+} $^5D_0 \rightarrow {}^7F_2$ (612.5 nm) transitions, respectively. (B) Emission spectrum of B6B–DPA. The Tb^{3+} $^5D_4 \rightarrow {}^7F_J$ (J=5,6) and the Eu^{3+} $^5D_0 \rightarrow {}^7F_J$ (J=2–4) transitions are identified. The asterisk marks the region were the overlap between the Eu^{3+} $^5D_0 \rightarrow {}^7F_{1,2}$ and the Tb^{3+} $^5D_4 \rightarrow {}^7F_4$ transitions is observed. The excitation wavelength is 280 nm.

Then, the temperature of B6B–DPA was changed at constant heating rate (1 K/min) in the temperature range 295–335–295–335K. Figure 8 shows the integrated areas I_1 and I_2 in the 295–335–295 K temperature cycling. As the temperature increase, the integrated intensity of Tb^{3+} $^5D_4 \rightarrow {}^7F_5$ (I_1) and Eu^{3+} $^5D_0 \rightarrow {}^7F_2$ (I_2) transitions decrease smoothly until 325 K. Between 325 and 335 K a stepper decrease on both integrated areas is observed (Figure 8). When the temperature decreases down to 295 K the integrated areas are restored to the initial values.

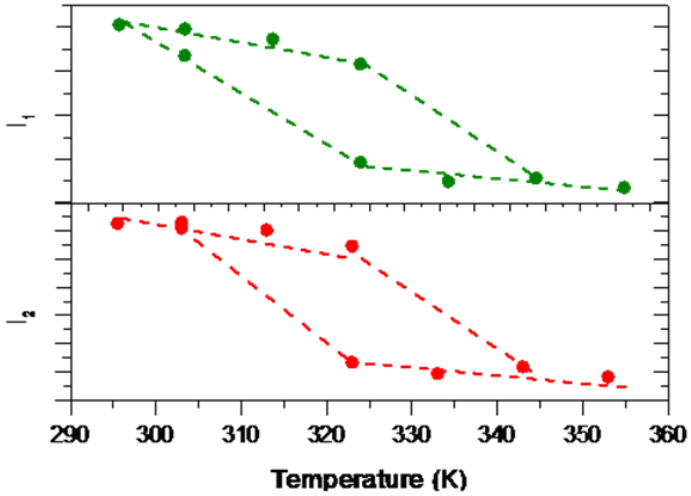

Figure 8: Hysteretic behavior of the integrated areas I1 and I2 in the temperature range 295–355–295 K. The emission spectra of B6B–DPA were recorded upon 280 nm excitation.

Taking advantage of the well-known[22] local environment probing of the Eu^{3+} $^5D_0 \rightarrow {}^7F_2$, it is possible to follow even minor changes in the local environment of the ion by simple analysis of the emission spectra.

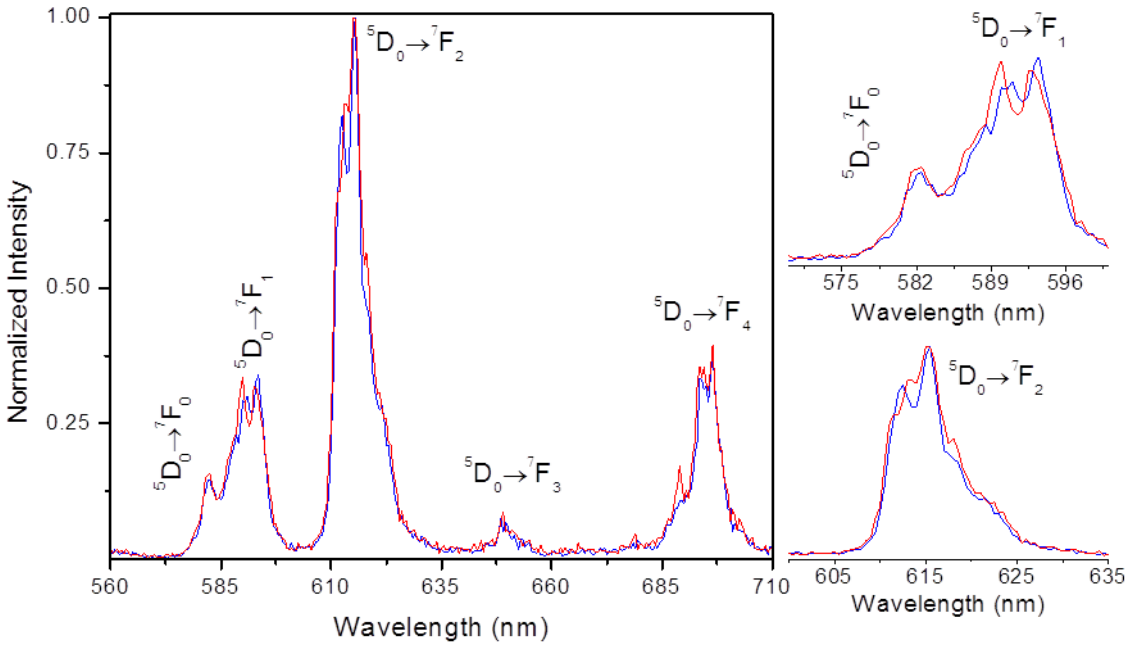

Figure 9: Emission spectra of B6B–DPA upon 280nm excitation. The red and blue lines correspond to the emission spectra recorded at 297 and 330K, respectively. The 5D0→7F2 transition is not significantly affected by the temperature increase, meaning that the local symmetry of the Eu3+ ion does not change significantly.

The definition of $\Delta=I_1/I_2$ makes the analysis of each emission spectrum straightforward and independent of the excitation power. The evolution of Δ in the temperature range 295–340 K in four consecutive cycles is presented in Figure 10. The Δ parameter follows essentially the same hysteretic cycle presented in Figure 8 for the integrated areas of I_1 and I_2. Moreover the heating and cooling cycles present the same dynamics.

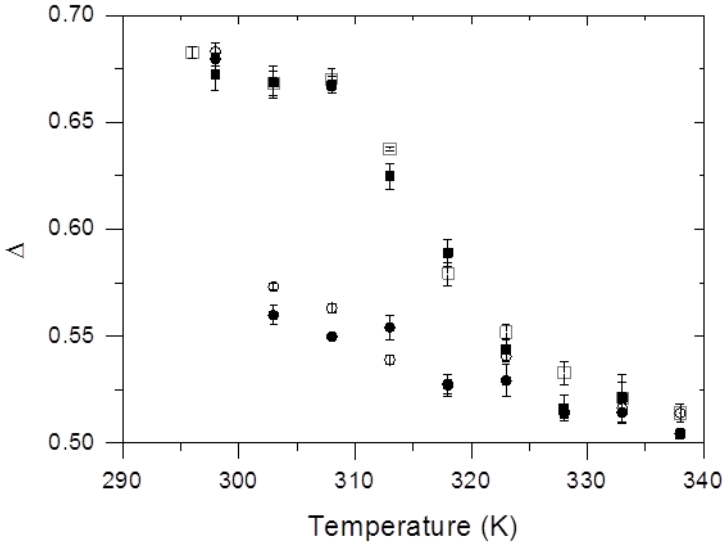

Figure 10: Temperature cycling in 295-335 K temperature range. The thermometric parameter was computed when the temperature was increased (squares) and decreased (circles). Solid symbols identify the first and the second cycles whereas the third and the fourth cycles are represented using open symbols. The error bars result from the propagation of the errors in the determination of I1 and I2.

Acknowledgments

Financial support from the Spanish Ministry of Science and Innovation research grants BFU2009-12763/BFI, MAT2011-259911 and Project Consolider-Ingenio in Molecular Nanoscience CSD2007-00010 are gratefully acknowledged. CDSB (SFRH/BPD/89003/2012) thank FCT for a grant.

References

1. E. Southern, K. Mir and M. Shchepinov, *Nat Genet*, 1999, **21**, 5-9.
2. S. A. Campbell, *The Science and Engineering of Microelectronic Fabrication*, Oxford, New York, 2001.
3. S. F. Bent, *Surf Sci*, 2002, **500**, 879-903.

4. R. C. Webb, A. P. Bonifas, A. Behnaz, Y. H. Zhang, K. J. Yu, H. Y. Cheng, M. X. Shi, Z. G. Bian, Z. J. Liu, Y. S. Kim, W. H. Yeo, J. S. Park, J. Z. Song, Y. H. Li, Y. G. Huang, A. M. Gorbach and J. A. Rogers, *Nat Mater*, 2013, **12**, 938-944.
5. C. D. S. Brites, P. P. Lima, N. J. O. Silva, A. Millán, V. S. Amaral, F. Palacio and L. D. Carlos, *Adv Mater*, 2010, **22**, 4499-4504.
6. C. D. S. Brites, P. P. Lima, N. J. O. Silva, A. Millán, V. S. Amaral, F. Palacio and L. D. Carlos, *New Journal of Chemistry*, 2011, **35**, 1177-1183.
7. C. D. S. Brites, P. P. Lima, N. J. O. Silva, A. Millán, V. S. Amaral, F. Palacio and L. D. Carlos, *Nanoscale*, 2013, **5**, 7572 - 7580.
8. A. M. Klonkowski, S. Lis, M. Pietraszkiewicz, Z. Hnatejko, K. Czarnobaj and M. Elbanowski, *Chem Mater*, 2003, **15**, 656-663.
9. L. S. Jang and H. J. Liu, *Biomed Microdevices*, 2009, **11**, 331-338.
10. R. Boukherroub and D. D. M. Wayner, *J Am Chem Soc*, 1999, **121**, 11513-11515.
11. H. Amiri, R. Bustamante, A. Millan, N. J. O. Silva, R. Pinol, L. Gabilondo, F. Palacio, P. Arosio, M. Corti and A. Lascialfari, *Magn Reson Med*, 2011, **66**, 1715-1721.
12. L. M. A. Ali, M. Gutierrez, R. Cornudella, J. A. Moreno, R. Pinol, L. Gabilondo, A. Millan and F. Palacio, *J Biomed Nanotechnol*, 2013, **9**, 1272-1285.
13. O. Penon, S. Novo, S. Duran, E. Ibanez, C. Nogues, J. Samitier, M. Duch, J. A. Plaza and L. Perez-Garcia, *Bioconjugate Chem*, 2012, **23**, 2392-2402.
14. O. Penon, D. Siapkas, S. Novo, S. Durán, G. Oncins, A. Errachid, L. Barrios, C. Nogués, M. Duch, J. A. Plaza and L. Pérez-García, *Colloids and Surfaces B: Biointerfaces*, 2014, **116**, 104-113.
15. L. K. Bera, K. S. Ong, Z. Z. Wong, Z. Fu, M. Nallani and S. O. Shea, *Conf Proc IEEE Eng Med Biol Soc. 2012*, 2012, 6563-6567.
16. J. A. Howarter and J. P. Youngblood, *Langmuir*, 2006, **22**, 11142-11147.
17. F. Mercier, C. Alliot, L. Bion, N. Thromat and P. Toulhoat, *Journal of Electron Spectroscopy and related Phenomena*, 2006, **150**, 21-26.
18. Y. Zhao, J.-G. Li, M. Guo and X. Yang, *J. Mater. Chem. C*, 2013, **1**, 3584-3592.
19. G. Blanco, J. M. Pintado, S. Bernal, M. A. Cauqui, M. P. Corchado, A. Galtayries, J. Ghijsen, R. Sporken, T. Eickhoff and W. Drube, *Surf. Interface Anal.*, 2002, **34**, 120-124.
20. M. Balaguer, C.-Y. Yoo, H. J. M. Bouwmeester and J. M. Serra, *J. Mater. Chem. A*, 2013, **1**, 10234-10242.
21. B. D. Padalia, W. C. Lang, P. R. Norris, L. M. Watson and D. J. Fabian, *Proc. R. Soc. Lond. A*, 1977, **354**, 269-290.
22. H. Y. Wu, Y. H. Hu, W. Zhang, F. W. Kang, N. N. Li and G. F. Ju, *J Sol-Gel Sci Techn*, 2012, **62**, 227-233.

4.4. Biofunctionalization of Quartz Tuning Fork Probes for the study of avidin-biotin interaction

Manuscript in preparation

Mafalda Rodrigues,[a] Laura González,[b] Manel Puig-Vidal,[b] Lluïsa Pérez-García.[a]

a Department of Pharmacology and Therapeutic Chemistry, Universitat de Barcelona, Av. Joan XXIII s/n 08028 Barcelona, Spain. Fax: +34 934024539, Tel: +34 934035849, E-mail: mlperez@ub.edu

b Department of Electronics, University of Barcelona, C/Martí i Franquès 1, 08028 Barcelona, Spain

Summary

Interaction between hosts and their respective ligands can be performed using Force Microscopy. For that, the probes and substrates have to be correctly functionalized with the appropriate biomolecules.

In this work, the functionalization of a recently developed Quartz Tuning Fork probe was performed, to be used as sensor to determine the binding force between streptavidin and biotin, a system that is well known. In order to do so, the best conditions were previously studies in patterned silicon surfaces, to allow and determine with which silane/solvent system the best coverage was achieved. The analysis was performed by immobilizing biomolecules that were conjugated with fluorophores and using fluorescence microscopy to determine the intensity of the fluorescence obtained with the different approaches. Two different silanes (APTES and TESUD) were used to immobilize biotin and streptavidin, respectively. Besides these silanes, with functional groups, other silanes were used, with no functional group where the biomolecules would bind, in order to have less density of biomolecules in the surface of the probe and substrate.

The QTF probes could be successfully used to study the interactions between biotin and streptavidin.

Functionalization of tuning fork probes with biotin for molecular recognition of streptavidin

Mafalda Rodrigues,[a] Laura González,[b] Manel Puig-Vidal,[b] Lluïsa Pérez-García.[a]

a Department of Pharmacology and Therapeutic Chemistry, Universitat de Barcelona, Av. Joan XXIII s/n 08028 Barcelona, Spain.
b Department of Electronics, University of Barcelona, C/Martí i Franquès 1, 08028 Barcelona, Spain

Abstract Force microscopy is nowadays gaining much attention for the study of molecular interactions on the biological level. In this study, different approaches were followed in order to achieve the biofunctionalization of tuning fork probes for the study of the binding forces between avidin and biotin. From the tested conditions, we chose APTES 2% in acetone and TESUD 2% in ethanol, which appeared as the systems showing better results. The study of the binding between ligand and host were performed. A hysteresis between the approach and the retraction curves is observed, as result of the interaction between the biotin and streptavidin. The area between approach and withdrawal curves is related to bond energy.

1. Introduction

The molecular interactions are a key process in biological processes. It is important to determine certain parameters in biological soft samples, whether they are affinities and bindings forces between ligands and host systems[1] or rigidity of cells.[2] Nowadays, many techniques can be used for that matter; one of them relies on using AFM to measure the binding forces between molecules on the tip and on a surface. To performed this study, it is of paramount importance to achieve correctly the immobilization of molecules on the AFM probe, which can be done by functionalization of the tip with a SAM where the molecules to be studied are later immobilized.[3] Recently, Quartz Tuning Fork (QTF) probes are gaining attention. QTF probes have already been used for the photoacoustic detection of gases,[4] or as force sensor for the imaging of surfaces with atomic resolution.[5]

Its original application was in the fabrication of apparatus that require high precision control, like clocks or watches. However it was found that the QTF could be used in scanning probe microscopy, due to their piezoelectric properties. When the QTF oscillates, it generates current which is linearly proportional to the oscillation amplitude.[6] The quality factor Q is defined as the ratio between the energy stored in the resonator and the energy lost during each oscillation

period.[7] The most direct benefit of using QTFs is their high quality factor Q when operating in liquid, which means high frequency stability in this media. As demonstrated before,[8] the QTF appears appropriate to use with soft samples in liquid as demonstrated before. The immersion of the tip in liquid causes a recovery of the vibration amplitude, and allows obtaining images of the soft samples with high resolution. Advantages in the potential applications are wide due to the fact that it is self-sensing, meaning that there is no need to use a laser and a photodiode to measure the interaction as in the case of AFM cantilevers.[5] It can be easily integrated with optical techniques and it opens a wide range of applications in biomedical research. The tip is millimetre long, so the sample access is much better than with standard cantilevers; and finally, with QTF the experiments can be performed in Petri dishes, well-plates and other array-like sample preparations.

For those reasons, recently QTF has been studied as an alterantive to AFM probes for use with biological samples. Atomic force microscopy using QTF was successfully used for recognition between the enzyme glucose oxidase and the ligand glucosamine. The process is self-sensing and the recognition was performed with the probe immersed in a selected buffer to optimize the interactions.[9] QTF probes were also used to detect Gram-negative bacteria and their endotoxins. The differences in the amplitude of oscillation of the QTF were used to detect viscosity changes in the medium upon the coagulation of the Limulus Amebocyte Lysate, an assay currently used to determine the levels of endotoxin.[10] QTF have also been used as impedance sensors for the monitorization of the formation of *Pseudomonas aeruginosa* biofilm. The formation of the biofilm was detected through changes in electrical properties of the sensor.[11]

Additionally, QTF using shear mode has already proved a useful tool for the imaging of biological samples such as antibodies patterned on a silicon oxide surface[12]or *Pseudomonas aeruginosa* bacteria.[13] Using shear mode was also possible to detect the morphology of Pseudomonas aeruginosa and changes in their mechanical properties.[14]

Molecular recognition between avidin and biotin and between lysozyme and an anti-lysozyme antibody was studied using a QTF and transverse dynamic force microscopy.[15] In this work we aimed at using shear force microscopy for the detection of the interactions between molecules. We performed the functionalization of the QTF probes with biotin and of glass substrates with streptavidin to use as model.

2. Results and Discussion

Force microscopy is an important tool in the study of biological interactions. In this work, QTF probes were functionalized with biotin and corning glass slides with avidin for the study of

intermolecular ligand/host interactions. To achieve the functionalization of the surfaces, we started by activating them with piranha and then with a solution of NH4/H2O2/H2O, in order to obtain hydroxyl groups. These groups then react with an appropriate silane, with a functional group that would allow us the reaction with the intended biomolecule (Scheme 1).

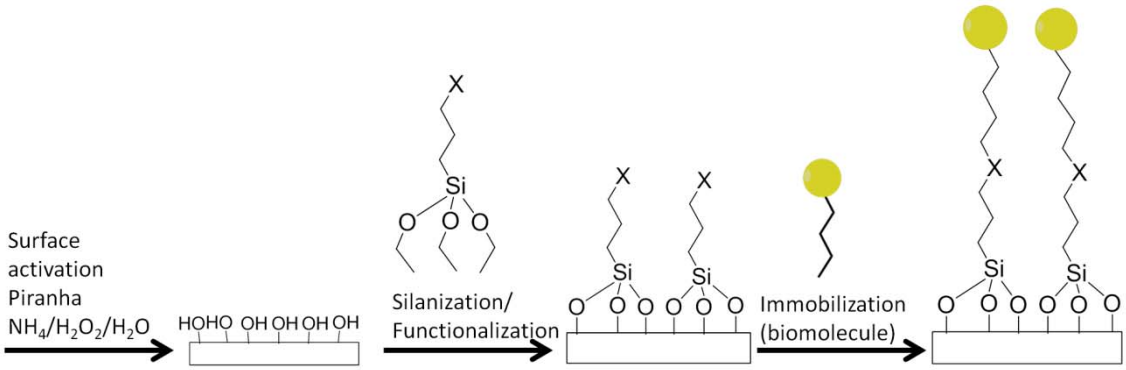

Scheme 1: Activation of silicon surfaces to introduce hydroxyl groups, silanization and immobilization of the biomolecules (avidin or biotin).

According to the functional group present in the biomolecules that was used to immobilize them on the surface, different silanes were chosen: a) TESUD was used to react with amine groups present in avidin-TR and streptavidin, and b) APTES, that has an amine that reacts with hydroxysuccinimide group, to immobilize the NHS-biotin.

Initially the surfaces used to study the correct functionalization were silicon wafers with an area of approximately 1cm2 and a pattern with 3x3 μm polysilicon particles on the thermal silicon oxide layer. These surfaces were previously described for biomolecules immobilization studies,[16,17] and due to the pattern, is easier to measure the fluorescence from the fluorophore-conjugated biomolecules. The first step was to prepare monolayers of TESUD and APTES and immobilize avidin-TR and NHS- biotin respectively. Since biotin was not conjugated with any fluorophore, its presence in the surfaces was detected by adding avidin-TR, which would bind the biotin. This complex is very strong and requires very harsh conditions to dissociate them. Therefore, the surfaces were washed with PBS containing EDTA and Triton X-100 in order to eliminate the molecules that were adsorbed on the surface and not bound.

Two different processes for the silanization process, described in literature, were tested, in order to see which showed more homogeneous covering with biotin. APTES or AUTES were used 5% in ethanol with 5% water, 2% in acetone, and APTES, AUTES or APDEMS were used 2% in toluene. After immobilizing biotin on the surface, avidin-TR was added, to bind to the biotin and the surfaces were observed on the fluorescence optical microscope. The results are shown in Figure 1, where the images from the fluorescence and a 3D representation of the fluorescence

intensity can be seen. The surfaces functionalized in toluene and with avidin-TR conjugated to the immobilized biotin showed some irregular coverage. Apart from this, the process was later discarded because the solvent also caused the QTF tip detachment from its holder.

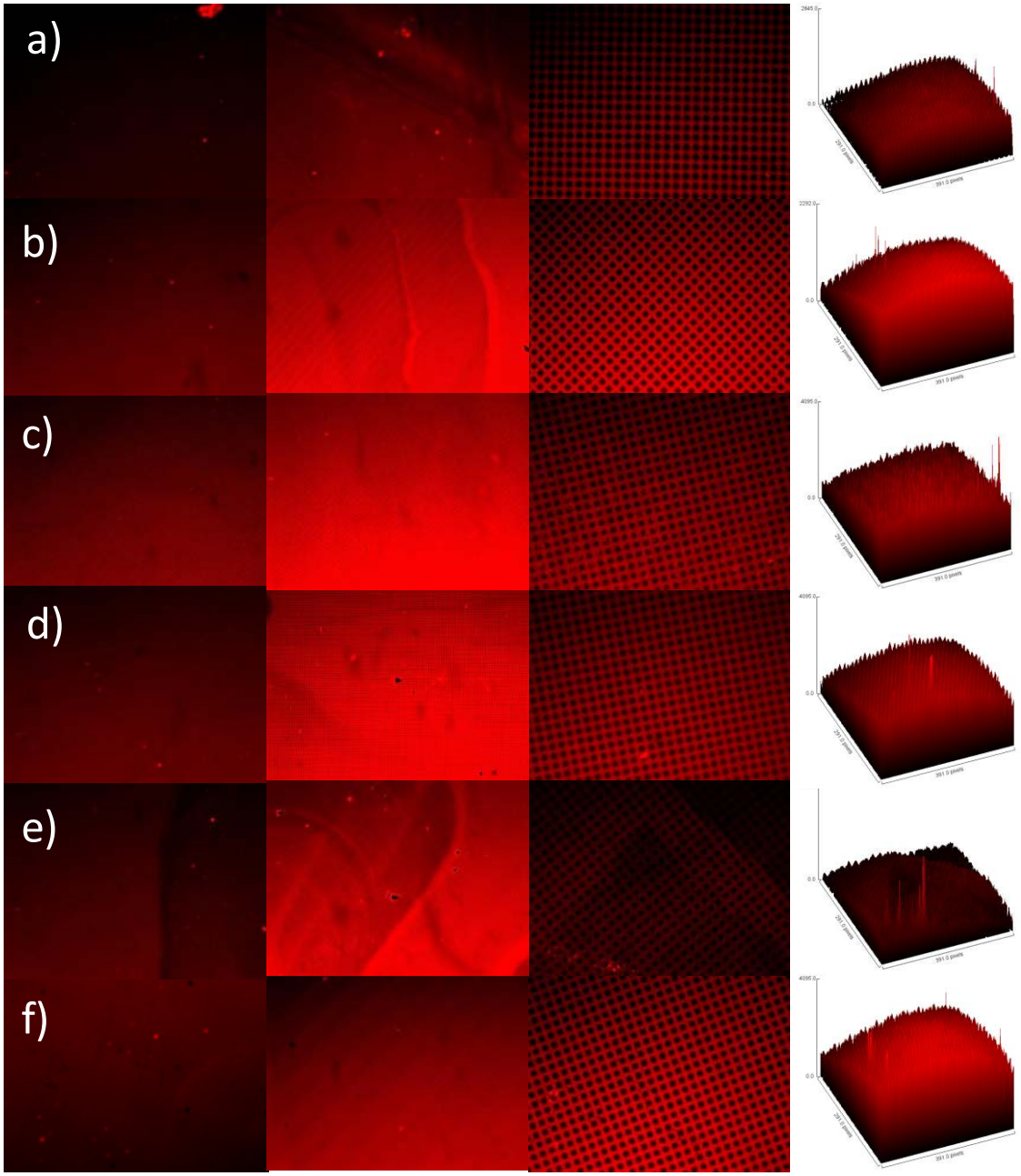

Figure 1: From left to right: fluorescence optical microscope image with 100x magnification and 3 seconds of exposition, 100x magnification and 6 second of exposition, 400x magnification and 1 second of exposition and corresponding surface plot showing the fluorescence intensity (right) of silicon surfaces with 3x3 µm polysilicon particles functionalized with: 2% in ethanol with 5% water, c) APTES and d) AUTES 2% in acetone; and e) APTES and f) AUTES 2% in toluene.

Functionalized surfaces with silane but without immobilized biotin were placed on the same avidin-TR solution, as negative control (Figure 2). The negative controls showed very low fluorescence, even though the images were taken with more exposition time, so that the square pattern could be appreciated.

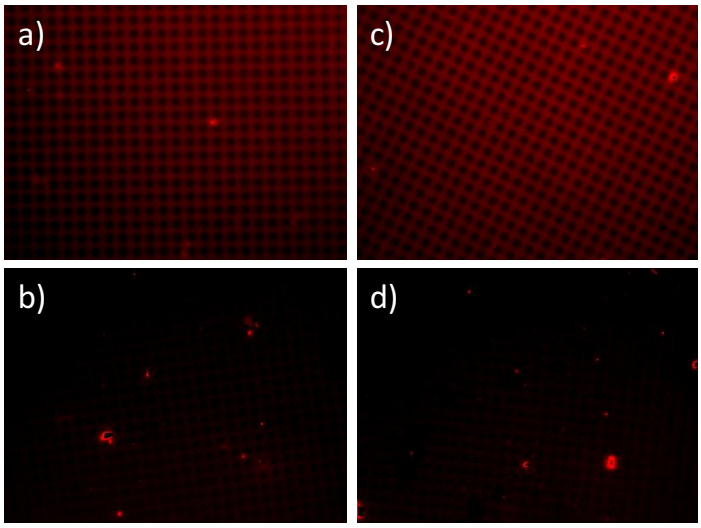

Figure 2: Fluorescence optical microscope image with 400x magnification and 3 seconds of exposition of silicon surfaces with 3x3 μm polysilicon particles functionalized with a) APTES 2% in toluene with avidin-TR conjugated with biotin and b) with avidin-TR (negative control); and c) APDEMS 2% in toluene with avidin-TR conjugated with biotin and d) with avidin-TR (negative control).

Additional silanes were introduced to form mixed monolayers: MTMS with polyethylene glycol (PEG) groups to form mixed monolayers with TESUD, and TEMS mixed with APTES, to decrease the density of the functional silanes in the surface. This is important because in the case of multivalent proteins, like avidin and streptavidin, they are present in tetrameric form and each of the subunits binds one biotin, meaning that one molecule can bind more than one ligand, and the force results would not be of the binding between the protein and one biotin. By forming the mixed monolayers, the biotin and protein molecules will be further apart, and the protein will bind just one ligand.[1,18] The mixed monolayer with APTES and TEMS has already been reported elsewhere,[18] but before the study of the interactions, monolayers with TEMS were prepared to assure that the NHS- biotin could not bind or adsorb on its surface.

Additionally, because avidin is a large protein with charges, is more likely to adsorb by electrostatic interactions to the surfaces. We proved also a mixed monolayer of TESUD (to bind avidin-TR) with TEMS, but it was found that avidin would also attach to the surface with the mixed monolayer by non-specific interactions. This was confirmed by placing a surface

funcitonalized with TEMS only, which showed the same fluorescence as the surface with TESUD or the surface with the mixed monolayer (Figure 3).

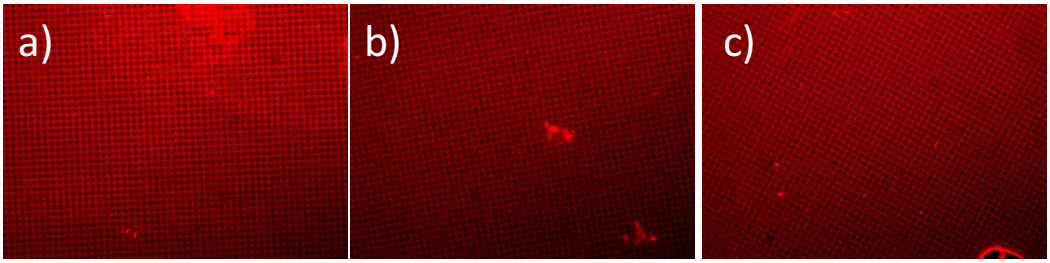

Figure 3: Fluorescence optical microscope image with 100x magnification and 2 seconds of exposition of silicon surfaces with 3x3 µm polysilicon particles functionalized with a) TESUD and avidin-TR, b) mixed monolayer of TESUD/TEMS 1:100 and avidin-TR, and c) TEMS and avidin-TR.

The functionalization with TEMS was repeated and apart from avidin-TR, wheat germ agglutinin (WGA) also conjugated with Texas Red was also tested. It was verified that between both, the fluorescence intensity observed was big, indicating that avidin is more prone to attach non-covalently to the surface covered with TEMS, as shown by the results from Figure 4. Therefore, to avoid the unspecific interactions, we chose MTMS, because the PEG groups prevents non-specific protein adhesion.[1] The mixed monolayers were also initially studied with the silicon wafers with the patterned polysilicon particles.

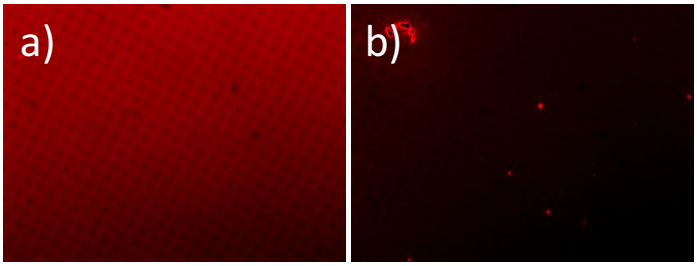

Figure 4: Fluorescence optical microscope image with 400x magnification and 4 seconds of exposition of silicon surfaces with 3x3 µm polysilicon particles functionalized with a) TEMS and avidin-TR, and b) TEMS and WGA-TR.

After the correct functionalization of the surfaces and QTF tips, the next step was the immobilization of strepavidin on the surfaces and of biotin on the tips. Scheme 2 shows the final conditions for the immobilization of the silanes APTES and TEMS and the functionalization with biotin, and the immobilization of TESUD and MTMS and the functionalization with streptavidin/avidin-TR through the amine groups present in the protein. Figure 5 shows the QTF functionalized with biotin and conjugated with avidin-TR. The presence of fluorescence

indicates that avidin is interacting with biotin on the surface, confirming the successful functionalization with biotin. The QTF probe functionalized with biotin was used to detect its interaction and binding with streptavidin, immobilized on a glass surface.

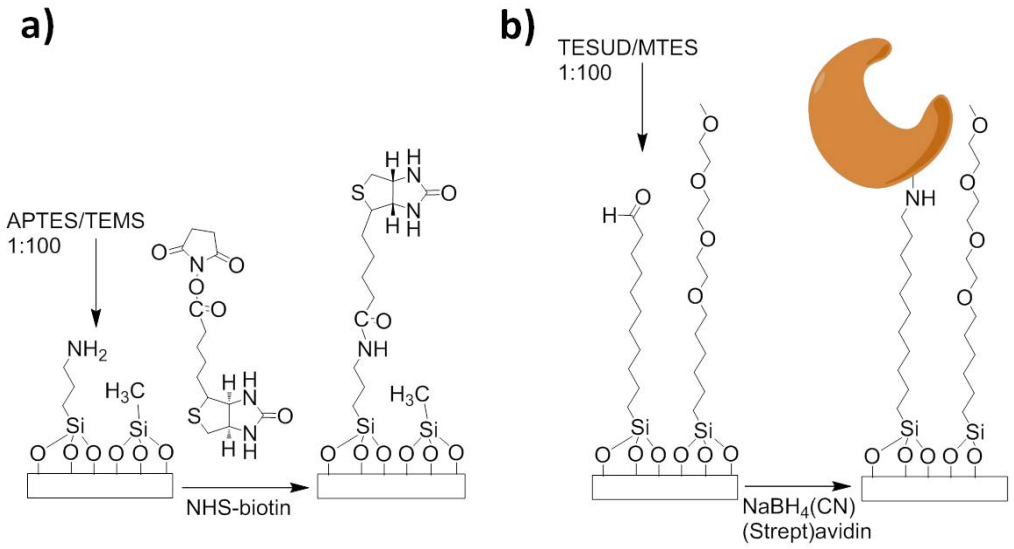

Scheme 2: a) Immobilization of APTES and TEMS, and functionalization with NHS-biotin, and b) immobilization of TESUD and MTES, and the functionalization with biomolecules containing amine groups.

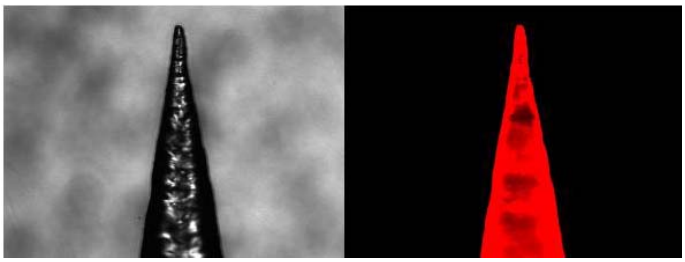

Figure 5: QTF functionalized with biotin and then conjugated with Avidin-TR. Optical microscopy images with normal light (left) and fluorescence filters (right); 200x magnification.

Amplitude versus tip–sample distance curves were performed by measuring the current, Irms, through the QTF when the functionalized biotin QTF probe was approaching onto the immobilized streptavidin on the sample surface at different retraction speeds. The QTF was driven at the resonance frequency; Irms was constant when the probe was far from the sample surface and diminished as the QTF approached the sample. Figure 4.a shows a representative graph of an amplitude-displacement curve for the biotin-streptavidin system for a retraction speed of 300 nm/s. The specificity of the interaction adding free biotin which cancels the adhesion forces was checked. The approach and withdrawal curves are almost identical without showing any distinct nonlinear jump. Interestingly, however, we observed hysteresis between

the approach and the retraction curves, indicating there is an interaction between the biotin-streptavidin system. The area confined between approach and withdrawal curves is related to bond energy and it is increased with retraction speed. However, it is difficult to quantify the unbinding force because there is no a complete mechanical model of the QTF sensor to obtain the magnitude of the forces when working in shear mode. Control curves over a non-functionalized bare glass surface were performed to confirm that the measured hysteresis was due to the specific interaction between biotin-streptavidin system and no hysteresis is observed in this case (Figure 6.b).

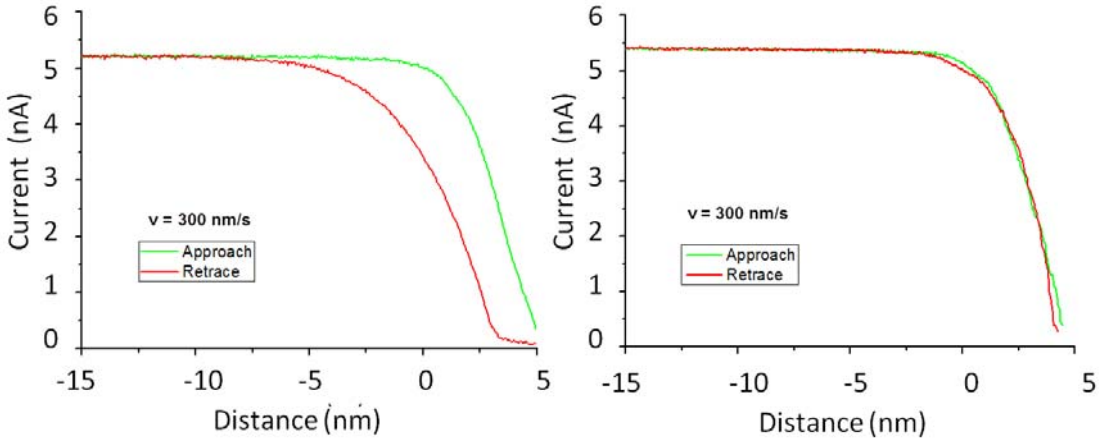

Figure 6: a) Representative amplitude-distance curve of the interaction between biotin functionalized QTF probe over streptavidin immobilized on the sample surface at retraction speeds of 300 nm/s, and b) Amplitude versus tip–sample distance control curve over a non-functionalized bare glass surface.

3. Conclusions

With this work it was confirmed that these newly developed QTF probes can be successfully functionalized to measure interactions between biomolecules. First results on molecular interaction measurements, as well as a recent publication19 show the ability of QTF to perform molecular recognition experiments. Using a well-known biochemical interaction (biotin/streptavidin or biotin/avidin[20]), the feasibility of the interaction detection with the tuning fork can be determined.

4. Experimental Section

3-aminopropyltriethoxysilane (APTES), 3-aminopropyldiethoxymethylsilane (APDEMS), triethoxymethylsilane (TEMS), Avidin-Sulforhodamine 101 (Avidin-Texas Red®), Streptavidin and (+)-Biotin N-hydroxysuccinimide ester (NHS-biotin) were purchased from Sigma,

Triethoxysilylundecanal (TESUD) from ABCR and (6-{2-[2-(2-Methoxy-ethoxy)-ethoxy]-ethoxy}-hexyl)trimethoxysilane (MTMS) from Sikemia.

The functionalized surfaces and QTF probes were observed using a Leica DMIRB wide-field transmitted light and fluorescence microscope at the CCiTUB, and the images were processed using ImageJ 1.48v.

In the experiments we used QTFs with a resonance frequency of 32,768 Hz (AB38T model, AbraconCorp., USA). The sensor was mounted on an adapted STM head integrated into a commercial AFM microscope (Cervantes model, Nanotec Electrónica, Spain) and measurements were done using a transimpedance amplifier (TIA) (model OPA656, Texas Instruments, USA).

4.1. Functionalization of the QTF and surfaces

Activation of the surfaces

The substrates (glass slides and QTF probes) were prepared as described elsewhere.16 Briefly, the surfaces were immersed in piranha solution (3:1 concentrated H2SO4 and 30% H2O2 solution) for 1 hour, rinsed with MilliQ water and dried under nitrogen. To activate the surface in order to obtain hydroxyl groups required for the functionalization step, the substrates were placed in a mixture of NH4/H2O2/H2O (1:1:5) for 30 minutes, then rinsed with MilliQ water and dried under nitrogen stream. The functionalization was done as follows:

Immobilization of streptavidin

The substrates were immersed overnight in a solution of TESUD/MTMS (1:100) 2 % in ethanol containing 2% acetate buffer pH 5.2, washed thrice with ethanol and dried under nitrogen, cured at 90°C for 20-30 minutes and placed in a 20 μg/mL solution of streptavidin in PBS (100 mM, pH 7.4) and with 5mM of sodium cianoborohydride for 6 hours, and then washed twice with a solution of EDTA 0.1% and triton x-100 1% in PBS, for 15 minutes, and in PBS for another 15 minutes, and dried with nitrogen.

Immobilization of biotin

The substrates were immersed overnight in a solution of APTES/TEMS (1:100) 2 % in acetone, washed thrice with acetone, cured at 90°C for 20-30 minutes and dried under nitrogen, and placed in a solution of NHS-biotin 20 μg/mL in PBS (100 mM, pH 7.4) (prepared from a stock of 1mg/mL in DMSO) for 6 hours, and then washed twice with a solution of EDTA 0.1% and

triton x-100 1% in PBS, for 15 minutes, and in PBS for another 15 minutes, and dried with nitrogen.

4.2. Sensors production and data adquisition

The QTF probes were custom made by attaching a chemically sharpened optical fiber (SiO2) to one of the prongs of a previously decapsulated commercial device. To sharpen the probes, a 125 µm optical fiber was immersed in a 40% HF solution, with an organic solvent on top to act as a protective layer (C8H18); then, at the interface between the acid and the solvent, a meniscus formed thereby creating a reaction gradient. The radius of the fiber decreased due to HF etching until the process automatically stopped, resulting in a 100 nm tip radius. The length of the part of the fiber protruding from the fork was between 3 and 4 mm, which was the minimum length necessary to work within the microscope liquid cell, while maintaining the QTF resonating in air. The QTFs were operated in shear mode: oscillating parallel to the sample surface. The probes were electrically driven to resonance and the amplitude of oscillation was obtained by measuring the current flowing through the sensor with a TIA amplifier.

For the experiments presented in this work, a QTF with a quality factor, Q, of 1500 and resonance frequency, f, of 34830 Hz was used (once the fiber was attached and immersed in the buffer solution). A driving amplitude of 20 mV was selected and the measured current at resonance was 5.2 nA. Force measurements were acquired bringing the biotin-coated QTF probe into contact with the substrate functionalized with immobilized avidin in phosphate-buffered saline (PBS) at room temperature. The retraction speed was varied from 200 to 1000 nm/s. The maximum indentation was controlled to minimize the contact area.

References

1. X. Zhang and V. K. Yadavalli, *Anal. Chim. Acta*, 2009, **649**, 1–7.
2. L. Alonso-Sarduy, G. Longo, G. Dietler and S. Kasas, *Nano Lett.*, 2013, **13**, 5679–5684.
3. R. Barattin and N. Voyer, in *Atomic Force Microscopy in Biomedical Research:Methods and Protocols*, eds. P. C. Braga and D. Ricci, Humana Press, Totowa, NJ, 2011, vol. 736, pp. 457–483.
4. A. A. Kosterev, F. K. Tittel, D. V. Serebryakov, A. L. Malinovsky and I. V. Morozov, *Rev. Sci. Instrum.*, 2005, **76**, 043105.
5. F. J. Giessibl, *Appl. Phys. Lett.*, 2000, **76**, 1470–1472.
6. Y. Qin and R. Reifenberger, *Rev. Sci. Instrum.*, 2007, **78**, 063704.
7. J.-M. Friedt and E. Carry, Am. J. Phys., 2007, 75, 415–422.
8. W. H. J. Rensen, N. F. van Hulst and S. B. Kämmer, *Appl. Phys. Lett.*, 2000, **77**, 1557.
9. A. Makky, P. Viel, S. W. Chen, T. Berthelot, J.-L. Pellequer and J. Polesel-Maris, *J. Mol. Recognit.*, 2013, **26**, 521–531.

10. A. Chałupniak, K. Waszczuk, K. Hałubek-Głuchowska, T. Piasecki, T. Gotszalk and J. Rybka, Biosens. *Bioelectron.*, 2014, **58**, 132–7.
11. T. Piasecki, G. Guła, K. Nitsch, K. Waszczuk, Z. Drulis-Kawa and T. Gotszalk, *Sensors Actuators B Chem.*, 2013, **189**, 60–65.
12. L. González, J. Otero, J. P. Agusil, J. Samitier, J. Adan, F. Mitjans and M. Puig-Vidal, *Ultramicroscopy*, 2014, **136**, 176–184.
13. J. Otero, L. Gonzalez and M. Puig-Vidal, *Sensors (Basel).*, 2012, **12**, 4803–4819.
14. J. Otero, R. Baños, L. González, E. Torrents, A. Juárez and M. Puig-Vidal, *Colloids Surf. B. Biointerfaces,* 2013, **102**, 117–123.
15. M. Hofer, S. Adamsmaier, T. S. van Zanten, L. A. Chtcheglova, C. Manzo, M. Duman, B. Mayer, A. Ebner, M. Moertelmaier, G. Kada, M. F. Garcia-Parajo, P. Hinterdorfer and F. Kienberger, *Ultramicroscopy,* 2010, **110**, 605–611.
16. O. Penon, D. Siapkas, S. Novo, S. Durán, G. Oncins, A. Errachid, L. Barrios, C. Nogués, M. Duch, J. A. Plaza and L. Pérez-García, *Colloids Surf. B. Biointerfaces*, 2014, **116**, 104–113.
17. O. Penon, S. Novo, S. Durán, E. Ibañez, C. Nogués, J. Samitier, M. Duch, J. A. Plaza and L. Pérez-García, *Bioconjug. Chem.,* 2012, **23**, 2392–3402.
18. Z.-H. Wang and G. Jin, *Colloids Surf. B. Biointerfaces*, 2004, **34**, 173–177.
19. J. Polesel-Maris, J. Legrand, T. Berthelot, A. Garcia, P. Viel, A. Makky and S. Palacin, *Sensors Actuators B Chem.,* 2012, **161**, 775–783.
20. G. Lee, D. Kidwell and R. Colton, *Langmuir*, 1994, **10**, 354–357.

4.5. Study of the affinity of monoclonal antibodies anti-EGFR for their antigen

Manuscript in preparation

Mafalda Rodrigues,[a,b] Jaume Adan,[c] Lluïsa Pérez-García.[a,b]

a Department of Pharmacology and Therapeutic Chemistry, Universitat de Barcelona, Av. Joan XXIII, s/n 08028 Barcelona, Spain. Fax: +34 934024539, Tel: +34 934035849, E-mail: mlperez@ub.edu

b Institute of Nanoscience and Nanotechnology IN2UB, Universitat de Barcelona, 08028 Barcelona, Spain.

c Biomed Division of Leitat Technological Center, Barcelona Science Park, 08028 Barcelona, Spain

Summary

In the same line of work of the study of molecular interactions using sensors, we aimed at studying the binding force and affinity between newly developed monoclonal antibodies, and their respective antigen EGFR. The binding affinities were determined using SPR. This technique also requires the immobilization of the biomolecules on a pre-prepared sensor chip. In this case, the immobilized molecule was the monoclonal antibodies, and their antigen was flown through the channels. Two different strategies for the immobilization of the monoclonal antibodies were tested: the first consisted of immobilizing the antibodies through interaction with Protein A, pre-loaded on the sensor chips. This strategy however did not give good results, as it has major drawbacks, and therefore a second strategy was used, where the antibodies were covalently attached to the surface through carboxymethyldextran activated with succinimide.

The analysis of the kinetic curves obtained for each of the monoclonal antibodies allowed the determination of their affinity constant and thus determine which ones had more affinity for the antigen EGFR.

Affinity study of Monoclonal Antibodies using Surface Plasmon Resonance

Mafalda Rodrigues,[a,b] Jaume Adan,[c] Lluïsa Pérez-García.[a,b]

a Department of Pharmacology and Therapeutic Chemistry, Universitat de Barcelona, Av. Joan XXIII, s/n 08028 Barcelona, Spain. Fax: +34 934024539, Tel: +34 934035849, E-mail: mlperez@ub.edu

b Institute of Nanoscience and Nanotechnology IN2UB, Universitat de Barcelona, 08028 Barcelona, Spain.

c Biomed Division of Leitat Technological Center, Barcelona Science Park, 08028 Barcelona, Spain

Abstract Surface Plasmon Resonance (SPR) was used to study the affinities of new monoclonal antibodies specific for the Epidermal Growth Factor Receptor (EGFR). Two approaches were used for the loading of the antibody into the sensor chip: using chips with Protein A and chips with carboxymethyldextran, but the second proved more suitable for the study. From the analysis of the binding of the antigen was possible to determine from all the study antibodies, which has bigger affinity for the antigen.

1. Introduction

Monoclonal antibodies are important tools for cancer therapy. Many growth factor receptors are overexpressed in many tumours, and these receptors can be targeted by monoclonal antibodies. The binding of the antibody to the receptor may help to normalize the growth rate of the tumour cell, can trigger apoptosis, and can serve to direct chemotherapeutic drugs to the tumour cells as well as to target these cells for imaging purposes, to detect the tumours.[1–3] Therefore it is of paramount importance that the antibody has high affinity and binds strongly to the antigen.

Recently, SPR has proved a powerful tool for the study of host-ligand affinity. Examples spawn from nucleic acid-ligand interactions, protein-protein interactions, lipid-protein interactions, epitope mapping and equilibrium kinetics. Characterization of biomolecular interactions of proteins associated with cellular membrane can be done through the determination of affinity and selectivity of the protein for the different lipids that can constitute the membrane.[4] Study of

the interaction between lectins and the complementary carbohydrates, which are involved in cell-adhesion events can also be performed. Examples found in literature include the binding between WGA and N-acetyl- D-glucosamine.[5] SPR was used along with AFM to obtain complementary information on the binding between the two molecules.

Antibody affinity was tested using both SPR and ELISA, to compare the results, using fibronectin and its antibody. It was demonstrated that the affinity values are not similar, because the kinetics constants of the interaction are different, but the results obtained by both methods are consistent.[6] SPR technology can also be applied to food-safety analysis, namely the detection of antimicrobial agents or growth promoters that are administered to animals and can accumulate in the meat, or the detection of microorganisms.[7] Example is the detection of ractopamine residues in pork meat using anti-ractopamine antibodies.[8]

Many detection strategies, that use the SPR as sensor, rely on the immobilization of specific antibodies, and therefore are called immunoassays. This type of assays have been used for the detection of cancer biomarker carcinoembryonic antigen (CEA),[9] of the influenza virus,[10] Immobilization of vascular endothelial growth factor VEGF was used to detect the presence of its growth factor receptor VEGFR in human blood plasma, which is overexpressed in myelodysplastic syndromes.[11]

To perform molecule immobilization, a widely used procedure is the activation of carboxylate groups present on the sensor with (N-(3-Dimethylaminopropyl)-N′-ethylcarbodiimide hydrochloride and N-hydroxysuccinimide (EDC and NHS, respectively) for the immobilization of the ligands through amine groups.[9,11] Commercially available sensors have the gold surface covered with dextran bearing carboxymethyl groups. The passivation of the surface is strong, with low unspecific adsorption of protein due to the dextran. It also allows a higher loading with functional groups to immobilize the proteins.[12] Nevertheless, other alteranative strategies are performed for the immobilization of macromolecules on the sensor chips. For example, proteins can be immobilized through non covalent bonds using histidine tags that are immobilized on the chip and interact with the protein.[13] another example found relies on the use of protein G for the immobilization of antibodies with appropriate orientation for antigen detection, because protein G interacts with antibodies through the Fc moiety, which is not involved in antigen recognition.[14] Another method found in literature consists on immobilizing neutravidin on biotin functionalized surface, and attachment of biotin-conjugated molecule, which can be proteins, like BSA, or DNA probes.[15]

One of the most known and widely used SPR-based system is the Biacore, where the changes in the refractive index close to the metal surface of the chip are detected. When ligands are

immobilized on the surface of the sensor the interfacial refractive index changes, which causes changes in the angle of reflectance. These changes are quantified by the optical part of the system.[16]

In this work, a Biacore system was used to study the affinity of different MAbs that recognize the Epidermal Growth Factor Receptor (EGFR) was studied by Surface Plasmon Resonance (SPR), in order to determine the binding constants for the EGFR. Covalent immobilization of the antibodies using EDC and NHS, and non-covalent immobilization through protein A interaction were performed.

2. Results and Discussion

The affinity between the antibodies and the antigen was studied by Surface Plasmon Resonance (SPR), using a Biacore T100. The equipment's software allowed the determination of the affinity constants of the different antibodies to the same antigen, based on the curves obtained for increasing concentrations of the antigen.

Initially we used SPR chips loaded with Protein A (Scheme 1) to immobilize the antibodies with the correct orientation, because Protein A has affinity and binds the antibodies through the Fc region, allowing the antigen-binding site to be available.

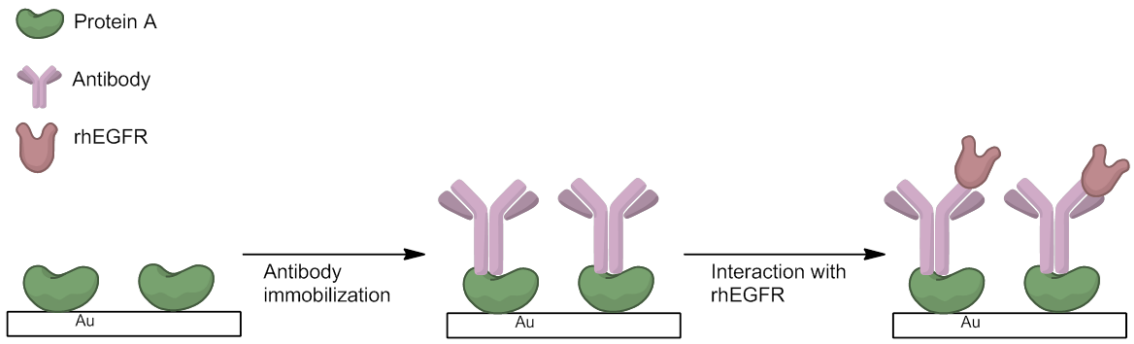

Scheme 1: Immobilization of MAbs through interaction with Protein A (Sensorchip SC PAP), and interaction between the immobilized MAbs on the surface of the chip and rhEGRF.

However, although initially this strategy seemed the most convenient, Protein A has different affinities for the different IgG subfamilies, and also depending on the origin of the MAbs (murine, human …), yielding poor binding of the MAbs to the chip. Apart from this drawback, the fact that the EGFR protein was a recombinant protein, possessing itself a Fc region, caused some of the antigen to bind to the free protein A in the chip and thus yielding RU that were not because of antibody-antigen interaction but because of the analyte binding to the chip. This, together with the fact that after each cycle the chip had to be regenerated, which implied that the

immobilized antibodies were released and a new immobilization step has to be performed, with the consequent loss of performance of the chip, caused this strategy to be abandoned. Therefore, the most common method was used, and the immobilization of the MAbs was performed using a carboxymethyldextran covered surface. The carboxymethyldextran has carboxylate groups that are activated with N-succinimide that reacts with amines present in the amino acid residues of the antibodies (Scheme 2). This immobilization is random and may immobilize the antibodies in an orientation where the antigen-binding site may not be available for epitope recognition. The advantages were that being a covalent binding, there is no need to immobilize again the MAb after each regeneration step, and the fact that there is no affinity required, the antibodies could be immobilized with higher RU, translated by higher amounts of antibody on the chip surface. Even though the antibodies were present randomly in the surface, this strategy gave better results than the previous one using protein A, and it was possible to establish the affinities of the different studied MAbs.

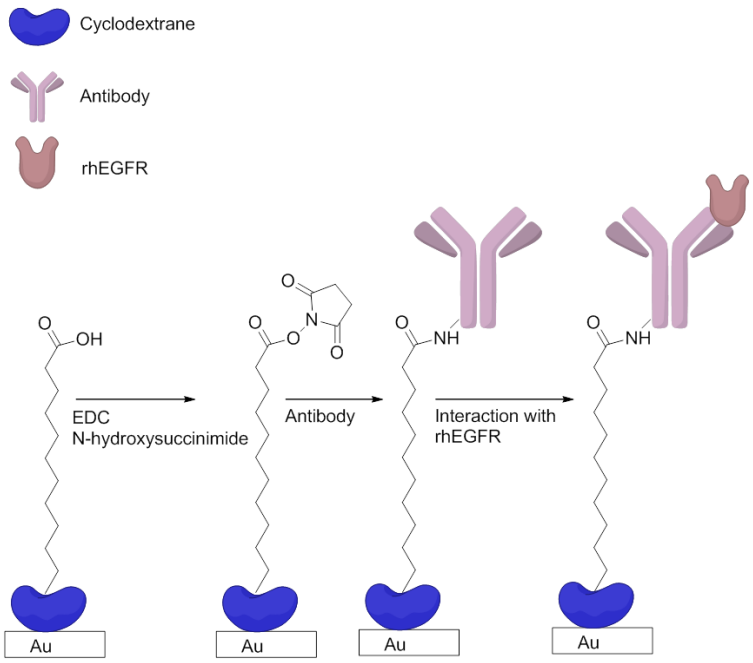

Scheme 2: Immobilization of MAbs through covalent linkage on the surface of a chip with carboxyl groups (Sensorchip SC CMDP) activated with N-succinimide, and interaction between the immobilized MAbs on the surface of the chip and rhEGRF.

The response obtained by the Biacore is proportional to the immobilized amount of MAb.

To determine the necessary amount of immobilized antibody, equation 1 is used:

$$Rmax = MWA/MWL \times RLS \quad (1)$$

where Rmax is the maximum binding for the analyte (antigen), MWA/MWL is the ratio between the molecular weight of the analyte and the immobilized ligand (antibody), RL is the response level that should be obtained for the immobilized ligand and S is the number of binding sites per ligand. In our case, the number of binding sites is 1.

Based on this, the three different MAbs were immobilized in distinct flow channels, in a way that similar RU were obtained in all three channels, assuring that similar amounts of antibodies were present on each channel. Afterwards, increasing concentrations of rhEGFR were flowed through the cells, and the response was recorded. The response obtained in each channel is proportional to the amount of rhEGFR present on the surface through its interaction with the MAb. This means that if the affinity is higher, we will have more rhEGFR present on surface, and thus a higher response signal. Increasing concentrations of the antigen were used, until the steady-state level was reached. The antigen solution is flown through the channels for a specific time, called contact time. Afterwards, the run buffer is flown during some time (dissociation time) to allow the dissociation of the antigen from the antibody. According to the different affinities, the steasy-state was achieved for higher concentrations in the case of some antibodies. It is also noteworthy that for antibodies MAb3 and MAb4 the contact time between the antigen and the flow rate had to be increased because with the same conditions used initially for MAb1 and MAb2 the RU were very low. By increasing these two parameters, more antigen is brought into contact with the antibody. Because a comparison between the antibodies had to be made, MAb1 was again tested with these new conditions, to compare the affinities with MAb3 and MAb4. Figure 1 includes the binding curves for different studied MAbs. MAB108 is a commercial antibody that was used as positive control and reference to compare the affinities.

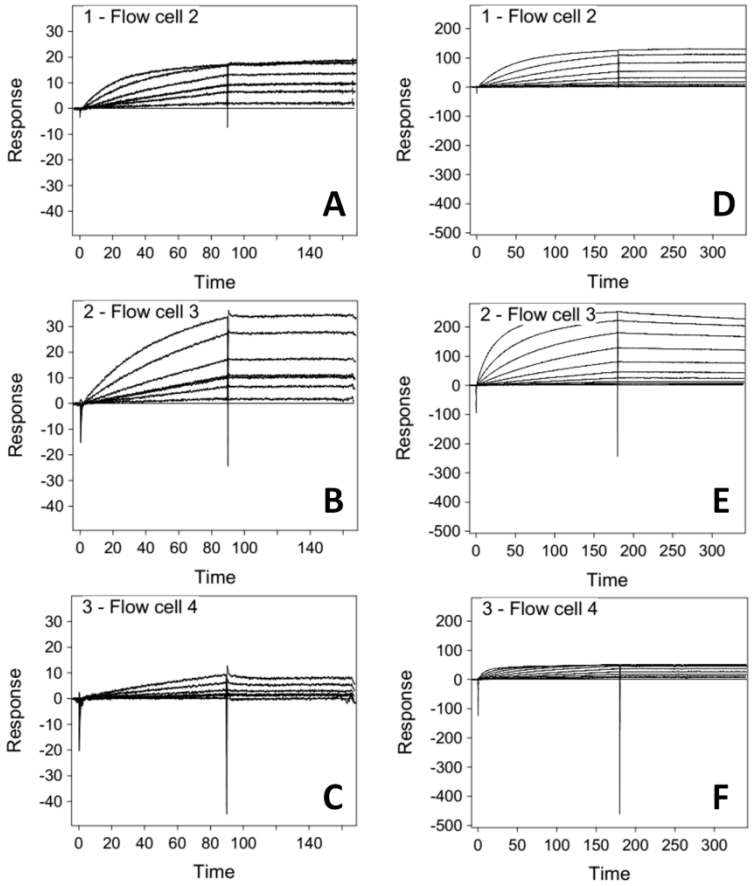

Figure 1: Binding curves obtained by SPR for commercial MAb108 (a), MAb1 (B) and MAb2 (C), using increasing concentrations of antigen (0.65 – 52.6 nM), and contact time of 90 s, dissociation time of 60 s and flow rate of 30 µL/min, and for MAb3 (D), MAb4 (E) and MAb1 (F), using increasing concentrations of antigen (0.65 – 105.2 nM for MAb3and MAb4, and 0.65 – 13.15 for MAb1) and contact time of 180 s, dissociation time of 60 s and flow rate of 60 µL/min

According to the results, the antibodies can be sorted by affinity, from higher to lower: MAb 2 > MAb 1 > MAb3. Based on the affinity constants calculated, no conclusions could be done regarding MAb4 because the steady-state could not be reached within the concentration range used.

3. Materials and methods

Recombinant human rhu-Fc-EGFR was purchased from Creative BioMart. SPR sensorchip with Protein A (SC PAP) and with carboxymethyldextran (SC CMDP) were purchased from Xantec. The anti-EGFR monoclonal antibodies MAb1, MAb2, MAb3, MAb4 were provided by Leitat. The Mab108 was obtained from ATCC. PBS buffer, BSA and Tween 20 were purchased from Sigma-Aldrich. Reagents for specific use with Biacore systems: amino coupling kit composed of (N-(3-Dimethylaminopropyl)-N′-ethylcarbodiimide hydrochloride (EDC), N-

hydroxysuccinimide (NHS), 1 M Ethanolamine hydrochloride-NaOH pH 8.5, and regeneration solution 10 mM glycine-HCl pH 2 were purchased from GE Healthcare Life Sciences and used according to the instructions from the manufacturer.

The SPR measurements were performed using a Biacore T100 (GE Healthcare Life Sciences) at the CCiTUB. Two different strategies were used:

a) SPR sensorchip with Protein A: the MAbs were immobilized through their interaction with the Protein A. An IgG1, not specific for EGFR, was immobilized in one of the flow cells to be used as control. The different MAbs were immobilized each in a flow cell, and rhu-Fc-EGFR solutions prepared in Run buffer (PBS 10 mM + Tween 20 0.05% + BSA 0.05%), with concentrations ranging from 2.6 nM to 0.1625 nM, were flowed through the channels, with a flow rate of 30 μL min-1, a contact time of 30 seconds and dissociation time of 60 seconds. After each cycle, the channels were regenerated by passing a solution of glycine 10 mM pH 2 and the MAbs were again immobilized in the corresponding flow cell.

b) SPR sensorchip with carboxymethyldextran: the MAbs were covalently linked to the sensorchip CMDP by activation it EDC and NHS, following the recommendations of the Biacore manufacturer: briefly, the first step consisted of determining the best pH for the immobilization of each antibody. The antibodies were resuspended in acetic acid solutions with pH ranging from 4 to 7, injected in the Biacore, and the response units (RU) were determined. The chosen pH for the immobilization of the antibody was the pH that allowed the highest RU to be obtained. The SPR chip was then activated by flowing through each channel a solution containing 1:1 v/v of the EDC and NHS solution. The immobilization was carried out so that similar response units (RU) for each of the MAbs were obtained in each channel. Ethanolamine was used as blocking agent, and was added after the successful immobilization of the MAbs. The rhu-Fc-EGFR was then flowed by the channels, as described previously. The regeneration was performed by passing a solution of glycine 10 mM pH 2.

In all chips, one of the four channels was reserved for the immobilization of an antibody not specific for the antigen EGFR as negative control. The final response is calculated subtracting the signal obtained for the negative control channel.

References

1. L. M. Weiner, R. Surana and S. Wang, *Nat. Rev. Immunol*., 2010, **10**, 317–327.
2. A. L. Nelson, E. Dhimolea and J. M. Reichert, *Nat. Rev. Drug Discov*., 2010, **9**, 767–774.
3. A. M. Scott, J. D. Wolchok and L. J. Old, *Nat. Rev. Cancer*, 2012, **12**, 278–287.
4. R. V Stahelin, *Mol. Biol. Cell*, 2013, **24**, 883–886.

5. M. Lienemann, A. Paananen, H. Boer, J. M. de la Fuente, I. García, S. Penadés and A. Koivula, *Glycobiology*, 2009, **19**, 633–643.
6. L. Heinrich, N. Tissot, D. J. Hartmann and R. Cohen, *J. Immunol. Methods*, 2010, **352**, 13–22.
7. C. Situ, M. H. Mooney, C. T. Elliott and J. Buijs, *TrAC Trends Anal. Chem*., 2010, **29**, 1305–1315.
8. X. Lu, H. Zheng, X.-Q. Li, X.-X. Yuan, H. Li, L.-G. Deng, H. Zhang, W.-Z. Wang, G.-S. Yang, M. Meng, R.-M. Xi and H. Y. Aboul-Enein, *Food Chem.,* 2012, **130**, 1061–1065.
9. Z. Altintas, Y. Uludag, Y. Gurbuz and I. E. Tothill, *Talanta,* 2011, **86**, 377–383.
10. C. E. Nilsson, S. Abbas, M. Bennemo, A. Larsson, M. D. Hämäläinen and A. Frostell-Karlsson, *Vaccine,* 2010, **28**, 759–766.
11. K. Pimková, M. Bocková, K. Hegnerová, J. Suttnar, J. Cermák, J. Homola and J. E. Dyr, *Anal. Bioanal. Chem.,* 2012, **402**, 381–387.
12. S. Löfås, B. Johnsson, K. Tegendal and I. Rönnberg, *Colloids Surf. B. Biointerfaces*, 1993, **1**, 83–89.
13. M. Fischer, A. Leech and R. Hubbard, *Anal. Chem*., 2011, **83**, 1800–1807.
14. G. Bergström and C.-F. Mandenius, *Sensors Actuators B Chem*., 2011, **158**, 265–270.
15. Z. Altintas, Y. Uludag, Y. Gurbuz and I. Tothill, *Anal. Chim. Acta*, 2012, **712**, 138–144.
16. S. C. B. Gopinath, *Sensors Actuators B Chem*., 2010, **150**, 722–733.

4.6. Appendix: Functionalization of Quartz Tuning Fork Probes for the study of Concanavalin A-mannose interaction

Besides the immobilization of biotin and avidin for the binding force studies (Chapter 4.4), the same was done with Concanavalin A and mannose, for its study using the QTF probe, because it's a host-ligand system already studied by AFM,[53,253,254] which would allow a direct comparison between these two techniques. However, the interaction study with the prepared QTF probes is yet to be performed.

The first step involved the chemical modification of mannose, because the molecule did not present any group that could be used for immobilization. An amine group was thus introduced as described elsewhere.[263]

As before, the first proofs were performed in a silicon surface with patterned polysilicon squares, and the mannosylamine molecule was immobilized through the amine onto the surface functionalized with TESUD, as described previously (Chapter 4). Concanvalin A conjugated with Fluoresceín Isothiocyanate (FITC) was then added, to bind to the mannosylamine and allow the surface to be observed by fluorescence microscopy. **Figure 4.11** shows the image taken of the functionalized surfaces.

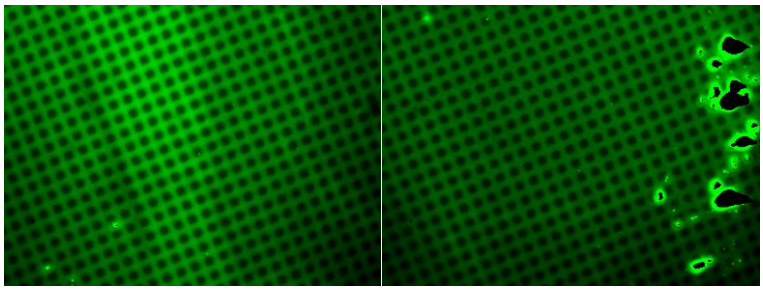

Figure 4.11: Optical microscopy images of silicon surface with mannosylamine and Concanavalin A-FITC, with 400x magnification and 60 seconds of exposure time.

From the above Figure, it is clear that we have the fluorescence of Concanavalin A, which could indicate the interaction with the immobilized sugar. However, in this experiment, we did not have proof that the presence of the Concanavalin A was not due to unspecific interactions or immobilization directly on the silane, caused by incomplete or absent immobilization of mannosylamine, and because Concanavalin A has also free amines that could react with the TESUD. Therefore, new experiments were performed in order to confirm that the presence of Concanavalin A was due to interaction with immobilized mannose.

Contact angle measurements were performed for the surfaces with a SAM of TESUD, and after the immobilization reaction with mannosylamine. To compare the values, a control was performed with the immobilization of Concanvalin A. The results are shown on **Table 4.1**.

Table 4.1: Contact angle measurements for the different surfaces, after functionalization with TESUD, and after immobilization with Mannosylamine or Concanavalin A.

surface	Contact angle
TESUD	76.5 ± 1.2
TESUD + Manosylamine	64.1 ± 3.2
TESUD + Concanavalin A	67.6 ± 7.1

As we can see, the variation between the surfaces before and after immobilization are not very big, and the one obtained between the samples with mannosylamine and Concanavalin A are very similar.

An experiment was performed, in order to assure that the mannose is on the surface and that the fluorescence observed comes from the interaction between the Concanavalin A and the immobilized sugar. The washing step after the addition of the proteins to the surfaces was performed with PBS with EDTA 0.1% and triton x-100 1%. The results obtained are presented in **Table 4.2**.

We can observe that Concanavalin A does not attach to the clean surface without any silane (surface 1). Then 2-(2-Aminoethoxy)ethanol was immobilized on the surface and two diferent proteins were attached: Concanavalin A (surface 2) and WGA (surface 3) in order to see if the 2-(2-Aminoethoxy)ethanol could block all the reacting sites of TESUD, but from the images is clear that the proteins still attach. Other surfaces were functionalized with TESUD, mannosylamine was immobilized, and again 2-(2-Aminoethoxy)ethanol was added before Concanavalin A (surface 4) or WGA (surface 5). It's noteworthy that in the surface with Concanavalin A we have some fluorescence, unlike the one with WGA. Since both showed good binding to the surfaces with just 2-(2-Aminoethoxy)ethanol, this means that in surfaces 4 and 5 we have the mannosylamine immobilized, and therefore Concanavalin A could attach, but not WGA. The fact that the fluorescence observed is so low is because the washing done with PBS with EDTA 0.1% and triton x-100 1% helps detach the Concanavalin A from its ligand sugar.

Table 4.2: Summary of the conditions used for different immobilization strategies on silicon surface and the corresponding fluorescence microscopy images, obtained with a 200x magnification and 60 seconds of exposure time.

Surface	Silane	Biomolecule	Block	Biomolecule	Fluorescence microscopy image
1	no	Conc. A	no	no	
2	TESUD	no	Aminoethoxy ethanol	Conc A	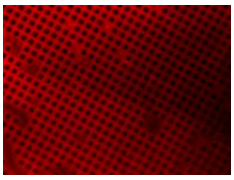
3	TESUD	no	Aminoethoxy ethanol	WGA	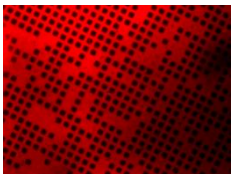
4	TESUD	Mannosyl amine	Aminoethoxy ethanol	Conc A	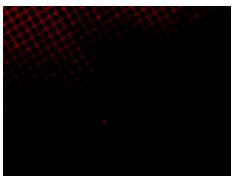
5	TESUD	Mannosyl amine	Aminoethoxy ethanol	WGA	

After the evidences of the correct immobilization of the biomolecules, we proceeded to perform the same procedure on the QTF probes.

Chapter 5

Summary of Results

Supramolecular chemistry represents the basic key to the synthesis of nanomaterials through a bottom-up approach, especially relying on phenomena such as self-assembly and self-organization. This thesis is focused on the usage of the self-assembly to build up nanomaterials. The self-assembly could be of molecules forming nanostructures (hydrogels), or on surfaces which could also be obtained through a bottom up approach, using chemical processes (gold nanoparticles), or a top down approach using physical processes (QTF probes and silicon surfaces). Distinct applications were explored in a biological context, whether it was therapy or sensing.

To facilitate the discussion of the results as a whole, this section was divided in two: the first dedicated to the results obtained for the synthesis of GNP and hydrogels with bis-imidazolium amphiphiles, and the second to the assembly of monolayers of thiols in GNP and of silanes in surfaces. Therefore, the discussion does not follow the chapter order.

Nanostructures based on bis-imidazolium amphiphiles

One of the main objectives was pursuing therapeutic applications using the components of a bis-imidazolium family that was previously discovered in the group, and it was known that could assemble into micelles due to their amphiphilic character. Other important feature was their ability to recognize and serve as host for anionic molecules, which has already been described in earlier publications.

Because of their amphiphilic character, the ability of the bis-imidazolium derivatives to be used in the synthesis of GNP was tried. One of the most commonly used methods to obtain monodisperse GNP in solution is the Brust-Schiffrin method in a byphasic system. Therefore, and having found precedents in literature, the synthesis using the amphiphilic bis-imidazolium-based ligands with open structure **1·2Br** and **2·2Br**, and an analogue macrocycle **3·2Br** (**Figure 5.1**) both as transfer agent as well as stabilizer was attempted. The GNP could be successfully obtained using any of the 3 ligands. This was initially confirmed by UV-visible absorption spectroscopy, where the obtained spectra showed an absorption peak around 520 nm, corresponding to the typical SPR peak of the GNP. It is important to remark that a ligand with the same polar head as **3·2Br**, but with alkyl chains with 1 carbon instead of 18, was also used to synthesize GNP, but without success, showing the importance of the amphiphilic character of

the molecules in the process.

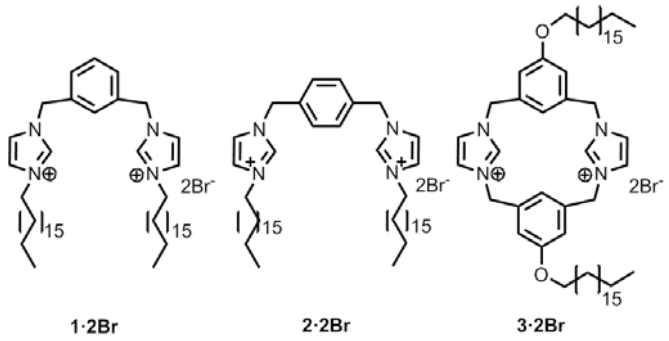

Figure 5.1: Structure of bis-imidazolium amphiphiles **1·2Br-3·2Br**

XPS showed the presence of the characteristic binding energies of Au^0 at 88.2 and 84.5 eV corresponding to the double peaks of Au $4f_{5/2}$ and Au $4f_{7/2}$ therefore confirming that the gold was in the reduced state. These peaks are only visible after sputtering of the sample, otherwise the gold core is below the outer layer of ligands and is not detected.

The size and morphology of the GNP was assessed through TEM, and it was found that all of the GNP were spherical. **1·GNP** have slightly bigger gold core size (8.8 nm) whereas **2·GNP** have 6.5 nm and **3·2Br** have 5.3 nm. DLS was used to determine the hydrodynamic size of the GNP. **1·GNP** showed a hydrodynamic size around 20 nm, which correlates well with the presence of a monolayer of ligand around the gold core, and **2·GNP** have 36.9 nm, which is slightly bigger. However **3·GNP** show a size of 73.5 nm, which is twice the one found for the GNP synthesized with open structure ligands. A possible explanation can be the bulky geometry of the cyclic ligands.

MALDI-TOF-MS was performed to help enlighten the nature of the interaction between the protophane and the gold core. the spectra were recorded in different conditions, and in the case of **1·GNP** all the most abundant peak was the singly charged peak corresponding to the gold complex with the two imidazolylidene moieties of one molecule of **1·2Br [(M-2Br-2H+Au)$^+$]**, but in the case of **3·GNP**, this peak was not visible. The most abundant peak corresponded to[**(M-2Br+Au)$^+$**], suggesting that maybe the differences on the polar head between **1·2Br and 3·2Br**, which are responsible for the stabilization of the GNP, may result in different interactions with the gold present in the core.

Elemental analysis was also performed, but no conclusive results could be obtained. The amount (in mass) of ligands present in the GNP samples was determined by Thermogravimetric Analysis (TGA). This value, along with the ligand:Au ration and the diameter of the gold core determined by TEM, allowed us to calculate the number of ligands present per nm^2 in the GNP. **1·GNP**, **2·GNP** and **3·GNP** have approximately 28, 30 and 3 molecules of ligand per nm^2

respectively. It is visible that in the case of **1·GNP** and **2·GNP**, which have both ligands with open chain polar heads, the number of ligands is very similar. However in the case of **3·GNP**, which has the cyclic polar head, the number of ligands is 10 times lower. This can be possible to the fact that the ligand has a bulkier head, and is more difficult to fit more molecules in the same area in comparison with the open chain analogues.

The incorporation of an anionic drug on the ligand layer of **1·GNP**, **2·GNP** and **3·GNP** was assessed using sodium ibuprofenate as model. After the successful incorporation of the drug, the *in vitro* release of the ibuprofenate from the GNP was studied at pH 5.5 and 7.4 (the first corresponds to the pH found in human skin and the second to physiological pH).

In the case of **1·GNP** the release rate and kinetics depended greatly on the pH used: at pH 7.4 it followed a first-order and at pH 5.5 it followed a zero-order release. The release rate at pH 5.5 was 1.265×10^{-5} mmol h^{-1} and 39.98 h^{-1} at pH 7.4. Observing the release curves in **Figure 5.2** it is visible the different release kinetics.

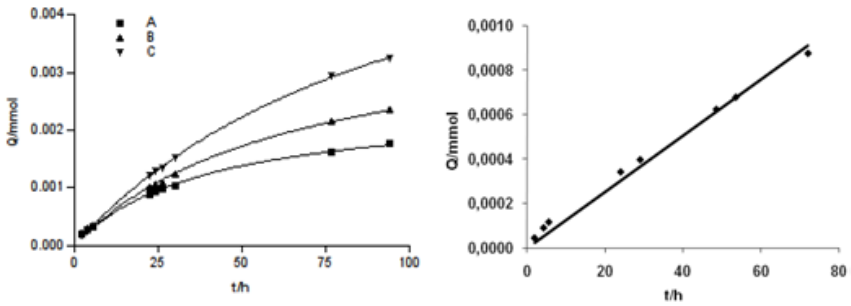

Figure 5.2: Release profile of sodium ibuprofenate at pH 7.4 (A) free in solution, (B) ibuprofenate-**1·2Br**, and (C) ibuprofenate-**1·GNP** (left); and at pH 5.5 from ibuprofenate-**1·GNP**.

Due to the fact that the ligand **3·2Br** has more affinity, it was expected a higher loading of drug. **3·GNP** could extract and incorporate 85% of the total sodium ibuprofenate, whereas in the case of **1·GNP** the value was 70%. However, it was found that the release was much slower. **Figure 5.3** shows the release curves of ibuprofenate from **3·GNP**. The release rates obtained were very similar: 0.0085 h^{-1} at pH 5.5 and 0.0060 h^{-1} at pH 7.4. The pH does not appear to affect the kinetic of the release: at both pH 5.5 and 7.4 the release follows a first order kinetic, unlike what was observed for **1·GNP**, where the release kinetic changed with the pH. Comparing these rates with the obtained at pH 7.4 with **1·GNP**, which also followed a first order kinetic, it can be seen that they differ by 3 orders of magnitude. It is important to remark that the amounts of drug being released from **3·GNP** are in the μmol range, whereas with **1·GNP** the amounts were in the mmol range.

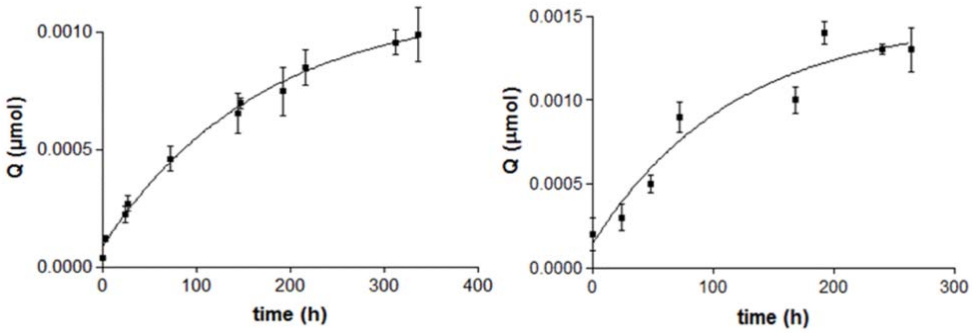

Figure 5.3: Release profile of ibuprofenate from **ibuprofenate-3•GNP** at pH 7.4 (left) and pH 5.5 (right).

After the successful synthesis of the GNP in a biphasic system, and following examples in the literature, the synthesis was performed in aqueous medium using ligand **1·2Br**. Because **2·2Br** and **3·2Br** are more hydrophobic that **1·2Br**, only the later was used. Different Au/ligand ratios were tested, and after finding the most adequate ones, the GNP were characterized. It was found by UV-visible absorption spectroscopy that the GNP solution presented a peak corresponding to the SPR at 534 nm. This value is slightly shifted from the one obtained with the ligands in organic medium, possibly because the medium is different, and also due to differences in the ligand layer around the GNP: it was postulated that to obtain GNP that are soluble in water there must be a double layer of ligands where the outer layer has the polar head facing outward.

The size of the gold core as determined by TEM was 10 nm, which similar to the ones obtained with the synthesis in biphasic system. DLS could not be used to determine the hydrodynamic size of the GNP. TGA was performed and it was calculated that these water-soluble GNP have approximately 72 ligands per nm^2, a value which is a bit more than the double of ligands found per nm^2 in **1·GNP** synthesized in organic medium. These results are in agreement with the proposed hypothesis that the gold core is surrounded by a bilayer of ligand.

To study the incorporation and *in vitro* release, piroxicam was chosen as a model drug, because it is a poorly water-soluble drug. The release was performed, as described before, at pH 5.5 and 7.4 (**Figure 5.4**).

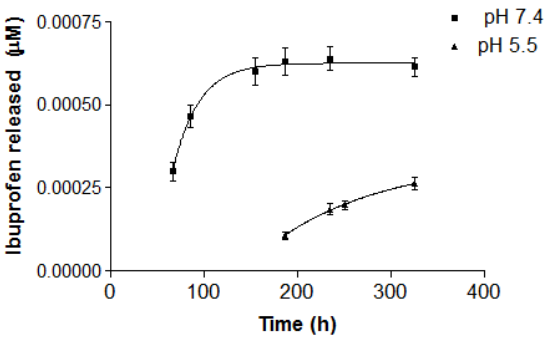

Figure 5.4: Release profile of piroxicam at pH 7.4 and pH 5.5 from **1·GNP**.

Although the profiles do not seem similar, the analysis of different models showed that the release of piroxicam followed the same kinetic in both cases: one phase exponential. Furthermore, the delay found at the beginning indicates the importance of the partition of the drug between the interior of the ligand layer of the GNP and the outer donor solution. This confirms that in this case the incorporation of the drug does not rely entirely in the affinity of the polar head for the drug; it depends on the hydrophobic environment that is present in-between the double layer of ligands. The release rates found were 0.0081 h^{-1} at pH 5.5 and 0.0367 h^{-1} at pH 7.4, which is an order of magnitude higher comparing with pH 5.5.

Additionally, the activity of the released piroxicam was also evaluated. In order to do so, the activity of the cyclooxygenase (COX) was assessed, to determine the inhibition exerted by the drug. The effect of piroxicam being released could be seen, as a decrease in the activity of the COX was obtained when comparing with GNP with no drug, nevertheless the GNP themselves were responsible for some inflammatory effect, and therefore the action of the drug was against the inflammation induced by an external agent, but also against the response to the GNP.

The cytotoxicity and genotoxicity of the ligands were performed to assess their safety for biological applications. The EC_{50} determined for **1·2Br**, **2·2Br** and **3·2Br** was 15 μM, 45 μM and 64 μM respectively. The values are all within the same range, but **1·2Br** presents a slightly lower value. Furthermore, the EC_{50} value for **1·GNP** was assessed but it proved to be higher than the maximum tested value (70 μg/mL). Water soluble **1·GNP** presented an EC_{50} value of 30 μg/mL. Comparing with the **1·GNP** soluble in organic medium, this difference can be explained by the disposition of the ligands that cover the gold core: the positive charges of the polar head facing outward can account for the higher cytotoxicity.

None of the analysed samples should genotoxicity, determined by the Comet Assay.

The internalization of the **1·GNP** was studied using Caco-2 Cells as model. It was found that the ones that are soluble in organic medium are found inside the cell, in early endosomes and lysosomes, but after 24 hours they are removed by some excretory process. However, the ones that are water soluble were found free in the cytoplasm. This finding can also be related to the double layer of ligand in the later that helps the GNP to enter through alternative routes to phagocytosis.

During the characterization of the compounds, it was found that some had the ability to form gels when in a solution of ethanol and water. Firstly, the conditions for the gel formation were tested, since the spontaneous assembly occurs with adequate ratios of ethanol and water.

After assessing the best ratios that allowed obtaining the gels, variable amounts of different anionic drugs were introduced: the non-steroidal anti-inflammatory drugs (NSAIDs) ibuprofenate (Ibu) and indomethacin (Ind) were chosen as model, besides methotrexate (Mtx), which is used in auto-immune diseases therapy such as rheumatoid arthritis (**Figure 5.5**).

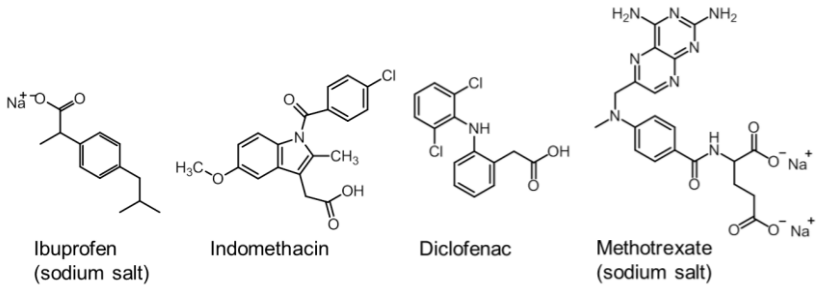

Figure 5.5: Structure of the gelator molecule **1·2Br** and of the model drugs that were studied.

The obtained gels were characterized and the results confirmed the size and tridimensional structure of the fibbers. It was found that the fibbers have 40–80 nm for **gel-1**, 100–120 nm for **gel-Ibu**, 60–100 nm for the **gel-Ind** and 100–120 nm for the **gel-Mtx**. ^{1}H NMR spectra were recorded for the gels with increasing amounts of drug, and it was found that no peak was visible in the case of ibuprofenate or methotrexate, but in the case of indomethacin, peaks corresponding to the drug were found. This indicates that the first two are interaction with the gel, probably included in the fibbers, but in the case of indomethacin part is dispersed in the interstitial space. The effect of the drug in the rheological behaviour of the gel was determined, and it was found that **gel-Mtx** presents a crossover value that is three times the value obtained for the other gels, indicating that **gel-Mtx** has higher resistance to applied tensions.

After characterization, a set of studies were made to assess the viability of the obtained nanomaterial to be used in therapy, namely, as vehicle for drug delivery. Therefore, a study of the release *in vitro* was performed with the gels incorporating drugs that could be successfully obtained (**Figure 5.6**).

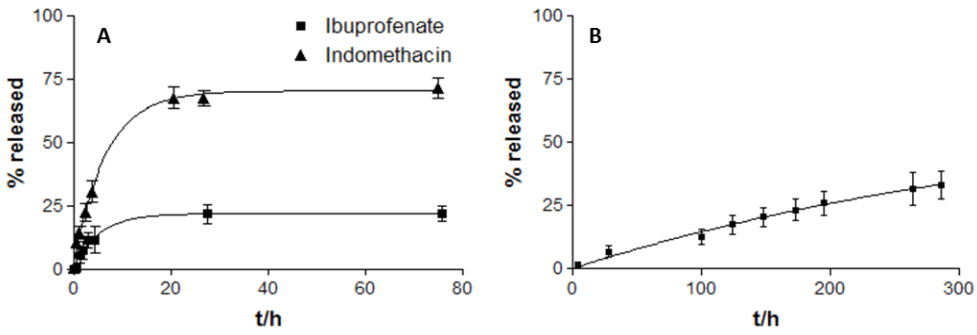

Figure 5.6: Release profile of sodium ibuprofenate and indomethacin (A) and sodium methotrexate (B) from respective gels at pH 5.5 and 32°C.

The release of the drugs from the hydrogel followed a first-order kinetic. **Gel-Ibu** and **gel-Ind** presented very similar release profiles with release rates of 0.19 and 0.15 h^{-1}. However the amount of indomethacin released from **gel-Ind** is more than three times the amount of released ibuprofenate. The release rate of methotrexate found was 0.0026 h^{-1}, which is much slower. In the case of ibuprofenate and indomethacin, 50% of the maximum released amount was achieved after approximately 4 hours, whereas in the case of the methotrexate it takes around 280 hours to achieve 50% of the maximum amount released.

Based on the results, indomethacin was chosen for an *ex vivo* experiment, and furthermore, the anti-inflammatory activity of the NSAIDs ibuprofenate and indomethacin were also assessed in vivo. Indomethacin-containing gel showed higher activity when compared with the ibuprofenate-containing gel. This was in agreement with the fact that indomethacin appeared to release faster, and could thus be more available.

After finding literature where GNP were synthesized *in situ* using gels as templates, this same approach was used, by incorporating the $HAuCl_4$ salt (precursor for the synthesis of the GNP) in the bis-imidazolium hydrogel. After the gel was formed, and aged for a couple of days, an aqueous solution of $NaBH_4$ was added. It was visible that the hydride was reducing the gold, because the gel, that presented a yellow colour, slowly turned into red, as seen in **Figure 5.7**.

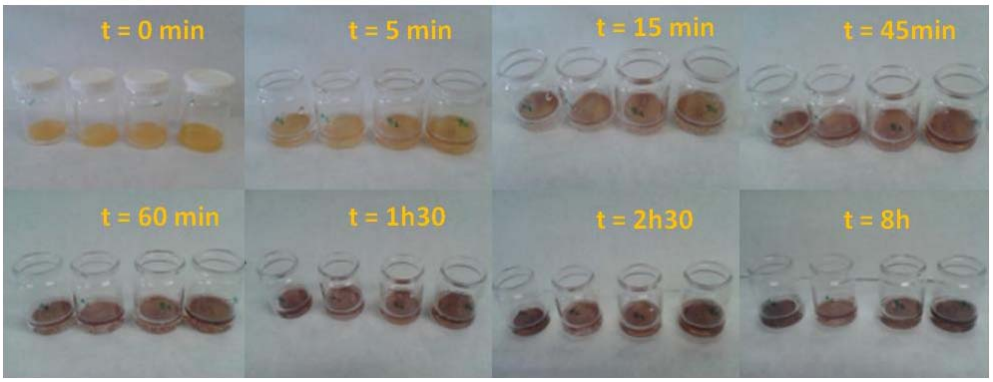

Figure 5.7: Gels with $HAuCl_4$ before (t=0 minutes) and after the adition of $NaBH_4$ at different times.

After a few hours, the remaining $NaBH_4$ solution was removed. The rheological behaviour of the gel was studied, and comparing with the **gel-1** it was found that the presence of GNP in the gel improves its rheological properties. The crossover value found was 1540 Pa, which is one order of magnitude higher when compared with **gel-1**. The crossover occurs at a value of shear stress of 118.9 Pa, which is approximately four times higher, meaning that besides being more viscous, it also has more resistance to sheer stress.

The **gel-GNP** was observed by AMF and TEM, and the fibbers were similar to **gel-1**, and GNP were visible by TEM, but not by AFM, which means that the GNP are within the fibbers of gel. The **gel-GNP** was disintegrated mechanically to characterize the GNP. The UV-visible spectrum showed the typical SPR peak at 520 nm, in agreement with the GNP obtained with **1·2Br** in organic medium, and XPS also confirmed that gold was in its reduced form. HRTEM allowed us to confirm that GNP had icosahedral shape, formed by 20 {111} facets, and a size of 5.4 ± 0.7 nm (**Figure 5.8**).

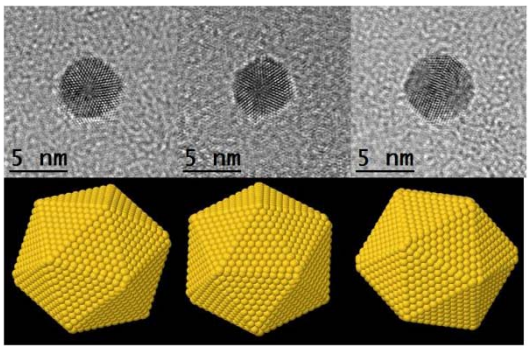

Figure 5.8: HRTEM micrographs and below, structural models of the icosahedral shape with relevant orientations are presented.

HRTEM was also performed for the **1·GNP** synthesized in solution soluble in organic medium and also the ones soluble in aqueous, and it was found that the sizes are smaller in the case of the GNP synthesized *in situ* in the gel, and that only one type of morphology was found for these GNP, whereas in the GNP obtained in solution, it could be found at least 3 different geometric shapes (spheroidal, tetrahedral and icosahedral) , and also different sizes which were also slightly bigger (12 ± 0,8 and 7,2 ± 0,7), meaning that the disposition of the imidazolium ligand in fibbers favours one type of geometry, also acting as template to obtain a more homogeneous size distribution.

Self-assembled monolayers on surfaces

Through collaboration with Prof. Lidia Feliu (LIPPSO group - Universitat de Girona), we also aimed at the use of GNP as vehicles to deliver small biomolecules with therapeutic applications. In this case, small synthetic cyclopeptides were chosen from a library of peptides that present antimicrobial activity and antitumor properties and that are synthesized by the group. **Figure 5.9** shows the structures of the different cyclopeptides used. Initially, different approaches were tested:

a) Synthesis of GNP by the citrate method and posterior functionalization with 11-

mercaptoundecanoic acid (MUA). Afterwards, the carboxylic acid group was activated with *N*-hydroxysuccinimide to later react with free amines from amino acid residues from the peptides (**Figure 5.9.a**);

b) Synthesis of GNP by the citrate method and posterior functionalization with 11-azidoundecanothiol and immobilization of peptide modified with an alkyne through the reaction between this group and the azide group present on the thiol (**Figure 5.9.b**);

c) Synthesis of the GNP using a thiol-bearing peptide (**Figure 5.9.c**).

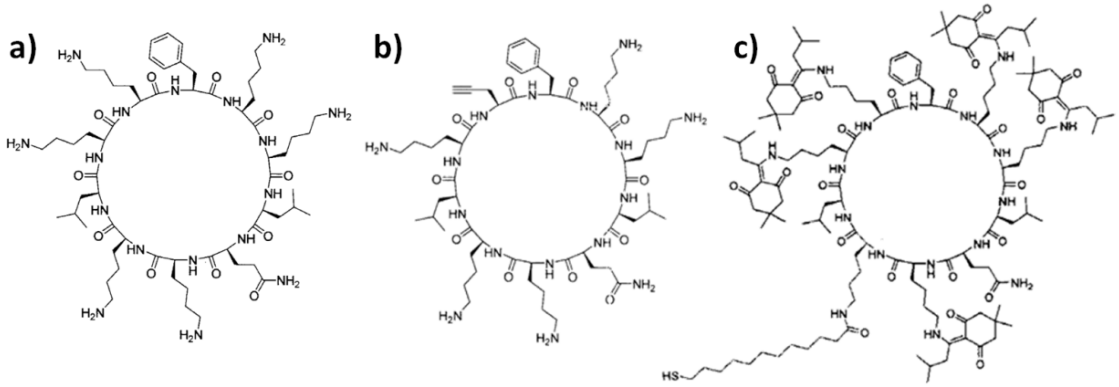

Figure 5.9: Structure of the cyclopeptides with free amines (a), with an alkyne (b) and with an alkyl chain with a thiol (c).

In the first approach (**Scheme 5.1**), the optimization of the process was time-consuming, since the concentration of the coupling agents (EDC and NHS) is an important factor because if too many carboxylic groups react, the equilibrium is disrupted and the GNP end up precipitating or aggregating.

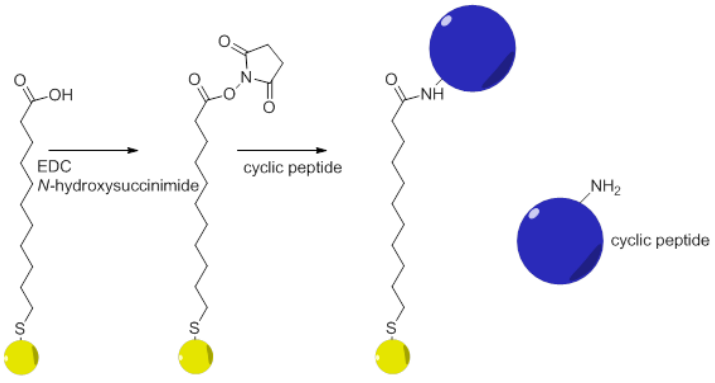

Scheme 5.1: GNP stabilized with MUA, activation of the carboxylic group with EDC and *N*-hydroxysuccinimide, and immobilization of peptide through the amine group.

The citrate GNP that were used showed a gold core with 18 nm (measured by TEM). DLS was used to characterize the size after the functionalization with the thiol and peptide

immobilization. It was found that after adding MUA the measured size was between 27 and 33 nm (depending on the amount of MUA added), and after the immobilization of the peptide, an increase of approximately 12-14 nm was observed in the size.

In the case of the second approach (**Scheme 5.2**), using thiol with an azide group, GNP were synthesised by the citrate reduction method and afterwards were modified. The synthesis cannot be performed directly with the thiol with azide group because the reducing agent that is used for the formation of the GNP also reduces the azide group. Therefore, the citrate stabilized GNP were mixed with a solution containing the thiol with the azide group. Two different thiols were proved: one thiol with PEG and other without PEG, to see if the PEG groups would influence the solubility of the GNP in aqueous medium, but no differences were observed. After the functionalization of the GNP with the thiols, both proved to be water soluble.

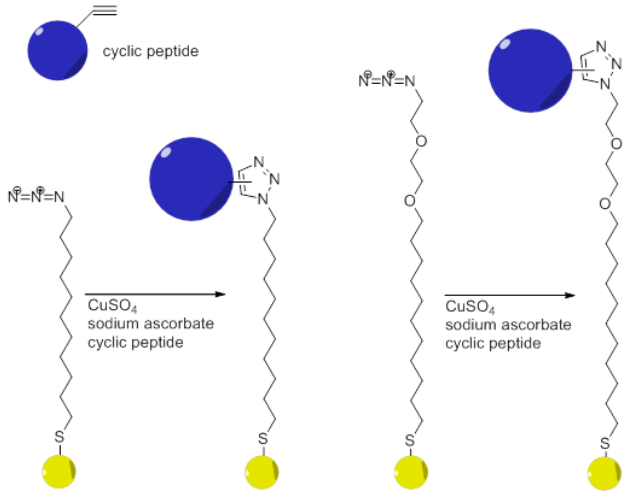

Scheme 5.2: Immobilization of the peptide bearing an alkyne group onto GNP (obtained by citrate reduction) using two different thiol molecules with azide group: one without PEG and other with PEG.

This approach, gave similar results: after functionalization the size increased to approximately 35 nm and after immobilization of the peptide it increased to 57 nm. These two results confirm that the peptides could be successfully immobilized in the GNP through self-assembled monolayers of thiols and functionalization with the peptides through functional groups.

The third approach was the most direct one, because it would allow obtaining the GNP with the peptides directly, without any additional functionalization or immobilization steps. The synthesis was performed in methanol. The thiol with the peptide was mixed with a thiol with PEG (in a ratio of 1:20). This way, we assure the presence of hydrophilic groups (PEG) that will render water-soluble GNP. The synthesis was also successful: TEM images showed that the GNP, synthesized in methanol using directly the peptide and another thiol with PEG groups, showed a size of 4 nm, which explains the absence of SPR peak in the UV-visible absorption

spectrum. DLS showed a size of 46 nm, which correlates well with the sizes found for the other GNP.The next step would be assessing the activity of the immobilized cyclopetides, and the targeting of the GNP (for instance conjugating with the adequate antibody or other biomolecule) to specific cells and tissues.

So far it was described the work regarding the assembly of ligands on the surface of gold nanoparticles, aiming at a therapeutic application. But the assembly of monolayers of molecules was also exploited for the functionalization of other type of materials not at the nanoscale.

Collaboration with the group of Prof. Fernando Palacio at ICMA (CSIC - Universidad de Zaragoza) was established and included one month stay at ICMA to perform the functionalization and characterization of different silicon based surfaces.

Through correct surface functionalization, we aimed at the immobilization of lanthanide complexes on silicon surfaces to be used as temperature sensors. The surfaces were activated with piranha solution and functionalized with APTES, in the same manner as described before. The immobilization of polymer **1** was performed between the acrylate group and the amine of APTES through a Michael's reaction. Two different lanthanides (Ln) were used, Europium and Terbium. The lanthanides were added to the surface, in solution, in the form of salt ($EuCl_3.6H_2O$ and $TbCl_3.6H_2O$ with a ratio of 1:3). The lanthanides would then complexate with the ketoester group of the polymer and a second ligand (phenantroline or 2,6-pyridinedicarboxylic acid) was added to complete the coordination with the lanthanide (**Scheme 5.3**).

The surfaces were characterized by measuring the contact angle, by Atomic Force Microscopy (AFM) and by X-ray Photoelectron Spectroscopy (XPS). AFM images were used to detect differences in the surface after each immobilization step. The contact angle technique was used to show differences in the hydrophobic/hydrophilic character of surfaces as a result of the deposition of molecules. XPS was used to confirm the presence of the lanthanides, therefore indicating if the complex was formed.

AFM images obtained before and after the APTES deposition following two different activation processes, either piranha solution or ozone showed little differences between them, however since the deposition was done using vapour, normally this implies a smoother and more homogeneous layer of silane. Analysis of the roughness values confirms that are almost no differences among them, indicating that the APTES layer is very homogeneous.

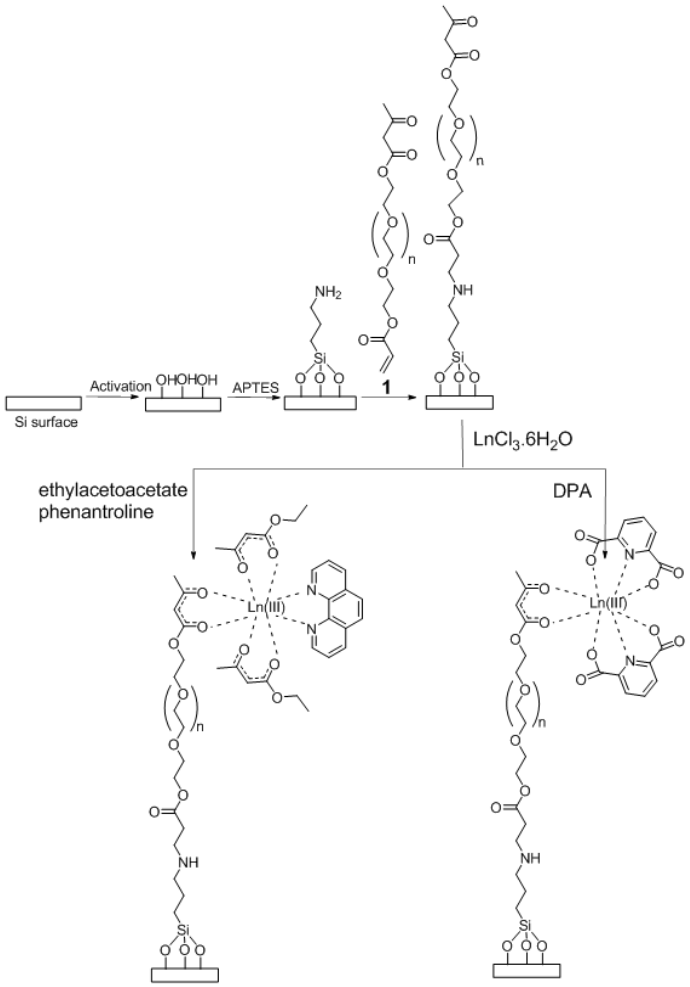

Scheme 5.3: Lanthanide complex immobilized on a silicon surface.

To confirm that APTES was in the surface, we used the contact angle measurement, and found that it changed from 45.9 ± 2.3 (after activation) to 93.4 ± 3.3 (after APTES deposition). The hydrophobicity changed from more hydrophilic (when activated, the surface has hydroxyl groups) to hydrophobic (due to the presence of the silane).The following steps were harder to characterize through the above techniques, instead XPS was used, and we found the energy binding peaks corresponding to the used lanthanides (Eu and Tb) were found on the samples where the complexes were already formed. The corresponding XPS spectra can be seen in **Figure 5.10**.

After characterization, the surfaces were studied to assess if the two lanthanides showed differences in the emission spectra derived from changes in the temperature. Hysteresis of optical emission with temperature variation between 305 and 345 K were found, indicating that the assembled complexes can be used as molecular thermometers.

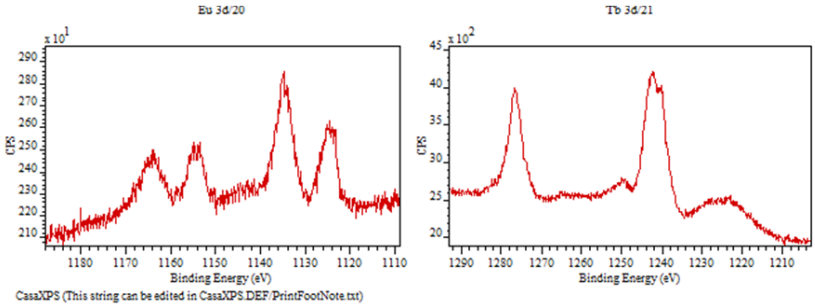

Figure 5.10. Binding energies (eV) from Europium (left) and Terbium (right) obtained by XPS for samples with lanthanides complexes.

On the other hand surface functionalization was applied to QTF probes, a work done in collaboration with Prof. Manel Puig (Facultat de Fisica, Universitat de Barcelona). The tasks included the correct functionalization of the QTF probes with a molecule, and also of glass surfaces with its corresponding ligand. The general method used is depicted in **Scheme 5.4**.

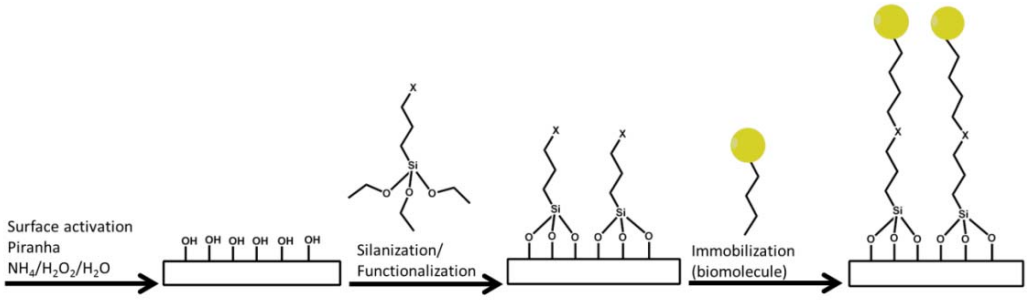

Scheme 5.4: General procedure for activation, silanization and biofunctionalization of the surfaces.

The QTF probe functionalized with biotin was used to detect its interaction and binding with avidin or streptavidin, immobilized on a glass surface. The strategies for the functionalization of the QTF probes and the glass surface are shown in **Scheme 5.5**.

The QTF could be successfully used to determine interactions between Avidin and Biotin, as demonstrated between the differences in the approach and retraction curves which is derived from the force of the interaction between the two molecules. No values could, however be obtained for the interaction forces.

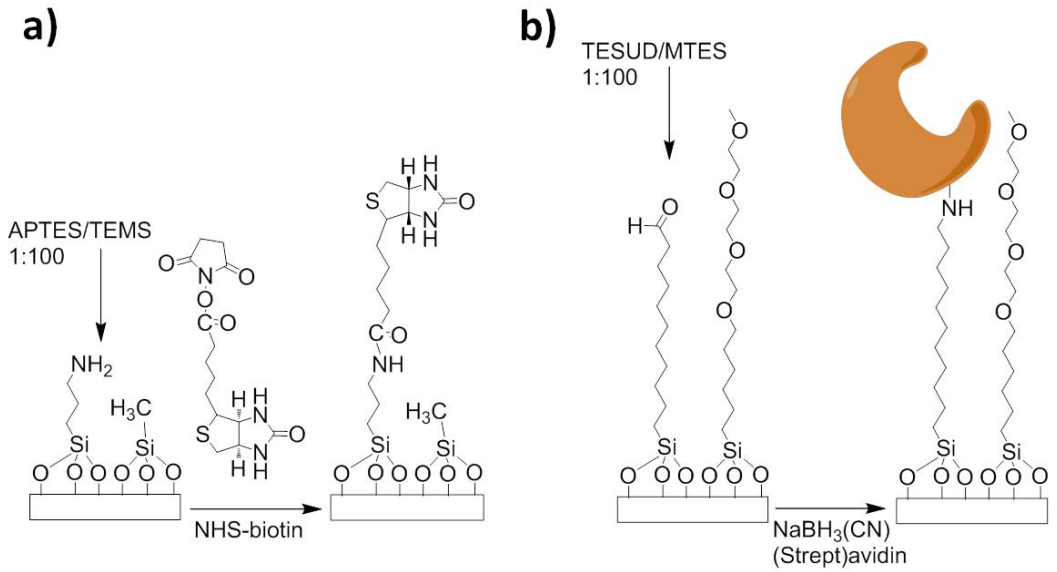

Scheme 5.5: a) Immobilization of APTES and TEMS, and functionalization with Biotin *N*-hydroxysuccinimide ester, and b) immobilization of TESUD and MTES, and the functionalization with biomolecules containing amine groups.

An assay based in surface chemistry and sensing using SPR was performed using Monoclonal Antibodies (MAbs) to determine their binding affinities for their antigen: the Epidermal Growth Factor Receptor (EGFR). Since these are newly synthesized MAbs, the affinity between the antibodies and the antigen was studied using the Biacore T100. This apparatus uses gold coated chips, that already have a self-assembled monolayer of molecules with functional groups that can be used to immobilize biomolecules, and measures the Surface Plasmon Resonance (SPR) profiles. The software then allows the determination of the affinity constants, in our case, of the different antibodies to the EGFR. The response obtained by the SPR analysis Biacore is proportional to the immobilized amount of MAb. Based on this, the different MAbs were immobilized in distinct flow channels, in a way that the same response was obtained in all channels, assuring that similar amounts of antibodies were present on each channel. Afterwards, increasing concentrations of rhEGFR were flowed through the cells, and the response was recorded, which allowed obtaining the binding curves for the different studied MAbs From these curves is possible to obtain the equilibrium dissociation constant K_D between the MAbs and EGFR. The found values for K_D were 1.41×10^{-9}, 2.52×10^{-8} and 1.73×10^{-8} for antibodies MAb1, MAb3 and MAb4 respectively, which means that from the analysed antibodies MAb1 has more affinity for EGFR and MAb3 is the one with less affinity.

Chapter 6

Conclusions

- Nanostructures based on self-assembled bis-imidazolium amphiphiles were successfully obtained.
  - The bis-imidazolium amphiphile proved, therefore, that is a gelator capable of forming a hydrogel when in a mixture of ethanol and water, maintaining this capability when other molecules were added to the solution;
  - The reported hydrogels showed properties that were suitable for drug delivery applications, namely: is thermoreversible, it has rheological behaviour adequate for topic application and it can incorporate drugs and released them across time;
  - Depending on the drug that was incorporated, different release rates were obtained: sodium ibuprofenate and indomethacin, which have one carboxylate group, were released with a faster rate than methotrexate, which has two carboxylate groups;
  - The drugs also had different effects on the overall resistance of the gel to sheer stress: methotrexate increased the resistance of the gel, whereas gels with ibuprofenate and indomethacin showed similar resistance to the unloaded gel;
  - The obtained hydrogel could be used as template for the preparation of GNP with good monodispersity and more specific geometry;
  - The presence of the GNP within the gel matrix improves the resistance of the gel to sheer stress.

- Synthesis of GNP stabilized by a self-assembled layer of bis-imidazolium ligands around the gold core was performed by different methods.
  - The bis-imidazolium ligands play a double role in the synthesis in the biphasic system: they act as both transfer agents and as stabilizers, simplifying the process. Additionally their ability to recognize and complexate anions is maintained while stabilizing the GNP, giving the GNP an extra role.
  - GNP could be obtained with open chain amphiphiles both in aqueous medium and organic medium using two different synthetic approaches: the GNP soluble in organic medium presented a monolayer of ligands around the core, whereas the water soluble GNP have a bilayer of ligands;
  - The nature of the ligand polar head (open or cyclic) is important for the anion recognition and consequent release from the ligand layer: the ligand with cyclic head

has more affinity for the anions, which causes the release to be slower when comparing with its open analogue;

- Zero-order or first-order release profiles were obtained for the different GNP and pH was found to have less influence when the affinity of the drug was higher for the ligand layer: for the ligand with cyclic head, the release followed the same release kinetic, whereas with the ligand with open structure the release followed first-order for pH 7.4 and zero-order for pH 5.5.

- GNP containing bioactive peptides on the surface were synthesized by the formation of a self-assembled monolayer of thiols.
  - It was found that the best results were obtained with the synthesis of the GNP in methanol using peptides bearing an alkyl chain with a terminal thiol group; the GNP obtained by citrate reduction and exchanged with azidoundecylthiol were successfully used to immobilize peptides using "click" chemistry;
  - The immobilization of peptides through amine groups using EDC/NHS activation requires more steps for the immobilization of the peptide, besides the fact that after the immobilization, the peptides need to be deprotrected.

- The functionalization of silicon surfaces for sensing purposes, through the formation of self-assembled monolayers of silanes, was successfully accomplished.
  - Functionalization with APTES was used for the reaction with a polymer containing PEG that forms a complex with lanthanides. The immobilized complexes showed hysteresis of optical emission with temperature variation between 305 and 345 K, which are promising results for their use as molecular thermometers;
  - Functionalization with APTES was also carried out in a tuning fork tip to allow the immobilization of biotin in the tip. The tip was then used to scan a surface with immobilized streptavidin, and the molecular interaction between the two molecules could be successfully detected, demonstrating the possible application of the tuning fork for the study of affinity binding between molecules.

- Commercial SPR sensors, based on gold surfaces with self-assembled layers of dextran or protein A, were used to determine the binding affinity of monoclonal antibodies for their antigen using SPR.

- Different approaches were used to allow for the immobilization of the antibodies on the surface;
- Through SPR it was possible to determine the kinetics of the association and dissociation between the antibody and the antigen and the affinity of the different antibodies for the antigen, which allowed the determination of the binding constants between the antibody and the antigen.

Bibliography

1. W. G. Kreyling, M. Semmler-Behnke, and Q. Chaudhry, *Nano Today*, 2010, **5**, 165–168.

2. D. Mijatovic, J. C. T. Eijkel, and A. van den Berg, *Lab Chip*, 2005, **5**, 492–500.

3. R. Thiruvengadathan, V. Korampally, A. Ghosh, N. Chanda, K. Gangopadhyay, and S. Gangopadhyay, *Rep. Prog. Phys.*, 2013, **76**, 066501.

4. M. Shimomura and T. Sawadaishi, *Curr. Opin. Colloid Interface Sci.*, 2001, **6**, 11–16.

5. E. Busseron, Y. Ruff, E. Moulin, and N. Giuseppone, *Nanoscale*, 2013, **5**, 7098–7140.

6. V. Vogel, Ed., *Nanotechnology Volume 5: Nanomedicine*, Wiley VCH, Verlag GMbH & Co. KGaA, Weinheim, 2009.

7. F. Caruso, T. Hyeon, and V. M. Rotello, Eds., *Nanomedicine (themed issue) in Chemical Society Reviews*, 2012.

8. J. Drbohlavova and J. Chomoucka, *Curr. Drug Metab.*, 2013, **14**, 547–564.

9. J. Gao, H. Gu, and B. Xu, *Acc. Chem. Res.*, 2009, **42**, 1097–107.

10. Y. Cheng, R. a Morshed, B. Auffinger, A. L. Tobias, and M. S. Lesniak, *Adv. Drug Deliv. Rev.*, 2014, **66**, 42–57.

11. M. Palombo, M. Deshmukh, D. Myers, J. Gao, Z. Szekely, and P. J. Sinko, *Annu. Rev. Pharmacol. Toxicol.*, 2014, **54**, 581–598.

12. M. S. Muthu, D. T. Leong, L. Mei, and S.-S. Feng, *Theranostics*, 2014, **4**, 660–677.

13. D. Mishra, J. R. Hubenak, and A. B. Mathur, *J. Biomed. Mater. Res. A*, 2013, **101**, 3646–3660.

14. D. Bera, L. Qian, T.-K. Tseng, and P. H. Holloway, *Materials (Basel).*, 2010, **3**, 2260–2345.

15. A. Kumari, R. Singla, A. Guliani, and S. Yadav, *EXCLI J.*, 2014, **13**, 265–286.

16. B. Guo and P. X. Ma, *Sci. China Chem.*, 2014, **57**, 490–500.

17. F. Kreppel and S. Kochanek, *Mol. Ther.*, 2008, **16**, 16–29.

18. W. J. Gradishar, *Expert Opin. Pharmacother.*, 2006, **7**, 1041–1053.

19. L. Klouda and A. G. Mikos, *Eur. J. Pharm. Biopharm.*, 2008, **68**, 34–45.

20. S. Van Vlierberghe, P. Dubruel, and E. Schacht, *Biomacromolecules*, 2011, **12**, 1387–1408.

21. T. R. Hoare and D. S. Kohane, *Polymer*, 2008, **49**, 1993–2007.

22. R. Jeetah, A. Bhaw-Luximon, and D. Jhurry, *Mutat. Res. Fundam. Mol. Mech. Mutagen.*, 2014, http://dx.doi.org/10.1016/j.mrfmmm.2014.04.009.

23. P. Kumar, R. A. Khan, Y. E. Choonara, and V. Pillay, *Future Med. Chem.*, 2013, **5**, 929–946.

24. T. Kim and T. Hyeon, *Nanotechnology*, 2014, **25**, 012001.

25. Y. Xing, J. Zhao, P. S. Conti, and K. Chen, *Theranostics*, 2014, **4**, 290–306.

26. R. Sperling, P. Gil, F. Zhang, M. Zanella, and W. J. Parak, *Chem. Soc. Rev.*, 2008, **37**, 1896–1908.

27. D. Pissuwan, T. Niidome, and M. B. Cortie, *J. Control. Release*, 2011, **149**, 65–71.

28. A. Kumar, X. Zhang, and X.-J. Liang, *Biotechnol. Adv.*, 2013, **31**, 593–606.

29. R. Cao-Milán and L. M. Liz-Marzán, *Expert Opin. Drug Deliv.*, 2014, **11**, 741–752.

30. J. Li, S. Gupta, and C. Li, *Quant. Imaging Med. Surg.*, 2013, **3**, 284–291.

31. C. Felton, A. Karmakar, Y. Gartia, P. Ramidi, A. S. Biris, and A. Ghosh, *Drug Metab. Rev.*, 2014, **46**, 142–154.

32. C. Tang, P. J. Russell, R. Martiniello-Wilks, J. E. J. Rasko, and A. Khatri, *Stem Cells*, 2010, **28**, 1686–1702.

33. S. Laurent, A. A. Saei, S. Behzadi, A. Panahifar, and M. Mahmoudi, *Expert Opin. Drug Deliv.*, 2014, 1–22.

34. J. T. Jenkins, D. L. Halaney, K. V Sokolov, L. L. Ma, H. J. Shipley, S. Mahajan, C. L. Louden, R. Asmis, T. E. Milner, K. P. Johnston, and M. D. Feldman, *Nanomedicine*, 2013, **9**, 356–365.

35. V. Biju, T. Itoh, and M. Ishikawa, *Chem. Soc. Rev.*, 2010, **39**, 3031–3056.

36. P. G. Luo, F. Yang, S.-T. Yang, S. K. Sonkar, L. Yang, J. J. Broglie, Y. Liu, and Y.-P. Sun, *RSC Adv.*, 2014, **4**, 10791–10807.

37. S. Y. Madani, N. Naderi, O. Dissanayake, A. Tan, and A. M. Seifalian, *Int. J. Nanomedicine*, 2011, **6**, 2963–2979.

38. B. A. Rzigalinski and J. S. Strobl, *Toxicol. Appl. Pharmacol.*, 2009, **238**, 280–288.

39. H. Ali-Boucetta and K. Kostarelos, *Adv. Drug Deliv. Rev.*, 2013, **65**, 2111–2119.

40. J. Puigmartí-Luis, W. J. Saletra, A. González, D. B. Amabilino, and L. Pérez-García, *Chem. Commun.*, 2014, **50**, 82–84.

41. B. Fabre, S. Pujari, L. Scheres, and H. Zuilhof, *Langmuir*, 2014, **30**, 7235–7243.

42. G.-J. Zhang, M. J. Huang, J. J. Ang, E. T. Liu, and K. V. Desai, *Biosens. Bioelectron.*, 2011, **26**, 3233–3239.

43. M. L. Y. Sin, T. Liu, J. D. Pyne, V. Gau, J. C. Liao, and P. K. Wong, *Anal. Chem.*, 2012, **84**, 2702–2707.

44. X. Chen, C.-Y. Hong, Y.-H. Lin, J.-H. Chen, G.-N. Chen, and H.-H. Yang, *Anal. Chem.*, 2012, **84**, 8277–8283.

45. D. Samanta and A. Sarkar, *Chem. Soc. Rev.*, 2011, **40**, 2567–2592.

46. E. Michelini and A. Roda, *Anal. Bioanal. Chem.*, 2012, **402**, 1785–1797.

47. O. Penon, S. Novo, S. Durán, E. Ibañez, C. Nogués, J. Samitier, M. Duch, J. A. Plaza, and L. Pérez-García, *Bioconjug. Chem.*, 2012, **23**, 2392–3402.

48. O. Penon, D. Siapkas, S. Novo, S. Durán, G. Oncins, A. Errachid, L. Barrios, C. Nogués, M. Duch, J. A. Plaza, and L. Pérez-García, *Colloids Surfaces B Biointerfaces*, 2014, **116**, 104–113.

49. X. Guo, *J. Biophotonics*, 2012, **5**, 483–501.

50. E. Wijaya, C. Lenaerts, S. Maricot, J. Hastanin, S. Habraken, J.-P. Vilcot, R. Boukherroub, and S. Szunerits, *Curr. Opin. Solid State Mater. Sci.*, 2011, **15**, 208–224.

51. M. Lienemann, A. Paananen, H. Boer, J. M. de la Fuente, I. García, S. Penadés, and A. Koivula, *Glycobiology*, 2009, **19**, 633–643.

52. A. Ebner, P. Hinterdorfer, and H. J. Gruber, *Ultramicroscopy*, 2007, **107**, 922–927.

53. X. Zhang and V. K. Yadavalli, *Anal. Chim. Acta*, 2009, **649**, 1–7.

54. P. J. Flory, *Faraday Discuss. Chem. Soc.*, 1974, **57**, 7–18.

55. P. Gupta, K. Vermani, and S. Garg, *Drug Discov. Today*, 2002, **7**, 569–579.

56. L. A. Estroff and A. D. Hamilton, *Chem. Rev.*, 2004, **104**, 1201–1218.

57. A. Vintiloiu and J.-C. Leroux, *J. Control. Release*, 2008, **125**, 179–192.

58. W. T. Truong, Y. Su, J. T. Meijer, P. Thordarson, and F. Braet, *Chem. Asian J.*, 2011, **6**, 30–42.

59. D. J. Abdallah and R. G. Weiss, *Adv. Mater.*, 2000, **12**, 1237–1247.

60. A. S. Hoffman, *Adv. Drug Deliv. Rev.*, 2002, **54**, 3–12.

61. K. Rehman and M. H. Zulfakar, *Drug Dev. Ind. Pharm.*, 2014, **40**, 433–40.

62. J. Le Bideau, L. Viau, and A. Vioux, *Chem. Soc. Rev.*, 2011, **40**, 907–925.

63. K. Oishi and Y. Maehata, *Chemosphere*, 2013, **91**, 302–306.

64. S. R. Shirsath, A. P. Patil, R. Patil, J. B. Naik, P. R. Gogate, and S. H. Sonawane, *Ultrason. Sonochem.*, 2013, **20**, 914–923.

65. H.-Y. Chen, L. Lin, X.-Y. Yu, K.-Q. Qiu, X.-Y. Lü, D.-B. Kuang, and C.-Y. Su, *Electrochim. Acta*, 2013, **92**, 117–123.

66. N. A. Choudhury, J. Ma, and Y. Sahai, *J. Power Sources*, 2012, **210**, 358–365.

67. I. Yoshimura, Y. Miyahara, N. Kasagi, H. Yamane, A. Ojida, and I. Hamachi, *J. Am. Chem. Soc.*, 2004, **126**, 12204–12205.

68. P. D. Wadhavane, M. A. Izquierdo, F. Galindo, M. I. Burguete, and S. V. Luis, *Soft Matter*, 2012, **8**, 4373–4381.

69. N. Sahiner, H. Ozay, O. Ozay, and N. Aktas, *Appl. Catal. B Environ.*, 2010, **101**, 137–143.

70. S. Ray, A. K. Das, and A. Banerjee, *Chem. Commun.*, 2006, 2816–2818.

71. C. Fan, L. Liao, C. Zhang, and L. Liu, *J. Mater. Chem. B*, 2013, **1**, 4251–4258.

72. M. De Colli, M. Massimi, A. Barbetta, B. L. Di Rosario, S. Nardecchia, L. Conti Devirgiliis, and M. Dentini, *Biomed. Mater.*, 2012, **7**, 055005.

73. S. Pok, J. D. Myers, S. V Madihally, and J. G. Jacot, *Acta Biomater.*, 2013, **9**, 5630–5642.

74. E. Ruel-Gariépy and J.-C. Leroux, *Eur. J. Pharm. Biopharm.*, 2004, **58**, 409–426.

75. C.-W. Lin, S.-J. Tseng, I. M. Kempson, S.-C. Yang, T.-M. Hong, and P.-C. Yang, *Biomaterials*, 2013, **34**, 4387–4393.

76. Y. S. R. Elnaggar, W. M. El-Refaie, M. a El-Massik, and O. Y. Abdallah, *J. Control. Release*, 2014, **180**, 10–24.

77. H. Kuang, H. He, Z. Zhang, Y. Qi, Z. Xie, X. Jing, and Y. Huang, *J. Mater. Chem. B*, 2014, **2**, 659–667.

78. C. Ju, J. Sun, P. Zi, X. Jin, and C. Zhang, *J. Pharm. Sci.*, 2013, **102**, 2707–2717.

79. B. Y. Swamy, J. H. Chang, H. Ahn, W.-K. Lee, and I. Chung, *Cellulose*, 2013, **20**, 1261–1273.

80. C. Alvarez-Lorenzo, B. Blanco-Fernandez, A. M. Puga, and A. Concheiro, *Adv. Drug Deliv. Rev.*, 2013, **65**, 1148–1171.

81. E. B. Anderson and T. E. Long, *Polymer*, 2010, **51**, 2447–2454.

82. J. Bandomir, A. Schulz, S. Taguchi, L. Schmitt, H. Ohno, K. Sternberg, K.-P. Schmitz, and U. Kragl, *Macromol. Chem. Phys.*, 2014, **215**, 716–724.

83. D. Batra and M. A. Firestone, *Chem. Mater.*, 2007, **19**, 4423–4431.

84. A. Ikeda, K. Sonoda, M. Ayabe, and S. Tamaru, *Chem. Lett.*, 2001, **11**, 1154–1155.

85. L. Viau, C. Tourné-Péteilh, J.-M. Devoisselle, and A. Vioux, *Chem. Commun.*, 2010, **46**, 228–230.

86. M. A. Firestone, P. G. Rickert, S. Seifert, and M. L. Dietz, *Inorganica Chim. Acta*, 2004, **357**, 3991–3998.

87. F. D'Anna, P. Vitale, S. Marullo, and R. Noto, *Langmuir*, 2012, **28**, 10849–10859.

88. J. Zhang and X. Shen, *J. Phys. Chem. B*, 2013, **117**, 1451–1457.

89. Y. Liu, T. Wang, and M. Liu, *Chem. Eur. J.*, 2012, **18**, 14650–14659.

90. M. Suzuki, M. Yumoto, M. Kimura, H. Shirai, and K. Hanabusa, *Helv. Chim. Acta*, 2003, **86**, 2228–2238.

91. P. K. Vemula, U. Aslam, V. A. Mallia, and G. John, *Chem. Mater.*, 2007, **19**, 138–140.

92. L. Casal-Dujat, M. Rodrigues, A. Yagüe, A. C. Calpena, D. B. Amabilino, J. González-Linares, M. Borràs, and L. Pérez-García, *Langmuir*, 2012, **28**, 2368–2381.

93. Z. Huaizhi and N. Yuantao, *Gold Bull.*, 2001, **34**, 24–29.

94. G. J. Higby, *Gold Bull.*, 1982, **15**, 130–140.

95. E. Boisselier and D. Astruc, *Chem. Soc. Rev.*, 2009, **38**, 1759–1782.

96. M. Faraday, *Philos. Trans. R. Soc. London*, 1857, **147**, 145–181.

97. M.-C. Daniel and D. Astruc, *Chem. Rev.*, 2004, **104**, 293–346.

98. M. M. Alvarez, J. T. Khoury, T. G. Schaaff, M. N. Shafigullin, I. Vezmar, and R. L. Whetten, *J. Phys. Chem. B*, 1997, **101**, 3706–3712.

99. J. Kimling, M. Maier, B. Okenve, V. Kotaidis, H. Ballot, and A. Plech, *J. Phys. Chem. B*, 2006, **110**, 15700–15707.

100. X. Liu, M. Atwater, J. Wang, and Q. Huo, *Colloids Surfaces B Biointerfaces*, 2007, **58**, 3–7.

101. W. Haiss, N. T. K. Thanh, J. Aveyard, and D. G. Fernig, *Anal. Chem.*, 2007, **79**, 4215–4221.

102. E. Ringe, M. R. Langille, K. Sohn, J. Zhang, J. Huang, C. A. Mirkin, R. P. Van Duyne, and L. D. Marks, *J. Phys. Chem. Lett.*, 2012, **3**, 1479–1483.

103. J. Turkevich, P. C. Stevenson, and J. Hillier, *Discuss. Faraday Soc.*, 1951, **11**, 55–75.

104. G. Frens, *Nat. Phys. Sci.*, 1973, **241**, 20–22.

105. S. Kumar, K. S. Gandhi, and R. Kumar, *Ind. Eng. Chem. Res.*, 2007, **46**, 3128–3136.

106. M. Brust, M. Walker, D. Bethell, D. J. Schiffrin, and R. Whyman, *J. Chem. Soc. Chem. Commun.*, 1994, 801–802.

107. R. Jin, *Nanoscale*, 2010, **2**, 343–362.

108. Y. Li, O. Zaluzhna, B. Xu, Y. Gao, J. M. Modest, and Y. J. Tong, *J. Am. Chem. Soc.*, 2011, **133**, 2092–2095.

109. M. Brust, J. Fink, D. Bethell, D. J. Schiffrin, and C. Kiely, *J. Chem. Soc. Chem. Commun.*, 1995, 1655–1656.

110. M. Giersig and P. Mulvaney, *Langmuir*, 1993, 3408–3413.

111. M. J. Hostetler, A. C. Templeton, and R. W. Murray, *Langmuir*, 1999, 3782–3789.

112. A. Templeton, W. P. Wuelfing, and R. W. Murray, *Acc. Chem. Res.*, 2000, **33**, 27–36.

113. S. Aryal, R. B K C, N. Dharmaraj, N. Bhattarai, C. H. Kim, and H. Y. Kim, *Spectrochim. Acta. A. Mol. Biomol. Spectrosc.*, 2006, **63**, 160–163.

114. C. A. Simpson, K. J. Salleng, D. E. Cliffel, and D. L. Feldheim, *Nanomedicine*, 2013, **9**, 257–263.

115. K. Ock, W. Il Jeon, E. O. Ganbold, M. Kim, J. Park, J. H. Seo, K. Cho, S.-W. Joo, and S. Y. Lee, *Anal. Chem.*, 2012, **84**, 2172–2178.

116. K. Siriwardana, A. Wang, and K. Vangala, *Langmuir*, 2013, **29**, 10990–10996.

117. H. Huang and X. Yang, *Biomacromolecules*, 2004, **5**, 2340–2346.

118. T. Phuoc, *J. Mater. Sci. Nanotechnol.*, 2014, **1**, 1–7.

119. W. Weare and S. Reed, *J. Am. Chem. Soc.*, 2000, **122**, 12890–12891.

120. P. M. Shem, R. Sardar, and J. S. Shumaker-Parry, *J. Colloid Interface Sci.*, 2014, **426**, 107–116.

121. J. Shan and H. Tenhu, *Chem. Commun.*, 2007, 4580–4598.

122. P. Alexandridis, *Chem. Eng. Technol.*, 2011, **34**, 15–28.

123. M. Wanunu, R. Popovitz-Biro, H. Cohen, A. Vaskevich, and I. Rubinstein, *J. Am. Chem. Soc.*, 2005, **127**, 9207–9215.

124. L. Zhang, X. Sun, Y. Song, X. Jiang, S. Dong, and E. Wang, *Langmuir*, 2006, **22**, 2838–2843.

125. B. Nikoobakht and M. El-Sayed, *Chem. Mater.*, 2003, **15**, 1957–1962.

126. J. Xiao and L. Qi, *Nanoscale*, 2011, **3**, 1383–1396.

127. Q. Liu, M. Guo, Z. Nie, J. Yuan, J. Tan, and S. Yao, *Langmuir*, 2008, **24**, 1595–1599.

128. T. Jain, A. R. Tehrani-Bagha, H. Shekhar, R. Crawford, E. Johnson, K. Nørgaard, K. Holmberg, P. Erhart, and K. Moth-Poulsen, *J. Mater. Chem. C*, 2014, **2**, 994–1003.

129. J. Dupont and J. D. Scholten, *Chem. Soc. Rev.*, 2010, **39**, 1780–1804.

130. O. P. Khatri, K. Adachi, K. Murase, K. Okazaki, T. Torimoto, N. Tanaka, S. Kuwabata, and H. Sugimura, *Langmuir*, 2008, **24**, 7785–7792.

131. H. S. Schrekker, M. A. Gelesky, M. P. Stracke, C. M. L. Schrekker, G. Machado, S. R. Teixeira, J. C. Rubim, and J. Dupont, *J. Colloid Interface Sci.*, 2007, **316**, 189–195.

132. M. Murawska, M. Wiatr, P. Nowakowski, K. Szutkowski, A. Skrzypczak, and M. Kozak, *Radiat. Phys. Chem.*, 2013, **93**, 160–167.

133. J. Y. Song, H.-K. Jang, and B. S. Kim, *Process Biochem.*, 2009, **44**, 1133–1138.

134. S. P. Dubey, M. Lahtinen, and M. Sillanpää, *Colloids Surfaces A Physicochem. Eng. Asp.*, 2010, **364**, 34–41.

135. K. Adavallan and N. Krishnakumar, *Adv. Nat. Sci. Nanosci. Nanotechnol.*, 2014, **5**, 025018.

136. S. Lokina, R. Suresh, K. Giribabu, A. Stephen, R. Lakshmi Sundaram, and V. Narayanan, *Spectrochim. Acta. A. Mol. Biomol. Spectrosc.*, 2014, **129**, 484–490.

137. A. Mishra, M. Kumari, S. Pandey, V. Chaudhry, K. C. Gupta, and C. S. Nautiyal, *Bioresour. Technol.*, 2014, **166C**, 235–242.

138. P. Mukherjee, S. Senapati, D. Mandal, A. Ahmad, M. I. Khan, R. Kumar, and M. Sastry, *Chembiochem*, 2002, **3**, 461–463.

139. P. Mukherjee, A. Ahmad, D. Mandal, S. Senapati, S. R. Saikar, M. I. Khan, R. Ramani, R. Parischa, P. V Ajayakumar, M. Alam, M. Sastry, and R. Kumar, *Angew. Chem. Int. Ed. Engl.*, 2001, **40**, 3585–3588.

140. S. He, Z. Guo, Y. Zhang, S. Zhang, J. Wang, and N. Gu, *Mater. Lett.*, 2007, **61**, 3984–3987.

141. B. S. Takale, M. Bao, and Y. Yamamoto, *Org. Biomol. Chem.*, 2014, **12**, 2005–2027.

142. M. Turner, V. B. Golovko, O. P. H. Vaughan, P. Abdulkin, A. Berenguer-Murcia, M. S. Tikhov, B. F. G. Johnson, and R. M. Lambert, *Nature*, 2008, **454**, 981–983.

143. X. Chen, H.-Y. Zhu, J.-C. Zhao, Z.-F. Zheng, and X.-P. Gao, *Angew. Chem. Int. Ed. Engl.*, 2008, **120**, 5433–5436.

144. T. Mitsudome and K. Kaneda, *Green Chem.*, 2013, **15**, 2636–2654.

145. C. Gryparis and M. Stratakis, *Org. Lett.*, 2014, **16**, 1430–1433.

146. S. K. Beaumont, *J. Chem. Technol. Biotechnol.*, 2012, **87**, 595–600.

147. S. Bhaviripudi, E. Mile, S. a Steiner, A. T. Zare, M. S. Dresselhaus, A. M. Belcher, and J. Kong, *J. Am. Chem. Soc.*, 2007, **129**, 1516–1517.

148. S. Rong-Hwa, T. Shiao-Shek, C. Der-Jiang, and H. Yao-Wen, *Food Chem.*, 2010, **118**, 462–466.

149. B. Ngom, Y. Guo, X. Wang, and D. Bi, *Anal. Bioanal. Chem.*, 2010, **397**, 1113–1135.

150. C. Hua, W. H. Zhang, S. R. M. De Almeida, S. Ciampi, D. Gloria, G. Liu, J. B. Harper, and J. J. Gooding, *Analyst*, 2012, **137**, 82–86.

151. R. Chandrawati and M. M. Stevens, *Chem. Commun.*, 2014, **50**, 5431–5434.

152. J.-S. Lee, M. S. Han, and C. A. Mirkin, *Angew. Chemie*, 2007, **119**, 4171–4174.

153. X. Xu, W. L. Daniel, W. Wei, and C. A. Mirkin, *Small*, 2010, **6**, 623–626.

154. T. E. Pylaev, E. K. Volkova, V. I. Kochubey, V. a. Bogatyrev, and N. G. Khlebtsov, *J. Quant. Spectrosc. Radiat. Transf.*, 2013, **131**, 34–42.

155. P. C. Ray, G. K. Darbha, A. Ray, J. Walker, and W. Hardy, *Plasmonics*, 2007, **2**, 173–183.

156. J. Matsui, K. Akamatsu, N. Hara, D. Miyoshi, H. Nawafune, K. Tamaki, and N. Sugimoto, *Anal. Chem.*, 2005, **77**, 4282–4285.

157. A. G. Tkachenko, H. Xie, Y. Liu, D. Coleman, J. Ryan, W. R. Glomm, M. K. Shipton, S. Franzen, and D. L. Feldheim, *Bioconjug. Chem.*, 2004, **15**, 482–490.

158. N. Khlebtsov and L. Dykman, *Chem. Soc. Rev.*, 2011, **40**, 1647–1671.

159. J. F. Hainfeld, D. N. Slatkin, T. M. Focella, and H. M. Smilowitz, *Br. J. Radiol.*, 2006, **79**, 248–253.

160. K. Saha, S. S. Agasti, C. Kim, X. Li, and V. M. Rotello, *Chem. Rev.*, 2012, **112**, 2739–2779.

161. S. Schlücker, *Angew. Chem. Int. Ed. Engl.*, 2014, **53**, 4756–4795.

162. M. H. Shin, W. Hong, Y. Sa, L. Chen, Y.-J. Jung, X. Wang, B. Zhao, and Y. M. Jung, *Vib. Spectrosc.*, 2014, **72**, 44–49.

163. U. S. Kadam, B. Schulz, and J. Irudayaraj, *FEBS Lett.*, 2014, **588**, 1637–1643.

164. Z. A. Nima, A. Biswas, I. S. Bayer, F. D. Hardcastle, D. Perry, A. Ghosh, E. Dervishi, and A. S. Biris, *Drug Metab. Rev.*, 2014, **46**, 155–175.

165. J. Ando, K. Fujita, N. Smith, and S. Kawata, *Nano Lett.*, 2011, **11**, 5344–5348.

166. M. Vendrell, K. K. Maiti, K. Dhaliwal, and Y.-T. Chang, *Trends Biotechnol.*, 2013, **31**, 249–257.

167. K. K. Maiti, U. S. Dinish, A. Samanta, M. Vendrell, K.-S. Soh, S.-J. Park, M. Olivo, and Y.-T. Chang, *Nano Today*, 2012, **7**, 85–93.

168. K. K. Maiti, U. S. Dinish, C. Y. Fu, J.-J. Lee, K.-S. Soh, S.-W. Yun, R. Bhuvaneswari, M. Olivo, and Y.-T. Chang, *Biosens. Bioelectron.*, 2010, **26**, 398–403.

169. L. Moriggi, C. Cannizzo, E. Dumas, C. R. Mayer, A. Ulianov, and L. Helm, *J. Am. Chem. Soc.*, 2009, **131**, 10828–10829.

170. J.-A. Park, H.-K. Kim, J.-H. Kim, S.-W. Jeong, J.-C. Jung, G.-H. Lee, J. Lee, Y. Chang, and T.-J. Kim, *Bioorg. Med. Chem. Lett.*, 2010, **20**, 2287–2291.

171. I. Miladi, C. Alric, S. Dufort, P. Mowat, A. Dutour, C. Mandon, G. Laurent, E. Bräuer-Krisch, N. Herath, J.-L. Coll, M. Dutreix, F. Lux, R. Bazzi, C. Billotey, M. Janier, P. Perriat, G. Le Duc, S. Roux, and O. Tillement, *Small*, 2014, **69100**, 1116–1124.

172. S. E. H. Murph, S. Jacobs, J. Liu, T. C.-C. Hu, M. Siegfired, S. M. Serkiz, and J. Hudson, *J. Nanoparticle Res.*, 2012, **14**, 658.

173. M. V Yigit, L. Zhu, M. a Ifediba, Y. Zhang, K. Carr, A. Moore, and Z. Medarova, *ACS Nano*, 2011, **5**, 1056–1066.

174. A. J. Mieszawska, W. J. M. Mulder, Z. a Fayad, and D. P. Cormode, *Mol. Pharm.*, 2013, **10**, 831–847.

175. P. Ghosh, C. Kim, G. Han, N. Forbes, and V. Rotello, *ACS Nano*, 2008, **2**, 2213–2218.

176. S. Guo, Y. Huang, Q. Jiang, Y. Sun, and L. Deng, *ACS Nano*, 2010, **4**, 5505–5511.

177. I. Venditti, L. Fontana, I. Fratoddi, C. Battocchio, C. Cametti, S. Sennato, F. Mura, F. Sciubba, M. Delfini, and M. V. Russo, *J. Colloid Interface Sci.*, 2014, **418**, 52–60.

178. X. Wang, X. Cai, J. Hu, N. Shao, F. Wang, Q. Zhang, J. Xiao, and Y. Cheng, *J. Am. Chem. Soc.*, 2013, **135**, 9805–9810.

179. Q.-Y. Bao, D.-D. Geng, J.-W. Xue, G. Zhou, S.-Y. Gu, Y. Ding, and C. Zhang, *Int. J. Pharm.*, 2013, **446**, 112–118.

180. Y. Tao, J. Han, C. Ye, T. Thomas, and H. Dou, *J. Mater. Chem.*, 2012, **22**, 18864–18871.

181. J. Song, Z. Fang, C. Wang, J. Zhou, B. Duan, L. Pu, and H. Duan, *Nanoscale*, 2013, **5**, 5816–5824.

182. N. Li, Y. Chen, Y.-M. Zhang, Y. Yang, Y. Su, J.-T. Chen, and Y. Liu, *Sci. Rep.*, 2014, **4**, 4164.

183. P. Murawala, A. Tirmale, A. Shiras, and B. L. V Prasad, *Mater. Sci. Eng. C. Mater. Biol. Appl.*, 2014, **34**, 158–167.

184. M. M. Afifi, L. A. Austin, M. A. Mackey, and M. A. El-Sayed, *Bioconjug. Chem.*, 2014, **25**, 207–215.

185. M. Ganeshkumar, M. Sathishkumar, T. Ponrasu, M. G. Dinesh, and L. Suguna, *Colloids Surf. B. Biointerfaces*, 2013, **106**, 208–216.

186. T. Stuchinskaya, M. Moreno, M. J. Cook, D. R. Edwards, and D. A. Russell, *Photochem. Photobiol. Sci.*, 2011, **10**, 822–831.

187. X. Sun, G. Zhang, R. S. Keynton, M. G. O'Toole, D. Patel, and A. M. Gobin, *Nanomedicine*, 2013, **9**, 1214–1222.

188. S.-M. Lee, H. J. Kim, S. Y. Kim, M.-K. Kwon, S. Kim, A. Cho, M. Yun, J.-S. Shin, and K.-H. Yoo, *Biomaterials*, 2014, **35**, 2272–2282.

189. J. Fang, H. Nakamura, and H. Maeda, *Adv. Drug Deliv. Rev.*, 2011, **63**, 136–151.

190. R. R. Arvizo, S. Rana, O. R. Miranda, R. Bhattacharya, V. M. Rotello, and P. Mukherjee, *Nanomedicine*, 2011, **7**, 580–587.

191. D. Bartczak, O. L. Muskens, T. Sanchez-Elsner, A. G. Kanaras, and T. M. Millar, *ACS Nano*, 2013, **7**, 5628–5636.

192. J. P. M. Almeida, E. R. Figueroa, and R. A. Drezek, *Nanomedicine*, 2014, **10**, 503–514.

193. A. Y. Lin, J. Lunsford, A. S. Bear, J. K. Young, P. Eckels, L. Luo, A. E. Foster, and R. A. Drezek, *Nanoscale Res. Lett.*, 2013, **8**, 72.

194. I.-H. Lee, H.-K. Kwon, S. An, D. Kim, S. Kim, M. K. Yu, J.-H. Lee, T.-S. Lee, S.-H. Im, and S. Jon, *Angew. Chemie*, 2012, **124**, 8930–8935.

195. R. P. Brinãs, A. Sundgren, P. Sahoo, S. Morey, K. Rittenhouse-Olson, G. E. Wilding, W. Deng, and J. J. Barchi, *Bioconjug. Chem.*, 2012, **23**, 1513–1523.

196. D. Safari, M. Marradi, F. Chiodo, H. a Th Dekker, Y. Shan, R. Adamo, S. Oscarson, G. T. Rijkers, M. Lahmann, J. P. Kamerling, S. Penadés, and H. Snippe, *Nanomedicine (Lond).*, 2012, **7**, 651–662.

197. J. F. Hainfeld, F. A. Dilmanian, D. N. Slatkin, and H. M. Smilowitz, *J. Pharm. Pharmacol.*, 2008, **60**, 977–985.

198. W. N. Rahman, N. Bishara, T. Ackerly, C. F. He, P. Jackson, C. Wong, R. Davidson, and M. Geso, *Nanomedicine Nanotechnology, Biol. Med.*, 2009, **5**, 136–142.

199. J. F. Hainfeld, F. A. Dilmanian, Z. Zhong, D. N. Slatkin, J. a Kalef-Ezra, and H. M. Smilowitz, *Phys. Med. Biol.*, 2010, **55**, 3045–3059.

200. P. Cherukuri, E. S. Glazer, and S. a Curley, *Adv. Drug Deliv. Rev.*, 2010, **62**, 339–345.

201. I. H. El-Sayed, X. Huang, and M. a El-Sayed, *Cancer Lett.*, 2006, **239**, 129–135.

202. J. F. Hainfeld, L. Lin, D. N. Slatkin, F. Avraham Dilmanian, T. M. Vadas, and H. M. Smilowitz, *Nanomedicine*, 2014, 1–10.

203. J. Nam, W. La, S. Hwang, Y. Ha, and N. Park, *ACS Nano*, 2013, **7**, 3388–3402.

204. I. J. Macdonald and T. J. Dougherty, *J. Porphyrins Phthalocyanines*, 2001, **05**, 105–129.

205. D. K. Chatterjee, L. S. Fong, and Y. Zhang, *Adv. Drug Deliv. Rev.*, 2008, **60**, 1627–1637.

206. D. Bechet, P. Couleaud, C. Frochot, M.-L. Viriot, F. Guillemin, and M. Barberi-Heyob, *Trends Biotechnol.*, 2008, **26**, 612–621.

207. D. C. Hone, P. I. Walker, R. Evans-Gowing, S. FitzGerald, A. Beeby, I. Chambrier, M. J. Cook, and D. A. Russell, *Langmuir*, 2002, **18**, 2985–2987.

208. M. Camerin, M. Magaraggia, M. Soncin, G. Jori, M. Moreno, I. Chambrier, M. J. Cook, and D. a Russell, *Eur. J. Cancer*, 2010, **46**, 1910–1918.

209. C. M. Goodman, C. D. Mccusker, T. Yilmaz, and V. M. Rotello, *Bioconjug. Chem.*, 2004, **15**, 897–900.

210. S. T. Kim, K. Saha, C. Kim, and V. M. Rotello, *Acc. Chem. Res.*, 2013, **46**, 681–691.

211. N. M. Schaeublin, L. K. Braydich-Stolle, A. M. Schrand, J. M. Miller, J. Hutchison, J. J. Schlager, and S. M. Hussain, *Nanoscale*, 2011, **3**, 410–420.

212. E. E. Connor, J. Mwamuka, A. Gole, C. J. Murphy, and M. D. Wyatt, *Small*, 2005, **1**, 325–327.

213. S. Wang, W. Lu, O. Tovmachenko, U. S. Rai, H. Yu, and P. C. Ray, *Chem. Phys. Lett.*, 2008, **463**, 145–149.

214. Y. Pan, S. Neuss, A. Leifert, M. Fischler, F. Wen, U. Simon, G. Schmid, W. Brandau, and W. Jahnen-Dechent, *Small*, 2007, **3**, 1941–1949.

215. W. Cui, J. Li, Y. Zhang, H. Rong, W. Lu, and L. Jiang, *Nanomedicine*, 2012, **8**, 46–53.

216. C. Lasagna-Reeves, D. Gonzalez-Romero, M. A. Barria, I. Olmedo, A. Clos, V. M. Sadagopa Ramanujam, A. Urayama, L. Vergara, M. J. Kogan, and C. Soto, *Biochem. Biophys. Res. Commun.*, 2010, **393**, 649–655.

217. Arnida, M. M. Janát-Amsbury, A. Ray, C. M. Peterson, and H. Ghandehari, *Eur. J. Pharm. Biopharm.*, 2011, **77**, 417–423.

218. H. I. Labouta and M. Schneider, *Nanomedicine*, 2013, **9**, 39–54.

219. J. D. Steckbeck, B. Deslouches, and R. C. Montelaro, *Expert Opin. Biol. Ther.*, 2014, **14**, 11–14.

220. I. Kosiova and P. Kois, *Collect. Czechoslov. Chem. Commun.*, 2007, **72**, 996–1004.

221. F. Schreiber, *Prog. Surf. Sci.*, 2000, **65**, 151–257.

222. J. C. Love, L. A. Estroff, J. K. Kriebel, R. G. Nuzzo, and G. M. Whitesides, *Chem. Rev.*, 2005, **105**, 1103–1169.

223. S.-Y. Lin, Y.-T. Tsai, C.-C. Chen, C.-M. Lin, and C. Chen, *J. Phys. Chem. B*, 2004, **108**, 2134–2139.

224. R. Barattin and N. Voyer, in *Atomic Force Microscopy in Biomedical Research:Methods and Protocols*, eds. P. C. Braga and D. Ricci, Humana Press, Totowa, NJ, 2011, vol. 736, pp. 457–483.

225. J. J. Gooding and S. Ciampi, *Chem. Soc. Rev.*, 2011, **40**, 2704–2718.

226. F. Rusmini, Z. Zhong, and J. Feijen, *Biomacromolecules*, 2007, **8**, 1775–1789.

227. R. A. Shircliff, P. Stradins, H. Moutinho, J. Fennell, M. L. Ghirardi, S. W. Cowley, H. M. Branz, and I. T. Martin, *Langmuir*, 2013, **29**, 4057–4067.

228. D. Prim, F. Rebeaud, V. Cosandey, R. Marti, P. Passeraub, and M. E. Pfeifer, *Molecules*, 2013, **18**, 9833–9849.

229. Renate Förch, H. Schönherr, and A. T. A. Jenkins, Eds., *Surface Design: Applications in Bioscience and Nanotechnology*, Wiley VCH, Verlag GMbH & Co. KGaA, Weinheim, 2009.

230. M. Mrksich, *ACS Nano*, 2008, **2**, 7–18.

231. H. Tsubery and M. Mrksich, *Langmuir*, 2008, **24**, 5433–5438.

232. R. Valiokas, G. Klenkar, A. Tinazli, A. Reichel, R. Tampé, J. Piehler, and B. Liedberg, *Langmuir*, 2008, **24**, 4959–4967.

233. B. D. Booth, S. G. Vilt, C. McCabe, and G. K. Jennings, *Langmuir*, 2009, **25**, 9995–10001.

234. K. B. Rodenhausen, B. a. Duensing, T. Kasputis, a. K. Pannier, T. Hofmann, M. Schubert, T. E. Tiwald, M. Solinsky, and M. Wagner, *Thin Solid Films*, 2011, **519**, 2817–2820.

235. M. J. Heller, *Annu. Rev. Biomed. Eng.*, 2002, **4**, 129–153.

236. X. Zhang and H. Hu, *Cent. Eur. J. Chem.*, 2014, **12**, 977–993.

237. A. J. Zaitouna and R. Y. Lai, *Anal. Chim. Acta*, 2014, **828**, 85–91.

238. S. K. Arya, P. Kongsuphol, C. C. Wong, L. J. Polla, and M. K. Park, *Sensors Actuators B Chem.*, 2014, **194**, 127–133.

239. S. Z. Bas, E. Maltas, B. Sennik, F. Yilmaz, and H. C. Vural, *J. Appl. Polym. Sci.*, 2014, **131**, 40638.

240. J. Yang, S.-E. Kim, M. Cho, I.-K. Yoo, W.-S. Choe, and Y. Lee, *Biosens. Bioelectron.*, 2014, **61**, 38–44.

241. M. Motaghedifard, M. Behpour, and S. M. Ghoreishi, *Sensors Actuators B Chem.*, 2014, **203**, 802–811.

242. C. Calas-Blanchard, G. Catanante, and T. Noguer, *Electroanalysis*, 2014, **26**, 1277–1286.

243. M. J. Langton and P. D. Beer, *Acc. Chem. Res.*, 2014, **47**, 1935–1949.

244. R. Zhang, J. Shang, J. Xin, B. Xie, Y. Li, and H. Möhwald, *Adv. Colloid Interface Sci.*, 2014, **207**, 361–375.

245. L. Ding, Y. Liu, Y. Cao, L. Wang, Y. Xin, and Y. Fang, *J. Mater. Chem.*, 2012, **22**, 11574–11582.

246. L. Gao, F. Lü, H. Xia, L. Ding, and Y. Fang, *Spectrochim. Acta. A. Mol. Biomol. Spectrosc.*, 2011, **79**, 437–442.

247. H. Lu, S. Qi, J. Mack, Z. Li, J. Lei, N. Kobayashi, and Z. Shen, *J. Mater. Chem.*, 2011, **21**, 10878–10882.

248. H. Ju, M. H. Lee, J. Kim, J. S. Kim, and J. Kim, *Talanta*, 2011, **83**, 1359–1363.

249. K. Nieradka, K. Kapczyńska, J. Rybka, T. Lipiński, P. Grabiec, M. Skowicki, and T. Gotszalk, *Sensors Actuators B Chem.*, 2014, **198**, 114–124.

250. V. K. Gupta, M. L. Yola, and N. Atar, *Sensors Actuators B Chem.*, 2014, **194**, 79–85.

251. P. Hinterdorfer and Y. Dufrêne, *Nat. Methods*, 2006, **3**, 347–355.

252. A. Touhami, B. Hoffmann, and A. Vasella, *Langmuir*, 2003, 1745–1751.

253. T. V Ratto, K. C. Langry, R. E. Rudd, R. L. Balhorn, M. J. Allen, and M. W. McElfresh, *Biophys. J.*, 2004, **86**, 2430–2437.

254. K. Lebed, G. Pyka-Fościak, J. Raczkowska, M. Lekka, and J. Styczeń, *J. Phys. Condens. Matter*, 2005, **17**, S1447–S1458.

255. A. M. Whited and P. S.-H. Park, *Biochim. Biophys. Acta*, 2014, **1838**, 56–68.

256. J. Polesel-Maris, J. Legrand, T. Berthelot, A. Garcia, P. Viel, A. Makky, and S. Palacin, *Sensors Actuators B Chem.*, 2012, **161**, 775–783.

257. A. Makky, P. Viel, S. W. Chen, T. Berthelot, J.-L. Pellequer, and J. Polesel-Maris, *J. Mol. Recognit.*, 2013, **26**, 521–531.

258. K. Mayer and J. Hafner, *Chem. Rev.*, 2011, **111**, 3828–3857.

259. Z. Altintas, Y. Uludag, Y. Gurbuz, and I. Tothill, *Anal. Chim. Acta*, 2012, **712**, 138–144.

260. W.-P. Hu, L.-Y. Huang, T.-C. Kuo, W.-W. Hu, Y. Chang, C.-S. Chen, H.-C. Chen, and W.-Y. Chen, *Anal. Biochem.*, 2012, **423**, 26–35.

261. T. Rispens, H. Te Velthuis, P. Hemker, H. Speijer, W. Hermens, and L. Aarden, *J. Immunol. Methods*, 2011, **365**, 50–57.

262. S. C. B. Gopinath, *Sensors Actuators B Chem.*, 2010, **150**, 722–733.

263. M. A. Brun, M. D. Disney, and P. H. Seeberger, *Chembiochem*, 2006, **7**, 421–424.

264. L. Casal-Dujat, P. C. Griffiths, C. Rodríguez-Abreu, C. Solans, S. Rogers, and L. Pérez-García, *J. Mater. Chem. B*, 2013, **1**, 4963–4971.

265. L. Casal-Dujat, O. Penon, C. Rodríguez-Abreu, C. Solans, and L. Pérez-García, *New J. Chem.*, 2012, **36**, 558–561.

APPENDIX

A: Abbreviations and acronyms

^{1}H NMR – Proton Nuclear Magnetic Resonance Spectroscopy

AFM – Atomic Force Microscopy

APTES – Aminopropyltriethoxysilane

CAC – Critical Aggregation Concentration

CGC – Critical Gelator Concentration

COX – Cyclooxygenase

DLS – Dynamic Light Scattering

DNA – Deoxyribonucleic acid

DPA – 2,6-Pyridinedicarboxylic acid

EC_{50} – Half effective concentration

EDC – *N*-(3-Dimethylaminopropyl)-*N*′-ethylcarbodiimide hydrochloride

EGFR – Epidermal Growth Factor Receptor

EPR – Enhanced Permeability and Retention

eV – Electron volt

FITC – Fluoresceín Isothiocyanate

GNP – Gold Nanoparticles

HRTEM – High Resolution Transmission Electron Microscopy

IR – Infrared

LMWG – Low Molecular Weight Gelator

MAbs – Monoclonal Antibodies

MALDI-TOF-MS – Matrix Assisted Laser Desorption Ionization Time-of-Flight Mass Spectroscopy

MPC – Monolayer-Protected Clusters

MRI – Magnetic Resonance Imaging

MUA – 11-Mercaptoundecanoic acid

NHS – *N*-Hydroxysuccinimide

NSAIDs – Non-steroidal anti-inflammatory drugs

PDT – Photodynamic Therapy

PEG – Polyethylene glycol

QTF – Quartz Tuning Fork

rhEGFR – Recombinant Human Epidermal Growth Factor Receptor

ROS – Reactive Oxygen Species

SAM – Self-Assembled Monolayer

SEM – Scanning Electron Microscopy

SERS – Surface-Enhanced Raman Scattering

sulfo-EMCS – *N*- [ε-Maleimidocaproyloxy]sulfosuccinimide ester

SPR – Surface Plasmon Resonance

TEM – Transmission Electronic Microscopy

TESUD – Triethoxysilylundecanal

TGA – Thermogravimetric Analysis

TOAB – Tetraoctylammonium Bromide

UV – Ultraviolet

VEGF – Vascular Endothelial Growth Factor

XPS – X-ray Photoelectron Spectroscopy

XRPD – X-ray Powder Diffraction

B: Divulgation of Results

CONGRESS CONTRIBUTIONS

Congress Publications:

Authors: A. C. Calpena, M. Rodrigues, L. Pérez-García
Title: *Gold Nanoparticles for Drug Delivery Based on Imidazolium-derived Ligand*
Publication: Revista Portuguesa de Farmácia (2011) Volume LII, 51-52

Oral Communications:

Authors: A. C. Calpena, M. Rodrigues and L. Pérez-García
Title: *Gold nanoparticles for drug delivery based on imidazolium-derived ligands*
Conference: III Congress of the Portuguese Society of Pharmaceutical Sciences and IX Spanish-Portuguese Conference on Controlled Drug Delivery
Place: Oporto (Portugal) 13-15 October 2011

Authors: M. Rodrigues, L. Casal-Dujat, A. Yagüe, A. Calpena, D. Amabilino, J. González-Linares, M. Borràs Suàrez and L. Pérez-García
Title: *Gemini-type imidazolium-based gold nanoparticles for drug delivery*
Conference: Jornada de Química de Catalunya i del Gran Sud-oest Francès
Place: Barcelona (Spain) 25th November 2011

Authors: M. Rodrigues, L. Casal-Dujat, A. Calpena, D. Amabilino, J. González-Linares, M. Borràs Suàrez and L. Pérez-García
Title: *Nanoestructures basadas en Lligands Catiònics tipus gemini per a l'alliberament de Fàrmcs*
Conference: VII Trobada de Joves Investigadors dels Països Catalans
Place: Palma de Mallorca (Spain) 16-17 February 2012

Authors: M. Rodrigues, A. Calpena, D. Amabilino, and L. Pérez-García
Title: *Imidazolium-based nanostructured gels for drug delivery*
Conference: Final International Workshop Magnifyco
Place: Barcelona (Spain) 20-22 February 2013

Authors: M. Rodrigues, O Penon and L. Pérez-García
Title: *Biofunctionalization of nano-microparticles for biomedical applications*
Conference: 6th European Summit for Clinical Nanomedicine and Targeted Medicine - CLINAM
Place: Basel (Switzerland) 23-26 June 2013

Authors: M. Rodrigues
Title: *Aplicacions biomèdiques de nanopartícules d'or*
Conference: VII Jornada de Recerca de la Facultat de Farmàcia de la Universitat de Barcelona
Place: Barcelona (Spain) 26th May 2014

Poster Communications:

Authors: M. Rodrigues, L. Casal-Dujat, A. Calpena, and L. Pérez-García
Title: *Ibuprofen release from Amphiphile-based Gold nanoparticles*
Conference: III Jornada IN2UB
Place: Barcelona (Spain) 13th October 2010

Authors: M. Rodrigues, L. Casal-Dujat, A. Calpena, and L. Pérez-García
Title: *Amphiphile-based Gold Nanoparticles for Drug Delivery*
Conference: 3rd IRUN Symposium on Nanotechnology
Place: Barcelona (Spain) 14-15 October 2010

Authors: M. Rodrigues, L. Casal-Dujat, A. Calpena, and L. Pérez-García
Title: *Anionic drug nanocarriers from bis-imidazolium amphiphiles*
Conference: ESF-UB Conference on Nanomedicine
Place: Sant Feliu de Guixols (Spain) 23-28 October 2010

Authors: M. Rodrigues, L. Casal-Dujat, A. Calpena, J. González-Linares, M. Borràs Suàrez and L. Pérez-García
Title: *Bis-imidazolium amphiphile-based gold nanoparticles for drug delivery*
Conference: NanoBio&Med
Place: Bilbao (Spain) 11-14 April 2011

Authors: M. Rodrigues, L. Casal-Dujat, A. Calpena, J. González-Linares, M. Borràs Suàrez, D. Amabilino and L. Pérez-García
Title: *Supramolecular chemistry in nanopharmacology: Imidazolium based nanostructures for Drug delivery*
Conference: IV Jornada IN2UB
Place: Barcelona (Spain) 14th November 2011

Authors: M. Rodrigues, D. Amabilino and L. Pérez-García
Title: *Bis-imidazolium amphiphile-based nanostructured gels*
Conference: Vth International Conference on Molecular Materials – MolMat 2012
Place: Barcelona (Spain) 3-6 July 2012

Authors: M. Rodrigues, L. Casal-Dujat, A. Calpena, J. González-Linares, M. Borràs Suàrez and L. Pérez-García
Title: *Imidazolium-derived nanostructures for drug delivery*
Conference: Colloids and Nanomedicine
Place: Amsterdam (The Netherlands) 15-17 July 2012

Authors: M. Rodrigues, L. Casal-Dujat, A. Calpena, D. Amabilino and L. Pérez-García
Title: *Imidazolium-derived nanostructures for drug delivery*
Conference: V Jornada IN2UB
Place: Barcelona (Spain) 15th November 2012

Authors: M. Rodrigues, A. Calpena, D. Amabilino and L. Pérez-García
Title: *Imidazolium-based nanogels for drug delivery*
Conference: III International Conference on Multifunctional, Hybrid and Nanomaterials
Place: Sorrento (Italy) 3-7 March 2013

Authors: M. Alea, E. Amirthalingam, L. Russo, M. Rodrigues, A. Gonzalez, L. Pérez-García
Title: *Synthesis of gold nanoparticles using gemini-type surfactant amphiphiles*
Conference: 2nd Whole Action Meeting of the COST Action CM1105
Place: Barcelona (Spain) 9-10 September 2013

Authors: M. Rodrigues, L. Gonzalez, M. Puig-Vidal and L. Pérez-García
Title: *Tunning fork biofunctionalization for the detection of biomolecular interactions*
Conference: Thematic Workshop of the COST Action TD1003
Place: Catania (Italy) 28-30 April 2014

Authors: M. Alea, E. Amirthalingam, L. Russo, M. Rodrigues, A. Gonzalez, L. Pérez-García
Title: *Gemini-type surfactant amphiphiles for the synthesis of gold nanoparticles*
Conference: VI Jornada IN2UB
Place: Barcelona (Spain) 5 June 2014